UNIVERSITÄT BAYREUTH

Biochemical and structural studies on the mitochondrial Sirtuins 4 and 5

Dissertation

zur Erlangung des akademischen Grades eines Doktors der Naturwissenschaften (Dr. rer. nat.) in der Bayreuther Graduiertenschule für Mathematik und Naturwissenschaften (BayNAT) der Universität Bayreuth

vorgelegt von

M. Sc. Biochemiker

Martin Pannek

aus Rödental, Landkreis Coburg

Bayreuth, Dezember 2017

Die vorliegende Arbeit wurde in der Zeit von März 2013 bis August 2017 in Bayreuth am Lehrstuhl Biochemie unter Betreuung von Herrn Professor Dr. Clemens Steegborn angefertigt.

Vollständiger Abdruck der von der Bayreuther Graduiertenschule für Mathematik und Naturwissenschaften (BayNAT) der Universität Bayreuth genehmigten Dissertation zur Erlangung des akademischen Grades eines Doktors der Naturwissenschaften (Dr. rer. nat.).

Dissertation eingereicht am: 15.12.2017

Zulassung durch das Leitungsgremium: 15.01.2018

Wissenschaftliches Kolloquium: 14.05.2018

Amtierender Direktor: Prof. Dr. Dirk Schüler

Prüfungsausschuss:

Prof. Dr. Clemens Steegborn   (Gutachter/in)
Prof. Dr. Andreas Möglich   (Gutachter/in)
Prof. Dr. Matthias Ullmann   (Vorsitz)
Prof. Dr. Birte Höcker

Table of contents

List of abbreviations

AceCS2:	Acetyl-CoA synthetase 2
ADP-ribose:	Adenosine diphosphate ribose
ATP:	Adenosine triphosphate
Cbz:	Benzyloxycarbonyl
CoA:	Coenzyme A
CPS1:	Carbamoylphosphate synthase 1
CypA:	Cyclophilin A
FdL:	Fluor-de-Lys®
G6PDH:	Glucose-6-phosphate dehydrogenase
GAPDH:	Glycerinaldehyd-3-phosphate dehydrogenase
GDH:	Glutamate dehydrogenase
HDAC:	Histone deacetylase
HMGCS2:	3-hydroxy-3-methylglutaryl-CoA synthase 2
ICD2:	Isocitrate dehydrogenase 2
KDAC:	Lysine deacetylase
KAT:	Lysine-acetyl-transferase
KO:	Knock out
LCAD:	Long-chain acyl-CoA dehydrogenase
MCD:	Malonyl-CoA decarboxylase
MS:	Mass-spectrometry
NAD^+/NADH:	Nicotinamide adenine dinucleotide (oxidized/reduced)
NADP+/NADPH:	Nicotinamide adenine dinucleotide phosphate (oxidized/reduced)
NAM:	Nicotinamide
PDH:	Pyruvate dehydrogenase
PPARα:	Peroxisome proliferator-activated receptor α
PTM:	Posttranslational modification
ROS:	Reactive oxygen species
s.d.:	Standard deviation
Sir2:	Silent information regulator 2
SirReal2:	Sirtuin-Rearranging Ligand 2
Sirt:	Sirtuin
SOD2:	Superoxid dismutase 2
UBCS:	Abbreviation code for the lab internal compound library (University of Bayreuth Clemens Steegborn

Inhibitory acyl abbreviations:

3PTS	3-phenyl-succinyl
3PMS	3-phenyl-3-methyl-succinyl
3BS	3-butyl-succinyl
3ZAS	3-Z-amino-succinyl
3BTS	3-(benzyl-thio)-succinyl
3PTS	3-(phenyl-thio)-succinyl
3MNTS:	3-(naphtylmethyl-thio)-succinyl

Summary

The Sirtuins constitute a conserved enzyme family, which is involved in the regulation of fundamental cellular processes like metabolic homeostasis, DNA repair or aging. In this context, they were linked to multiple aging-related pathologies such as neurodegenerative diseases and cancer. Sirtuins catalyze the NAD^+-dependent hydrolysis of posttranslational acyl-modifications from protein lysine side chains. Mammalian cells possess seven Sirtuin isoforms (Sirt1-7), which are primarily located to either the nucleus/nucleolus (Sirt1/6/7), cytosol (Sirt2) or mitochondria (Sirt3/4/5). While lysine deacetylation was initially supposed to be the conserved function of all Sirtuins, recent research has revealed a broader range of lysine deacylase activities, like demyristoylation by Sirt6 or desuccinylation by Sirt5. Of the mitochondrial Sirtuins, Sirt3 is a robust deacetylase, while no efficient Sirt4 activity was reported so far. Also the acyl-specificity of Sirt5, albeit identified as desuccinylase/demalonylase, was never systematically characterized. However, investigating Sirtuin catalysis, their influence on substrate proteins and relation to organismal pathophysiology demands precise knowledge about Sirtuin acyl-specificity. Notably, specific Sirtuin modulators provide another possibility for characterizing Sirtuins *in vitro* and *in vivo* and have a potential in prospective medical treatments of Sirtuin-related dysfunctions like type 2 diabetes (Sirt4) or neurodegeneration (Sirt2/5). However, only a few specific Sirtuin modulators were developed yet.

In this thesis, the acyl specificities of the mitochondrial Sirtuins 4 and 5 were investigated in collaborative projects. Our collaborators synthesized an acyl-peptide library to screen Sirt5 activity, which revealed a superior lysine deglutarylation efficiency compared to the reported desuccinylase/demalonylase activities. We solved crystal structures of Sirt5 in complex with several acylated peptides to elucidate the molecular background of these activities. Supposedly, the more strained conformation of the glutaryl-ADP-ribose product is responsible for the improved turnover by enhancing the rate-limiting product release. Concerning Sirt4, we screened activities with the same acyl-peptide library and identified the hydrolysis of 3,3-dimethyl-succinyl as a robust, but unphysiologic activity. Testing chemically similar acyls with a physiologic background revealed 3-hydroxy-3-methyl-glutaryl as a robust Sirt4 substrate acyl.

Furthermore, this work includes the first Sirt4 crystal structures obtained by using the orthologue *Xenopus tropicalis* Sirt4, which shares a high sequence identity and the same catalytic activities with the human isoform. These crystal structures revealed three interesting features providing deeper insights into the function and regulation of Sirt4. Firstly, Sirt4 comprises a significantly elongated zinc-binding domain loop, which sequence is present in all chordate Sirt4, but unique in the Sirtuin family. It contributes to the active-site lining and might be involved in Sirt4 regulation, since loop mutants showed changed catalytic turnovers. Secondly, the nucleotide-binding pocket is more positively charged compared to other isoforms,

which appears to correlate with a unique sensitivity among Sirtuins to physiologic NADH concentrations, indicating a distinct regulation mechanism for Sirt4. Thirdly, an additional channel to the acyl-lysine binding site was identified, which might either expand the substrate acyl-lysine binding pocket or serve as a binding-site for regulatory molecules.

We utilized the insights in Sirt5 structure and function to develop specific small molecule inhibitors in collaborative projects. Our contribution to these projects was the analysis of complex crystal structures to guide the inhibitor synthesis and kinetic studies performed by our collaborators. We chose a peptide with succinyl-lysine as a starting point and transformed this robust and Sirt5-specific substrate into Sirt5-selective peptide inhibitors by derivatization of the succinyl with alkyl-side chains. These inhibitory peptides initially showed weak potencies in the two-digit micromolar range and competed with NAD^+ binding through the alkyl moieties as revealed by structural analysis. We rationally derivatized these inhibitors by substitution of the alkyl-side chains with thio-alkyls, which increased potency into the two-digit nanomolar range and showed a similar inhibitory mechanism in structural analysis. Since peptidic inhibitors often comprise poor cellular resorption and half-life, the strongest inhibitory acyl was attached to a lysine or lysine-mimetics to create small molecule modulators, but resulted in a decrease of potency by at least three orders of magnitude. However, we could obtain structural information about inhibitor scaffold-optimization in another collaborative structure-activity relationship study, which pursued a Sirtuin mechanism-based inhibition approach. Herein, short peptide(-like) inhibitors were developed and structurally analyzed, which resulted in potencies in the sub-micromolar range. Combining this information about Sirt5 affinity hot spots around the lysine binding-site with the inhibitory acyls of the peptide approach should constitute a starting point for the development of small molecule Sirt5 inhibitors. These will contribute to the elucidation of Sirt5 physiology and have a potential as therapeutics for the treatment of Sirt5-related diseases.

Zusammenfassung

Die Sirtuine sind eine konservierte Familie von Enzymen, welche in die Regulation fundamentaler zellulärer Prozesse wie der metabolischen Homöostase, der Aufrechterhaltung der genomischen Stabilität oder dem Altern involviert ist. In diesem Zusammenhang wurden die Sirtuine mit mehreren alterungsbedingten Pathologien wie neurodegenerativen Krankheiten und Krebs in Verbindung gebracht. Sirtuine katalysieren die NAD^+-abhängige Hydrolyse von posttranslationalen Acyl-Modifikationen von Protein Lysin Seitenketten. Wirbeltiere weisen sieben Sirtuin Isoformen auf (Sirt1-7), welche primär im Nukleus/Nukleolus (Sirt1/6/7), dem Zellplasma (Sirt2) oder den Mitochondrien (Sirt3/4/5) lokalisiert sind. Während die Hydrolyse von Lysin-Acetylierungen zunächst als konservierte Funktion aller Sirtuine angesehen wurde, offenbaren neuere Studien, dass Sirtuine eine größere Bandbreite von Lysin-Deacylase Aktivitäten aufweisen, wie die Demyristoylierung durch Sirt6 oder Desuccinylierung durch Sirt5. Von den mitochondrialen Sirtuinen ist Sirt3 als effiziente Deacetylase bekannt, wohingegen für Sirt4 bislang keine robuste Aktivität beschrieben wurde und die Sirt5 Acyl-Spezifität nach Entdeckung ihrer Demalonylase/Desuccinylase Aktivität nie umfassend charakterisiert wurde. Die detaillierte Kenntnis der Acyl-Präferenz ist jedoch essentiell für die Untersuchung der Sirtuin Katalyse, den Einfluss der Sirtuine auf ihre Substrat-Proteine und deren Zusammenhang mit der Pathophysiologie des Organismus. Bei solchen Untersuchungen spielen wirksame und Isoform-spezifische Sirtuin-Modulatoren eine bedeutende Rolle, da sie eine weitere Option für die *in vitro* und *in vivo* Charakterisierung der Sirtuine darstellen. Zusätzlich sind solche Modulatoren potentielle Therapeutika für Krankheiten, welche in Zusammenhang mit Sirtuinen stehen, wie neurodegenerative Erkrankungen (Sirt2/5) oder Typ 2 Diabetes (Sirt4). Allerdings sind bislang nur wenige spezifische Modulatoren für Sirtuine bekannt.

Im Rahmen dieser Doktorarbeit wurden die Acyl-Spezifitäten der mitochondrialen Sirtuine 4 und 5 in Kollaborationsprojekten untersucht. Unsere Kollaborateure synthetisierten eine Acyl-Peptid Bibliothek zur systematischen, kinetischen Charakterisierung der Sirt5 Acyl-Spezifität und entdeckten eine gesteigerte Lysin Deglutarylierungs-Effizienz gegenüber den zuvor berichteten Demalonylase und Desuccinylase Aktivitäten. Durch Lösen von Sirt5 Kristallstrukturen in Komplex mit verschiedenen acylierten Peptiden wurde der molekulare Hintergrund dieser Aktivitäten analysiert. Diese legten die Hypothese nahe, dass die effizientere Lysin Deglutarylierung von der stärkeren Stauchung des Glutaryl-ADP-Ribose Produktes rührt, welche die Katalyse-Geschwindigkeit limitierende Produkt-Freisetzung beschleunigen könnte. Die generierte Acyl-Peptid Bibliothek ermöglichte es uns weiterhin, die Acyl-Spezifität von Sirt4 zu charakterisieren, wodurch die Hydrolyse von 3,3-Dimethyl-Succinyl von Lysinen als robuste, aber unphysiologische Sirt4 Aktivität identifiziert wurde. Durch Experimente mit chemisch ähnlichen, potentiell physiologischen Acylen konnte die Hydrolyse von 3-Hydroxy-3-Methyl-Glutaryl von Lysin Seitenketten als robuste Sirt4 Aktivität gezeigt werden.

Die vorliegende Arbeit beinhaltet zudem die ersten Kristallstrukturen von Sirt4, welche unter Verwendung des *Xenopus tropicalis* Sirt4 Orthologs gelöst werden konnten. Dieses Ortholog weist eine hohe Sequenzidentität zur humanen Isoform und dieselben enzymatischen Aktivitäten auf. Die Kristallstrukturen zeigten drei besondere Merkmale von Sirt4, welche zum besseren Verständnis dieser Isoform beitragen. Erstens besitzt die Zink-Bindedomäne einen verhältnismäßig langen *Loop*, dessen Sequenz konserviert in Chordata Sirt4 Orthologen, aber einzigartig in der Sirtuin-Familie ist. Dieser steuert Aminosäuren zum Aufbau des Aktivzentrums bei und scheint in die Regulation der Enzymaktivität involviert zu sein, da *Loop*-Deletionsmutanten veränderte katalytische Werte zeigten. Zweitens weißt die Nukleotid-Bindetasche eine positivere elektrostatische Ladung auf, was die unter den Sirtuinen einzigartige Sensitivität gegenüber physiologischen NADH-Konzentrationen erklären könnte. Drittens zeigen die Strukturen einen zusätzlichen Kanal zum Aktivzentrum, welcher als vergrößerte Substrat Acyl-Lysin Bindestelle oder als Interaktionsfläche für regulatorische Moleküle dienen könnte.

Die Einblicke in die Struktur und Funktion von Sirt5 flossen in die Entwicklung spezifischer Modulatoren für diese Isoform ein. Unser Beitrag war die Analyse von Komplex Kristallstrukturen, um die Inhibitor-Synthese und kinetischen Studien unserer Partner rational zu führen. Dafür wählten wir ein Peptid mit succinyliertem Lysin als Startpunkt und transformierten dieses robuste und Sirt5-spezifische Substrat durch Derivatisierung des Succinyls mit Alkyl-Seitenketten in Sirt5-selektive Peptid-Inhibitoren. Die zunächst schwachen Inhibitoren mit Wirksamkeiten im zweistelligen mikromolaren Bereich zeigten in den strukturellen Analysen eine Kompetition der Alkyl-Seitenketten mit dem Co-Substrat NAD$^+$. Durch rationale Derivatisierung des Succinyls mit Thio-Alkylen konnte die Wirksamkeit der Peptid-Inhibitoren jedoch in den zweistelligen nanomolaren Bereich verbessert werden, wobei diese Derivate den gleichen inhibitorischen Mechanismus in strukturellen Analysen zeigten. Durch Abtrennen des Peptids sollte der Schritt zu niedermolekularen Wirkstoffen vollzogen werden, um deren zelluläre Resorption und Halbwertszeit zu verbessern. Allerdings verringerte dies die Wirksamkeit um mindestens drei Größenordnungen, je nach Derivatisierung des inhibitorischen Acyls mit verschiedenen Lysin-Mimetika. In einer weiteren kollaborativen Studie, welche einen Sirtuin-Mechanismus basierten Ansatz der Inhibition verfolgte, wurden kleinere Peptid(-Mimetika) mit Wirksamkeiten im sub-mikromolaren Bereich entwickelt und strukturelle Informationen zur Optimierung des Inhibitor-Rückgrats rund um die Bindung im Lysin Kanal gewonnen. Die Kombination der Erkenntnisse über Affinitäts-Hotspots am Lysin-Kanal mit den Acylen aus dem Peptid-Inhibitoren Ansatz ergibt einen Startpunkt zur Entwicklung potenter und selektiver Sirt5 Kleinmolekül-Inhibitoren. Diese werden einen wichtigen Beitrag zur Aufklärung der Sirt5 Physiologie leisten und besitzen Potential als Therapeutika für die Behandlung von Krankheiten, welche in Zusammenhang mit Sirt5 stehen.

1. __Introduction__

1.1. Proteins and posttranslational modifications

Proteins are key-players in many cellular functions by catalyzing complex chemical reactions, providing structural frameworks or tuning gene expression, to name only a few of their manifold tasks. Thus, changing the performance or fate of a cell requires the regulation of proteins, which is achieved through several means like enzyme modulation by effector molecules [1] or altering protein expression [2]. Additionally, an outstandingly complex and adaptable machinery regulates proteins by attaching and removing posttranslational modifications (PTMs) on protein termini or amino acid side chains [3].

The human genome encodes for roughly 30,000 proteins, but this diversity is tremendously extended by mRNA splicing and PTMs to a two to three orders of magnitude more complex, so called, proteome **(Figure 1A)** [3]. PTMs include the cleavage of the protein backbone as well as the covalent modification of amino acids. In fact, 5% of the genes in higher eukaryotes encode for protein modifying enzymes and 15 of the 20 natural amino-acids are PTM targets [3]. The best characterized PTMs are phosphorylation, glycosylation, acetylation, methylation, ubiquitylation and sumoylation, which are studied for more than half a century, demonstrating their complex roles in protein folding, degradation, stability and function **(Figure 1B)** [3].
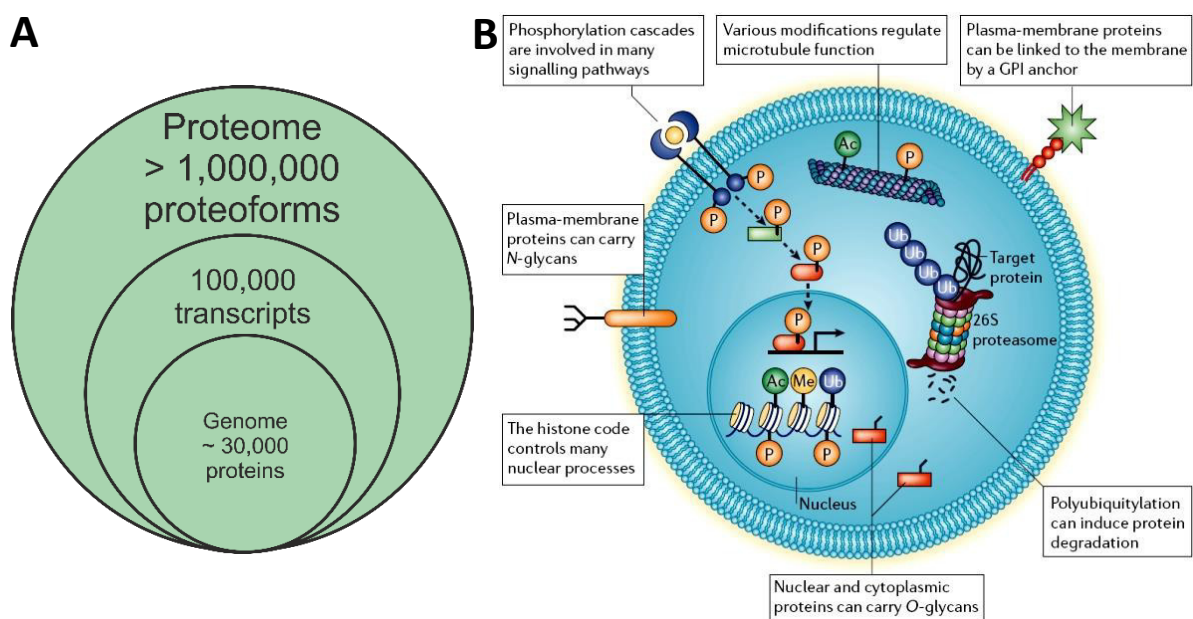

Figure 1: PTMs augment human proteome complexity and account for multifaceted effects on target proteins. (A) Illustration of the increasing complexity of the human proteome by mRNA splicing and PTMs. (B) Examples of protein modifications and their respective function (reproduced from Jensen, 2006 [4] with permission of Nature publishing group).

The most prominent function of (poly-)ubiquitylation is the proteosomal degradation of target proteins [5,6], but also histone regulation and endocytosis of membrane proteins have been reported [3,7]. Glycosylation mainly occurs in eukaryotic cells and plays roles in, e.g., chaperone-

mediated protein folding [8], signaling of cell surface proteins [9] and transcription factor regulation [10]. Protein phosphorylation is probably the best studied PTM and comprises multifaceted roles like changing ordered/disordered protein conformations, protein-ligand association/dissociation and enzyme activity [3,11].

Recent technical advances, especially in the field of high resolution mass-spectrometry (MS) [4,12], enabled the in-depth investigation of lysine side chain-acetylation and -acylation. These PTMs attracted immense scientific attention and might have as much impact on protein regulation as phosphorylation or glycosylation, as will be presented in the following.

1.2. Protein lysine acetylation & acylation

Protein acetylation on lysine side chain N_ε-amines **(Figure 2A)** occurs in all branches of life, implicating an evolutionarily conserved significance [13–15]. It is in the scientific focus for 50 years, since Allfrey and co-workers for the first time discovered reversible acetylation on histones [16]. Thereafter, it took more than two decades to discover the first acetylated non-histone proteins, which were the microtubule major component α-tubulin [17], the tumor suppressor p53 [18] and the HIV transcriptional regulator Tat [19]. Since then, the technical advances in MS and the generation of acetyl-lysine antibodies to specifically enrich acetylated proteins or peptides, enabled the assembly of "acetylomes", which revealed this modification to be as widespread and abundant as phosphorylation [13,20–25]. Interestingly, the majority of acetylation sites reside on nonnuclear proteins and a huge number of them is present on mitochondrial proteins. In fact, since phosphorylation rarely occurs in mitochondria, acetylation seems to be the prevalent PTM in this organelle, implying key regulatory roles [25,26].
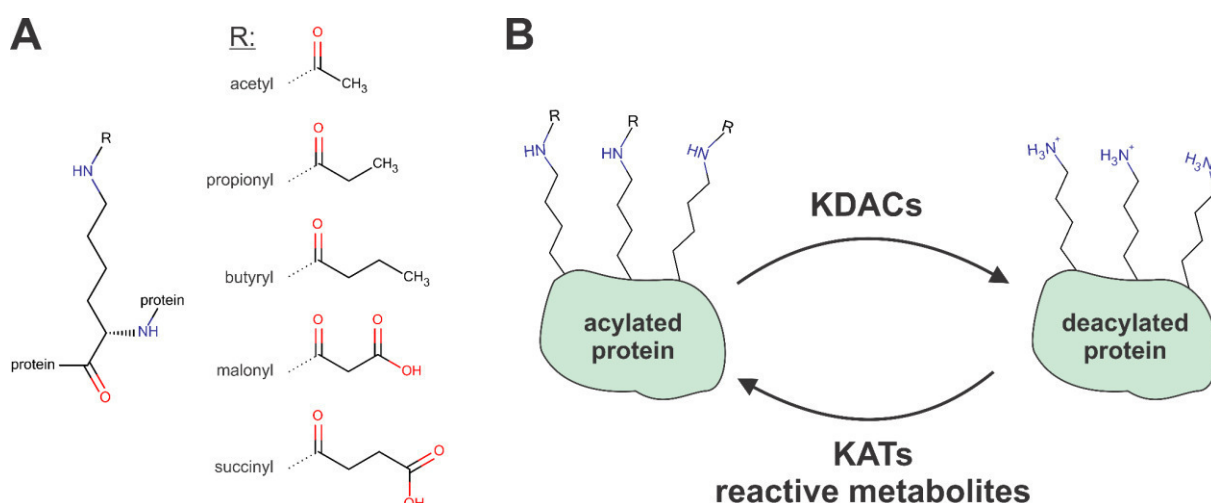
Figure 2: Diversity and regulation of protein acylation. (A) Examples for known lysine side chain acylations. (B) Acyls are attached to lysine side chains by KATs or reactive metabolites and are removed by KDACs.

Besides acetylation, several other lysine acylations were reported in the last decade **(Figure 2A)**. Among those are butyrylation, propionylation [27–29] and crotonylation [30], which are chemically similar to acetylation, but vary in size. In contrast, the short carboxyls malonylation

and succinylation are chemically dissimilar due to their charged terminal group [31–33]. Additionally, myristoylation of lysine side chains was described and seems to play an important role in membrane association [34,35].

The mechanisms of lysine acylation are not fully elucidated, but two pathways have been proposed **(Figure 2B)**. Firstly, acetyl-moieties are attached to lysine side chains by acetyl-transferases (KATs) of the three major families GCN5, CREB-Binding-Protein/p300 and MYST using acetyl-Coenzyme A (acetyl-CoA) as donor molecule [13,36]. Furthermore, some KATs can also utilize bigger hydrophilic acyl-CoA molecules like propionyl-, butyryl- or crotonyl-CoA to modify lysines [28,29,37–40]. It was also reported that CREB-Binding-Protein/p300 has the ability to catalyze lysine succinylation *in vitro* [41], but there are contrary implications based on a structural study, questioning that its aliphatic pocket can bind charged acyl-CoA variants [37]. Secondly, several *in vitro* studies suggested that non-enzymatic lysine acetylation and acylation in cells is feasible through reactive metabolites with good leaving groups like the above-mentioned CoA [42–44]. Indeed, the physiologic significance of this non-enzymatic pathway could be shown *in vivo* by adding the reactive precursors to cell feeds or accumulating/diminishing them by deleting distinct metabolic genes [44,45]. Specific properties of the mitochondrial matrix like the alkaline pH, which increases lysine nucleophilicity, and the relatively high concentration of several acyl-CoA species could explain the high abundance of respective lysine-acylations in mitochondria [45–47]. Additional to reactive CoA-species, lysine side chains can be modified by other reactive metabolites like acetyl-phosphate or 1,3-bisphosphoglycerate *in vitro* and *in vivo* [44,48], augmenting the theoretically possible diversity of lysine modifications.

The reversible acylation of lysine side chains is counteracted by the lysine deacylases (KDACs) **(Figure 2B)**, which are phylogenetically grouped in four classes in higher eukaryotes. Class I, II and IV are constituted by the historically termed histone deacetylases 1-11 (HDAC1-11) [49]. These utilize a zinc ion bound to the active-site, which polarizes the lysine-Nε-acetyl carbonyl to facilitate deacetylation by hydrolysis [50,51]. The KDAC Class III, in contrast, uses a completely different enzymatic mechanism, and is constituted by the "Sirtuins" [49].

1.3. Deacylase Class III: The Sirtuin Family

The name Sirtuin is derived from the yeast homolog Sir2 (**S**ilent **i**nformation **r**egulator **2**), which was discovered in 1987 and regulates transcriptional silencing [52]. It was initially proposed to transfer ribose-phosphate moieties, because of its close homology to the bacterial cobalamine synthesis proteins cobB and cobT [53,54]. Later, Frye reported the ability of Sir2 to transfer the adenosine diphosphate ribose (ADP-ribose) moiety of nicotinamide adenine dinucleotide (NAD+) to proteins [55], and, finally, Imai and co-workers (2000) showed, that Sir2 deacetylates the histones H3 and H4 using an NAD+ dependent mechanism [56]. Recent studies showed, that some human Sirtuins comprise other robust lysine deacylase activities, like desuccinylation by

Sirt5 or demyristoylation by Sirt6 [57,58]. The molecular basis of these activities will be described later. Remarkably, homologs of Sir2 were identified in organisms ranging from archaea over bacteria to humans, which again implicates a vital role for reversible lysine acylation [59]. A lot of effort was and is still spent on the investigation of Sirtuin functions, which demonstrated regulatory roles in DNA-repair, energy homeostasis and tumorigenesis. Furthermore, Sirtuins were implied to play a significant role in the process of aging (see below) [60,61].

Mammals possess seven Sirtuin isoforms (Sirt1-7) with different primary location either in the nucleus (Sirt1,6), nucleolus (Sirt7), cytosol (Sirt2) or mitochondria (Sirt3,4,5) [62]. However, localization can vary under certain circumstances, e.g. appearance of Sirt1 in the cytosol in different mouse tissues [65] or Sirt2 shuttling between cytoplasm and nucleus with implications in mitosis [66]. Concerning the mitochondrial Sirtuins, full-length Sirt3 was detected in the cytosol and nucleus, whereas an N-terminal truncated form resides solely in the mitochondria [63,67]. A shuttling of Sirt4 and 5 was not reported yet, but a cytosolic Sirt5 demalonylase activity has been shown in quantitative MS-experiments [68].

1.4. Sirtuin regulatory functions

The Sirtuins primarily raised attention because of their involvement in aging and mediation of lifespan extension upon caloric restriction (CR) [69]. Deletion of the yeast Sir2 gene shortened lifespan, whereas a second copy promoted longevity [69], and similar results were obtained in *C. elegans* (homologue sir-2.1) [70,71], *D. melanogaster* (homologue dSir2) [72,75,76] and male mice (Sirt6-dependent) [77]. However, other studies disproved the relation of Sirtuins with CR and aging in yeast, *C. Elegans* and *D. melanogaster*, which started an ongoing controversy [78–83]. A model was proposed, in which Sirtuins are not the only mediators of CR on lifespan extension, but contribute together with other mechanisms [78]. Additionally, Sirtuins are reported to delay aging-related diseases, diabetes and cancer [84–86] and are linked to central molecular functions like genomic maintenance, metabolic homeostasis or stress response [60,61], which all influence lifespan.

Acylation of lysine side chains has two primary effects. First, the potentially positively charged lysine side chain is either neutralized (e.g. by acetylation) or becomes negatively charged (e.g. by succinylation). Second, it introduces sterical hindrance in the lysine's microenvironment. These primary effects are responsible for the regulation of protein-ligand-, protein-DNA- or protein-protein-interactions, enzymatic activity or even the subcellular localization of proteins [13,32,87].

The nuclear Sirt1, 6 and 7 are involved in, e.g., transcriptional regulation and genome stability [60,88]. They deacetylate histones to regulate gene-silencing and participate in DNA repair,

e.g., by recruiting DNA-damage response enzymes [60,89–93], but also modulate non-histone proteins like the transcriptional Hypoxia-inducible factor 1-α and 2-α to decrease the expression of glycolytic genes [94,95]. Sirt1 controls p53 function in cell cycle arrest, apoptosis and DNA-damage repair [96]. Sirt6 was found to demyristoylate tumor necrosis factor alpha to release it from the membrane, which can thereafter enable one of its multifaceted effects ranging from apoptosis over cell survival to proliferation [58,97].

The cytosolic Sirt2 deacetylates the main component of microtubules, α-tubulin, and thereby influences their stability and structure [98]. Several other functions have been reported, e.g., a Sirt2 control function in cell cycle progression [99,100] and adipogenesis [61,101].

1.5. Functions of mitochondrial Sirtuins

An important regulatory role of mitochondrial processes is accounted to Sirt3, 4 and 5, since they are the only deacylases in mitochondria and acylations are the prevalent PTMs in this organelle **(Figure 3)** [24,25].
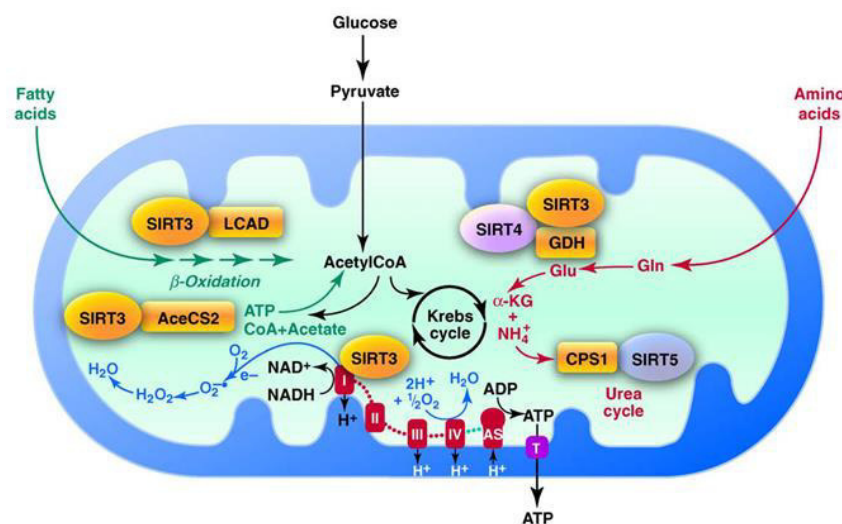

Figure 3. Exemplary regulatory roles of the mitochondrial Sirtuins 3, 4 and 5. Sirt3 deacetylates and activates long-chain acyl-CoA-dehydrogenase (LCAD), acetyl-CoA synthetase 2 (AceCS2), glutamate dehydrogenase (GDH) and enzymes of the respiratory electron transport chain to stimulate catabolic pathways and ATP supply. Sirt4 inhibits GDH activity, which increases insulin secretion. Sirt5 deacylates and activates carbamoyl-phosphate synthase 1 (CPS1), the key entry point to the urea cycle (Figure reproduced from Verdin et al., 2010 [102] with permission of Elsevier).

Sirt3 exhibits robust deacetylase activity and mainly targets metabolic enzymes. It deacetylates and thereby activates acetyl-CoA synthetase 2 (AceCS2) to replenish acetyl-CoA for the Krebs cycle or other biosynthesis pathways [103]. Furthermore, Sirt3 activates complex I and II of the respiratory chain to enhance ATP generation [104,105], long-chain acyl-CoA dehydrogenase (LCAD) to stimulate fatty acid oxidation [106] and glutamate dehydrogenase (GDH) to support metabolic intermediate anaplerosis [107]. Interestingly, Sirt3 is also involved in the regulation of reactive oxygen species (ROS) suppression by activating superoxid dismutase 2 (SOD2) [108]. In summary, Sirt3 activity stimulates catabolic pathways and simultaneously represses ROS generation to dodge emerging cellular damage.

The regulatory function of Sirt4 was less studied yet. Sirt4 was reported to oppose Sirt3 by attenuating GDH-activity [109], which subsequently increases insulin secretion and reduces blood glucose levels [110]. Furthermore, it deacetylates malonyl-CoA decarboxylase (MCD), which inhibits the turnover of malonyl-CoA to acetyl-CoA and thereby decreases fatty acid oxidation and promotes lipogenesis [111]. It influences hepatic peroxisome proliferator-activated receptor α (PPARα) to decrease expression of genes involved in fatty acid catabolism [112]. Additionally, Sirt4 was reported to abolish pyruvate dehydrogenase (PDH) activity by delipoylating a catalytic lysine residue, which hinders the glycolysis product pyruvate to enter the Krebs cycle [113]. In sum, Sirt4 influences metabolic pathways to favor lipid anabolism and reduce lipolysis. Remarkably, it is the highest induced Sirtuin upon DNA-damage and facilitates repair mechanisms by inhibiting GDH, which contributes to cell cycle arrest [60,109].

Only a few regulatory roles of Sirt5 have been reported, but information might increase soon, since its specificity for carboxylic acyls has only recently been uncovered [57]. Sirt5 was reported to stimulate the glycolytic enzyme glycerinaldehyld-3-phosphat-dehydrogenase (GAPDH) [68], the ketogenic enzyme 3-hydroxy-3-methyl-glutaryl-CoA synthase 2 (HMGCS2) and lipolytic enzymes [114]. It is important for nicotinamide adenine dinucleotide phosphate (NADPH) homeostasis by deacylating isocitrate dehydrogenase 2 (ICD2) and glucose-6-phosphate dehydrogenase (G6PDH) to stimulate their NADPH production, which in turn promotes biosynthetic pathways or scavenges ROS by reducing glutathione [115]. Furthermore, it facilitates the disposal of ammonia by deacylating and activating carbamoyl-phosphate synthase 1 (CPS1), the key entry point to the urea cycle [116]. Like Sirt3, it boosts energy supply by enhancing glycolysis, lipolysis and ketogenesis, and protects from consequential ROS-induced cellular damage. This contrasts Sirt4 functions and suggests a balancing regulatory axis of metabolic processes by Sirt3/5 opposing Sirt4.

1.6. Mammalian Sirtuins – Structure and enzymatic mechanism

The highly conserved Sirtuin catalytic core is constituted by 275 amino acids, flanked by N- and C-terminal extensions of varying length **(Figure 4A)**. These are long for Sirt1, where they comprise nuclear localization signals as well as stabilizing and regulatory domains [117,118], and are shorter for Sirt2-7, where they mainly function as mitochondrial (Sirt3,4,5) [116,119,120] or nuclear/nucleolar (Sirt6,7) [121,122] targeting sequences. The catalytic core of each isoform consists of a Rossmann-fold domain, typical for NAD^+ binding proteins [123], and a smaller zinc-binding domain **(Figure 4B)** [124]. In contrast to HDACs of Class I, II and IV, the zinc ion does not participate in catalysis, but is important for the enzyme's stability by clamping two β-sheets of the zinc-ribbon [125]. The active-site is located in a cleft between the two core domains, which are connected by several loops **(Figure 4B,C)**. It consists of a (poly)peptide binding groove, a relatively conserved NAD^+ pocket and a more variable acyl-lysine binding site. A conserved active-site histidine is of crucial importance for NAD^+ binding and activation [88,126–129].
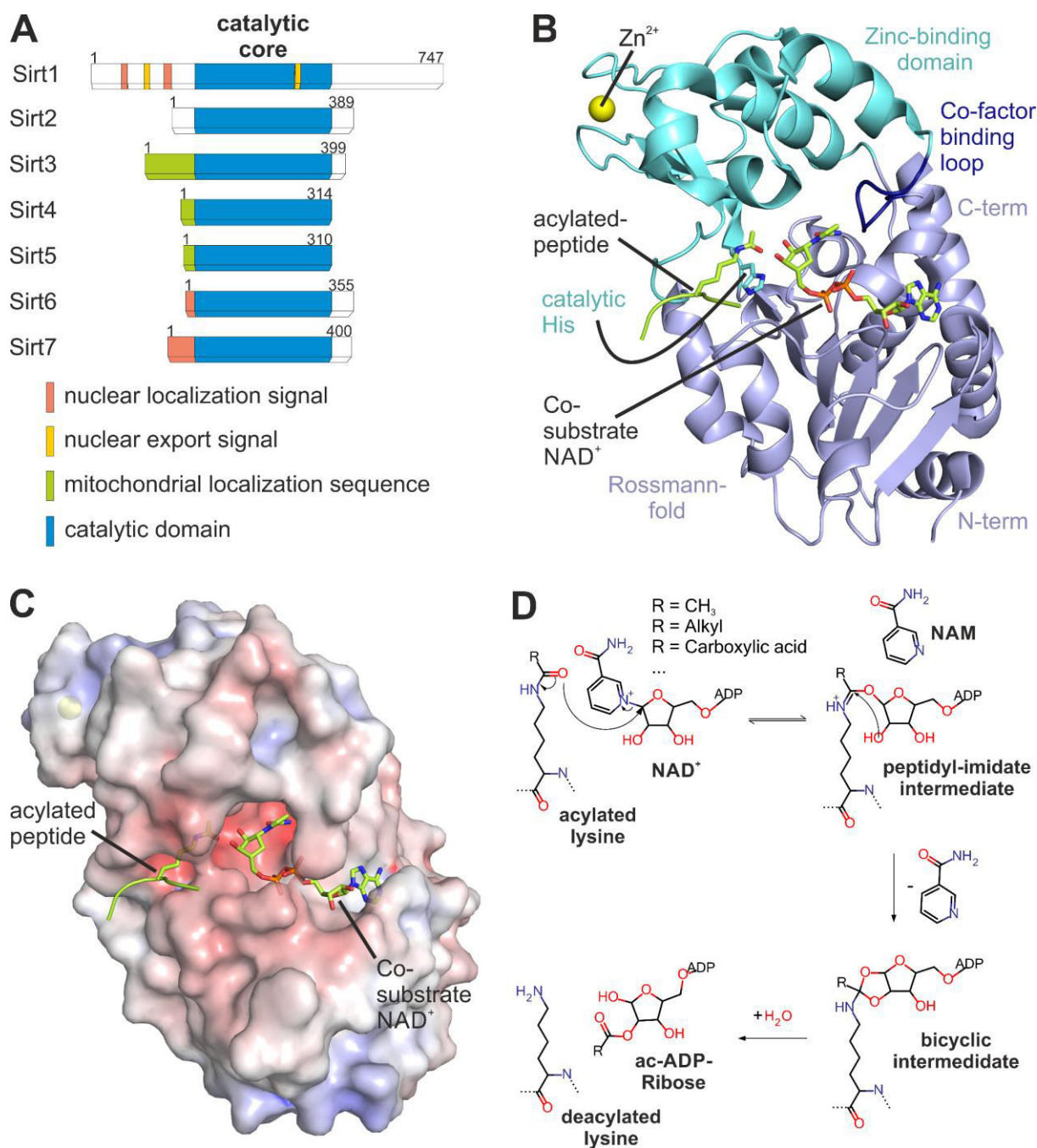
Figure 4. Conserved features of Sirtuin isoforms. (A) The Sirtuins' catalytic cores are flanked by N- and C-terminal extensions, which consist of stabilizing and regulatory domains for Sirt1 and comprise localization sequences for Sirt3-7. (B) The conserved structure of the Sirtuin catalytic core consists of a Rossmann-fold (light blue) and a Zn^{2+}-binding domain (cyan) connected by several loops. The active-site is located between the two core domains. The so-called cofactor-binding loop (dark blue) plays an important role in cofactor binding and catalysis. Protein (blue/cyan) and peptide (green) are shown in cartoon representation, the zinc ion as yellow sphere and the catalytic histidine (catalytic His) as well as the peptide acetyl-lysine and NAD^+ (green) as cpk color-coded sticks (PDB 4FVT). (C) The surface representation of the Sirtuin catalytic core shows the binding pockets for the acylated peptide and NAD^+, colored by electrostatic potential ranging from -10 to +10 K_bT/e_c (PDB 4FVT). (D) Scheme of the Sirtuin catalyzed deacylation reaction (NAM: nicotinamide, ac-ADP-Rbose: acylated ADP-Rbose).

The relative conformation of Rossmann-fold and zinc-binding domain changes during catalysis. Substrate binding induces a closed conformation constituting the acyl-lysine tunnel and positioning the reacting substrate moieties close to each other. Furthermore, it orders the initially flexible "co-factor binding loop" and forces the co-substrate NAD^+ in a kinked, so called

"productive" conformation, which is indispensable for catalysis **(Figure 4B,C)** [124,130]. In the first reaction step, the nicotinamide (NAM) moiety of NAD^+ is released and the instable, not yet evidenced as free or highly dissociative, C1' oxacarbenium ion is instantly attacked by the acetyl-lysine's carbonyl oxygen to form an ADP-ribose-peptidyl imidate **(Figure 4D)** [129,131]. This first intermediate can either be attacked on its β-face by NAM to reconstitute NAD^+ or be processed to a second, cyclic intermediate by collapse of the ADP-ribose 2'-OH group [129]. Sirtuins favor the downstream deacetylation reaction by a conserved Phe/Tyr residue of the co-factor binding loop, which flips in upon NAM-release, probably expelling NAM and hindering the reverse reaction [132,133]. Furthermore, collapse of the ADP-ribose 2'-OH is promoted by the conserved catalytic histidine, which acts as a base to deprotonate the ADP-ribose 3'-OH subsequently activating its 2'-OH [128,131,134]. The second, bicyclic intermediate gets hydrolyzed and the deacetylated protein and 2'-acetyl-ADP-ribose, which spontaneously equilibrates with 3'-acetyl-ADP-ribose, are finally released as reaction products [131].

1.7. Diverse Sirtuin deacylation functions

Robust deacetylation activity was demonstrated for Sirt1, 2 and 3 [61]. However, the mitochondrial Sirt4 and 5 as well as the nuclear/nucleolar Sirt6 and 7 display very weak or undetectable deacetylase activity *in vitro.* It was reported, that Sirt4 and 6 possess ADP-ribosyltransferase activity [120,135,136], but a follow-up study showed that this is an inefficient side reaction for both isoforms [137]. In recent years, crystal structures and biochemical characterizations revealed novel, robust functions of Sirt5 and 6, which correlates with the afore-mentioned discovery of new acyl-modifications on lysine side chains.

Sirt5 was shown to efficiently turnover short carboxylic acyl modifications such as malonyl or succinyl [57], which have been reported as physiological lysine PMTs [31–33]. Consistent with these studies, a recent proteomics approach demonstrated that Sirt5 knock-out (KO) mouse embryonic fibroblasts showed increased protein succinylation, while acetylation levels remained relatively constant [138]. The reason for this acyl-selectivity was revealed by crystal structure analysis. Sirt3 Phe180 caps the acyl-lysine binding site **(Figure 5A)**, but is substituted by Ala86 in Sirt5, which widens the pocket **(Figure 5B)**. Additionally, a Tyr-X-X-Arg motif at the back of the acyl-lysine binding site recognizes the negatively charged acyl **(Figure 5B)**. Kinetics for Sirt5 demalonylation and desuccinylation are in the range of other robust Sirtuin activities, like Sirt2 deacetylation, with low micromolar K_M and catalytic efficiencies of a few thousand $s^{-1} M^{-1}$ [57,139]. Confirming the physiological relevance, experiments with Sirt5 KO mice showed that CPS1 activity is regulated by Sirt5 desuccinylation [57].

In contrast, Sirt6 was reported to efficiently hydrolyze long-chain fatty acyls from lysine side chains [58]. The Sirt6/myristoyl-peptide complex crystal structure revealed a large pocket lined by hydrophobic residues, ideal for binding fatty acyl-lysine substrates and explaining Sirt6

specificity **(Figure 5C)** [58]. A follow-up study reported that the low Sirt6 deacetylation activity is significantly increased by the addition of free long-chain fatty acids [140]. Biochemical data suggested that the free fatty acid binds in the hydrophobic substrate pocket, thereby increasing the affinity for the acetyl-lysine substrate and enhancing Sirt6 deacetylase activity. Interestingly, also Sirt1-3 and 5 were shown to hydrolyze fatty acyls from lysine side chains. However, only Sirt6 but not Sirt1 deacetylation could be activated by the addition of free fatty acids [140].
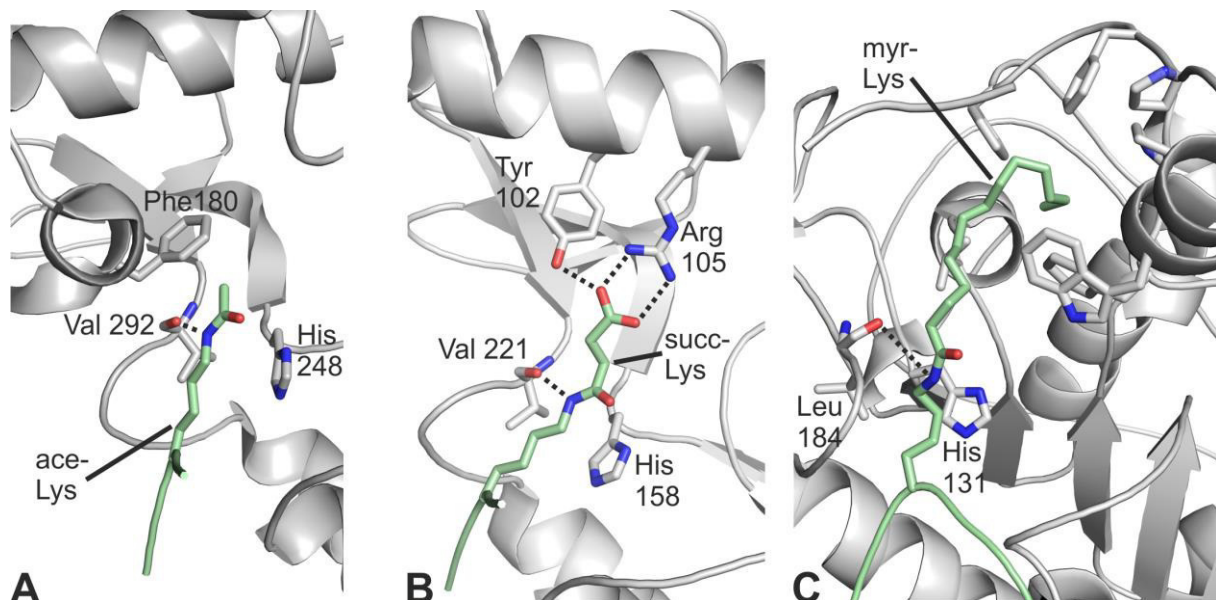

Figure 5: Sirtuin isoforms comprise diverse acyl-specificities due to variable acyl-lysine binding sites. (A) The Sirt3 acyl-lysine binding site is short due to capping by Phe180 and can accommodate short lysine modifications like an acetyl-group (ace-Lys), which fits to its strong deacetylase activity. (B) The Sirt5 acyl-lysine binding site is wider than in Sirt3 and a Tyr-X-X-Arg motif at the back of the pocket recognizes the negatively charged carboxyl function of carboxylic acyls, e.g. succinyl (succ-Lys). (C) Sirt6 comprises a broad acyl-lysine channel lined by hydrophobic residues facilitating long-chain fatty-acyl-lysine, e.g. myristoyl-lysine (myr-Lys), binding. The proteins Sirt3 (PDB 4FVT), Sirt5 (PDB 4G1C) and Sirt6 (PDB 3ZG6) are represented in grey cartoon style with the proteins' amino acids of interest shown as cpk color-coded sticks. The substrate peptides (green) are shown in cartoon style with the acyl-lysines as cpk color-coded sticks. Dashed lines indicate protein-ligand interactions.

Due to these findings, it is worthwhile considering that Sirt4 and 7, which do not display robust *in vitro* deacetylase activity, bear an unrevealed primary function or can be activated by physiologic small molecules in a similar way as Sirt6. Indeed, a Sirt4 *in vivo* deacetylation activity was reported [111], which suggests that this activity is stimulated by an unknown mechanism. In 2014, Mathias and co-workers reported a delipoylase activity for Sirt4 on PDH protein and peptide *in vitro* and *in vivo*, but the kinetics were orders of magnitude weaker than robust primary functions of other Sirtuins [113].

1.8. Modulation of Sirtuin activity

Sirtuins are regulators of multiple key cellular functions and therefore have to be tightly controlled [60,61]. Cells achieve this by either changing Sirtuin transcription levels, by regulatory proteins binding to Sirtuins, PTMs or physiological small molecules. Of these multifaceted possibilities, only the small molecules will be discussed in the following due to their implications for drug development studies.

1.8.1. Physiological small molecule modulators

The characterization of physiological small molecule modulators contributed to both characterization of Sirtuin catalysis and drug development studies. The availability and redox status of NAD^+/NADH regulates Sirtuin activity. NAD^+ is the co-substrate with K_M values between 10 and 600 µM, depending on the Sirtuin isoform [129,141], which is in the range of the physiological concentration of 300 to 400 µM NAD^+ in mammalian cells [142,143]. The fact that Sirtuins require NAD^+ to catalyze lysine deacylation renders them metabolic sensors for sufficient nutrient supply (low NAD^+ level) or starvation (high NAD^+ level) [144]. In contrast, NADH is a weak inhibitor with one-digit millimolar IC_{50} values for human Sirt1,2,3,5 and 6 [145] and possibly also for the other, not yet tested isoforms due to the high conservation of the co-factor binding site. Molecular dynamic simulations predicted NADH binding to Sirtuins solely in an elongated, unproductive conformation, whereas NAD^+ with the oxidized NAM was more stably binding in the kinked, productive conformation, an essential feature for catalysis [145]. A physiological pan Sirtuin inhibitor is NAM, which is generated by several metabolic pathways and released from NAD^+ during the Sirtuin deacylation process as a by-product [129]. NAM inhibited all tested Sirtuins (human Sirt1, 2, 3, 5 (desuccinylation), Sir2, Hst2, Sir2Tm) with IC_{50} values of 20-140 µM [146–148], which is in the range of physiological NAM concentrations (10-400 µM) implying a regulatory mechanism [149]. However, a few exceptions like the bacterial Sir2Af2 (from *Archaeoglobus fulgidus*) and the human Sirt5 deacetylation function showed weak inhibition with IC_{50} values in the millimolar range. Thus, NAM appears to be a deacylase activity discriminating inhibitor, but a comprehensive investigation of its effects on Sirtuins with multiple weak and strong activities was not performed yet.

1.8.2. Pharmacological Sirtuin modulation

Specific Sirtuin modulators are essential tools for the characterization of Sirtuin mechanism, activity and regulatory function in *in vitro* and *in vivo* experiments. Furthermore, Sirtuins are potential drug-targets due to their multiple physiological and pathophysiological roles in, e.g., neurodegenerative disorders, metabolic and aging-related diseases or cancer [61,150]. Unfortunately, most drug-development projects concerning Sirtuins yielded compounds lacking isoform specificity or exhibiting low potency [88,150], but a few exceptions (e.g. EX527) will be described briefly below.

Modulators extensively occupying the NAD^+ pocket often lack isoform specificity due to the high conservation of this site in Sirtuins [124] and regularly affected other enzymes binding NAD^+ or adenosine derivatives [88,126,150–152]. Interestingly, the structures of human Sirt5 and 6 revealed substantial variations in the acyl-lysine binding site among the Sirtuin family, which might facilitate isoform selectivity and is therefore an attractive site for the development of specific modulators [57,58].

Notably, either Sirtuin activation or inhibition, depending on the disease or condition to be treated, would be required for medical purposes. In order to promote longevity, boosting Sirtuin activity related to lifespan extension would be desired. Concerning the medication of obesity or metabolic defects, activation or inhibition of a subset of mitochondrial Sirtuins would be helpful, since they have different regulatory functions on metabolism as described above.

One of the first discovered and extensively studied Sirtuin compounds is the plant stilbene resveratrol, which activates Sirt1, 3 and 5 [153,154]. Similar to CR, it extended lifespan and showed positive health effects [155–157], but it is unclear in which extent this resulted from Sirtuin activation, since this compound targets a variety of proteins [151,158]. Remarkably, resveratrol induced either positive, negative or no effects on Sirt1 deacetylase activity in a peptide array with ~6500 physiological acetylation motifs [159]. This adds another level of complexity to Sirtuin modulation, since compound effects appear not to depend only on the isoform, but also on the acyl-modification (see NAM – Sirt5) or the substrate sequence (see Resveratrol – Sirt1).

One of the best studied Sirtuin inhibitors is EX-527 **(Figure 6A,B)**, which inhibits Sirt1 (IC_{50} 0.1 µM) and has two orders of magnitude weaker potencies towards Sirt2 and 3 and no effect on Sirt5 [160,161]. It was reported to bind to the NAM pocket with NAM-like H-bonds to Ile230 and Asp231 and inhibit Sirtuin catalysis by stabilization of the Sirtuin/inhibitor/acetyl-ADP-ribose complex **(Figure 6B)** [160]. This mechanism explains the insensitivity of Sirt5, which comprises substantial structural differences blocking this site for EX-527 [160].

1.8.3. Mitochondrial Sirtuin modulators

Most initial drug development studies concerned Sirt1 and 2, whereas mitochondrial Sirtuins have not been extensively targeted yet [88]. Concerning Sirt5, efforts were hampered due to the lack of *in vitro* assay systems, until its efficient demalonylation and desuccinylation activities were reported a few years ago in 2011 [57]. Likewise, no Sirt4 modulator was developed yet, since there was no robust *in vitro* activity reported for this isoform. Thus, only a few modulators for Sirt3 and 5 were discovered so far, which will be described in the following.

Suramin was the first Sirtuin compound for which inhibition data as well as structural information were obtained. The compound shows single-digit micromolar IC_{50} on Sirt1, but also inhibits Sirt2 and 5 with similar potencies. This can be explained by the crystal structure of Sirt5 with bound Suramin, which shows that the compound broadly and non-specifically targets the peptide-lysine and NAD^+ binding sites [162,163]. Furthermore, it has strong off-target effects on G-proteins, reverse transcriptase and growth factors [164–166], all together rendering it unusable as a specific Sirtuin modulator.

The "extended library technology" (ELT) inhibitor class comprises the strongest Sirtuin inhibitors reported so far, which unfortunately affect Sirt1, 2 and 3 equally **(Figure 6A,C)** [167]. The

top compound inhibited Sirt3 with an IC_{50} of 4 nM. Complex crystal structures demonstrated that the inhibitors partially occupy the acyl-lysine tunnel and the NAM pocket [167], where its carboxamide forms NAM-like H-bonds to the protein **(Figure 6C)**. Furthermore, ELTs interact by π-stacking of the thieno[3,2-d]pyrimidine with the highly conserved phenylalanine (Phe157 in Sirt3) of the co-factor binding loop **(Figure 6C)** without affecting the loops regular conformation. These compounds did not show off-target effects, which renders them starting points for derivatization to develop potent and selective Sirtuin inhibitors [88,167].

SRT1720 is a potent (K_i 0.6 µM) Sirt3 inhibitor, which does not affect Sirt5, but activates Sirt1 with a similar potency ($EC_{1.5}$ 0.16 µM) **(Figure 6A,D)** [155,168]. Its mechanism towards Sirt3 has been extensively characterized by kinetic and structural studies. It is a competitive inhibitor towards the acetyl-lysine substrate and uncompetitively inhibits NAD^+ binding to Sirt3. This was explained by complex crystal structures, which showed that SRT1720 tightly binds between the protein and the NAM-moiety of NAD^+ in the Sirt3 active-site, leading to a rearrangement of the co-factor binding loop and a stable, inactive Sirt3/NAD^+/inhibitor complex [168]. Derivatization of SRT1720 is promising to yield the first selective and highly potent Sirt3 inhibitor.

Finally, the indole GW5074 is an acyl- and possibly sequence-dependent Sirt5 inhibitor [152]. It efficiently inhibits Sirt5 desuccinylation (IC_{50} 20 µM), while Sirt5 deacetylation is an order of magnitude less potently affected (IC_{50} 200-400 µM). Unfortunately, it has strong off-target effects on kinases and Sirt2 [169], rendering it a difficult starting point for further drug development.
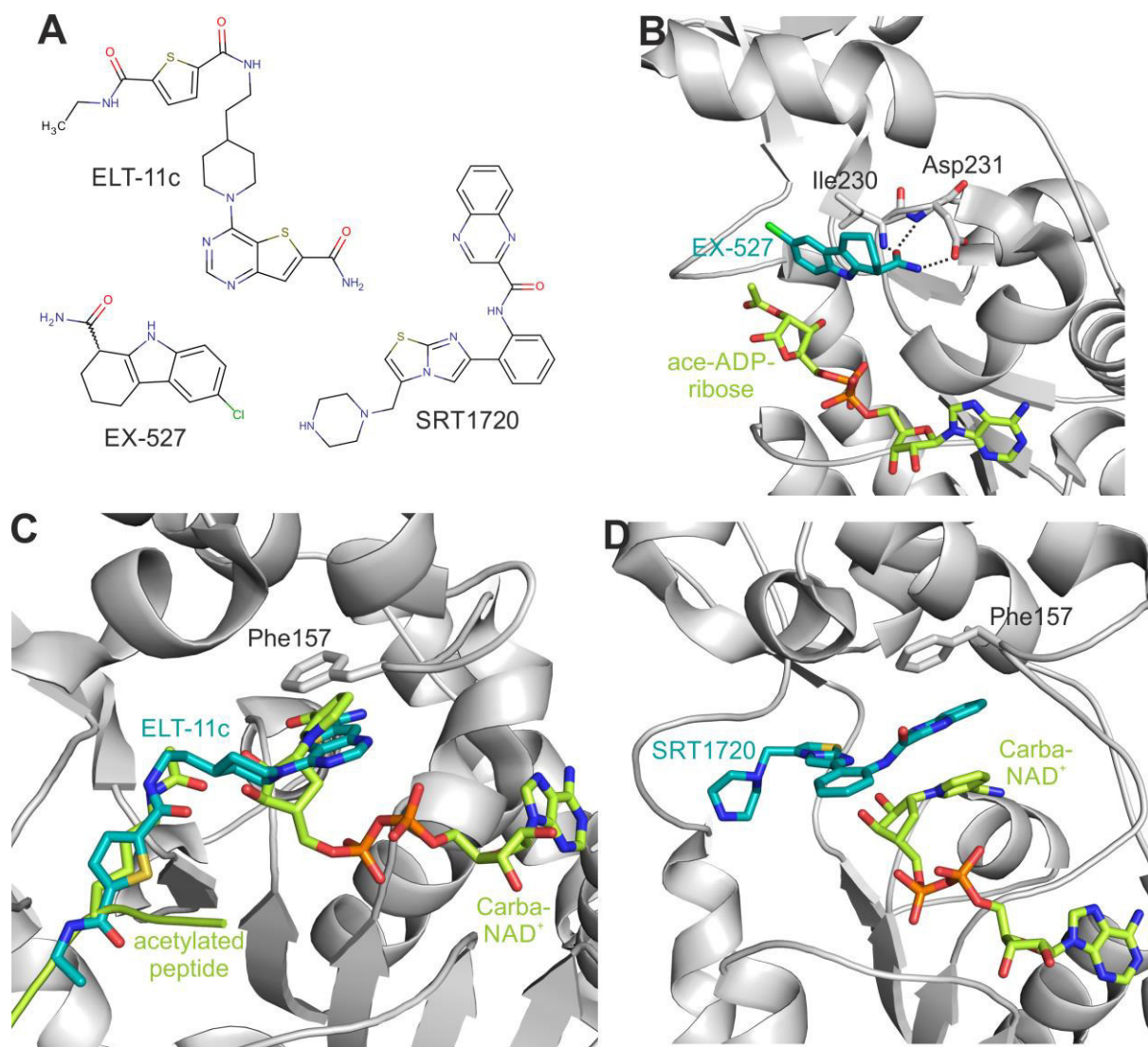
Figure 6: Examples of small molecule mitochondrial Sirtuin modulators. (A) Chemical structures of the Sirtuin inhibitors ELT11-c, EX-527 and SRT1720. (B) Complex crystal structure of Sirt3 with acetyl-ADP-ribose (ace-ADP-ribose) and the inhibitor EX-527 (PDB 4BVH). EX-527 binds to Sirt3 in the NAM pocket and adjacent area with NAM-like H-bonding interactions to Ile230 and Asp231 (indicated by dashed lines). It inhibits Sirtuins by stabilizing the Sirtuin/EX-527/acetyl-ADP-ribose complex, which blocks the active site. (C) Complex crystal structure of Sirt3 with ELT-11c (PDB 4JSR). The NAD^+ analog Carba-NAD^+ and the acetylated peptide were modeled from the Sirt3/acetyl-ACS2-peptide/carba-NAD^+ complex structure (PDB 4FVT). ELT-11c binds in the acyl-lysine channel and part of the NAD^+ binding site and thereby competitively inhibits Sirt1, 2 and 3 with high potency. ELT-11c binds to Sirtuins through π-stacking of the thieno[3,2-d]pyrimidine with the highly conserved phenylalanine of the co-factor binding loop (Phe157 in Sirt3) and NAM-like interactions (compare carba-NAD^+ NAM moiety with ELT-11c pyrimidine group). (D) The crystal structure of Sirt3 in complex with SRT1720 and Carba-NAD^+ (PDB 4BN5) shows the binding of SRT1720 between Sirt3 (e.g. π-stacking to co-substrate binding loop Phe157) and co-substrate. The compound stabilizes the inactive Sirt3/NAD^+/SRT1720 complex. Proteins are shown in grey cartoon representation with amino acids of interest as cpk color-coded sticks. Inhibitors are represented as cyan cpk color-coded sticks, while peptides, Carba-NAD^+ and acetyl-ADP-ribose are shown as green cartoon and cpk color-coded sticks.

Summarizing, there is undoubtedly need for the development of Sirtuin modulators for pharmacological as well as scientific purposes, especially in the field of the mitochondrial isoforms, which were not investigated as thoroughly as Sirt1 and 2 so far.

2. <u>Aims of this work</u>

2.1. <u>Characterization of Sirt5 acyl-specificity and Sirt5 inhibitor development</u>

Even though the first structure of the mitochondrial Sirtuin 5 was already solved in 2006 [162], the first robust activities of this isoform, demalonylation and desuccinylation of target protein lysines, were only discovered in 2011 [57]. However, the acyl-specificity of Sirt5 was never systematically characterized, although this could reveal further physiologic activities, which in turn should stimulate investigations to uncover their regulatory function. Therefore, a collaborative study will be set up to synthesize a peptide-based acyl-library for screening Sirt5 activity and investigating the molecular background of distinct activities by crystal structure analysis of Sirt5/peptide complexes.

Specific Sirt5 inhibitors would be valuable tools for biochemical investigations of Sirt5 catalysis or physiologic roles and might one day serve as leads for medicating Sirt5 related diseases, e.g., for its possible involvement in neurodegeneration [88,170]. Thus, the obtained insights in Sirt5 structure and function should be used to develop inhibitors for this isoform. The rationale is to create succinyl-derivatives on a peptide lysine to transform the robust and Sirt5-specific substrate into Sirt5 peptide inhibitors. Our collaborators will synthesize and test the inhibitors, while we guide the study by crystal structure analysis revealing their inhibition mode and potential for optimization. It will be necessary to truncate the peptidic part of these inhibitors to improve *in vivo* availability, which is assumed to result in a significant loss of potency. Thus, a collaborative structure-activity relationship (SAR) study should be performed to decrease peptide-length while retaining inhibitor potency. Our collaborators will synthesize and test small peptide-(like) inhibitors, while we guide the process by crystal structure analysis to reveal their binding and inhibition mode and further potential for small molecule inhibitor development.

### 2.2. <u>Biochemical and structural studies of Sirtuin 4</u>

In contrast to most other Sirtuins, the mitochondrial Sirtuin 4 is poorly understood. Its structure could not be resolved so far and its primary enzymatic activity is unknown. However, a few regulatory roles of Sirt4 were discovered through *in vivo* studies, e.g., deacetylation of MCD [111], ADP-ribosylation of GDH [120] or delipoylation of PDH [113], but corresponding *in vitro* kinetics were much weaker than for primary activities of other Sirtuins. Probably, many trials to explore this isoform were hampered by its intrinsically high insolubility. Therefore, constructs and protocols for efficient production of human Sirt4 and, if a breakthrough cannot be achieved, Sirt4 orthologues from other species will be established. In case of success, Sirt4 will be biochemically characterized and its deacylation activity screened using the peptide-based acyl-library of the Sirt5 study. Furthermore, a Sirt4 crystal structure is a major objective of this work, since it could provide valuable information to enable further investigations concerning Sirt4 acyl-recognition, catalysis or physiologic regulation.

3. **Summary and discussion of results**

3.1. Systematic characterization of the Sirt5 acyl-specificity

Ever since it was discovered, Sirt5 was supposed to be a relatively weak deacetylase with reported regulatory functions [107,116]. Only a few years ago, Du and co-workers found that Sirt5 features strong demalonylase and desuccinylase activity [57], which prompted studies linking these activities with regulatory roles [33,68,114]. However, a systematic probing of Sirt5's acyl specificity was never performed, but could unravel further physiologic activities. Therefore, our collaborators modified a peptide derived from the Sirt5 substrate CPS1 (CPS1-K527) with a library of acyls on its central lysine residue side chain and tested them as Sirt5 substrates in Michaelis-Menten kinetics. This library included a series of acyls of incremental length with distal carboxyl groups **(Figure 7A,B)** and a variety of succinyl- and glutaryl-modifications with small substitutions or heteroatoms in 2' or 3' positions **(see scheme 1, 2, 3 in publication 1)**.

A **1** Bz-Gly-Val-Leu-Lys-Glu-Tyr-Gly-Val-NH$_2$

peptide	K_M [μM]	k_{cat} [s^{-1}]	k_{cat}/K_M [M^{-1}s^{-1}]
2	24.3 ± 9.1	$3.9 \times 10^{-4} \pm 6 \times 10^{-5}$	16
3	416 ± 24	$1.6 \times 10^{-3} \pm 8 \times 10^{-5}$	4
4	5.1 ± 1.1	$1.9 \times 10^{-2} \pm 1 \times 10^{-3}$	3758
5a	3.8 ± 0.6	$5.3 \times 10^{-2} \pm 2 \times 10^{-3}$	13995
6a	4.1 ± 1.0	$7.7 \times 10^{-2} \pm 2 \times 10^{-3}$	18699
7	6.5 ± 1.6	$1.0 \times 10^{-2} \pm 6 \times 10^{-4}$	1538
8	80.5 ± 22.9	$2.8 \times 10^{-4} \pm 4 \times 10^{-5}$	4
9	409 ± 283	$5.3 \times 10^{-4} \pm 2 \times 10^{-5}$	1
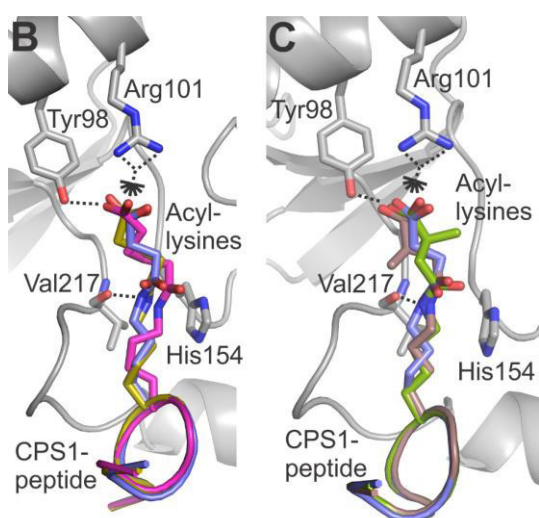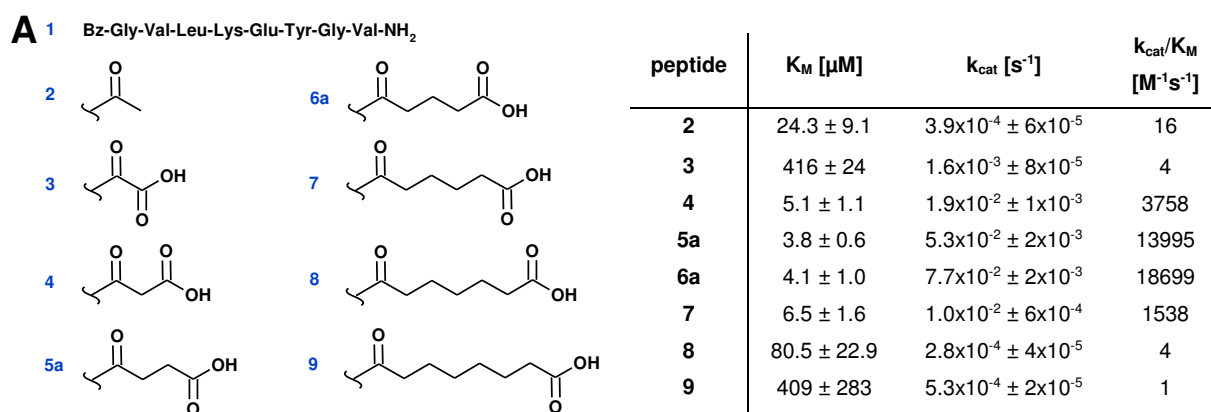
Figure 7: Sirt5 specificity screening and structural binding mode analysis of acylated peptides. (A) A CPS1-K527 peptide **(1)** was modified with an acetyl- **(2)**, oxalyl- **(3)**, malonyl- **(4)**, succinyl- **(5a)**, glutaryl- **(6a)**, adipoyl- **(7)**, suberoyl- **(8)** or pimeloyl-group **(9)** on the lysine side chain. The table on the right shows kinetic parameters of Sirt5 towards these acylated CPS1 peptides. Error is the standard deviation (s.d.) of two independent experiments. (B) zSirt5/CPS1 peptide complexes with succinyl-, glutaryl- and adipoyl- or (C) succinyl, 3-methyl-succinyl- and 3,3-di-methyl-succinyl-CPS1 peptide were overlaid to investigate their binding mode and differences in catalytic efficiency. All acyl-lysines interacted with side chains of Sirt5 residues Tyr98/Arg101 and Val217 backbone (except adipoyl for Val217), as indicated by dashed lines. zSirt5 is shown in grey cartoon style with amino acids of interest as cpk color-coded sticks, while peptides are shown as blue (succinyl), yellow (glutaryl), magenta (adipoyl), brown (3-methyl-succinyl) or green (3,3-di-methyl-succinyl) cartoon with the acyl-lysine as respectively cpk color-coded sticks.

These assays confirmed the several orders of magnitude increased catalytic efficiency of lysine demalonylation **(4)** and desuccinylation **(5a)** compared to its low deacetylase **(2)** activity. Interestingly, Sirt5 exhibited even higher catalytic efficiency for the glutarylated peptide **(6a)** due to the elevated k_{cat} compared to desuccinylation and demalonylation. Further elongation

of the carboxylic acyl **(7-9)** or the introduction of any kind of substitutions or heteroatoms reduced Sirt5 activity **(see Table 1 in publication 1).**

Since the molecular basis of the enhanced Sirt5 deglutarylation activity was unclear, we solved crystal structures of zebrafish Sirt5 (zSirt5) in complex with several CPS1 peptides. zSirt5 was used instead of human Sirt5 (hSirt5), since it showed a high (75%) sequence identity of the catalytic core and crystallized more reliably. The crystals exhibited moderate diffraction around 3 Å resolution, which allowed modeling of the complete peptide including the acyl. Structural analysis showed that succinyl-, glutaryl- and adipoyl-modifications tightly interacted with the Tyr98/Arg101 motif at the back of the Sirt5 substrate pocket and that the Val217 backbone carbonyl fixed the acyl-lysine Nε in a conserved position (residue numbering refers to zSirt5) **(Figure 7B)**. Both observations concerning succinyl-lysine binding are in congruency with a reported hSirt5/succinyl-peptide crystal structure [57]. Thus, the acyls need to arrange themselves between the two interaction motifs, leading to increasingly twisted conformations for glutaryl- and adipoyl-lysine compared to succinyl-lysine and weaker contact between adipoyl-lysine and Val217 due to a slight substrate shift **(Figure 7B)**. Consistently, a docking study of our collaborators with pimeloylated and suberoylated CPS1-K527 peptides indicated weaker interaction and unfavorable conformations of acyl and protein side chains due to an extension beyond the normal acyl-lysine channel. This explains the increasingly weakened K_M and turnover of acyls longer than glutaryl **(see Figure 1b and Table 1 in publication 1)**.

The kinetic analysis showed similar K_M (3.8/4.1 µM), but changing k_{cat} values for CPS1-K527 desuccinylation (5.3 x 10^{-2} s^{-1}) and deglutarylation (7.7 x 10^{-2} s^{-1}). Two hypotheses were built on the obtained structural data, which could explain the different turnovers. First, the more winded acyl of the substrate glutaryl-lysine compared to the unstrained succinyl-lysine **(Figure 7B)** implies a more strained glutaryl-ADP-ribose product, which might prompt faster product release, probably the rate-limiting step in Sirtuin catalysis [128]. Second, a slight carbamide rotation was observed for glutaryl- compared to succinyl-lysine, which might enable a more efficient nucleophilic attack during intermediate formation. Supporting this idea, a similar rotation of the carbamide's carbonyl-function towards the NAD^+ pocket correlated with decreasing k_{cat} values for succinyl- (5.3 x 10^{-2} s^{-1}), 3' mono-methyl-succinyl (2.4 x 10^{-3} s^{-1}) and 3,3' di-methyl-succinyl-CPS1 peptides (2.2 x 10^{-4} s^{-1}), while all of them showed similar K_M and interactions with Tyr98/Arg101/Val217 **(Figure 7C)**.

Another independent study confirmed the Sirt5 deglutarylation activity and provided proteomic data evidencing lysine glutarylation as a physiologic PTM [171]. Interestingly, glutarylation was mapped on proteins in bacteria, yeast, drosophila, mouse and human cells, which – as for acetylation – implies an evolutionarily conserved function [171,172]. Glutarylation and succinylation sites significantly overlapped in samples derived from mouse liver and hyperglutarylation as

well as hypersuccinylation reduced CPS1 activity [57,171], both suggesting similar roles for these acylations. Like acetylation, also succinylation and glutarylation were abundantly found on metabolic proteins, underlining their presumable regulatory role as well as Sirt3's and Sirt5's control function in metabolic homeostasis [114,138,171,173,174].

3.2. Development of peptidic Sirt5 inhibitors

Despite several attempts, Sirt5 drug discovery projects so far only yielded compounds with weak potency or lacking isoform selectivity, e.g., GW5074, Suramin and compounds of the thiobarbiturate family [152,175,176]. Hence, our collaborators expanded the acyl-peptide library described in chapter 3.1 and screened for inhibitory acyls exploiting Sirt5 affinity- or selectivity-hot spots to propose starting points for non-peptidic, drug-like inhibitor development. The succinylated CPS1-K527 peptide was used as a scaffold to target the Sirt5 Tyr/Arg motif, which is a distinct selectivity feature among the mammalian Sirtuins [57,176]. The succinyl-moiety was modified by alkyls or bulky rings at positions 2' or 3' to transform the robust substrate into inhibitors. In parallel, we solved complex crystal structures of zSirt5 with inhibitory CPS1-K527 peptides to rationalize results and guide the derivatization process.

Initially, 3-phenyl-succinyl (3PS) was identified as a weak inhibitor of Sirt5 desuccinylation (Ki = 100 µM) **(Figure 8A)**. As expected, the zSirt5 complex crystal structure showed the substrate-like binding of the 3PS-CPS1 peptide to Tyr98/Arg101 and Val217, while its phenyl-group protruded to the NAD$^+$ pocket and clashed with modeled NAD$^+$, which suggests a competitive inhibition of substrate and co-substrate binding **(Figure 8B)**. Follow-up trials yielded the more potent inhibitory acyl 3-butyl-succinyl (3BS; K_i 17.2 µM), which showed similar binding in the zSirt5 complex crystal structure and clashing of the butyl moiety with modeled NAD$^+$ **(Figure 8A,B)**. Interestingly, introducing an additional methyl group on the succinyl 3' increased potency of the weak 3PS by two orders of magnitude (3-phenyl-3-methyl-succinyl; 3PMS; Ki 4.3 µM) **(Figure 8A)**, yielding a potent and selective inhibitory peptide, not affecting Sirt1/3 and weakly inhibiting Sirt2 deacetylase activity (4% inhibition at 50 µM dose).

Since several potent Sirtuin inhibitors like EX-527 occupy the NAM-site [160], a methyl-carbamate linker was introduced to move the phenyl moiety into this pocket (3(S)-Z-aminosuccinyl (3ZAS)) **(Figure 8A,C)**. This approach yielded moderate potency (K_i 38 µM), but fixing the loose ring (indicated by its weak electron density, **see SI Figure S14c in publication 1**) in the NAM-site by adding a carboxamide function to the phenyl, similar to NAM or EX-527 [88,160], and additional 3'-methylation like in 3PMS might yield a compound with enhanced potency.
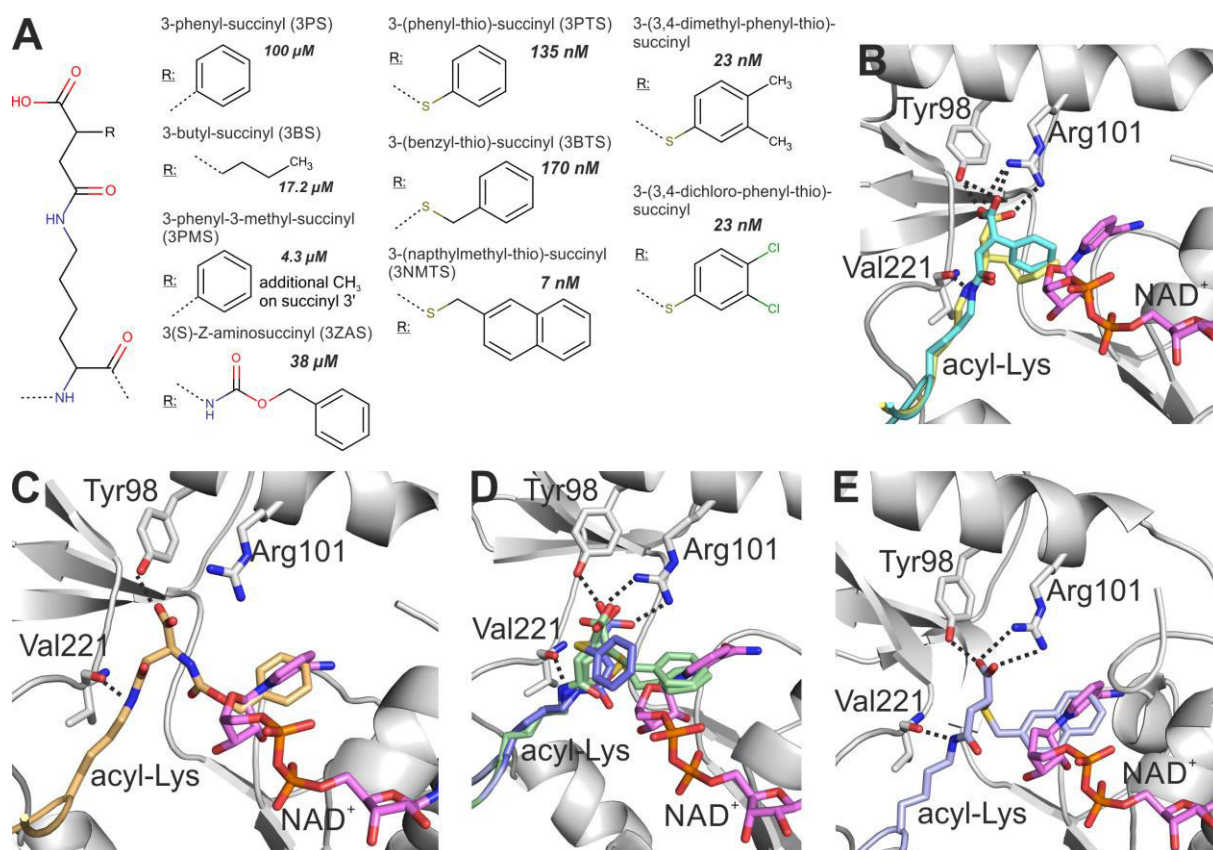
Figure 8: Chemical structures and binding mode analysis of Sirt5 inhibiting acyls. (A) Chemical structures of inhibitory acyls, which were created by different substitutions (R) on a succinyl-lysine at the 3'-position. K_i values are given in bold for each derivative. Complex crystal structures of zSirt5 with (B) 3PS- (cyan) and 3BS- (yellow), (C) 3ZAS- (orange), (D) 3PTS- (blue) and 3BTS- (green) and (E) 3NMTS-CPS1 peptide (light blue), each overlaid with NAD$^+$ (magenta) modeled from hSirt5/succinyl-H3K9/NAD$^+$ complex (PDB 3RIY). zSirt5 (grey) and CPS1 peptides are represented in cartoon style with zSirt5 amino acids of interest and acyl-lysines shown as respectively cpk color-coded sticks. Interactions between zSirt5 and acyl-lysines are indicated by dashed lines.

Exchanging the polar carbamate linker on the succinyl 3' position of 3ZAS by a more hydrophobic thioether function was supposed to enhance affinity. Furthermore, it enabled the synthesis of a comprehensive set of 3-(alkyl-thio)-succinylated CPS1-K527 peptides by coupling thiols to maleinyl-lysines via Michael-addition **(see Table 1 in publication 2)**. Addition of a thioether-linked phenyl (3-(phenyl-thio)-succinyl; 3PTS) or benzyl (3-(benzyl-thio)-succinyl; 3BTS) to the succinyl 3' position resulted in highly improved K_i values of 135 nM (3PTS) and 170 nM (3BTS) **(Figure 8A)**. Notably, 3S and 3R enantiomers of the chemical synthesis could be separated in the chromatography purification process and showed significantly different K_i values, but it is unclear which enantiomer of 3PTS and 3BTS is the more potent one. Complex structures showed a binding of 3PTS close to modeled NAD$^+$, while 3BTS was clashing heavily with the NAM and NAM-ribose of modeled NAD$^+$ **(Figure 8D)**. However, electron density was too weak to distinguish enantiomers. Adding chlorines or methyls to 3PTS in meta- and para-position (K_i 23 nM for both, **Figure 8A**) or introducing a bulkier naphthyl moiety instead of the phenyl-ring (K_i 30 nM, **see compound 33.2 in Table 1/S1 in publication 2**) both increased potency by another order of magnitude. Finally, introduction of a methylene into the linker to

create the 3-(2-naphthylmethyl-thio)-succinyl-CPS1-K527 peptide yielded the strongest inhibitor of this study (3NMTS). It showed a similar inhibition mode in the solved Sirt5 complex crystal structure by clashing with modeled NAD$^+$ and for the first time reached single-digit nanomolar potency (Ki 7 nM) **(Figure 8A,E)**.

3.3. Development of Sirt5 small molecule inhibitors

Truncation of the peptidic Sirt5 inhibitors to small molecules is desired, since it enhances drug properties like cell-permeability or *in vivo* half-life and decreases susceptibility to proteolysis after resorption in the body/cell [177]. Thus, a collaborative SAR study was performed to optimize the lysine-scaffold and shrink peptide size while retaining potency. In this study, our collaborators synthesized and tested the inhibitors, while we solved crystal structures to reveal their binding and inhibition mode.

A lysine side chain was initially modified with a thio-glutaryl moiety, since glutaryl- and succinyl-lysine share a comparable K_M **(see publication 1)** and thio-succinylated peptides were shown to inhibit Sirt5 with single-digit micromolar IC_{50} [178]. The N-terminus was Cbz protected and the C-terminus modified with an ethyl-indole, which indeed yielded a moderate Sirt5 inhibitor as starting point of the study (IC_{50} 25 µM, **compound 1, see scheme 2 in publication 3**). In the course of the SAR study, more than 70 compounds with different N-terminal, C-terminal and lysine side chain modifications were synthesized and tested by our collaborators. Strikingly, the first iterative cycle yielded the sub-micromolar inhibitors "compound 10" (IC_{50} 830 nM) and "compound 29" (IC_{50} 370 nM) **(Figure 9A)**. These only differed in their lysine acylation, which was either a thio-glutaryl (compound 10) or a thio(urea)-glutaryl (compound 29). As expected, the most potent compound 29 was highly specific for Sirt5, as it did not affect any other tested Sirtuin at a 10 µM dose **(Figure 9A)**. These compounds were proposed to inhibit Sirt5 by stalling catalysis through the slowly dissociating peptidyl-thioimidate or bicyclic intermediate, thereby permanently blocking the active-site [178,179].

We solved crystal structures of Sirt5 in complex with compounds 10 and 29 to test this hypothesis and to investigate the molecular details of the improved lysine-scaffold. Incubating Sirt5 with compound and NAD$^+$ prior to setting up crystallization trials yielded well diffracting crystals with around 2 Å resolution or better in combinations of hSirt5/compound29, zSirt5/compound10 and zSirt5/compound29. These indeed comprised the reaction intermediates stalled either in the peptidyl-thioimidate or bicyclic state **(Figure 9B,C and Figure 1 in publication 3)**.
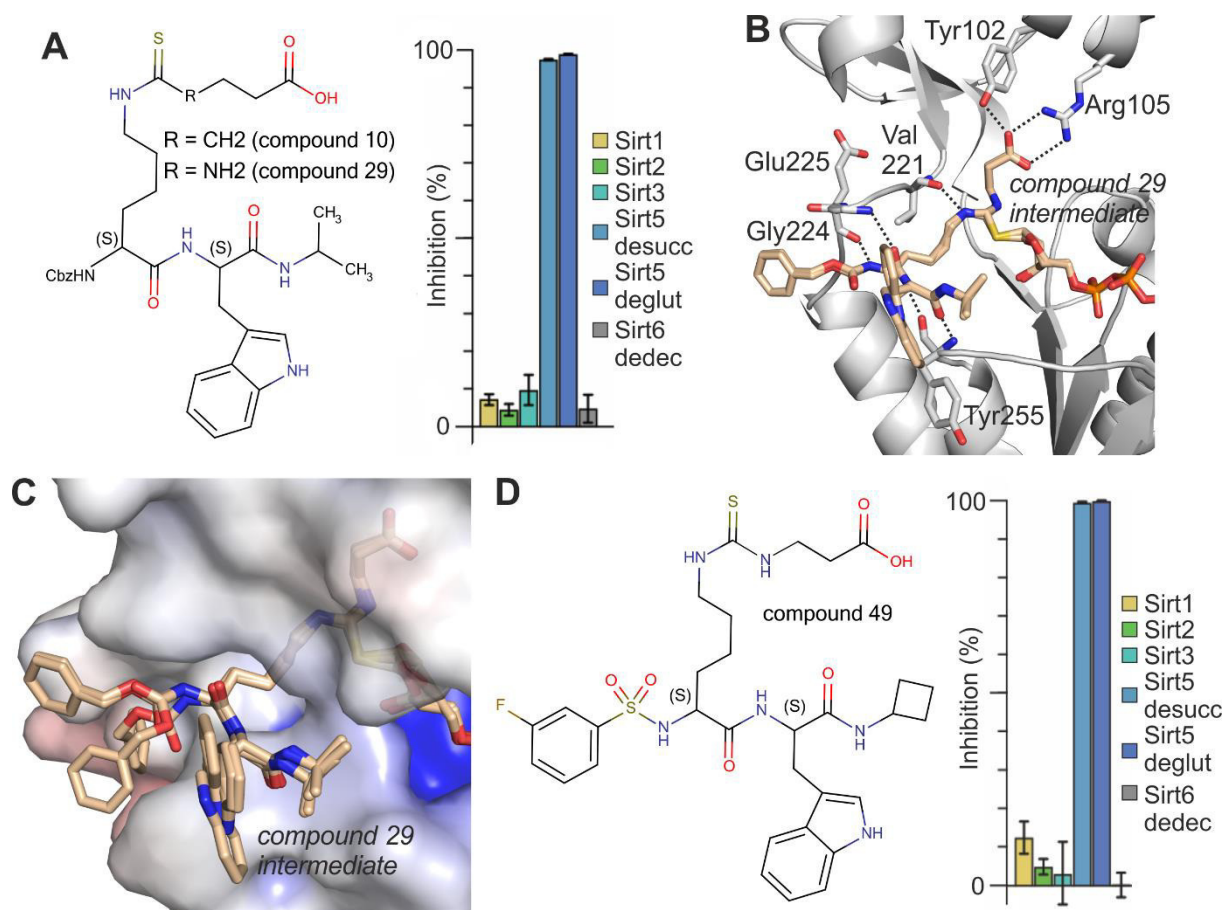
Figure 9: Characterization of Sirt5 inhibitory compound 10, 29 and 49 selectivity, binding and mechanism. (A) Chemical structures of compounds 10 and 29 and selectivity testing of compound 29 on Sirt1/2/3 deacetylation, Sirt5 desuccinylation/deglutarylation and Sirt6 de-decanoylation at a 10 µM dose. (B) Zoom view of the hSirt5 active-site with bound peptidyl-thioimidate intermediate of compound 29. Interactions between protein and compound 29 are indicated by dashed lines. (C) Sirt5 bound compound 29 Cbz- and indole-moieties adopt multiple conformations. hSirt5 protein is shown as grey cartoon with amino acids of interest as cpk color-coded sticks in (B) or as surface colored by electrostatic potential (-10 (red) to +10 K_bT/e_c (blue)) in (C). The compound 29 peptidyl-thioimidate intermediate is shown in orange cpk color-coded stick representation. (D) Chemical structure and selectivity profile (tested against activities as in (A)) of the most potent compound 49 at a 10 µM dose.

The improved lysine scaffold bound similarly in all of our above mentioned crystal structures and thus the 1.32 Å high resolution hSirt5/compound29 complex was used for structural analysis **(Figure 9B,C)**. As predicted, the thio(urea)glutaryl-lysine interacted with Tyr102/Arg105/Val221 in a substrate-like manner (residue numbering refers to hSirt5). Furthermore, hydrogen bonding interactions between hSirt5 backbone of Gly224, Glu225 and Tyr255 with N- and C-terminal extensions of the compound's lysine could be identified, leading to a rigid conformation of this part, whereas the Cbz and indole groups showed higher flexibility **(Figure 9B,C)**. However, introduction of the bulky indole led to 4-fold increased potency compared to unsubstituted derivatives **(see compounds 10 and 13, scheme 2 in publication 3)**, although its flipping conformation indicates weak binding and further potential for improvement. Substitution of the N-terminal Cbz with a sulfone-linked fluoro-benzene or naphthalene resulted in only a maximum of 2-fold improved potency **(see compounds 29 and 42/43, scheme 2 in publication 3)** and the flexibility of the Cbz group in the crystal structure indicates difficulties to improve potency in this compound part. However, it was interesting to see that

the peptide bond can be replaced by a sulfone linker, which decreases susceptibility to prote-olysis. In contrast, the C-terminal isopropyl-moiety is bound in a stable conformation and exploits a binding site on the Sirt5 surface. This is consistent with increasing potency from a free C-terminal amine over substitution with an isopropyl to a bulkier cyclobutyl moiety by more than an order of magnitude **(see compounds 7, 10, 48, 49, scheme 2 in publication 3)**. Finally, the study yielded compound 49**,** which comprised the highest potency (IC_{50} 110 nM) and Sirt5 selectivity **(Figure 9D)**.

Still, the inhibitors proposed by the afore-mentioned study comprise several weak properties like their size (compound 10/29/49: 637/638/674 Da) or the amounts of H-bond donors (6/7/6) disobeying Lipinski's "rule of 5" [180] and thus suggesting low bioavailability. Additionally, they contain two to three peptide bonds, which are targets for proteolytic cleavage that by rationale would significantly decrease inhibitor potency. Our collaborators thus tested a series of lysine substitutions carrying the strongly inhibiting 3-(2-naphthylmethyl-thio)-succinyl acyl derived from the peptide inhibitor study **(publication 2)**. A tripeptide still comprised a K_i of 180 nM (compound 40, **Figure 10**), while further truncation to an acetyl-/amine-protected lysine de-creased potency to 7 µM (compound 41, **Figure 10**), i.e. a decrease of three orders of magnitude compared to the parent inhibitory CPS1-peptide (K_i 7 nM, **Figure 8A**). Removing the residual lysine-backbone decreased potency by another order of magnitude (compound 42, K_i 77 µM, **Figure 10**), but could partially be recovered by testing a few substitutions of the lysine side chains (compounds 43-46, K_i 36-79 µM, **Figure 10**).
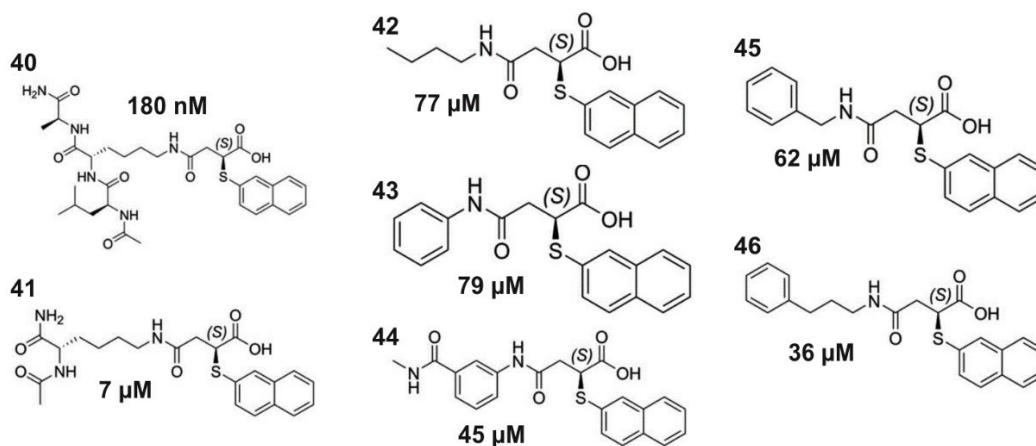
Figure 10: Small molecule inhibitors derived from the 3-(2-naphthylmethyl-thio)-succinyl inhibitory acyl. Chemical structures of the inhibitors and their potency (in bold) are shown. Truncation of the highly potent inhibitory peptide 3NMTS-CPS1-K527 **(Figure 8A)** resulted in an order of magnitude less potent tripeptide (compound 40, Ki 180 nM) and another order of magnitude less potent acetyl-/amine-protected 3NMTS-lysine (compound 41, Ki 7µM). Further trimming and substitutions of the lysine-scaffold yielded several small molecule inhibitors carrying the 3NMTS acyl with Kis in the two-digit micromolar range (compounds 42-46).

Future studies can build on the highly potent and selective acyls identified in **publication 1 and 2**, but need to improve the lysine scaffold to recover the loss of potency arising from peptide truncation. High-resolution structural data obtained within **publication 3** can be used to grow and develop such small molecule scaffolds to recover potency by targeting affinity hot

spots around the Sirt5 lysine binding-site. Furthermore, prospective studies need to address the cellular resorption and *in vivo* half-life of such compounds, which are important features to enable their use not only for *in vitro* investigations, but also for *in vivo* studies or pharmacologic treatments of Sirt5-related pathologies like metabolic dysfunctions or neurodegeneration [88,170].

3.4. SirReal2 is a potent and selective Sirt2 inhibitor

Our efforts to optimize the recombinant production of human Sirt4 (hSirt4) resulted in low yields of about 30 µg per liter of *E. Coli* culture, but the purification process could be optimized to obtain > 95% pure and active hSirt4 protein. The ability to produce hSirt4 protein enabled the participation in a collaborative drug development project, which aimed to establish a selective and drug-like Sirt2 inhibitor. Therefore, our collaborators screened an in-house compound library and identified molecules of the aminothiazole-family as *in vitro* Sirt2 inhibitors with sub-micromolar potency. Of those, SirReal2 (**Sir**tuin-**rea**rranging **l**igand 2) was the most potent compound (IC$_{50}$ 140 nM) and did not significantly affect other Sirtuin activities (Sirt1/3 deacetylation, Sirt5 desuccinylation, Sirt6 demyristoylation) *in vitro* **(Figure 11A,B)**, while NAM inhibited all Sirtuins as a positive control. We contributed to this project by testing SirReal2 and NAM against Sirt4 deacetylation of acetyl-NNT397 peptide **(sequence given in publication 4)**, which was found to yield interpretable signals in our lab.
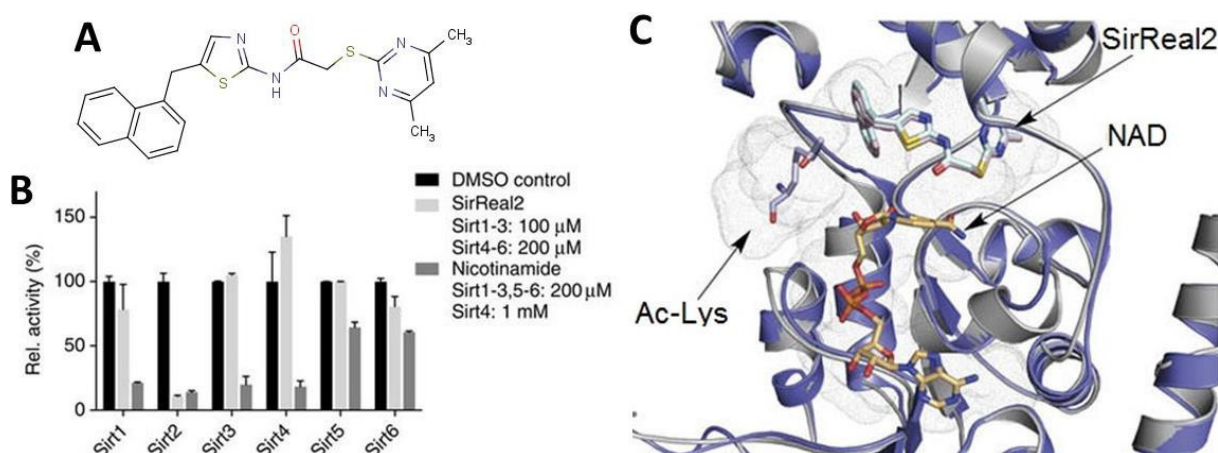

Figure 11: Characterization of the Sirt2 specific inhibitor SirReal2. (A) Chemical structure of SirReal2. (B) Selectivity study of SirReal2 against Sirt1-6, revealing its isoform specificity for Sirt2. SirReal2 was tested at 0, 100 or 200 µM dose, while NAM was tested at a 200 µM dose on Sirt1-6 except Sirt4, where it was tested at a 1 mM dose. Compounds were tested on Sirt1-4 deacetylation, Sirt5 desuccinylation and Sirt6 demyristoylation. (C) SirReal2 binds in vicinity to co-substrate NAD+ and protrudes into the acetyl-lysine channel, thereby repulsing the substrate lysine.

Our collaborators solved complex crystal structures of Sirt2 with SirReal2 in presence or absence of substrate and NAD$^+$. These led to the conclusions that SirReal2 introduces major rearrangements in the Sirt2 structure, occupies part of the acetyl-lysine binding site and forces the acetyl-lysine 5 Å out of its physiological position **(Figure 11C)**. Kinetic analysis confirmed that SirReal2 hampers acetyl-lysine binding, which, together with the structural Sirt2 rearrangements, appears to be responsible for efficient Sirt2 inhibition. Interestingly, *in vivo* experiments

identified two inhibited Sirt2 functions upon SirReal2 treatment, BubR and α-tubulin deacety-lation, proving the compound's cellular availability. Therefore, SirReal2 is suitable as a modulator of Sirt2 activity in *in vitro* and *in vivo* studies and could serve as a lead for prospective therapeutic treatments of Sirt2 related pathologies like neurodegenerative diseases (Alzheimer) or glioma and brain cancer [61].

3.5. Biochemical and structural characterization of Sirt4

In contrast to most other isoforms, the mitochondrial Sirtuin 4 is poorly understood. Its structure was not resolved so far and its primary activity is unknown. Deacetylase [111], ADP-ribosyltransferase [109] and delipoylase [113] activities were reported, but the *in vitro* kinetics of these activities are weak compared to robust primary functions of other Sirtuins. A sequence dependent activity is conceivable and thus a microarray study testing 6800 different acetylated peptides as Sirt4 substrates was conducted [181]. However, it showed a significant impact of peptide sequence on Sirt4 activity, but did not enhance it by the orders of magnitude, which would be necessary to draw level with other robust Sirtuin activities. These results and other reported features of Sirt4 indicating a functional deacylase activity, e.g., the conserved catalytic core [182] or its low deacetylase [111,181] and delipoylase activity [113], suggested an unidentified, robust activity or the necessity of a stimulating ligand, as in the case of Sirt6 [140].

Thus, hSirt4 acyl-specificity was screened using the CPS1-K527 acyl-library described in chapter 3.1. Initial screening at high peptide concentration in a coupled Sirtuin assay showed weak deacetylase activity and confirmed the slightly increased delipoylation and debiotinylation activity [113] **(Figure 12A,B)**. Strikingly, Sirt4 showed an 8-fold increased activity towards the non-physiologic 3,3-dimethyl-succinyl (DMS) modification. Testing chemically similar lysine acylations, which might be physiologic PTMs due to an existing reactive metabolite, identified 3-hydroxy-3-methyl-glutaryl (HMG) as a Sirt4 substrate-acyl with 3-fold improved activity compared to deacetylation **(Figure 12A,B)** (activity will be abbreviated as de-HMG-ylation in the following). We collaboratively demonstrated that the metabolite HMG-CoA modifies the model protein Cyclophilin-A (CypA) and that Sirt4 de-HMG-ylates CypA *in vitro*, indicating a physiological significance **(see Figure 1e,f and SI figure 1d,e in publication 5)**. Confirmingly, an independent study proved the existence of HMG as a physiologic lysine-PTM and demonstrated Sirt4 de-HMG-ylase activity *in vivo* by using HMG-lysine specific antibodies [183].

Determining Michaelis-Menten kinetics for the above mentioned CPS1-K527 peptide substrates confirmed weak deacetylation efficiency (3.7 ± 0.7 M^{-1} s^{-1}) due to a very high K_M, whereas the lipoylated peptide showed an improved K_M but lower k_{cat} with a huge error due to poor peptide solubility (170 ± 230 M^{-1} s^{-1}) **(Figure 12C)**. Remarkably, DMS- and HMG- modified CPS1-K527 peptides showed both, enhanced K_M and k_{cat}, leading to two orders of magnitude increased catalytic efficiencies (HMG: 546 ± 67 $M^{-1}s^{-1}$; DMS: 412 ± 41 $M^{-1}s^{-1}$) compared to

deacetylation **(Figure 12C)**. These are close to the range of primary functions of other Sirtuins, such as Sirt2 deacetylation (1400 $M^{-1}s^{-1}$ for acetyl-H3K27 peptide) [139] or Sirt5 desuccinylation (2000 $M^{-1}s^{-1}$ for succinyl-GDH-K503 peptide) [57].
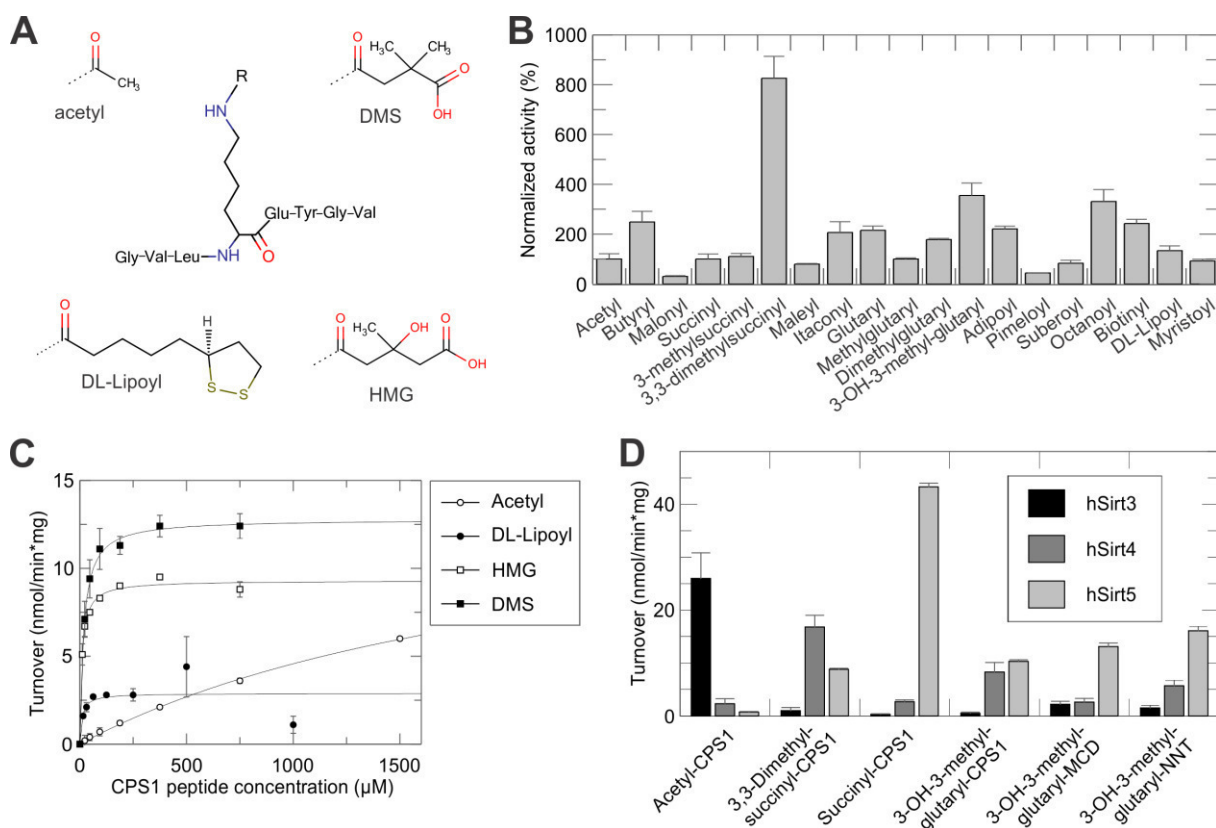

Figure 12: Sirt4 selectivity profiling and testing mitochondrial Sirtuin activity on improved Sirt4 substrate-acyls. (A) Chemical structure of the CPS1-K527 peptide and Sirt4 substrate acyls. (B) Screening hSirt4 activity towards a variety of acylated CPS1-K527 peptides. (C) Michaelis-Menten kinetics of hSirt4 for acetyl-, DL-lipoyl-, DMS- and HMG-CPS1-K527 peptides and (D) comparison of mitochondrial hSirt3,4 and 5 activities towards acetyl, DMS-, succinyl-, HMG-CPS1 and two other HMG-modified substrate peptides (HMG-MCD, HMG-NNT; **peptide sequences are given in publication 5)**.

However, testing Sirt4 activity on HMG-CPS1 peptide in an MS-based assay revealed a similar K_M, but significantly lower v_{max} **(see Figure 12C and SI Figure 1c in publication 5)**. Over time course assays, a significantly increasing amount of a 560 Da UV_{280} absorbing molecule, likely to be ADP-ribose, was detected in assays with HMG-, but not with acetyl-CPS1-K527 peptide. The discrepancy between the coupled and MS-based assay systems might thus rely on their different readouts. The MS-based assay detects substrate and product peptides directly, which contrasts the indirect detection of substrate turnover via the by-product NAM in the coupled assay [184]. Generation of ADP-ribose as revealed by MS-based assays implies a Sirt4 glycohydrolase activity stimulated by HMG-CPS1-K527 peptide, and both glycohydrolase and de-HMG-ylase activity would contribute to the strong signal in the coupled continuous assay. In contrast, only the acyl-hydrolysis is taken into account in the MS-based assay for quantification of the Sirt4 deacylation reaction. A similar effect has been reported for Hst2 assays with an

artificial homocitrulline-lysine peptide substrate, which yielded NAM, ADP-ribose and the recovered homocitrulline-lysine as products [185]. However, further work is clearly necessary to elucidate this issue.

Testing the specificity of mitochondrial Sirtuins towards the improved Sirt4 substrates showed no significant overlap of Sirt3 and 4, since the robust deacetylase Sirt3 showed negligible activity on DMS- and HMG-CPS1 peptide. However, Sirt5 showed lower activity on DMS-CPS1 peptide than Sirt4, but de-HMG-ylated peptides with comparable or better efficiency as Sirt4, depending on substrate sequence **(Figure 12D)**. It is tempting to speculate that Sirt4 exhibits a not yet identified deacylase activity due to the similar Sirt4/5 de-HMGylase efficiencies, which contrast the clearly discriminated primary activities of the other mitochondrial Sirtuins 3 (deacetylation) and 5 (acting on acyls with distal carboxylic groups) [88,102].

Clearly, the crystal structure of Sirt4 would provide valuable information to unveil its activity and other specific features. Since crystallization trials using hSirt4 were unsuccessful due to low yield and solubility, the highly similar orthologues from *D. rerio* (zebrafish; zSirt4) and *X. tropicalis* (western clawed frog; xSirt4) were recombinantly expressed in *E. Coli* and purified for crystallization experiments. Aligning hSirt4, xSirt4 and zSirt4 catalytic core sequences showed roughly 80% similarity and the orthologues shared comparable activity profiles **(see Figure 1g in publication 5)**. Strikingly, xSirt4 constructs yielded crystals with high resolution below 2 Å in presence of ADP-ribose, which enabled the determination of the first Sirt4 structure **(Figure 13A,B)**.
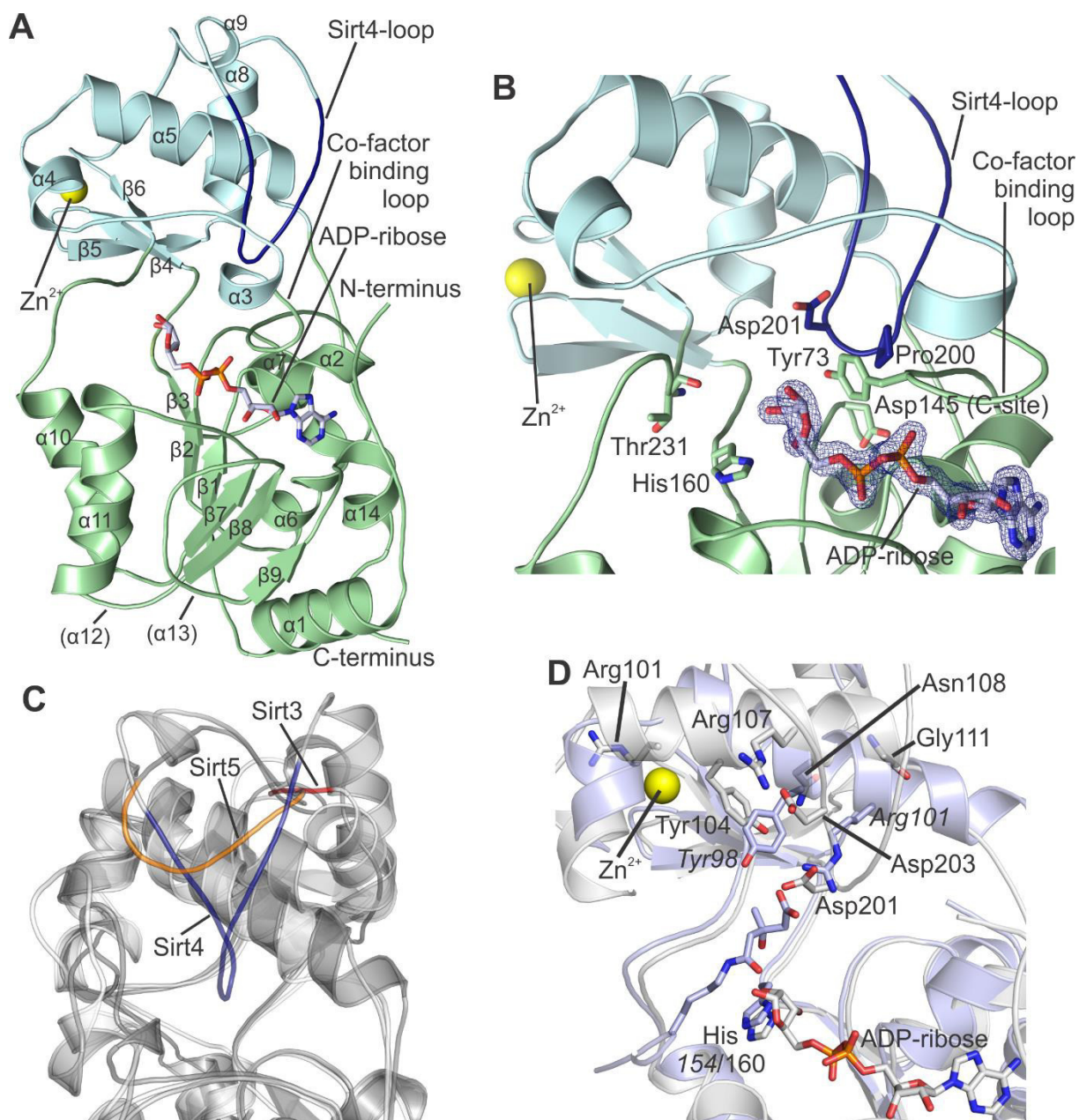
Figure 13: Analysis of the Sirt4 crystal structure. (A) Overall xSirt4/ADP-ribose complex structure with universal Sirtuin secondary structure labeling. (B) Sirt4 active-site with electron-density for the ligand ADP-ribose shown (2FoFc, σ = 1.0). xSirt4 is shown in green (Rossmann-fold), light-blue (zinc-binding domain) or dark blue ("Sirt4-loop") cartoon representation, while important amino acids are shown as respectively domain cpk color-coded sticks and ligands as grey cpk color-coded sticks. (C) Overlay of Sirt3 (light grey, red), 4 (grey, blue) and 5 (dark grey, orange) structures in cartoon representation, demonstrating the different length of their zinc-binding domain loop. (D) Overlay of xSirt4/ADP-ribose (grey) and zSirt5/HMG-CPS1-K527 (light blue) complexes with proteins and peptide shown in cartoon style and amino acids of interest, ADP-ribose and acyl-lysine shown as respectively color-coded cpk sticks. The bound zinc ion is shown as a yellow sphere in (A), (B) and (D).

The xSirt4/ADP-ribose complex resembled the typical Sirtuin overall structure with a Rossmann-fold and a zinc-binding domain connected by several loops and the active-site located in between the two domains **(Figure 13A)**. Interestingly, Sirt4 comprises an elongated Zinc-binding domain loop, which is highly conserved among chordate Sirt4 orthologues, but unique in the Sirtuin family **(see alignments in Figure 2c,d or SI Figures 2c,d in publication 5)** and extensive enough to contribute to the active-site lining **(Figure 13A,B)**. The loop's core can be deleted and is thus dispensable for the protein's integrity, but mutants showed

slightly higher K_M and increased k_{cat} for acetyl- and HMG-CPS1-K527 peptide, suggesting a role in active-site dynamics **(see Table 3 in publication 5)**. This hypothesis is supported by another crystal structure of an xSirt4/thioacetyl-ADP-ribose product complex, in which the Sirt4-loop is flexible and detached from the active-site, suggesting changing conformations during catalysis **(see SI Figure 2e in publication 5)**. However, it is also flexible in another solved xSirt4/ADP-ribose complex, thus, determining its role in active-site dynamics clearly needs further investigation.

Another Sirt4 feature is an additional entry channel on top of the acyl-lysine binding site, which is constituted by amino acids mostly conserved in Sirt4, while other isoforms comprise variable residues in this area. This structural feature is reminiscent of the hydrophobic pocket of Sirt6, which either enables its demyristoylation activity or probably binds free fatty acids and thereby enhances deacetylation [140]. Although the Sirt4 and 6 channels are of different shape and size, a similar effect of additional ligands is conceivable. Therefore, several fatty and (di)carboxylic acids were tested as effectors on Sirt4 deacetylation and de-HMG-ylation and showed that DL-lipoic acid acts as an inhibitor at high concentrations **(see SI Figure 3b in publication 5)**. Consistently, a lipoyl-lysine docked in the active-site partially occupied the acyl-lysine binding-site and the additional channel **(see Figure 3a in publication 5)**, which rationalizes both inhibition by DL-lipoic acid and delipoylation of a substrate lysine by Sirt4. It is also conceivable that the channel serves as a binding site for a substrate anchor to enhance the deacylation of a nearby lysine residue similar to the recently reported SirTM, which ADP-ribosylates peptides and proteins after recognition of an adjacent biotinylation site [186].

Since a Sirt4/peptide complex could not be crystallized, a zSirt5/HMG-CPS1-K527 complex was solved and overlaid with the xSirt4/ADP-ribose structure to investigate Sirt4 acyl recognition **(Figure 13D)**. Like glutaryl-lysine, HMG-lysine is recognized by the Sirt5 Tyr-X-X-Arg-motif at the back of the acyl-lysine binding site. Sirt4 comprises the same motif in this region, but it is shifted by one helix winding, with Tyr104 pointing back to the active-site, but Arg107 away from it. Mutating both residues lead to a 2- to 4-fold increased K_M for HMG-CPS1-K527 peptide, suggesting a role in acyl-recognition and a reorientation of Arg107 upon substrate-binding. Interestingly, Asp201 of the Sirt4-loop overlays with Arg101 of the Sirt5 Tyr-X-X-Arg motif and is thus in an ideal position for acyl-recognition. Therefore, acyls of varying length with terminal amines to complement the negative charge of Asp201 were tested, but did not show significant Sirt4 activity. Additionally, an Asp201Ala mutant only showed minor differences in kinetic parameters for deacetylation and de-HMG-ylation. Thus, both experimental setups indicated that this residue is not directly involved in acyl-recognition. It is tempting to speculate, that the Sirt4 active-site and the zinc-binding domain loop rearrange upon substrate binding and possibly throughout the catalytic cycle. This would explain the influence of the offside Arg107 on

de-HMG-ylation activity, the lacking acyl-recognition of the well-positioned Asp201, and the detached loop in the xSirt4/thioacetyl-ADP-ribose product structure.

A third structural feature of Sirt4 is a more pronounced positive charge in its nucleotide-binding site compared to other Sirtuins. We hypothesized, that this could influence binding of co-substrate NAD$^+$ and inhibition by NAM or NADH. The K_M of 62 µM for NAD$^+$ was within the lower range of 10 to 600 µM reported for Sirtuins [129,141]. NAM potently inhibited Sirt4 (IC$_{50}$ 31 ± 2 µM), which strongly indicates an influence at physiologic concentrations of 10-400 µM [149], but the effect is comparable to other Sirtuins (e.g. IC$_{50}$ Sirt1: 62 µM, Sirt3: 43 µM and Sirt5 desuccinylation: 21 µM) [146]. Interestingly, in comparison to the weak effects of NADH on other Sirtuins in the millimolar range [145], Sirt4 is much more sensitive (IC$_{50}$ 126 ± 12 µM (at 500 µM NAD$^+$)) and probably affected at the physiologic 30 µM free NADH in mitochondria [187]. The more positively charged nucleotide-binding site could be the key-driver for this effect. It might facilitate NADH binding in an inhibiting, so called unproductive, conformation with the reduced NAM residing outside the so called "C-site", which favors oxidized nucleotides for productive NAD$^+$ binding [145]. Our data implies a unique regulation mechanism by NADH and a distinct metabolic sensory function of Sirt4 demanding further investigation in a cellular context.

The last classification of Sirtuins was performed using sequence alignments by Frye in 2000 [182] **(Figure 14A)**, but several structures of bacterial and eucaryotic Sirtuins have been determined since then, which could be used to structurally investigate Sirtuin phylogeny. Therefore, we conducted a new structure-based alignment with all known bacterial, yeast and Sirt1-6 structures. Additionally, the 195 verified UniProt chordate sequences of Sirt1-7 were aligned to this structure-based alignment to generate a more redundant phylogenetic tree of the Sirtuin family **(Figure 14B)**.
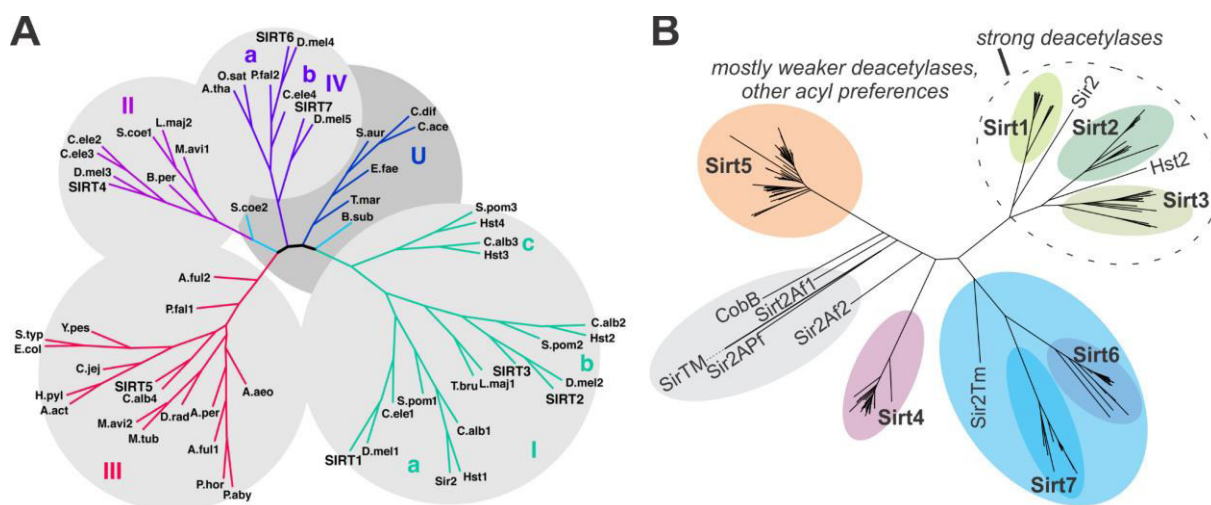

Figure 14: Phylogenetic trees of bacterial and eukaryotic Sirtuins. (A) Phylogenetic tree from Frye, 2000 [182] based on sequence alignments (used with permission of Elsevier). (B) New phylogenetic tree derived from a structure-based alignment supplemented with 195 sequences of chordate Sirt1-7.

Overall, the new tree mostly confirms the phylogenetic analysis of Frye, but displays a few differences **(Figure 14A,B)**. The ancient *T. maritima* Sir2Tm (Frye nomenclature: T.mar) is now closer to the Sirt6/7 branch and Sirt5 is more separated from the bacterial Sirs like *E. Coli* CobB (E.col) and *A. fulgidus* Sir2Af1 (A.ful1). The latter are now grouped together with the other bacterial *A. fulgidus* Sir2Af2 (A.ful2) and *P. falciparum* Sir2Apf (P.fal1) in the new classification. Remarkably, both trees discriminate Sirtuins with different deacylase activity. While the robust deacetylases Sirt1, 2 and 3 are grouped together, the weak deacetylases Sirt4-7 are clearly separated. Interestingly, both trees place Sirt6 and 7 on neighboring branches, which is reminiscent to the Sirt1-3 deacetylase branch and implies a similar structure and/or deacylase activity. Including more sequences and structures of ancestral Sirtuins could reconstruct the evolution from bacterial Sirtuins to the seven mammalian isoforms and might be of avail to understand their function and regulatory role.

4. **Literature**

1. Laskowski, R. A., Gerick, F. & Thornton, J. M. The structural basis of allosteric regulation in proteins. *FEBS Lett.* **583,** 1692–1698 (2009).

2. Gilbert, S. F. Differential Gene Transcription. (2000).

3. Walsh, C. T., Garneau-Tsodikova, S. & Gatto, G. J. Protein posttranslational modifications: the chemistry of proteome diversifications. *Angew. Chem. Int. Ed Engl.* **44,** 7342–7372 (2005).

4. Jensen, O. N. Interpreting the protein language using proteomics. *Nat. Rev. Mol. Cell Biol.* **7,** 391–403 (2006).

5. Chau, V. *et al.* A multiubiquitin chain is confined to specific lysine in a targeted short-lived protein. *Science* **243,** 1576–1583 (1989).

6. Thrower, J. S., Hoffman, L., Rechsteiner, M. & Pickart, C. M. Recognition of the polyubiquitin proteolytic signal. *EMBO J.* **19,** 94–102 (2000).

7. Hicke, L. Protein regulation by monoubiquitin. *Nat. Rev. Mol. Cell Biol.* **2,** 195–201 (2001).

8. Xu, C. & Ng, D. T. W. Glycosylation-directed quality control of protein folding. *Nat. Rev. Mol. Cell Biol.* **16,** 742–752 (2015).

9. Haines, N. & Irvine, K. D. Glycosylation regulates Notch signalling. *Nat. Rev. Mol. Cell Biol.* **4,** 786–797 (2003).

10. Wells, L., Whelan, S. A. & Hart, G. W. O-GlcNAc: a regulatory post-translational modification. *Biochem. Biophys. Res. Commun.* **302,** 435–441 (2003).

11. Johnson, L. N. & Lewis, R. J. Structural basis for control by phosphorylation. *Chem. Rev.* **101,** 2209–2242 (2001).

12. Choudhary, C. & Mann, M. Decoding signalling networks by mass spectrometry-based proteomics. *Nat. Rev. Mol. Cell Biol.* **11,** 427–439 (2010).

13. Choudhary, C., Weinert, B. T., Nishida, Y., Verdin, E. & Mann, M. The growing landscape of lysine acetylation links metabolism and cell signalling. *Nat. Rev. Mol. Cell Biol.* **15,** 536–550 (2014).

14. Kim, G.-W. & Yang, X.-J. Comprehensive lysine acetylomes emerging from bacteria to humans. *Trends Biochem. Sci.* **36,** 211–220 (2011).

15. Soufi, B., Soares, N. C., Ravikumar, V. & Macek, B. Proteomics reveals evidence of cross-talk between protein modifications in bacteria: focus on acetylation and phosphorylation. *Curr. Opin. Microbiol.* **15,** 357–363 (2012).

16. Allfrey, V. G., Faulkner, R. & Mirsky, A. E. ACETYLATION AND METHYLATION OF HISTONES AND THEIR POSSIBLE ROLE IN THE REGULATION OF RNA SYNTHESIS. *Proc. Natl. Acad. Sci. U. S. A.* **51,** 786–794 (1964).

17. L'Hernault, S. W. & Rosenbaum, J. L. Chlamydomonas .alpha.-tubulin is posttranslationally modified by acetylation on the .epsilon.-amino group of a lysine. *Biochemistry (Mosc.)* **24,** 473–478 (1985).

18. Gu, W. & Roeder, R. G. Activation of p53 sequence-specific DNA binding by acetylation of the p53 C-terminal domain. *Cell* **90,** 595–606 (1997).

19. Ott, M. *et al.* Acetylation of the HIV-1 Tat protein by p300 is important for its transcriptional activity. *Curr. Biol. CB* **9,** 1489–1492 (1999).

20. Kim, S. C. *et al.* Substrate and functional diversity of lysine acetylation revealed by a proteomics survey. *Mol. Cell* **23,** 607–618 (2006).

21. Choudhary, C. *et al.* Lysine acetylation targets protein complexes and co-regulates major cellular functions. *Science* **325,** 834–840 (2009).

22. Wang, Q. *et al.* Acetylation of metabolic enzymes coordinates carbon source utilization and metabolic flux. *Science* **327,** 1004–1007 (2010).

23. Zhao, S. *et al.* Regulation of cellular metabolism by protein lysine acetylation. *Science* **327,** 1000–1004 (2010).

24. Lundby, A. *et al.* Proteomic analysis of lysine acetylation sites in rat tissues reveals organ specificity and subcellular patterns. *Cell Rep.* **2,** 419–431 (2012).

25. Weinert, B. T. *et al.* Proteome-wide mapping of the Drosophila acetylome demonstrates a high degree of conservation of lysine acetylation. *Sci. Signal.* **4,** ra48 (2011).

26. Gnad, F. *et al.* Evolutionary constraints of phosphorylation in eukaryotes, prokaryotes, and mito-chondria. *Mol. Cell. Proteomics MCP* **9,** 2642–2653 (2010).

27. Garrity, J., Gardner, J. G., Hawse, W., Wolberger, C. & Escalante-Semerena, J. C. N-lysine propio-nylation controls the activity of propionyl-CoA synthetase. *J. Biol. Chem.* **282,** 30239–30245 (2007).

28. Chen, Y. *et al.* Lysine propionylation and butyrylation are novel post-translational modifications in histones. *Mol. Cell. Proteomics MCP* **6,** 812–819 (2007).

29. Cheng, Z. *et al.* Molecular characterization of propionyllysines in non-histone proteins. *Mol. Cell. Proteomics MCP* **8,** 45–52 (2009).

30. Tan, M. *et al.* Identification of 67 histone marks and histone lysine crotonylation as a new type of histone modification. *Cell* **146,** 1016–1028 (2011).

31. Kawai, Y. *et al.* Formation of Nepsilon-(succinyl)lysine in vivo: a novel marker for docosahexaenoic acid-derived protein modification. *J. Lipid Res.* **47,** 1386–1398 (2006).

32. Zhang, Z. *et al.* Identification of lysine succinylation as a new post-translational modification. *Nat. Chem. Biol.* **7,** 58–63 (2011).

33. Peng, C. *et al.* The first identification of lysine malonylation substrates and its regulatory enzyme. *Mol. Cell. Proteomics MCP* **10,** M111.012658 (2011).

34. Stevenson, F. T., Bursten, S. L., Locksley, R. M. & Lovett, D. H. Myristyl acylation of the tumor ne-crosis factor alpha precursor on specific lysine residues. *J. Exp. Med.* **176,** 1053–1062 (1992).

35. Stevenson, F. T., Bursten, S. L., Fanton, C., Locksley, R. M. & Lovett, D. H. The 31-kDa precursor of interleukin 1 alpha is myristoylated on specific lysines within the 16-kDa N-terminal propiece. *Proc. Natl. Acad. Sci. U. S. A.* **90,** 7245–7249 (1993).

36. Berndsen, C. E. & Denu, J. M. Catalysis and substrate selection by histone/protein lysine acetyl-transferases. *Curr. Opin. Struct. Biol.* **18,** 682–689 (2008).

37. Kaczmarska, Z. *et al.* Structure of p300 in complex with acyl-CoA variants. *Nat. Chem. Biol.* **13,** 21–29 (2017).

38. Sabari, B. R. *et al.* Intracellular crotonyl-CoA stimulates transcription through p300-catalyzed his-tone crotonylation. *Mol. Cell* **58,** 203–215 (2015).

39. Berndsen, C. E., Albaugh, B. N., Tan, S. & Denu, J. M. Catalytic mechanism of a MYST family histone acetyltransferase. *Biochemistry (Mosc.)* **46,** 623–629 (2007).

40. Ringel, A. E. & Wolberger, C. Structural basis for acyl-group discrimination by human Gcn5L2. *Acta Crystallogr. Sect. Struct. Biol.* **72,** 841–848 (2016).

41. Hu, A., Britton, L. M. & Garcia, B. A. Investigating the specificity of histone acetyltransferase activity for producing rare modifications on histones using mass spectrometry. (2014).

42. Wagner, G. R. & Payne, R. M. Widespread and enzyme-independent Nε-acetylation and Nε-suc-cinylation of proteins in the chemical conditions of the mitochondrial matrix. *J. Biol. Chem.* **288,** 29036–29045 (2013).

43. Simic, Z., Weiwad, M., Schierhorn, A., Steegborn, C. & Schutkowski, M. The ε-Amino Group of Pro-tein Lysine Residues Is Highly Susceptible to Nonenzymatic Acylation by Several Physiological Acyl-CoA Thioesters. *Chembiochem Eur. J. Chem. Biol.* **16,** 2337–2347 (2015).

44. Weinert, B. T. *et al.* Acetylation dynamics and stoichiometry in Saccharomyces cerevisiae. *Mol. Syst. Biol.* **10,** 716 (2014).

45. Wagner, G. R. & Hirschey, M. D. Nonenzymatic protein acylation as a carbon stress regulated by sirtuin deacylases. *Mol. Cell* **54,** 5–16 (2014).

46. Garland, P. B., Shepherd, D. & Yates, D. W. Steady-state concentrations of coenzyme A, acetyl-coenzyme A and long-chain fatty acyl-coenzyme A in rat-liver mitochondria oxidizing palmitate. *Biochem. J.* **97,** 587–594 (1965).

47. Hansford, R. G. & Johnson, R. N. The steady state concentrations of coenzyme A-SH and coenzyme A thioester, citrate, and isocitrate during tricarboxylate cycle oxidations in rabbit heart mitochondria. *J. Biol. Chem.* **250,** 8361–8375 (1975).

48. Moellering, R. & Cravatt, B. Functional lysine modification by an intrinsically reactive primary glycolytic metabolite. *Science* **341,** 549–553 (2013).

49. Haberland, M., Montgomery, R. L. & Olson, E. N. The many roles of histone deacetylases in development and physiology: implications for disease and therapy. *Nat. Rev. Genet.* **10,** 32–42 (2009).

50. Somoza, J. R. *et al.* Structural snapshots of human HDAC8 provide insights into the class I histone deacetylases. *Struct. Lond. Engl. 1993* **12,** 1325–1334 (2004).

51. Lombardi, P. M., Cole, K. E., Dowling, D. P. & Christianson, D. W. Structure, Mechanism, and Inhibition of Histone Deacetylases and Related Metalloenzymes. *Curr. Opin. Struct. Biol.* **21,** 735–743 (2011).

52. J, R. & I, H. Four genes responsible for a position effect on expression from HML and HMR in Saccharomyces cerevisiae. *Genetics* **116,** 9–22 (1987).

53. Tsang, A. W. & Escalante-Semerena, J. C. CobB, a new member of the SIR2 family of eucaryotic regulatory proteins, is required to compensate for the lack of nicotinate mononucleotide:5,6-dimethylbenzimidazole phosphoribosyltransferase activity in cobT mutants during cobalamin biosynthesis in Salmonella typhimurium LT2. *J. Biol. Chem.* **273,** 31788–31794 (1998).

54. Blander, G. & Guarente, L. The Sir2 family of protein deacetylases. *Annu. Rev. Biochem.* **73,** 417–435 (2004).

55. Frye, R. A. Characterization of five human cDNAs with homology to the yeast SIR2 gene: Sir2-like proteins (sirtuins) metabolize NAD and may have protein ADP-ribosyltransferase activity. *Biochem. Biophys. Res. Commun.* **260,** 273–279 (1999).

56. Imai, S., Armstrong, C. M., Kaeberlein, M. & Guarente, L. Transcriptional silencing and longevity protein Sir2 is an NAD-dependent histone deacetylase. *Nature* **403,** 795–800 (2000).

57. Du, J. *et al.* Sirt5 is a NAD-dependent protein lysine demalonylase and desuccinylase. *Science* **334,** 806–809 (2011).

58. Jiang, H. *et al.* SIRT6 regulates TNF-α secretion through hydrolysis of long-chain fatty acyl lysine. *Nature* **496,** 110–113 (2013).

59. Brachmann, C. B. *et al.* The SIR2 gene family, conserved from bacteria to humans, functions in silencing, cell cycle progression, and chromosome stability. *Genes Dev.* **9,** 2888–2902 (1995).

60. Mei, Z. *et al.* Sirtuins in metabolism, DNA repair and cancer. *J. Exp. Clin. Cancer Res. CR* **35,** 182 (2016).

61. Carafa, V. *et al.* Sirtuin functions and modulation: from chemistry to the clinic. *Clin. Epigenetics* **8,** 61 (2016).

62. Michishita, E., Park, J. Y., Burneskis, J. M., Barrett, J. C. & Horikawa, I. Evolutionarily conserved and nonconserved cellular localizations and functions of human SIRT proteins. *Mol. Biol. Cell* **16,** 4623–4635 (2005).

63. Iwahara, T., Bonasio, R., Narendra, V. & Reinberg, D. SIRT3 functions in the nucleus in the control of stress-related gene expression. *Mol. Cell. Biol.* **32,** 5022–5034 (2012).

64. Kiran, S. *et al.* Intracellular distribution of human SIRT7 and mapping of the nuclear/nucleolar localization signal. *FEBS J.* **280,** 3451–3466 (2013).

65. Tanno, M., Sakamoto, J., Miura, T., Shimamoto, K. & Horio, Y. Nucleocytoplasmic shuttling of the NAD+-dependent histone deacetylase SIRT1. *J. Biol. Chem.* **282,** 6823–6832 (2007).

66. North, B. J. & Verdin, E. Interphase Nucleo-Cytoplasmic Shuttling and Localization of SIRT2 during Mitosis. *PLoS ONE* **2,** (2007).

67. Sundaresan, N. R., Samant, S. A., Pillai, V. B., Rajamohan, S. B. & Gupta, M. P. SIRT3 Is a Stress-Responsive Deacetylase in Cardiomyocytes That Protects Cells from Stress-Mediated Cell Death by Deacetylation of Ku70. *Mol. Cell. Biol.* **28,** 6384–6401 (2008).

68. Nishida, Y. *et al.* SIRT5 Regulates both Cytosolic and Mitochondrial Protein Malonylation with Glycolysis as a Major Target. *Mol. Cell* **59,** 321–332 (2015).

69. Kaeberlein, M., McVey, M. & Guarente, L. The SIR2/3/4 complex and SIR2 alone promote longevity in Saccharomyces cerevisiae by two different mechanisms. *Genes Dev.* **13,** 2570–2580 (1999).

70. Berdichevsky, A., Viswanathan, M., Horvitz, H. R. & Guarente, L. C. elegans SIR-2.1 interacts with 14-3-3 proteins to activate DAF-16 and extend life span. *Cell* **125,** 1165–1177 (2006).

71. Pan, K. Z. *et al.* Inhibition of mRNA translation extends lifespan in Caenorhabditis elegans. *Aging Cell* **6,** 111–119 (2007).

72. Rogina, B. & Helfand, S. L. Sir2 mediates longevity in the fly through a pathway related to calorie restriction. *Proc. Natl. Acad. Sci. U. S. A.* **101,** 15998–16003 (2004).

73. Wood, J. G. *et al.* Sirtuin activators mimic caloric restriction and delay ageing in metazoans. *Nature* **430,** 686–689 (2004).

74. Bauer, J. H. *et al.* dSir2 and Dmp53 interact to mediate aspects of CR-dependent lifespan extension in D. melanogaster. *Aging* **1,** 38–48 (2009).

75. Aström, S. U., Cline, T. W. & Rine, J. The Drosophila melanogaster sir2+ gene is nonessential and has only minor effects on position-effect variegation. *Genetics* **163,** 931–937 (2003).

76. Frankel, S., Ziafazeli, T. & Rogina, B. dSir2 and longevity in Drosophila. *Exp. Gerontol.* **46,** 391–396 (2011).

77. Kanfi, Y. *et al.* The sirtuin SIRT6 regulates lifespan in male mice. *Nature* **483,** 218–221 (2012).

78. Dang, W. The controversial world of sirtuins. *Drug Discov. Today Technol.* **12,** e9–e17 (2014).

79. Kaeberlein, M. Lessons on longevity from budding yeast. *Nature* **464,** 513–519 (2010).

80. Lee, G. D. *et al.* Dietary deprivation extends lifespan in Caenorhabditis elegans. *Aging Cell* **5,** 515–524 (2006).

81. Hansen, M. *et al.* Lifespan extension by conditions that inhibit translation in Caenorhabditis elegans. *Aging Cell* **6,** 95–110 (2007).

82. Wang, Y. *et al.* C. elegans 14-3-3 proteins regulate life span and interact with SIR-2.1 and DAF-16/FOXO. *Mech. Ageing Dev.* **127,** 741–747 (2006).

83. Burnett, C. *et al.* Absence of effects of Sir2 overexpression on lifespan in C. elegans and Drosophila. *Nature* **477,** 482–485 (2011).

84. Mattison, J. A. *et al.* Impact of caloric restriction on health and survival in rhesus monkeys from the NIA study. *Nature* **489,** 318–321 (2012).

85. Colman, R. J. *et al.* Caloric restriction delays disease onset and mortality in rhesus monkeys. *Science* **325,** 201–204 (2009).

86. Hall, J. A., Dominy, J. E., Lee, Y. & Puigserver, P. The sirtuin family's role in aging and age-associated pathologies. *J. Clin. Invest.* **123,** 973–979 (2013).

87. Xiong, Y. & Guan, K.-L. Mechanistic insights into the regulation of metabolic enzymes by acetylation. *J. Cell Biol.* **198,** 155–164 (2012).

88. Gertz, M. & Steegborn, C. Using mitochondrial sirtuins as drug targets: disease implications and available compounds. *Cell. Mol. Life Sci. CMLS* **73,** 2871–2896 (2016).

89. Vaquero, A. *et al.* Human SirT1 interacts with histone H1 and promotes formation of facultative heterochromatin. *Mol. Cell* **16,** 93–105 (2004).

90. Dobbin, M. M. *et al.* SIRT1 collaborates with ATM and HDAC1 to maintain genomic stability in neurons. *Nat. Neurosci.* **16,** 1008–1015 (2013).

91. Vazquez, B. N. *et al.* SIRT7 promotes genome integrity and modulates non-homologous end joining DNA repair. *EMBO J.* **35,** 1488–1503 (2016).

92. Michishita, E. *et al.* SIRT6 is a histone H3 lysine 9 deacetylase that modulates telomeric chromatin. *Nature* **452,** 492–496 (2008).

93. Toiber, D. *et al.* SIRT6 recruits SNF2H to DNA break sites, preventing genomic instability through chromatin remodeling. *Mol. Cell* **51,** 454–468 (2013).

94. Lim, J.-H. *et al.* Sirtuin 1 modulates cellular responses to hypoxia by deacetylating hypoxia-inducible factor 1alpha. *Mol. Cell* **38,** 864–878 (2010).

95. Hubbi, M. E., Hu, H., Kshitiz, null, Gilkes, D. M. & Semenza, G. L. Sirtuin-7 inhibits the activity of hypoxia-inducible factors. *J. Biol. Chem.* **288,** 20768–20775 (2013).

96. Lee, J. T. & Gu, W. SIRT1: Regulator of p53 Deacetylation. *Genes Cancer* **4,** 112–117 (2013).

97. Olmos, G., Lladó, Jerò & nia. Tumor Necrosis Factor Alpha: A Link between Neuroinflammation and Excitotoxicity. *Mediators Inflamm.* **2014,** e861231 (2014).

98. Li, L. & Yang, X.-J. Tubulin acetylation: responsible enzymes, biological functions and human diseases. *Cell. Mol. Life Sci. CMLS* **72,** 4237–4255 (2015).

99. Serrano, L. *et al.* The tumor suppressor SirT2 regulates cell cycle progression and genome stability by modulating the mitotic deposition of H4K20 methylation. *Genes Dev.* **27,** 639–653 (2013).

100. Inoue, T. *et al.* SIRT2, a tubulin deacetylase, acts to block the entry to chromosome condensation in response to mitotic stress. *Oncogene* **26,** 945–957 (2007).

101. Jing, E., Gesta, S. & Kahn, C. R. SIRT2 regulates adipocyte differentiation through FoxO1 acetylation/deacetylation. *Cell Metab.* **6,** 105–114 (2007).

102. Verdin, E., Hirschey, M. D., Finley, L. W. S. & Haigis, M. C. Sirtuin regulation of mitochondria: energy production, apoptosis, and signaling. *Trends Biochem. Sci.* **35,** 669–675 (2010).

103. Schwer, B., Bunkenborg, J., Verdin, R. O., Andersen, J. S. & Verdin, E. Reversible lysine acetylation controls the activity of the mitochondrial enzyme acetyl-CoA synthetase 2. *Proc. Natl. Acad. Sci. U. S. A.* **103,** 10224–10229 (2006).

104. Cimen, H. *et al.* Regulation of succinate dehydrogenase activity by SIRT3 in mammalian mitochondria. *Biochemistry (Mosc.)* **49,** 304–311 (2010).

105. Ahn, B.-H. *et al.* A role for the mitochondrial deacetylase Sirt3 in regulating energy homeostasis. *Proc. Natl. Acad. Sci. U. S. A.* **105,** 14447–14452 (2008).

106. Hirschey, M. D. *et al.* SIRT3 regulates mitochondrial fatty-acid oxidation by reversible enzyme deacetylation. *Nature* **464,** 121–125 (2010).

107. Schlicker, C. *et al.* Substrates and regulation mechanisms for the human mitochondrial sirtuins Sirt3 and Sirt5. *J. Mol. Biol.* **382,** 790–801 (2008).

108. Rangarajan, P., Karthikeyan, A., Lu, J., Ling, E.-A. & Dheen, S. T. Sirtuin 3 regulates Foxo3a-mediated antioxidant pathway in microglia. *Neuroscience* **311,** 398–414 (2015).

109. Ahuja, N. *et al.* Regulation of insulin secretion by SIRT4, a mitochondrial ADP-ribosyltransferase. *J. Biol. Chem.* **282,** 33583–33592 (2007).

110. Csibi, A. *et al.* The mTORC1 pathway stimulates glutamine metabolism and cell proliferation by repressing SIRT4. *Cell* **153,** 840–854 (2013).

111. Laurent, G. *et al.* SIRT4 coordinates the balance between lipid synthesis and catabolism by repressing malonyl CoA decarboxylase. *Mol. Cell* **50,** 686–698 (2013).

112. Laurent, G. *et al.* SIRT4 represses peroxisome proliferator-activated receptor α activity to suppress hepatic fat oxidation. *Mol. Cell. Biol.* **33,** 4552–4561 (2013).

113. Mathias, R. A. *et al.* Sirtuin 4 is a lipoamidase regulating pyruvate dehydrogenase complex activity. *Cell* **159,** 1615–1625 (2014).

114. Rardin, M. J. *et al.* SIRT5 regulates the mitochondrial lysine succinylome and metabolic networks. *Cell Metab.* **18,** 920–933 (2013).

115. Zhou, L. *et al.* SIRT5 promotes IDH2 desuccinylation and G6PD deglutarylation to enhance cellular antioxidant defense. *EMBO Rep.* **17,** 811–822 (2016).

116. Nakagawa, T., Lomb, D. J., Haigis, M. C. & Guarente, L. SIRT5 Deacetylates carbamoyl phosphate synthetase 1 and regulates the urea cycle. *Cell* **137,** 560–570 (2009).

117. Pan, M., Yuan, H., Brent, M., Ding, E. C. & Marmorstein, R. SIRT1 contains N- and C-terminal regions that potentiate deacetylase activity. *J. Biol. Chem.* **287,** 2468–2476 (2012).

118. Lakshminarasimhan, M. *et al.* Molecular architecture of the human protein deacetylase Sirt1 and its regulation by AROS and resveratrol. *Biosci. Rep.* **33,** (2013).

119. Schwer, B., North, B. J., Frye, R. A., Ott, M. & Verdin, E. The human silent information regulator (Sir)2 homologue hSIRT3 is a mitochondrial nicotinamide adenine dinucleotide-dependent deacetylase. *J. Cell Biol.* **158,** 647–657 (2002).

120. Haigis, M. C. *et al.* SIRT4 inhibits glutamate dehydrogenase and opposes the effects of calorie restriction in pancreatic beta cells. *Cell* **126,** 941–954 (2006).

121. Ardestani, P. M. & Liang, F. Sub-cellular localization, expression and functions of Sirt6 during the cell cycle in HeLa cells. *Nucleus* **3,** 442–451 (2012).

122. Kiran, S. *et al.* Intracellular distribution of human SIRT7 and mapping of the nuclear/nucleolar localization signal. *FEBS J.* **280,** 3451–3466 (2013).

123. Bellamacina, C. R. The nicotinamide dinucleotide binding motif: a comparison of nucleotide binding proteins. *FASEB J. Off. Publ. Fed. Am. Soc. Exp. Biol.* **10,** 1257–1269 (1996).

124. Sanders, B. D., Jackson, B. & Marmorstein, R. Structural basis for sirtuin function: what we know and what we don't. *Biochim. Biophys. Acta* **1804,** 1604–1616 (2010).

125. Min, J., Landry, J., Sternglanz, R. & Xu, R.-M. Crystal Structure of a SIR2 Homolog–NAD Complex. *Cell* **105,** 269–279 (2001).

126. Moniot, S., Weyand, M. & Steegborn, C. Structures, substrates, and regulators of Mammalian sirtuins - opportunities and challenges for drug development. *Front. Pharmacol.* **3,** 16 (2012).

127. Jin, L. *et al.* Crystal structures of human SIRT3 displaying substrate-induced conformational changes. *J. Biol. Chem.* **284,** 24394–24405 (2009).

128. Smith, B. C. & Denu, J. M. Sir2 protein deacetylases: evidence for chemical intermediates and functions of a conserved histidine. *Biochemistry (Mosc.)* **45,** 272–282 (2006).

129. Sauve, A. A. Sirtuin chemical mechanisms. *Biochim. Biophys. Acta* **1804,** 1591–1603 (2010).

130. Cosgrove, M. S. *et al.* The structural basis of sirtuin substrate affinity. *Biochemistry (Mosc.)* **45,** 7511–7521 (2006).

131. Sauve, A. A. *et al.* Chemistry of gene silencing: the mechanism of NAD+-dependent deacetylation reactions. *Biochemistry (Mosc.)* **40,** 15456–15463 (2001).

132. Chang, J.-H. *et al.* Structural basis for the NAD-dependent deacetylase mechanism of Sir2. *J. Biol. Chem.* **277,** 34489–34498 (2002).

133. Hoff, K. G., Avalos, J. L., Sens, K. & Wolberger, C. Insights into the sirtuin mechanism from ternary complexes containing NAD+ and acetylated peptide. *Struct. Lond. Engl. 1993* **14,** 1231–1240 (2006).

134. Hawse, W. F. *et al.* Structural insights into intermediate steps in the Sir2 deacetylation reaction. *Struct. Lond. Engl. 1993* **16,** 1368–1377 (2008).

135. Liszt, G., Ford, E., Kurtev, M. & Guarente, L. Mouse Sir2 homolog SIRT6 is a nuclear ADP-ribosyl-transferase. *J. Biol. Chem.* **280,** 21313–21320 (2005).

136. North, B. J., Marshall, B. L., Borra, M. T., Denu, J. M. & Verdin, E. The human Sir2 ortholog, SIRT2, is an NAD+-dependent tubulin deacetylase. *Mol. Cell* **11,** 437–444 (2003).

137. Du, J., Jiang, H. & Lin, H. Investigating the ADP-ribosyltransferase activity of sirtuins with NAD analogues and 32P-NAD. *Biochemistry (Mosc.)* **48,** 2878–2890 (2009).

138. Park, J. *et al.* SIRT5-mediated lysine desuccinylation impacts diverse metabolic pathways. *Mol. Cell* **50,** 919–930 (2013).

139. Jin, J., He, B., Zhang, X., Lin, H. & Wang, Y. SIRT2 Reverses 4-Oxononanoyl Lysine Modification on Histones. *J. Am. Chem. Soc.* **138,** 12304–12307 (2016).

140. Feldman, J. L., Baeza, J. & Denu, J. M. Activation of the protein deacetylase SIRT6 by long-chain fatty acids and widespread deacylation by mammalian sirtuins. *J. Biol. Chem.* **288,** 31350–31356 (2013).

141. Feldman, J. L. *et al.* Kinetic and Structural Basis for Acyl-Group Selectivity and NAD(+) Dependence in Sirtuin-Catalyzed Deacylation. *Biochemistry (Mosc.)* **54,** 3037–3050 (2015).

142. Yang, H. *et al.* Nutrient-sensitive mitochondrial NAD+ levels dictate cell survival. *Cell* **130,** 1095–1107 (2007).

143. Yamada, K., Hara, N., Shibata, T., Osago, H. & Tsuchiya, M. The simultaneous measurement of nicotinamide adenine dinucleotide and related compounds by liquid chromatography/electrospray ionization tandem mass spectrometry. *Anal. Biochem.* **352,** 282–285 (2006).

144. Li, X. & Kazgan, N. Mammalian sirtuins and energy metabolism. *Int. J. Biol. Sci.* **7,** 575–587 (2011).

145. Madsen, A. S. *et al.* Investigating the Sensitivity of NAD+-dependent Sirtuin Deacylation Activities to NADH. *J. Biol. Chem.* **291,** 7128–7141 (2016).

146. Fischer F *et al.* Sirt5 deacylation activities show differential sensitivities to nicotinamide inhibition. *PloS One* **7,** e45098–e45098 (2012).

147. Landry, J., Slama, J. T. & Sternglanz, R. Role of NAD(+) in the deacetylase activity of the SIR2-like proteins. *Biochem. Biophys. Res. Commun.* **278,** 685–690 (2000).

148. Chiang, Y.-L. & Lin, H. An improved fluorogenic assay for SIRT1, SIRT2, and SIRT3. *Org. Biomol. Chem.* **14,** 2186–2190 (2016).

149. Bitterman, K. J., Anderson, R. M., Cohen, H. Y., Latorre-Esteves, M. & Sinclair, D. A. Inhibition of Silencing and Accelerated Aging by Nicotinamide, a Putative Negative Regulator of Yeast Sir2 and Human SIRT1. *J. Biol. Chem.* **277,** 45099–45107 (2002).

150. Cen, Y. Sirtuins inhibitors: the approach to affinity and selectivity. *Biochim. Biophys. Acta* **1804,** 1635–1644 (2010).

151. Pirola, L. & Fröjdö, S. Resveratrol: one molecule, many targets. *IUBMB Life* **60,** 323–332 (2008).

152. Suenkel, B., Fischer, F. & Steegborn, C. Inhibition of the human deacylase Sirtuin 5 by the indole GW5074. *Bioorg. Med. Chem. Lett.* **23,** 143–146 (2013).

153. Howitz, K. T. *et al.* Small molecule activators of sirtuins extend Saccharomyces cerevisiae lifespan. *Nature* **425,** 191–196 (2003).

154. Baur, J. A. & Sinclair, D. A. Therapeutic potential of resveratrol: the in vivo evidence. *Nat. Rev. Drug Discov.* **5,** 493–506 (2006).

155. Milne, J. C. *et al.* Small molecule activators of SIRT1 as therapeutics for the treatment of type 2 diabetes. *Nature* **450,** 712–716 (2007).

156. Barger, J. L. *et al.* A low dose of dietary resveratrol partially mimics caloric restriction and retards aging parameters in mice. *PloS One* **3,** e2264 (2008).

157. Baur, J. A. *et al.* Resveratrol improves health and survival of mice on a high-calorie diet. *Nature* **444,** 337–342 (2006).

158. Baur, J. A. Biochemical effects of SIRT1 activators. *Biochim. Biophys. Acta* **1804,** 1626–1634 (2010).

159. Lakshminarasimhan, M., Rauh, D., Schutkowski, M. & Steegborn, C. Sirt1 activation by resveratrol is substrate sequence-selective. *Aging* **5,** 151–154 (2013).

160. Gertz, M. *et al.* Ex-527 inhibits Sirtuins by exploiting their unique NAD+-dependent deacetylation mechanism. *Proc. Natl. Acad. Sci. U. S. A.* **110,** E2772-2781 (2013).

161. Napper, A. D. *et al.* Discovery of indoles as potent and selective inhibitors of the deacetylase SIRT1. *J. Med. Chem.* **48,** 8045–8054 (2005).

162. Schuetz, A. *et al.* Structural basis of inhibition of the human NAD+-dependent deacetylase SIRT5 by suramin. *Struct. Lond. Engl. 1993* **15,** 377–389 (2007).

163. Trapp, J. *et al.* Structure-activity studies on suramin analogues as inhibitors of NAD+-dependent histone deacetylases (sirtuins). *ChemMedChem* **2,** 1419–1431 (2007).

164. Kudlacek, O. *et al.* Biased inhibition by a suramin analogue of A1-adenosine receptor/G protein coupling in fused receptor/G protein tandems: the A1-adenosine receptor is predominantly coupled to Goalpha in human brain. *Naunyn. Schmiedebergs Arch. Pharmacol.* **365,** 8–16 (2002).

165. Jentsch, K. D., Hunsmann, G., Hartmann, H. & Nickel, P. Inhibition of human immunodeficiency virus type I reverse transcriptase by suramin-related compounds. *J. Gen. Virol.* **68 (Pt 8),** 2183–2192 (1987).

166. Doggrell, S. A. Suramin: potential in acute liver failure. *Expert Opin. Investig. Drugs* **13,** 1361–1363 (2004).

167. Disch, J. S. *et al.* Discovery of thieno[3,2-d]pyrimidine-6-carboxamides as potent inhibitors of SIRT1, SIRT2, and SIRT3. *J. Med. Chem.* **56,** 3666–3679 (2013).

168. Nguyen, G. T. T., Schaefer, S., Gertz, M., Weyand, M. & Steegborn, C. Structures of human sirtuin 3 complexes with ADP-ribose and with carba-NAD+ and SRT1720: binding details and inhibition mechanism. *Acta Crystallogr. D Biol. Crystallogr.* **69,** 1423–1432 (2013).

169. Trapp, J. *et al.* Adenosine mimetics as inhibitors of NAD+-dependent histone deacetylases, from kinase to sirtuin inhibition. *J. Med. Chem.* **49,** 7307–7316 (2006).

170. Lutz, M. I., Milenkovic, I., Regelsberger, G. & Kovacs, G. G. Distinct Patterns of Sirtuin Expression During Progression of Alzheimer's Disease. *NeuroMolecular Med.* **16,** 405–414 (2014).

171. Tan, M. *et al.* Lysine glutarylation is a protein posttranslational modification regulated by SIRT5. *Cell Metab.* **19,** 605–617 (2014).

172. Xie, L. *et al.* Proteome-wide Lysine Glutarylation Profiling of the Mycobacterium tuberculosis H37Rv. *J. Proteome Res.* **15,** 1379–1385 (2016).

173. Weinert, B. T. *et al.* Lysine succinylation is a frequently occurring modification in prokaryotes and eukaryotes and extensively overlaps with acetylation. *Cell Rep.* **4,** 842–851 (2013).

174. Hirschey, M. D. & Zhao, Y. Metabolic Regulation by Lysine Malonylation, Succinylation, and Glutarylation. *Mol. Cell. Proteomics MCP* **14,** 2308–2315 (2015).

175. Maurer, B. *et al.* Inhibitors of the NAD(+)-Dependent Protein Desuccinylase and Demalonylase Sirt5. *ACS Med. Chem. Lett.* **3,** 1050–1053 (2012).

176. Yang, L. *et al.* Sirtuin 5: a review of structure, known inhibitors and clues for developing new inhibitors. *Sci. China Life Sci.* **60,** 249–256 (2017).

177. Di, L. Strategic approaches to optimizing peptide ADME properties. *AAPS J.* **17,** 134–143 (2015).

178. He, B., Du, J. & Lin, H. Thiosuccinyl peptides as Sirt5-specific inhibitors. *J. Am. Chem. Soc.* **134,** 1922–1925 (2012).

179. Smith, B. C. & Denu, J. M. Mechanism-based inhibition of Sir2 deacetylases by thioacetyl-lysine peptide. *Biochemistry (Mosc.)* **46,** 14478–14486 (2007).

180. Lipinski, C. A., Lombardo, F., Dominy, B. W. & Feeney, P. J. Experimental and computational approaches to estimate solubility and permeability in drug discovery and development settings. *Adv. Drug Deliv. Rev.* **46,** 3–26 (2001).

181. Rauh, D. *et al.* An acetylome peptide microarray reveals specificities and deacetylation substrates for all human sirtuin isoforms. *Nat. Commun.* **4,** 2327 (2013).

182. Frye, R. A. Phylogenetic classification of prokaryotic and eukaryotic Sir2-like proteins. *Biochem. Biophys. Res. Commun.* **273,** 793–798 (2000).

183. Anderson, K. A. *et al.* SIRT4 Is a Lysine Deacylase that Controls Leucine Metabolism and Insulin Secretion. *Cell Metab.* **25,** 838–855.e15 (2017).

184. Smith, B. C., Hallows, W. C. & Denu, J. M. A Continuous Microplate Assay for Sirtuins and Nicotinamide Producing Enzymes. *Anal. Biochem.* **394,** 101–109 (2009).

185. Smith, B. C. & Denu, J. M. Acetyl-lysine analog peptides as mechanistic probes of protein deacetylases. *J. Biol. Chem.* **282,** 37256–37265 (2007).

186. Rack, J. G. M. *et al.* Identification of a Class of Protein ADP-Ribosylating Sirtuins in Microbial Pathogens. *Mol. Cell* **59,** 309–320 (2015).

187. Zhao, Y. *et al.* Genetically Encoded Fluorescent Sensors for Intracellular NADH Detection. *Cell Metab.* **14,** 555–566 (2011).

UNIVERSITÄT BAYREUTH

5. <u>List of publications</u>

5.1. <u>Publication 1</u>

Chemical Probing of the Human Sirtuin 5 Active Site Reveals Its Substrate Acyl Specificity and Peptide-Based Inhibitors

Roessler, C.*, Nowak, T.*, Pannek, M.*, Gertz, M., Nguyen, G.T.T., Scharfe, M., Born, I., Sippl, W., Steegborn, C., Schutkowski, M. (2014). Chemical Probing of the Human Sirtuin 5 Active Site Reveals Its Substrate Acyl Specificity and Peptide-Based Inhibitors. *Angew. Chem.*, 126(40):10904-10908.

* These authors contributed equally to this work.

This publication resulted from a collaborative study of the groups of Mike Schutkowski, Clemens Steegborn and Wolfgang Sippl. Mike Schutkowski, Clemens Steegborn, Wolfgang Sippl, Claudia Roessler and me designed the study. Claudia Roessler, Theresa Nowak and Illona Born synthesized acylated CPS1 peptides and executed all *in vitro* assays. Giang Nguyen established the zSirt5 construct used for complex crystallization, which was either expressed and purified by our technical assistant Norbert Grillenbeck (not listed as author) or me. I produced the Sirt5/peptide complex crystals and solved, refined and deposited the structures in the PDB, supported by Melanie Gertz and Clemens Steegborn. Michael Scharfe created the models of human Sirt5 with acylated substrate peptides. Claudia Roessler, Mike Schutkowski, Wolfgang Sippl, Clemens Steegborn and me drafted the manuscript.

<u>Please note:</u> Supplementary Information Figure S16 (MS-spectra of peptides) was omitted to limit the number of pages, but is available on the CD-ROM attached to this work.

Chemical Probing of the Human Sirtuin 5 Active Site Reveals Its Substrate Acyl Specificity and Peptide-Based Inhibitors**

Claudia Roessler, Theresa Nowak, Martin Pannek, Melanie Gertz, Giang T. T. Nguyen, Michael Scharfe, Ilona Born, Wolfgang Sippl, Clemens Steegborn, and Mike Schutkowski*

Abstract: Sirtuins are NAD$^+$-dependent deacetylases acting as sensors in metabolic pathways and stress response. In mammals there are seven isoforms. The mitochondrial sirtuin 5 is a weak deacetylase but a very efficient demalonylase and desuccinylase; however, its substrate acyl specificity has not been systematically analyzed. Herein, we investigated a carbamoyl phosphate synthetase 1 derived peptide substrate and modified the lysine side chain systematically to determine the acyl specificity of Sirt5. From that point we designed six potent peptide-based inhibitors that interact with the NAD$^+$ binding pocket. To characterize the interaction details causing the different substrate and inhibition properties we report several X-ray crystal structures of Sirt5 complexed with these peptides. Our results reveal the Sirt5 acyl selectivity and its molecular basis and enable the design of inhibitors for Sirt5.

The reversible acetylation of lysine side chains represents one of the most frequent posttranslational modifications in proteins conserved from bacteria to eukaryotes.[1] Acetylation states are regulated by the action of lysine acetyltransferases and lysine deacetylases. One class of lysine deacetylases, the sirtuins, require NAD$^+$ as a cosubstrate, linking their activity to energy levels of the cell. They transfer the acetyl group from the lysine side chain to the 2′-hydroxyl group of the ADP ribose moiety of NAD$^+$ under nicotinamide release.[2] Sirtuins are involved in many metabolic and stress response

processes, and modulators of human isoforms are interesting drug candidates for aging-related diseases including diabetes, cancer, and neurodegeneration.[3] Some sirtuin isoforms were found to be specific for other acyl modifications on the lysine side chain. Besides acetylation, modifications like propionylation,[4] butyrylation,[4a] crotonylation,[5] malonylation,[6] succinylation,[7] myristoylation,[8] and 3-phosphoglycerylation[9] were detected in vivo. The mitochondrial isoform sirtuin 5 (Sirt5) and the nuclear isoform sirtuin 6 (Sirt6) have a much lower deacetylation activity than several other isoforms.[10] For Sirt6 it could be demonstrated that long acyl chains, such as myristoyl residues, represent much better substrates as a result of improved K_M values,[10b] similar to findings for the *Plasmodium falciparum* sirtuin 2A.[11]

Sirt5 was also found to remove octanoyl and decanoyl residues from model peptides.[12] In particular, this isoform was recently shown to be an effective demalonylase/desuccinylase in vitro[13] and in vivo.[6,13b] Du et al. were able to demonstrate that the change from acetyl to succinyl residues in three different model peptide sequences increased catalytic efficiencies (k_{cat}/K_M) between 75- and 1000-fold but individual K_M and k_{cat} values could not be determined for acetylated substrates.[13a] Crystal structure analysis identified an interaction between the carboxyl function of the succinylated peptide lysine and the Sirt5 side chains of Arg105 and Tyr102,[13a] indicating a mechanism for substrate acyl discrimination. Interestingly, these residues also cause isoforms and substrate acyl specific inhibitor effects.[14] Here we investigated the effects of substrate lysine modifications in a more systematic way and developed novel peptide-based Sirt5 inhibitors through acyl group modifications. As the peptide we used a carbamoyl phosphate synthetase I (CPS1)-derived sequence (**1**) identified through high-density peptide micro-

[*] C. Roessler,[+] Dr. I. Born, Prof. Dr. M. Schutkowski
Department of Enzymology
Institute of Biochemistry and Biotechnology
Martin-Luther-University Halle-Wittenberg
Kurt-Mothes-Strasse 3, 06120 Halle/Saale (Germany)
E-mail: mike.schutkowski@biochemtech.uni-halle.de

T. Nowak,[+] M. Scharfe, Prof. Dr. W. Sippl
Department of Medical Chemistry, Institute of Pharmacy
Martin-Luther-University Halle-Wittenberg
Halle/Saale (Germany)

M. Pannek,[+] Dr. M. Gertz, G. T. T. Nguyen, Prof. Dr. C. Steegborn
Department of Biochemistry, University of Bayreuth (Germany)

[+] These authors contributed equally to this work.

1 Bz-Gly-Val-Leu-Lys-Glu-Tyr-Gly-Val-NH$_2$
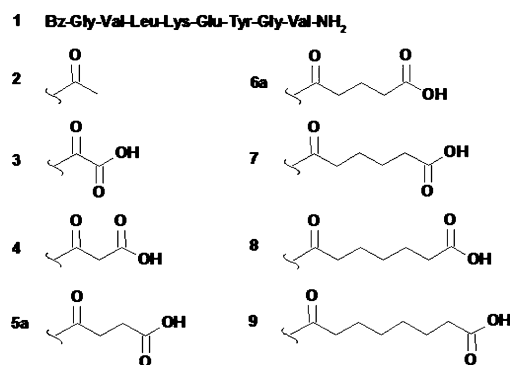
Scheme 1. Homologous row of dicarbonic acyl (**3–9**) and acetyl (**2**) residues attached to the lysine side chain of CPS1 peptide **1**.

array experiments[1] and shown to serve as a Sirt5 substrate in its acetylated form (Scheme 1).[14a]

In Sirt5 crystal structures Arg105 adopts different conformations suggesting that larger acyl residues might be able to interact with Tyr102 and Arg105, too. Therefore, we synthesized CPS1 substrate analogues acylated at the lysine side chain with oxalyl (**3**), malonyl (**4**), succinyl (**5a**), glutaryl (**6a**), adipoyl (**7**), pimeloyl (**8**), and suberoyl (**9**) residues (Scheme 1). Moreover, we introduced double bonds (**5e–5g**), heteroatoms (**6e–6g**), and additional substituents to succinyl and/or glutaryl moieties like methyl groups (**5b**, **5c**, **6b**, **6c**, **6g**, and **6d**), methylidene groups (**5e**), hydroxyl groups (**6d**), and amino groups (**5d**). Additionally, we replaced the carboxyl group of the succinyl residue with a nitro function (**5l**) as well as a methyl group (**5n**) (Scheme 2 and Scheme 3). Finally, we introduced larger substituents to the 3-position of succinyl (**5h–k** and **5m**) (Scheme 2) and the 4-position of glutaryl residues (**6h**) (Scheme 3).

Kinetic constants for the substrates (Table 1) were determined using an HPLC-based assay. Controls without NAD$^+$ under identical conditions yielded no conversion of the substrates. Inspection of the kinetic constants uncovers the surprising fact that the introduction of an additional carboxyl group to the acyl chain did not significantly influence
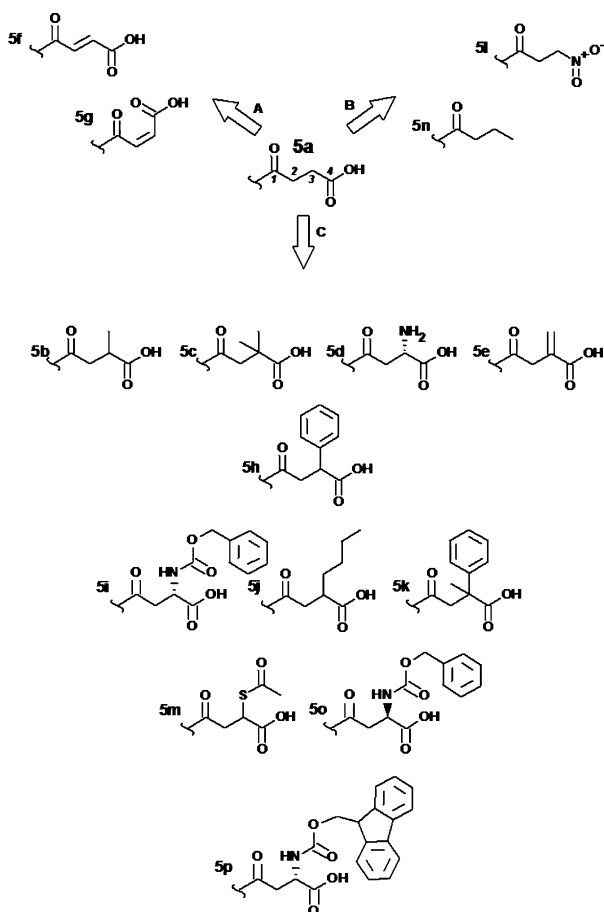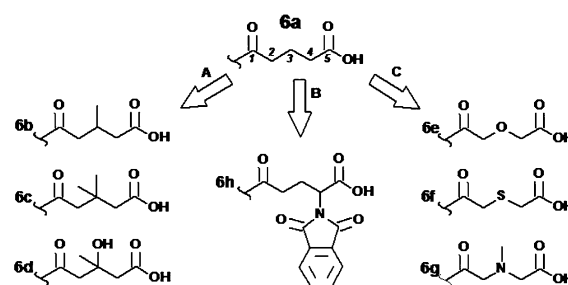
Scheme 3. Derivatization of **6a**: A) substitutions on C3; B) substitutions on C4; C) replacement of the C3-carbon by oxygen, sulfur, or methylated nitrogen.

Table 1: Kinetic constants for differently acylated CPS1-derived peptides.

Compound	K_M [μM]	k_{cat} [s^{-1}]	k_{cat}/K_M [M^{-1} s^{-1}]
2	24.3 ± 9.1	3.9×10^{-4} ± 6×10^{-5}	16
3	415.8 ± 24.3	1.6×10^{-3} ± 8×10^{-5}	4
4	5.1 ± 1.1	1.9×10^{-2} ± 1×10^{-3}	3758
5a	3.8 ± 0.6	5.3×10^{-2} ± 2×10^{-3}	13995
5b	3.1 ± 0.3	2.4×10^{-3} ± 4×10^{-5}	774
5c	5.3 ± 1.0	2.2×10^{-4} ± 8×10^{-6}	42
5d	130.3 ± 57.2	8.4×10^{-2} ± 2×10^{-3}	644
5e	8.2 ± 0.7	2.5×10^{-3} ± 5×10^{-5}	307
5f	46.7 ± 8.0	1.7×10^{-3} ± 1×10^{-4}	37
5g	191.8 ± 99.0	1.5×10^{-3} ± 5×10^{-4}	8
5l	44.8 ± 17.1	5.2×10^{-3} ± 8×10^{-4}	116
6a	4.1 ± 1.0	7.7×10^{-2} ± 2×10^{-3}	18699
6b	5.7 ± 0.6	3.3×10^{-3} ± 5×10^{-5}	579
6c	16.3 ± 3.5	1.1×10^{-4} ± 8×10^{-6}	7
6d	7.6 ± 0.92	3.8×10^{-3} ± 1×10^{-4}	500
6e	10.1 ± 2.0	1.0×10^{-1} ± 7×10^{-3}	9906
6f	2.7 ± 0.5	2.3×10^{-2} ± 7×10^{-4}	8613
6g	12.1 ± 2.7	1.6×10^{-2} ± 1×10^{-3}	1325
7	6.5 ± 1.6	1.0×10^{-2} ± 6×10^{-4}	1538
8	80.5 ± 22.9	2.8×10^{-4} ± 4×10^{-5}	4
9	409.1 ± 283.0	5.3×10^{-4} ± 2×10^{-5}	1

the apparent affinity to the active site of Sirt5, as reflected by the almost comparable K_M values for **2** and **4**. Instead, the respective k_{cat} value is increased about 50-fold demonstrating that this modification either influences the velocity or changes the nature of the rate-limiting step of the Sirt5-catalyzed reaction. Insertion of one (**5a**) and two (**6a**) additional methylene groups did not improve the K_M value but increased the k_{cat} value 140-fold and 200-fold, respectively, as compared to **2**. Insertion of an additional methylene group (**7**) yields a substrate with a similar apparent affinity to the active site but 7-fold reduced k_{cat} value compared to **6a**. Insertion of more methylene groups (**8** and **9**) resulted in substrates with k_{cat} values similar to that of **2** and increased K_M values. Replacement of the methyl group of the acetyl residue in **2** by a carboxyl function (**3**) increased the K_M value by more than 15-fold. Molecular docking of **3** shows that the distance between the carboxyl group of **3** and Tyr102 as well as Arg105 is too large for interaction with these residues. Additionally, one oxygen of the carboxyl group of **3** clashes with the backbone carbonyl of Val221 which might explain why the K_M value of **3** is lower than that of **5a** (Figure S9).

Scheme 2. Derivatization of **5a**: A) dehydrogenation; B) replacement of carboxyl group by methyl or nitro function; C) substitution on C3. **5j** represents a mixture of 2- and 3-butylsuccinyl CPS1.

Obviously, **4**, **5a**, and **6a** represent most likely physiological substrates for Sirt5; this is reflected by the superior specificity constants k_{cat}/K_M. The very similar apparent affinities, indicated by K_M values, of Sirt5 for **5a** and **6a** could be confirmed by the determination of dissociation constants (K_D) using isothermal titration calorimetry (Figure S8). We found K_D values of 700 ± 50 nM and 710 ± 110 nM for **5a** and **6a**, respectively. The improved turnover of **5a** relative to that of **2** is not simply caused by the increased length of the acyl chain because **5n** showed kinetic constants comparable to those of **2** (data not shown). Introduction of a double bond into the succinyl residue resulted in **5f** and **5g**, which showed an about 30-fold decrease in the turnover. The K_M value is increased about 12-fold for **5f** but by more than 50-fold for **5g** with a *cis*-configured double bond. We compared the structure of the zebrafish Sirt5 (zSirt5)/**5a** complex with docking poses of **5f** and **5g**. Due to the double bond, the acylated lysine residues are forced into a planar orientation, which is not suited to form an optimal hydrogen bond to Tyr102 and a salt bridge to Arg105 (Figure S17).

We solved crystal structures of zSirt5, which is highly homologous to the less reproducibly crystallizing human enzyme (Figure S11), in complex with **5a**, **6a**, and **7** to analyze the binding details of the modifications on the lysine side chain. The final models are composed of two zSirt5 molecules, each complexing one zinc cation. The active site of one molecule is occupied by the respective substrate peptide, with a consistent salt bridge between the carboxyl group of the acyl moiety and Arg101 as well as a hydrogen bond to Tyr98 (Figure 2a), whereas a buffer ion interacts with Arg101 in the active site of the second zSirt5 molecule. In comparison to the succinyl moiety of **5a**, the glutaryl and adipoyl modifications show an increasingly twisted conformation, allowing very similar positions for the distal carboxyl group despite different chain lengths (Figure 1a). The adipoyl modification shows a slight movement toward the catalytic His154 to accommodate the broader, helically arranged carbon chain, resulting in a strained conformation and an elongation of the conserved


Figure 2. Crystal structures of zSirt5 active-site with superposed **5a** (gray), **5b** (dark gray), and **5c** (light gray). The protein is shown only once for clarity (zSirt5/**5a** complex; gray), since all protein residues superpose well. Polar interactions between active-site residues and substrate peptides' acylated lysine are indicated by dotted lines.

hydrogen bond between the lysine ε-amino group and the Val217 main-chain carboxyl oxygen. Additional extension of the substrate acyl chain (**8** and **9**) could not be bound in the same mode as for **5a**, **6a**, and **7** by twisting the chain, resulting in the loss of the conserved hydrogen bond to oxygen of Val217 but a similar carboxyl interaction with Arg101/Tyr98.

Flexible docking of **8** and **9** indicates that Arg105 changes its conformation to enable similar interactions. This Arg105 conformation is also observed in the Sirt5/thioacetyl-H3K9/CHES complex structure (3RIG), showing that this conformation is possible for the protein. The substrate hydrogen bond to Tyr102 is completely lost, however. This lost interaction and possibly a nonoptimal Arg105 conformation thus appear to be the reasons for the weaker apparent binding and lowered catalytic efficiencies for these substrates. Further extending the acyl chain would lead to a complete loss of the Arg105 interaction and to energetically unfavorable acyl conformations due to limited space within the substrate-binding pocket of Sirt5 (Figure 1b).

Crystal structures of **5a** and **6a** bound to zSirt5 revealed that there is some space around position 3 of the acyl residue and docking studies with **5b**, **5c**, and **6b**, **6c** suggested that they could bind to Sirt5 similar to **5a** and **6a**, respectively. The substituents do not disturb the NAD$^+$ productive conformation, as suggested by docking studies (Figure S10) and indicated by crystal structure analysis of zSirt5 in complex with **5b** or **5c** (Figure 2). We thus tested single (**5b**, **5e**, **5d**, and **6b**) and double substitutions on this position (**5c**, **6c**, and **6d**) and replacement of the methylene moiety at position 3 by oxygen (**6e**) and sulfur (**6f**), and by methyl-substituted nitrogen (**6g**). Introduction of heteroatoms into the acyl chain seems to be tolerated by Sirt5 at least in position 3 of glutaryl derivatives. Kinetic constants for **6e** and **6f** are similar to that of **6a**, and for **6g** similar to that for **6b**.

All compounds with methyl/hydroxyl substitutions are substrates for Sirt5 with K_M values in the low micromolar range but with dramatically reduced k_{cat} values. Determination of kinetic constants for the cosubstrate under saturating conditions for peptides **5a** and **5b** yielded very similar results (Figure S5) with NAD$^+$ K_M values of 29.6 ± 15.2 μM and 35.5 ± 11.7 μM, respectively, confirming that the additional

Figure 1. a) Crystal structures of zSirt5 with superposed **5a** (gray), **6a** (light gray), and **7** (dark gray). The protein is shown only once for clarity (zSirt5/**5a** complex; gray), since all protein residues superpose well. b) Docking of **8** (dark gray) and **9** (light gray) is only possible if Arg105 adopts another conformation that is also observed in the X-ray structure of PDB entry 3RIG. Polar interactions between ligand and protein are indicated as dashed lines.

methyl group in the acyl chain of the peptide substrate does not interfer with NAD^+ binding. Solving zSirt5 structures in complex with **5b** and **5c** reveals molecular reasons for this effect on k_{cat}. Compared to the structure with **5a**, the acyl side chain in **5b** and **5c** is twisted to position the hydrophobic methyl groups in appropriate active site cavities (Figure 2). This reorientation requires a rotation of the amide bond of the acylated lysine side chain, resulting in a carbonyl orientation that is probably not optimal for the nucleophilic attack at C1 of the ribose ring in the cosubstrate.

Determination of the respective K_D values using ITC yielded 830 ± 170 nM and 290 ± 40 nM for **5b** and **5c**, which is very similar to the K_D value for nonsubstituted parent peptide **5a**, indeed confirming that the unchanged K_M correctly indicates similar affinities to the active site. In contrast, substrate **5d** showed a 30-fold increased K_M value, likely due to the positive charge of the introduced primary amino function, since assuming that the binding is similar to that of **5b** would place this function in a hydrophobic environment. These results suggest the assumption that the chain length of the dicarbonic acyl residue as well as the orientation of the carboxyl group has a high impact on the k_{cat} value but less on the apparent affinity of the peptidic substrate.

Small acyl modifications can show significant effects on the substrate properties, suggesting the development of inhibitory binding groups: Exploiting the Sirt5 specific active site cavities should make it possible to further increase the binding affinity, in a nonproductive, inhibitory conformation, and it should enable isoform selective binding and inhibition.

We tested the idea of introducing bulkier acyl substituents to generate steric hindrance for NAD^+ binding by analyzing succinyl CPS1 derivatives with larger substitutions on C3 like **5j** and **5h**. These compounds could not be deacylated by the enzyme even when prolonged reaction times (up to 24 h) and higher Sirt5 concentrations (up to 2 µM) were used. Consistent with our hypothesis that they still bind to the active site of Sirt5 and block the NAD^+ site, these compounds are inhibitors for Sirt5 with K_i values of 100 ± 45 and 17.2 ± 1.3 µM for **5h** and **5j**, respectively (Table S2, Figures S6 and S7). Solving their complex structures with zSirt5 revealed that both modifications allow binding of the succinyl moiety like in substrate **5a**, and that these substitutions point toward the NAD^+ binding pocket (Figure S14a,b). Modeling NAD^+ from PDB ID 3RIY (Sirt5/succinyl-H3K9-peptide/$NAD^{+[13a]}$) into our zSirt5 structures shows that the modifications would clash with ribose atoms of the NAD^+ cosubstrate (Figure S18). For **5h** a mixture of *S* and *R* enantiomers appear to be bound, with slightly differing succinyl conformations but distal carboxyl groups and the phenyl moieties still in the same position. Our CPS1 derivatives thus reveal a novel principle for sirtuin inhibition based on peptides, which can also reveal valuable information for the development of small-molecule inhibitors.

Several sirtuin inhibitors, such as Ex527[15] and 4′-bromo-resveratrol,[16] were recently shown to bind to the nicotinamide-accommodating C-site, indicating it as an attractive pocket for obtaining binding affinity. We therefore attempted to move the phenyl residue of **5h** deeper into the NAD^+ site, toward the C-site, by introducing a methylcarbamate linker

between the succinyl and the phenyl group (**5i**). During the synthesis of this compound we were able to control the stereochemistry by using *Z*-protected aspartic acid derivatives in *S* and *R* configuration for the acylation reaction, yielding **5i** and **5o**, respectively. Testing benzyloxycarbonyl-protected aminosuccinyl derivatives showed that **5i** is an inhibitor for Sirt5 with about 3-fold improved K_i value (38.1 ± 0.6 µM) as compared to **5h** (Table S2). Peptide **5o** is an inhibitor with considerably reduced affinity to the active site of Sirt5 underlining the binding specificity for the *S* configuration. A crystal structure of the complex between **5i** and zSirt5 confirms that extending the linker in the *S* configuration moved the phenyl ring deeper into the C-site (Figure S14c). Only the methylcarbamate linker is well defined by electron density, while less pronounced spherical density is observed for the phenyl moiety in the C-site. The phenyl ring is in fact well positioned to mimic nicotinamide binding (Figure 3) but appears to be rotationally flexible, and adding a more nicotinamide-like carboxamide moiety to the phenyl ring is an obvious next step to improve binding of this acyl modification. Other large moieties can also be employed for binding to this active site region.
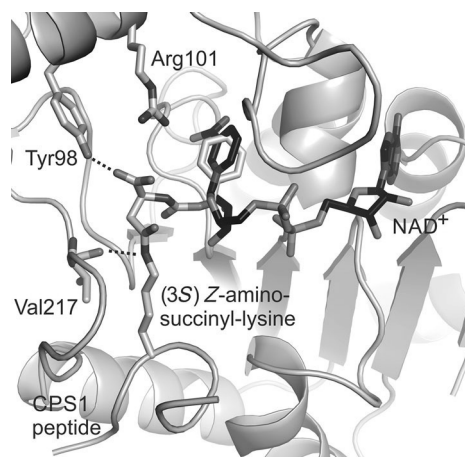

Figure 3. Crystal structure of zSirt5 active site with inhibitor **5i** (light gray). NAD^+ molecule was modeled in by an overlay with PDB entry 3RIG (dark gray). The protein is shown only once for clarity (zSirt5/**5i** complex; gray). Polar interactions between active-site residues and substrate peptides' acylated lysine are indicated by dotted lines.

Thus, introduction of a fluorenyl ring (**5p**) yielded an inhibitor with similar preference for the *S* configuration ($K_i = 46.0 \pm 0.23$ µM). Also, targeting additional active site areas could increase inhibitor affinity. Disubstitution at position 3 with a phenyl and a methyl moiety led to an about 20-fold increase in binding affinity of **5k** ($K_i = 4.3 \pm 0.32$ µM) compared to **5h**. Supposing that the observed orientation of **5h** for the phenyl group is similar, the methyl substituent at C3 can be assumed to occupy a position similar to the second methyl group in **5c** (Figure S10), indicating it as an interesting extension site for inhibitor development. Testing inhibition of human sirtuin isoforms by **5k** confirms that this approach achieved selectivity for Sirt5 versus Sirt1, 2, and 3 (Table S3).

Next steps in converting our peptide derivatives into small-molecule Sirt5 inhibitors comprise removal of the peptide part without losing sufficient affinity and replacement of the carboxyl moiety to enable membrane passage.

Substitution of the carboxyl group by a nitro function (**5l**) resulted in about 10-fold decrease of both K_M and k_{cat} values, that is, it is a well binding substrate. Crystal structure analysis of its zSirt5 complex shows that the nitropropionylated lysine indeed binds very similar to **5a** (Figure S13c).

Combining this nitro substitution with our novel acyl-based inhibition principle should now enable the systematic development of small-molecule inhibitors for Sirt5. This approach would lead to the first potent and selective Sirt5 inhibitors, which are anxiously awaited as research tools and as lead compounds for drug development.

[1] D. Rauh, F. Fischer, M. Gertz, M. Lakshminarasimhan, T. Bergbrede, F. Aladini, C. Kambach, C. F. Becker, J. Zerweck, M. Schutkowski, C. Steegborn, *Nat. Commun.* **2013**, *4*, 2327.

[2] A. A. Sauve, C. Wolberger, V. L. Schramm, J. D. Boeke, *Annu. Rev. Biochem.* **2006**, *75*, 435–465.

[3] a) M. C. Haigis, D. A. Sinclair, *Annu. Rev. Pathol.* **2010**, *5*, 253–295; b) S. Sanchez-Fidalgo, I. Villegas, M. Sanchez-Hidalgo, C. A. de La Lastra, *Curr. Med. Chem.* **2012**, *19*, 2414–2441; c) J. Schemies, U. Uciechowska, W. Sippl, M. Jung, *Med. Res. Rev.* **2010**, *30*, 861–889.

[4] a) Y. Chen, R. Sprung, Y. Tang, H. Ball, B. Sangras, S. C. Kim, J. R. Falck, J. Peng, W. Gu, Y. Zhao, *Mol. Cell. Proteomics* **2007**, *6*, 812–819; b) Z. Cheng, Y. Tang, Y. Chen, S. Kim, H. Liu, S. S. Li, W. Gu, Y. Zhao, *Mol. Cell. Proteomics* **2009**, *8*, 45–52; c) J. Garrity, J. G. Gardner, W. Hawse, C. Wolberger, J. C. Escalante-Semerena, *J. Biol. Chem.* **2007**, *282*, 30239–30245.

[5] M. Tan, H. Luo, S. Lee, F. Jin, J. S. Yang, E. Montellier, T. Buchou, Z. Cheng, S. Rousseaux, N. Rajagopal, Z. Lu, Z. Ye, Q. Zhu, J. Wysocka, Y. Ye, S. Khochbin, B. Ren, Y. Zhao, *Cell* **2011**, *146*, 1016–1028.

[6] C. Peng, Z. Lu, Z. Xie, Z. Cheng, Y. Chen, M. Tan, H. Luo, Y. Zhang, W. He, K. Yang, B. M. Zwaans, D. Tishkoff, L. Ho, D. Lombard, T. C. He, J. Dai, E. Verdin, Y. Ye, Y. Zhao, *Mol. Cell. Proteomics* **2011**, *10*, M111 012658.

[7] a) Z. Zhang, M. Tan, Z. Xie, L. Dai, Y. Chen, Y. Zhao, *Nat. Chem. Biol.* **2011**, *7*, 58–63; b) B. T. Weinert, C. Scholz, S. A. Wagner, V. Iesmantavicius, D. Su, J. A. Daniel, C. Choudhary, *Cell Rep.* **2013**, *4*, 842–851; c) G. R. Wagner, R. M. Payne, *J. Biol. Chem.* **2013**, *288*, 29036–29045.

[8] a) F. T. Stevenson, S. L. Bursten, R. M. Locksley, D. H. Lovett, *J. Exp. Med.* **1992**, *176*, 1053–1062; b) F. T. Stevenson, S. L. Bursten, C. Fanton, R. M. Locksley, D. H. Lovett, *Proc. Natl. Acad. Sci. USA* **1993**, *90*, 7245–7249.

[9] a) G. Boël, V. Pichereau, I. Mijakovic, A. Maze, S. Poncet, S. Gillet, J. C. Giard, A. Hartke, Y. Auffray, J. Deutscher, *J. Mol. Biol.* **2004**, *337*, 485–496; b) R. E. Moellering, B. F. Cravatt, *Science* **2013**, *341*, 549–553.

[10] a) M. Gertz, C. Steegborn, *Biochim. Biophys. Acta Proteins Proteomics* **2010**, *1804*, 1658–1665; b) H. Jiang, S. Khan, Y. Wang, G. Charron, B. He, C. Sebastian, J. Du, R. Kim, E. Ge, R. Mostoslavsky, H. C. Hang, Q. Hao, H. Lin, *Nature* **2013**, *496*, 110–113.

[11] A. Y. Zhu, Y. Zhou, S. Khan, K. W. Deitsch, Q. Hao, H. Lin, *ACS Chem. Biol.* **2012**, *7*, 155–159.

[12] J. L. Feldman, J. Baeza, J. M. Denu, *J. Biol. Chem.* **2013**, *288*, 31350–31356.

[13] a) J. Du, Y. Zhou, X. Su, J. J. Yu, S. Khan, H. Jiang, J. Kim, J. Woo, J. H. Kim, B. H. Choi, B. He, W. Chen, S. Zhang, R. A. Cerione, J. Auwerx, Q. Hao, H. Lin, *Science* **2011**, *334*, 806–809; b) J. Park, Y. Chen, D. X. Tishkoff, C. Peng, M. Tan, L. Dai, Z. Xie, Y. Zhang, B. M. Zwaans, M. E. Skinner, D. B. Lombard, Y. Zhao, *Mol. Cell* **2013**, *50*, 919–930.

[14] a) F. Fischer, M. Gertz, B. Suenkel, M. Lakshminarasimhan, M. Schutkowski, C. Steegborn, *PLoS One* **2012**, *7*, e45098; b) B. Maurer, T. Rumpf, M. Scharfe, D. A. Stolfa, M. L. Schmitt, W. He, E. Verdin, W. Sippl, M. Jung, *ACS Med. Chem. Lett.* **2012**, *3*, 1050–1053.

[15] M. Gertz, F. Fischer, G. T. Nguyen, M. Lakshminarasimhan, M. Schutkowski, M. Weyand, C. Steegborn, *Proc. Natl. Acad. Sci. USA* **2013**, *110*, E2772–2781.

[16] G. T. Nguyen, M. Gertz, C. Steegborn, *Chem. Biol.* **2013**, *20*, 1375–1385.

Angewandte Chemie

Eine Zeitschrift der Gesellschaft Deutscher Chemiker

Supporting Information

Chemical Probing of the Human Sirtuin 5 Active Site Reveals Its Substrate Acyl Specificity and Peptide-Based Inhibitors**

Claudia Roessler, Theresa Nowak, Martin Pannek, Melanie Gertz, Giang T. T. Nguyen, Michael Scharfe, Ilona Born, Wolfgang Sippl, Clemens Steegborn, and Mike Schutkowski*

ange_201402679_sm_miscellaneous_information.pdf

Table of contents

Chemicals and general methods

All chemicals were purchased from Sigma (Saint Louis, USA) if not stated otherwise. Rink amide MBHA resin was obtained from Iris Biotech (Marktredwitz, Germany). Fmoc-protected amino acid derivatives and Benzotriazole-1-yl-oxy-tris-pyrrolidino-phosphonium hexafluorophosphate (PyBOP) were purchased from Merck (Darmstadt, Germany). Trifluoroacetic acid was obtained from Roth (Karlsruhe, Germany).

For HPLC separations solvents consisting of water (solvent A) and ACN (solvent B), both containing 0.1 % TFA were used. Eluting compounds were detected at 260 nm. Analytical runs were performed on an Agilent 1100 HPLC (Boeblingen, Germany) with a quaternary pump, a well-plate autosampler and a variable wavelength detector. 40 to 80 µl of compounds or reaction solutions were injected and separated using a linear gradient from 30 % to 60 % solvent B within 5min on a 3.0 x 7.5 mm reversed phase column (Agilent Poroshell 120 EC-C18, 2.7 µm) with a flow-rate of 0.8 mL/min. A Merck-Hitachi High Speed LC system (Darmstadt, Germany) with a Merck Hibar LiChrosorb RP-8 column (250-25 mm, 7 µm) was used for preparative separations. For separation a linear gradient from 20 % to 50 % solvent B in 60 min was used (flow-rate: 8mL/min). Eluted compounds were analyzed by LC/ESI-MS (HPLC: Agilent 1100, ESI-ion trap-mass spectrometer: BrukerDaltonics Esquire LC (Bremen, Germany)). The runs were performed with a linear gradient from 5 % to 100 % solvent B in 20 min on a Machery Nagel (Dueren, Germany) RP-C18 column (ET 125/2 Nukleosil 500-5 C18 PPN).

Synthesis of CPS1 derivative 1

1 was synthesized by standard solid-phase-peptide synthesis protocols using 9-fluorenylmethoxy-carbonyl (Fmoc) protected amino acid derivatives. Rink amide MBHA resin was treated with *N,N*-dimethylformamide (DMF) at RT for 10 min. The Fmoc protecting group was removed with 20 % piperidine in DMF for 15 min. After washing with DMF (5 min, 5 times) the resin was incubated with 4 eq of amino acid derivative, 4 eq PyBOP and 8 eq of *N,N*-diisopropylethylamine (DIPEA) in DMF at RT for 45 min. The *N*-terminus of the glycine residue was modified using 4 eq benzoic anhydride and 8 eq DIPEA in DMF at RT for 45 min. The resin was washed with dichloromethane (DCM, 3 min, 5 times), methanol (5 min, 3 times) and again with dichloromethane (DCM, 3 min, 5 times). The peptide was cleaved from the resin and side-chain deprotected by treatment with 97 % trifluoroacetic acid (TFA) at RT for 2.5 h. Crude peptide was precipitated with cold diethylether, filtrated and dried. The peptide was purified by preparative HPLC yielding> 97 % of pure **1**. Identity was confirmed by ESI-MS (calculated mass: 967.5 Da, found: 967.5 Da).
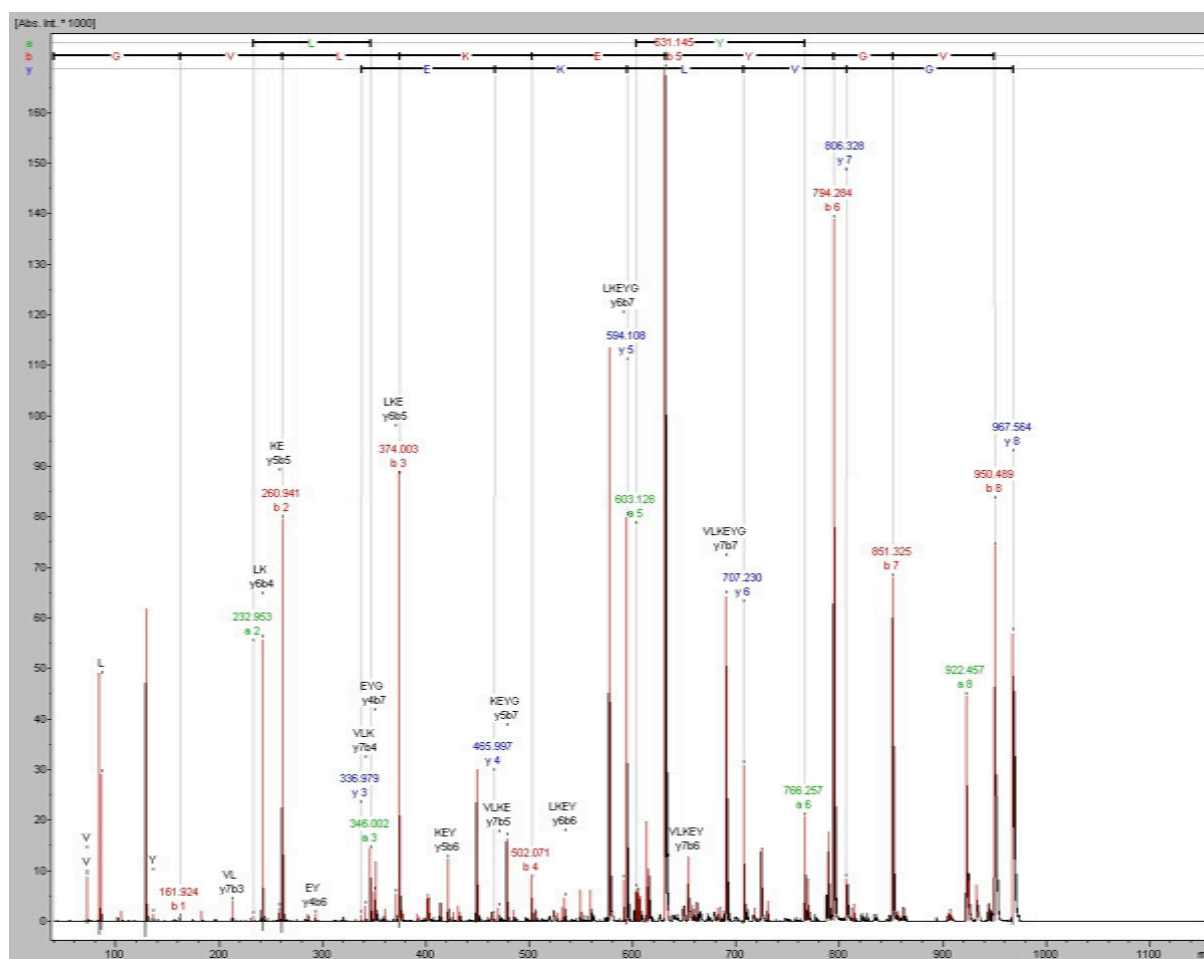
Figure S1. Fragment MS-spectra of compound **1**.

Synthesis of acylated CPS1 peptide derivatives

Method 1 - anhydrides Treatment of **1** with 1.5 eq of different anhydrides (Table S1) in dry DMF in the presence of 3 eq DIPEA at RT yielded the corresponding lysine-modified CPS1-peptide derivate. The mixture was stirred at RT for 4 to 16h. Ester bonds formed at tyrosine residue of **1** were cleaved by alkaline hydrolysis using sodium hydroxide. The reaction was monitored using analytical HPLC. The acylated CPS1 derivatives were purified by preparative HPLC and product-containing fractions were lyophilized. The identity of purified peptide derivatives was confirmed by HPLC-ESI-MS (Table S1 and Figure S16)

Method 2 - carboxylic acids Treatment of **1** with 1.5 eq of different carboxylic acids (Table S1) in dry DMF in the presence of 1.5 eq PyBOP and 3 eq DIPEA yielded the corresponding lysine-modified peptide derivative. The mixture was stirred at RT for 4 to 16h. The acyl residues at the tyrosine side chain of **1** and resulting mono-methyl/ethyl-ester (compound **3**, **5f**, **7**, **8**, **9**; Table S1) were removed by alkaline hydrolysis using sodium hydroxide. The mono-*tert*-butyl-ester and the Boc-protecting groups were removed by treated with 50 % TFA in DCM to yield deprotected compounds **4** and **5d**. The reaction was monitored using analytical HPLC. The modified CPS1-peptides were purified by preparative HPLC and product-containing fractions were lyophilized. The identity of purified peptide derivatives was confirmed by HPLC-ESI-MS (Table S1 and Figure S16)

Method 3 – 3-hydroxy-3-methylglutaryl-CoA Reaction mixture containing 8.6 mg of compound **1** and 1.5 eq of DL-3-hydroxy-3-methylglutaryl coenzyme A sodium salt hydrate was incubated in buffer (100 mM TrisHCl, pH 9.5) at RT for 96 h. 4-Dimethylaminopyridine (DMAP) was used as catalyst. Compound **6d** was isolated

using reverse phase HPLC. Molecular weight was confirmed by MALDI-ToF and purity checked by HPLC-ESI-MS (Table S1 and Figure S16).

Table S1. Lysine modifications in CPS1 substrate peptide

1   Benzoyl-Gly-Val-Leu-Lys-Glu-Tyr-Gly-Val-amide

no.	modification reagent	method	mass calculated for [M+H]$^+$ [g/mol]	mass found [M+H]$^+$ [g/mol]
2	Acetic anhydride	1	1008.0	1031.4[a]
3	Ethyl-Chlorooxoacetat	2	1039.0	1022.4[b]
4	Mono-*tert*-butyl malonate	2	1053.1	1036.4[b]
5a	Succinic anhydride	1	1067.1	1050.4[b]
5b	Methylsuccinic anhydride	1	1081.1	1081.3
5c	2,2-Dimethyl succinic anhydride	1	1095.1	1095.3
5d	Boc-Asp-O*t*Bu	2	1082.1	1082.5
5e	Itaconic anhydride	1	1079.1	1079.3
5f	mono-Ethyl fumarate	2	1065.1	1048.4[b]
5g	Maleic anhydride	1	1065.1	1048.4[b]
5h	Phenylsuccinic anhydride	1	1143.2	1126.3[b]
5i	*N*-Z-L-aspartic anhydride	1	1216.2	1199.3[b]
5j	Butylsuccinic anhydride	1	1123.2	1123.3
5k	3-Methyl-3-phenyldihydrofuran-2,5-dione	1	1157.2	1157.3
5l	3-Nitropropionic acid	2	1068.1	1091.8[a]
5m	*S*-Acetylmercaptosuccinic anhydride	1	1141.2	1163.3[a]
5o	*N*-Z-D-aspartic anhydride	1	1216.2	1216.3
5p	Fmoc-L-Asp-O*t*Bu	2	1304.0	1304.3

no.	modification reagent	method	mass calculated for [M+H]+ [g/mol]	mass found [M+H]+ [g/mol]
6a	Glutaric anhydride	1	1081.5	1064.4[b]
6b	3-Methyl glutaric anhydride	1	1095.1	1078.3[b]
6c	3,3-Dimethyl glutaric anhydride	1	1109.1	1109.3
6d	HMG-CoA	3	1111.0	1111.3
6e	Diglycolic anhydride	1	1083.1	1106[a]
6f	Thiodiglycolic anhydride	1	1099.1	1082.3[b]
6g	4-Methylmorpholine-2,6-dione	1	1096.1	1096.5
6h	*N*-Phthaloyl-D,L-glutamic anhydride	1	1226.2	1248.3[a]
7	Adipic acid monoethyl ester	2	1096.1	1078.5[b]
8	Pimelic acid monoethyl ester	2	1109.2	1131.3[a]
9	Suberic acid monomethyl ester	2	1123.2	1106.5[b]

[a] $[M+Na]^+$ [b] $[M-NH_2]^+$

Expression and purification of human Sirt5

The expression and purification of hSirt5 was done as described by Gertz et al. [17].

Expression and purification of zebrafish Sirt5

Expression of the zebrafish Sirt5 isoform (zSirt5) used for crystallization was done as described for human Sirt5, except that *E. coli* BL21-CodonPlus™ (DE3) cells (Stratagene, La Jolla, CA, USA) were used for expression. Purification of His_6-zSirt5(30-298) was done via cell-disruption of harvested cells in lysis buffer (50 mM Tris/HCl pH 8.5, 200 mM NaCl) followed by affinity-chromatography using Co^{2+}-Talon beads (Clontech, Mountain View, CA, USA). Resin was washed with 20 column volumes high-salt (50 mM Tris/HCl pH 8.5, 500 mM NaCl) and low imidazole buffer (50 mM Tris/HCl pH 8.5, 200 mM NaCl, 5 mM imidazole), respectively, and target protein was subsequently eluted using high imidazole concentration (50 mM Tris/HCl pH 8.5, 200 mM NaCl, 250 mM imidazole). Pooled eluate fractions were dialyzed against 30 mM HEPES pH 6.5, 50 mM NaCl and treated with TEV-protease at 4 °C in a 1:20 ration in an overnight step, followed by reverse affinity-chromatography on Co^{2+}-Talon to remove the hexa-Histidine tag. Flowthrough was collected, subjected to gelfiltration on a Sephacryl S-200 HR 50/100 column in 20 mM Tris/HCl pH 8.5, 150 mM NaCl and zSirt5-fractions were pooled, concentrated and stored at -80 °C.

HPLC based activity assay

For determination of kinetic constants for the Sirt5 mediated reactions solutions containing 20 mM TRIS/HCl pH 7.8, 150 mM NaCl, 5 mM MgCl$_2$, 0.5 mM NAD$^+$ and varying substrate concentrations (2-200μM) were used. Deacylation was started by adding human Sirt5 to reach a final concentration of 0.5 μM. Enzyme-catalyzed reaction was stopped using TFA (1% final concentration) after 1 to 180 min of incubation at 37°C depending on substrate reactivity. Reaction mixtures containing compound **5e**, **5f** and **5g** were stopped by pH shift through adding of 5μl sodium citrate buffer (100 mM, pH 4.0) caused by sensibility acidic hydrolysis. A control reaction (100 μM compound **4a**, 0.5 μM NAD$^+$, 0.5 μM Sirt5 in reaction buffer and 5μl sodium citrate buffer pH 4.0, 37 °C, overnight) verified that the reaction was completely stopped. The cleavage rate of the different CPS1 peptide derivatives was analyzed using analytical reversed phase HPLC. The product and substrate peaks were quantified using absorbance at 260 nm (absorption of *N*-terminal benzoyl moiety). The peak areas were integrated and converted to initial velocity rates calculated from the ratio of product area to total peak area. Linear regression of conversions plotted against time yielded reaction rates in μM/min (relative conversion below 20 % of substrate). Non-linear regression according to Michaelis-Menten of the reaction rates at different substrate concentrations yielded K_M- and k_{cat}-values using the program SigmaPlot (Systat Software, San Jose, USA). All measurements were done in duplicates.

The analysis of kinetic constants for NAD$^+$ was performed equally. The reaction mixtures contained 100 μM of **5a** or **5b**, 0.5 μM human Sirt5 and varying concentrations of NAD$^+$ (10 - 2000 μM). The resulting velocity-substrate-plots were fitted with Michaelis-Menten-equation.
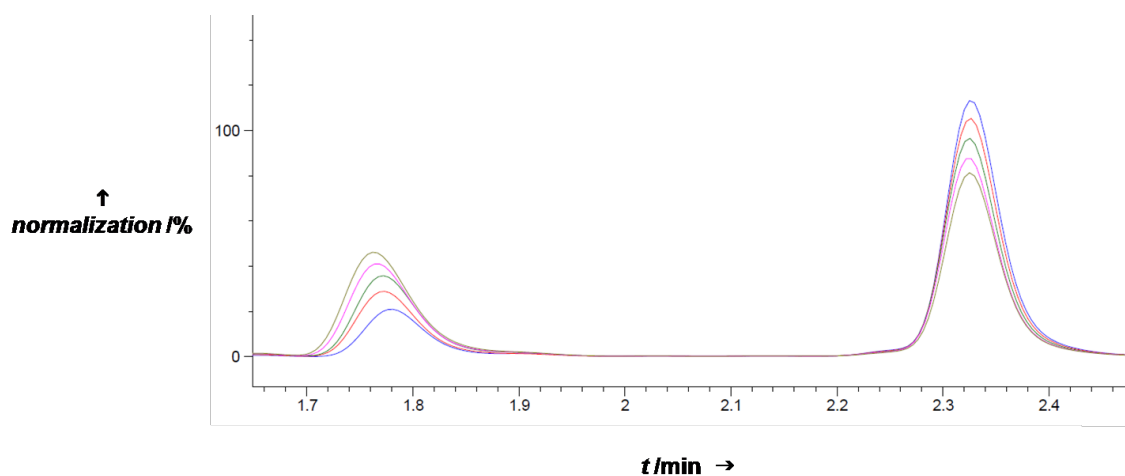

Figure S2. HPLC traces (260 nm) of **5a** after different incubation times with Sirt5. Reaction conditions: 100 μM compound **5a**, 500 μM NAD$^+$ and 0.5 μM Sirt5. Detection wavelength: 260 nm. Incubation time 20 min (blue), 30 min (red), 40 min (green), 50 min (pink) and 60 min (olive green).
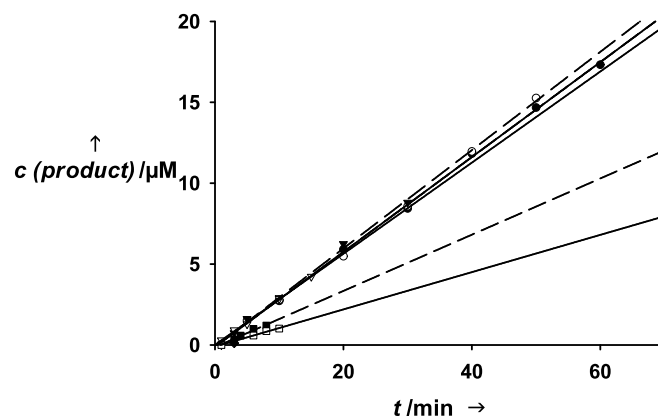
Figure S3. Progress curves for **5a**. Reaction conditions: 500 µM NAD$^+$, 0.5 µM Sirt5 and different concentrations of **5a** (2µM – white square, 5µM – black square, 25µM – white triangle, 50µM black triangle, 75µM white spot, 100µM black spot). Reaction was monitored by HPLC.
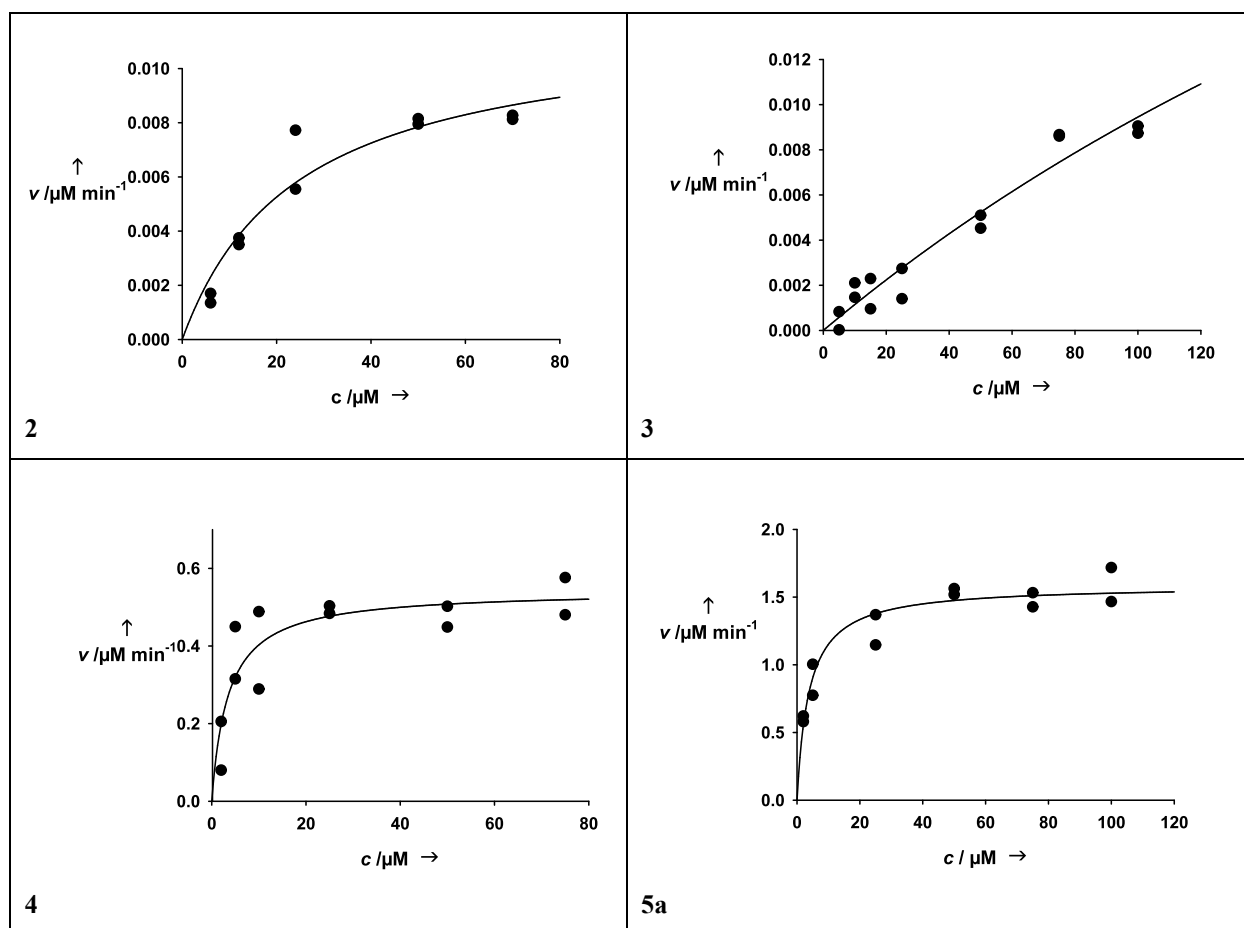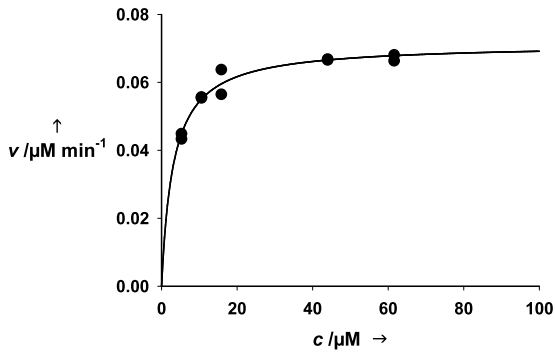
5b
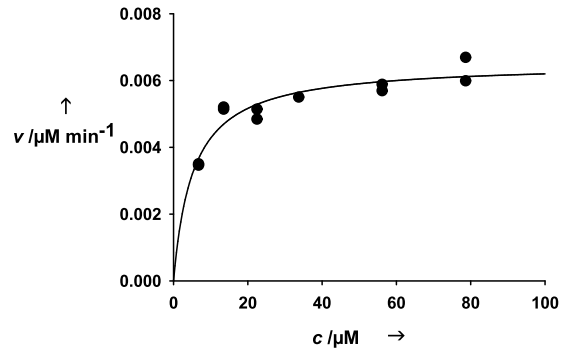
5c
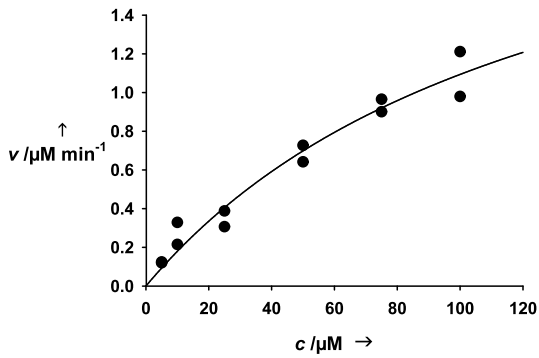

5d
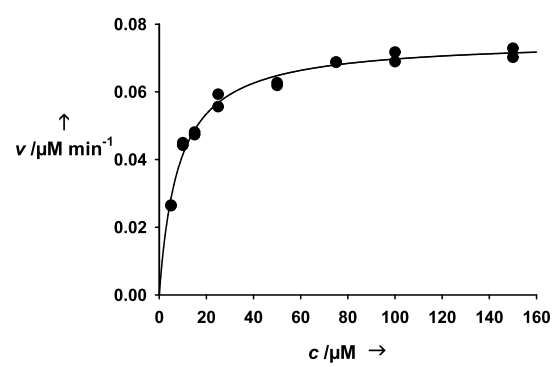
5e
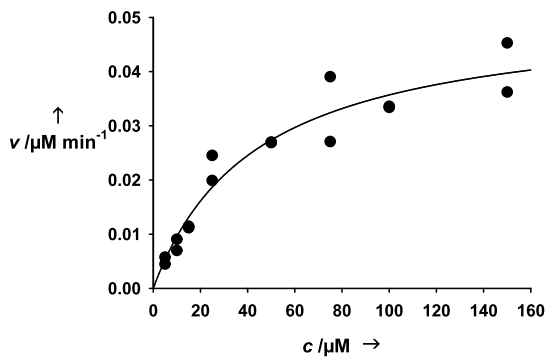
5f
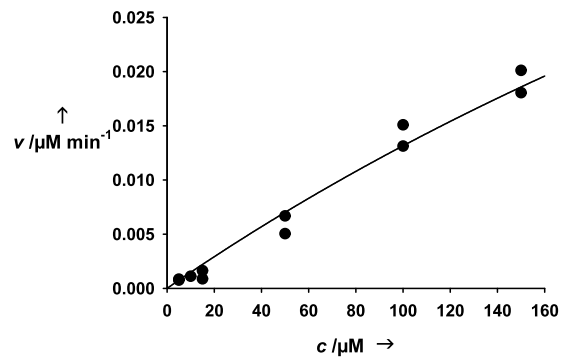
5g
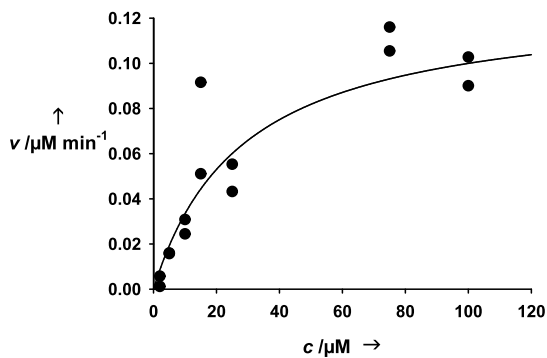
5l
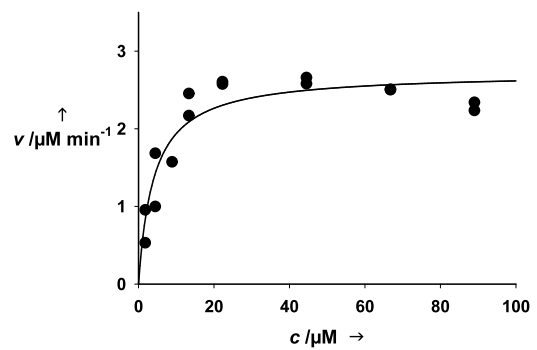
6a

6b

6c

6d

6e

6f

6g

7

8

9
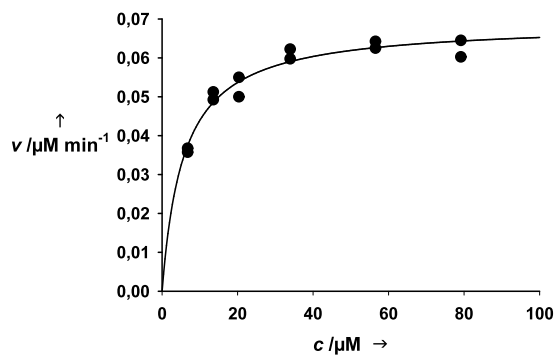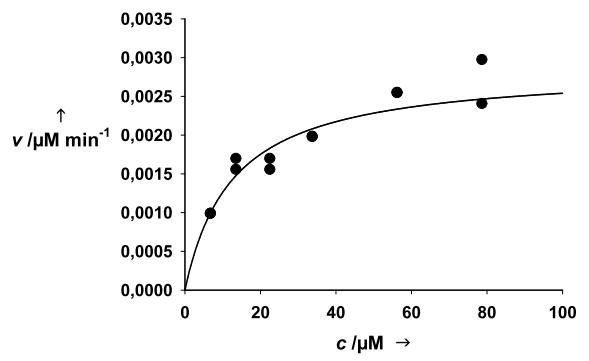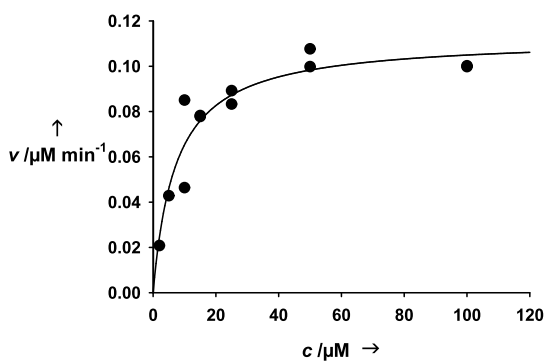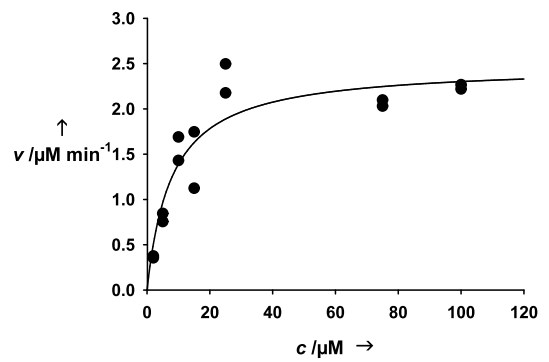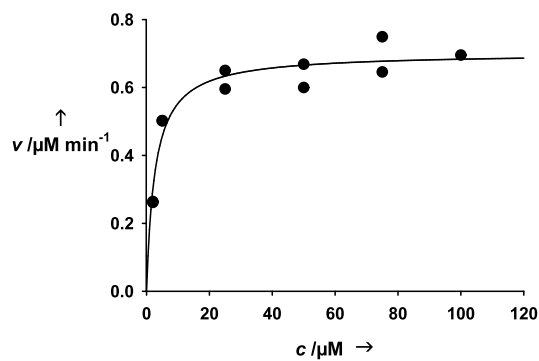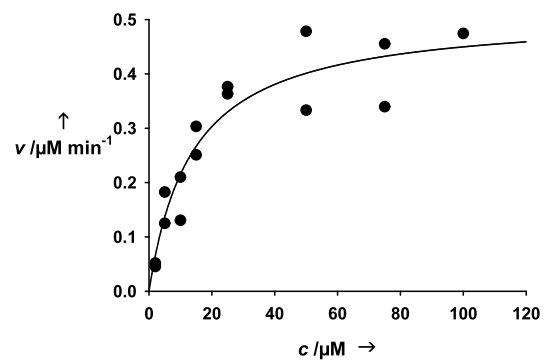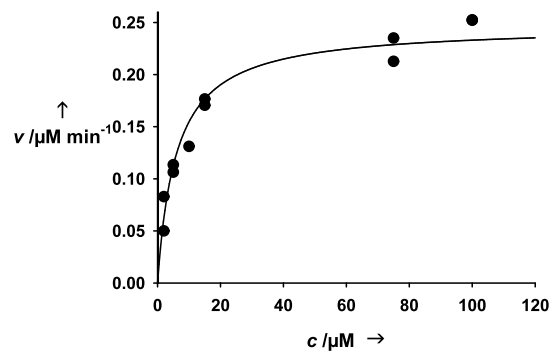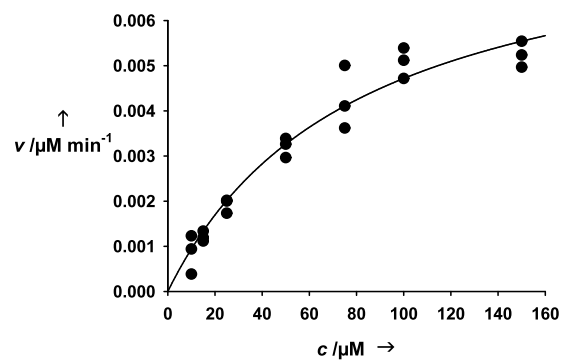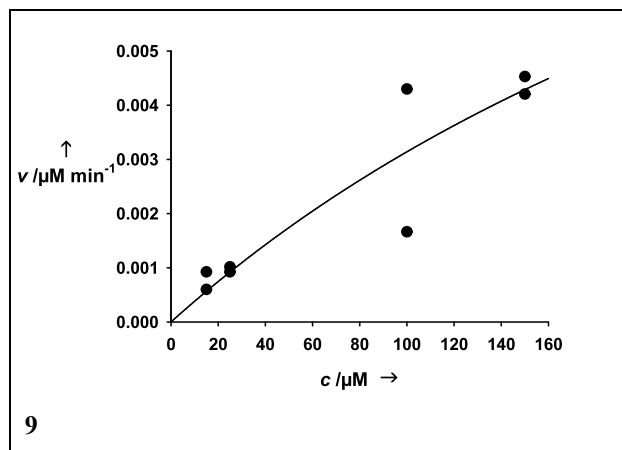
Figure S4. Kinetic characteristics for Sirt5 substrates. The reactions were performed with 0.5 µM Sirt5, 500 µM NAD$^+$ and varying concentrations of substrates (2-150 µM). All reactions were done in duplicates. Lines represent the Michaelis-Menten-plot.

c	compound	5a	5b
	K$_M$ [µM]	40.7± 5.2	25.4 ± 5.5
	k$_{cat}$[s^{-1}]	6.3x10^{-2} ± 2x10^{-3}	1.5x10^{-3} ± 7x10^{-5}
	k$_{cat}$/K$_M$ [µM^{-1}s^{-1}]	1551	58
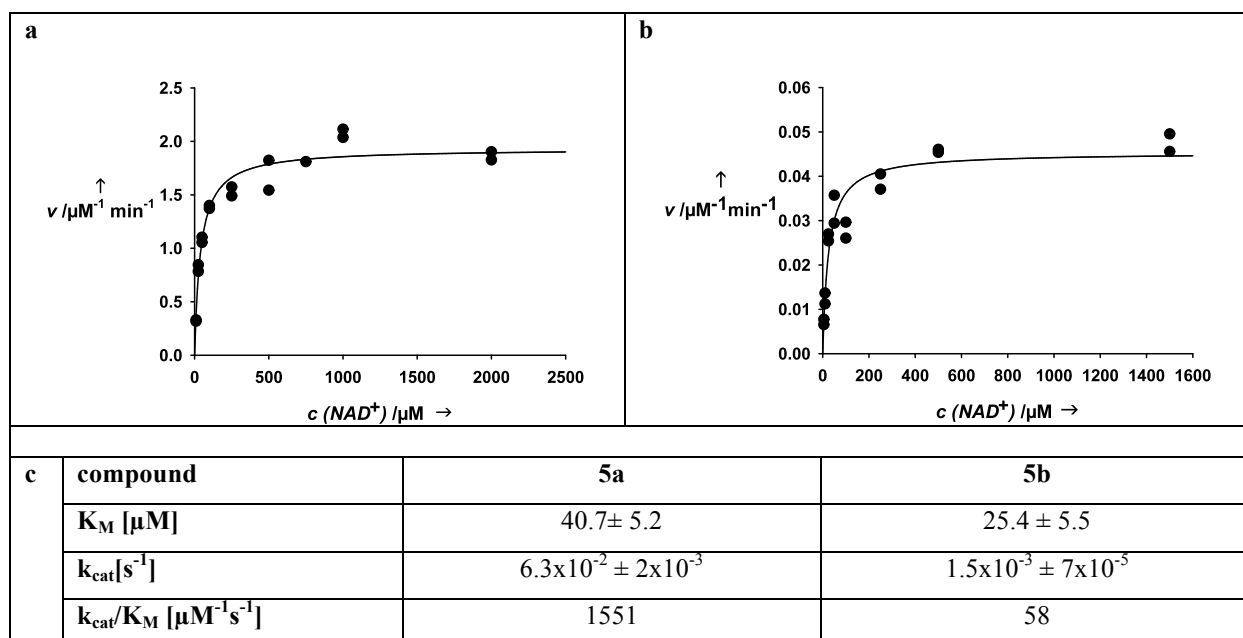
Figure S5. Kinetic characteristics for NAD$^+$ with **5a** (a) and **5b** (b). The reactions were performed with 0.5 µM Sirt5, 100 µM compound **5a** or **5b** and varying concentrations of NAD$^+$ (10-2000 µM). All reactions were done in duplicates and monitored by HPLC. The curves represent Michaelis-Menten plots resulting in kinetic constants given in (c).

Determination of the inhibitor constants K$_i$

K$_i$ values of the inhibitors were determined recording k$_{cat}$ and K$_M$ values for **5a** in the presence of varying inhibitor concentrations (50-250 µM). The program SigmaPlot was used for generation of the respective plots. The linear regression of the apparent K$_M$-values against the corresponding inhibitor concentration yielded the inhibitor constant K$_i$.

5h

5i

5j

5k

5m

5p

6h
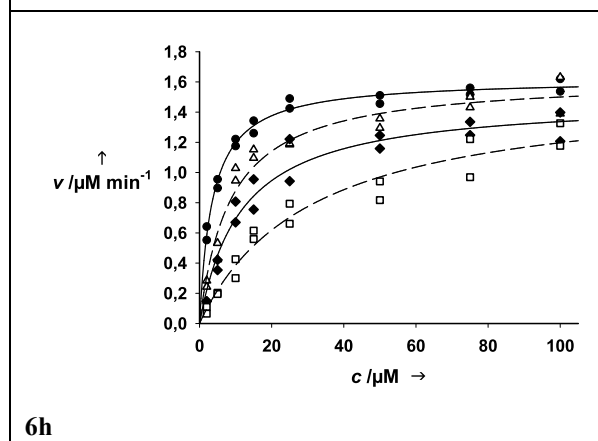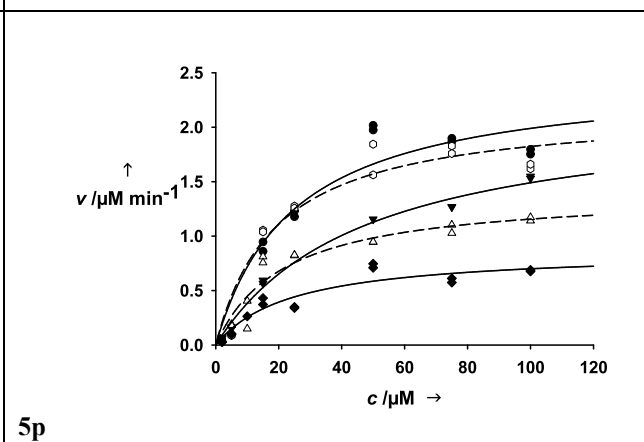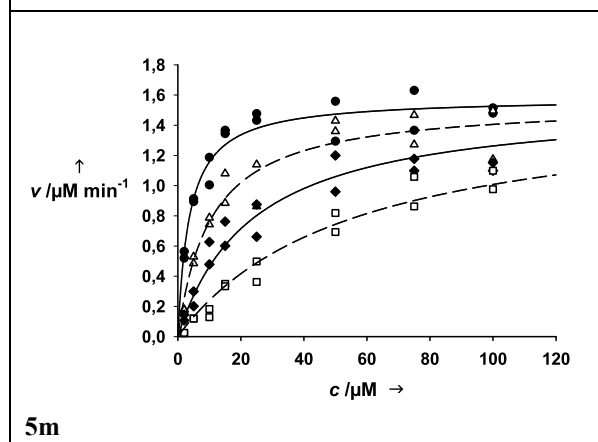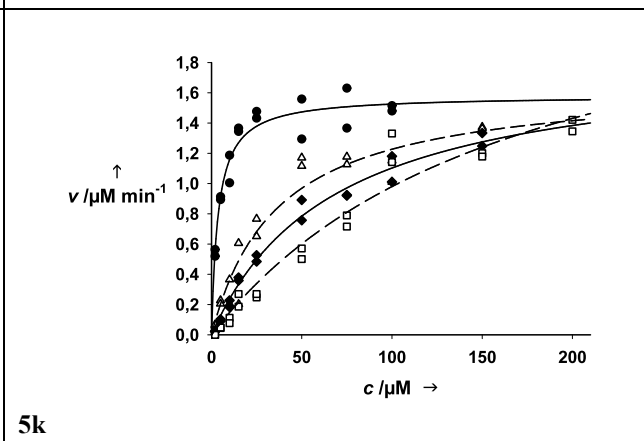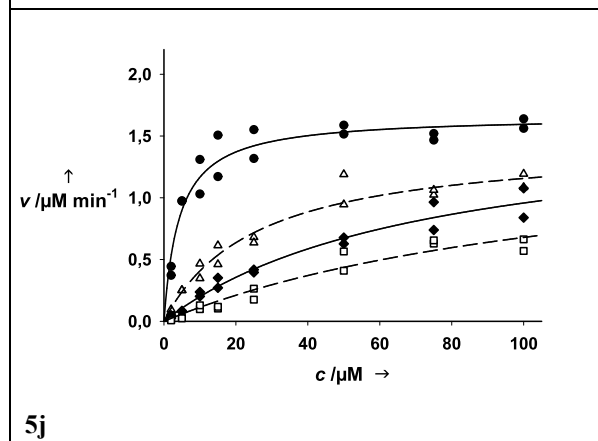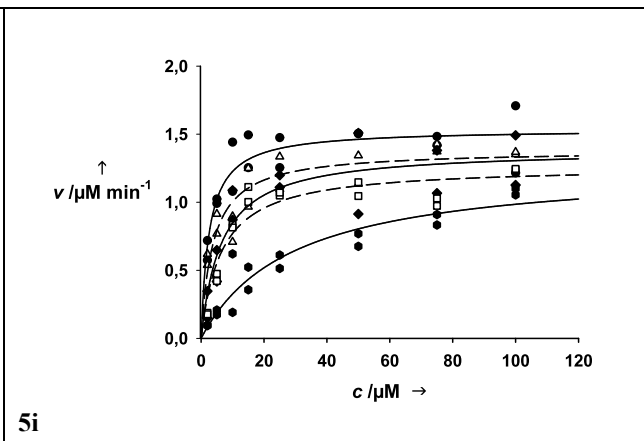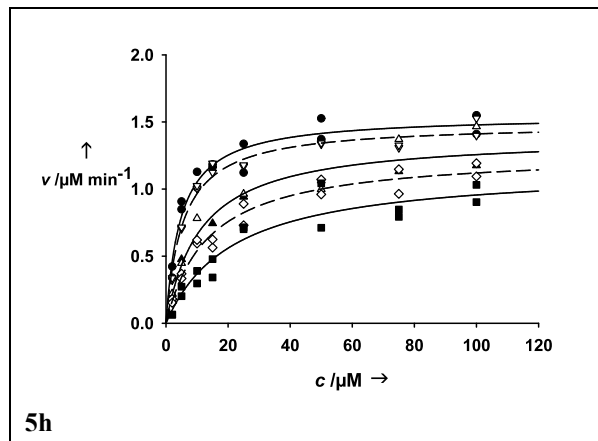
Figure S6. Kinetic characteristics for Sirt5 inhibitors. The reactions were performed with 0.5 μM Sirt5, 500 μM NAD$^+$ and varying concentrations of substrates/inhibitors (2-150 μM). For determination of the K$_i$ values different concentrations of inhibitor (10μM – hexagon, 25μM - triangle down, 50 μM - triangle up, 100 μM - diamond, 250 μM- square) were used. All reactions were done in duplicates. Lines represent the Michaelis-Menten-plots.

5k

5m

5p

6h

13
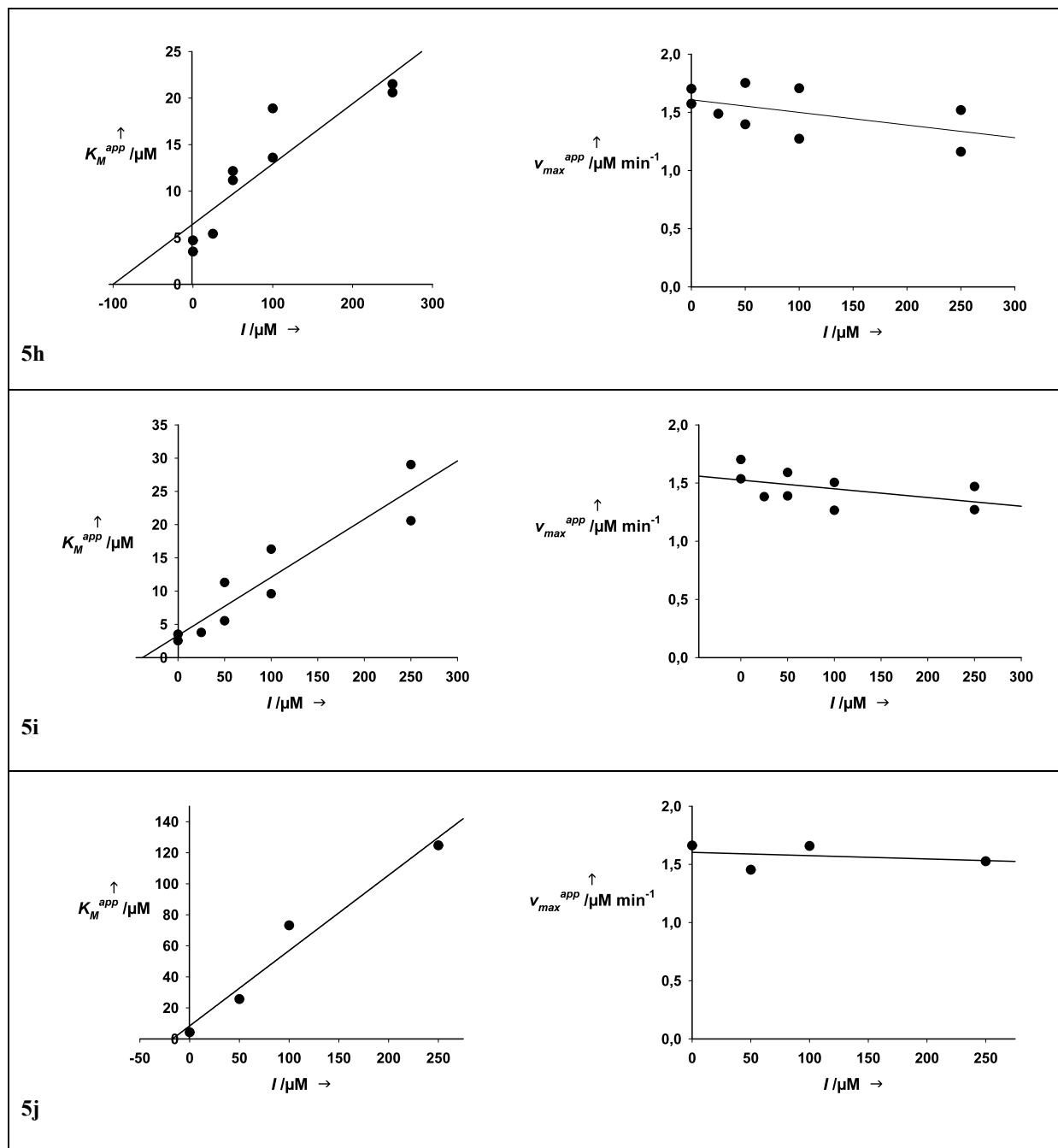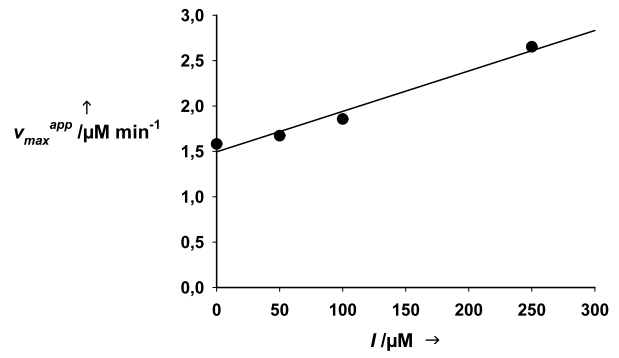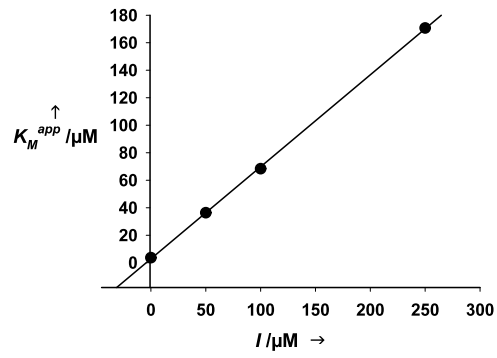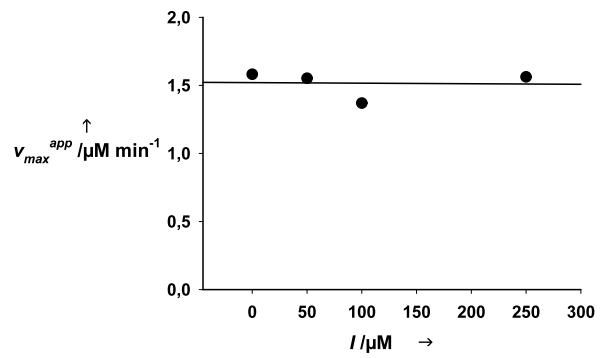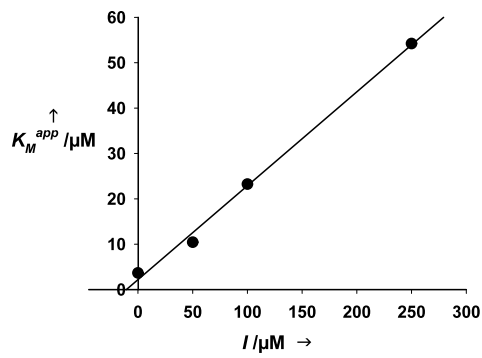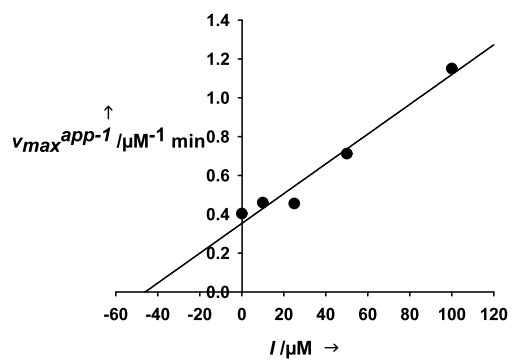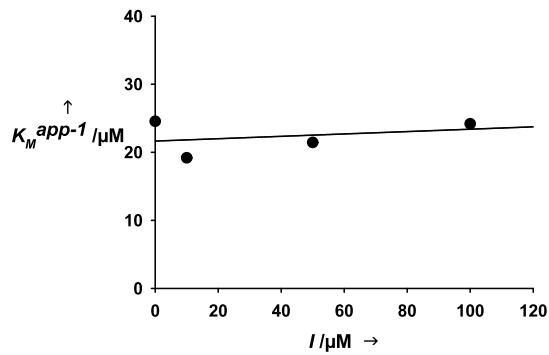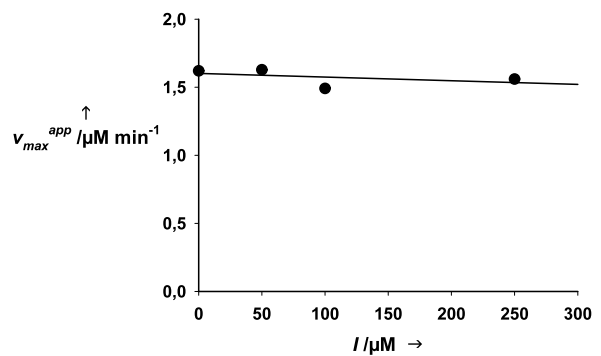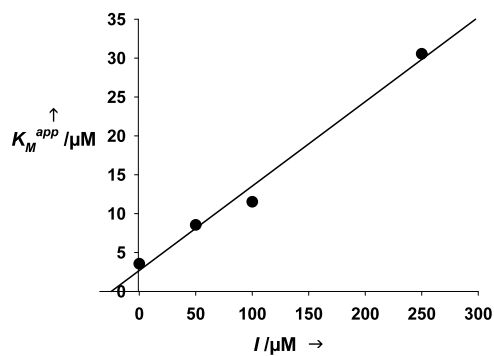
Figure S7. Secondary plots for Sirt5 inhibitors. The apparent K_M and V_{max} values from v/S characteristics were plotted against the corresponding inhibitor concentration. The negative K_i value can be determined as intersection with the X-axis from the K_M^{app}/I plot respectively from the v_{max}^{app-1}/I plot.

Table S2. Inhibition constants for different Sirt5 inhibitors.

compound	K_i [μM]
5h	100.0 ± 0.45
5i	38.1 ± 0.63
5j	17.2 ± 1.31
5k	4.3 ± 0.32
5m	10.6 ± 0.66
5p	46.0 ± 0.22
6h	24.9 ± 0.54

Determination of specificity of sirtuin inhibition by 5k

The inhibitor specificity was tested against Sirt1-3 by determination of cleavage rates in the presence of **5k**. The reaction mixture contained 20 mM TRIS/HCl pH 7.8, 150 mM NaCl, 5 mM $MgCl_2$, 0.5 mM NAD^+, 10 μM of substrate and 50μM of inhibitor **5k**. Compound **2** was used as substrate for Sirt1 and 3, compound **5a** for Sirt5, the peptide derivative H-PSDK(Ac)TIGGWW-NH_2 derived from α-tubulin for Sirt2. Deacylation was started by adding enzyme to reach a final concentration of 0.5 μM. The reaction was stopped using TFA (1% final concentration) after 2 to 10 min of incubation at 37°C depending on substrate reactivity. The inhibition was analyzed by analytical HPLC as described above.

Table S3: Inhibition of different Sirtuins by compound **5k**.

sirtuin	inhibition at 50 μM [%]
Sirt1	< 1
Sirt2	4.23 ± 2.16
Sirt3	< 1
Sirt5	70.43 ± 11.75

Isothermal Titration Calorimetry (ITC)

To minimize unspecific heat effects, human Sirt5 had to be dialyzed again against buffer A. The CPS1 peptide derivatives were then diluted with this buffer. All ITC measurements were performed at 10°C using a MicroCalVP-ITC isothermal titration calorimeter (MicroCal Inc., Northampton, USA). The sample cell (1.4 ml) was filled with a 5 μM solution of human Sirt5 and a 200-500 μM solution of peptide was loaded into the injection syringe (280 μl). Each titration experiment was started with a 300 s delay followed by 28 or 56 injections of 10 or 5 μl of the peptide solution, respectively, in intervals of 250 seconds. The sample cell was stirred at 300 rpm. Control experiments where peptide was injected in the absence of protein allowed the subtraction of heats of dilution. The data was analyzed using the Origin 5.0 software (Microcal Inc.,

Northampton, USA). The corrected data were analyzed by nonlinear regression with a single-site binding model. The area under each peak of the resulting heat profile was integrated and plotted against the molar ratio of Sirt5 to titrant.


5a

5b

5c

5h
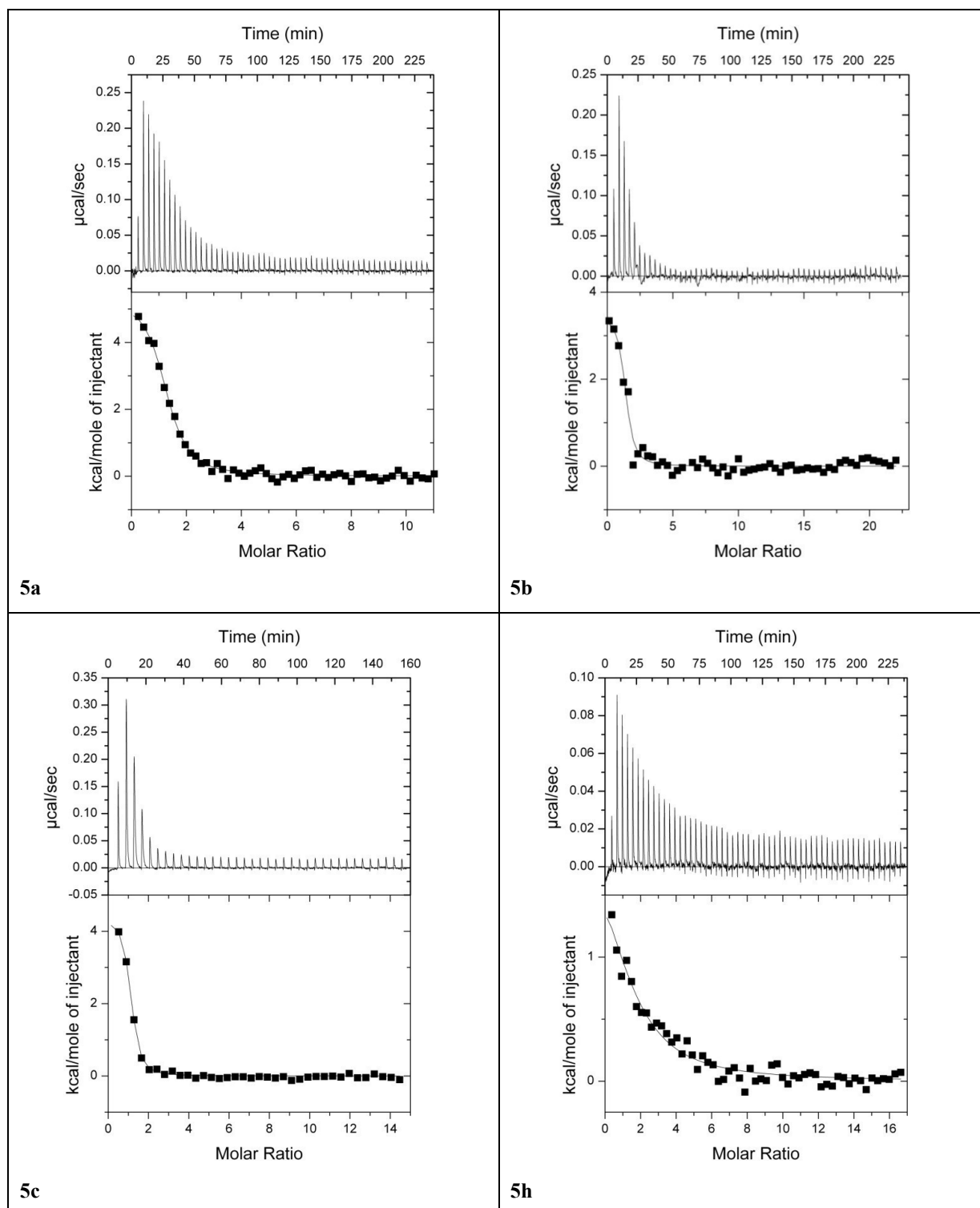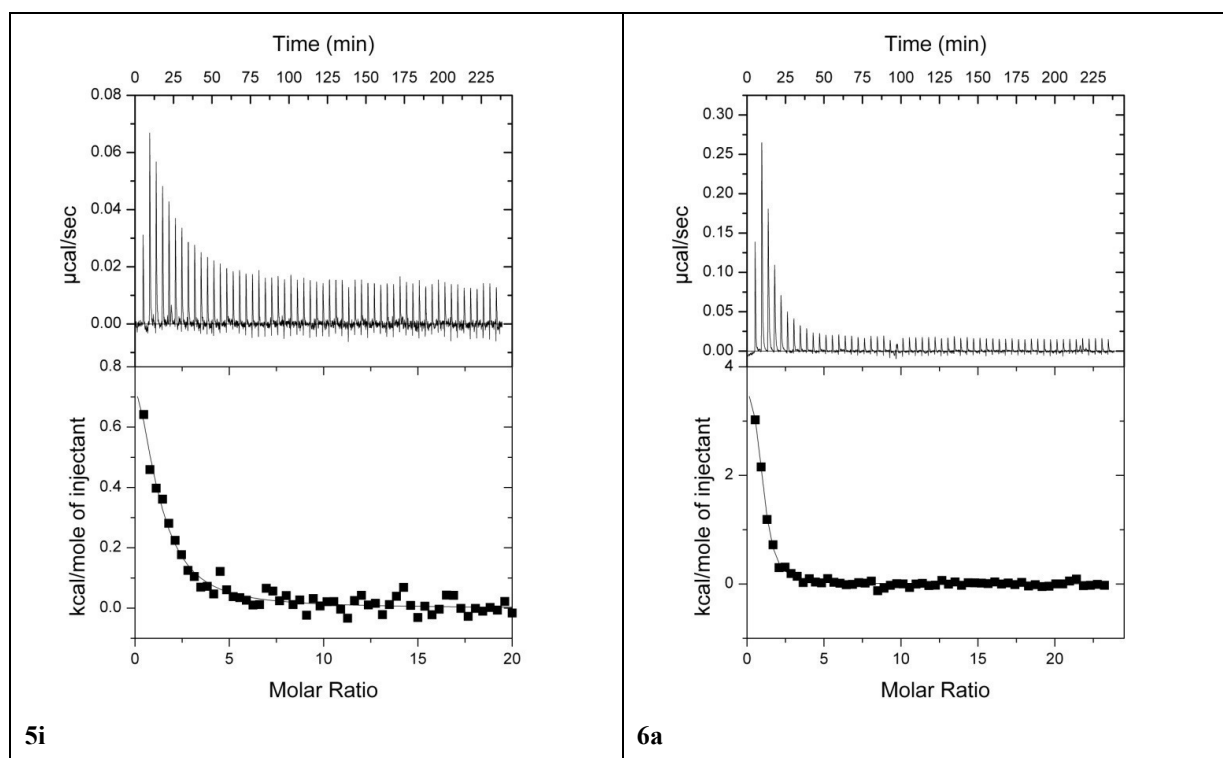
Figure S8. Isothermal titration calorimetry of different Sirt5 substrates and inhibitors. The compounds (20-100µM end concentration) were titrated into 5 µM Sirt5 diluted in dialysis buffer containing 20 mM TRIS/HCl pH 7.8, 150 mM NaCl, 5 mM $MgCl_2$. Titration was carried out in 56 steps à 5 µl at 10°C with in an incubation time of 250 s (upper graphs). The area under each peak of the resulting heat profile was integrated and plotted against the molar ratio of Sirt5 to titrant (lower graphs). The data were analyzed by nonlinear regression with a single-site binding model.

Table S4. K_D-values.

compound	K_D [µM]
5a	0.71 ± 0.05
5b	0.83 ± 0.17
5c	0.29 ± 0.04
5h	8.20 ± 0.55
5i	5.78 ± 2.36
6a	0.70 ± 0.11

Fluorescence titration

Tryptophan fluorescence titration experiments were carried out on a Hitachi F-4500 spectrometer (Tokyo, Japan) using an excitation wavelength of 280 nm. Emission was measured at 330 nm at 25°C. Peptide solution was added successively (2-10 µM end concentration) to 5 µM human Sirt5 in buffer containing 20 mM TRIS/HCl pH 7.8, 150 mM NaCl. Fluorescence intensities were recorded subsequent to reaching equilibrium for each titration step. Dissociation constants were determined using a single-site binding model.

Modeling

The molecular structures of all peptides described in the present work were generated using the MOE 2012.10 program (Chemical Computing Group, Montreal, Canada).[18] The initial conformations resulted from energy minimization using the Amber99SB force field as implemented in MOE.[19] Two crystal structures of human Sirt5, one in complex with a succinylated peptide and NAD^+, and another one with a thioacetylated peptide and CHES were retrieved from the Protein Databank (PDB code 3RIY and 3RIG). For the subsequent docking studies, all water and ligand molecules were removed and both structures were protonated and minimized using the Amber99SB force field.

All dockings studies were carried out using the GOLD5.1 docking program (Cambridge Crystallographic Data Centre, Cambridge, UK) in exhaustive sampling mode.[20] The binding cavity was defined by the co-crystallized succinylated peptide. To guide the search process, the position of the co-crystallized lysine of 3RIY was used as a substructure constraint. Using Goldscore as fitness function, the co-crystallized peptides were correctly docked into the Sirt5 catalytic site.

All tested peptides were docked in both crystal structures and 20 docking poses were stored. The resulting poses were manually analyzed and docking solutions with the highest overlap to the crystal structure position of the co-crystallized peptide were selected for subsequent refinement runs. For each binding hypothesis, an energy minimization of the peptide and proximal pocket residues was carried out using the Amber99SB force field. This procedure resulted in a final docking model for each of the synthesized peptides.
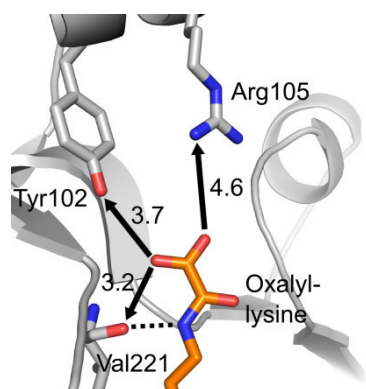

Figure S9. Model of hSirt5 in complex with **3** (orange). The distances (given in Å) between the carboxyl group of **3** and proximal protein atoms are drawn as black arrows and hydrogen bonds are indicated as dashed lines. The carboxyl moiety is too far away to form hydrogen bonds to Tyr102 and Arg105.

Figure S10. Model of hSirt5 in complex with **5c** (cyan) superimposed with the NAD$^+$ conformation observed in the X-ray structures of hSirt5 (NAD$^+$ from 3RIY). The distances (given in Å) between the methyl group of **5c** and NAD$^+$ in the productive conformation are drawn as black arrows and hydrogen bonds are indicated as dashed lines. The methyl group of **5c** might hinder the nucleophilic attack on the *C*1 atom of NAD.


Figure S11. Sequence alignment of zSirt5 and hSirt5. Both proteins are highly similar (blue) with a sequence identity of 75%. Most of the substitutions are located in the *N*-terminal region (red) which comprises a ~35 residue mitochondrial localization sequence removed during transport into the organelle.

Crystallization and structure solution

The zSirt5 protein (10 mg/mL; 20 mM TRIS/HCl pH 8.5, 150 mM NaCl) was co-crystallized with 1 mM CPS1-peptides at 20 °C. Protein and peptide (peptide 50 mM stocks in DMSO, 10% final DMSO concentration for crystallization) were mixed and pre-incubated for 30 min on ice before setting up hanging-drop vapor-diffusion crystallization experiments. 2 µL crystallization drops were constituted of a 2:1, 1:1 or 1:2 ratio of protein:reservoir solutions (reservoir: 18-24% PEG3350, 0.1 M HEPES pH 7.2 to 7.8; depending on the acylated peptide) and equilibrated against 250 µL reservoir. Crystals grew up to 300 x 300 x 300 µM in size in about two weeks (again depending on acylated peptide). They were transferred to a cryo-solution drop composed of the respective reservoir and peptide, supplemented with 25% glycerol, prior to shock-freezing using liquid nitrogen. Diffraction data collection was performed at BESSY II beamline MX14.1[21] (operated by the Helmholtz-Zentrum Berlin, Germany) with an MX-225 CCD (Rayonix, Evanston, IL, USA) or a Pilatus 6M detector (Dectris, Baden, Switzerland). Indexing, scaling and merging of diffraction data were done using XDS.[22] Structures were solved by molecular replacement using MolRep[23a] using human Sirt5 (PDB entry NYR) as a search model for the first zSirt5 structure, which was then used as search model for subsequent complex structures.[23b] Refinement was performed with Refmac5.[24] For refinement of structures with resolution around 3 Å or less (all complexes except for those with the **5h** or **5j**, respectively, as a ligand), local NCS restraints and the Prosmart function using protein chain A from PDB-ID 3RIY as a model was used during refinement.[25] Furthermore, TLS-refinement was used during the last refinement steps.[26] Manual modeling and structure validation were done with Coot.[27] Geometry parameter files for the peptides' acylated lysine-residues were generated using the PRODRG server[28] and structure figures created with PyMol (www.pymol.org).

Table S5. Data collection and refinement statistics.

	zSirt5 + 5h	zSirt5 + 5a	zSirt5 + 6a	zSirt5 + 7	zSirt5 + 5i
Data processing					
Space group	P 6_5 2 2	P 6_5 2 2	P 6_5 2 2	P 6_5 2 2	P 6_5 2 2
Unit cell (a / b / c) [Å]	88.9/88.9/305.3	87.4/87.4/314.9	87.2/87./314.0	87.3/87.3/314.6	87.2/87.2/313.9
Resolution (outermostshell)	100.00 - 2.40 (2.45 - 2.40)	100.00 - 3.00 (3.10 - 3.00)	100.00 - 2.90 (3.00 - 2.90)	50.00 - 3.30 (3.40 - 3.30)	20.00 - 2.80 (2.90 - 2.80)
Unique reflections (o. s.)	29005 (1681)	15155 (1362)	16586 (1549)	11477 (948)	18292 (1784)
Observations (o. s.)	207062 (12353)	123469 (11516)	1164771 (11295)	114909 (9814)	191409 (19772)
Completeness (o. s.)	100.0% (100.0%)	99.9% (99.9%)	99.8% (100.0%)	99.9% (100.0%)	99.6% (100.0%)
Mutliplicity (o. s.)	7.1 (7.3)	8.1 (8.5)	7.0 (7.3)	10.0 (10.4)	10.5 (11.1)
R-meas (o. s.) [a]	13.4% (130.5%)	19.9% (155.9%)	17.5% (133.6%)	34.7% (132.1%)	26.1% (218.0%)
I/sigma (o. s.)	14.4 (1.9)	10.6 (1.5)	11.3 (1.7)	9.1 (2.4)	10.6 (1.3)
Refinement					
amino acids (aa range)	33 - 298	33 - 298	35 - 298	33 - 298	33 - 298
protein atoms	4026	4094	4054	4057	4103
peptide atoms	162[d]	75	76	77	86
zincs	2	2	2	2	2
waters	134	17	57	30	52
solvent atoms	20	23	17	24	32
Resolution (outermostshell)	47.85-2.40 (2.46-2.40)	75.73-3.00 (3.08-3.00)	75.53-2.90 (2.98-2.90)	48.41-3.30 (3.39-3.30)	19.87-2.80 (2.87-2.80)
R_{cryst}[b]/ R_{free}[c]	19.7 / 22.7	21.5 / 26.7	21.8 / 26.1	20.9 / 25.4	20.8 / 26.1
B factor protein [Å^2]	44.271	71.169	61.104	68.418	70.707
B factor peptide [Å^2]	42.196	65.457	55.932	64.548	72.053
B factor Zn [Å^2]	38.195	74.475	63.590	67.170	79.355
B factor water[Å^2]	37.113	39.804	57.029	23.935	43.432
B factor solvent atoms [Å^2]	59.381	69.627	37.739	63.260	68.051
RMSD bond lengths / target [Å]	0.016 / 0.019	0.011 / 0.019	0.012 / 0.019	0.011 / 0.019	0.012 / 0.019
RMSD angles / target [°]	1.922 / 1.968	1.673 / 1.965	1.794 / 1.960	1.687 / 1.963	1.690 / 1.968
RMSD planes / target [Å]	0.010 / 0.021	0.008 / 0.021	0.009 / 0.021	0.009 / 0.021	0.008 / 0.021

	zSirt5 + 5l	zSirt5 + 5j '[e]	zSirt5 + 5b	zSirt5 + 5c	
Data processing					
Space group	P 6_5 2 2	P 6_5 2 2	P 6_5 2 2	P 6_5 2 2	
Unit cell (a / b / c) [Å]	87.5/87.5/313.8	87.4/87.4/315.1	87.5/87.5/314.4	87.5/87.5/314.8	
Resolution (outermost shell)	50.00 - 3.10 (3.20 - 3.10)	50.00 - 2.90 (3.00 - 2.90)	50.00 - 3.00 (3.10 - 3.00)	50.00 - 2.90 (3.00 - 2.90)	
Unique reflections (o. s.)	13762 (1203)	16737 (1569)	15155 (1378)	16749 (1569)	
Observations (o. s.)	158350 (12752)	135088 (9991)	78545 (7388)	211283 (20615)	
Completeness (o. s.)	99.9% (100.0%)	99.9% (99.9%)	99.8% (99.9%)	99.9% (100.0%)	
Mutliplicity (o. s.)	11.5 (10.6)	8.1 (6.4)	5.2 (5.4)	12.6 (13.1)	
R-meas (o. s.) [a]	22.3% (137.2%)	17.9% (110.2%)	14.9% (98.8%)	17.0% (161.6%)	
I/sigma (o. s.)	14.3 (2.1)	13.3 (1.9)	12.5 (2.1)	15.8 (2.0)	
Refinement					
amino acids (aa range)	33 - 298	33 - 298	33 - 298	33 - 298	
protein atoms	4050	4083	4111	4111	

peptide atoms	75	79	152[d]	77	
zincs	2	2	2	2	
waters	34	58	41	54	
solvent atoms	32	28	36	24	
Resolution (outermost shell)	48.38 – 3.10 (3.18 – 3.10)	48.44-2.90 (2.98-2.90)	48.39 – 3.00 (3.08 – 3.00)	48.42 – 2.90 (2.98 – 2.90)	
R_{cryst}[b] / R_{free}[c]	19.4 / 26.2	20.3 / 25.4	19.9 / 27.0	19.2 / 25.2	
B factor protein [Å2]	68.693	53.300	65.068	73.805	
B factor peptide [Å2]	66.963	47.064	57.426	67.833	
B factor Zn [Å2]	72.240	57.420	71.470	85.195	
B factor water [Å2]	33.970	26.874	33.835	46.885	
B factor solvent atoms [Å2]	62.783	49.472	62.289	73.300	
RMSD bond lengths / target [Å]	0.013 / 0.019	0.011 / 0.019	0.014 / 0.019	0.013 / 0.019	
RMSD angles / target [°]	1.704 / 1.963	1.558 / 1.962	1.730 / 1.967	1.709 / 1.965	
RMSD planes / target [Å]	0.008 / 0.021	0.007 / 0.021	0.008 / 0.021	0.008 / 0.021	

[a] $$R_{meas} = \frac{\sum_h \sqrt{\frac{nh}{nh-1}} \sum_i^{nh} |\hat{I}_h - I_{h,i}|}{\sum_h \sum_i^{nh} I_{h,i}} \quad \text{with} \quad \hat{I}_h = \frac{1}{nh} \sum_i^{nh} I_{h,i}$$ [b]. $R_{cryst} = \frac{\sum ||F_{obs}| - k|F_{calc}||}{\sum |F_{obs}|}$ $|F_{obs}|$ is the

observed and $|F_{calc}|$ the calculated structure factor amplitude. [c] R_{free} was calculated from 5% of measured reflections omitted from refinement.[d] Peptide was modeled in two possible conformations. [e] Only the C2 substituted derivative of **5j** was observed in the crystals.
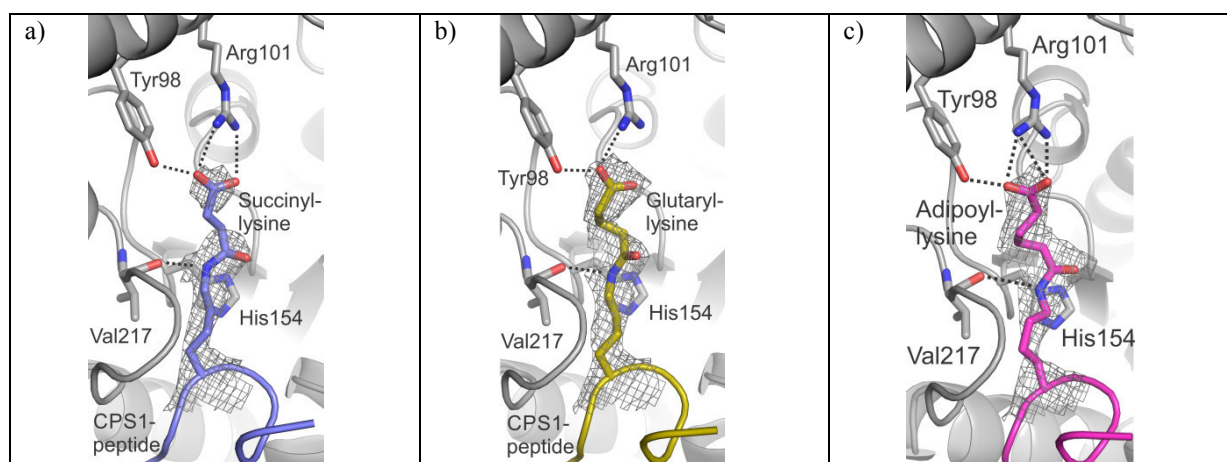

Figure S12. a) Crystal structure of zSirt5 in complex with **5a**. 2Fo-Fc electron density for the acylated lysine of the peptide ligand (blue) is contoured at 1σ. Polar interactions to the backbone of Val217 and the side-chains of Tyr98 and Arg101 are indicated by dotted lines; b) Crystal structure of zSirt5 in complex with **6a**. 2Fo-Fc electron density for the acylated lysine of the peptide ligand (yellow) is contoured at 1σ. Polar interactions to the backbone of Val217 and the side-chains of Tyr98 and Arg101 are indicated by dotted lines; c) Crystal structure of zSirt5 in complex with **7**. 2Fo-Fc electron density for the acylated lysine of the peptide ligand (magenta) is contoured at 1σ. Polar interactions to the backbone of Val217 and the side-chains of Tyr98 and Arg101 are indicated by dotted lines.
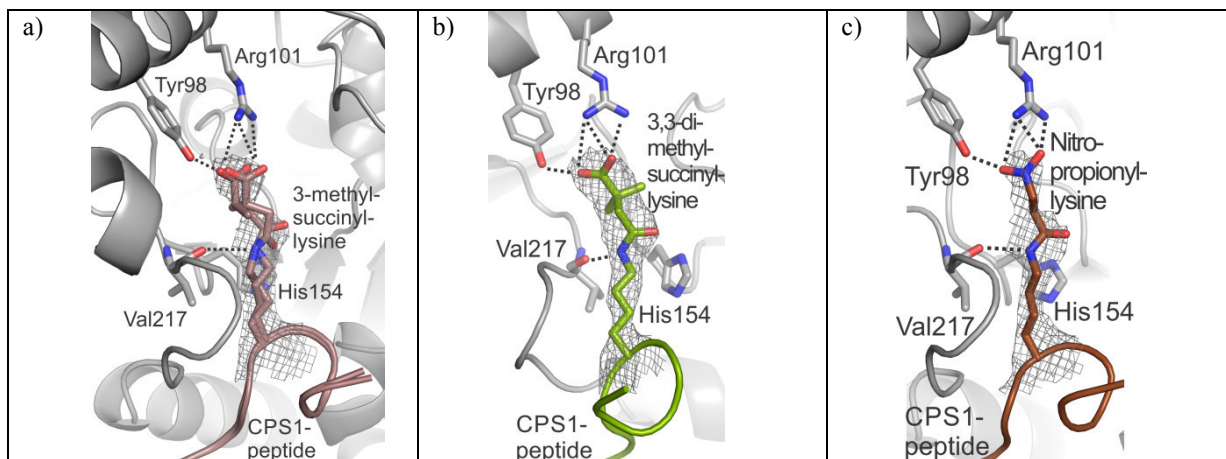
Figure S13. a) Crystal structure of zSirt5 in complex with **5b**. 2Fo-Fc electron density for the acylated lysine of the peptide ligand (brown) is contoured at 1σ. Polar interactions to the backbone of Val217 and the side-chains of Tyr98 and Arg101 are indicated by dotted lines; b) Crystal structure of zSirt5 in complex with **5c**. 2Fo-Fc electron density for the acylated lysine of the peptide ligand (green) is contoured at 1σ. Polar interactions to the backbone of Val217 and the side-chains of Tyr98 and Arg101 are indicated by dotted lines; c) Crystal structure of zSirt5 in complex with **5l**. 2Fo-Fc electron density for the acylated lysine of the peptide ligand (dark brown) is contoured at 1σ. Polar interactions to the backbone of Val217 and the side-chains of Tyr98 and Arg101 are indicated by dotted lines.
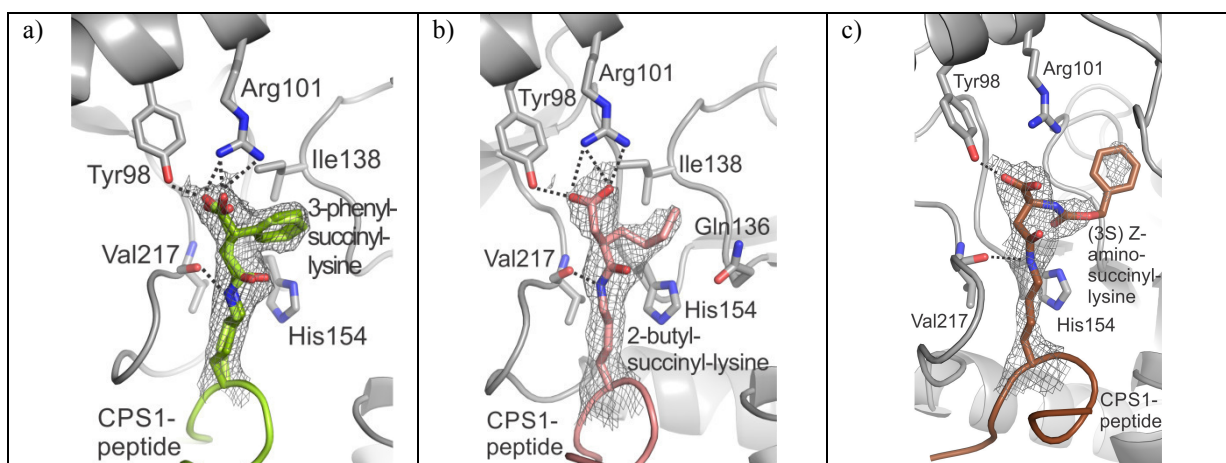
Figure S14. a) Crystal structure of zSirt5 in complex with **5h**. 2Fo-Fc electron density for the acylated lysine of the peptide ligand (green) is contoured at 1σ. Polar interactions to the backbone of Val217 and the side-chains of Tyr98 and Arg101 are indicated by dotted lines; b) Crystal structure of zSirt5 in complex with **5j'**. 2Fo-Fc electron density for the acylated lysine of the peptide ligand (skin-coloured) is contoured at 1σ. Polar interactions to the backbone of Val217 and the side-chains of Tyr98 and Arg101 are indicated by dotted lines; c) Crystal structure of zSirt5 in complex with **5i**. 2Fo-Fc electron density for the acylated lysine of the peptide ligand (dark brown) is contoured at 1σ. Polar interactions to the backbone of Val217 and the side-chain of Tyr98 are indicated by dotted lines.
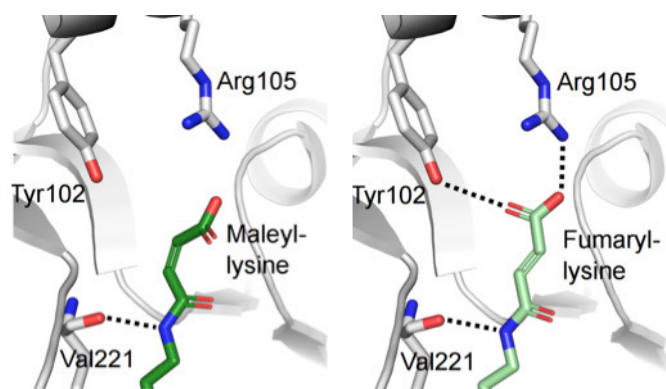
Figure S17. Docking of **5f** (light green) and **5g** (dark green) into hSirt5/**5a** complex. Only in case of **5f** hydrogen bonds with Tyr102 and Arg105 are observed. Hydrogen bonds between ligand and protein are indicated as dashed lines.
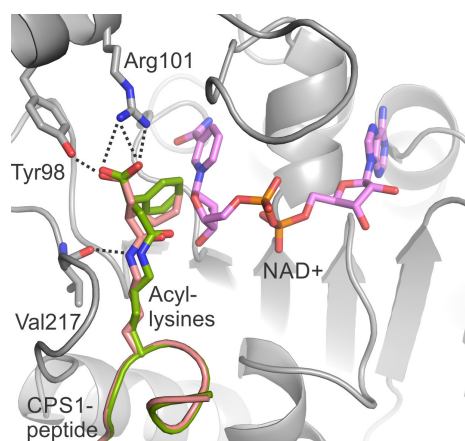

Figure S18. Active-site supperposition of crystal structures of zSirt5 complexes with inhibitory **5j** (skin coloured) and **5h** (green). The protein is shown only once for clarity (zSirt5/5h complex; grey), since all protein residues superpose well.

References

[17] M. Gertz, G. T. Nguyen, F. Fischer, B. Suenkel, C. Schlicker, B. Franzel, J. Tomaschewski, F. Aladini, C. Becker, D. Wolters, C. Steegborn, *PLoS One* **2012**, *7*, e49761.

[18] C. C. G. Inc., Montreal, QC, Canada, **2012**.

[19] D. A. D. Case, T. A.; Cheatham, I. T. E.; Simmerling, C. L.; Wang, J.; Duke, R. E.; Luo, R.; Crowley, M.; Walker, R. C.; Zhang, W.; Merz, K. M.; Wang, B.; Hayik, S.; Roitberg, A.; Seabra, G.; KolossvaÌry, I.; Wong, K. F.; Paesani, F.; Vanicek, J.; Wu, X.; Brozell, S. R.; Steinbrecher, T.; Gohlke, H.; Yang, L.; Tan, C.; Mongan, J.; Hornak, V.; Cui, G.; Mathews, D. H.; Seetin, M. G.; Sagui, C.; Babin, V.; Kollman, P. A., **2010**.

[20] G. Jones, P. Willett, R. C. Glen, A. R. Leach, R. Taylor, *J Mol Biol* **1997**, *267*, 727-748.

[21] U. Mueller, N. Darowski, M. R. Fuchs, R. Förster, M. Hellmig, M. S. Paithankar, S. Pühringer, M. Steffien, G. Zocher, M. S. Weiss, *J Synchrotron Radiat* **2012**, *May 1*, 442-449.

[22] W. Kabsch, *Acta Crystallogr D Biol Crystallogr* **2010**, *66*, 125-132.

[23] a) A. A. Vagin, M. N. Isupov, *Acta Crystallogr D Biol Crystallogr* **2001**, *57*, 1451-1456; b) A. Schuetz, J. Min, T. Antoshenko, C. L. Wang, A. Allali-Hassani, A. Dong, P. Loppnau, M. Vedadi, A. Bochkarev, R. Sternglanz, A. N. Plotnikov, *Structure* **2007**, *15*, 377-389.

[24] G. N. Murshudov, A. A. Vagin, E. J. Dodson, *Acta Crystallogr D Biol Crystallogr* **1997**, *53*, 240-255.

[25] R. A. Nicholls, F. Long, G. N. Murshudov, *Acta Crystallogr D Biol Crystallogr* **2012**, *68*, 404-417.

[26] M. D. Winn, M. N. Isupov, G. N. Murshudov, *Acta Crystallogr D Biol Crystallogr* **2001**, *57*, 122-133.

[27] P. Emsley, K. Cowtan, *Acta Crystallogr D Biol Crystallogr* **2004**, *60*, 2126-2132.

[28] A. W. Schuttelkopf, D. M. van Aalten, *Acta Crystallogr D Biol Crystallogr* **2004**, *60*, 1355-1363.

5.2. Publication 2

Potent and Selective Inhibitors of Human Sirtuin 5

Kalbas, D.*, Liebscher, S.*, Nowak, T.*, Meleshin, M., Pannek, M., Popp, C., Alhalabi, Z., Bordusa, F., Sippl, W., Steegborn, C., Schutkowski, M. (2017). Potent and Selective Inhibitors of Human Sirtuin 5. *J. Med. Chem.* 61(6):2460-2471.

* These authors contributed equally to this work.

This work is the result of a collaborative study between the labs of Mike Schutkowski, Clemens Steegborn, Wolfang Sippl and Frank Bordusa. The lab leaders and Diana Kalbas, Sandra Liebscher and Theresa Nowak designed the study and experiments. Diana Kalbas, Marat Meleshin and Corinna Popp synthesized the acylated peptides and small molecules. Sandra Liebscher produced Sirt5 protein and performed the BIAcore and affinity pulldown experiments. Diana Kalbas performed HPLC-assays, while fluorescence assays were performed by Diana Kalbas, Theresa Nowak and Corinna Popp. The zSirt5 protein used for complex crystallization was either expressed and purified by our technical assistant Norbert Grillenbeck (not listed as author) or me. The zSirt5/peptide complex crystals were produced and structures solved, refined and deposited in the PDB by me with comments from Clemens Steegborn. The manuscript was drafted by Mike Schutkowski and Diana Kalbas, while the manuscript's crystallographic section was commented and figures prepared by Clemens Steegborn and me.

Please note: _Supplementary Information Figures S28-S107 (UPLC-runs/MS-spectra of peptides/compounds) were omitted to limit the number of pages, but are available on the CD-ROM attached to this work._

Potent and Selective Inhibitors of Human Sirtuin 5

Diana Kalbas,[†,∥] Sandra Liebscher,[‡,∥] Theresa Nowak,[§,∥] Marat Meleshin,[†] Martin Pannek,[⊥]
Corinna Popp,[†] Zayan Alhalabi,[§] Frank Bordusa,[‡] Wolfgang Sippl,[§] Clemens Steegborn,[⊥]
and Mike Schutkowski[*,†]

[†]Department of Enzymology, Institute of Biochemistry and Biotechnology, Martin-Luther-University Halle-Wittenberg, 06120 Halle/Saale, Germany

[‡]Department of Natural Product Biochemistry, Institute of Biochemistry and Biotechnology, Martin-Luther-University Halle-Wittenberg, 06120 Halle/Saale, Germany

[§]Department of Medical Chemistry, Institute of Pharmacy, Martin-Luther-University Halle-Wittenberg, 06120 Halle/Saale, Germany

[⊥]Department of Biochemistry, University of Bayreuth, 95447 Bayreuth, Germany

Ⓢ *Supporting Information*

ABSTRACT: Sirtuins are protein deacylases that regulate metabolism and stress responses and are implicated in aging-related diseases. Modulators of the human sirtuins Sirt1−7 are sought as chemical tools and potential therapeutics, e.g., for cancer. Selective and potent inhibitors are available for Sirt2, but selective inhibitors for Sirt5 with K_i values in the low nanomolar range are lacking. We synthesized and screened 3-arylthiosuccinylated and 3-benzylthiosuccinylated peptide derivatives yielding Sirt5 inhibitors with low-nanomolar K_i values. A biotinylated derivative with this scaffold represents an affinity probe for human Sirt5 that is able to selectively extract this enzyme out of complex biological samples like cell lysates. Crystal structures of Sirt5/inhibitor complexes reveal that the compounds bind in an unexpected manner to the active site of Sirt5.
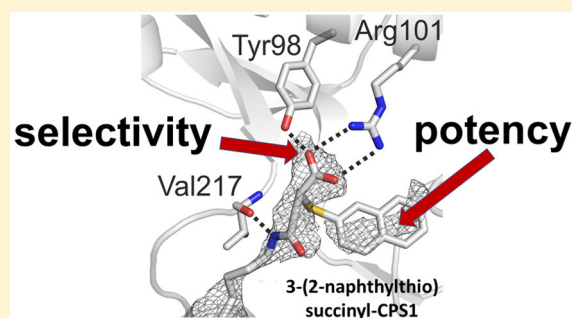
INTRODUCTION

Sirtuins (Sirt) represent an evolutionarily conserved family of NAD⁺-dependent lysine deacylases. Seven sirtuin isoforms have been identified in mammals, Sirt1 to Sirt7, which differ in their biochemical activities and subcellular localization. Sirt1 and Sirt2 are localized in the nucleus and cytoplasm, Sirt3−5 are mitochondrial enzymes, and Sirt6 and Sirt7 are localized exclusively in the nucleus. Sirtuins catalyze different lysine deacylation reactions, including removal of fatty acid modifications (Sirt1−6),[1] decrotonylation (Sirt1−3),[2] and removal of 3-hydroxy-3-methylglutaryl and lipoyl residues (Sirt4),[3] but only Sirt5 possesses a strong desuccinylase, demalonylase, and deglutarylase activity *in vitro* and *in vivo*.[4] The removal of negatively charged acyl moieties by Sirt5 results in up to 1000-fold higher catalytic activities compared to the respective deacetylation reaction.[4c]

The role of Sirt5 in metabolic pathways like glycolysis, tricarboxylic acid cycle, fatty acid oxidation, ammonia detoxification, reactive oxygen defense, or apoptosis makes this enzyme an interesting target for drug development.[4b,5] Deregulation or noncontrolled activation of Sirt5 is involved in several human diseases, including cancer, Alzheimer's disease, and Parkinson's disease.[6] Inhibition of Sirt5 resulted in suppressed tumor cell proliferation caused by increased succinylation of lysine residue 498 in pyruvate kinase M2.[6a]

Recently, it was shown that Sirt5-mediated desuccinylase activity is involved in pro-inflammatory response of macrophages by changing pyruvate kinase M2 enzymatic activity.[7] Moreover, Sirt5 is overexpressed in human non-small-cell lung cancer, and this overexpression is correlated with poor prognosis.[8] Effectors of Sirt5 activity are therefore needed as potential therapeutics and as chemical probes to investigate Sirt5 function in more detail. Here we present the development of selective and potent Sirt5 inhibitors with K_i values in the low nanomolar range.

RESULTS AND DISCUSSION

The 3-phenylsuccinyl moiety on a lysine side chain represents a specific Sirt5 inhibitor which acts by blocking the NAD⁺ binding pocket.[4c] Compound **I** (Figure 1) is one of the most effective and selective Sirt5 inhibitors with a K_i value of 4.3 μM. Other reported Sirt5 inhibitors are shown in Figure 1, but selectivity has not been determined for all of them. Inspection of the crystal structure of zebrafish Sirt5 (zSirt5) in complex with the structurally similar 3-phenylsuccinyl-carbamoyl phosphate synthetase (CPS1)-derived peptide (**47**; PDB ID 4UTV) revealed that the phenyl ring on the succinyl residue
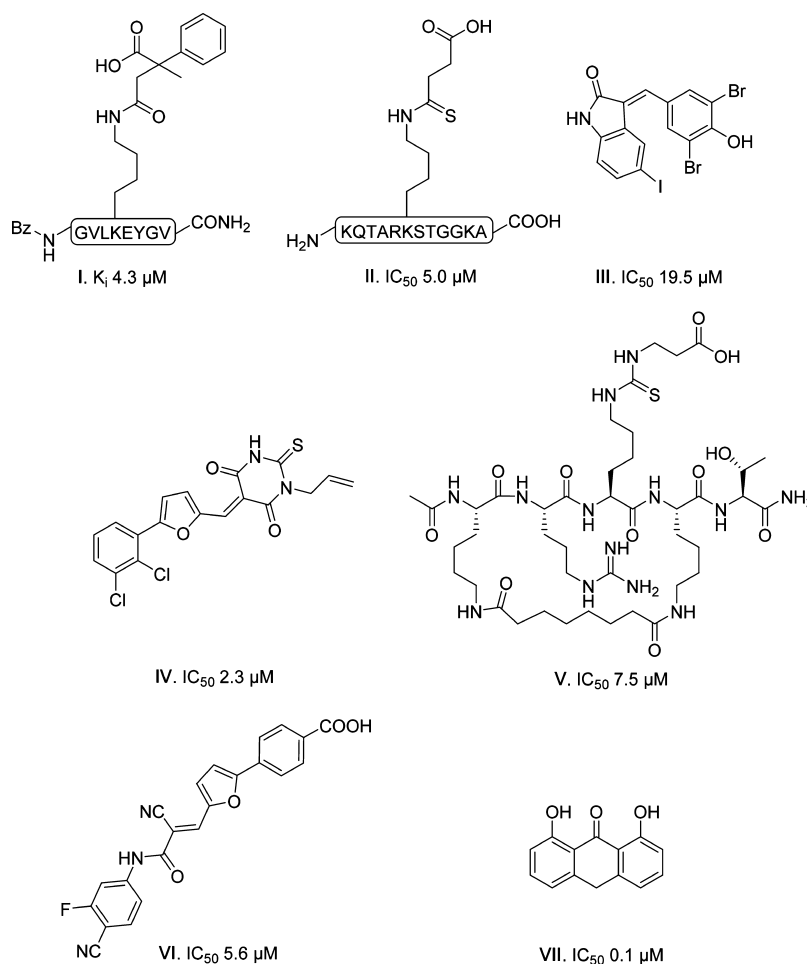
Figure 1. Reported Sirt5 inhibitors: **I**,[4c] **II**,[9] **III**,[10] **IV**,[11] **V**,[12] **VI**,[13] **VII**.[14]

points to the nicotinamide binding pocket (C-pocket) but is not able to reach the C-pocket.[4c] Therefore, we started to analyze a 3-benzylsuccinyl derivative of CPS1 peptide, resulting in **1** (Table 1) with a K_i value of 263 ± 48 nM (Table S1). Reaction of substituted succinic anhydrides with the lysine side chain represents a convenient route to 3-alkyl(aryl)succinyl peptide derivatives.[4c] However, because of limited access to such reagents and unsatisfactory regioselectivity of the reaction (often 2-substituted regioisomers are formed by alternative opening of the anhydride), we investigated another way to substitute succinyl peptides. Maleamic acid derivatives react with thiols, affording 2-(alkylthio)succinamic acid as the sole product.[15] Because a large number of thiols are available commercially and respective Michael addition can be performed directly on the solid support, this method was chosen for the preparation of a library of 3-substituted succinyl-CPS1 peptides (Scheme 1). Treatment of resin-bound maleylated peptides with a thiol in the presence of tertiary base afforded expected diastereomeric mixtures of 3-substituted target peptides along with minor amounts of 2-substituted regioisomers. Treatment with trifluoroacetic acid at room temperature yielded four diastereomers/regioisomers. Surprisingly, reaction products were easily separated with HPLC, enabling convenient and simultaneous route to both (*S*)-3- and (*R*)-3-(alkyl(aryl)thio)succinyl-CPS1 peptide derivatives (2-substituted derivatives were formed in minor amounts and were not isolated). For convenience, we denote inseparable

equal mixtures of diastereomers as a number **N**, and fast- and slow-eluting diastereomers as **N.1** and **N.2**, respectively.

Using this reaction, we systematically optimized the acyl residue of the CPS1-derived peptide inhibitor (Table 1), resulting in a K_i value of 7 nM for **35.2** (Table S1). Compound **2** showed a K_i value similar to that of **1**. Nevertheless, we were able to demonstrate that the slower-migrating diastereomer, due to the substitution at position 3 of the succinyl residue **2.2**, is a more efficient inhibitor for Sirt5, with a K_i value of 135 nM. Insertion of one, two, or three methylene groups between the sulfur and the phenyl ring, resulting in **15**, **27**, and **32**, respectively, did not improve the inhibition constants. Additionally, replacement of the phenyl ring by heterocycles (see **28–31**) yielded inhibitors with K_i values between 3.5 and 11 μM. To analyze Sirt5/inhibitor interaction details, we solved crystal structures of **15**, respectively **2**, in complex with zSirt5 (Figure 2 and Table S2) and compared them with the previously solved structure of zSirt5/**47**[4c] (PDB ID 4UTV). Surprisingly, the substituents at position 3 of the succinyl group occupy different binding pockets (Figure 2). The benzyl group of **15** is oriented similar to the phenyl ring of **I**, toward the C-pocket, and reaches deeper into this pocket yet still cannot fill it completely. In contrast, the phenyl group of **2** is positioned toward a hydrophobic patch formed by Ala78 and Phe219 and opened through rearrangements of the cofactor binding loop. Apparently, both sites can provide interactions for tight binding and potent inhibition. To explore the binding pocket of the phenyl ring of compound **2** in more detail, we generated all

Table 1. Chemical Structures of Succinyl-CPS1-Derived Peptide Inhibitors (Bz-GVLK(X)EYGV-NH$_2$)

X = (structure with R substituent)

R*
IC$_{50}$(nM)

1 1122.0 ± 168.4	**8.1** 1606.9 ± 164.3 **8.2** 45.9 ± 11.3	**15.1** 644.1 ± 112.5 **15.2** 335.7 ± 39.7	**22.1** 2202.7 ± 245.7 **22.2** 803.5 ± 110.3	**29** 13243.9 ± 1931.5
2.1 1798.8 ± 200.4 **2.2** 273.5 ± 31.	**9.1** 2013.7 ± 586.7 **9.2** 176.6 ± 20.7	**16.1** 352.4 ± 48.2 **16.2** 533.3 ± 105.2	**23.1** 1148.2 ± 131.7 **23.2** 1124.6 ± 141.0	**30** 6966.3 ± 1261.6
3.1 3097.4 ± 361.4 **3.2** 857.0 ± 93.6	**10.1** 647.1 ± 73.2 **10.2** 86.1 ± 10.5	**17.1** 2673.0 ± 405.9 **17.2** 2710.2 ± 421.3	**24.1** 431.5 ± 57.0 **24.2** 543.3 ± 28.5	**31.1** 18492.7 ± 3575.3 **31.2** 8749.8 ± 1989.4
4.1 1383.6 ± 215.3 **4.2** 119.9 ± 7.4	**11.1** 12502.6 ± 2812.5 **11.2** 576.8 ± 77.9	**18.1** 1020.9 ± 169.4 **18.2** 893.3 ± 142.6	**25.1** 779.8 ± 40.0 **25.2** 739.6 ± 37.9	**32.1** 2060.6 ± 251.9 **32.2** 1129.8 ± 188.1
5.1 1614.4 ± 187.1 **5.2** 101.9 ± 9.5	**12.1** 1258.9 ± 153.2 **12.2** 46.1 ± 4.5	**19.1** 1235.9 ± 171.0 **19.2** 792.5 ± 92.8	**26.1** 631.0 ± 91.2 **26.2** 5200.0 ± 640.4	**33.1** 1181.0 ± 312.8 **33.2** 30.3 ± 3.5
6.1 3388.4 ± 410.6 **6.2** 714.5 ± 105.7	**13.1** 9078.2 ± 745.2 **13.2** 325.8 ± 42.9	**20.1** 4027.2 ± 445.4 **20.2** 3732.5 ± 489.9	**27.1** 591.6 ± 68.0 **27.2** 2741.6 ± 350.5	**34.1** 2196.2 ± 612 **34.2** 95.0 ± 14.2
7.1 1977.0 ± 251.1 **7.2** 295.1 ± 39.1	**14.1** > 14000** **14.2** > 4000**	**21.1** 1111.7 ± 120.8 **21.2** 1047.1 ± 103.9	**28** 22803.4 ± 4586.4	**35.1** 207 ± 21.1 **35.2** 15.4 ± 9.5

*Hereinafter an equal mixture of diastereomers is denoted as **N**, with **N.1** the fast- and **N.2** the slow-eluting diastereomer. **Cannot be determined more precisely because of solubility problems.

possible monochloro- and dichloro-substituted compounds, resulting in **3−5** and **6−11**, respectively. Substitution in the *o*-position seems not to be beneficial (Table 1) because it could lead to steric clash with the protein (Figure 2), but replacement of hydrogen by chlorine in the *m*- or *p*-position yielded inhibitors with K_i values between 50 and 60 nM for the better binding diastereomer. This improvement in binding is maybe caused by beneficial interactions with Sirt5 residues Phe66 and Arg67 (Figure 2). Chloro substitution in both the *p*- and *m*-positions led to **8**, with a K_i value of 23 nM for **8.2**. Flexible docking of **8.2** into the crystal structure of zSirt5 cocrystallized

with **2** showed that the dichlorophenyl ring fits perfectly into the hydrophobic pocket formed between Arg67 and Phe219 (Figure S25). Combined *m*- and *p*-substitution using methyl (**12**) and methoxy (**13**) moieties resulted in similar Sirt5 affinities. Inspired by this substitution pattern, we created 3-(2-naphthylthio)succinyl derivative **33.2**, which represents the most efficient Sirt5 inhibitor with the 3-(arylthio)succinyl scaffold (IC$_{50}$ value = 40 nM). Moreover, **33.2** is selective for Sirt5, evidenced by the fact that no effect on catalysis mediated by Sirt1, Sirt2, Sirt3, or Sirt6 could be detected with concentration of **33.2** up to 50 μM (Figure S22). When the

Scheme 1. Chemical Reaction Used for the Preparation of Peptidyl Derivatives Carrying 3-(Aryl- or Alkylthio)succinyl Residues at the Lysine Side Chain


Figure 2. Comparison of the binding modes of **2** and **15** to a 3-phenylsuccinyl-Lys inhibitor (**47**) in the Sirt5 active site. The zSirt5 complex with **2** (ligand shown in green) was overlaid with the complexes with **15** (cyan) and with **47** (PDB ID 4UTV; yellow). NAD$^+$ (light blue) was modeled from a Sirt5/peptide/NAD$^+$ complex (PDB ID 4G1C) to indicate the C-pocket. The protein part is only shown for zSirt5/**2** in brackets (gray cartoon); dotted lines indicate polar interactions with the acyl group, and for **2**, **5**, and **47** respectively, one enantiomer was omitted for clarity.

aryl ring in **2** was replaced by a cyclohexyl ring (**14**), the resulting diastereomers showed about 500-fold reduced IC$_{50}$ values.

The IC$_{50}$ value of the more potent diastereomer of 3-(benzylthio)succinyl derivative **15.2** is comparable to the IC$_{50}$ value of 3-(phenylthio)succinyl derivative **2.2**. This fact prompted us to analyze substituted benzyl derivatives **16−26**. With the exception of *o*-chloro-substituted benzylthio derivative **16.1**, all of the modifications resulted in higher IC$_{50}$ values. In contrast to the phenylthio series (compounds **2−13**), the diastereomer (regarding position 3 of the succinyl residue) with the longer retention time is not in every case the more potent compound. The IC$_{50}$ values are very similar for both isomers in

the case of **21**, **23**, and **25**. On the other hand, there is a >8-fold difference in the IC$_{50}$ values for 2,4,6-trimethyl-substituted derivatives **25.1** and **25.2**. Generation of the naphthyl-methylthio derivative **35.2**, homologous to the naphthyl derivative **34.2**, resulted in an improvement of inhibition, with an IC$_{50}$ value of 15.4 ± 9.5 nM, resulting in a calculated K_i value of 7 nM. Double substitution at position 3 of the succinyl residue can increase Sirt5's inhibitory potency. The K_i value of compound **I** (Figure 1) is about 20-fold better than the K_i value of the respective 3-phenylsuccinyl-CPS1 peptide derivative.[4c] Therefore, we decided to analyze a similar double substitution and generated **36** by acylation of resin-bound CPS1 peptide with 2-methyl-2-(2-naphthylthio)succinic anhydride according to methods described in ref 4c. As mentioned above, that method yielded four different regio-/diastereomers (two diastereomers with substitution at C2 of succinyl residue and two diastereomers with substitution at C3 of succinyl residue). We could not separate all four isomers by RP-HPLC but were able to isolate two isomers (**36.1** and **36.2**) together with a mixture of the other two isomers (**36.3**). We determined the IC$_{50}$ values for the three HPLC fractions of **36** and determined IC$_{50}$ values between 60 and 90 nM. Obviously, affinity of 3-(2-naphthylthio)succinyl derivatives could not be improved by additional methyl substitutions at the same carbon atom. To explore the importance of the succinyl carboxyl group interacting with the arginine and tyrosine residues in the active site of Sirt5 (Figure 2) for efficient inhibition, we replaced this carboxyl function by either a methyl group or a hydrogen, resulting in 3-(2-naphthylthio)butyryl derivative **37** and 3-(2-naphthylthio)propionyl derivative **38** (Table 2). Surprisingly, both compounds are not inhibitors but rather substrates for human Sirt5, as demonstrated by an HPLC-based activity assay.[4c]

In order to define the absolute configuration of the best inhibitor, we decided to synthesize **33** in a stereocontrolled manner. The key intermediate in this synthesis was optically pure 4-methoxybenzyl-protected (*S*)-2-(2-naphthylthio)-succinate (**e**), which was prepared from commercially available (*S*)-malic acid (**a**) (Scheme 2). First, *O*-trifluoroacetyl (*S*)-malic acid anhydride (**b**) was reacted with 4-methoxybenzyl alcohol, affording the respective monoester (**c**).[16] Intramolecular cyclization of the β-hydroxyl ester using Mitsunobu conditions afforded (*R*)-β-lactone (**d**), which was not isolated but treated *in situ* with 2-naphthalenethiol, yielding (*S*)-2-(2-naphthylthio)-succinic acid 1-(4-methoxybenzyl) ester (**e**). Coupling of the acid to the resin-bound CPS1-peptide using standard DIC/HOSu activation and cleavage of the peptide from the resin

Table 2. Chemical Structures of CPS1-Derived Peptide Inhibitors and Substrates (Bz-GVLK(X)EYGV-NH$_2$)

	X	
	IC$_{50}$(nM)	
36.1 89.9 ± 8.8 **36.2** 59.0 ± 5.8	**37** >40000**	**38** >40000**

**Cannot be determined more precisely because of solubility problems.

Scheme 2. Synthesis of (S)-3-(Alkylthio/arylthio)succinyl Derivatives from (S)-Malic Acid


PMB = 4-methoxybenzyl; R₁ = 2-naphthyl;

Figure 3. HPLC profiles of **33**: (a) derived by Michael addition of 2-naphthalenethiol to maleyl-CPS1; (b) **33.2** prepared by coupling of (S)-2-(2-naphthylthio)succinic acid-1-(4-methoxybenzyl) ester to the CPS1-peptide (Scheme 2); and (c) mixed sample containing (a) and (b).

Table 3. Chemical Structures of Biotinylated Peptides 39 and 39.2

with TFA led to a single diastereomer according to HPLC. Figure 3 shows the HPLC chromatogram of crude reaction product **33** using the Michael addition reaction. The two minor peaks are the two 2-substituted succinyl derivatives, and the two major peaks are the 3-substituted arylthiosuccinyl derivatives **33.1** and **33.2**. The migration time of the reaction product derived from **e** shown in Scheme 2 is comparable to that of **33.2**, enabling assignment of **33.2** to the (S)-3-(2-naphthylthio)succinyl derivative. Additionally, spiking the reaction mixture of the Michael reaction with the product of the stereocontrolled synthesis resulted in an increase of the area of the signal caused by **33.2** (see Figure 3c). Encouraged by the unique selectivity of the potent inhibition of Sirt5 by **33.2**, we decided to develop an affinity probe for human Sirt5. Analysis of crystal structures of **15** and **2** in complex with zSirt5 (Figure 2) uncovered no interaction of the N-terminal benzoyl residue with the enzyme. Therefore, we replaced the benzoyl moiety in

33 by a spacer molecule and a biotinyl residue (compound **39**), enabling immobilization on (strept)avidin-coated surfaces (Table 3). Mixture of 3-substituted diastereomers (compound **39**) generated by Michael addition reaction yielded an inhibitor with a K_i value of 83.2 ± 15.4 nM, but stereoisomer **39.2**, synthesized according to the method shown in Scheme 2, is a more effective Sirt5 inhibitor, with a K_i value of 13.6 ± 3.8 nM. The inhibition is in both cases competitive regarding the peptide substrate (Figure 4). To analyze our Sirt5 affinity probe in more detail, we used real-time, label-free surface plasmon resonance (SPR) measurements to investigate the interaction of surface-bound inhibitor and human Sirt5 (Figure 5). Biotinylated peptide derivative **39.2** was immobilized on a streptavidin-coated SPR sensorchip. Sirt5 binds to immobilized **39.2** in a dose-dependent manner (Figure 5a). Rate constants $k_{on} = (1.3 \pm 1.0) \times 10^{-6}$ M^{-1} s^{-1} and $k_{off} = (1.5 \pm 0.6) \times 10^{-4}$ M^{-1} s^{-1} result in a K_D value of about 0.12 nM. Binding was
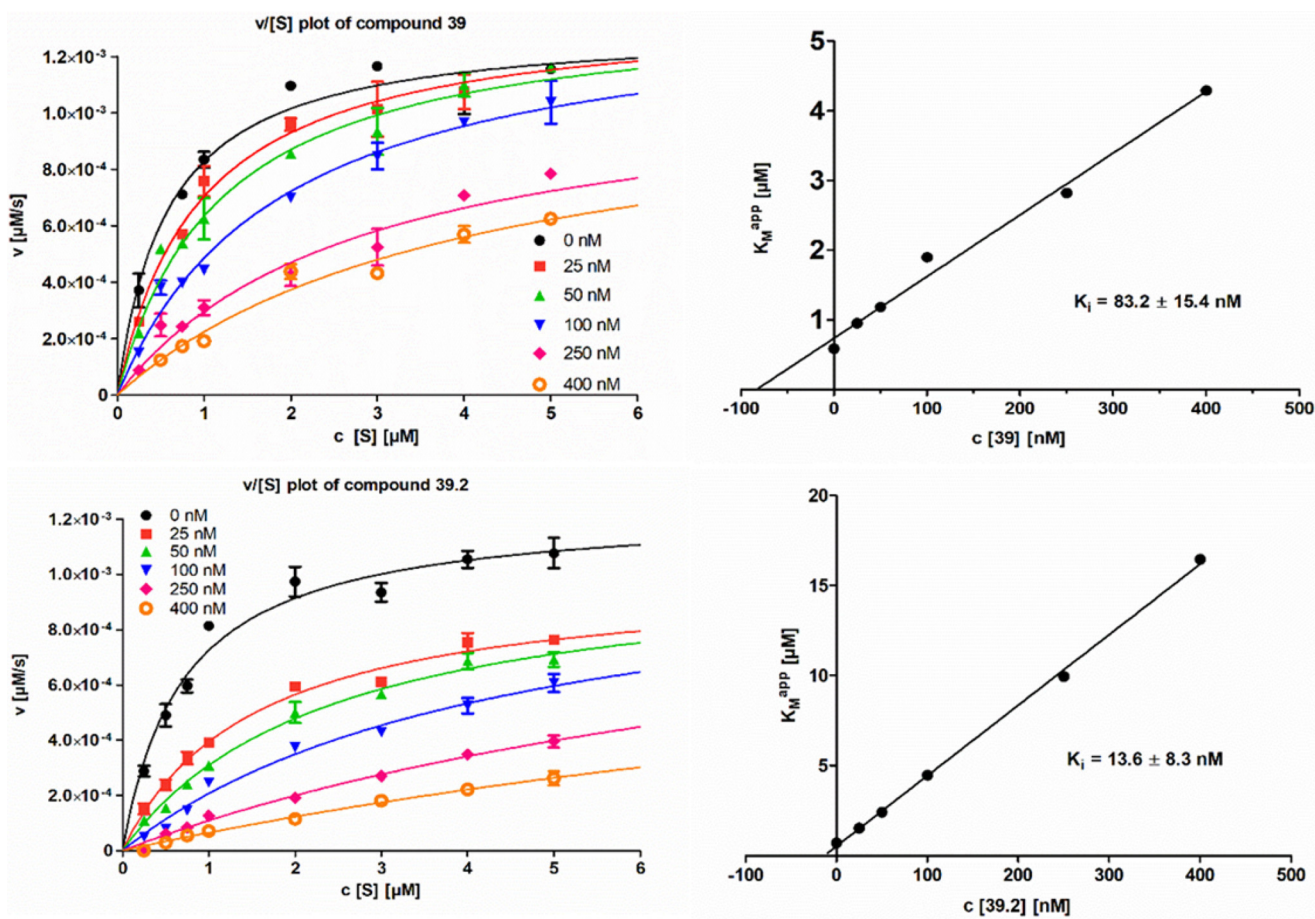
Figure 4. $v/[S]$ plots and fitting curves for compounds **39** and **39.2** generated using human Sirt5 in the presence of 500 μM NAD$^+$ cosubstrate.

linear up to 100 nM, representing the evaluation range for the rate constants ($R^2 = 0.9971$; Figure S22). This interaction seems to be very specific for Sirt5 because all other human sirtuin isoforms showed negligible K_D values (Figure 5b). The higher affinity of **39.2** for the active site of Sirt5 in the SPR experiment as compared to the kinetic measurements could be explained by the immobilization of the inhibitor leading to an avidity effect. However, in the presence of non-biotinylated inhibitor **33.2**, Sirt5 was unable to bind to surface-bound **39.2** (Figure 5c), indicating the expected peptide–substrate competitive binding mode. Consistently, reduced but detectable binding was observed in the presence of **19.2**, an inhibitor with a K_i value of 714 nM, or in the presence of succinylated CPS1-derived substrate peptide, demonstrating that surface-bound **39.2** competes with the substrate peptide. Analyzing interaction details of **33.2** with Sirt5 by solving a zSirt5/**33.2** crystal structure (Figure 6, Figure S24, Table S2) revealed a surprising binding mode. Although it was based on *m*- and *p*-modified **2**, the substituent of **33.2** occupies the C-pocket. Its bulky aromatic system fills much of the pocket yet remains flexible, as indicated by fragmented electron density and higher B factors. Further modifications that exploit polar groups, such as an addition at position 8 of the naphthyl moiety for beneficial interaction with Asp139 (Figure 2), might be a route for even further increased potency. Nevertheless, our data demonstrate that the combination of a succinyl scaffold for Sirt5 selectivity and a 3-(2-naphthyl)succinyl modification for potency yields compounds that bind Sirt5 tightly and specifically. We reversed the assembly by regioselective

immobilization of biotinylated Sirt5 to a streptavidin-coated sensorchip. Sirt5 was biotinylated at the N-terminus by the trypsiligase method.[17] For that purpose, we elongated Sirt5 with *Strep*II-tagged Tyr-Arg-His tripeptide at the N-terminus. This introduces a recognition sequence for trypsiligase which cleaves the Tyr-Arg bond and transfers a biotinyl-Gly to the Arg residue, resulting in a Sirt5 variant with biotinyl-Gly-Arg-His at the N-terminus (Figure S19d). Biotinylated Sirt5 showed similar enzymatic activity compared to the enzyme without modification (Figure S20b). Treatment of the immobilized Sirt5 with **33.2** showed a very fast association and hardly detectable dissociation (Figure 5d), resulting in an estimated K_D value of about 10 pM. We were not able to remove bound inhibitor by extensive washing of the sensorchip (several days).

To test the suitability of **39.2** for pull-down experiments using more complex biological samples, we immobilized **39.2** on streptavidin-coated agarose beads and loaded the beads with *E. coli* BL21 (DE3) lysate expressing Sirt5. There was no Sirt5 detected in the flow-through using SDS-PAGE analysis. Extensive washings removed a lot of different proteins but not Sirt5 (Figure 7a). Virtually pure Sirt5 could be eluted using 200 mM sodium hydroxide. ESI-MS analysis of the elution fraction yielded a protein with a molecular mass of 30.798 Da (Figure 7b), which matches the calculated mass of 30.796 Da. Lysates of *E. coli* expressing either Sirt2 or Sirt3 were used for similar pull-down experiments. There was no capture of these two sirtuins by **39.2** detectable, as demonstrated by the empty elution fraction lanes (Figure S18a,b). Additionally, an equimolar mixture of Sirt2, Sirt3, and Sirt5 was applied to
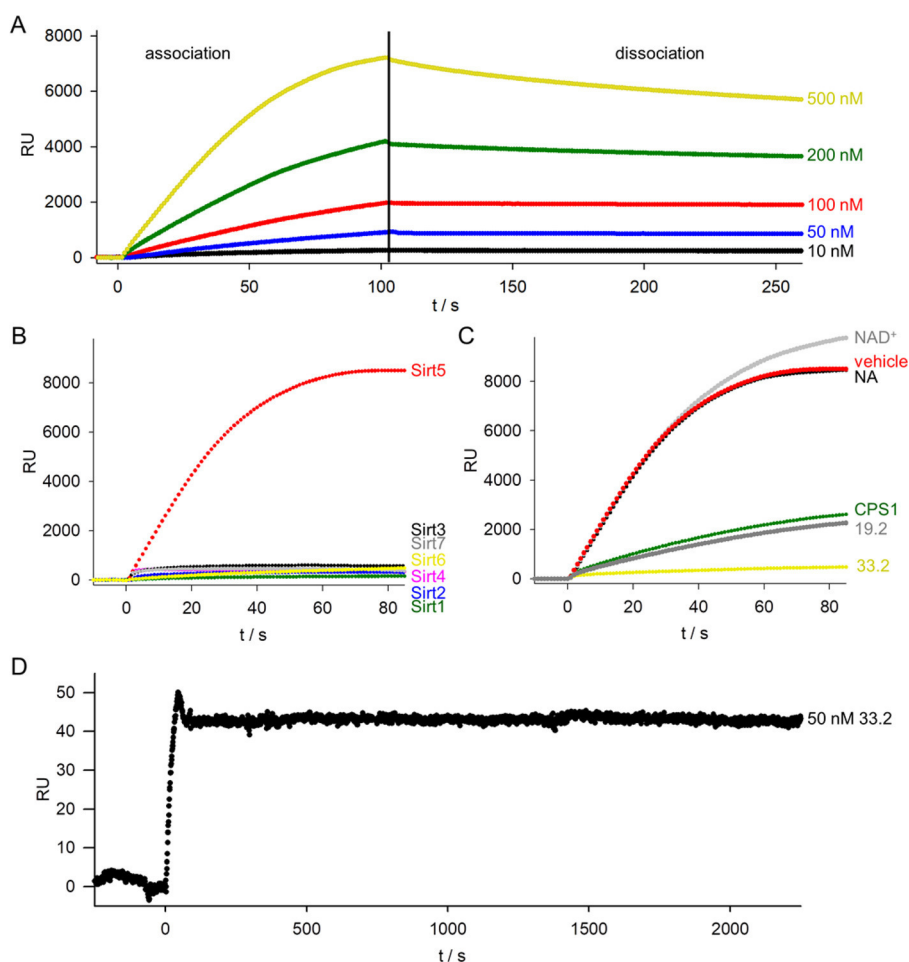
Figure 5. Biophysical characterization of compounds **33.2** and **39.2** by surface plasmon resonance spectroscopy. (a) SPR sensorgrams demonstrating binding of Sirt5 to immobilized **39.2**. (b) Association phase of sensorgrams representing binding of different sirtuin isoforms (1 μM) to immobilized **39.2**. (c) Association phase of SPR sensorgrams representing binding of Sirt5 to the immobilized inhibitor in the presence of CPS1-derived peptide substrate with succinyl residue on the lysine side chain (2 μM) or inhibitors **33.2** (2 μM) and **6.2** (2 μM); vehicle is PBS buffer. (d) Binding of compound **33.2** to immobilized, biotinylated Sirt5. Regioselective biotinylation of the N-terminus of Sirt5 was performed via trypsiligase reaction[17] (Figure S20).
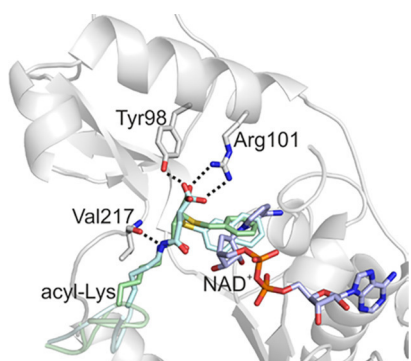
Figure 6. Comparison of the binding modes of **33.2** and **15** (in the Sirt5 active site). The zSirt5 complex with **33.2** (PDB ID 6FLG, cyan) was overlaid with the **15** complex (PDB ID 6FKY, ligand shown in green; one enantiomer omitted for clarity) and a Sirt5/NAD$^+$ complex (PDB ID 4G1C) that indicates the C-pocket. NAD$^+$ (light blue) was modeled from a Sirt5/peptide/NAD$^+$ complex. The protein is only shown for zSirt5/**33.2**, and dotted lines indicate polar interactions to the acyl group.

the inhibitor matrix and analyzed via SDS-PAGE (Figure S18c). Sirt2 and Sirt3 were exclusively detected in the flow-through and the wash fractions. Protein-containing elution fractions were analyzed using ESI-MS, and eluted protein was clearly identified as Sirt5 (Figure S18d).

CONCLUSIONS

For development of more drug-like Sirt5 inhibitors, we started to analyze the contribution of the peptide backbone to the affinity of (S)-3-(2-naphthylthio)succinyl derivatives. We shortened the peptide sequence to a tripeptide and generated **40.2** (see Table 4) using enantiomerically pure precursor **e**. This tripeptide binds 6-fold less strongly to Sirt5 as compared to **39.2**, but still with sub-micromolar inhibitory activity. Generation of an α-acetylated lysine amide, acylated with the (S)-3-(2-naphthylthio)succinyl moiety at the ε-amino group, resulted in **41**, showing a K_i value of 7 μM, which is about 40-fold higher than the K_i value for **40.2**, yet close to those of the most potent Sirt5 selective inhibitors known so far. The peptide part of the peptidic inhibitors thus contributes to affinity and potency, but omitting these contributions from our inhibitors with optimized acyl moieties still allows for tight binding. Further shortening by formal removal of the acetylated glycine amide part of **41** yielded **42**, which binds about 20-fold less effectively to Sirt5 as compared to **41**. Replacement of the
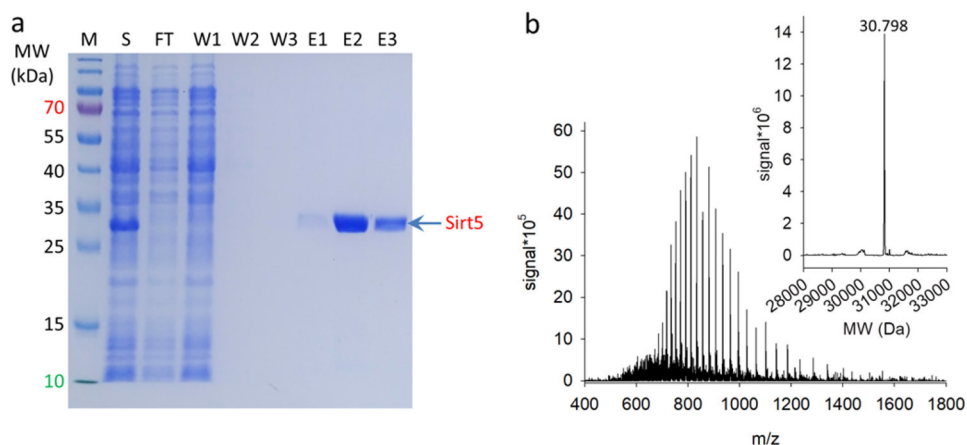
Figure 7. Immobilized **39.2** captures Sirt5 out of *E. coli* lysate. (a) SDS-PAGE analysis (Coomassie staining) of **39.2** bound to streptavidin-coated agarose interacting with *E. coli* BL21 (DE3) lysate expressing Sirt5. Exclusively Sirt5 was eluted from the matrix by addition of 200 mM NaOH. Abbreviations: S, supernatant after cell rupture; FT, flow-through; W, wash fractions; E, elution fractions. (b) ESI-MS analysis of the elution fraction E2; $M_{calc} = 30.796$ Da, $M_{found} = 30.798$ Da.

Table 4. Chemical Structures of Tripeptide and Small Molecules

Structure IC$_{50}$(nM)		
40 1075.4 ± 117.7	**43** 157200 ± 18900	**IV** 25200 ± 2700
40.2 350.4 ± 20.6	**44** 90000 ± 12500	**VII** 453400 ± 37600
41 7400 ± 750	**45** 124000 ± 17200	
42 154000 ± 19300	**46** 72560 ± 9300	

butylamide part in **42** by anilides (**43** and **44**) and benzylamide (**45**) is well tolerated, resulting in similar IC$_{50}$ values, indicating potential for further improvement of this compound moiety through focused library screens or structure-based design. Replacement of the methyl group in **42** by a phenyl ring (**46**) already improves the IC$_{50}$ value more than 2-fold, and our

structural data provide a basis for further optimizing this compound part to obtain potencies comparable to that of **41** or even better without having the peptide backbone, which is unfavorable for drug applications. For comparison, we analyzed known small-molecule inhibitors **IV** and **VII** (Table 4) using similar assay conditions. In our hands these compounds

showed much weaker affinity to SIRT5 in comparison to published values.[11,14] Collectively, these results show that the (S)-3-(2-naphthylthio)succinylamide scaffold represents a useful starting point for systematic development of small molecules that potently and selectively target Sirt5.

In this study we developed a peptide-based selective Sirt5 affinity probe by optimizing the acyl moiety in a systematic manner. Probe design was guided by analysis of a known crystal structure of Sirt5 in complex with **47** and crystal structures solved in this study. The developed affinity probe **39.2** is able to bind to Sirt5 in different matrixes and environments, accompanied by excellent selectivity and inhibitory activity. The high potency is caused by slow dissociation rate and fast association of the inhibitor−enzyme complex, making this probe to a multifunctional tool for investigation of Sirt5 biology at a new level.

■ EXPERIMENTAL SECTION

Chemicals and General Methods. Solutions of 0.1% trifluoro-acetic acid (TFA) in H_2O (solvent A) and 0.1% TFA in acetonitrile (solvent B) were used as mobile phase for HPLC measurements. For sample analysis, an Agilent 1100 HPLC with a quaternary pump, a well-plate autosampler, and a variable-wavelength detector was used. Separations were performed on a Phenomenex Kinetex XB C-18 column (2.6 μm, 3.0 × 50 mm) with a linear gradient from 25 to 55% solvent B in 4 min at a flow rate of 0.6 mL min^{-1}. The compounds were detected at 260 nm. A Shimadzu LC system with a Phenomenex Kinetex 5 μm XB-C18 column (250 × 21.1 mm, 100 Å) was used for purification of peptides. The preparative separations were performed with a linear gradient from 25 to 90% solvent B in 80 min at a flow rate of 15 mL min^{-1}. The eluting compounds were detected at 220 and 260 nm. UPLC-MS analysis was performed using a Waters Acquity UPLC-MS system (Milford, USA) with a Waters Acquity UPLC-MS-BEH C18 column (1.7 μM, 2.1 × 50 mm; 30 Å). Data analysis was performed using Waters MassLynx software. NMR spectroscopy was carried out using a Varian Gemini 2000 spectrometer and deuterated chloroform or deuterated dimethyl sulfoxide (DMSO). All chemicals were purchased from Sigma-Aldrich if not stated otherwise.

Solid-Phase Peptide Synthesis. The peptide derivatives Bz-GVLK(Ns)EYGV-NH$_2$ and Ac-LK(Ns)A-NH$_2$ were synthesized on an MBHA Rink amide resin with a loading density of 0.59 mmol/g (IRIS Biotech), using standard Fmoc-based solid-phase peptide synthesis. At first the resin was treated with DMF for 20 min. Next, 4 equiv of Fmoc-protected amino acid derivatives (Anaspec) was activated with 4 equiv of HBTU and 8 equiv of DIPEA in DMF and was coupled for at least 1 h. Afterward the Fmoc deprotection was performed two times for 10 min with 20% piperidine in DMF followed by washing with DMF for 5 min, five times. Finally, the amino group of glycine was modified with 4 equiv of benzoic acid and 8 equiv of DIPEA in DMF or 4 equiv of acetic anhydride and 8 equiv of DIPEA in DMF for 30 min. The lysine to be modified was used as the ε-nosyl (Ns, 2-nitrobenzenesulfonyl)-protected derivative, allowing a selective on-resin modification of the lysine side chain. This derivative, Fmoc-Lys(Ns)-OH, was prepared as described elsewhere.[20] The nosyl protecting group was removed by using 5 equiv of thiophenol and 5 equiv of DBU in DMF for 90 min, two times. The free lysine side chain was modified with 4 equiv of maleic anhydride and 8 equiv of DIPEA in DMF for 4 h, followed by washing with DMF. Afterward a Michael addition reaction was performed with 4 equiv of mercapto derivative (**2−13**, **15−35**, **39**, **40**) and 8 equiv DIPEA in DMF overnight. After sequential washing with DMF, DCM, methanol, and again with DCM for 4 min, five times, each peptide was cleaved from the resin using TFA−water solution (95:5 v/v) for 1 h, two times. The TFA was evaporated, and the peptide was dissolved in acetic acid. After purification by reversed-phase HPLC, collected fractions were analyzed with HPLC-MS and checked for purity. The purity was above 95% for all peptides (Figure S26−S105). The fractions containing target peptide were lyophilized.

(S)-2-Hydroxysuccinic Acid 1-(4-Methoxybenzyl) Ester (c). First, 3.2 g (15 mmol, 1 equiv) of (S)-2-trifluoroacetoxysuccinic anhydride (**b**), prepared from (S)-malic acid using a known method,[18] was mixed with 9.3 mL (75 mmol, 5 equiv) of 4-methoxybenzyl alcohol, and the reaction mixture was stirred overnight. The resulting oil was dissolved in 50 mL of ethyl acetate (EtOAc) and extracted several times with saturated NaHCO$_3$ solution. The combined aqueous phases were washed with EtOAc and acidified with diluted HCl solution. The mixture was extracted with DCM, and the organic phase was washed with water, dried over Na$_2$SO$_4$, and evaporated, affording 3.16 g of crude ester. Recrystallization from 14 mL of EtOAc−petroleum ether mixture (1:1) yielded 2.2 g of pure compound.

^{1}H NMR (300 MHz, DMSO-d_6): δ 7.29 (d, J = 8.7 Hz, 2H), 6.91 (d, J = 8.7 Hz, 2H), 5.03 (s, 2H), 4.34 (dd, J = 7.5, 5.1 Hz, 1H), 3.73 (s, 3H), 2.61 (dd, J = 15.8, 5.1 Hz, 1H), 2.52−2.40 (m, 1H).

(S)-2-(2-Naphthylthio)succinic Acid 1-(4-Methoxybenzyl) Ester (e). First, 508.5 mg (2 mmol) of 1-(4-methoxybenzyl) malate and 525 mg (2 mmol) of Ph$_3$P were dissolved in 9 mL of dry tetrahydrofuran (THF), and the flask was cooled with an ice−water bath. To this mixture was added 393 μL (404 mg, 2 mmol) of diisopropyl azodicarboxylate in 2 mL of THF dropwise over 5 min. The reaction mixture was stirred overnight at room temperature. The next day the yellow solution was cooled to −15 °C with an ice−salt mixture, and 320 mg of crystalline 2-naphthalenethiol (2 mmol) was added, followed by 276 mg (2 mmol) of solid K$_2$CO$_3$. After 20 min the cooling bath was removed, and the mixture was stirred at room temperature for 1 h. The product was isolated with acid−base extraction as described in the previous procedure, to yield 0.53 g of crude product, which contains around 25% of starting material. Recrystallization from methanol can be used for further purification.

^{1}H NMR (300 MHz, DMSO-d_6): δ 7.98−7.78 (m, 4H), 7.59−7.43 (m, 3H), 7.06 (d, J = 8.7 Hz, 2H), 6.75 (d, J = 8.7 Hz, 2H), 4.96 (dd, J = 28.2, 12.1 Hz, 2H), 4.15 (dd, J = 8.6, 6.6 Hz, 1H), 3.70 (s, 3H), 2.77 (dd, J = 7.6, 2.0 Hz, 2H).

General Procedure for the Synthesis of Maleamic Acid Derivatives 41−46. To the solution containing 20 mg (0.05 mmol) of (S)-2-(2-naphthylthio)succinic acid 1-(4-methoxybenzyl) ester and 7 mg (0.06 mmol) of N-hydroxysuccinimide (HOSu) in 500 μL of dry THF was added 9 μL (0.06 mmol) of N,N′-diisopropylcarbodiimide. After 30 min, 2 equiv (0.1 mmol) of the appropriate amino derivative was added. The progress of the reaction was monitored by TLC or HPLC. In the case of aromatic amines, longer reaction times and addition of 2 equiv of triethylamine were necessary to achieve satisfactory yields. After completion of the reaction, THF was evaporated, and the residue was redissolved in 500 μL of TFA−water (95:5 v/v) solution and left for 30 min. The reaction solution was then concentrated *in vacuo*, and the residue was purified by RP-HPLC. The fractions containing target product were lyophilized, affording pure compound.

Synthesis of 2-Methyl-2-(2-naphthylthio)succinic Anhydride. This compound was prepared according to the method described for preparation of 2-methyl-2-(4-chlorophenylthio)succinic anhydride.[19] Briefly, 1.12 g (10 mmol) of citraconic anhydride and 1.6 g (10 mmol) of 2-naphthalenethiol were mixed with 1 mL of toluene, and 4 μL of triethylamine was added. The mixture was stirred and heated at 70−80 °C for 1 h. Volatiles were removed *in vacuo*, and the residue was purified by flash chromatography. Additional recrystallization from petroleum ether−EtOAc (3:1 v/v) solution gave pure material.

^{1}H NMR (700 MHz, CDCl$_3$): 8.08 (d, J = 1.9 Hz, 1H), 7.88−7.82 (m, 3H), 7.59−7.51 (m, 3H), 3.14 (d, J = 18.8 Hz, 1H), 3.07 (d, J = 18.8 Hz, 1H), 1.70 (s, 3H).

Fluorescence Inhibition Assay. The inhibitory activity of all compounds was measured in black low-binding 96-well microtiter plates, and each well contained 0.025−5 μM substrate Abz-GVLK(glutaryl)AY(NO$_2$)GV-NH$_2$, 500 μM NAD$^+$, 500 nM trypsin, 10 nM SIRT5, 5% DMSO, and 0.01−20 μM inhibitor (compounds **1**−**46**) in assay buffer. The assay buffer contained 20 mM Tris, 150 mM NaCl, and 5 mM MgCl$_2$ at pH 7.8. The reaction mixture without enzymes was incubated for 5 min at 37 °C, followed by pipetting

trypsin and further incubation for 5 min at 37 °C. After addition of SIRT5, the measurements started, and the fluorescence was measured at an excitation wavelength of 320 nm and emission wavelength of 420 nm. The measurements were carried out in a plate reader (TECAN) and in a double determination.[20] IC_{50} values were obtained with 0.03 μM substrate, and the resulting data were fitted by log(inhibitor) vs normalized response equation:

$$Y = \frac{100}{(1 + 10^{(X - \log IC_{50})})} \qquad (1)$$

HPLC Assay. Reaction mixtures contained 0 μM or 50 μM inhibitor, 500 μM NAD^+, 5% DMSO, 0.1 μM SIRT1, 2, 3, 5, or 6, and 50 μM Bz-GVLK(acetyl)EYGV-NH_2 for SIRT1−3, Bz-GVLK-(succinyl)EYGV-NH_2 for SIRT5, and Ac-EALPKK(myristoyl)TGG-NH_2 for SIRT6 in assay buffer. The reactions were performed at 37 °C for 6 min (SIRT6), 8 min (SIRT1−3), or 10 min (SIRT5). After these time points, reaction was stopped with TFA−water solution (1:9 v/v), and samples were analyzed by HPLC. The stability of compounds **1**−**46** was determined by incubating 50 μM inhibitor in assay buffer at 37 °C for 24 h and measuring by HPLC. All measurements were carried out in duplicate.

Cloning, Expression, and Purification of Recombinant Proteins. Human Sirt5 was cloned with *N*-terminal *Strep*II-tag into pET-21a(+) vector. Sirt2$_{43-356}$ and Sirt3$_{114-380}$ were cloned with *N*-terminal *Strep*II-tag into pET-28a(+)-vector. All proteins were expressed using *E. coli* BL21 (DE3) in LB media supplemented with ampicillin or kanamycin, respectively. Overexpression was induced by the addition of IPTG (1 mM final concentration) at an OD_{600} of 0.6. Cells were harvested, resuspended in lysis buffer (100 mM Tris-HCl, 250 mM NaCl, 10 mM DTT, 1 mM EDTA, pH 8.0), and lysed by sonication. Supernatant after centrifugation was loaded onto a StrepTrap column (GE Healthcare, Uppsala, Sweden). The loaded column was intensively washed before elution with 5 mM desthiobiotin in 100 mM Tris, 250 mM NaCl, pH 8.0. Sirt5-containing fractions were concentrated and further purified using a Superdex 75 5/150 gel filtration column (GE Healthcare). Expression of Sirt4 was performed using the IMPACT system (NEB, Frankfurt am Main, Germany). The corresponding gene was cloned into pTWIN2 via *Sap*I/*Pst*I and transformed in *E. coli* ER2566 (NEB). Overexpression was induced by the addition of IPTG (0.5 mM final concentration) at an OD_{600} of 0.6 at 16 °C for 12 h. Chitin binding-domain-mediated affinity chromatography was performed as described in the supplier's manual. Enzymatic activity of the expressed Sirtuin isoforms was determined as described previously.[17] Biotinylation of Sirt5 was conducted via trypsiligase using biotinyl-4-guanidino-phenyl ester as described previously.[17]

Real-Time Biomolecular Interaction Analysis. Surface plasmon resonance spectroscopy was performed on a BIAcore X instrument (BIAcore, Uppsala, Sweden). Biotinylated inhibitor **39.2** (100 μM in PBS) was immobilized on an SAHC 200 M sensorchip (Xantec, Düsseldorf, Germany). Sirt5 was injected in a dilution series using PBS (4 mM KH_2PO_4, 16 mM Na_2HPO_4, 115 mM NaCl, pH 7.4) as running buffer. Vice versa, *N*-terminal biotinylated Sirt5 was immobilized on a second strepatvidin-coated sensorchip, resulting in a surface density of approximately 1800 response units (RU), and 50 nM **39.2** in PBS was injected. Each complex formation was observed at a continuous flow rate of 30 μL/min. Kinetic parameters were determined by fitting the data to the 1:1 Langmuir binding model with the BIAevaluation software (BIAcore). After each measurement the inhibitor matrix was regenerated by injection of 100 μL of NaOH (200 mM).

Affinity Pull-Down Experiments. A 0.5 mL bed-volume of streptavidin-conjugated agarose (Sigma-Aldrich, Munich, Germany) was applied to a gravity column and equilibrated with 5 CV PBS. Agarose beads were loaded with the biotinylated inhibitor **39.2** (100 μM in PBS). After 30 min incubation, agarose was washed with 10 CV PBST (4 mM KH_2PO_4, 16 mM Na_2HPO_4, 115 mM NaCl, 0.05% Tween, pH 7.4). As protein samples, pellets of 20 mL induced *E. coli* BL21 (DE3) cells expressing the respective Sirt isoform were

resuspended in 100 mM Tris, 250 mM NaCl, 1 mM EDTA, 10 mM DTT, pH 8.0, and lyzed by sonication. After removal of cell debris, supernatant was applied to the inhibitor matrix. Conjugated agarose beads were washed three times with 3 CV PBST. Bound protein was eluted by the addition of 200 mM NaOH. Elution fractions were analyzed by SDS-PAGE and LC-MS.

Crystal Structure Analyses. zSirt5 protein was purified by Co-Talon affinity chromatography, TEV proteolysis, reverse affinity chromatography, and gel filtration as reported, with the modification that 0.5 mM TCEP was added to the gel filtration buffer. For crystallization, zSirt5 (10 mg/mL) was mixed with 1 mM inhibitory peptide (20 mM stock in DMSO) and incubated on ice for 30 min. Complexes were crystallized in 2 μL sitting-drop vapor diffusion experiments at 20 °C using 0.1 M HEPES, pH 7.5, 20% PEG3350 as reservoir solution. After 2−4 days, crystals were transferred to a cryo-protection solution composed of reservoir and ligand supplemented with 25% glycerol. Crystals were shock-frozen and diffraction data collected at 100 K at BESSY II beamline MX14.1 (operated by the Helmholtz-Zentrum, Berlin, Germany) with a Pilatus 6 M detector (Dectris, Baden, Switzerland). Indexing, scaling, and merging were done in XDS,[21] and structures were solved by molecular replacement with search model PDB 4UTV (zSirt5/**47**). Refinement was done with Refmac5,[22] and manual modeling as well as structure validation were done with Coot.[23] Geometry parameters for the modified lysines were generated using PRODRG.[24]

Computational Methods. The molecular structures of all peptides described in the present work were generated using the MOE 2014.09 program.[25] The initial conformations resulted from energy minimization using the Amber12:EHT force field as implemented in MOE. The crystal structure of zSirt5 in complex with peptides **2.2** and **15.2** were considered for the flexible docking study. For the subsequent docking studies, all water and ligand molecules were removed, and the structure was protonated and minimized using the Amber12:EHT force field.

All docking studies were carried out using the GOLD5.2 docking program (Cambridge Crystallographic Data Centre, Cambridge, UK) in exhaustive sampling mode.[26] The binding cavity was defined by the cocrystallized peptide. To guide the search process, the position of the cocrystallized succinyl-lysine of the peptides was used as a scaffold constraint. Using Goldscore as fitness function, the cocrystallized peptide was correctly docked into the zSirt5 catalytic site, with RMSD values of 1.25 Å (**2.2**) and 1.41 Å (**15.2**).

All tested peptides were docked in both crystal structures, and 100 docking poses were stored. The resulting poses were rescored using the Amber12:EHT force field and the MM-GB/SA approach. Partial charges were fixed using the MOE Protonate3D tool according to the used force field, followed by a short minimization. An in-house script for rescoring the zSirt5−ligand complexes and calculating the binding free energies was applied for the docking poses of ligands. During complex minimization, heavy atoms of protein were tethered with a deviation of 0.5 Å (force constant $(3/2)kT/(0.5)^2$). Complexes that showed the most favorable MM-GB/SA energy were selected and visually analyzed using the MOE program.

■ ASSOCIATED CONTENT

ⓢ Supporting Information

The Supporting Information is available free of charge on the ACS Publications website at DOI: 10.1021/acs.jmedchem.7b01648.

> Detailed description of peptide synthesis including LC-MS runs for each derivative and NMR data for selected compounds, results of kinetic measurements, experimental details of crystallization, and SPR experiments, including Tables S1 and S2 and Figures S1−S108 (PDF)
>
> Molecular formula strings (CSV)

AUTHOR INFORMATION

Corresponding Author

*E-mail: mike.schutkowski@biochemtech.uni-halle.de.

ORCID

Wolfgang Sippl: 0000-0002-5985-9261

Mike Schutkowski: 0000-0003-0919-7076

Author Contributions

‖D.K., S.L., and T.N. contributed equally.

Notes

The authors declare no competing financial interest.

ABBREVIATIONS USED

CPS1, carbamoyl phosphate synthetase 1; DIAD, diisopropyl azodicarboxylate; DIC, diisopropylcarbodiimide; DIPEA, diisopropylethylamine; EtOAc, ethyl acetate; HBTU, (2-(1*H*-benzotriazol-1-yl)-1,1,3,3-tetramethyluronium hexafluorophosphate; HOSu, *N*-hydroxysuccinimide; Ph$_3$P, triphenylphosphine; MBHA, 4-methylbenzhydrylamine; ε-nosyl, 2-nitrobenzenesulfonyl; Sirt, Sirtuin; TCEP, tris(2-carboxyethyl)phosphine; TEV, tobacco etch virus

REFERENCES

(1) (a) Feldman, J. L.; Baeza, J.; Denu, J. M. Activation of the protein deacetylase SIRT6 by long-chain fatty acids and widespread deacylation by mammalian sirtuins. *J. Biol. Chem.* **2013**, *288* (43), 31350−31356. (b) Feldman, J. L.; Dittenhafer-Reed, K. E.; Kudo, N.; Thelen, J. N.; Ito, A.; Yoshida, M.; Denu, J. M. Kinetic and structural basis for acyl-group selectivity and NAD(+) dependence in sirtuin-catalyzed deacylation. *Biochemistry* **2015**, *54* (19), 3037−3050.

(2) Bao, X.; Wang, Y.; Li, X.; Li, X. M.; Liu, Z.; Yang, T.; Wong, C. F.; Zhang, J.; Hao, Q.; Li, X. D. Identification of 'erasers' for lysine crotonylated histone marks using a chemical proteomics approach. *eLife* **2014**, *3*, e02999.

(3) (a) Anderson, K. A.; Huynh, F. K.; Fisher-Wellman, K.; Stuart, J. D.; Peterson, B. S.; Douros, J. D.; Wagner, G. R.; Thompson, J. W.; Madsen, A. S.; Green, M. F.; Sivley, R. M.; Ilkayeva, O. R.; Stevens, R. D.; Backos, D. S.; Capra, J. A.; Olsen, C. A.; Campbell, J. E.; Muoio, D. M.; Grimsrud, P. A.; Hirschey, M. D. SIRT4 Is a lysine deacylase that controls leucine metabolism and insulin secretion. *Cell Metab.* **2017**, *25* (4), 838−855. (b) Mathias, R. A.; Greco, T. M.; Oberstein, A.; Budayeva, H. G.; Chakrabarti, R.; Rowland, E. A.; Kang, Y.; Shenk, T.; Cristea, I. M. Sirtuin 4 is a lipoamidase regulating pyruvate dehydrogenase complex activity. *Cell* **2014**, *159* (7), 1615−1625. (c) Pannek, M.; Simic, Z.; Fuszard, M.; Meleshin, M.; Rotili, D.; Mai, A.; Schutkowski, M.; Steegborn, C. Crystal structures of the mitochondrial deacylase Sirtuin 4 reveal isoform-specific acyl recognition and regulation features. *Nat. Commun.* **2017**, *8* (1), 1513.

(4) (a) Du, J.; Zhou, Y.; Su, X.; Yu, J. J.; Khan, S.; Jiang, H.; Kim, J.; Woo, J.; Kim, J. H.; Choi, B. H.; He, B.; Chen, W.; Zhang, S.; Cerione, R. A.; Auwerx, J.; Hao, Q.; Lin, H. Sirt5 is a NAD-dependent protein lysine demalonylase and desuccinylase. *Science* **2011**, *334* (6057), 806−809. (b) Tan, M.; Peng, C.; Anderson, K. A.; Chhoy, P.; Xie, Z.; Dai, L.; Park, J.; Chen, Y.; Huang, H.; Zhang, Y.; Ro, J.; Wagner, G. R.; Green, M. F.; Madsen, A. S.; Schmiesing, J.; Peterson, B. S.; Xu, G.; Ilkayeva, O. R.; Muehlbauer, M. J.; Braulke, T.; Muhlhausen, C.; Backos, D. S.; Olsen, C. A.; McGuire, P. J.; Pletcher, S. D.; Lombard, D. B.; Hirschey, M. D.; Zhao, Y. Lysine glutarylation is a protein posttranslational modification regulated by SIRT5. *Cell Metab.* **2014**, *19* (4), 605−617. (c) Roessler, C.; Nowak, T.; Pannek, M.; Gertz, M.; Nguyen, G. T.; Scharfe, M.; Born, I.; Sippl, W.; Steegborn, C.; Schutkowski, M. Chemical probing of the human sirtuin 5 active site reveals its substrate acyl specificity and peptide-based inhibitors. *Angew. Chem., Int. Ed.* **2014**, *53* (40), 10728−10732.

(5) (a) Nishida, Y.; Rardin, M. J.; Carrico, C.; He, W.; Sahu, A. K.; Gut, P.; Najjar, R.; Fitch, M.; Hellerstein, M.; Gibson, B. W.; Verdin, E. SIRT5 Regulates both cytosolic and mitochondrial protein malonylation with glycolysis as a major target. *Mol. Cell* **2015**, *59* (2), 321−332. (b) Lin, Z. F.; Xu, H. B.; Wang, J. Y.; Lin, Q.; Ruan, Z.; Liu, F. B.; Jin, W.; Huang, H. H.; Chen, X. SIRT5 desuccinylates and activates SOD1 to eliminate ROS. *Biochem. Biophys. Res. Commun.* **2013**, *441* (1), 191−195.

(6) (a) Xiangyun, Y.; Xiaomin, N.; Linping, G.; Yunhua, X.; Ziming, L.; Yongfeng, Y.; Zhiwei, C.; Shun, L. Desuccinylation of pyruvate kinase M2 by SIRT5 contributes to antioxidant response and tumor growth. *Oncotarget* **2017**, *8* (4), 6984−6993. (b) Lutz, M. I.; Milenkovic, I.; Regelsberger, G.; Kovacs, G. G. Distinct patterns of sirtuin expression during progression of Alzheimer's disease. *NeuroMol. Med.* **2014**, *16* (2), 405−414. (c) Liu, L.; Peritore, C.; Ginsberg, J.; Shih, J.; Arun, S.; Donmez, G. Protective role of SIRT5 against motor deficit and dopaminergic degeneration in MPTP-induced mice model of Parkinson's disease. *Behav. Brain Res.* **2015**, *281*, 215−221.

(7) Wang, F.; Wang, K.; Xu, W.; Zhao, S.; Ye, D.; Wang, Y.; Xu, Y.; Zhou, L.; Chu, Y.; Zhang, C.; Qin, X.; Yang, P.; Yu, H. SIRT5 Desuccinylates and activates pyruvate kinase M2 to block macrophage IL-1beta production and to prevent DSS-induced colitis in mice. *Cell Rep.* **2017**, *19* (11), 2331−2344.

(8) Lu, W.; Zuo, Y.; Feng, Y.; Zhang, M. SIRT5 facilitates cancer cell growth and drug resistance in non-small cell lung cancer. *Tumor Biol.* **2014**, *35* (11), 10699−10705.

(9) He, B.; Du, J.; Lin, H. Thiosuccinyl peptides as Sirt5-specific inhibitors. *J. Am. Chem. Soc.* **2012**, *134* (4), 1922−1925.

(10) Suenkel, B.; Fischer, F.; Steegborn, C. Inhibition of the human deacylase Sirtuin 5 by the indole GW5074. *Bioorg. Med. Chem. Lett.* **2013**, *23* (1), 143−146.

(11) Maurer, B.; Rumpf, T.; Scharfe, M.; Stolfa, D. A.; Schmitt, M. L.; He, W.; Verdin, E.; Sippl, W.; Jung, M. Inhibitors of the NAD(+)-dependent protein desuccinylase and demalonylase Sirt5. *ACS Med. Chem. Lett.* **2012**, *3* (12), 1050−1053.

(12) Liu, J.; Huang, Y.; Zheng, W. A selective cyclic peptidic human SIRT5 inhibitor. *Molecules* **2016**, *21* (9), 1217−1229.

(13) Liu, S.; Ji, S.; Yu, Z. J.; Wang, H. L.; Cheng, X.; Li, W. J.; Jing, L.; Yu, Y.; Chen, Q.; Yang, L. L.; Li, G. B.; Wu, Y. Structure-based discovery of new selective small-molecule sirtuin 5 inhibitors. *Chem. Biol. Drug Des.* **2018**, *91* (1), 257−268.

(14) Guetschow, E. D.; Kumar, S.; Lombard, D. B.; Kennedy, R. T. Identification of sirtuin 5 inhibitors by ultrafast microchip electrophoresis using nanoliter volume samples. *Anal. Bioanal. Chem.* **2016**, *408* (3), 721−731.

(15) Augustin, M.; Mueller, W. Umsetzung von N-Maleyl-aminosäuren mit Nucleophilen. *Z. Chem.* **1985**, *25* (2), 61−62.

(16) Miller, M. J.; Bajwa, J. S.; Mattingly, P. G.; Peterson, K. Enantioselective syntheses of 3-substituted 4-(alkoxycarbonyl)-2-azetidinones from malic acid. *J. Org. Chem.* **1982**, *47* (25), 4928−4933.

(17) Liebscher, S.; Schopfel, M.; Aumuller, T.; Sharkhuukhen, A.; Pech, A.; Hoss, E.; Parthier, C.; Jahreis, G.; Stubbs, M. T.; Bordusa, F. N-terminal protein modification by substrate-activated reverse proteolysis. *Angew. Chem., Int. Ed.* **2014**, *53* (11), 3024−3028.

(18) Miller, M. J.; Bajwa, J. S.; Mattingly, P. G.; Peterson, K. Base-catalyzed addition of thiols to α,β-unsaturated anhydrides. *J. Org. Chem.* **1982**, *47* (25), 4928−4933.

(19) Zienty, F. B.; Vineyard, B. D.; Schleppnik, A. A. Base-catalyzed addition of thiols to α,β-unsaturated anhydrides. *J. Org. Chem.* **1962**, *27* (9), 3140−3146.

(20) Schuster, S.; Roessler, C.; Meleshin, M.; Zimmermann, P.; Simic, Z.; Kambach, C.; Schiene-Fischer, C.; Steegborn, C.; Hottiger, M. O.; Schutkowski, M. A continuous sirtuin activity assay without any coupling to enzymatic or chemical reactions. *Sci. Rep.* **2016**, *6*, 22643−33655.

(21) Kabsch, W. XDS. *Acta Crystallogr., Sect. D: Biol. Crystallogr.* **2010**, *66*, 125−132.

(22) Vagin, A. A.; Steiner, R. S.; Lebedev, A. A.; Potterton, L.; McNicholas, S.; Long, F.; Murshudov, G. N. REFMAC5 dictionary: organisation of prior chemical knowledge and guidelines for its use. *Acta Crystallogr., Sect. D: Biol. Crystallogr.* **2004**, *60*, 2284−2295.

(23) Emsley, P.; Lohkamp, B.; Scott, W. G.; Cowtan, K. Features and development of Coot. *Acta Crystallogr., Sect. D: Biol. Crystallogr.* **2010**, *66*, 486−501.

(24) Schüttelkopf, A. W.; van Aalten, D. M. F. PRODRG: a tool for high-throughput crystallography of protein-ligand complexes. *Acta Crystallogr., Sect. D: Biol. Crystallogr.* **2004**, *60*, 1355−1363.

(25) Chemical Computing Group. *Molecular Operating Environment* (MOE), 2014.09; Chemical Computing Group Inc.: Montreal, Canada, 2014.

(26) Jones, G.; Willett, P.; Glen, R. C.; Leach, A. R.; Taylor, R. *J. Mol. Biol.* **1997**, *267*, 727−748.

Supporting Information

Potent and selective inhibitors of human Sirtuin 5

Diana Kalbas[§‡], Sandra Liebscher[‡‡], Theresa Nowak[†‡], Marat Meleshin[§], Martin Pannek[‖],

Corinna Popp[§], Zayan Alhalabi[3], Frank Bordusa[‡], Wolfgang Sippl[†], Clemens Steegborn[‖], Mike

Schutkowski[§] *

[§] Department of Enzymology, Institute of Biochemistry and Biotechnology, Martin-Luther-

University Halle-Wittenberg, 06120 Halle/Saale (Germany)

[‡] Department of Natural Product Biochemistry, Institute of Biochemistry and Biotechnology,

Martin-Luther-University Halle-Wittenberg, 06120 Halle/Saale (Germany)

[†] Department of Medical Chemistry, Institute of Pharmacy, Martin-Luther-University Halle-

Wittenberg, 06120 Halle/Saale (Germany)

[‖] Department of Biochemistry, University of Bayreuth, 95447 Bayreuth (Germany)

TABLE OF CONTENTS

Table S1. K_i values of compound **1-44**, **N.1** are fast- and **N.2** are slow-eluting diastereomers

Nr.	K_i [nM]	Nr.	K_i [nM]	Nr.	K_i [nM]	Nr.	K_i [nM]
1	236 ± 48.1*	11.2	290	21.2	525	33.1	382.8 ± 75.1*
2.1	900	12.1	630	22.1	1100	33.2	30.1 ± 6.1*
2.2	135	12.2	23	22.2	400	34.1	1100 ± 150*
3.1	1550	13.1	4540	23.1	1075	34.2	85 ± 18*
3.2	430	13.2	165	23.2	1060	35.1	155.2 ± 28.4*
4.1	690	14.1	> 7000	24.1	215	35.2	7
4.2	60	14.2	> 2000	24.2	270	36.1	45
5.1	805	15.1	320	25.1	390	36.2	30
5.2	50	15.2	170	25.2	370	37	> 40000
6.1	1695	16.1	175	26.1	315	38	> 40000
6.2	355	16.2	265	26.2	2600	39	83.2 ± 15.4*
7.1	990	17.1	1335	27.1	295	39.2	13.6 ± 3.8*
7.2	150	17.2	1355	27.2	1370	40	664.8 ± 78.0*
8.1	800	18.1	510	28	11400	40.2	179.8 ± 41.1*
8.2	23	18.2	445	29	6620	41	7012 ± 124*
9.1	1005	19.1	620	30	3485	42	77000
9.2	90	19.2	395	31.1	9245	43	78600
10.1	325	20.1	2015	31.2	4375	44	45000
10.2	43	20.2	1870	32.1	1030	45	62000
11.1	6250	21.1	550	32.2	565	46	36280

* K_i values were determined using the coupled fluorescence assay

all other Ki values were calculated with Cheng-Prusoff equation

Table S2. Data collection and refinement statistics

	zSirt5/compound 2	zSirt5/ compound 15	zSirt5/compound 33.2
Space group	P6$_5$22	P6$_5$22	P6$_5$22
Unit cell constants (Å)	87.2, 87.2, 318.9	87.1, 87.1, 316.7	87.2, 87.2, 317.6
Resolution [a] (Å)	50.00 – 3.30	50.00 – 2.98	20.00 – 2.50
	(3.39 – 3.30)	(3.16 – 2.98)	(2.56 – 2.50)
Unique reflections	10989 (1671)	15459 (2399)	25573 (1857)
Multiplicity	4.1 (4.3)	15.5 (16.0)	10.6 (11.1)
Completeness	99.5% (99.3%)	99.8% (99.1%)	99.6% (99.9%)
R_{meas}	39.3% (121.8%)	35.8% (210.0%)	35.1% (822.4%)
CC1/2	93.8 (49.6)	99.4 (51.3)	99.5 (12.8)
I/σI	5.0 (1.4)	9.8 (1.3)	7.2 (0.3)
Protein atoms	4135	4103	4128
Ligand atoms	164	166	86
Solvent atoms	59	75	90
Resolution (Å)	48.73 – 3.30	48.51 – 2.98	19.85 – 2.50
	(3.39 – 3.30)	(3.06 – 2.98)	(2.56 – 2.50)
R_{cryst}/R_{free} [b][c]	22.2 / 28.4	19.8 / 27.5	24.9 / 31.7
Average B- factors protein			
	62.3	69.0	74.3
ligands	73.8	72.4	97.6
solvent	35.3	47.8	75.7
RMSD bond-lengths	0.012	0.014	0.012
RMSD angles	1.7	1.9	1.963

[a] Values in parentheses refer to outermost shell.

[b] $R_{cryst} = \dfrac{\sum ||F_{obs}| - k|F_{calc}||}{\sum |F_{obs}|}$. |F$_{obs}$| is the observed and |F$_{calc}$| the calculated structure factor amplitude.

[c] R_{free} was calculated from 5% of reflections omitted from refinement.
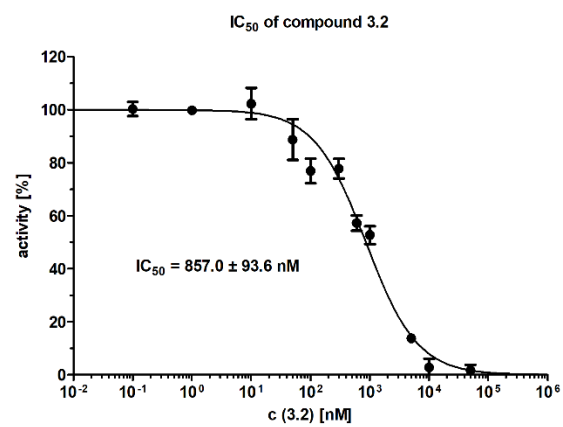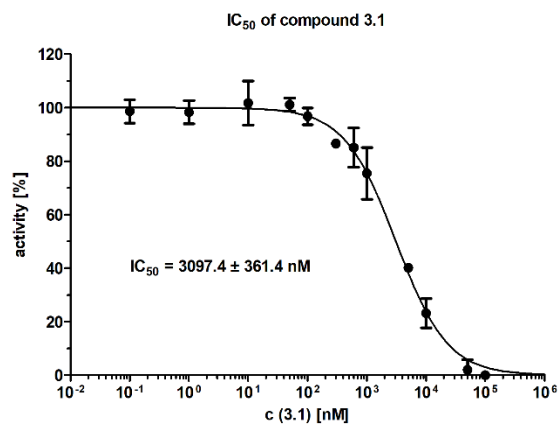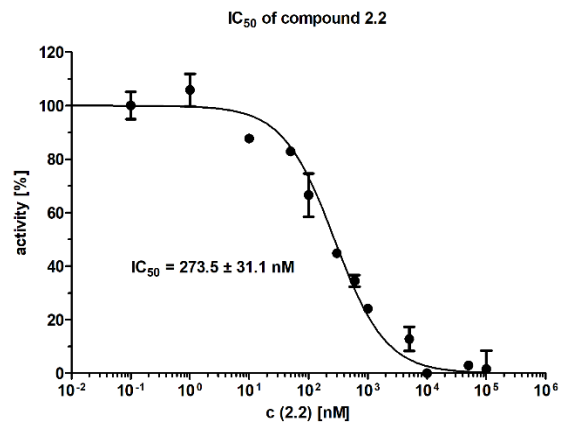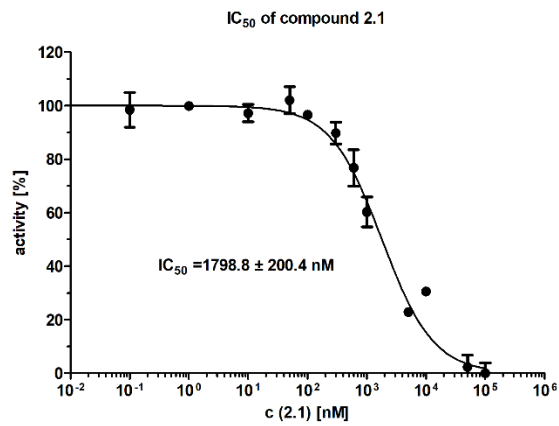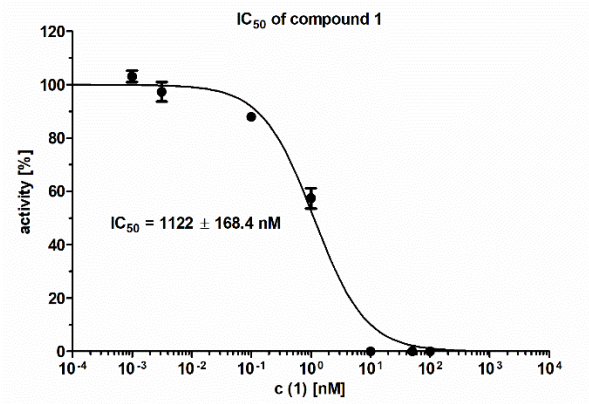
**Figure S1.** Dose-response analysis of compound **1-3** for SIRT5
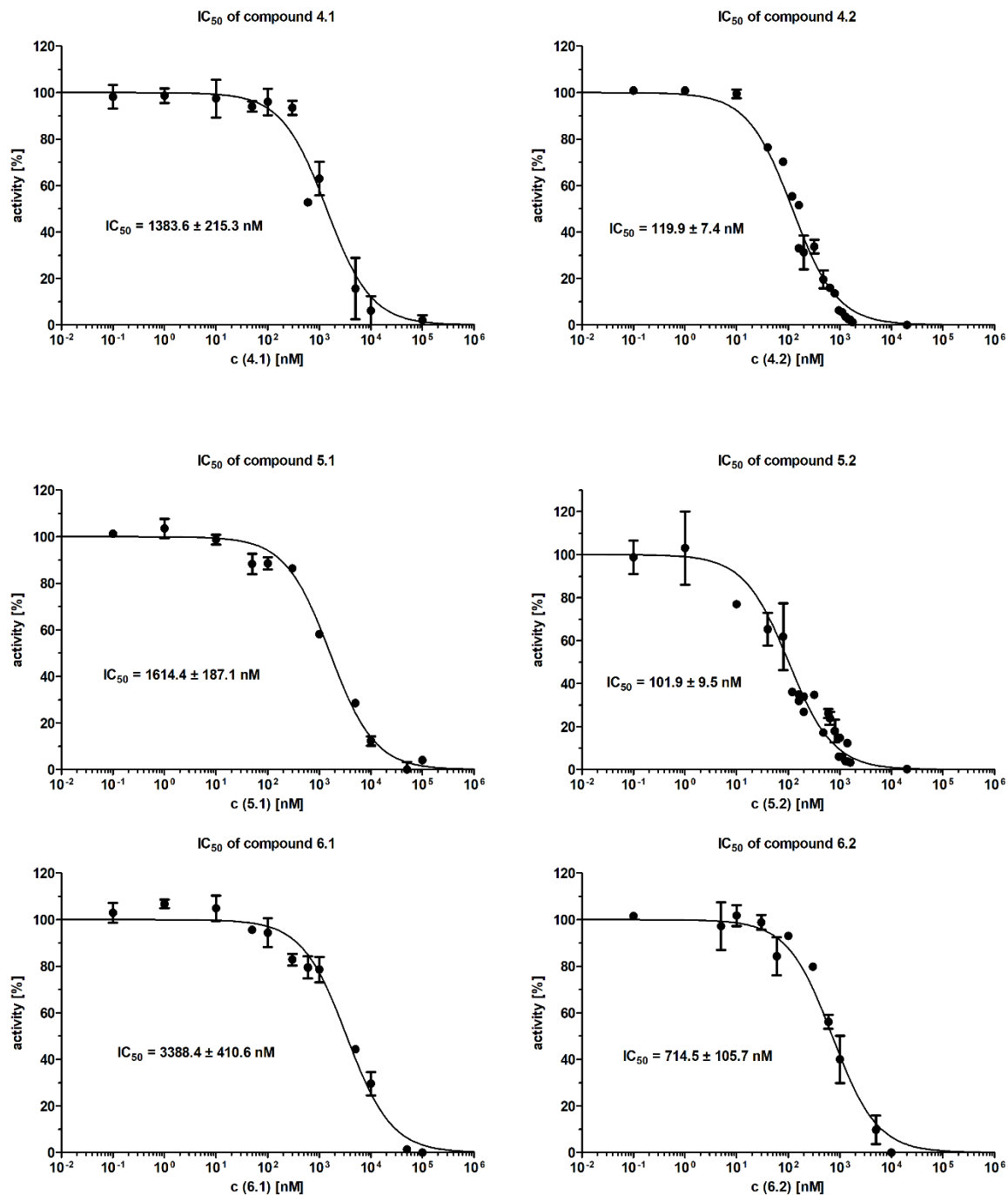
**Figure S2.** Dose-response analysis of compound **4-6** for SIRT5
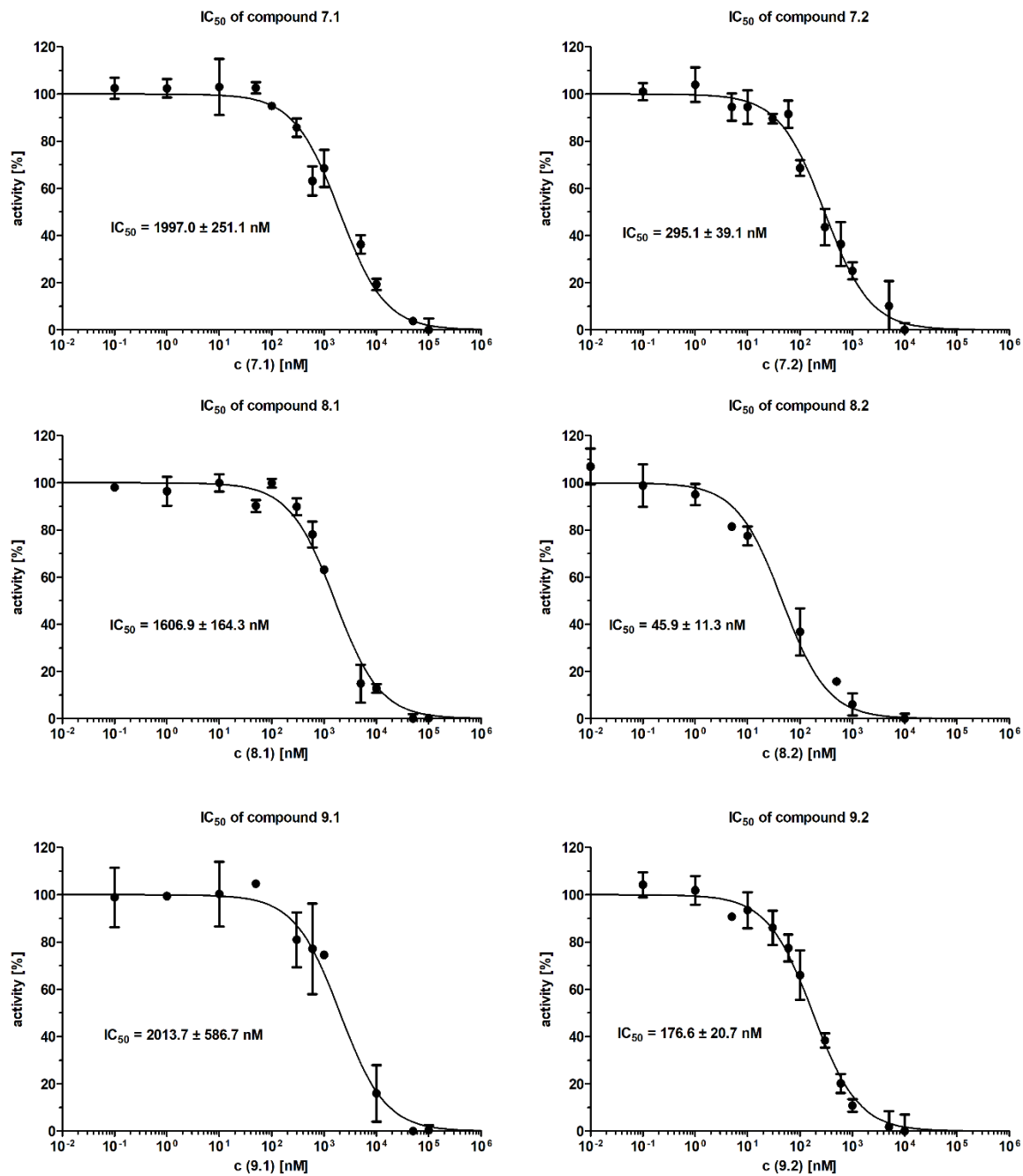
Figure S3. Dose-response analysis of compound **7-9** for SIRT5
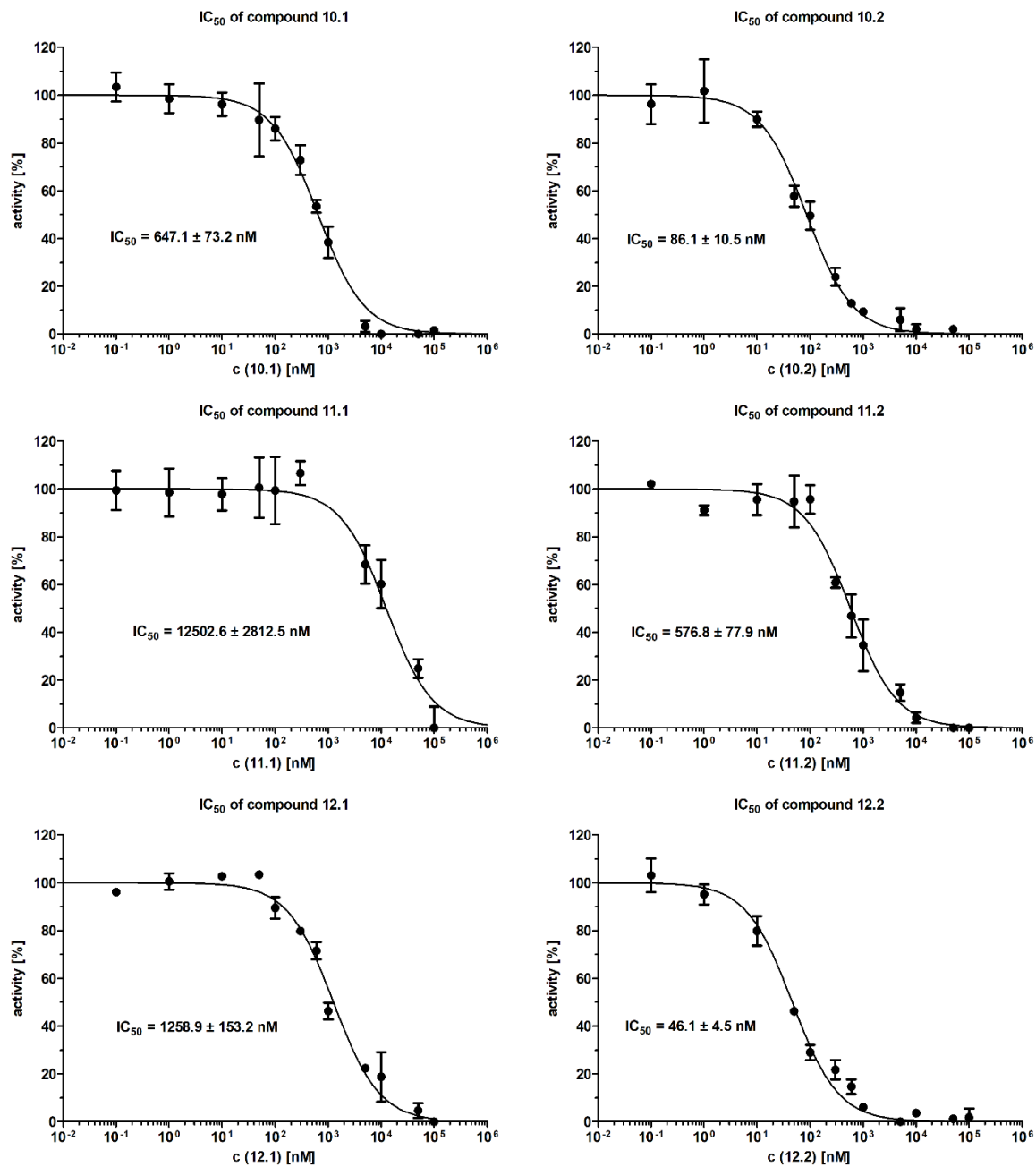
**Figure S4.** Dose-response analysis of compound **10-12** for SIRT5
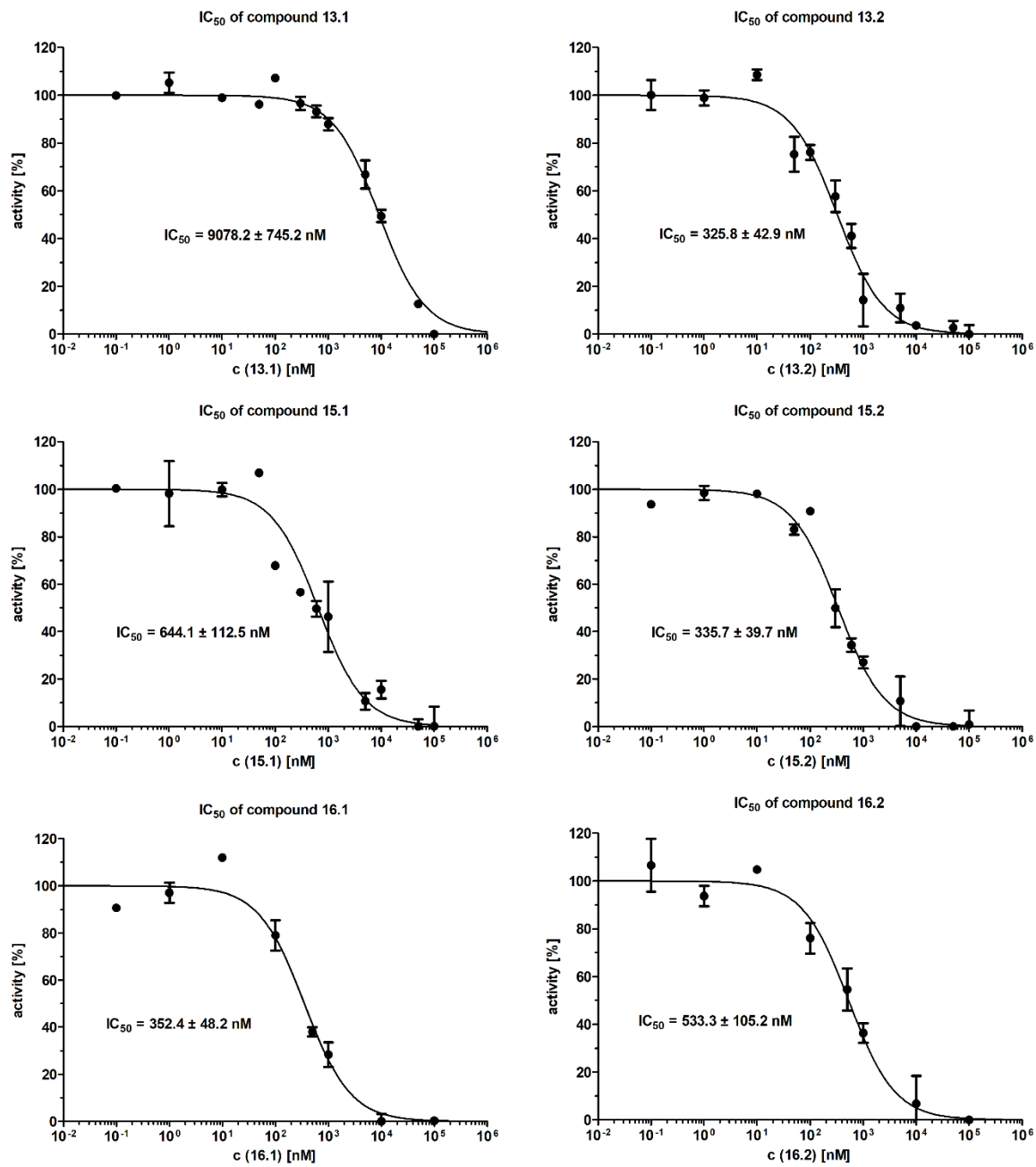
Figure S5. Dose-response analysis of compound **13,15,16** for SIRT5
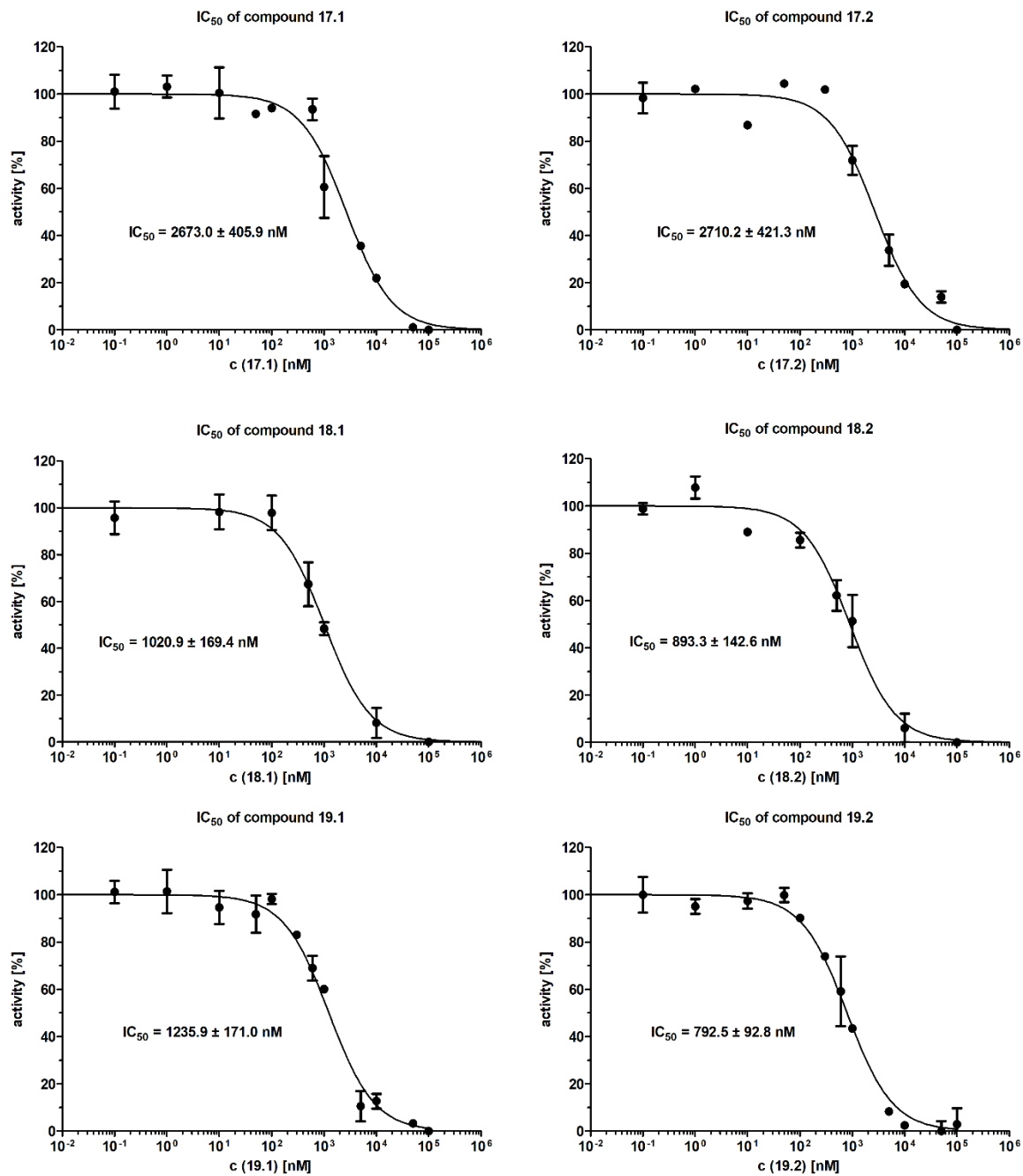
Figure S6. Dose-response analysis of compound **17-19** for SIRT5
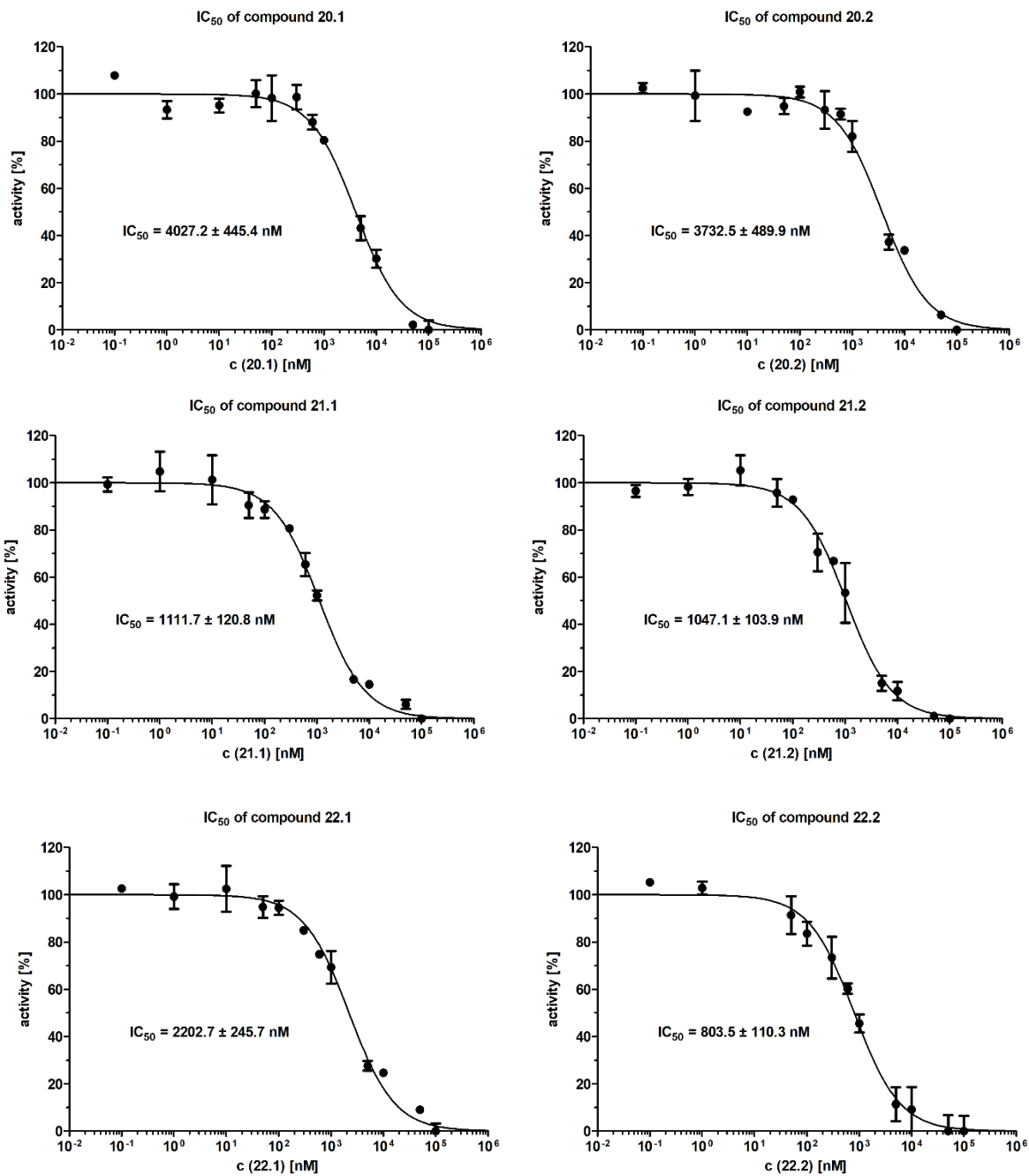
Figure S7. Dose-response analysis of compound **20-22** for SIRT5
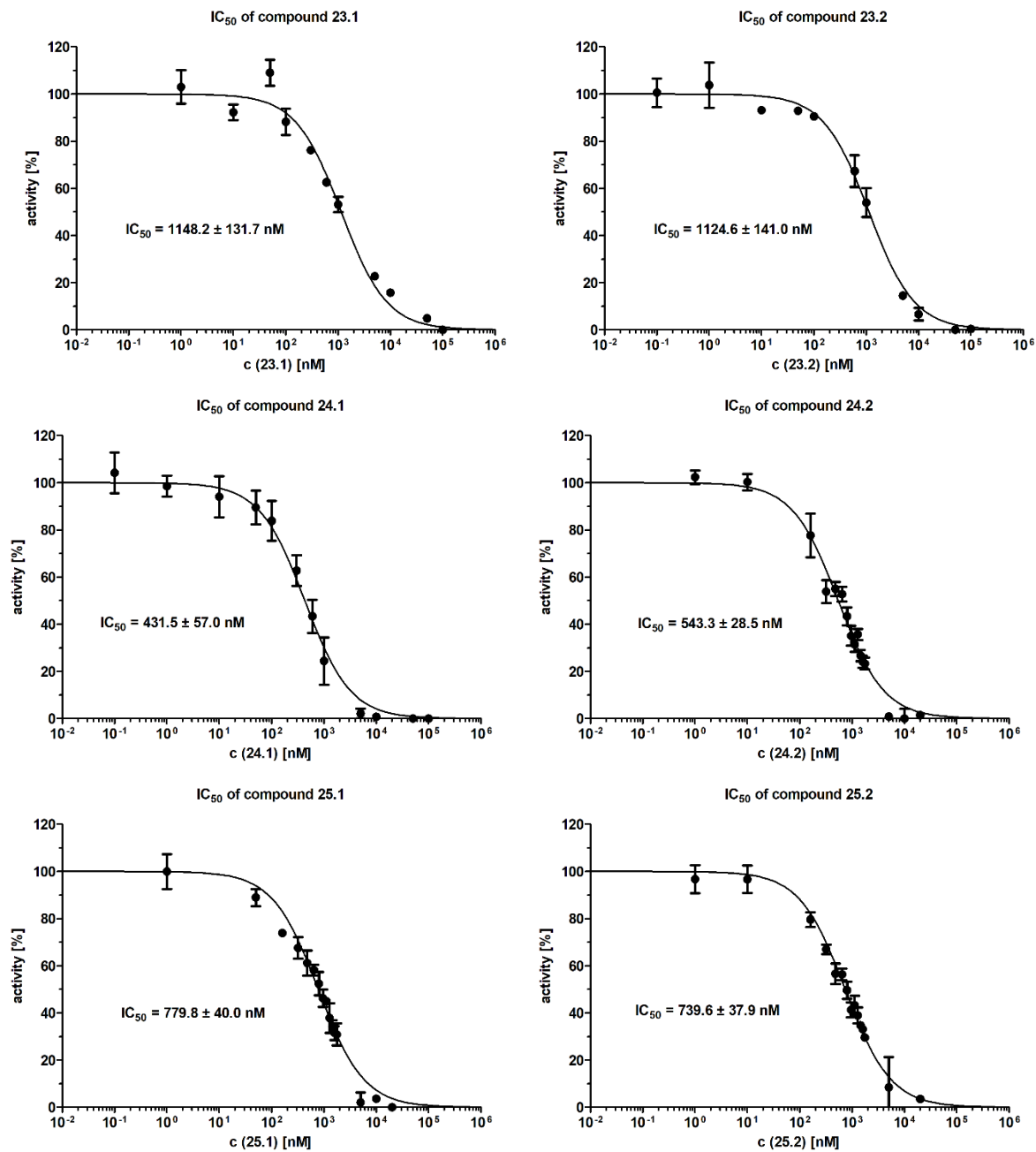
Figure S8. Dose-response analysis of compound **23-25** for SIRT5
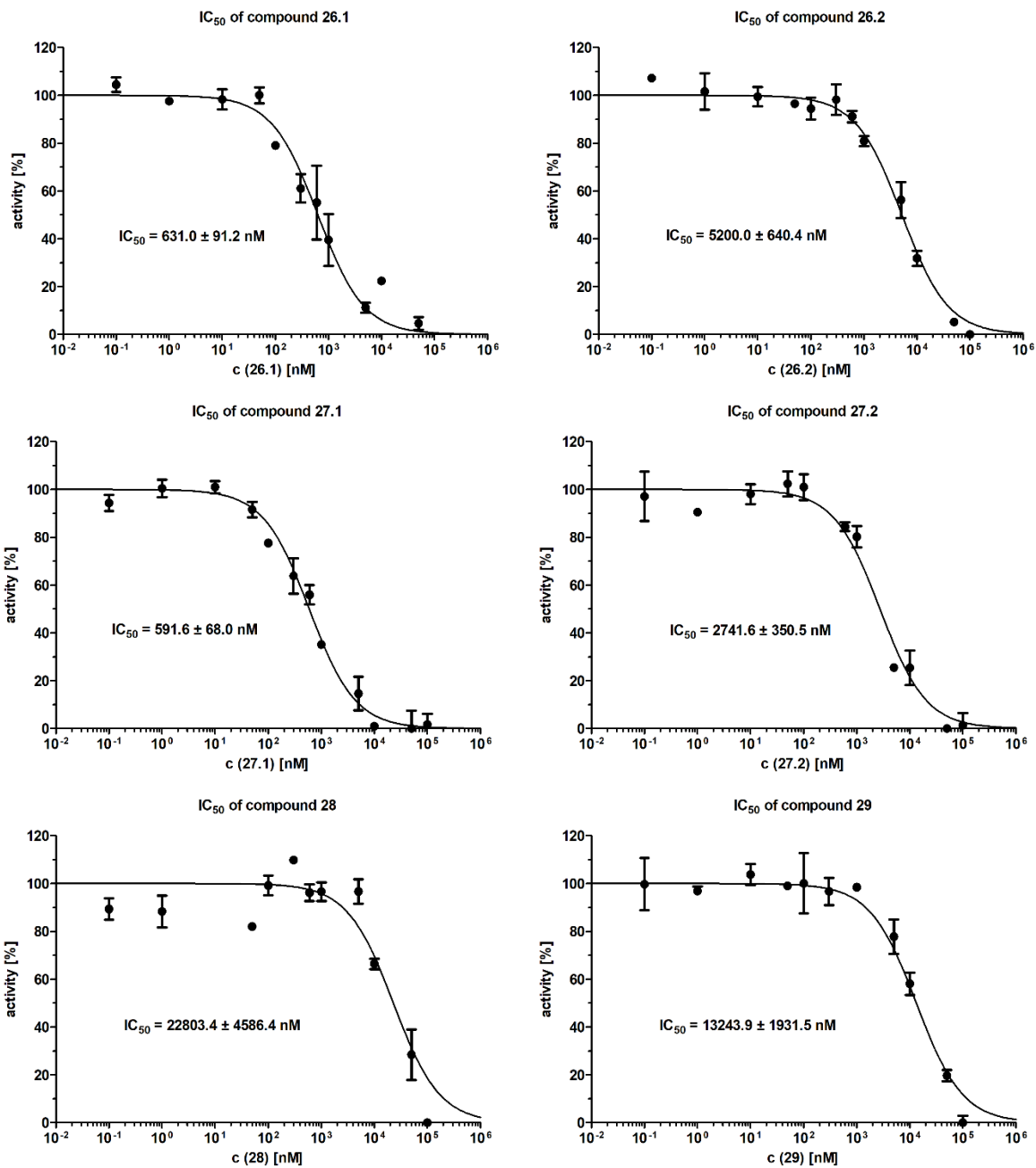
Figure S9. Dose-response analysis of compound **26-29** for SIRT5
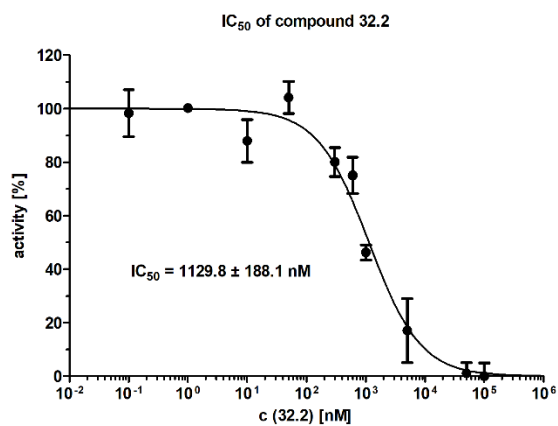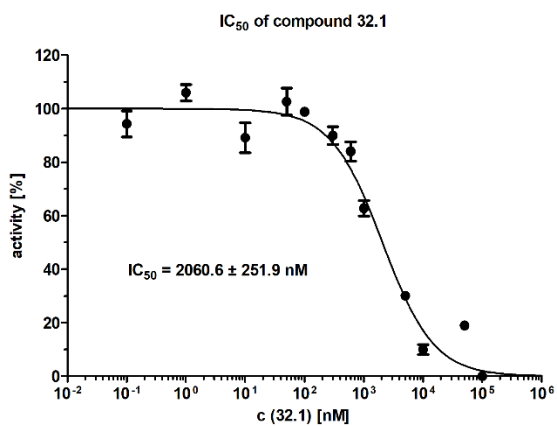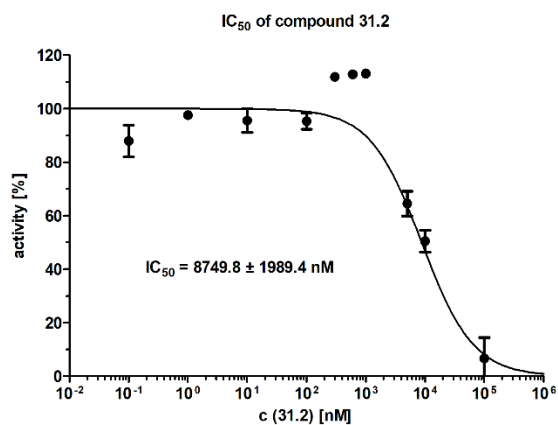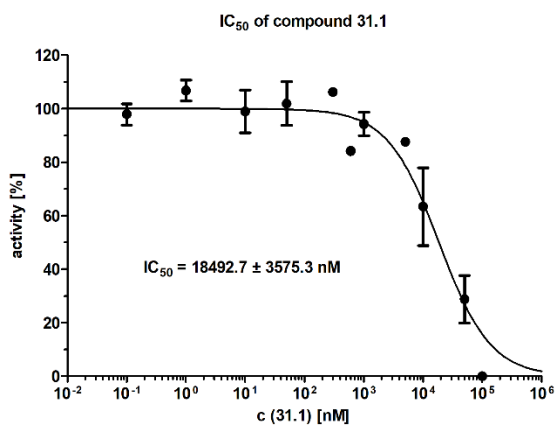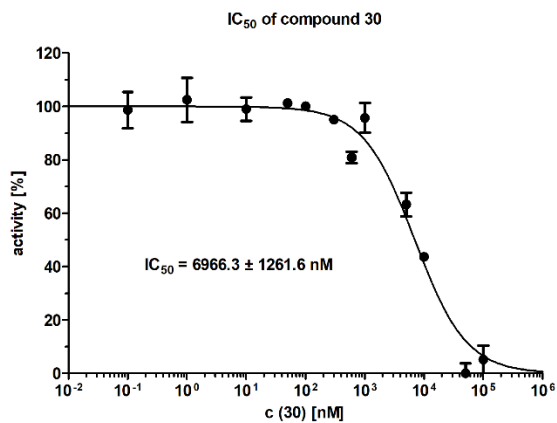
Figure S10. Dose-response analysis of compound **30-32** for SIRT5
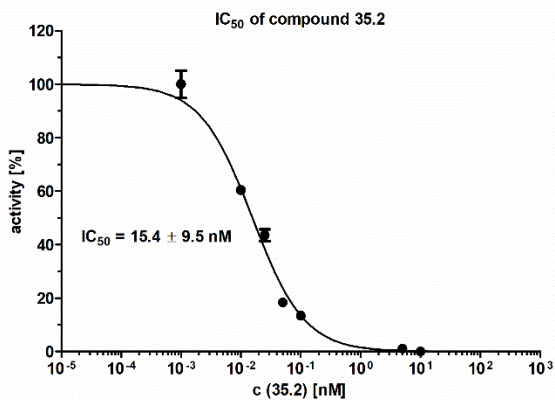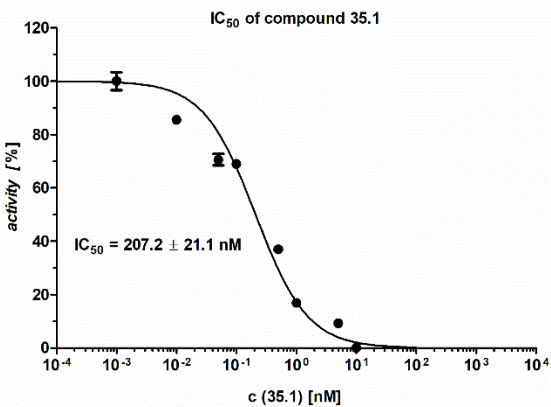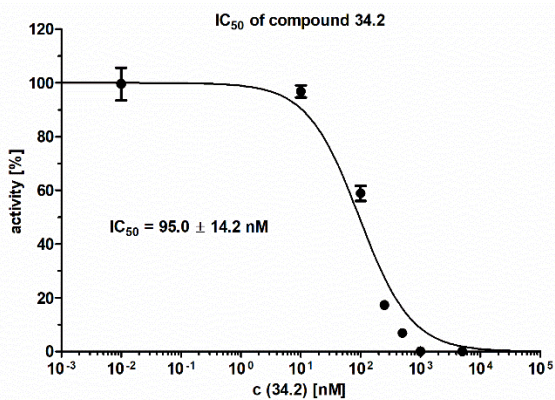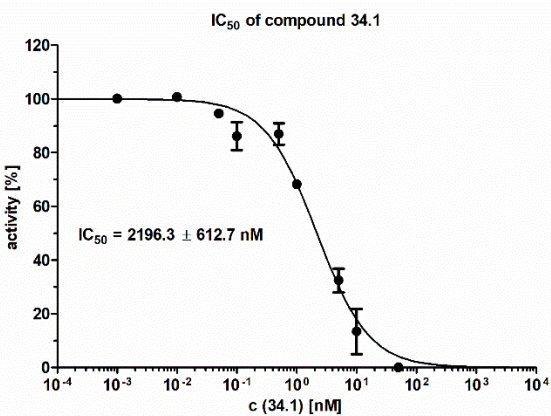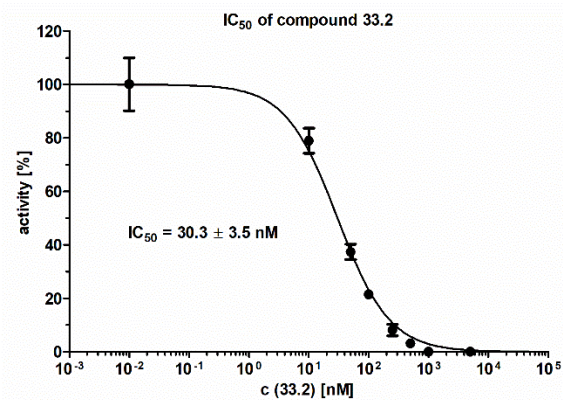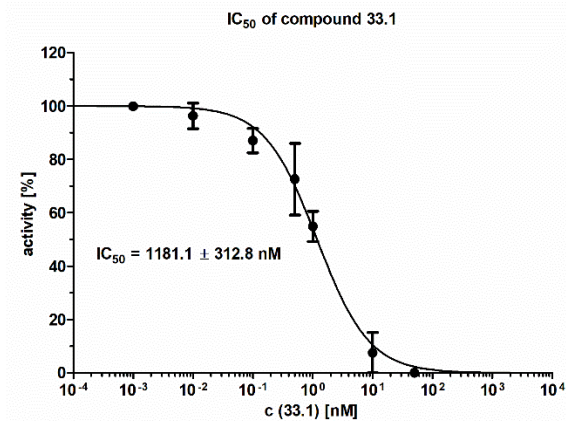
Figure S11. Dose-response analysis of compound **33-35** for SIRT5
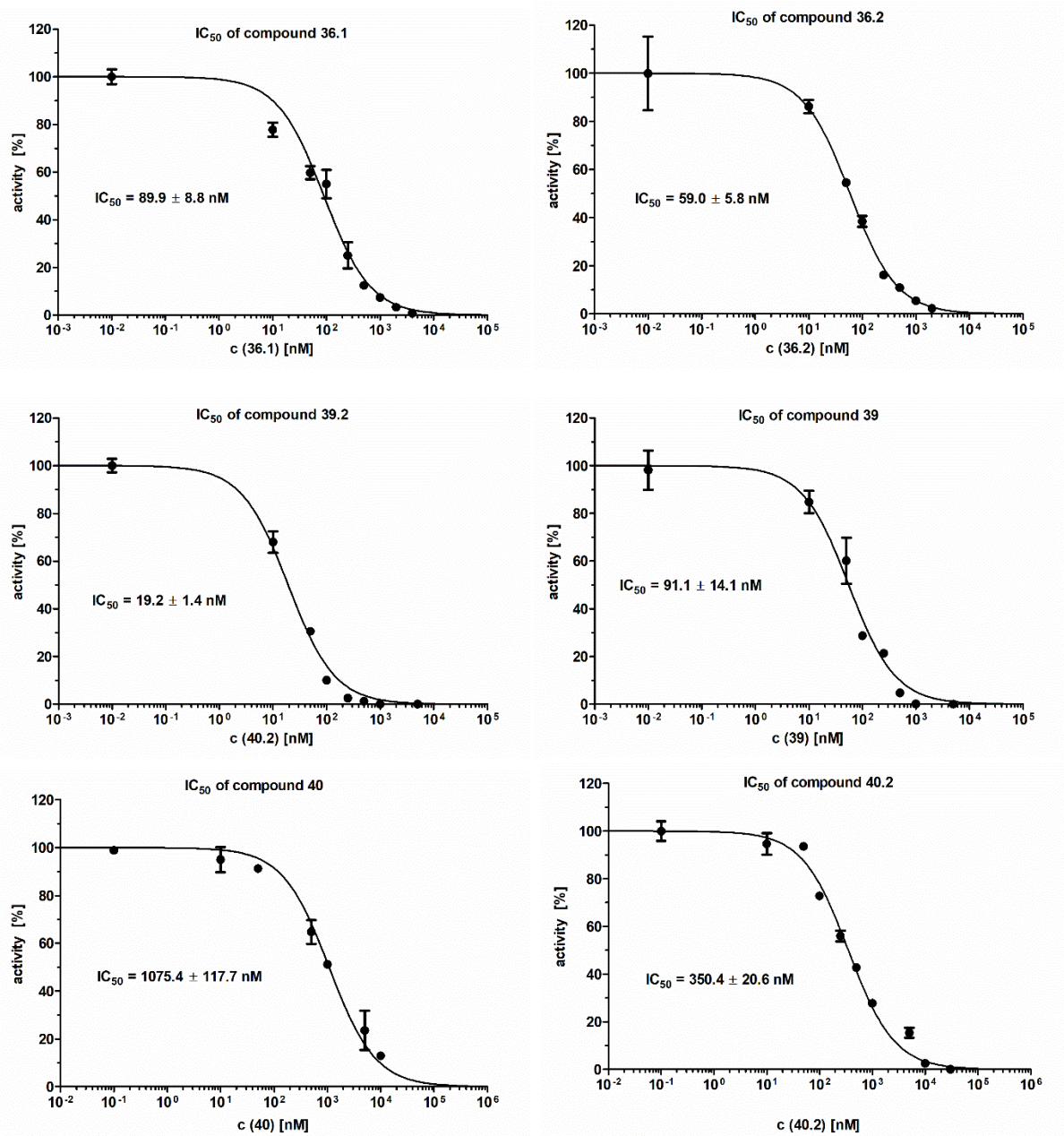
Figure S12. Dose-response analysis of compound **336,39,40** for SIRT5
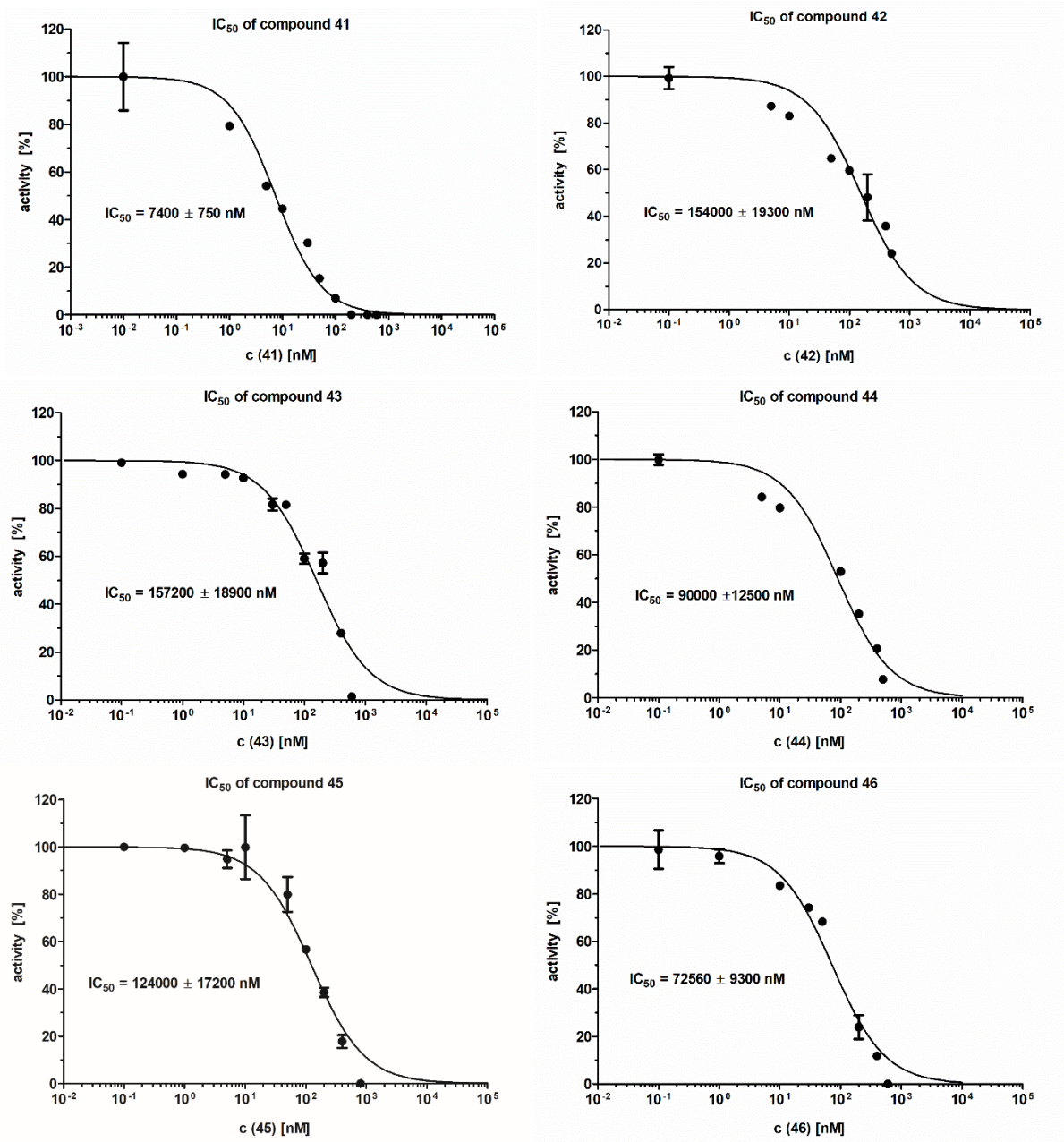
Figure S13. Dose-response analysis of compound **41-46** for SIRT5
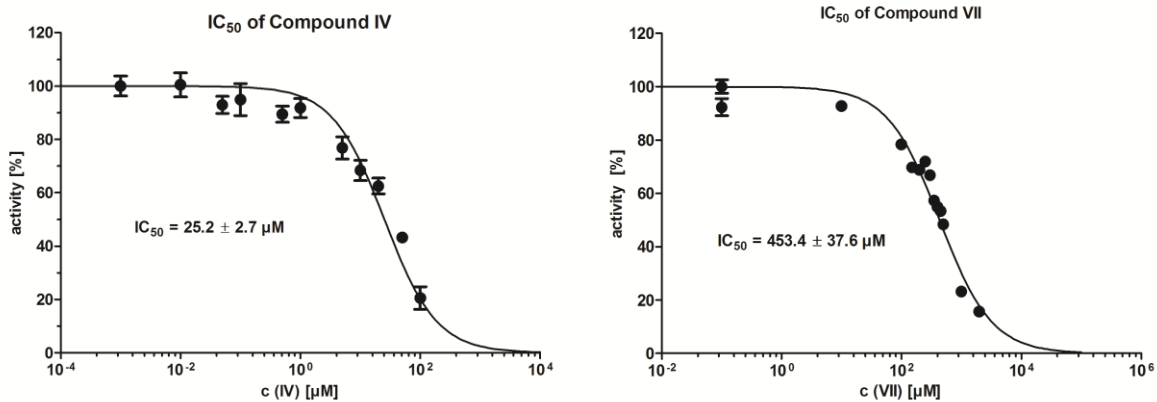
Figure S14. Dose-response analysis of compound **IV** and **VII** for SIRT5
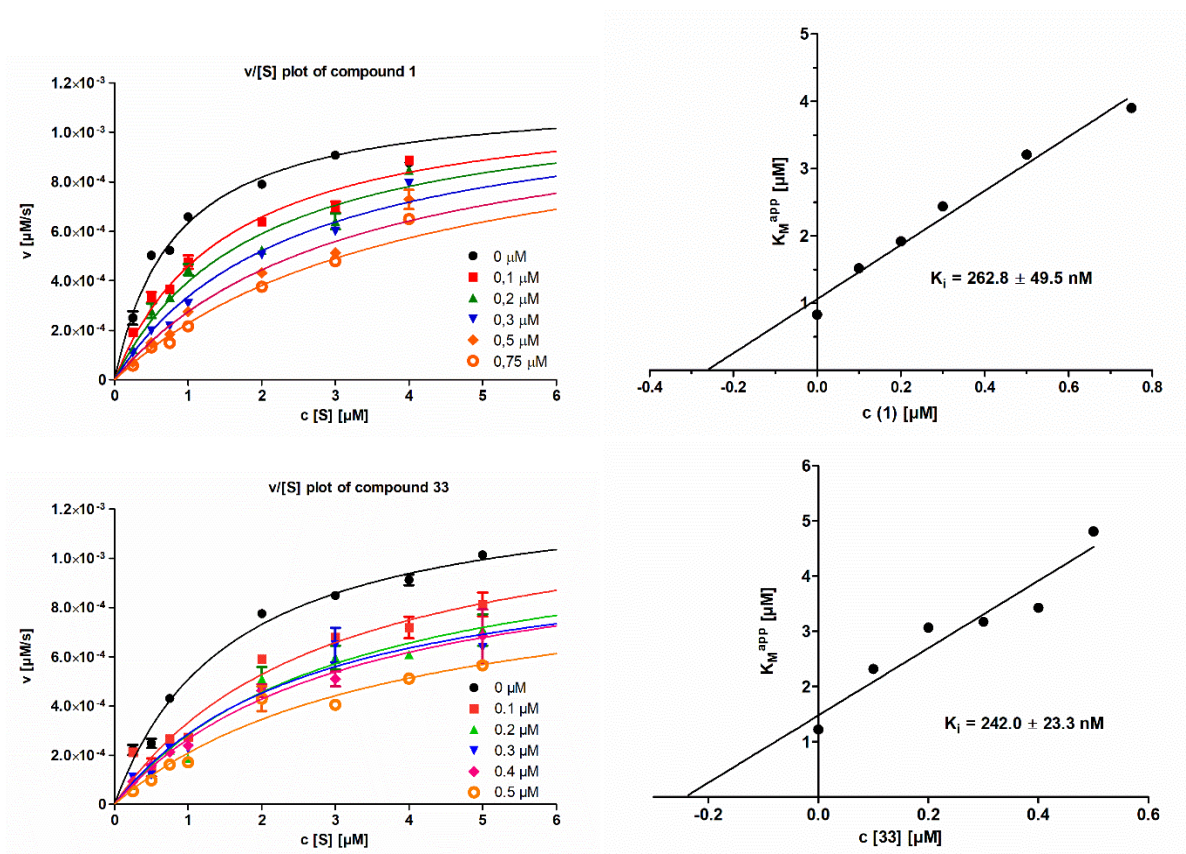
Figure S15. v/[S]-plots and fitting curves of inhibition of compound **1**, mixture of **33** for SIRT5
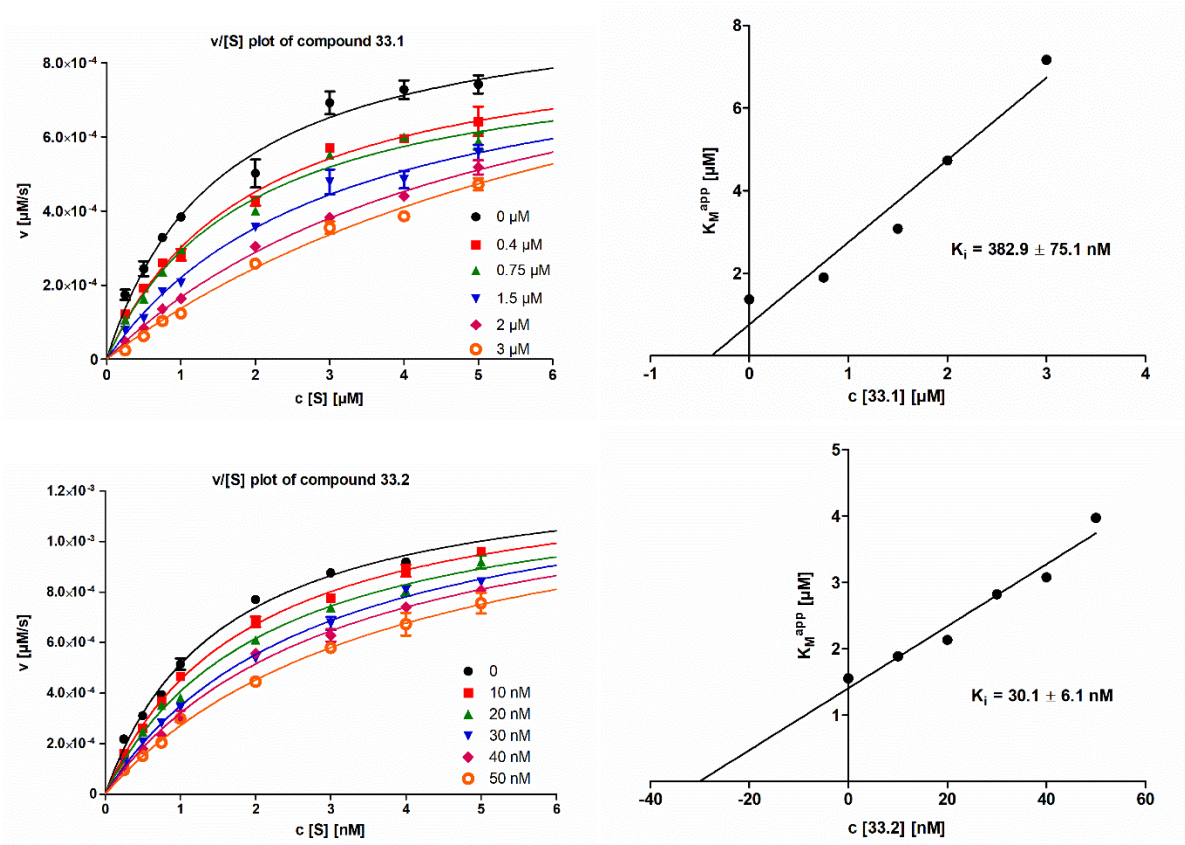
Figure S16. v/[S]-plots and fitting curves of inhibition of compound **33.1** and **33.2** for SIRT5
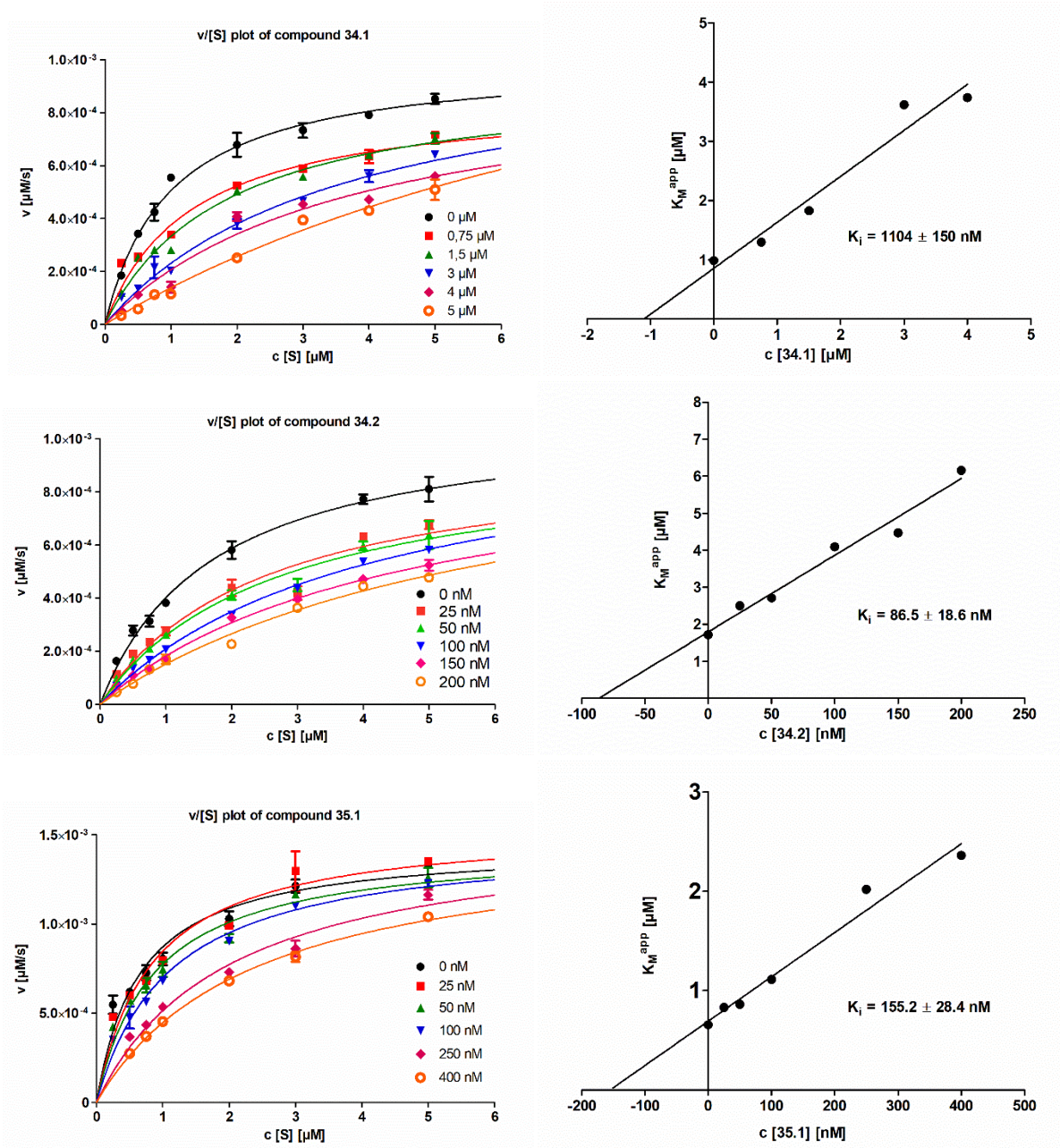
Figure S17. v/[S]-plots and fitting curves of inhibition of compound **34.1, 34.2**, and **35.1** for SIRT5
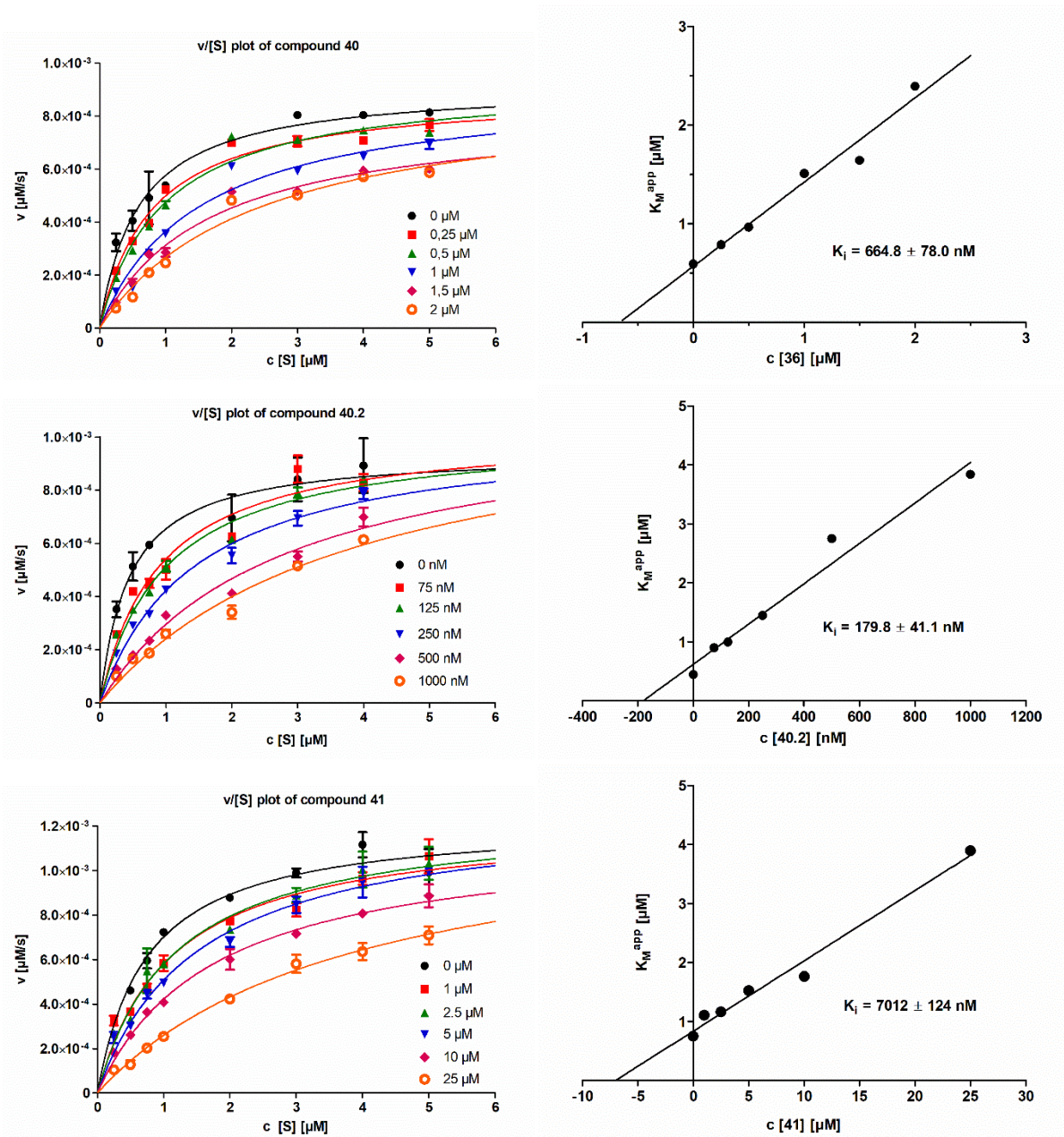
Figure S18. v/[S]-plots and fitting curves of inhibition for mixture of compound **40** and stereoselective synthesized compound **40.2** and **41** for SIRT5
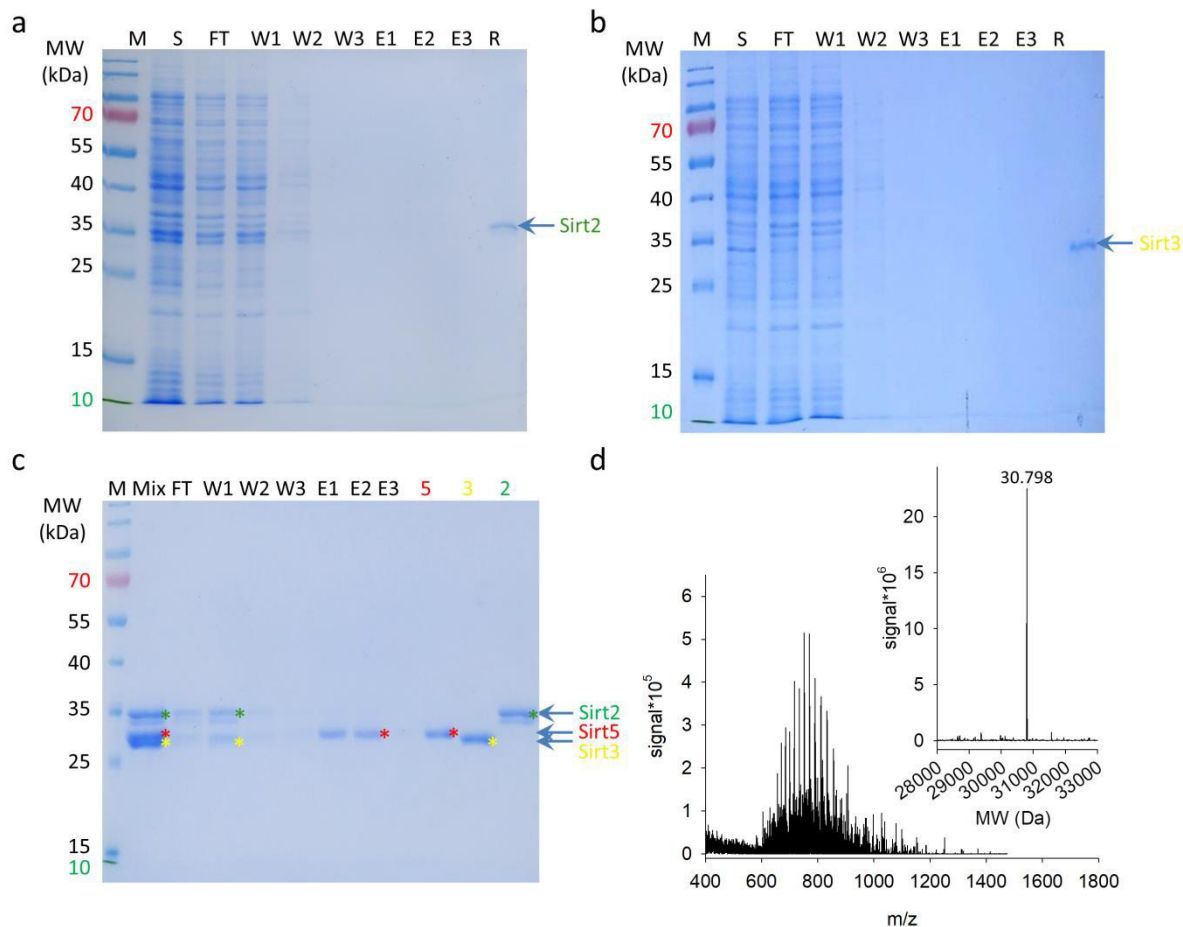
Figure S19: Immobilized **39.2** selectively captures Sirt5 out of E. coli lysate. a) SDS-Page analysis (coomassie staining) of biotinylated **39.2** bound to Streptavidin-coated agarose interacting with E.coli BL21 (DE3) lysate expressing Sirt2 in a column chromatographic manner. In contrast to Sirt5-expressing E.coli cells (figure x) no protein was eluted from the matrix indicating that Sirt2 did not bind to the inhibitor. b) Capture-studies with Sirt3-expressing E. coli cells show similar results as Sirt2: Sirt3 was not eluted from the inhibitor-matrix although Sirt3 seems to interact slightly more with the inhibitor than Sirt2 resulting in a weaker Sirt2-band in the flow through in comparison to the supernatant. c) Finally, an equimolar mixture of Sirt2, Sirt3 and Sirt5 was applied to the inhibitor-matrix in a column chromatographic manner and analyzed via SDS-Page. Sirt2 and Sirt3 were exclusively detected in the flow through and the wash fractions. Protein-containing elution fractions were analyzed via mass spectrometry (d).

The eluted protein was clearly identified as Sirt5 ($M_{calc.}$= 30.796 Da, M_{found}= 30.798 Da).

S…supernatant after cell rupture, FT…flow through, W…wash fractions, E…Elution fractions.
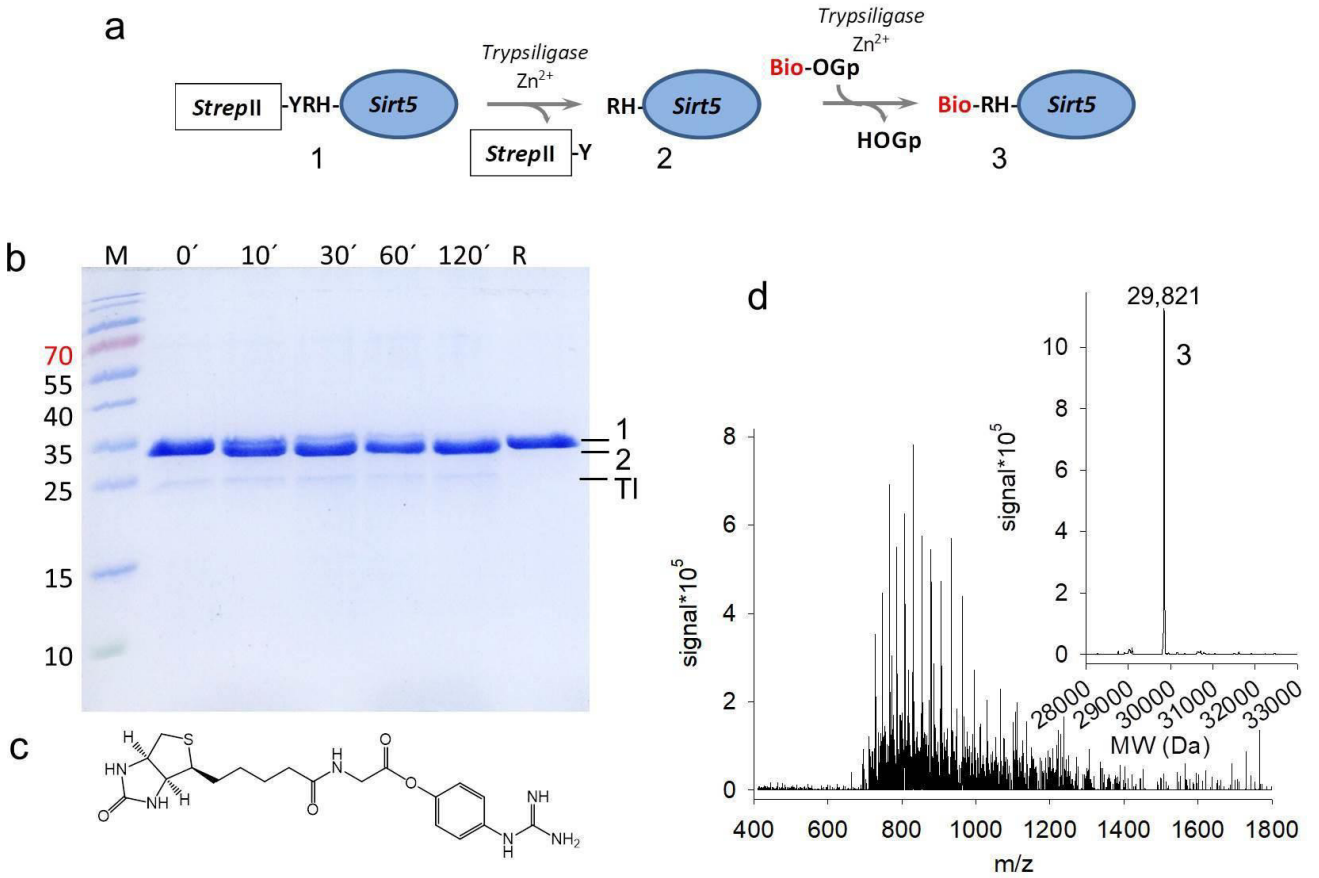
Figure S20. Trypsiligase-catalyzed biotinylation of Sirt5.
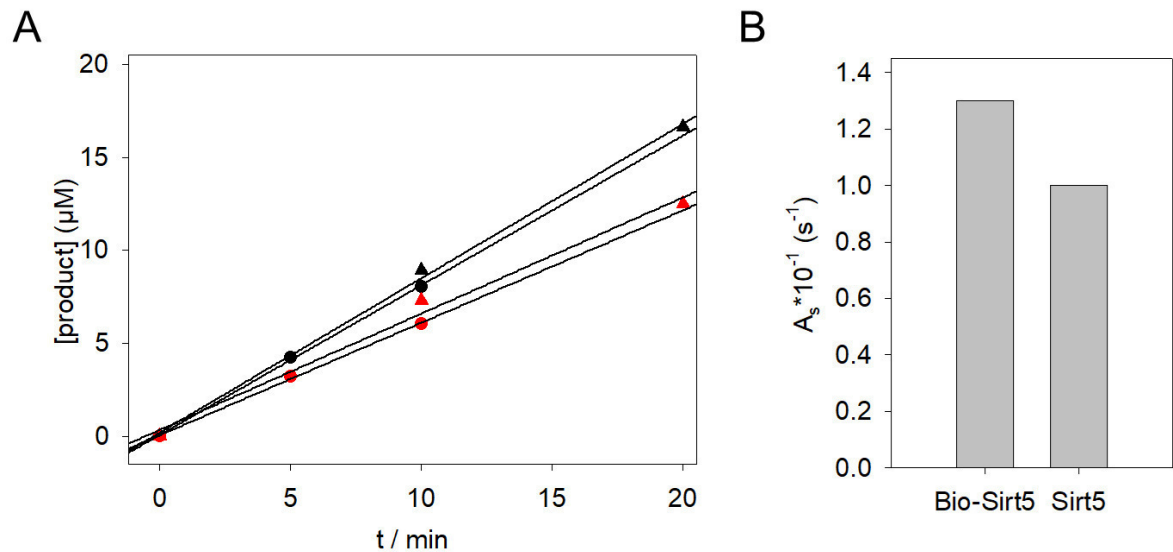
Figure S21. Biotinylated Sirt5 shows similar activity compared to the unmodified Sirt5. A) Product formation in a deacetylation assay for Bio-Sirt5 (black) and Sirt5 (red) at [substrate] = 10 µM (circle) and 50 µM (triangle), respectively. B) Specific activity of Bio-Sirt5 (0.13 s^{-1}) and Sirt5 (0.1 s^{-1}). Conditions: 100 nM Sirt5, [CPS1] = 10 µM, 50 µM, 20 mM Tris, 150 mM NaCl, 5 mM MgCl$_2$ pH 7.8, T=37°C, each point represent the average of two independent measurements (deviation <1%).
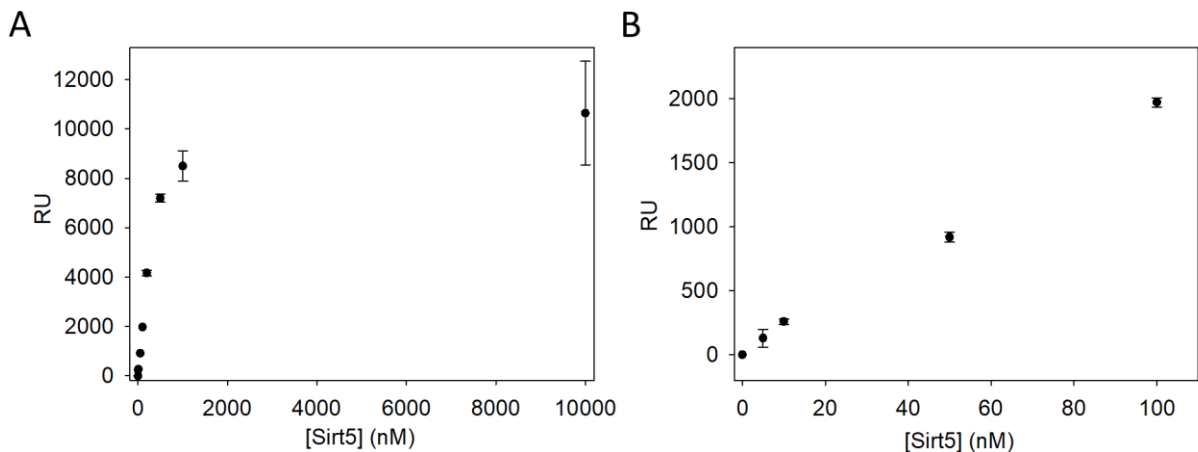
Figure S22. Maximum RU shift detected at the end of the association phase plotted against Sirt5 concentration (n = 3). A) RU vs Sirt5-concentration up to 10 µM. B) Linear range (0-100 nM Sirt5).
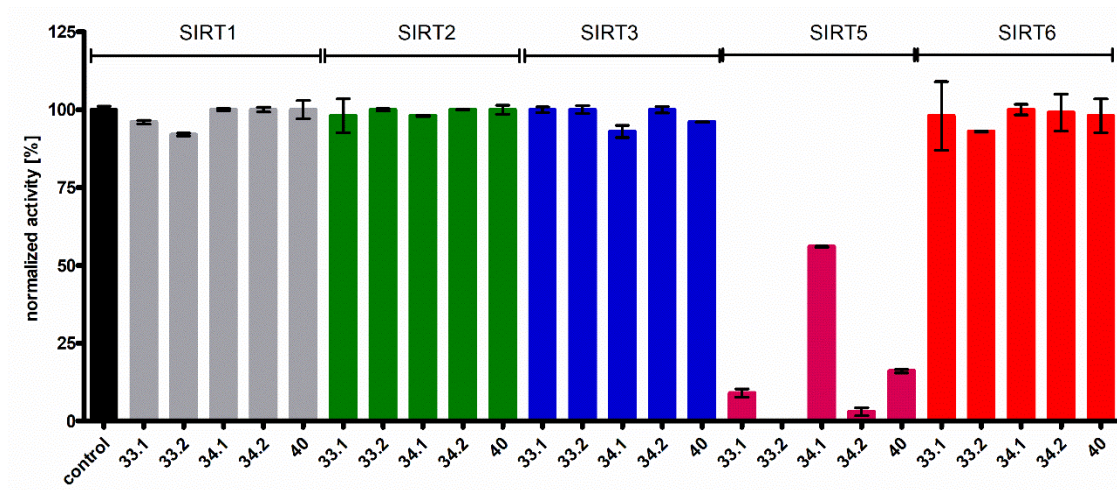
Figure S23: Specificity test of compounds **33.1, 33.2, 34.1 34.2** and **40** for SIRT1-3 and **5-6**. For SIRT 1-3 substrate Bz-GVLK(Acetyl)EYGV-NH$_2$ for SIRT Bz-GVLK(Succinyl)EYGV-NH$_2$ and for SIRT6 Ac-EALPKK(Myristoyl)TCG-NH$_2$ were used.
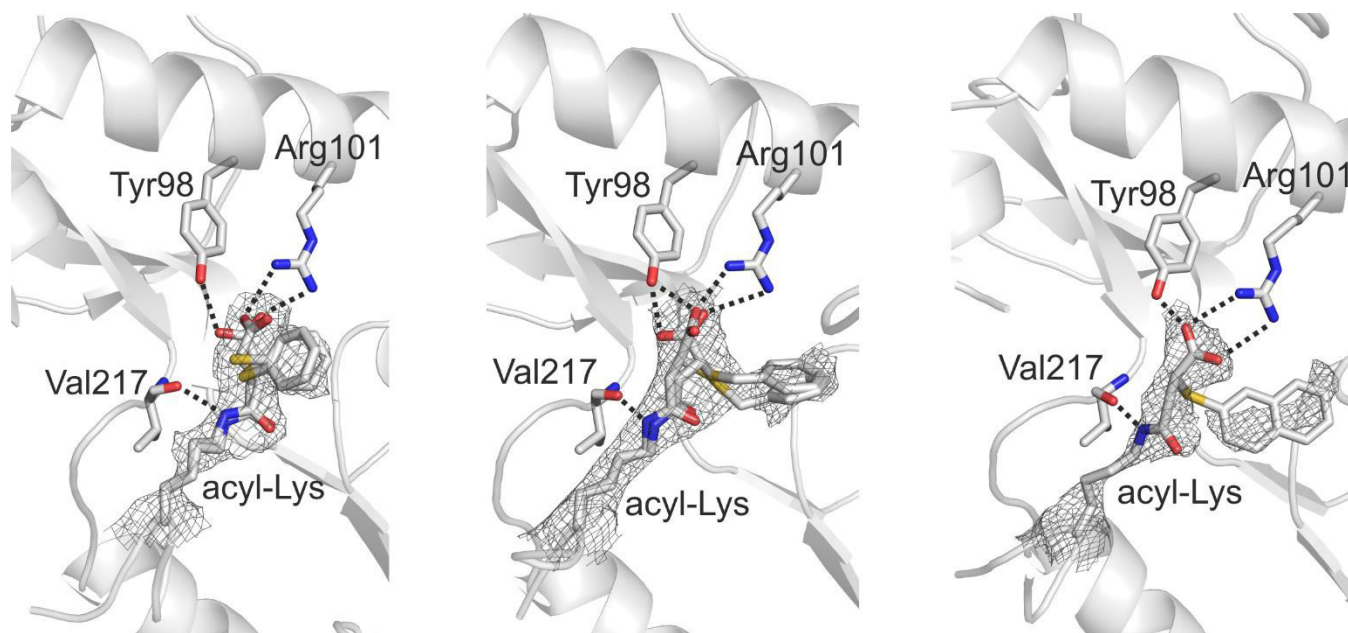
Figure S24. Left: Crystal structure of a zSirt5/**2** complex. The acyl-Lys and interacting residues are shown as sticks, and 2Fo-Fc electron density for the inhibitor is contoured at 1σ. **Middle:** Crystal structure of a zSirt5/**15** complex. The acyl-Lys and interacting residues are shown as sticks, and 2Fo-Fc electron density for the inhibitor is contoured at 1σ. **Right:** Crystal structure of a zSirt5/**33.2** complex. The acyl-Lys and interacting residues are shown as sticks, and 2Fo-Fc electron density for the inhibitor is contoured at 0.9σ.
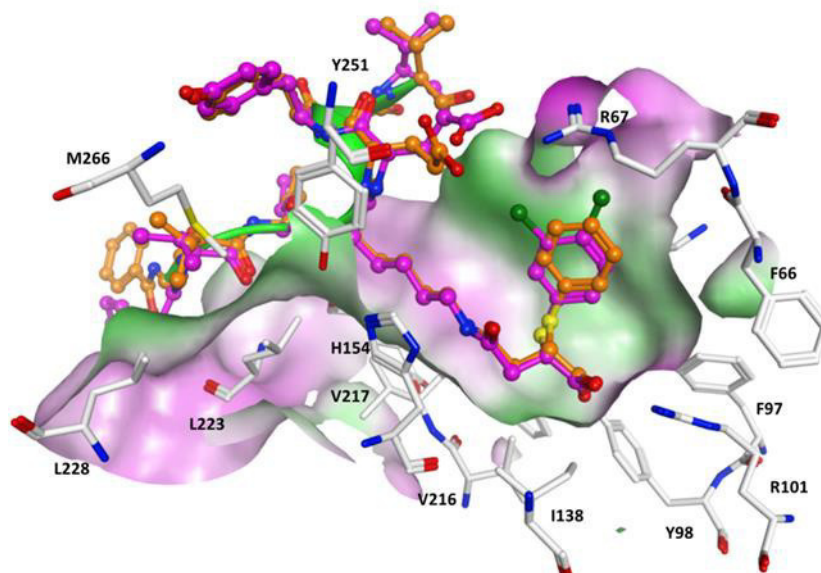
Figure S25. Comparison of the top-ranked docking pose of **8.2** (colored magenta) and the crystal structure of zSirt5/**2.2** (colored orange). The molecular surface of the zSirt5 binding pocket is displayed and colored according to the hydrophobicity (polar areas are colored magenta, hydrophobic areas are colored green).
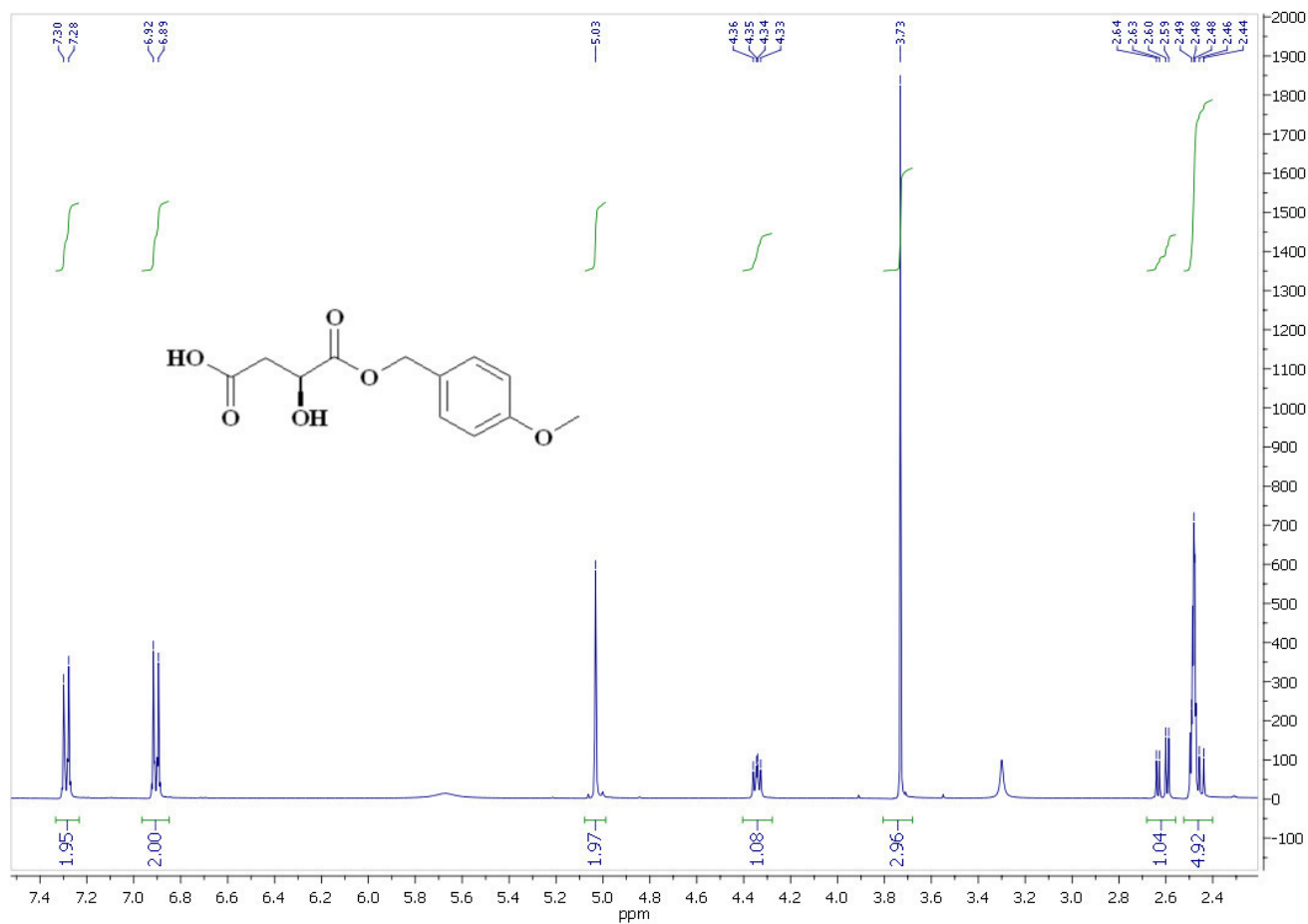
Figure S106. NMR-spectrum of (S)-2-hydroxysuccinic acid 1-(4-methoxybenzyl) ester
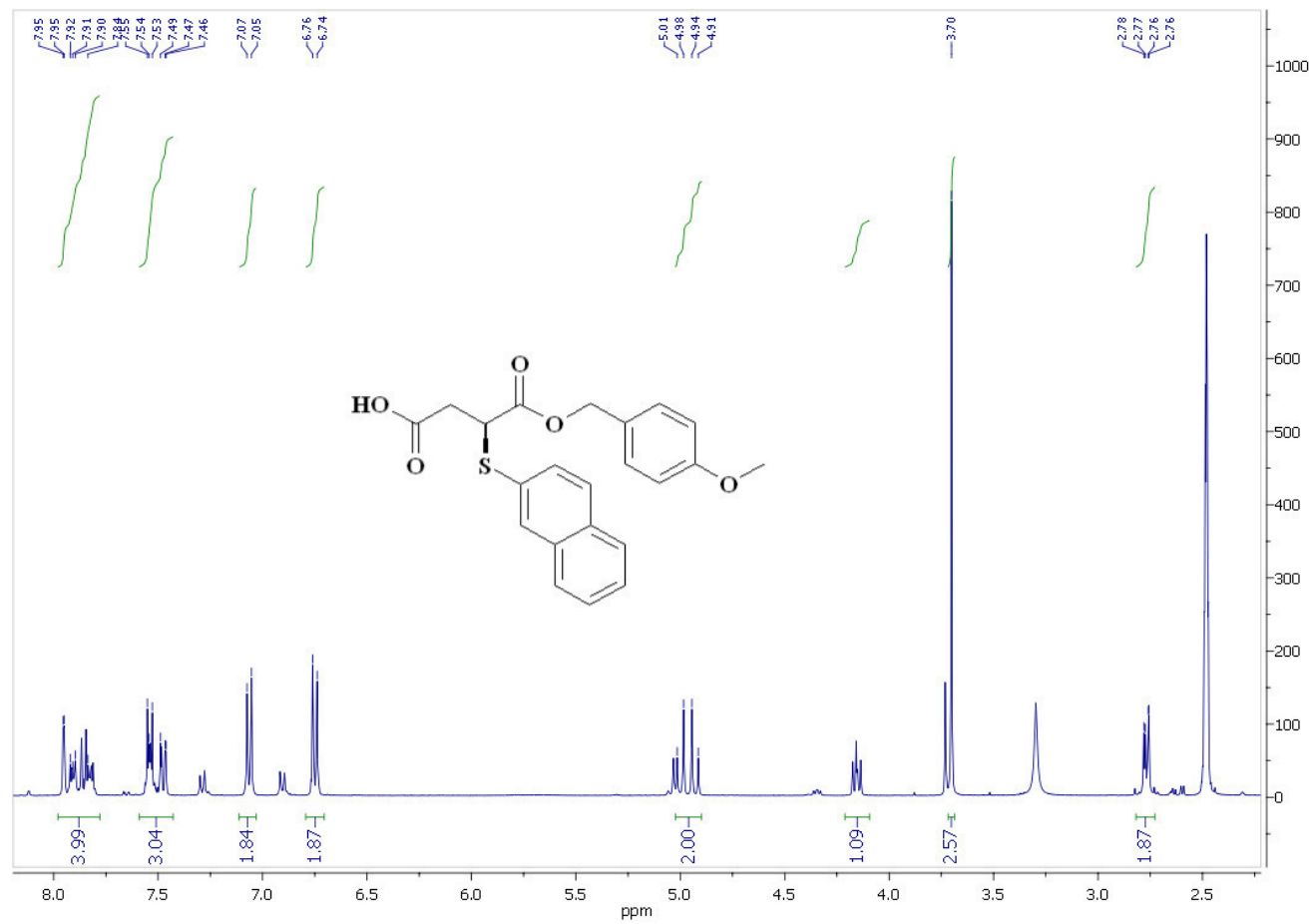
Figure S107. NMR-spectrum of (S)-2-(2-naphthylthio)succinic acid 1-(4-methoxybenzyl) ester
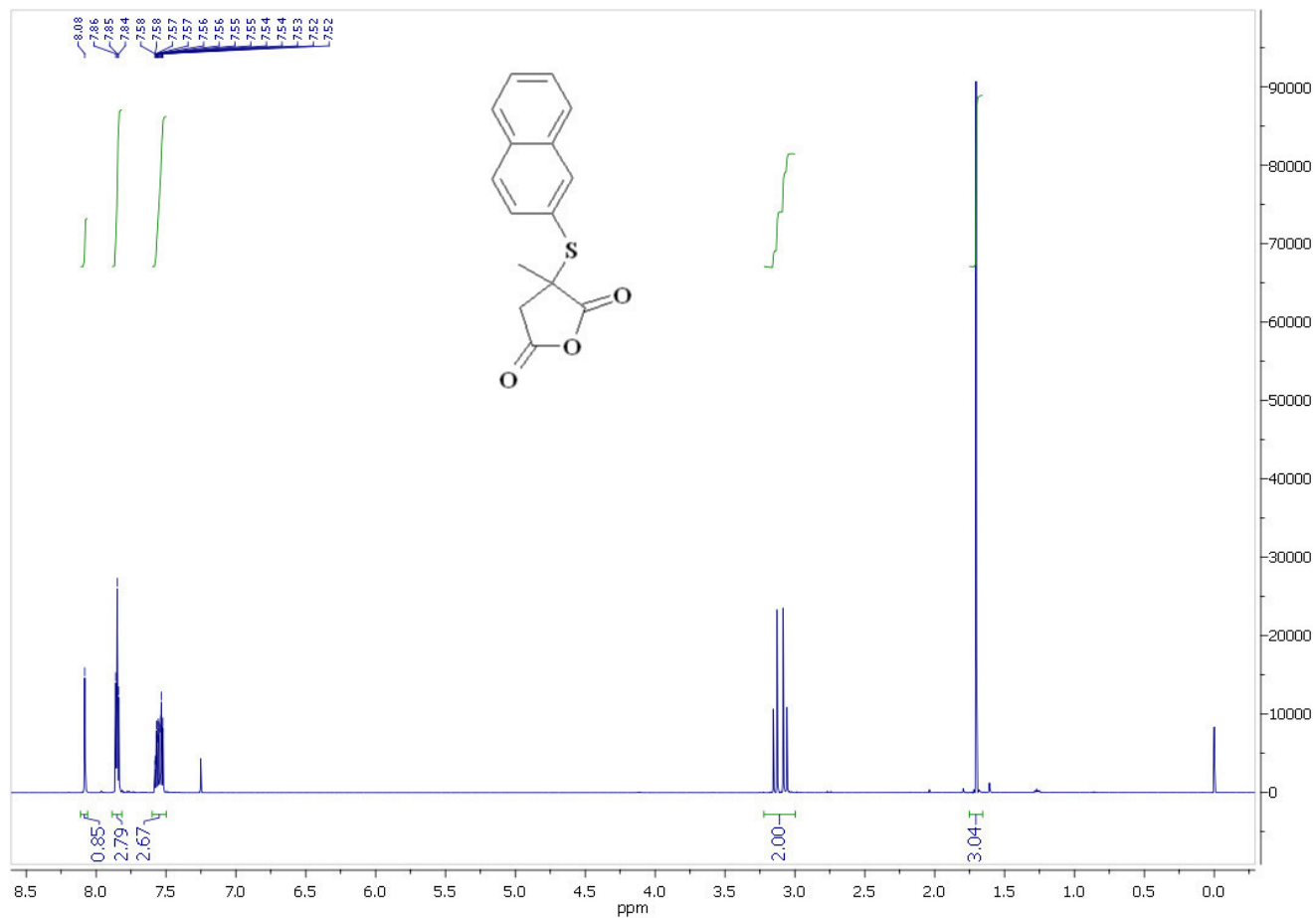
Figure S108. NMR-spectrum of 2-methyl-2-(2-naphthylthio)succinic anhydride

5.3. Publication 3

Mechanism-based Inhibitors of the Human Sirtuin 5 Deacylase: Structure-Activity Relationship, Biostructural, and Kinetic Insight

This paper resulted from a collaborative study between the labs of Christian A. Olsen, Andreas S. Madsen, Matthew D. Hirschey and Clemens Steegborn. Christian A. Olsen, Andreas S. Madsen and Nima Rajabi designed the study. Chrisian A. Olsen and Nima Rajabi designed the Sirt5 inhibitors, while Marina Auth, Kathrin R. Troelsen, Martin Fontenas and Nima Rajabi synthesized them. Andreas S. Madsen designed the assay substrates. Marina Auth, Kathrin R. Troelsen and Nima Rajabi performed the *in vitro* assays. Matthew D. Hirschey and Dhaval P. Bhatt designed and performed the Western-Blot experiments. Christian A. Olsen, Andreas S. Madsen and Nima Rajabi drafted the manuscript, while Clemens Steegborn and I contributed crystal structure figures and description.

Please note: Supplementary Information pages 25-92 (detailed chemical synthesis and NMR-analysis (in words) of compounds) and pages 98-254 (NMR spectra of compounds) were omitted to limit the number of pages, but are available on the CD-ROM attached to this work.

Mechanism-Based Inhibitors of the Human Sirtuin 5 Deacylase: Structure–Activity Relationship, Biostructural, and Kinetic Insight

Nima Rajabi, Marina Auth, Kathrin R. Troelsen, Martin Pannek, Dhaval P. Bhatt, Martin Fontenas, Matthew D. Hirschey, Clemens Steegborn, Andreas S. Madsen, and Christian A. Olsen*
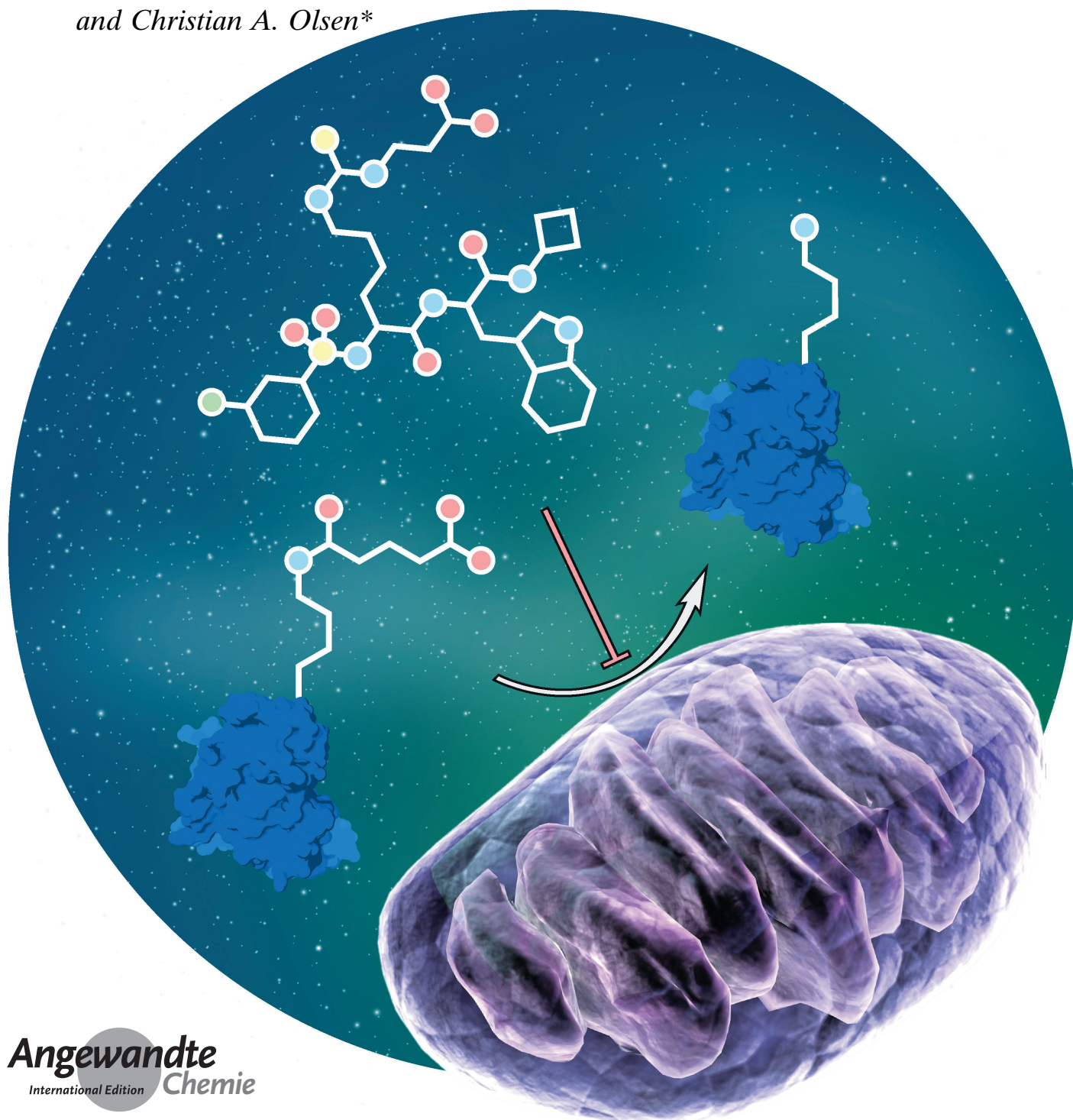
Abstract: *The sirtuin enzymes are important regulatory deacylases in a variety of biochemical contexts and may therefore be potential therapeutic targets through either activation or inhibition by small molecules. Here, we describe the discovery of the most potent inhibitor of sirtuin 5 (SIRT5) reported to date. We provide rationalization of the mode of binding by solving co-crystal structures of selected inhibitors in complex with both human and zebrafish SIRT5, which provide insight for future optimization of inhibitors with more "drug-like" properties. Importantly, enzyme kinetic evaluation revealed a slow, tight-binding mechanism of inhibition, which is unprecedented for SIRT5. This is important information when applying inhibitors to probe mechanisms in biology.*

Sirtuins are a family of NAD⁺-dependent silent information regulator 2 (Sir2) enzymes that catalyze the removal of acyl groups from ε-N-amino groups of lysine residues in the proteome.[1] The human genome codes for seven different sirtuin isoforms (SIRT1-7), which are classified according to sequence similarity and localize to different cellular compartments.[2] Recently, it has become evident that different enzyme isoforms exhibit preference for different ε-N-acyl-lysine posttranslational modifications (PTMs).[1c,d,3] Thus, ε-N-acetyllysine (Kac) functionalities are targeted primarily by SIRT1 and 6 in the nucleus, SIRT2 in the cytoplasm, and SIRT3 in the mitochondria.[3a] In addition, long chain acyl groups, such as ε-N-myristoyllysine (Kmyr), are also cleaved by SIRT1-3 and 6.[4] SIRT5 has been shown to selectively cleave ε-N-carboxyacyllysine derivatives based on malonate (Kmal),[5] succinate (Ksuc),[5b] and glutarate (Kglu).[6] Recently, the ability of SIRT4 to cleave the negatively charged ε-N-(3-methylglutaryl)lysine (Kmg) and ε-N-(3-methylglutaconyl)lysine (Kmgc) has also been demonstrated.[7]

Although the role of SIRT5 is not fully understood, it has been shown to regulate several metabolic enzymes, e.g., carbamoyl phosphate synthetase 1 (CPS1), succinate dehydrogenase (SDH), and 3-hydroxy-3-methylglutaryl-CoA synthase 2 (HMGCS2).[8] Additionally, SIRT5 is involved in

detoxification of reactive oxygen species, by deacylating proteins such as SOD1,[9] IDH2, and G6PD.[10] Furthermore, SIRT5 has been implicated in tumor growth in non-small cell lung cancer[10b,11] and has an anti-apoptotic effect in neuroblastoma cells,[12] highlighting the potential of SIRT5 as a therapeutic target.

Insight into the NAD⁺-dependent hydrolytic mechanism of the sirtuins has been exploited for design of highly potent substrate-mimicking inhibitors that contain thioamide or thiourea functionalities, forming stalled intermediates with ADP-ribose in the sirtuin active sites (Scheme 1A).[13]

Taking advantage of the acyl-substrate specificity of SIRT5, this strategy has been successfully adapted to selectively inhibit this isozyme (Scheme 1B).[6b,15] Here, we performed an extensive iterative structure–activity relationship (SAR) study, evaluating more than 70 compounds, which furnished SIRT5-selective inhibitors exhibiting nanomolar potency via a slow, tight-binding mechanism. These are the most potent SIRT5 inhibitors reported to date; however, our

[*] N. Rajabi, M. Auth, K. R. Troelsen, M. Fontenas,
    Prof. Dr. A. S. Madsen, Prof. Dr. C. A. Olsen
    Center for Biopharmaceuticals & Department of Drug Design and
    Pharmacology, University of Copenhagen
    Universitetsparken 2, 2100 Copenhagen (Denmark)
    E-mail: cao@sund.ku.dk

    M. Pannek, Prof. Dr. C. Steegborn
    Universität Bayreuth, Lehrstuhl Biochemie und Forschungszentrum
    für Biomakromoleküle
    Universitätsstrasse 30, 95447 Bayreuth (Germany)

    D. P. Bhatt, Prof. Dr. M. D. Hirschey
    Duke University Medical Center, Sarah W. Stedman Nutrition and
    Metabolism Center
    4321 Medical Park Drive, Durham, NC 27704 (USA)

Scheme 1. A) Sirtuin hydrolytic mechanism. B) Previous mechanism-based SIRT5 inhibitors. C) Inhibitor optimization in this study. X = O or S, NAD⁺ = reduced nicotinamide adenine dinucleotide, ADP = adenosine diphosphate, Cbz = carboxybenzyl.

study also highlights the necessity for thorough assessment of inhibitor mechanism and calls into question the application of IC$_{50}$ values as the sole measure of potency for these chemotypes.

As starting point, we chose ε-N-thioglutaryllysine over ε-N-thiosuccinyllysine due to the lower K_M value of glutarylated substrates.[6a] The α-amino group was kept Cbz protected to address the C-terminal, first by introduction of

a series of amines (**1–6**, Scheme 2 and Supporting Scheme S1). Inspired by examination of co-crystal structures of SIRT5 with a peptide substrate (PDB 3RIY and 4GIC), we then extended the series to di- and tripeptides (**7–17**), addressing the importance of side chain bulkiness, stereochemistry, and presence of backbone secondary amide (Scheme 2, gray area). The two latter proved important with a preference for L-configuration at position $i+1$ (**10** vs. **11**),
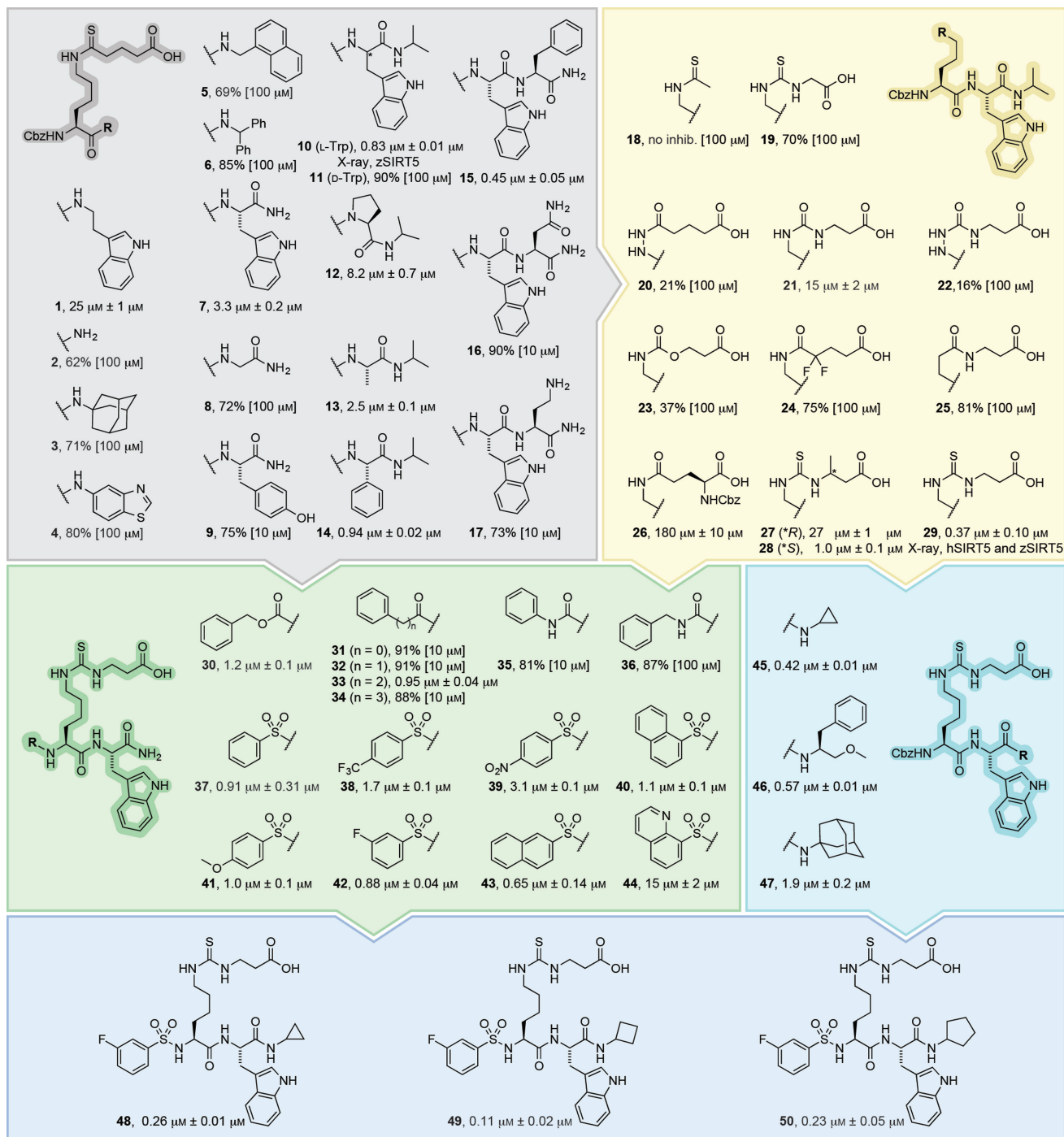
Scheme 2. Subset of the structure–activity relationship study, measuring compound potency against recombinant SIRT5 as previously described.[6a,14] Potencies are given as IC$_{50}$ values or %-inhibition at the highest tested concentration (see Figure S1 for dose-response curves). Please consult the Supporting Information for a list of additional compounds and their potencies (Scheme S1) as well as synthetic Schemes S2–S25.

while the steric bulk of the side chain had minor effect (**12** vs. **14**).

Furthermore, alkylation of the C-terminal amide was beneficial for potency and extending the structure with an $i+2$ amino acid resulted in a slight increase in potency for compound **15**. However, to limit the peptidic nature of the ligand, we chose **10** for further SAR. Next, we explored modifications of the PTM and the ε-amide bond (**18–29**, Scheme 2, yellow area). Inspired by work on Kac surrogates by Cole and Denu, introducing hydrazide[16] and urea[17] functionalities, respectively, we designed compounds **20** and **21**, as well as extended the series with semicarbazide **22** and carbamate **23**. Compound **24** was inspired by work on fluorinated acetamides,[17,18] and inverted amide (**25**) as well as Glu(Cbz) **26** have been introduced as side chains previously.[6b,15c] Finally, 3-methylglutaryl-mimicking[7] analogues (**27** and **28**) were prepared along with compound **29**, the thiourea analogue of **10**. Collectively, this exercise showed that thioamide- and thiourea-based compounds were the most potent and thus, compound **29** was chosen for individual optimization of the N-terminal (**30–44**, Scheme 2, green area) and modifications to the C-terminal *N*-alkyl group (**45–47**, Scheme 2, cyan area).

Co-crystal structures of NAD$^+$-derived intermediates of both lead compounds **10** and **29** in complex with SIRT5 from either zebrafish (zSIRT5) or man (hSIRT5) were solved (Supporting Table S1). These structures revealed detailed insight into the binding modes of the two compounds (Figure 1 A–D). Both structures of zSIRT5 contained the compound (**10** or **29**) bound as bicyclic intermediate with ADP-ribose, similar to structure **III** in Scheme 1 A (mixed with a fraction bound as intermediate **II** in Scheme 1 A for compound **29**), and with expected interactions of the carboxylate with Y98 and R101 (Figure 1 A,B and Supporting Figure S2). Slight structural deviations between the complexes were observed in a Zn-domain loop, the co-factor binding loop, and helix α3, presumably due to the subtle differences in the ligand acyl groups. Interestingly, the structure of **29** in complex with hSIRT5 revealed only the ADP-ribose-1′-thioimidate intermediate **II** of Scheme 1 and no bicyclic intermediate (Figure 1 C). However, the protein chains of the hSIRT5 and zSIRT5 complexes with **29** were almost identical (rmsd 0.31 Å for 225 Cα atoms), and the reason for partially stalling at different intermediate states remains to be elucidated. Whereas thioamides have been co-crystallized with sirtuins previously,[19] these are the first structures with thiourea-based
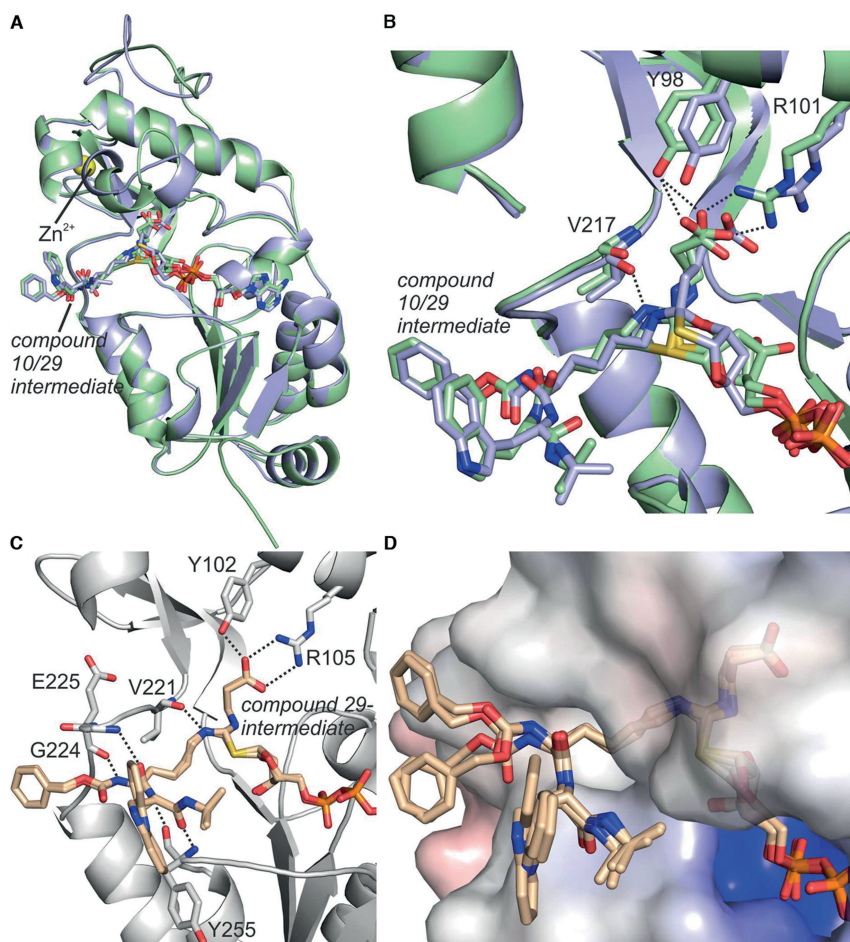
Figure 1. Co-crystal structures resulting from incubation of zSIRT5 with NAD$^+$ and inhibitors **10** or **29** as well as hSIRT5 with NAD$^+$ and inhibitor **29**. A) Superposition of co-crystal structures of zSIRT5 with either bicyclic intermediate **III** (compound **10** shown in pale blue) or an indistinguishable mixture of bicyclic intermediate **III** and ADP-ribose-1′-thioimidate intermediate **II** (compound **29** shown in pale green). B) Active site zoom of the zSirt5 complexes in panel A with interactions between protein and ligand represented as dashed lines. C) Active site of the co-crystal structure of hSIRT5 and ADP-ribose-1′-thioimidate intermediate **II** with compound **29**. Hydrogen bonding interactions between protein and ligand are shown as dashed lines. D) Surface view of the hSIRT5 complex containing the ADP-ribose–**29** intermediate, showing the different positions of the Cbz and indole moieties, while the rest of the ligand is tightly bound.

inhibitors. It is reassuring to observe examples for both intermediates **II** and **III**, confirming that this functionality behaves similarly to thioamides. Important interactions of the compound with hSIRT5 were again the glutaryl carboxylate with Y102 and R105 as well as the ε-NH to the backbone carbonyl of V221 and additional backbone–backbone amide interactions (Figure 1 C). Four SIRT5 chains with variations in the rotation of the Cbz and indole moieties of the ligand were resolved (Figure 1 D). The varying end group conformations are influenced by crystal packing, and the indole positions indicate a flexibility in the SIRT5 complex that is in agreement with the minor effect of this group observed in the SAR.

Furthermore, the observed flexibility of the Cbz group as well as its lack of specific interactions with the protein surface (Figure 1 D) indicated that a variety of functionalities could

be tested in the continued SAR. Thus, for the ease of synthesis, we decided to investigate the N-terminal relative to compound **30**, which is devoid of the C-terminal *i*-propyl group, allowing for ready preparation of the series **30–44** by solid-phase synthesis. We included amide, urea, and sulfonamide analogues of the Cbz group, including various lengths (**30–37**). Due to the potency of **37** and the high abundance of sulfonamides in approved drugs, we prepared analogues **38–44** as well.

In parallel, we briefly re-investigated the importance of steric bulk at the C-terminus, now in the context of compound **29** (**45–47**, Scheme 2, cyan area). Combining the results of these two series, we prepared compounds **48–50** in a final iteration, providing compound **49** as the most potent inhibitor with an improvement in IC_{50} value of > 100-fold from compound **1**. Not surprisingly based on the well-documented substrate specificity of SIRT5, selected compounds (**29** and **48–50**) exhibited excellent selectivity for SIRT5 over SIRT1–3 and 6 (Figure 2A). We were then interested in gaining insight into the kinetic behavior of our most potent compound (**49**) along with intermediate lead compounds **10** and **29** as well as compound **1** and patented compound **V** (Scheme 1) as a control. To achieve this, we first performed a continuous assay[14] to establish whether the inhibition occurred at steady-state kinetics. Not surprisingly, since this has been reported previously for mechanism-based inhibitors of SIRT1,[20] compounds **10**, **29** and **49** exhibited slow, tight-binding kinetics (Figure 2B and Supporting Figure S3). Interestingly, the less potent compounds **1** and **V** behaved like standard fast-on–fast-off inhibitors (Figure 2B and Supporting Figure S3), indicating that the change in mechanism is not solely associated with the thioamide or thiourea amide bond surrogate, but rather developing as the backbone-interacting part of the molecule gains affinity.

Nevertheless, slow binding could be associated with interaction with NAD^+ and enzyme or enzyme alone, so we performed pre-incubation experiments of selected inhibitors and SIRT5 with or without NAD^+ to address these scenarios and to evaluate whether compounds **19–25** exhibited slow-binding as well (Figure 2C). Not surprisingly, the slow-binding behavior of compounds **10**, **19**, **29** and **49** was
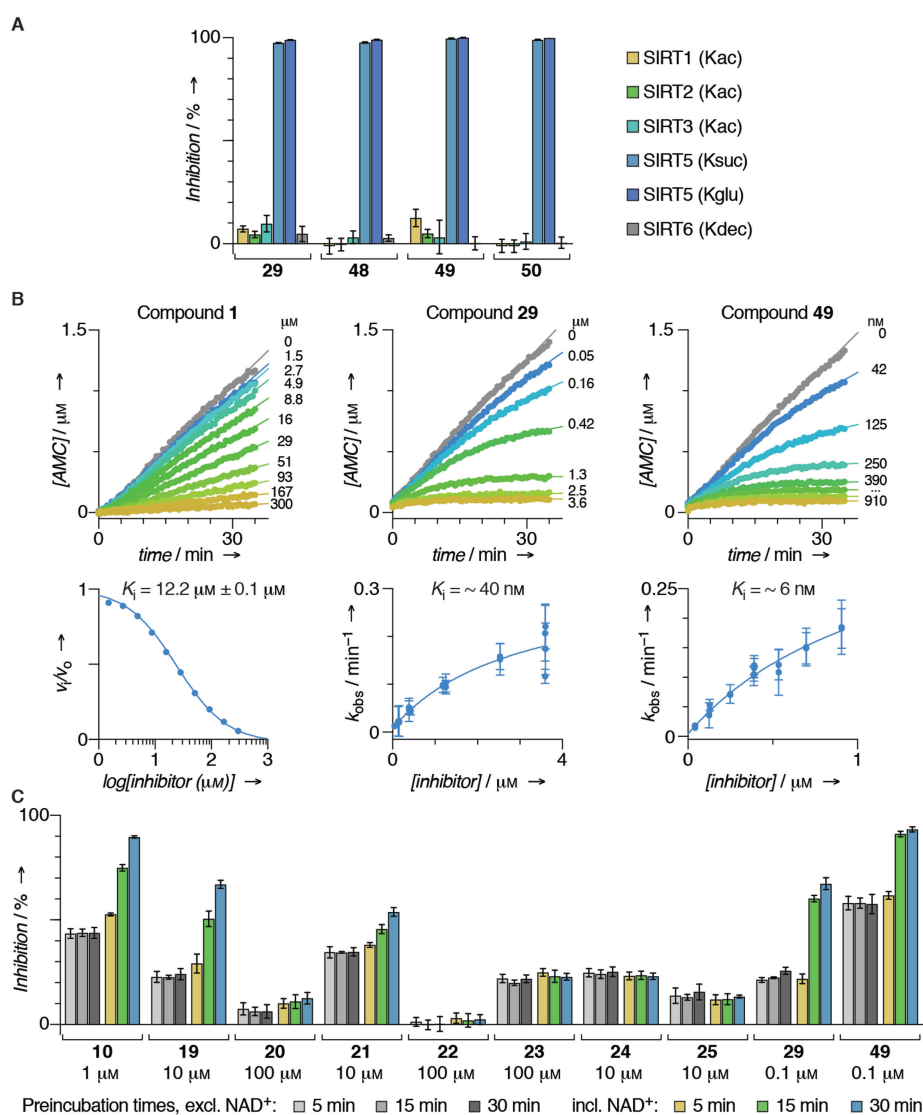
Figure 2. Biochemical evaluation in vitro. A) Selectivity of compounds **29** and **48–50**, measured at an inhibitor concentration of 10 μM. Acyllysines of substrates used are indicated for individual sirtuins. B) Progression curves and data fitting for inhibition of recombinant SIRT5 by compounds **1**, **29**, and **49**. C) Preincubation experiments of compounds **10**, **19–25**, **29**, and **49**.

depending on the presence of NAD^+, indicating that it involves formation of the stalled intermediate. However, it is intriguing that optimization of the scaffold's contribution to affinity imposes a change in mechanism of inhibition. Interestingly, the urea-containing compound **21** also exhibited NAD^+-dependent slow-binding, which may revive the use of this functionality for future inhibitor design. The remaining compounds did not exhibit slow-binding within the time-frame of the pre-incubation experiments (Figure 2C).

Finally, we tested an ethylester prodrug version of compound **29** (**Et-29**) for its ability to affect the degree of lysine glutarylation in cells. However, it is unfortunately not trivial to detect changes in either lysine malonylation, succinylation, or glutarylation even when comparing wildtype to a control CRISPR-Cas9 SIRT5 knockout cell line (Supporting Figures S4 and S5). Further optimization of the experimental design and subsequent evaluation of these

compounds in a cellular context will thus be of immediate future interest.

In summary, we describe mechanism-based inhibitors of sirtuin 5 that exhibit up to a 100-fold improvement in IC_{50} values compared to a patented reference compound included in our assays. Importantly, we show that kinetic analyses of inhibitors of these enzymes is important for appropriate comparison of potencies as we disclose the first examples of slow, tight-binding behavior for SIRT5 inhibitors. This calls for more thorough investigations of mechanism-based inhibitors for all sirtuins. We also describe structural information for the binding mode of thiourea-based sirtuin inhibitors for the first time, which provides important insight for future inhibitor design.

Conflict of interest

The authors declare no conflict of interest.

[1] a) J. Landry, A. Sutton, S. T. Tafrov, R. C. Heller, J. Stebbins, L. Pillus, R. Sternglanz, *Proc. Natl. Acad. Sci. USA* **2000**, *97*, 5807–5811; b) S. Imai, C. M. Armstrong, M. Kaeberlein, L. Guarente, *Nature* **2000**, *403*, 795–800; c) C. A. Olsen, *Angew. Chem. Int. Ed.* **2012**, *51*, 3755–3756; *Angew. Chem.* **2012**, *124*, 3817–3819; d) P. Bheda, H. Jing, C. Wolberger, H. Lin, *Annu. Rev. Biochem.* **2016**, *85*, 405–429.

[2] a) R. A. Frye, *Biochem. Biophys. Res. Commun.* **2000**, *273*, 793–798; b) R. Marmorstein, *Structure* **2001**, *9*, 1127–1133; c) E. Michishita, J. Y. Park, J. M. Burneskis, J. C. Barrett, I. Horikawa, *Mol. Biol. Cell* **2005**, *16*, 4623–4635.

[3] a) B. Chen, W. Zang, J. Wang, Y. Huang, Y. He, L. Yan, J. Liu, W. Zheng, *Chem. Soc. Rev.* **2015**, *44*, 5246–5264; b) B. R. Sabari, D. Zhang, C. D. Allis, Y. Zhao, *Nat. Rev. Mol. Cell Biol.* **2017**, *18*, 90–101.

[4] a) H. Jiang, et al., *Nature* **2013**, *496*, 110–113; b) J. L. Feldman, J. Baeza, J. M. Denu, *J. Biol. Chem.* **2013**, *288*, 31350–31356; c) I. Galleano, M. Schiedel, M. Jung, A. S. Madsen, C. A. Olsen, *J. Med. Chem.* **2016**, *59*, 1021–1031; d) A. S. Madsen, et al., *J. Biol. Chem.* **2016**, *291*, 7128–7141.

[5] a) C. Peng, et al., *Mol. Cell. Proteomics* **2011**, *10*, M111.012658; b) J. Du, et al., *Science* **2011**, *334*, 806–809.

[6] a) M. Tan, et al., *Cell Metab.* **2014**, *19*, 605–617; b) C. Roessler, et al., *Angew. Chem. Int. Ed.* **2014**, *53*, 10728–10732; *Angew. Chem.* **2014**, *126*, 10904–10908.

[7] K. A. Anderson, et al., *Cell Metab.* **2017**, *25*, 838–855.

[8] M. Gertz, C. Steegborn, *Cell. Mol. Life Sci.* **2016**, *73*, 2871–2896.

[9] Z. F. Lin, H. B. Xu, J. Y. Wang, Q. Lin, Z. Ruan, F. B. Liu, W. Jin, H. H. Huang, X. Chen, *Biochem. Biophys. Res. Commun.* **2013**, *441*, 191–195.

[10] a) L. Zhou, et al., *EMBO Rep.* **2016**, *17*, 811–822; b) Y. Xiangyun, N. Xiaomin, G. Linping, X. Yunhua, L. Ziming, Y. Yongfeng, C. Zhiwei, L. Shun, *Oncotarget* **2017**, *8*, 6984–6993.

[11] W. Lu, Y. Zuo, Y. Feng, M. Zhang, *Tumour Biol.* **2014**, *35*, 10699–10705.

[12] F. Liang, X. Wang, S. H. Ow, W. Chen, W. C. Ong, *Neurotox. Res.* **2017**, *31*, 63–76.

[13] Y. Jiang, J. Liu, D. Chen, L. Yan, W. Zheng, *Trends Pharmacol. Sci.* **2017**, *38*, 459–472.

[14] A. S. Madsen, C. A. Olsen, *J. Med. Chem.* **2012**, *55*, 5582–5590.

[15] a) B. He, J. Du, H. Lin, *J. Am. Chem. Soc.* **2012**, *134*, 1922–1925; b) H. Lin (Cornell University), WO 2014/197775 A1, **2014**; c) Y. He, L. Yan, W. Zang, W. Zheng, *Org. Biomol. Chem.* **2015**, *13*, 10442–10450; d) W. Zang, Y. Hao, Z. Wang, W. Zheng, *Bioorg. Med. Chem. Lett.* **2015**, *25*, 3319–3324; e) L. Polletta, et al., *Autophagy* **2015**, *11*, 253–270.

[16] B. C. R. Dancy, et al., *J. Am. Chem. Soc.* **2012**, *134*, 5138–5148.

[17] B. C. Smith, J. M. Denu, *J. Biol. Chem.* **2007**, *282*, 37256–37265.

[18] a) B. C. Smith, J. M. Denu, *Biochemistry* **2007**, *46*, 14478–14486; b) B. C. Smith, J. M. Denu, *J. Am. Chem. Soc.* **2007**, *129*, 5802–5803.

[19] M. Gertz, F. Fischer, G. T. Nguyen, M. Lakshminarasimhan, M. Schutkowski, M. Weyand, C. Steegborn, *Proc. Natl. Acad. Sci. USA* **2013**, *110*, E2772–E2781.

[20] a) B. M. Hirsch, Z. Du, X. Li, J. A. Sylvester, C. Wesdemiotis, Z. Wang, W. Zheng, *MedChemComm* **2011**, *2*, 291; b) T. Asaba, T. Suzuki, R. Ueda, H. Tsumoto, H. Nakagawa, N. Miyata, *J. Am. Chem. Soc.* **2009**, *131*, 6989–6996; c) T. Suzuki, T. Asaba, E. Imai, H. Tsumoto, H. Nakagawa, N. Miyata, *Bioorg. Med. Chem. Lett.* **2009**, *19*, 5670–5672.

Supporting Information

Mechanism-Based Inhibitors of the Human Sirtuin 5 Deacylase: Structure–Activity Relationship, Biostructural, and Kinetic Insight

Nima Rajabi, Marina Auth, Kathrin R. Troelsen, Martin Pannek, Dhaval P. Bhatt, Martin Fontenas, Matthew D. Hirschey, Clemens Steegborn, Andreas S. Madsen, and Christian A. Olsen*

anie_201709050_sm_miscellaneous_information.pdf

Contents

V, 8 ± 1 µM
Rate inhib. assay:
K_i = 13 ± 1 µM

Et-29, 54% [100 µM]

S1, 87% [100 µM]

S2, 82% [100 µM]

S3, 80% [100 µM]

S4, 72% [100 µM]

S5, 63% [100 µM]

S6, 71% [100 µM]

S7, 71% [100 µM]

S8, 0.98 ± 0.02 µM

S9, 0.45 ± 0.03 µM

S10, 76% [10 µM]

S11, 86% [10 µM]

S12, 92% [100 µM]

S13, 78% [100 µM]

S14, 52% [100 µM]

S15, 76% [100 µM]

S16, 53% [100 µM]

S17, 84% [100 µM]

S18, 24% [100 µM]

S19, 240 ± 10 µM

S20, 14% [100 µM]

S21, 63% [100 µM]

S22, 18% [100 µM]

S23, 32% [100 µM]

Scheme S1. Additional inhibitors for the structure–activity relationship study. Potencies are given as IC$_{50}$ values or inhibition (%) at the highest tested concentration (given in brackets)
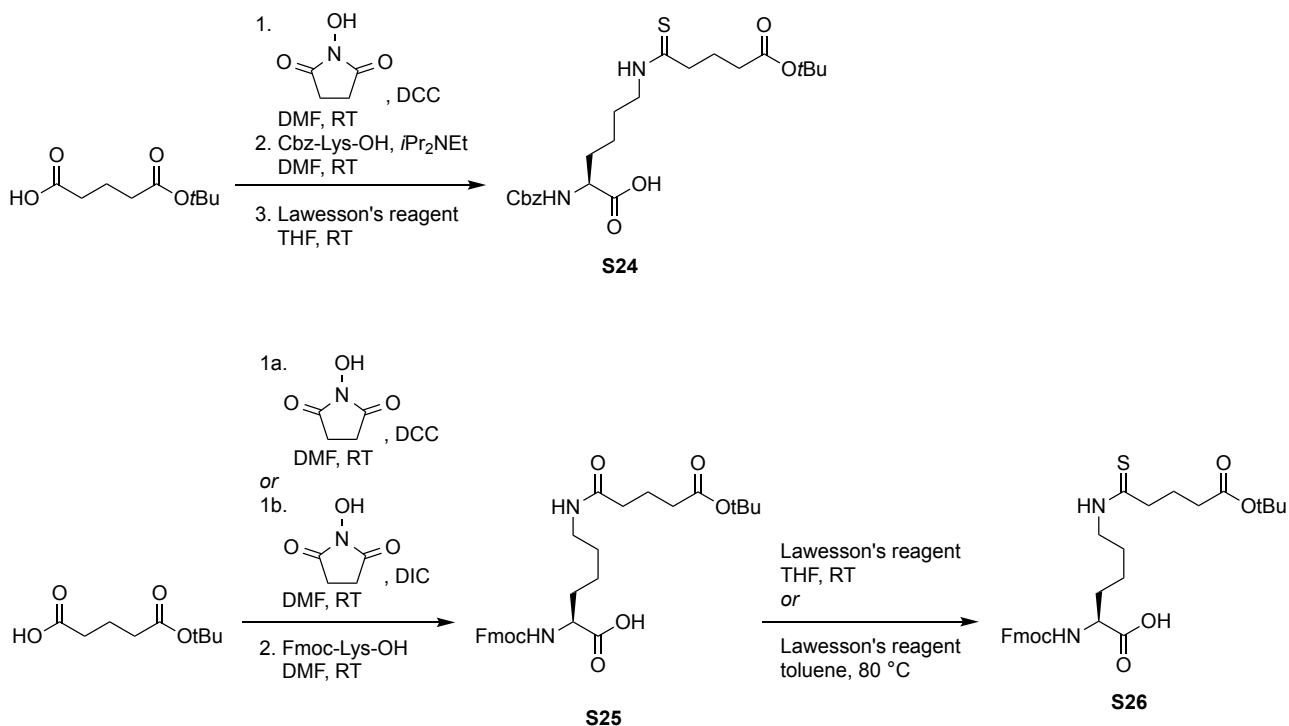
Scheme S2. Synthesis of thioamide building blocks
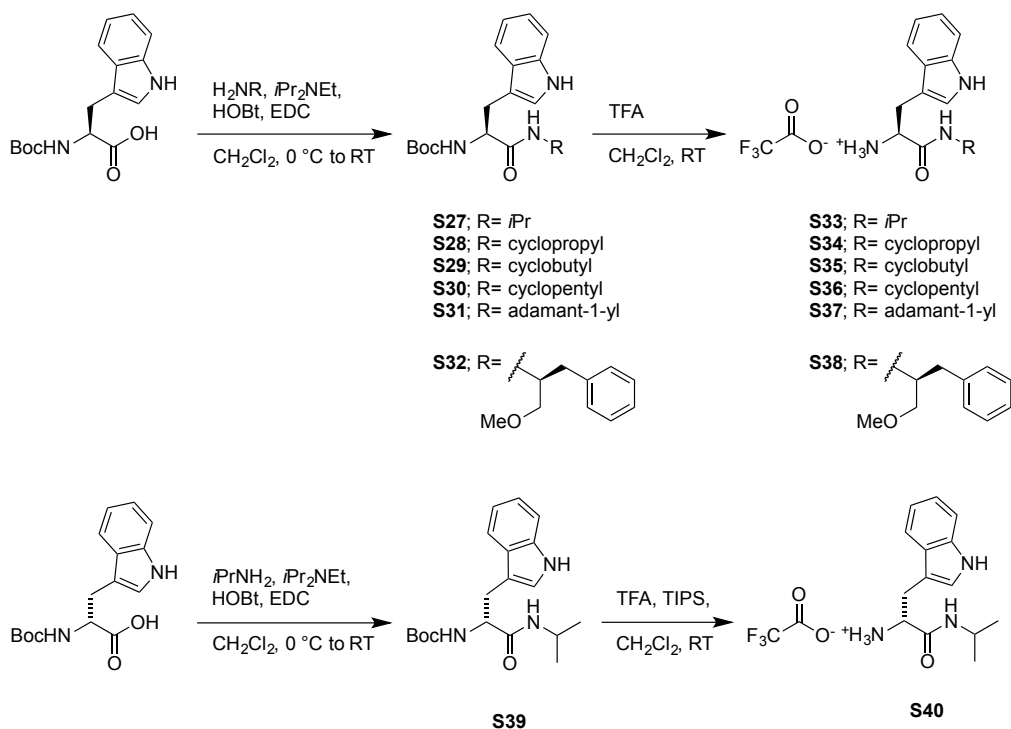
Scheme S3. Synthesis of tryptophan building blocks
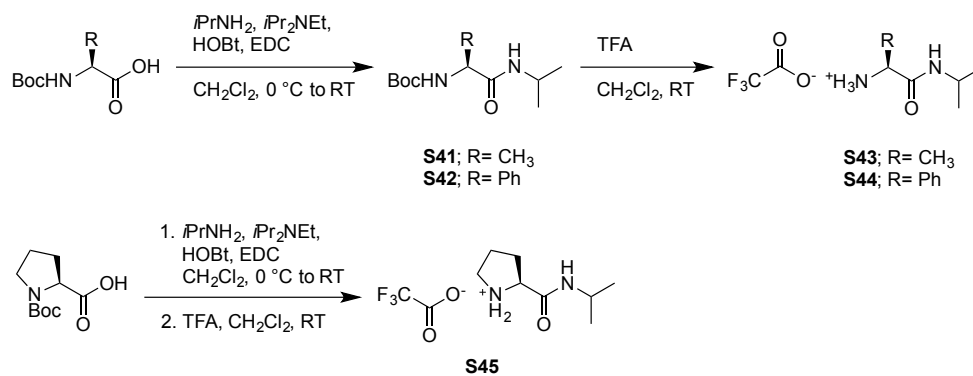
Scheme S4. Synthesis of other amino acid building blocks
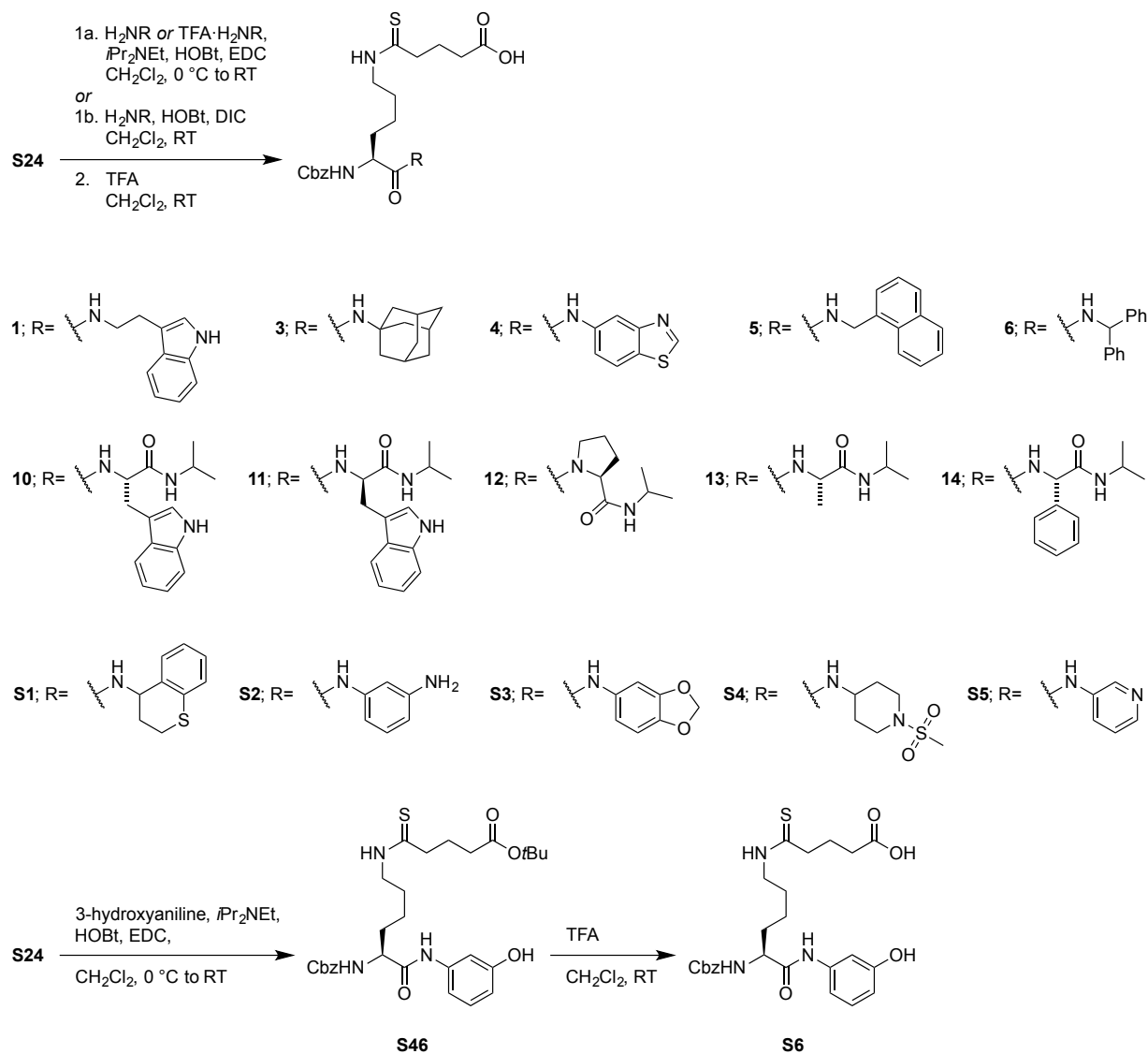
Scheme S5. Synthesis of thioamide inhibitors, part I
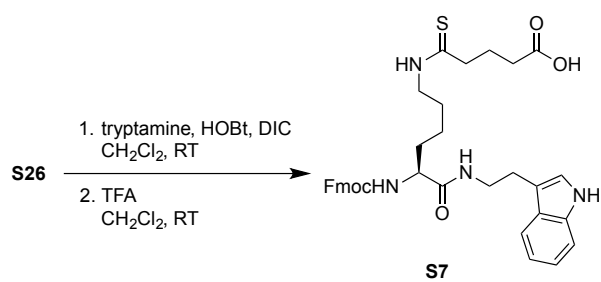
Scheme S6. Synthesis of thioamide inhibitor, part II
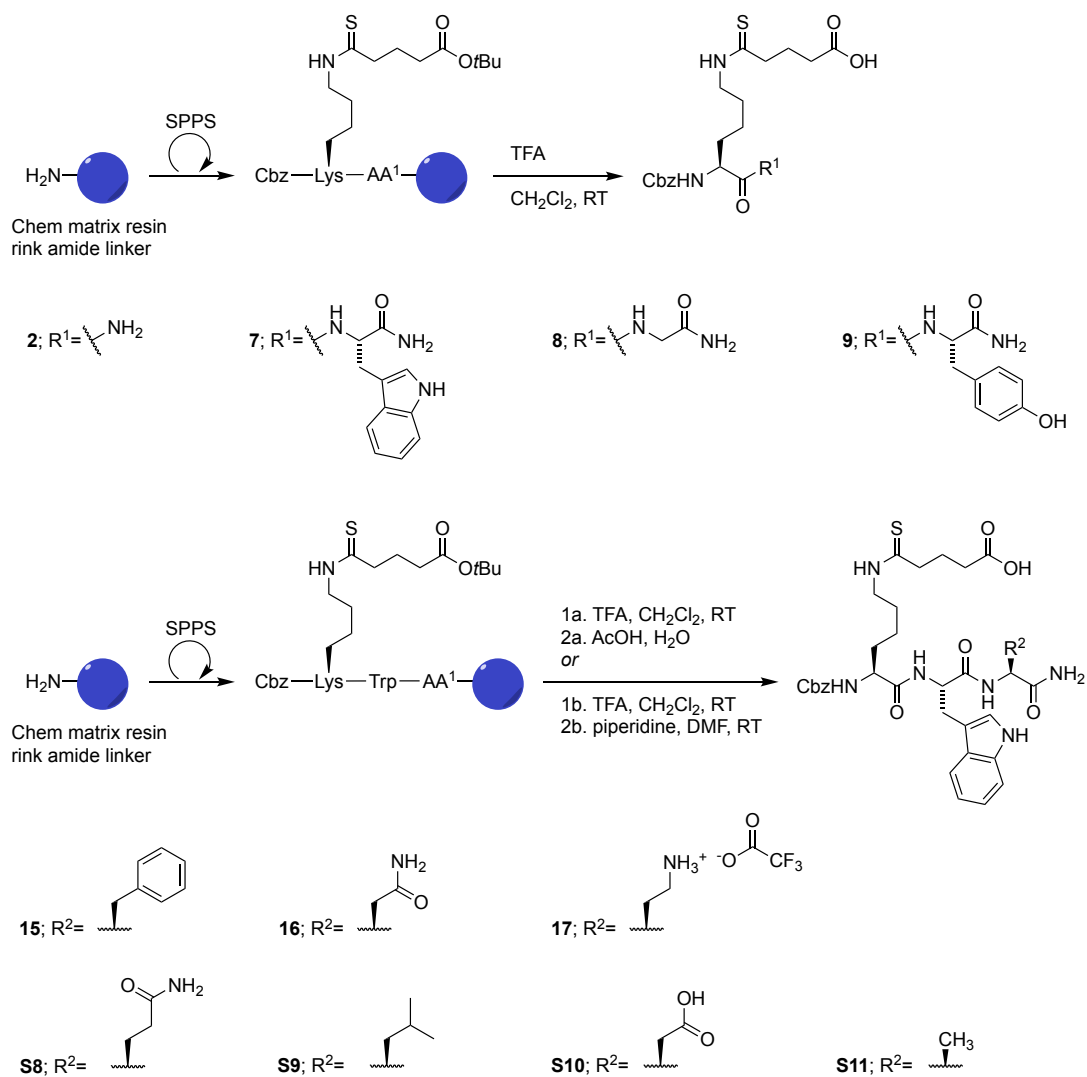
Scheme S7. Solid phase synthesis of tripeptide thioamide inhibitors
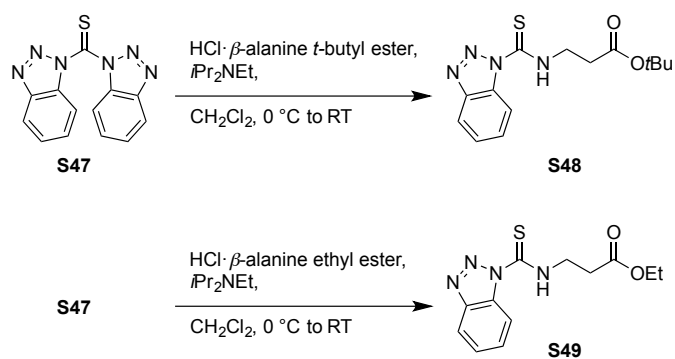
Scheme S8. Synthesis of benotriazole carbothioamido reagents
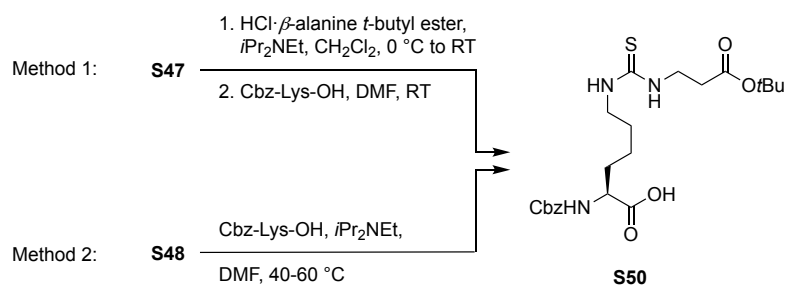
Scheme S9. Synthesis of thiourea building block **S50**
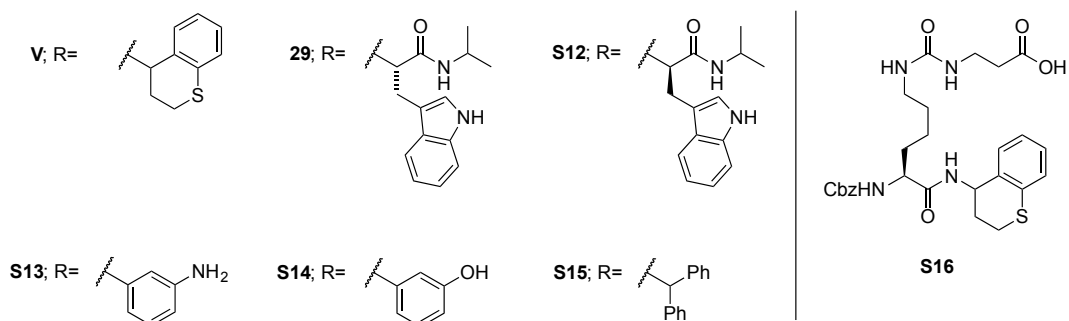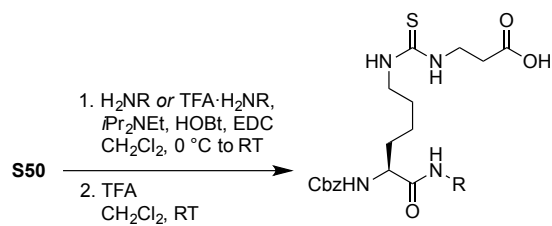
Scheme S10. Synthesis of thiourea inhibitors, part I
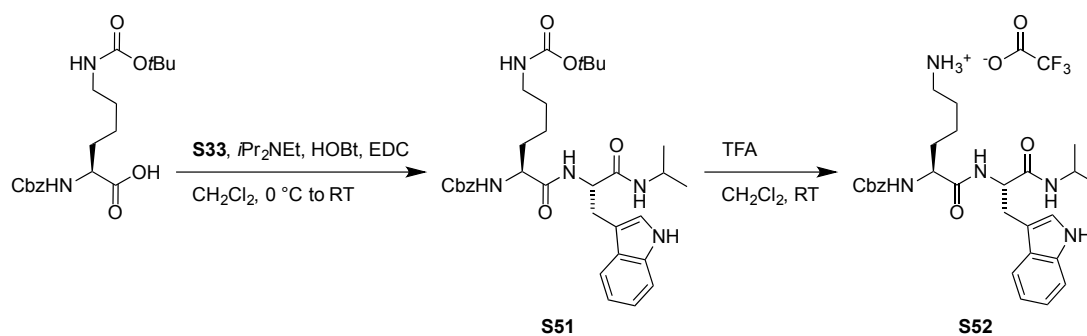
Scheme S11. Synthesis of common intermediate **S52**
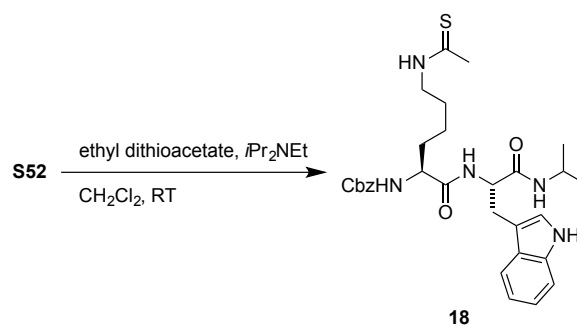
Scheme S12. Synthesis of thioacetamide **18**
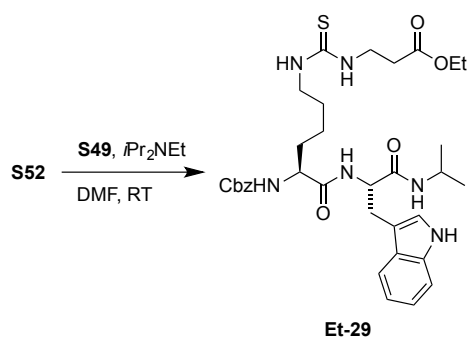
Scheme S13. Synthesis of compound **Et-29**
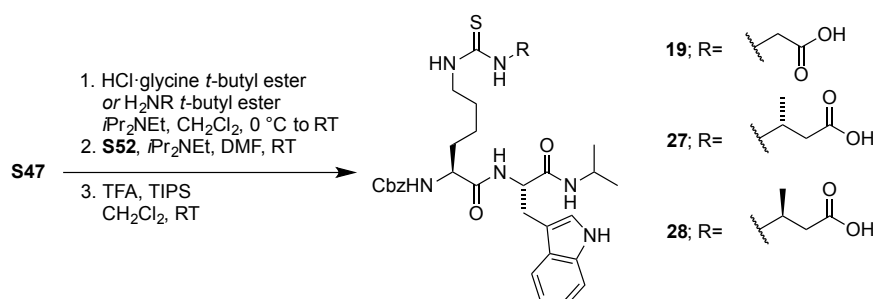
Scheme S14. Synthesis of thiourea inhibitors, part II
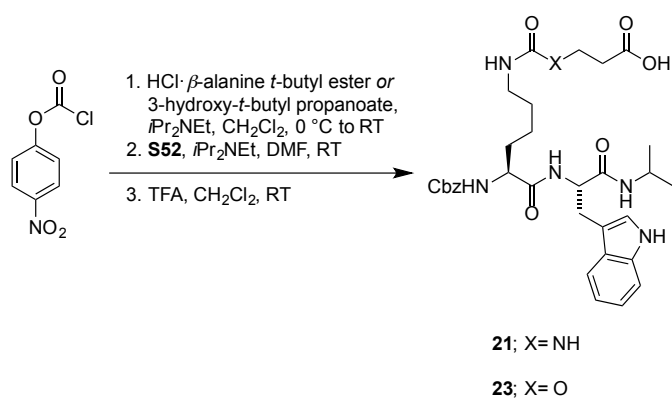
Scheme S15. Synthesis of inhibitors **21** and **23**
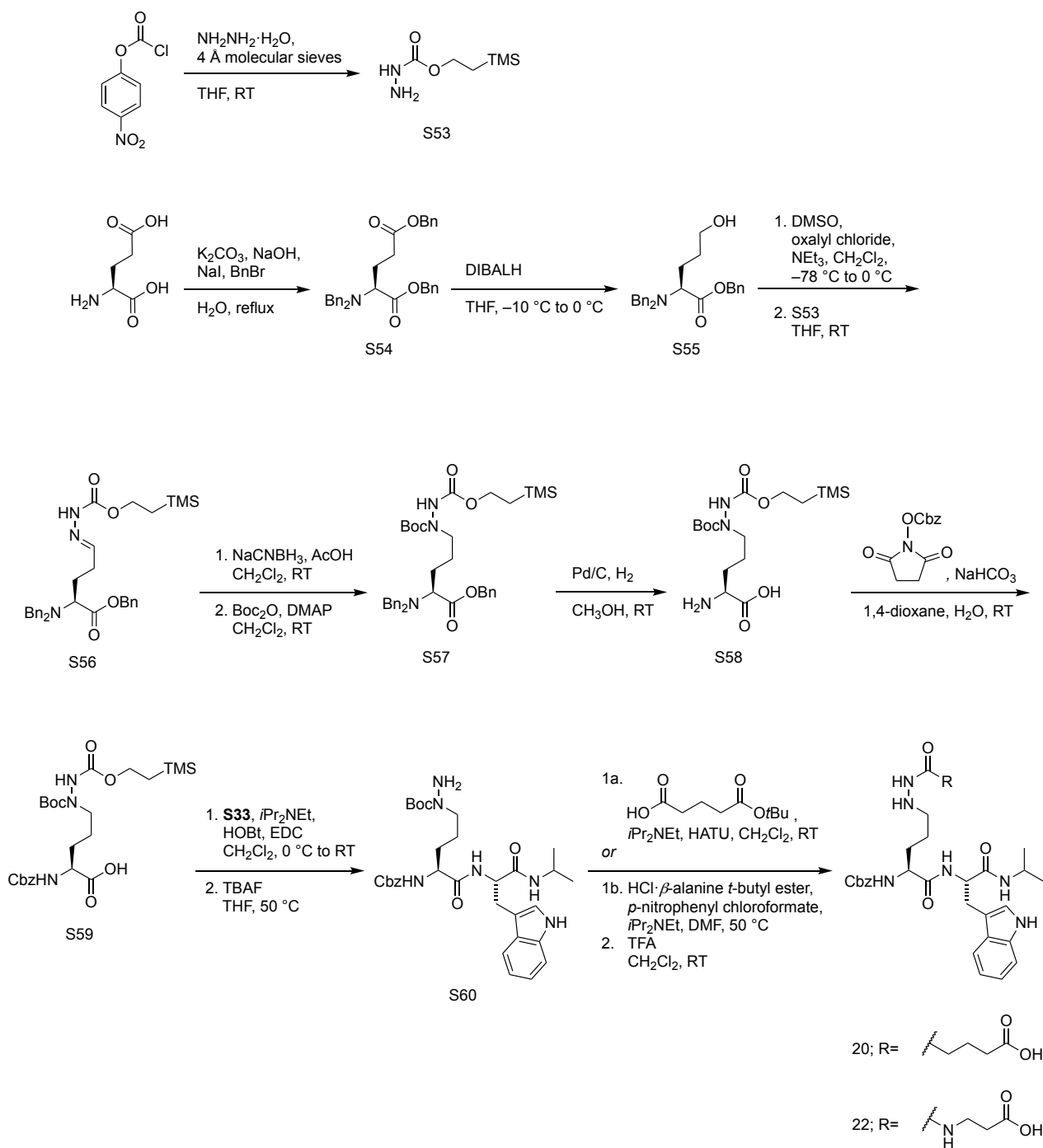
Scheme S16. Synthesis of hydrazide and semicarbazide inhibitors
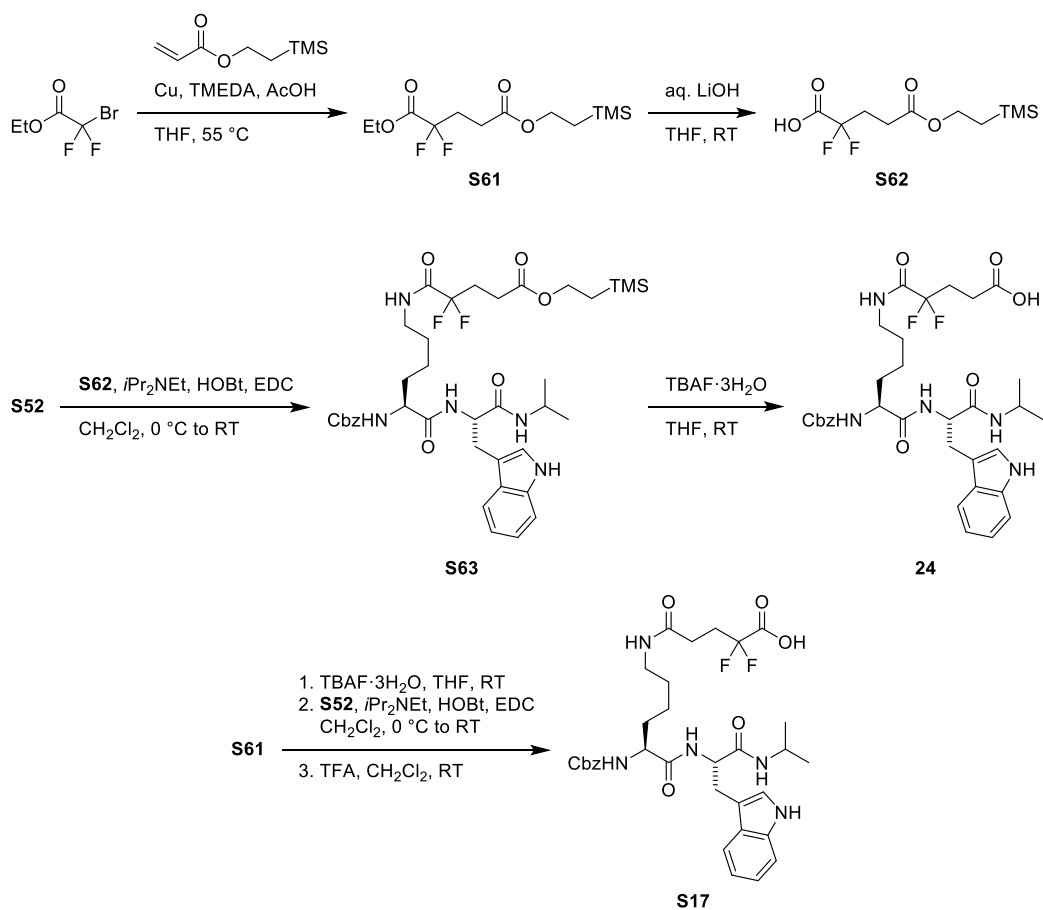
Scheme S17. Synthesis of fluorinated inhibitors **24** and **S17**
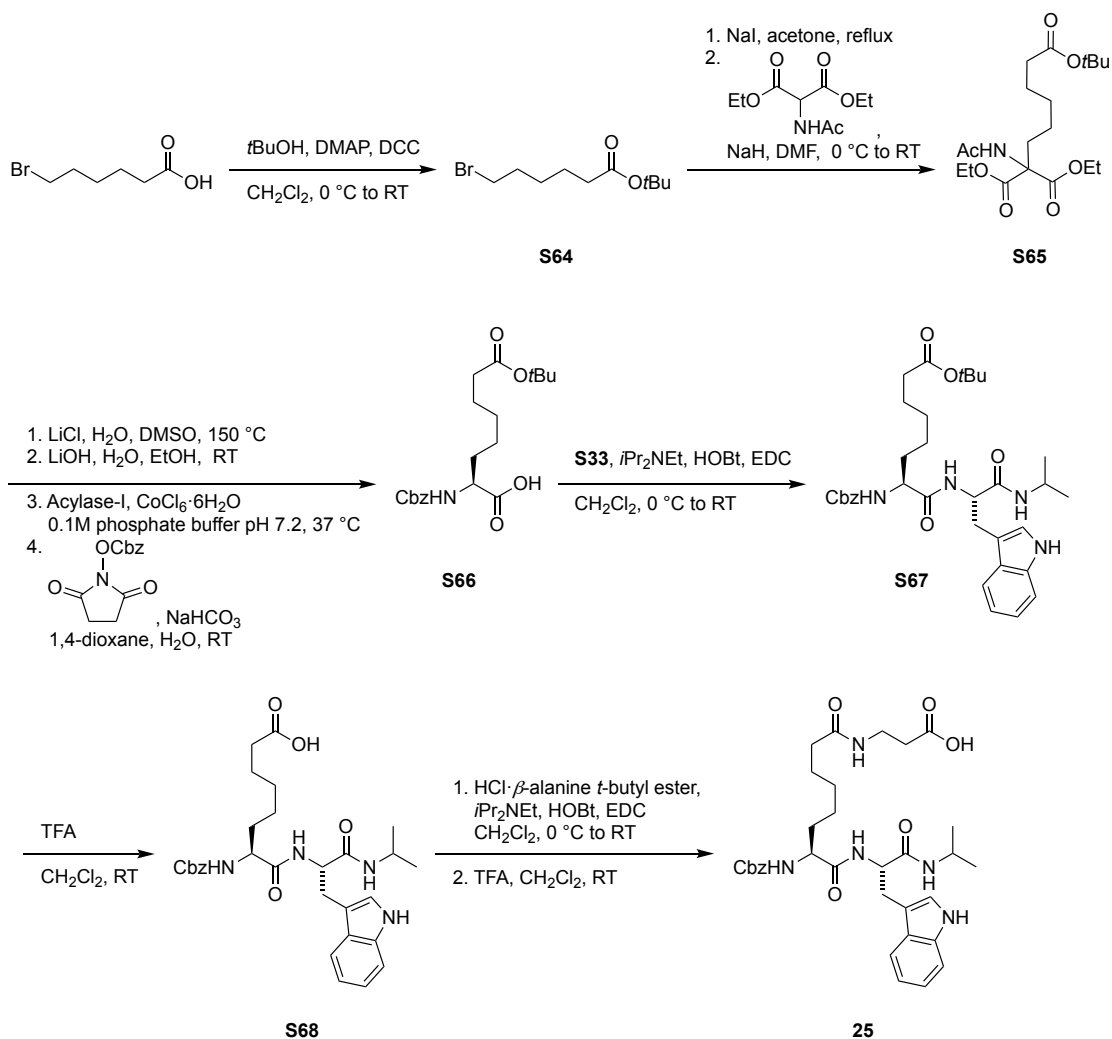
Scheme S18. Synthesis of inverted amide inhibitor **25**
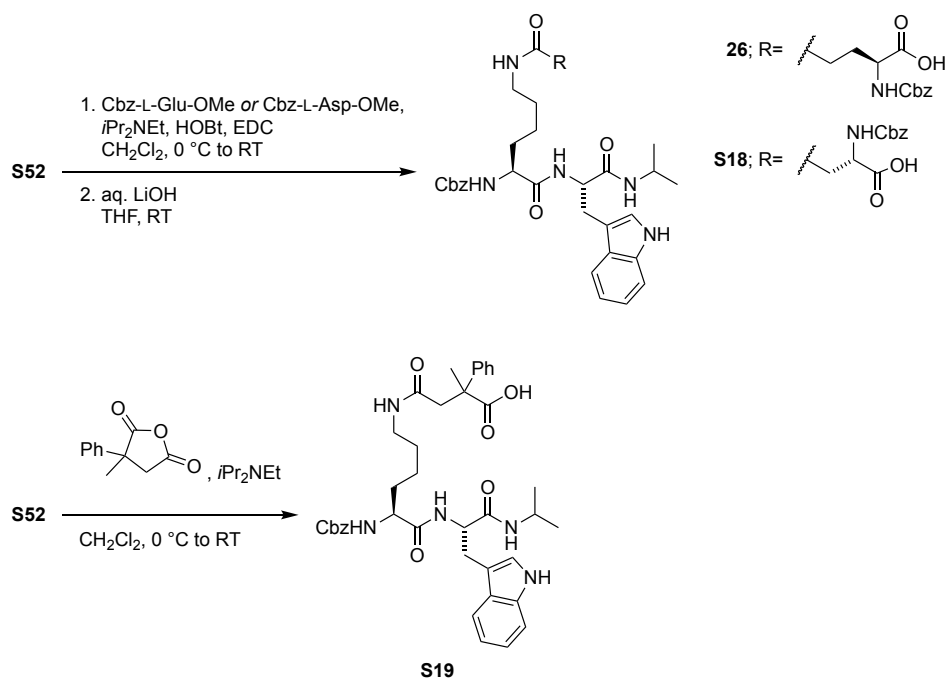
Scheme S19. Synthesis of amide inhibitors

S69; R= cyclopropyl
S70; R= adamant-1-yl

S71; R=

S72; R= cyclopropyl
S73; R= adamant-1-yl

S74; R=

45; R= cyclopropyl
47; R= adamant-1-yl

46; R=
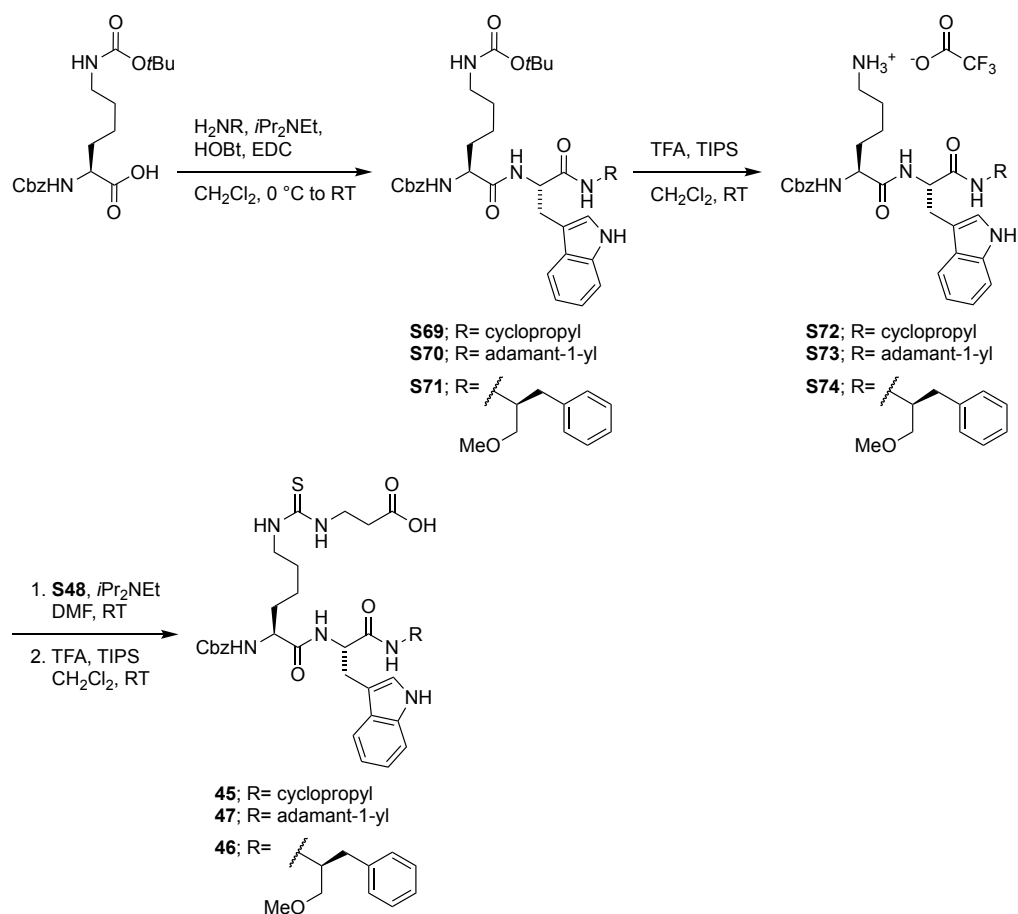
Scheme S20. Synthesis of thiourea inhibitors, part III
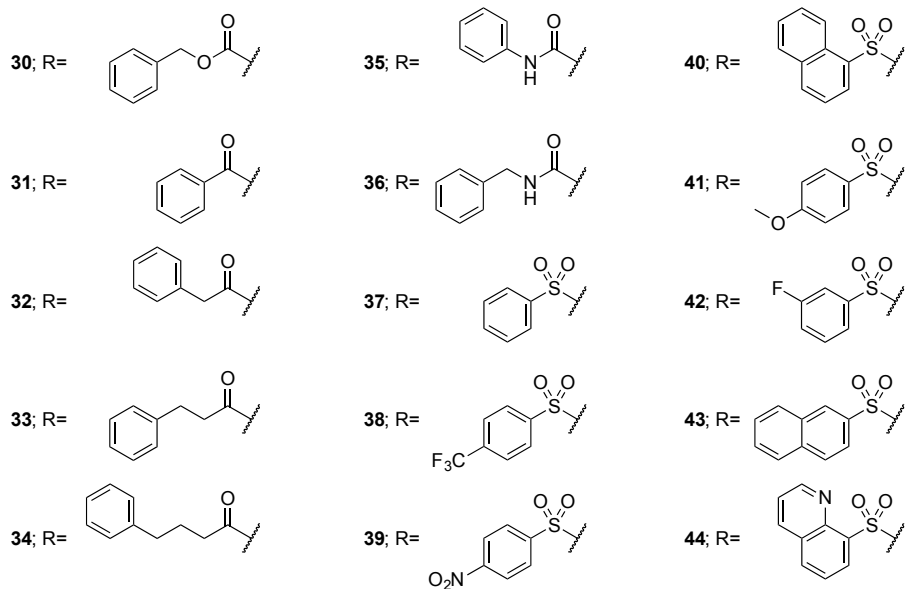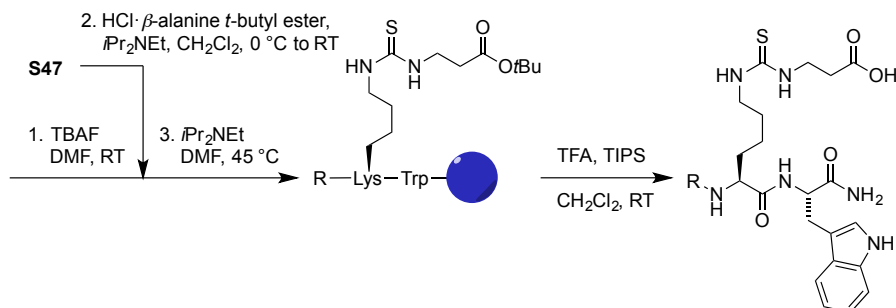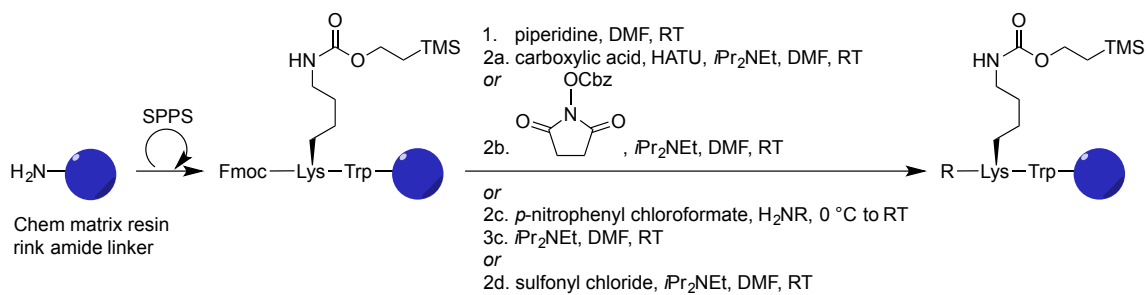
Scheme S21. Solid-phase synthesis of N-terminal modified thiourea inhibitors
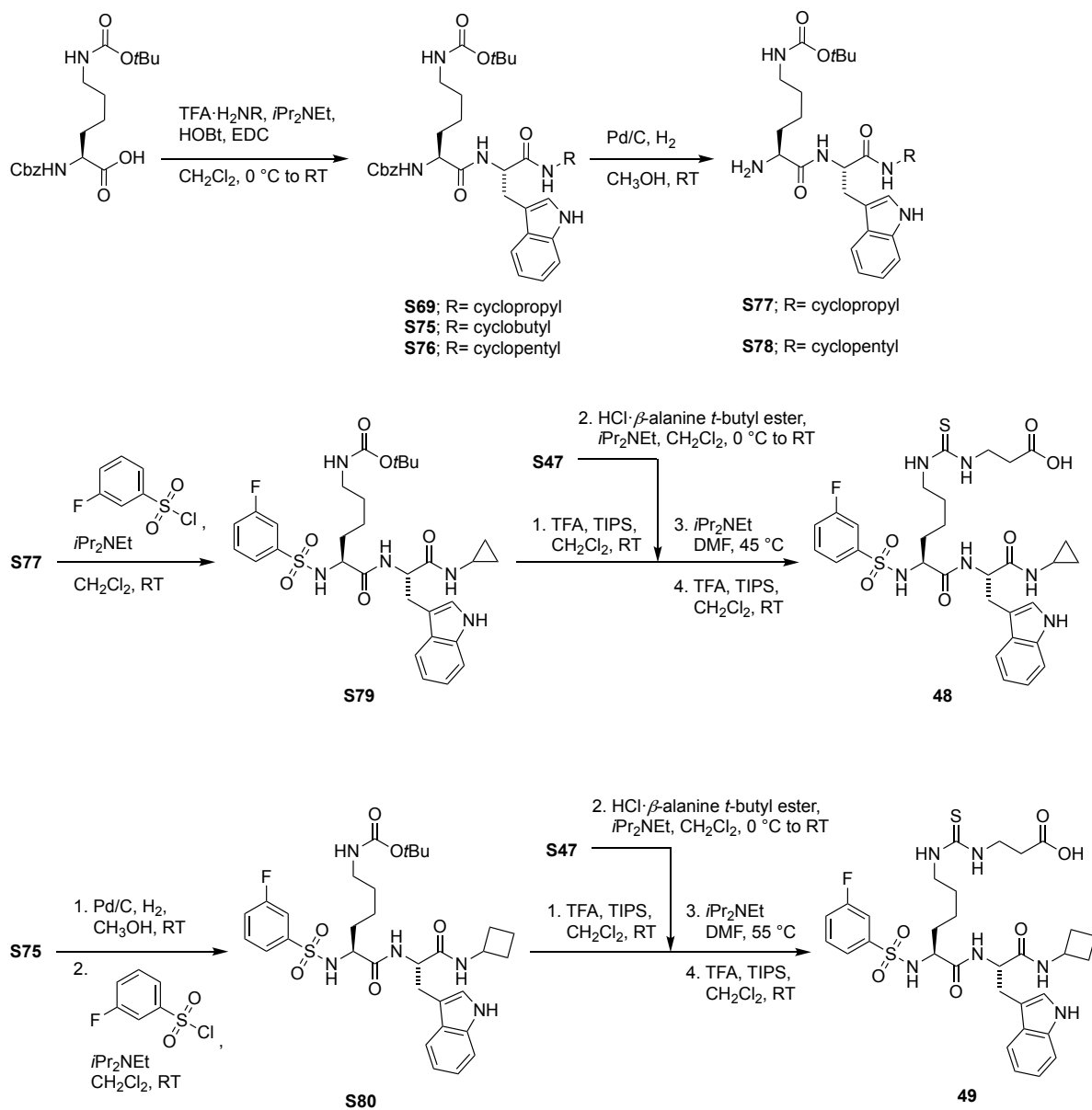
Scheme S22. Synthesis of thiourea inhibitors **48** and **49**

S15
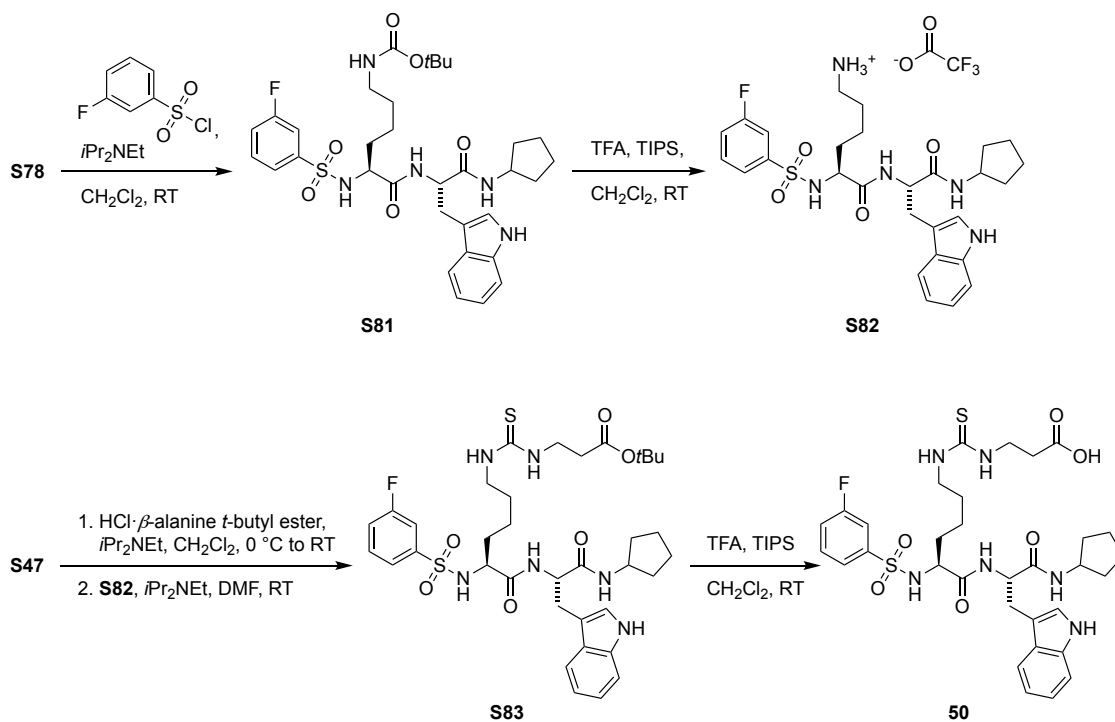
Scheme S23. Synthesis of thiourea inhibitor **50**
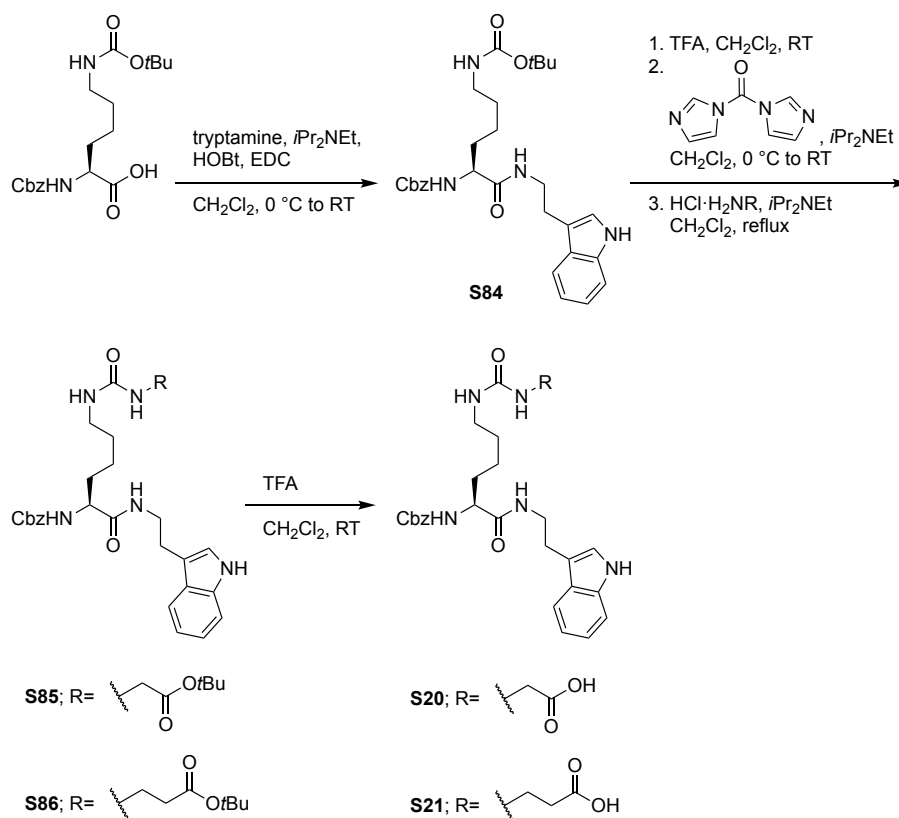
Scheme S24. Synthesis of urea inhibitors, part I
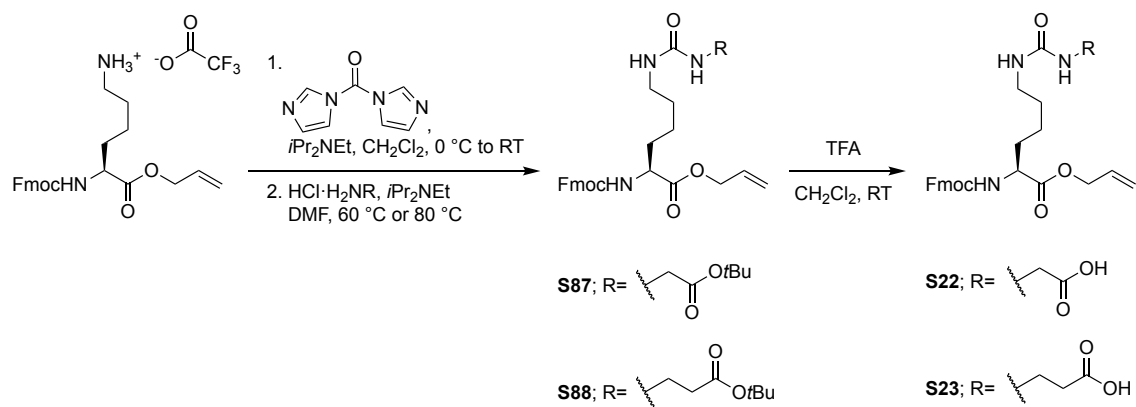
Scheme S25. Synthesis of urea inhibitors, part II
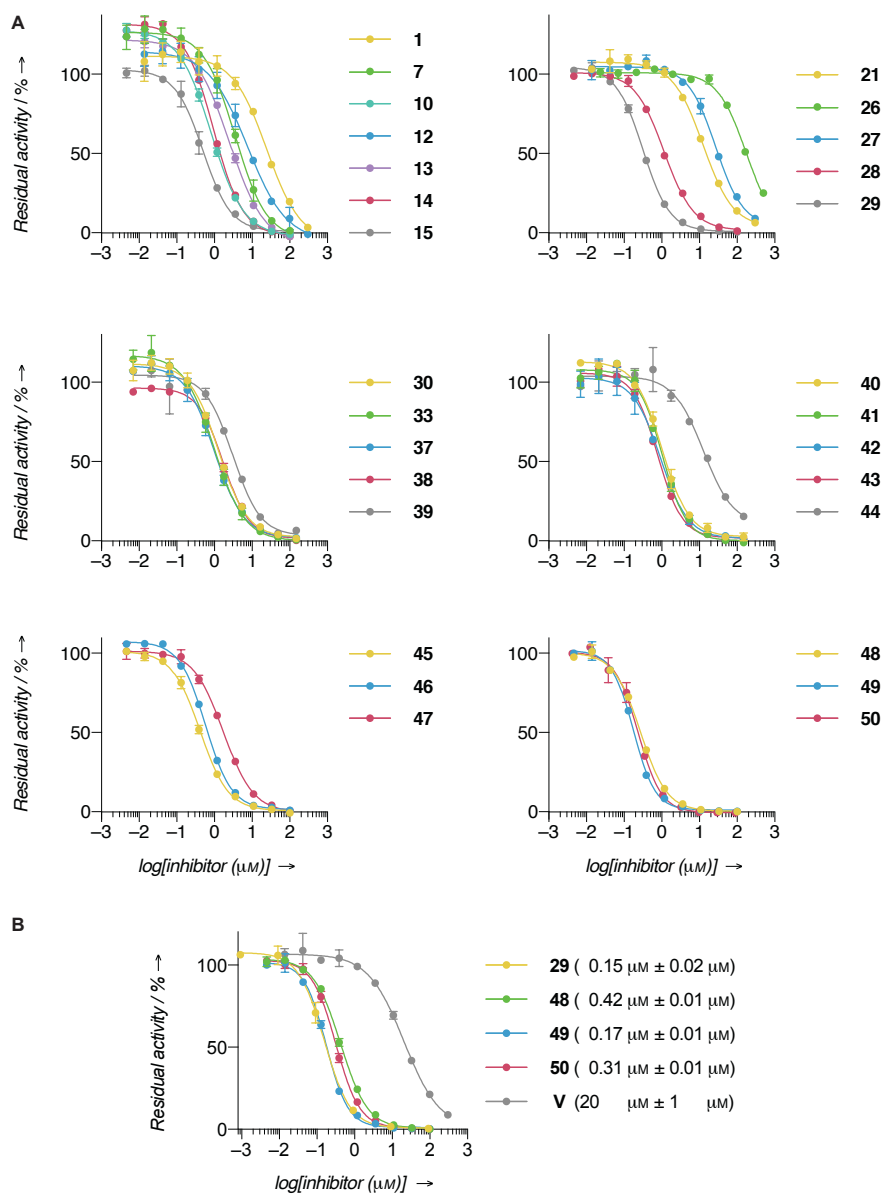
Figure S1. Concentration–response curves for SIRT5 inhibition of representative compounds using (A) Ac-LGKglu-AMC or (B) Ac-LGKsuc-AMC as substrate, respectively.
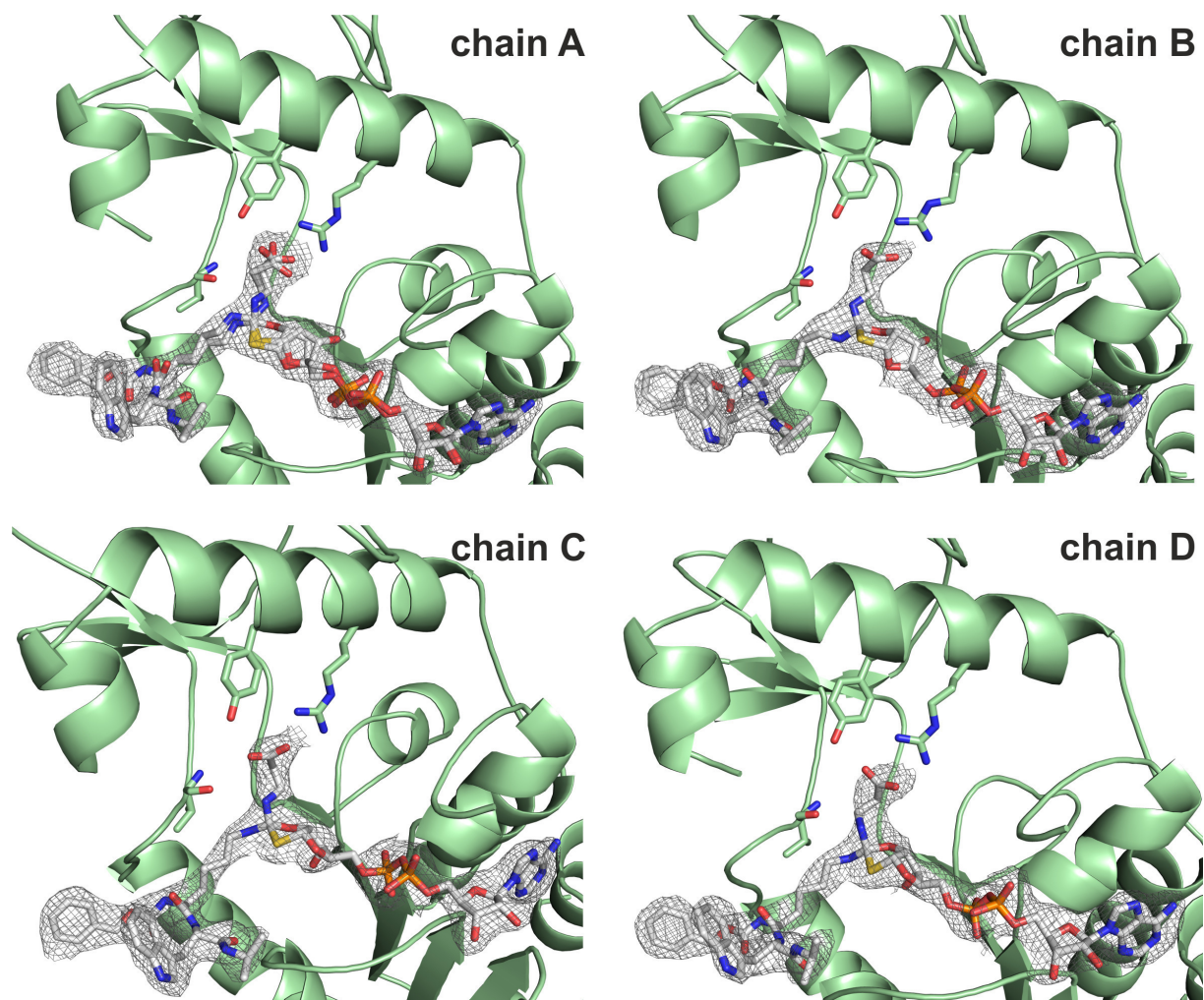
Figure S2. Co-crystal structures of **29**:zSIRT5. The complex crystal structure of **29**:zSIRT5 is composed of four protein chains (chain A to D) per asymmetric unit, one of which comprised an indistinguishable mixture of peptidyl-thioimidate and bicyclic intermediate. $2F_o$-F_c electron density (σ = 1.0) is shown for the intermediate ligand of each protein chain. SIRT5 is represented as green cartoon with amino acids of interest in stick style, while the intermediates are shown in white cpk colored stick representation.
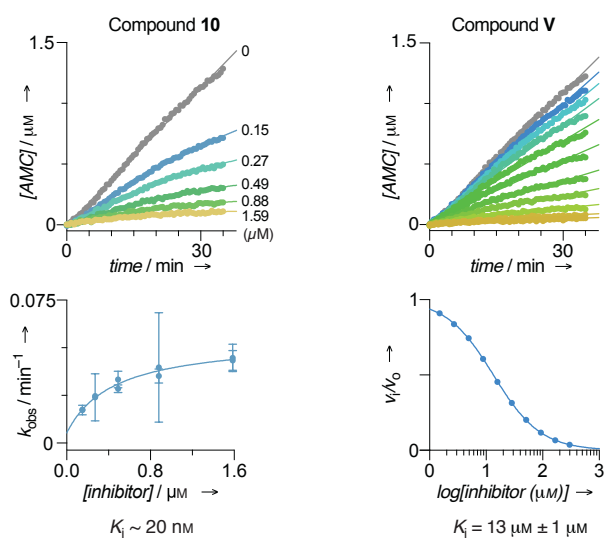
Figure S3. Progression curves and data fitting for SIRT5 inhibition by compound **10** and **V**.

A

SIRT5	+	−	+	−	+	−	+	−
DMSO (1 μM control)	+	+	−	−	−	−	−	−
Et-29 1 μM	−	−	+	+	−	−	−	−
DMSO (10 μM control)	−	−	−	−	+	+	−	−
Et-29 10 μM	−	−	−	−	−	−	+	+

IB: Glut-K
IB: β-actin
IB: SIRT5
IB: β-actin

SIRT5	+	−	+	−	+	−	+	−
DMSO (1 μM control)	+	+	−	−	−	−	−	−
Et-29 1 μM	−	−	+	+	−	−	−	−
DMSO (10 μM control)	−	−	−	−	+	+	−	−
Et-29 10 μM	−	−	−	−	−	−	+	+

IB: Suc-K
IB: β-actin

Protein glutarylation

B

SIRT5	+	-
Fraction	Mito	Mito

IB: Suc-K

SIRT5	+	-
Fraction	Mito	Mito

IB: Glut-K

SIRT5	+	-	+	-	+	-
Fraction	Mito	Mito	Cyt	Cyt	WCI	WCI

IB: β-actin
IB: GAPDH
IB: UQCRSF1
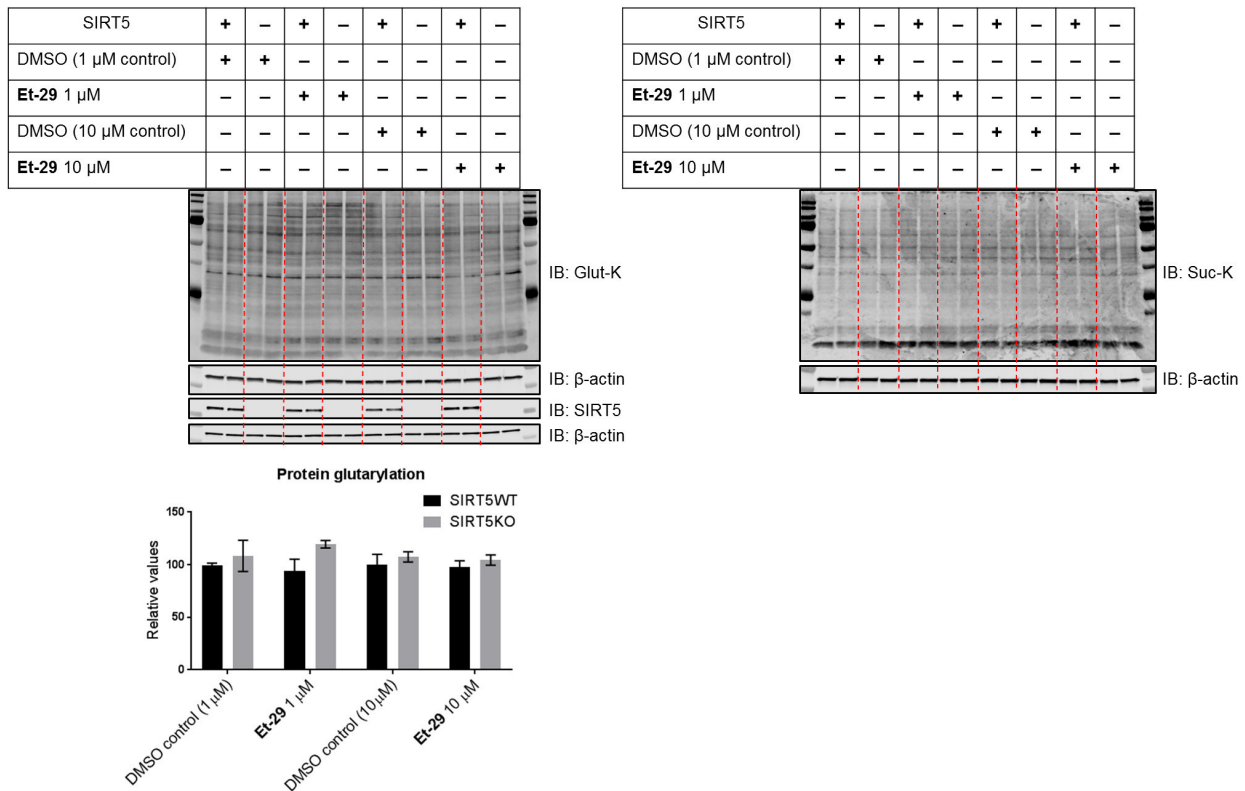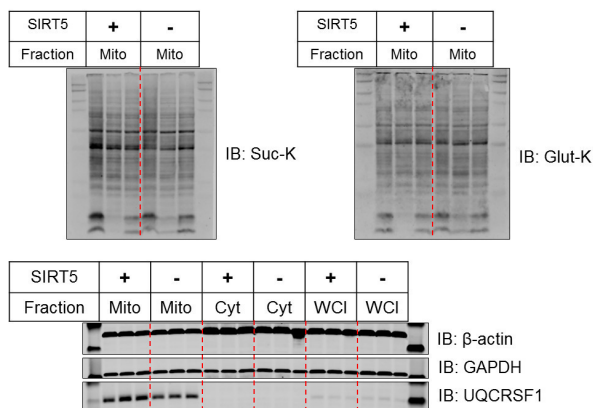
Figure S4. Western blot analysis of whole cell lysates after **Et-29** treatment or mitochondrial enrichment. (A) Effects of **Et-29** on lysine glutarylation and malonylation in HEK293T WT and crSIRT5KO cells (whole cell lysates). (B) Analysis of lysine succinylation and glutarylation in mitochondria enriched fractions of HEK293T WT and crSIRT5KO cells (Mito=mitochondrial fraction, Cyt=cytosolic fraction, WCl=Whole cell lysate). Anti-UQCRSF1 was used to analyze mitochondrial enrichment.

To assess the effect of **Et-29** in cells, we treated HEK293T WT and CRISPR/Cas9 SIRT5 knock out (crSIRT5KO) whole cell lysates, analyzing for changes in lysine glutarylation and succinylation levels. However, we observed no significant changes in the levels of either glutarylation or succinylation (Fig. S4A). Interestingly, no significant difference could be observed between untreated WT and crSIRT5KO cells either. Since succinyl and glutaryl modification of lysines are found on many mitochondrial proteins, we hypothesized that a larger difference in acylation levels between WT and crSIRT5KO cells could be detectable when analyzing this fraction—potentially making this a more suitable assay for evaluation of **Et-29**. However, mitochondrial enrichment of WT and crSIRT5KO cells did not show any significant changes in acylation levels between the cell lines either (Fig S4B).
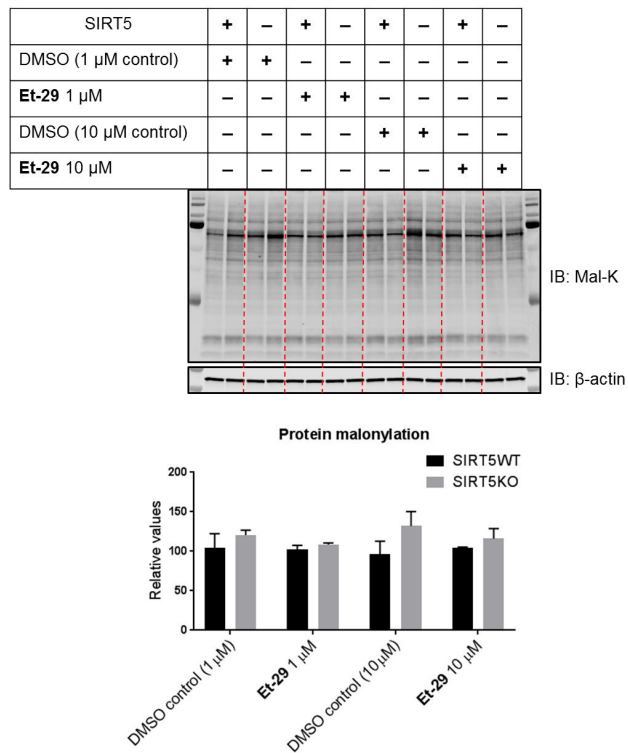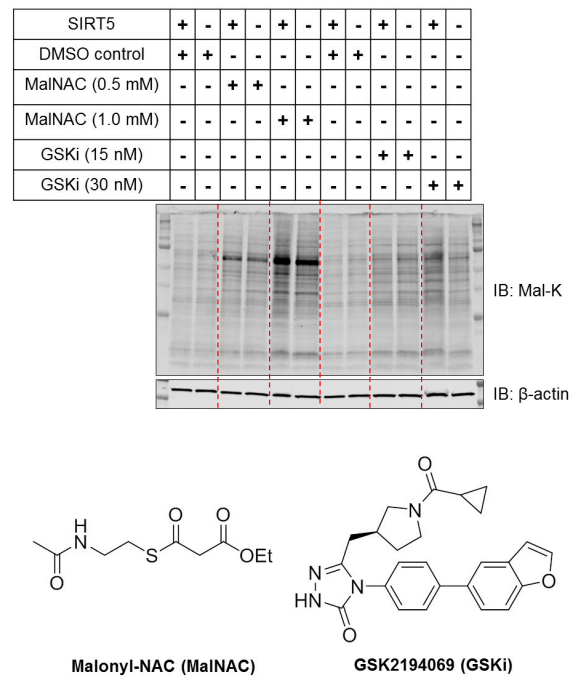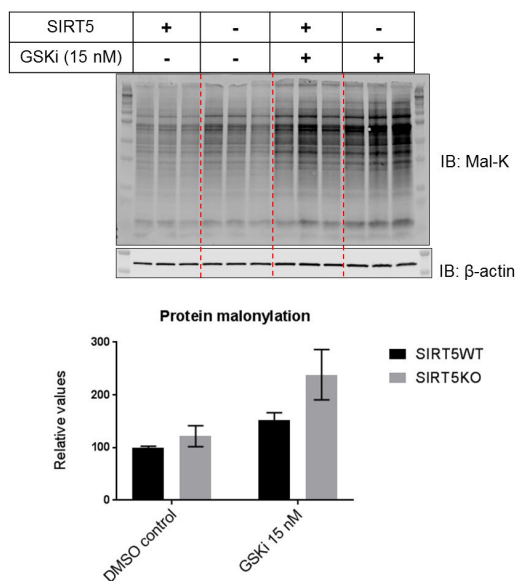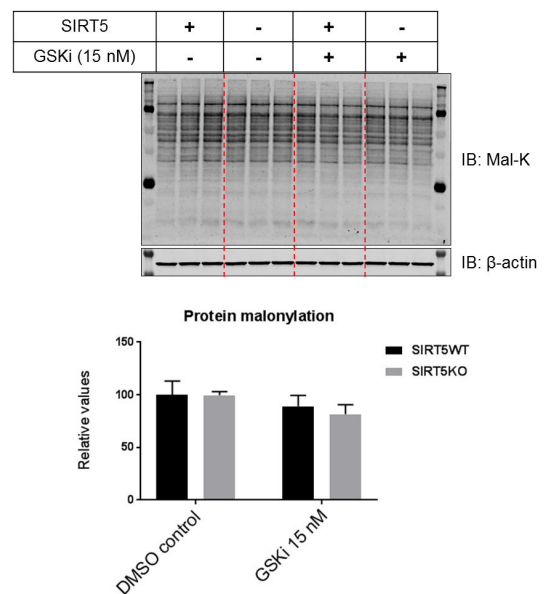
Figure S5. Western blot analysis of whole cell lysates after **Et-29**, MalNAC or GSKi treatments. (A) Effects of **Et-29** on lysine malonylation in HEK293T WT and crSIRT5KO cells. (B) Effects of MalNAC and GSKi on lysine malonylation in HEK293T WT and crSIRT5KO cells (initial experiment, one sample of the triplicate loaded). (C) Effects of GSKi on lysine malonylation in HEK293T WT and crSIRT5KO cells (initial experiment, all samples of the triplicate loaded). (D) Effects of GSKi on lysine malonylation in HEK293T WT and crSIRT5KO cells (second experiment, all samples of the triplicate loaded).

Since our initial efforts were unable to detect any significant differences in glutarylation or succinylation between WT and crSIRT5KO cells, we turned our attention to lysine malonylation, which is also regulated by SIRT5. We treated cells with **Et-29** and analyzed whole cell lysates for changes in malonyl-lysine levels. The results showed no significant changes in malonylation, nor were there any differences between the two cell lines (Figure S5A). A recent report by Kulkarni et al. have demonstrated that treating cells with an acylating reagent, Malonyl-NAC (MalNAC, Figure S5B), could considerably increase lysine malonylation in cells.[1] Additionally, they showed a similar effect when treating cells with a fatty acid synthase inhibitor (orlistat), which leads to increased availability of malonyl-CoA, the acyl donor in lysine malonylation. Inspired by this study, we hypothesized that increasing the on-rate of acylation by using MalNAC (obtained from Jordan L. Meier's lab) or the fatty acid synthase inhibitor GSK2194059 (GSKi, Figure S5B, Sigma-Aldrich, #SML1259-5MG) would increase our chances of observing changes in acylation levels between WT and crSIRT5KO cells. In our initial assay, both treatment with MalNAC and GSKi increased malonylation significantly in both cell lines (Figure S5B). However, no significant difference in malonylation was observed between the two cell lines, except when treated with a low concentration of GSKi (Figure S5C). Although these results were promising, the levels of malonylation upon GSKi treatment turned out to be considerably variable. In subsequent assays only minor or no apparent increase in malonylation could be observed (one example, Figure S5D, compare with Figure S5C).

The variability in cell culture acylation response and lack of observable changes between WT and crSIRT5KO cells prevented accurate evaluation of the effect of **Et-29** on SIRT5 regulated acylation in cells. Furthermore, western blot quantification of complete lanes is not an accurate representation of acylation. Consequently, probing specific SIRT5 targets or utilizing quantitative proteomics to measure changes in acylation may be more suitable assays to evaluate the effect of SIRT5 inhibitors, including prodrugs like **Et-29**.

Table S1. Kinetic parameters and dissociation constants for slow-binding inhibitors **29** and **49** derived from rate inhibition assays.

		10	**29**	**49**
k_{-2}	(min^{-1})	0.053 ± 0.0050	0.0080 ± 0.0098	0.0042 ± 0.0051
k_2	(min^{-1})	0.050 ± 0.003	0.32 ± 0.08	0.41 ± 0.08
$K_{i,1}$	(µM)	0.23 ± 0.10	1.5 ± 0.8	0.62 ± 0.19
K_i	(µM)	~0.022	~0.037	~0.006

Table S2. Data collection and refinement statistics

	zSirt5/ 10-ADPr-1′-thioimidate	zSirt5/ 29-ADPr-1′-thioimidate	hSirt5/ 29-ADPr-1′-thioimidate
Space group	C2	P2$_1$	P1
Unit cell constants (Å; °)	116.5 / 38.3 / 75.6;	64.9 / 113.6 / 72.3;	40.3 / 56.0 / 123.0;
	90.0 / 122.5 / 90.0	90.0 / 103.2 / 90.0	97.4 / 99.3 / 90.5
Resolution[a] (Å)	50.00–1.95	50.00–2.40	43.77–1.32
	(2.00–1.95)	(2.50–2.40)	(1.40–1.32)
Unique reflections	20704 (1518)	38453 (4467)	227669 (35569)
Multiplicity	4.1 (4.1)	3.8 (3.8)	2.0 (1.9)
Completeness (%)	99.1 (99.2)	96.2 (97.3)	91.5 (88.1)
R_{meas} (%)	21.3 (156.5)	25.2 (170.2)	5.9 (95.9)
$CC1/2$ (%)	98.9 (46.3)	98.9 (51.7)	99.9 (72.3)
$I/\sigma I$	6.8 (1.1)	6.1 (0.9)	6.8 (1.1)
Protein atoms	2088	8579	8501
Ligand atoms	80	400	640
Solvent atoms	177	193	1244
Resolution (Å)	49.11–1.95 (2.00–1.95)	48.41–2.40 (2.46–2.40)	43.77–1.32 (1.35–1.32)
R_{cryst}/R_{free}[b,c] (%)	19.5 / 24.2	25.3 / 30.5	16.0 / 20.9
Average B-factors (Å^2)			
protein	26.8	53.5	20.5
ligands	20.4	49.3	17.4
solvent	34.4	44.2	40.3
RMSD bond lengths	0.016	0.013	0.031
RMSD bond angles	2.0	2.0	2.9

[a] Values in parentheses refer to outermost shell.

[b] $R_{cryst} = \frac{\sum ||F_{obs}| - k|F_{calc}||}{\sum |F_{obs}|}$. $|F_{obs}|$ is the observed and $|F_{calc}|$ the calculated structure factor amplitude.

[c] R_{free} was calculated from 5% (zSirt5 complexes) or 1.1% (hSirt5 complex) of reflections omitted from refinement.

General experimentals

All reagents and solvents were of analytical grade and used without further purification as obtained from commercial suppliers. Anhydrous solvents were obtained from a PureSolv-system. Reactions were conducted under an atmosphere of argon or nitrogen whenever anhydrous solvents were used. All reactions were monitored by thin-layer chromatography (TLC) using silica gel coated plates (analytical SiO_2-60, F-254). TLC plates were visualized under UV light and by dipping in either (a) a solution of potassium permanganate (10 g/L), potassium carbonate (67 g/L) and sodium hydroxide (0.83 g/L) in water, (b) a solution of ninhydrin (3 g/L) in 3% acetic acid in water (v/v), or (c) a solution of molybdato-phosphoric acid (12.5 g/L) and cerium(IV)sulfate (5 g/L) in 3% conc. sulfuric acid in water (v/v) followed by heating with a heat gun. Vacuum liquid chromatography (VLC) was performed with silica gel 60 (particle size 15–40 μm). After column chromatography, appropriate fractions were pooled and dried at high vacuum (<2 mbar) for at least 12 hours to give obtained products in high purity (>95%) unless otherwise stated. Evaporation of solvents was carried out under reduced pressure at a temperature below 40 °C. UPLC−MS analyses were performed on a Phenomenex Kinetex column (1.7 μm, 50×2.10 mm) using a Waters Acquity ultra high–performance liquid chromatography (UPLC) system. Gradient A with eluent I (0.1% HCOOH in H_2O) and eluent II (0.1% HCOOH in MeCN) rising linearly from 0% to 95% of II during t = 0.00–5.20 min was applied at a flow rate of 0.6 mL/min. Preparative reversed-phase HPLC purification was performed on a C18 Phenomenex Luna column (5 μm, 100 Å, 250×20 mm) using an Agilent 1260 LC system equipped with a diode array UV detector and an evaporative light scattering detector (ELSD). Gradient B with eluent III (H_2O/MeCN/TFA, 95:5:0.1) and eluent IV (0.1% TFA in MeCN) rising linearly from 0% to 95% of IV during t = 5−45 min, then isocratically at 95% during t = 45–50 min was applied at a flow rate of 20 mL/min; *or* 0% to 95% of IV during t = 5−65 min, then isocratically at 95% during t = 65–70 min was applied at a flow rate of 20 mL/min. Analytical HPLC was performed on a C18 phenomenex Luna column (3 μm, 100 Å, 150×4.60 mm) using an Agilent 1100 series system equipped with a diode array UV detector. Gradient C using eluent III and eluent IV, rising linearly from 0% to 95% of IV during t = 5−35 min was applied at a flow rate of 1 mL/min. High-resolution mass spectrometry (HRMS) measurements were recorded either on a maXis G3 quadrupole time-of-flight (TOF) mass spectrometer (Bruker Daltonics, Bremen, Germany) equipped with an electrospray (ESI) source or on an Agilent 1290 UHPLC equipped with a diode array detector and coupled to Agilent 6550 QTOF mass spectrometer operated in positive electrospray or on a Bruker Solarix WR by either matrix assisted laser desorption/ionization, or electrospray ionization (ESI). Nuclear magnetic resonance (NMR) spectra were recorded either on a Bruker Avance III HD equipped with a cryogenically cooled probe (^{1}H NMR and ^{13}C NMR recorded at 600 and 151 MHz, respectively), a Bruker Avance III (^{1}H NMR, ^{13}C NMR and ^{19}F NMR recorded at 400, 101, and 377 MHz, respectively), or a Bruker Ascend 400 MHz (^{1}H NMR and ^{13}C NMR recorded at 400 and 101 MHz, respectively). All spectra were recorded at 298 K unless otherwise stated. Chemical shifts are reported in ppm relative to deuterated solvent as internal standard ($δ_H$ DMSO-d_6 2.50 ppm; $δ_C$ DMSO-d_6 39.52 ppm; $δ_H$ CDCl$_3$ 7.26 ppm; $δ_C$ CDCl$_3$ 77.16 ppm; $δ_H$ Methanol-d_4 3.31 ppm; $δ_C$ Methanol-d_4 49.0 ppm). Assignments of NMR spectra are based on 2D correlation spectroscopy (COSY, HSQC, and HMBC spectra). Melting point measurements were performed on a Stanford Research Systems DigiMelt MPA161 apparatus.

Fluorescence-based *in vitro* sirtuin deacylase assays

Materials—SIRT1 (aa 193–741 with N-terminal GST-tag, >60% purity), SIRT2 (aa 50–356 with C-terminal His-tag, >90% purity), and SIRT6 (full length with N-terminal GST-tag, >75% purity) were purchased from BPS Biosciences (San Diego, CA); SIRT3 (aa 102–399 with N-terminal His-tag; ~75% purity) and SIRT5 (aa 37–310 with N-terminal His-tag, >90% purity) were purchased from Enzo Life Sciences (Farmingdale, NY). Purities were based on SDS-PAGE and Coomassie blue stain according to the supplier, and all enzyme concentrations given are based on stock concentrations according to the supplier. Assay buffer was prepared as described in Biomol International product sheets BML-KI-143 [http://www.enzolifesciences.com/BML-AK500/fluor-de-lys-hdac-fluorometric-activity-assay-kit/] [TRIS HCl (50 mM), NaCl (137 mM), KCl (2.7 mM), MgCl$_2$ (1 mM), pH 8.0] with addition of BSA (1.0 mg/mL). Trypsin (10,000 units/mg, TPCK treated from bovine pancreas, T1426) was purchased from Sigma-Aldrich (Steinheim, Germany). All chemicals and solvents were of analytical grade were and used without further purification as obtained from commercial suppliers.

Fluorescence-based sirtuin deacylase assays—All reactions were performed in black low binding 96-well microtiter plates (Corning half area wells), with duplicate series in each assay and each assay performed at least twice. Control wells without enzyme were included in each plate. All reactions were performed in assay buffer, with appropriate concentrations of substrates and inhibitors obtained by dilution from 3.8–50 mM stock solutions in either water or DMSO, and appropriate concentration of enzyme obtained by dilution of the stock provided by the supplier. DMSO concentration in the final assay solution did not exceed 2% (v/v) and control wells without either enzyme (negative control) or inhibitor (positive control) were included in each plate. All plates were analyzed using a Perkin Elmer Enspire plate reader with excitation at 360 nm and detecting emission at 460 nm. Fluorescence measurements (RFU) were converted to [AMC] concentrations based on a [AMC]–fluorescence standard curve, and all data analysis was performed using GraphPad Prism.

End-point sirtuin 5 inhibition assays, initial screening—Relevant substrate and inhibitor was added to each well, and the experiment initiated by addition of a freshly prepared solution of sirtuin 5, for a final volume of 25 μL per well. The following final concentrations were used: SIRT5 (172 nM), Ac-LGKglu-AMC (50 μM), NAD$^+$ (500 μM), and inhibitor (100 μM or 10 μM). The plate was incubated at 37 °C for 30 min, then a solution of trypsin and nicotinamide (25 μL, 0.4 mg/mL and 8 mM, respectively; final concentration 0.2 mg/mL and 4 mM, respectively) was added and the assay development was allowed to proceed for 15 min at room temperature, before fluorescence measurement and calculation of residual activity.

End-point sirtuin 5 inhibition assays, concentration–response—Relevant substrate and inhibitor was added to each well, and the experiment initiated by addition of a freshly prepared solution of sirtuin 5, for a final volume of 25 μL per well. The following final concentrations were used: SIRT5 (172 nM), Ac-LGKglu-AMC (50 μM) or Ac-LGKsuc-AMC (50 μM), NAD$^+$ (500 μM), and inhibitor (3-fold dilution series). The plate was incubated at 37 °C for 30 min, then a solution of trypsin and nicotinamide (25 μL, 0.4 mg/mL and 4 mM, respectively; final concentration 0.2 mg/mL and 2 mM, respectively) was added and the assay development was allowed to proceed for 15 min at room temperature, before fluorescence measurement. Residual activity was calculated, and assuming a standard fast-on/fast-off mechanism, IC$_{50}$ values were obtained by fitting the resulting data to the concentration–response equation (**Eq. 1**).

$$\textbf{Eq. 1} \quad v_i = v_{bottom} + \frac{v_{top} - v_{bottom}}{1 + 10^{(\log IC_{50} - \log[I])h}}$$

End-point sirtuin inhibition assays, sirtuin selectivity—Using the protocol described above, SIRT1–3 (SIRT1: 250 nM; SIRT2 250 μM; SIRT3: 500 nM) and Ac-QPKKac-AMC (50 μM), SIRT5 (100 nM) and Ac-QPKKsuc-AMC (50 μM) or Ac-QPKKglu-AMC (50 μM), or SIRT6 (500 nM) and Ac-QPKKdec-AMC (50 μM) were incubated with NAD$^+$ (500 μM) and inhibitor (100 μM or 10 μM).[16] The plate was incubated at 37 °C for 60 min, then a solution of trypsin and nicotinamide (25 μL, 5 mg/mL and 4 mM, respectively; final concentration 2.5 mg/mL and 2 mM, respectively) was added and the assay development was allowed to proceed for 90 min at room temperature, before fluorescence measurement and calculation of residual activity.

End-point sirtuin 5 pre-incubation assays—Sirtuin 5 and inhibitor was pre-incubated with or without NAD$^+$ for 5 min at rt or 15 or 30 min at 37 °C in a total volume of 40 µL, prior to addition of substrate (and NAD$^+$ if excluded in pre-incubation), for a final volume of 45 µL. For pre-incubation excluding NAD$^+$, the following concentrations were used: SIRT5 (113 nM during pre-incubation, giving 100 nM after substrate and NAD$^+$ addition), inhibitor (113/100 µM, 11.3/10 µM, 1.13/1.0 µM, or 0.11/0.10 µM), substrate (0/50 µM), NAD$^+$ (0/500 µM); For pre-incubation including NAD$^+$, the following concentrations were used: SIRT5 (113 nM during pre-incubation, giving 100 nM after substrate addition), inhibitor (113/100 µM, 11.3/10 µM, 1.13/1.0 µM, or 0.11/0.10 µM), NAD$^+$ (563/500 µM), and substrate (0/50 µM). The plate was incubated at 37 °C for 30 min, then a solution of trypsin and nicotinamide (5 µL, 2.0 mg/mL and 40 mM, respectively; final concentration 0.2 mg/mL and 4 mM, respectively) was added and the assay development was allowed to proceed for 15 min at room temperature, before fluorescence measurement and calculation of residual activity.

Rate inhibition assays, concentration–response—Rate experiments for determination of kinetic parameters were evaluated under varying inhibitor concentrations. Sirtuin 5 was incubated with the relevant substrate, inhibitor and trypsin in assay buffer in a total volume of 50 µL per well using the following final concentrations: SIRT5 (100 nM); Ac-LGKglu-AMC (23 µM), NAD$^+$ (500 µM) and trypsin (0.125 ng/µL). *In situ* fluorophore release was monitored immediately by fluorescence readings recorded every 30 seconds for 35 min at 25 °C. The data were fitted to the relevant equations (**Eq. 2** or **3**) to obtain either initial linear rates (v) or apparent first-order rate constant (k_{obs}) for each inhibitor concentration. Secondary plots were then fitted to the relevant equations (**Eq. 1**, **4**, or **5**) to obtain the desired dissociation constants (K_i and $K_{i,1}$) and/or kinetic parameters (k_1, k_{-1}, k_2 and k_{-2}).

Eq. 2 $$[P] = vt$$

Eq. 3 $$[P] = v_{ss}t + \frac{v_{in} - v_{ss}}{k_{obs}}\left(1 - e^{-k_{obs}t}\right)$$

Eq. 4 $$k_{obs} = k_1\left(1 + \frac{[S]}{K_M}\right)[I] + k_{-1}$$

Eq. 5 $$k_{obs} = \frac{k_2}{[I] + K_{i,1}\left(1 + \frac{[S]}{K_M}\right)}[I] + k_{-2}$$

Expression and purification of hSirt5 and zSirt5

hSirt5(34-302) and zSirt5(30-298) proteins were expressed in *E. coli* Rosetta2 (DE3) cells and *E. coli* BL21-CodonPlus™ (DE3) cells, respectively, and purified through Co-Talon affinity chromatography, TEV-proteolysis, reverse affinity chromatography and gel filtration as previously reported[17], except that zSirt5 gel filtration buffer was 20 mM TRIS HCl, pH 8.5, 150 mM NaCl, 0.5 mM TCEP.

Crystallization and structure solution

10 mg/mL zSirt5 or hSirt5 protein, 1 mM compound **10** or **29** and 5 mM NAD$^+$ were mixed and pre-incubated for 30 min on ice (DMSO concentration 10% during incubation; compound stocks 20 mM in DMSO, NAD$^+$ stock 50 mM in sodium phosphate buffer pH 8.0) before setting up sitting-drop vapor-diffusion crystallization experiments at 20 °C. Co-crystallization was achieved by using 20% PEG8000, 0.2 M MgCl$_2$, 0.1 M TRIS HCl, pH 8.5, 0.1 M glycine for zSirt5 complexes and 30% PEG3350, 0.2 M NaCl, 0.1 M BIS-TRIS, pH 5.5, 5% 1,3-butandiol for the hSirt5 complex as reservoir solution. 2 µL crystallization drops were prepared with a 1:1 ratio of protein/ligand and reservoir solution, which were equilibrated against 200 µL reservoir solution in MRC Maxi 48-well crystallization plates (Hampton Research, Aliso Viejo, USA, # HR3-179). After 2–4 days, tiny crystal cubes (zSirt5) or large cubes, rods and bundles of rods (hSirt5) appeared. The crystals were transferred to a cryo-solution drop composed of reservoir and ligands supplemented with 25% glycerol prior to shock-freezing in liquid nitrogen and data collection. hSirt5 diffraction was mostly anisotropic, but one of the rods showed clearer diffraction images and was used for structure solution. Diffraction data collection was performed at 100 K at BESSY II beamline MX14.1[18] (operated by the Helmholtz-Zentrum Berlin, Germany) with a Pilatus 6M detector (Dectris, Baden, Switzerland) or at Swiss Light Source beamline

X06DA - PXIII (Paul Scherrer Institut, Villigen, Switzerland) with a Pilatus 2M-F detector (Dectris, Baden, Switzerland). Indexing, scaling and merging of diffraction data were done using XDS.[19] Structures were solved by Phaser[20] molecular replacement with search models PDB 3RIY (hSirt5/succinyl-H3K9/NAD$^+$ complex) for the hSirt5 complex and PDB 4UTV (zSirt5/3-phenyl-succinyl-CPS1) for the zSirt5 complexes. Refinement was performed using Refmac5[21] and manual modeling as well as structure validation were done with Coot.[22] Geometry parameters for compounds and intermediates were generated using PRODRG[23] and structure figures created with PyMOL Molecular Graphics System (Version 1.7 Schrödinger, LLC).

Cell culture and generation of crSIRT5KO cells

HEK293T were obtained from Dr. Eric Verdin's lab. The HEK293T crSIRT5KO cell line was generated with Dharmacon's Edit-R gene engineering system that uses plasmid-driven Cas9 nuclease expression, synthetic tracrRNA and crRNA for gene of interest as per manufacturer's protocol. Briefly, an Edit-R hCMV-Puro-Cas9 (#U-005100-120) was co-transfected with Edit-R tracrRNA (#U-002000-120) and Edit-R crRNA's for SIRT5 into HEK293T cells using the DharmaFECT Duo (#T-2010-03) transfection reagent. After 48 hours of transfection, positively transfected cells were selected using 2 µg/mL puromycin for 3 days and mono-clonal populations were selected using serial dilution technique. The guide sequence targeting the sense strand at sequence 5'-GAT GAG CTG CAC CGC AAG GC-3' in Exon 5 of human SIRT5 was selected from Dharmacon's online CRISPR RNA configurator tool (http://dharmacon.gelifesciences.com/gene-editing/crispr-rna-configurator/). Control cells underwent the same procedure as the crSIRT5KO cells, except they did not receive the gene-specific crRNA. Each clonal population was cultured and analyzed for loss of SIRT5 protein by Western blotting. Both cell lines were maintained at 37 °C and 5% CO_2 in Dulbecco's modified Eagle's medium (DMEM, Thermo Scientific #11965118) supplemented with 10% (v/v) fetal bovine serum (FBS, Thermo Scientific #26140079).

Western blotting and Antibodies

Equal amounts of denatured protein samples (30–60 µg) were uniformly loaded and run on BioRad AnykD Criterion TGX Precast Midi Protein Gels, 14 well (#5671123), 18 well (#5671124), or 26 well (#5671125), 15–40 uL at 150–180 V for 45–60 minutes. The proteins were wet-transferred to a 0.45 µm nitrocellulose membrane in a BioRad Criterion™ Blotter at 100 V for 90 minutes at 4 °C. The membranes were blocked for 1 hour in LI-COR blocking buffer (20 mM TRIS base, 150 mM NaCl, 0.45% fish gelatin, 0.1% casein and 0.02% azide, pH 7.5). Primary antibodies (1:1000–1:2000) were diluted in LI-COR blocking buffer (containing 0.1–0.2% Tween-20) overnight at 4 °C. Membranes were washed with TRIS-buffered saline (TBS, 20 mM TRIS base, 150 mM NaCl, containing 0.1% Tween-20), 4–6 times for 5–10 minutes each. Infra-red dye-conjugated secondary antibodies were diluted 1:10,000 in LI-COR blocking buffer containing 0.1–0.2% Tween-20 and incubated for 1 hour at room temperature. Western blots were visualized on a LI-COR Odyssey CLx imager. Un-stripped blots were re-probed for loading control and image analysis to quantify band-intensity was performed using the LI-COR Image Studio software (version 3.0.12). Antibodies: anti-SIRT5 (Sigma-Aldrich #HPA022002), anti-β-actin (Cell Signaling Technologies, #3700), anti-GAPDH (Santa Cruz Biotechnology, #sc-32233), anti-UQCRFS1 (Abcam, #ab14746), anti-glutaryl-lysine (Cell Signaling Technologies, non-commercial and PTM-Biolabs #1151), anti-succinyl-lysine (Cell Signaling Technologies, non-commercial and PTM-Biolabs #401), anti-malonyl-lysine (Cell Signaling Technologies, #14942), IRDye 680RD Donkey anti-mouse IgG (LI-COR, #926-68072), and IRDye 800CW Donkey anti-rabbit IgG (LI-COR, #926-32213).

Drug treatment of HEK293T WT and crSIRT5KO cells

Et-29 treatment—The crSIRT5KO and WT cells at passage 11 were treated with 1 or 10 µM of **Et-29** or respective volume of DMSO as control, in duplicate. Cells were plated at a density of 120,000 cell per well in 6-well plates and the SIRT5 inhibitor/DMSO were included in the plating media. After incubation for 48 hours, cells were washed in phosphate-buffered saline (PBS, pH 7.4, Thermo Scientific #10010023) and collected in ice-cold radio immunoprecipitation assay buffer (RIPA buffer, 20 mM TRIS base, 150 mM NaCl, 0.5%

sodium deoxycholate, 0.1% sodium dodecyl sulphate, 0.1% triton-X-100, 1 mM EDTA, 1 mM EGTA, pH 7.4) buffer containing protease- (Sigma-Aldrich, #P8340) and/or phosphatase (Sigma-Aldrich, #P0044 and P5726) inhibitors, 10 µM Trichostatin A (Selleckchem, #S1045), 10 mM nicotinamide (Sigma-Aldrich, #N5535) and 10 mM sodium butyrate (Sigma-Aldrich, #303410). Cells were lysed by sonication (10 intermittent pulses with a probe sonicator) after which samples were vortexed and centrifuged at 14,000×g for 1 hour. Supernatants were collected and protein concentration was determined using a Bicinchoninic Acid Protein Assay Kit (BCA assay, Sigma-Aldrich # BCA1). Western blot analysis of lysine glutarylation was performed as described above.

Malonyl-NAC[1] *and GSK2194069 treatement*—Malonyl-NAC (MalNAC) was obtained from Jordan L. Meier's lab. Fatty acid synthase inhibitor GSK2194069 (GSKi) was purchase from Sigma-Aldrich (#SML1259-5MG). The crSIRT5KO and WT cells at passage 11 were plated at a density of 200,000 cell per well in 6-well plates, in triplicate. After 48 hours cells were treated with MalNAC (0.5 or 1.0 mM) or GSKi (30 or 15 nM) or respective volume of DMSO as control. After incubation for 24 hours, cells were collected in RIPA buffer and western blot analysis of lysine malonylation was performed, as described above.

Mitochondrial enrichment

crSIRT5KO and WT cells at passage 11 were plated at a density of 2,200,000 cells in tissue-culture dishes (100×20 mm), in triplicate. After 48 hours in culture, media was aspirated and cells were collected in ice-cold PBS (12 mL). The cell suspension was centrifuged at 1000×g for 5 minutes at 4 °C and the resulting supernatant was aspirated. The pellet was resuspended in MHS buffer (220 mM mannitol, 70 mM sucrose, 5 mM potassium-HEPES, 10 mM nicotinamide, pH 7.5, 750 µL). An aliquot (50 µL) was mixed with aq. triton-X-100 (10%, containing Halt protease inhibitors 10× (Halt, Thermo Scientific, #78441), 5 µL), representing the whole cell lysate. The remaining cell lysate was transferred to a dounce homogenizer, and stroked 50 times. The dounced suspension was pelleted at 750×g for 5 minutes at 4 °C and the supernatant was collected. The pellet was resuspended in MHS buffer (300 µL) and transferred to a dounce homogenizer and stroked 50 times. The homogenate was centrifuged at 750×g for 5 minutes at 4 °C and the resulting supernatant was pooled with the previously collected supernatant. The pooled supernatants were pelleted at 14000×g for 10 minutes at 4 °C and an aliquot (100 µL) of the supernatant was mixed with aq. Triton-X-100 (10%, containing Halt (10×), 10 µL), representing the cytosolic fraction. The remaining supernatant was aspirated and the pellet was washed with MHS buffer (200 µL) and pelleted at 14000×g for 10 minutes at 4 °C and the supernatant was aspirated. This washing step was repeated 3 times, and after the last wash the pellet was resuspended in isolation buffer (30 µL) and mixed with aq. Triton-X-100 (10%, containing Halt (10×), 3 µL), representing the mitochondrial fraction. The three fractions (whole cell lysate, cytosolic and mitochondrial) were vortexed and protein concentration was determined using a BCA assay. Western blot analysis of lysine succinylation and lysine glutarylation was performed, as described above.

Full bibliography for references with more than 10 authors in the manuscript

[4a]   H. Jiang, S. Khan, Y. Wang, G. Charron, B. He, C. Sebastian, J. Du, R. Kim, E. Ge, R. Mostoslavsky, H. C. Hang, Q. Hao, H. Lin, *Nature* **2013**, *496*, 110-113

[4d]   A. S. Madsen, C. Andersen, M. Daoud, K. A. Anderson, J. S. Laursen, S. Chakladar, F. K. Huynh, A. R. Colaço, D. S. Backos, P. Fristrup, M. D. Hirschey, C. A. Olsen, *J. Biol. Chem.* **2016**, *291*, 7128-7141.

[5a]   C. Peng, Z. Lu, Z. Xie, Z. Cheng, Y. Chen, M. Tan, H. Luo, Y. Zhang, W. He, K. Yang, B. M. M. Zwaans, D. Tishkoff, L. Ho, D. Lombard, T. C. He, J. Dai, E. Verdin, Y. Ye, Y. Zhao, *Mol. Cell. Proteomics* **2011**, *10*, M111.012658.

[5d]   J. Du, Y. Zhou, X. Su, J. J. Yu, S. Khan, H. Jiang, J. Kim, J. Woo, J. H. Kim, B. H. Choi, B. He, W. Chen, S. Zhang, R. A. Cerione, J. Auwerx, Q. Hao, H. Lin, *Science* **2011**, *334*, 806-809.

[6a]   M. Tan, C. Peng, K. A. Anderson, P. Chhoy, Z. Xie, L. Dai, J. Park, Y. Chen, H. Huang, Y. Zhang, J. Ro, G. R. Wagner, M. F. Green, A. S. Madsen, J. Schmiesing, B. S. Peterson, G. Xu, O. R. Ilkayeva, M. J. Muehlbauer, T. Braulke, C. Mühlhausen, D. S. Backos, C. A. Olsen, P. J. McGuire, S. D. Pletcher, D. B. Lombard, M. D. Hirschey, Y. Zhao, *Cell Metab.* **2014**, *19*, 605-617.

[6b]   C. Roessler, T. Nowak, M. Pannek, M. Gertz, G. T. T. Nguyen, M. Scharfe, I. Born, W. Sippl, C. Steegborn, M. Schutkowski, *Angew. Chem. Int. Ed.* **2014**, *53*, 10728-10732.

[7]   K. A. Anderson, F. K. Huynh, K. Fisher-Wellman, J. D. Stuart, B. S. Peterson, J. D. Douros, G. R. Wagner, J. W. Thompson, A. S. Madsen, M. F. Green, R. M. Sivley, O. R. Ilkayeva, R. D. Stevens, D. S. Backos, J. A. Capra, C. A. Olsen, J. E. Campbell, D. M. Muoio, P. A. Grimsrud, M. D. Hirschey, *Cell Metab.* **2017**, *25*, 838-855.

[10a] L. Zhou, F. Wang, R. Sun, X. Chen, M. Zhang, Q. Xu, Y. Wang, S. Wang, Y. Xiong, K. L. Guan, P. Yang, H. Yu, D. Ye, *EMBO Rep.* **2016**, *17*, 811-822.

[15e] L. Polletta, E. Vernucci, I. Carnevale, T. Arcangeli, D. Rotili, S. Palmerio, C. Steegborn, T. Nowak, M. Schutkowski, L. Pellegrini, L. Sansone, L. Villanova, A. Runci, B. Pucci, E. Morgante, M. Fini, A. Mai, M. A. Russo, M. Tafani, *Autophagy* **2015**, *11*, 253-270.

[16]   B. C. R. Dancy, S. A. Ming, R. Papazyan, C. A. Jelinek, A. Majumdar, Y. Sun, B. M. Dancy, W. J. Drury, 3rd, R. J. Cotter, S. D. Taverna, P. A. Cole, *J. Am. Chem. Soc.* **2012**, *134*, 5138-5148.

Supporting references

[1]   R. A. Kulkarni, A. J. Worth, T. T. Zengeya, J. H. Shrimp, J. M. Garlick, A. M. Roberts, D. C. Montgomery, C. Sourbier, B. K. Gibbs, C. Mesaros, Y. C. Tsai, S. Das, K. C. Chan, M. Zhou, T. Andresson, A. M. Weissman, W. M. Linehan, I. A. Blair, N. W. Snyder, J. L. Meier, *Cell Chem. Biol.* **2017**, *24*, 231-242.

[2]   M. Gude, J. Ryf, P. D. White, *Lett. Pep. Sci.* **2002**, *9*, 203-206.

[3]   D. E. Levy, F. Lapierre, W. Liang, W. Ye, C. W. Lange, X. Li, D. Grobelny, M. Casabonne, D. Tyrrell, K. Holme, A. Nadzan, R. E. Galardy, *J. Med. Chem.* **1998**, *41*, 199-223.

[4]   Y. S. Oh, T. Yamazaki, M. Goodman, *Macromolecules* **1992**, *25*, 6322-6331.

[5]   P. Sebök, A. Levai, T. Timár, *Heterocycl. Commun.* **1998**, *4*, 547-552.

[6]   B. Zacharie, D. Fortin, N. Wilb, C. Penney (Proteomic Bioscience Inc.), US 8,080,555 B2, **2011**.

[7]   A. R. Katritzky, H. Tao, K. Kirichenko, *Arkivoc* **2007**, *10*, 142-151.

[8]   C. Larsen, K. Steliou, D. N. Harpp, *J. Org. Chem.* **1978**, *43*, 337-339.

[9]   a) J. T. Randolph, H.-J. Chen, A. Degoey, C. A. Flentge, W. Flosi, D. J. Grampovnik, P. Huang, D. K. Hutchinson, D. J. Kempf, L. L. Klein, M. C. Yeung (Abbott Laboratories), WO 2005/061487 A1, **2005**; b) H. Mitchell, Y. Leblanc, *J. Org. Chem.* **1994**, *59*, 682-687.

[10]   M. Rodriquez, M. Taddei, *Structure* **2005**, *2005*, 493-495.

[11]   Y. Kaburagi, Y. Kishi, *Org. Lett.* **2007**, *9*, 723-726.

[12]   C. Caumes, T. Hjelmgaard, O. Roy, M. Reynaud, D. Servent, C. Taillefumier, S. Faure, *Med. Chem. Commun.* **2012**, *3*, 1531.

[13]   C. Hardouin, M. J. Kelso, F. A. Romero, T. J. Rayl, D. Leung, I. Hwang, B. F. Cravatt, D. L. Boger, *J. Med. Chem.* **2007**, *50*, 3359-3368.

[14]   P. Kahnberg, A. J. Lucke, M. P. Glenn, G. M. Boyle, J. D. Tyndall, P. G. Parsons, D. P. Fairlie, *J. Med. Chem.* **2006**, *49*, 7611-7622.

[15]   a) S. Oriana, Y. Cai, J. W. Bode, Y. Yamakoshi, *Org. Biomol. Chem.* **2017**, *15*, 1792-1800; b) J. Wright (Bind Therapeutics Inc.), WO 2014/210485 A1, **2014**.

[16]   a) I. Galleano, M. Schiedel, M. Jung, A. S. Madsen, C. A. Olsen, *J. Med. Chem.* **2016**, *59*, 1021-1031; b) A. S. Madsen, C. Andersen, M. Daoud, K. A. Anderson, J. S. Laursen, S. Chakladar, F. K. Huynh, A. R. Colaço, D. S. Backos, P. Fristrup, M. D. Hirschey, C. A. Olsen, *J. Biol. Chem.* **2016**, *291*, 7128-7141; c) A. S. Madsen, C. A. Olsen, *J. Med. Chem.* **2012**, *55*, 5582-5590.

[17]   a) C. Roessler, T. Nowak, M. Pannek, M. Gertz, G. T. T. Nguyen, M. Scharfe, I. Born, W. Sippl, C. Steegborn, M. Schutkowski, *Angew. Chem. Int. Ed.* **2014**, *53*, 10728-10732; b) M. Gertz, G. T. Nguyen, F. Fischer, B. Suenkel, C. Schlicker, B. Fränzel, J. Tomaschewski, F. Aladini, C. Becker, D. Wolters, C. Steegborn, *PloS one* **2012**, *7*, e49761.

[18]   U. Mueller, N. Darowski, M. R. Fuchs, R. Förster, M. Hellmig, K. S. Paithankar, S. Pühringer, M. Steffien, G. Zocher, M. S. Weiss, *J. Synchrotron. Radiat.* **2012**, *19*, 442-449.

[19]   W. Kabsch, *Acta Crystallogr. Sect. D* **2010**, *66*, 133-144.

[20]   A. J. McCoy, R. W. Grosse-Kunstleve, P. D. Adams, M. D. Winn, L. C. Storoni, R. J. Read, *J. Appl. Crystallogr.* **2007**, *40*, 658-674.

[21]   G. N. Murshudov, A. A. Vagin, E. J. Dodson, *Acta Crystallogr. Sect. D* **1997**, *53*, 240-255.

[22]   P. Emsley, B. Lohkamp, W. G. Scott, K. Cowtan, *Acta Crystallogr. Sect. D* **2010**, *66*, 486-501.

[23]   A. W. Schuttelkopf, D. M. van Aalten, *Acta Crystallogr. Sect. D* **2004**, *60*, 1355-1363.

5.4. Publication 4

Selective Sirt2 inhibition by ligand-induced rearrangement of the active site

Rumpf, T. Schiedel, M., Karaman, B., Roessler, C., North, B.J., Lehotzky, A., Oláh, J., Ladwein, K.I., Schmidtkunz, K., Gajer, M., Pannek, M., Steegborn, C., Sinclair, D.A., Gerhardt, S., Ovádi, J., Schutkowski, M., Sippl, W., Einsle, O. and Jung, M. (2015). Selective Sirt2 inhibition by ligand-induced rearrangement of the active site. *Nat. Commun.* 6:6263.

This work resulted from a collaboration of the labs of Matthias Jung, Oliver Einsle, Wolfgang Sippl, Mike Schutkowski, Judith Ovádi, David Sinclair and Clemens Steegborn. Tobias Rumpf, Wolfgang Sippl, Oliver Einsle and Manfred Jung designed the study and drafted the manuscript. Tobias Rumpf performed the crystallization experiments, collected the data, solved, refined and deposited the structures with support of Stefan Gerhardt. Matthias Schiedel synthesized the SirReal inhibitors. Tobias Rumpf, Claudia Roessler, Matthias Schiedel, Markus Gajer and me performed the inhibition tests. Tobias Rumpf, Claudia Roessler, Matthias Schiedel and Mike Schutkowski analyzed *in vitro* data. Brian North, Tobias Rumpf, Karin Schmidtkunz, Katharina Ladwein, Attila Lehotzky, Judit Oláh and Judit Ovádi performed the cellular biology experiments. Tobias Rumpf, Brian North, Attila Lehotzky, Judith Ovádi and David Sinclair analyzed the data from cellular biology experiments. Berin Karaman and Wolfgang Sippl performed computational studies. All authors commented on the manuscript.

This work is publicly available and licensed under a Creative Commons Attribution 4.0 International License. This license can be found at the following adress:

https://creativecommons.org/licenses/by/4.0/legalcode

The whole publication including all supplementary information is shown on the following pages.

Selective Sirt2 inhibition by ligand-induced rearrangement of the active site

Tobias Rumpf[1], Matthias Schiedel[1], Berin Karaman[2], Claudia Roessler[3], Brian J. North[4], Attila Lehotzky[5], Judit Oláh[5], Kathrin I. Ladwein[1], Karin Schmidtkunz[1], Markus Gajer[1], Martin Pannek[6], Clemens Steegborn[6], David A. Sinclair[4], Stefan Gerhardt[7], Judit Ovádi[5], Mike Schutkowski[3], Wolfgang Sippl[2], Oliver Einsle[7] & Manfred Jung[1]

Sirtuins are a highly conserved class of NAD^+-dependent lysine deacylases. The human isotype Sirt2 has been implicated in the pathogenesis of cancer, inflammation and neuro-degeneration, which makes the modulation of Sirt2 activity a promising strategy for pharmaceutical intervention. A rational basis for the development of optimized Sirt2 inhibitors is lacking so far. Here we present high-resolution structures of human Sirt2 in complex with highly selective drug-like inhibitors that show a unique inhibitory mechanism. Potency and the unprecedented Sirt2 selectivity are based on a ligand-induced structural rearrangement of the active site unveiling a yet-unexploited binding pocket. Application of the most potent Sirtuin-rearranging ligand, termed SirReal2, leads to tubulin hyperacetylation in HeLa cells and induces destabilization of the checkpoint protein BubR1, consistent with Sirt2 inhibition *in vivo*. Our structural insights into this unique mechanism of selective sirtuin inhibition provide the basis for further inhibitor development and selective tools for sirtuin biology.

[1] Institute of Pharmaceutical Sciences, Albert-Ludwigs-University Freiburg, Albertstraße 25, 79104 Freiburg im Breisgau, Germany. [2] Institute for Pharmacy, Martin-Luther-University Halle-Wittenberg, Wolfgang-Langenbeck-Straße 4, 06120 Halle (Saale), Germany. [3] Institute for Biochemistry and Biotechnology, Martin-Luther-University Halle-Wittenberg, Kurt-Mothes-Straße 3, 06120 Halle (Saale) Germany. [4] Department of Genetics, Harvard Medical School, 77 Avenue Louis Pasteur, Boston, Massachusetts 02115, USA. [5] Institute of Enzymology, Research Centre for Natural Sciences, Hungarian Academy of Sciences, Magyar Tudósok körútja 2, H-1117 Budapest, Hungary. [6] Department of Biochemistry, University of Bayreuth, Universitätsstraße 30, 95445 Bayreuth, Germany. [7] Institute for Biochemistry and BIOSS Centre for Biological Signalling Studies, Albert-Ludwigs-University Freiburg im Breisgau, Albertstraße 21, 79104 Freiburg im Breisgau, Germany. Correspondence and requests for materials should be addressed to O.E. (email: einsle@biochemie.uni-freiburg.de) or to M.J. (email: manfred.jung@pharmazie.uni-freiburg.de).

N AD[+]-dependent protein deacylases (sirtuins) constitute a unique class of enzymes that are conserved from bacteria to humans. Initially recognized as protein deacetylases, they were recently shown to catalyse further post-translational modifications such as demyristoylation[1,2], desuccinylation[3] or ADP-ribosylation[4]. Through a multitude of protein substrates, they are involved in key cellular processes, including metabolic sensing, regulation of mitosis and aging. The human isotype Sirtuin 2 (Sirt2) deacetylates both nuclear and cytoplasmatic proteins and thereby functions as a major cell cycle regulator[5,6], a determinant of myelination[7], a regulator of autophagy[8] and a suppressor of brain inflammation[9]. Generally deemed as a tumour suppressor[10,11] in some types of cancer, Sirt2 was also shown to adopt a contrary role by promoting tumorigenesis[12,13]. In addition, recent reports link Sirt2 to bacteria-induced reprogramming of host cell gene expression[14].

Owing to its multiple regulatory roles, Sirt2 has been implicated as a potential drug target to combat cancer[12,13], neurodegeneration[15,16] and inflammation[7] but other reports question the suitability of Sirt2 as a drug target[17]. The physiological studies of Sirt2 have so far been hampered by the lack of potent and isotype-specific modulators of sirtuin activity.

The biochemistry of sirtuins has been studied extensively in recent years and three-dimensional structures of the catalytic domain of several human isotypes provided insight into different stages of the catalytic cycle[18–23]. Despite a highly conserved amino-acid sequence and a high structural similarity of the catalytic core between the members of the sirtuin family, recent screening campaigns have identified several isotype-selective inhibitors[15,24–27]. But for only a few of them structural information is available (Supplementary Fig. 1a) and a strategy for structure-based optimization of isotype-selective inhibitors remains mostly elusive. In particular, a structure-derived rationale for Sirt2-selective inhibition is also lacking so far.

Most recently, the first X-ray structure of Sirt2 in complex with a potent macrocyclic peptidic inhibitor was reported, but this inhibitor lacked the desired isotype selectivity[28] and, due to its physicochemical properties, might be of limited use for drug discovery. In this work, we present the first crystal structures of Sirt2 in complex with a potent and Sirt2-selective small-molecule inhibitor with drug-like properties. The basis for the high potency and unprecedented isotype selectivity is a ligand-induced structural rearrangement of the active site, exploiting an adjacent binding pocket. Along with kinetic studies, the structures give insight into a unique and isotype-selective inhibition mechanism. The relevance of the observed biochemical activity is further supported by cellular studies.

Results

Identification and crystallization of SirReal inhibitors. In search for new sirtuin inhibitors, we screened an internal compound library using an *in vitro* assay[29] based on a fluorophore-labelled acetyl-lysine derivative for human Sirt1–3. In this screening campaign, a family of aminothiazoles that we have termed Sirtuin-rearranging ligands (SirReals) was discovered as potent, Sirt2-selective inhibitors. Of these, SirReal2 (**1**) showed the most promising inhibitory properties (Fig. 1a,b). AGK2 was used as a reference inhibitor. Under the same assay conditions it is 38-fold less potent with an IC$_{50}$ of $15.4 \pm 0.7\,\mu$M. The activity of Sirt1 or Sirt3 was not affected at 50 μM. Additional confirmation of Sirt2-selective *in vitro* inhibition and binding by SirReal2 was obtained by using non-labelled peptidic substrates in a high-performance liquid chromatography (HPLC)-based conversion assay (Fig. 1c, Supplementary Fig. 1b) and from thermal stability assays, where the presence of SirReal2 led to increased melting temperatures due to ligand-induced stabilization of the protein (Fig. 1d). SirReal2 only inhibits Sirt2 potently with an IC$_{50}$ value
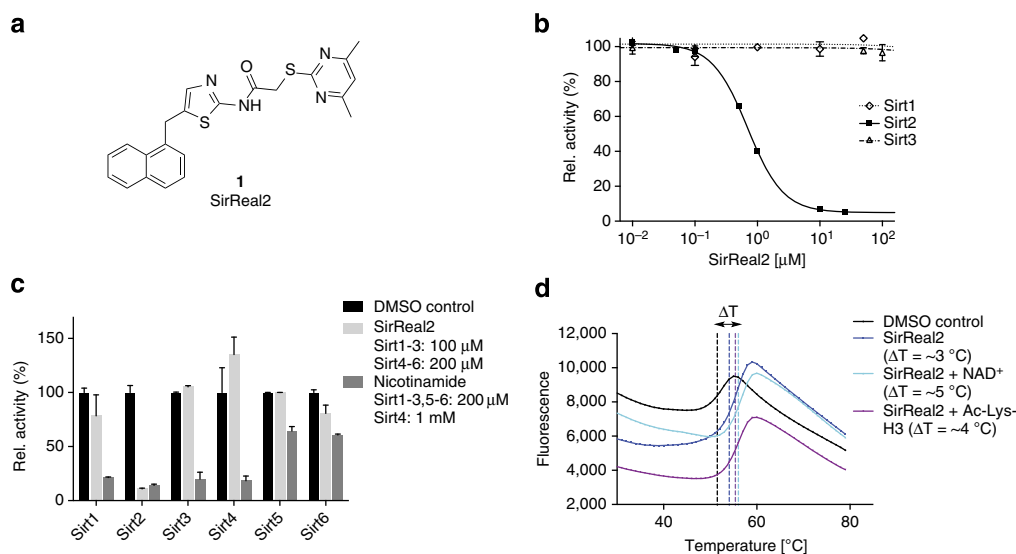
Figure 1 | SirReal2 selectively inhibits Sirt2 in a dose-dependent manner. (**a**) Chemical structure of SirReal2 (**1**). (**b**) Representative dose–response curve for Sirt1–3 and SirReal2 using the substrates ZMAL (Z-Lys(Acetyl)-AMC, Sirt1-2) resp. Fluor-de-Lys (Sirt3). Compared with the peptide-HPLC assay, SirReal2 was slightly less potent using ZMAL with an IC$_{50}$ value of 0.4 μM. Data are presented as mean ± s.d. ($n = 3$). (**c**) *In vitro* inhibition data for SirReal2 (Sirt1–3: 100 μM; Sirt4–6: 200 μM) in an assay using non-labelled acyl-lysine oligopeptide as a substrate (Sirt1–4, acetyl-lysine substrate; Sirt5, succinyl-lysine substrate; Sirt6, myristoyl-lysine substrate). A solution containing DMSO was used as a negative control, a solution with nicotinamide (NCA, 200 μM or 1 mM) was used as a positive control. Only the activity of Sirt2 is substantially reduced in the presence of SirReal2. Data are presented as mean ± s.d. ($n = 2$) (**d**) Representative thermal stability plots for Sirt2 in the presence of SirReal2 (25 μM) and either the cofactor NAD$^+$ (5 mM) or an acetyl-lysine H3 peptide (5 mM). The presence of NAD$^+$ or of an acetyl-lysine peptide substrate enhances the stability of the Sirt2–SirReal2 complex ($n = 3$). Representative thermal stability plots of Sirt2 in the absence of SirReal2 and in the presence of NAD$^+$ or an acetyl-lysine oligopeptide are shown in Supplementary Fig. 1d. Rel., relative.
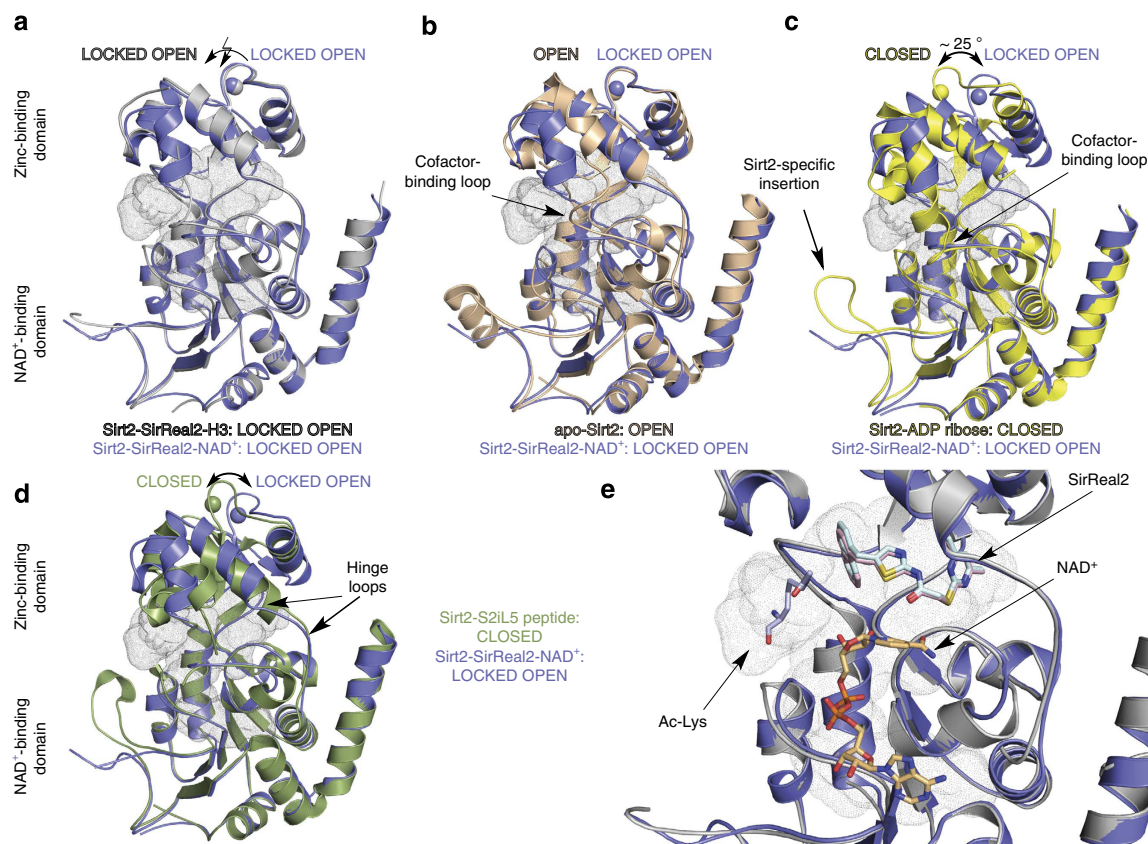
Figure 2 | SirReal2 functions as a molecular wedge locking Sirt2 in an open conformation. (a) Overlay of Sirt2–SirReal2–NAD$^+$ (slate blue) and Sirt2–SirReal2–H3 (light grey). Both structures are very similar (r.m.s.d. (C$_\alpha$ atoms) = 0.8 Å) and feature an open conformation. The active site is indicated by small grey dots. **(b)** Superposition of Sirt2–SirReal2–NAD$^+$ (slate blue) with Sirt2-apo (PDB-ID 3ZGO, salmon, residues 34–45 are omitted for better clarity). Both structures feature an open state despite major structural differences in the zinc-binding domain. **(c)** Superposition of Sirt2–SirReal2–NAD$^+$ (slate blue) with the Sirt2-ADPR complex (PDB-ID 3ZGV, yellow, residues Tyr139-Gly141 of one hinge loop were not defined in the electron density map). The structures display major conformational differences in the orientation of the zinc-binding domain. While the ADPR complex is in a closed state, Sirt2–SirReal2–NAD$^+$ adopts an open state. **(d)** Superposition of Sirt2–SirReal2–NAD$^+$ with Sirt2 in complex with a macrocyclic peptide inhibitor S2iL5 (PDB-ID 4L3O, green). Similar to the Sirt2–ADPR complex, the Sirt2–S2iL5 complex assumes a closed conformation. While the Rossmann fold domain is very similar in both structures, major structural differences can be seen at the zinc-binding domain and at the Sirt2-specific insertion. **(e)** Close-up view on the active site using the superposition shown in **a**. SirReal2 (Sirt2–SirReal2–NAD$^+$, light pink sticks; Sirt2–SirReal–H3, light cyan sticks) occupies the extended C-site of Sirt2. Binding of SirReal2 neither prevents binding of the acetyl-lysine substrate (light blue sticks) nor the cosubstrate NAD$^+$ (light orange sticks). The cofactor-binding loop of both structures is omitted for clarity.

of 140 nM and has very little effect on the activities of Sirt3-5. Only the activity of Sirt1 (22% inhibition at 100 μM) and Sirt6 (19% inhibition at 200 μM) are slightly affected at higher SirReal2 concentrations, making SirReal2 one of the most selective sirtuin inhibitors up to date. However, any attempts to identify a putative-binding site and to rationalize initial structure–activity relationships by docking to available X-ray structures of Sirt2 were not successful. We, therefore, proceeded to determine the structures of Sirt2-inhibitor complexes by protein X-ray crystallography.

For that, we used a truncated form of Sirt2$_{56–356}$ lacking the flexible N- and C termini. To validate the suitability of our expression construct, we also crystallized this truncated form of Sirt2 in the presence of ADP ribose (ADPR) and the physiological inhibitor nicotinamide (NCA, Supplementary Fig. 2, structure termed Sirt2–ADPR–NCA). As the binding mode of these ligands corresponded to other published sirtuin structures in complex with NCA[30], we concluded that our expression construct was suitable for the investigation of Sirt2–ligand interactions. Further thermal stability experiments indicated an additional stabilization of the Sirt2–SirReal2 complex in the presence of either NAD$^+$ or a peptidic acetyl-lysine substrate (Fig. 1d). These findings were

the key to a successful crystallization of Sirt2 in complex with SirReal2 that was only achieved in the presence of either substrate or cosubstrate.

Overall structure of Sirt2–SirReal2 complexes. We solved the structure of Sirt2 in complex with SirReal2 and the cosubstrate NAD$^+$ (structure termed Sirt2–SirReal2–NAD$^+$) as well as in complex with SirReal2 and an acetyl-lysine peptide derived from histone H3 (residues 11–17, structure termed Sirt2–SirReal2-H3). Both Sirt2–SirReal2 crystals belonged to different monoclinic space groups and contained one monomer per asymmetric unit. They had the two-domain structure typical for sirtuins-a larger domain with a Rossmann fold and a smaller zinc-binding domain that are separated through a large groove that constitutes the active site (Fig. 2a). The structures are highly similar (root mean squared deviation, r.m.s.d. (C$_\alpha$ atoms) = 0.8 Å) with the main differences in the cofactor-binding loop and its adjacent residues (r.m.s.d. (C$_\alpha$ residues 92–115) = 1.3 Å). In addition, we observed the Sirt2-specific insertion (residues 289–304) that mediates crystal contacts as was reported for the Sirt2–ADPR complex (ADPR, PDB-ID 3ZGV[19]) and apo-Sirt2 (PDB-ID 1J8F, refined
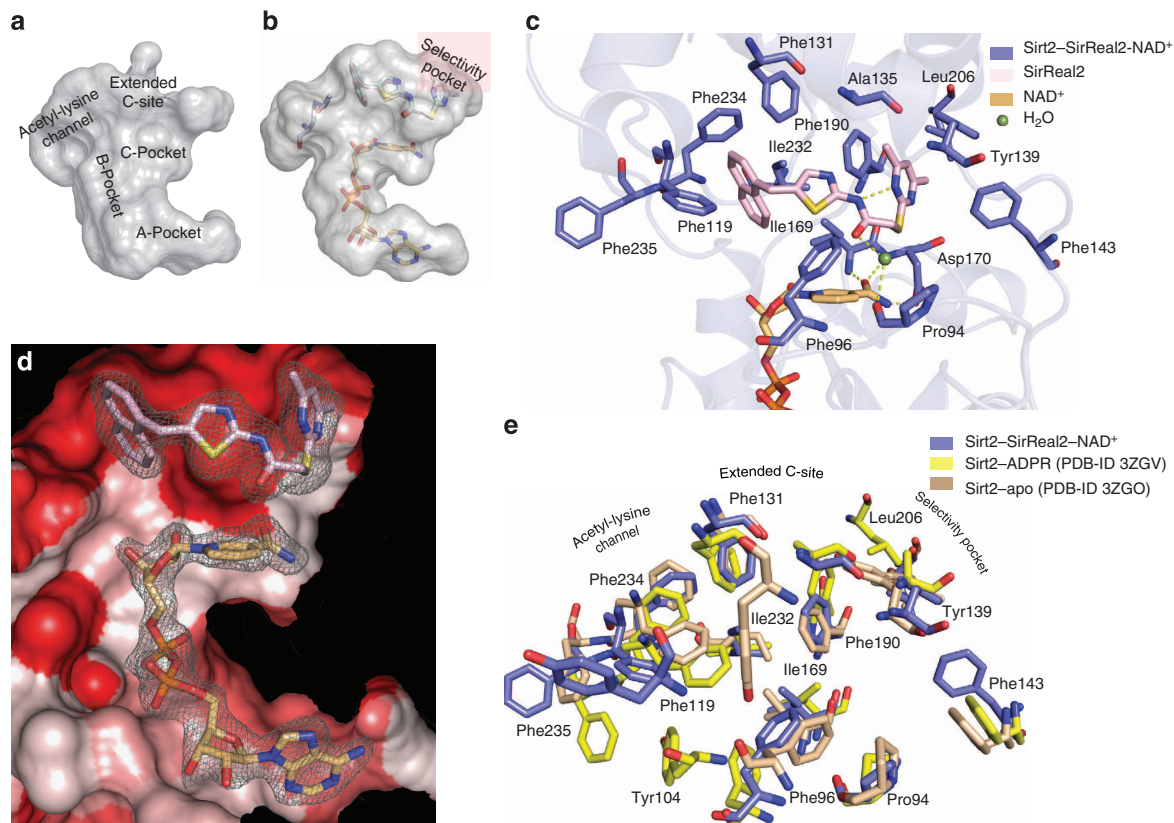
Figure 3 | SirReal2 occupies the extended C-site and induces a major rearrangement of Sirt2's active site. (a) Surface representation of the active site of apo-Sirt2, designating the individual subsites referred to in the text. **(b)** Orientation of SirReal2 in the active site of the Sirt2–SirReal2 complexes. The binding of SirReal2 induces the formation of the yet-unexploited selectivity pocket. **(c)** Interactions of SirReal2 (light pink) with Sirt2 in complex with the cosubstrate NAD$^+$ (light orange). Interacting residues are represented as sticks (slate blue). Hydrogen bonds are shown as dashed yellow lines. **(d)** SirReal2 (light pink sticks, overall B-factor of 32.2 Å^2) occupies the very hydrophobic extended C-site adjacent to the cosubstrate NAD$^+$ (light orange sticks, overall B-factor of 41.8 Å^2). The surface of Sirt2–SirReal2–NAD$^+$ is coloured according to its hydrophobicity (red colour indicating increasing hydrophobicity). The σ-weighted $2F_o - F_c$ electron density map is contoured at 1.0 σ. A stereo image of **d** is shown in Supplementary Fig. 4b. σ-weighted $F_o - F_c$ electron density OMIT maps for both ligands are shown in Supplementary Fig. 4d. **(e)** Comparison of the positions of the interacting residues of Sirt2-apo (PDB-ID 3ZGO, salmon), Sirt2–ADPR (PDB-ID 3ZGV, yellow) and Sirt2–SirReal2–NAD$^+$ (slate blue). Residues are shown as sticks. The binding of SirReal2 results in a reorganization of the side chains of several residues. The most drastic side chain movement was observed for the residues that form the acetyl-lysine substrate channel and the selectivity pocket. The side chain of Tyr139 of Sirt2–ADPR complex was not defined in the electron density map. The position of the interacting residues of Sirt2 in complex with the macrocyclic peptide inhibitor S2iL5 are very similar to the ones of Sirt2–ADPR and are therefore not shown.

3ZGO[18,19]). The cofactor-binding loop in both Sirt2–SirReal2 complexes adopts a conformation similar to the one observed in Sirt2 in complex with the product analogue ADPR (PDB-ID 3ZGV).

When compared with the available Sirt2 structures (apo-Sirt2: PDB-ID 1J8F, 3ZGO; Sirt2-ADPR: PDB-ID 3ZGV; Sirt2–S2iL5 peptide: PDB-ID 4L3O[28]) the zinc-binding domains in the Sirt2–SirReal2 structures adopt a conformation similar to the one in apo-Sirt2 (Fig. 2b–d, Supplementary Fig. 3a–c). On binding of the acetyl-lysine peptide substrate, the zinc-binding domain rotates towards the Rossmann fold domain. This has been termed as the 'closure' of the two domains and can be observed in several other human and bacterial sirtuin structures in complex with an acetyl-lysine peptide substrate[20,21,31]. This domain closure induces the formation of the acetyl-lysine-binding tunnel and the β-staple motif that mediates the acetyl-lysine peptide substrate-sirtuin interactions[32]. Despite the absence of an acetyl-lysine peptide substrate, the Sirt2–ADPR complexes also adopt the closed conformation. This is due to the Sirt2-specific insertion that acts as a pseudo-substrate in the crystal and binds to the acetyl-lysine-binding site of a neighbouring Sirt2 molecule.

Despite the 'open' conformation of the Sirt2–SirReal2 structures, SirReal2-inhibited Sirt2 adopts a substantially different structure from the one observed in Sirt2–apo (r.m.s.d. (C$_\alpha$ atoms) = 1.4 Å, Fig. 2b), the complex of Sirt2 and ADPR (r.m.s.d. (C$_\alpha$ atoms) = 1.6 Å, Fig. 2c) and the complex of Sirt2 and the S2iL5 peptide (r.m.s.d. (C$_\alpha$ atoms) = 1.7 Å, Fig. 2d). Our structures feature a completely new and unexpected Sirt2 conformation, where SirReal2 functions as a 'molecular wedge' that traps Sirt2 in the open conformation even in the presence of an acetyl-lysine peptide substrate. We call this a 'locked open' state.

SirReal2 occupies a yet-unexploited binding pocket. SirReal2 binds to the active site of Sirt2 (Figs 2e and 3) at the interface of the Rossmann fold domain and the zinc-binding domain, the site of the deacylation of ε-amino groups of lysines. The active site of Sirt2 has previously been divided into different sites (Fig. 3a). The A- and B-pocket, respectively, bind the ADPR moiety, whereas the C-pocket binds the NCA of NAD$^+$. NAD$^+$ is able to adopt different conformations. However, only a kinked conformation where the NCA moiety of NAD$^+$ occupies the C-pocket is considered productive for catalytic deacylation. The hydrophobic
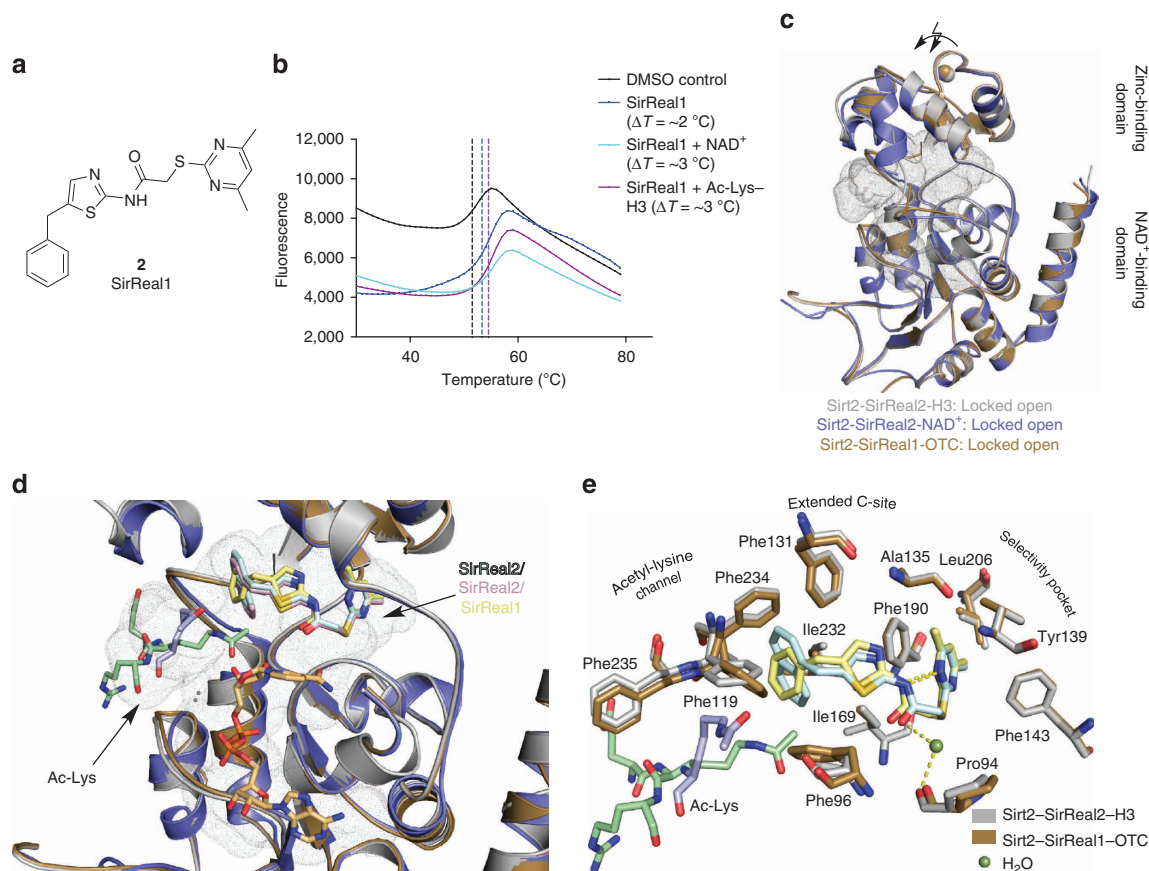
Figure 4 | SirReal1 selectively inhibits Sirt2 and functions as a molecular wedge to lock Sirt2 in an open conformation. (**a**) Chemical structure of SirReal1 (**2**). (**b**) Representative thermal stability plots for Sirt2 in the presence of SirReal1 (50 μM) and either the cofactor NAD$^+$ (5 mM) or an acetyl-lysine H3 peptide (5 mM). The presence of the cosubstrates enhances the stabilization of the Sirt2–SirReal1 complex ($n = 3$). Representative thermal stability plots of Sirt2 in the absence of SirReal2 and the presence of NAD$^+$ or an acetyl-lysine oligopeptide are shown in Supplementary Fig. 1d. (**c**) Overlay of Sirt2–SirReal1–OTC (brown) with Sirt2 structures in complex with SirReal2 (Sirt2–SirReal2–H3, light grey; Sirt2–SirReal2–NAD$^+$, slate blue). All Sirt2–SirReal complexes share a high similarity (r.m.s.d. (C$_\alpha$ atoms) = 0.44 Å to Sirt2–SirReal2–H3, 0.59 Å to Sirt2–SirReal2–NAD$^+$) and represent the locked open conformation. The active site is represented as grey dots. (**d,e**) SirReal1 (light yellow sticks) occupies the extended C-site in a very similar fashion as observed for SirReal2 (light blue in Sirt2–SirReal2–H3, light pink in Sirt2–SirReal2–NAD$^+$). Differences can be observed for the position of the side chains of Phe119, Phe235 and the acetyl-lysine peptides. The acetyl-lysine-binding site as well as the selectivity pocket are also the sites of major conformational changes compared with Sirt2–apo (PBD-ID 3ZGO) and Sirt2-ADPR (PDB-ID 3ZGV, see Fig. 3e). Hydrogen bonds are shown in dashed yellow lines. The cofactor-binding loop of **d** is omitted for clarity. A stereo image of the σ-weighted $2F_o - F_c$ electron density maps for SirReal1 and the Ac-Lys-OTC oligopeptide as well as σ-weighted $F_o - F_c$ electron density OMIT maps of both ligands are shown in Supplementary Fig. 5b,d.

acetyl-lysine-binding tunnel is formed by several phenylalanines and connects the NAD$^+$-binding site to the acetyl-lysine-binding site. The pocket adjacent to the C-pocket has been termed extended C-site (EC-site)[33].

The aminothiazole SirReal2 occupies this EC-site adjacent to the C-pocket, which is the physiological site for product inhibition by the feedback inhibitor NCA[30] (Supplementary Fig. 2). It binds at this highly hydrophobic site in vicinity to the zinc-binding domain, where it does not interfere with the binding of NCA or the NCA moiety of NAD$^+$ (Fig. 3b–d). The naphthyl moiety of SirReal2 protrudes into the substrate channel and the dimethylmercaptopyrimidine substituent (DMP) induces the formation of a binding pocket beyond the EC-site. This region is formed by two loops (residues 136–144, residues 188–191) of the hinge region that connect the Rossmann fold domain with the zinc-binding domain. We refer to this binding pocket in the following as the 'selectivity pocket'. The position of SirReal2 in the EC-site of Sirt2 is very similar in both structures with either NAD$^+$ or the acetyl-lysine peptide substrate (r.m.s.d. of 0.47 Å), and we will primarily describe the binding of SirReal2 in the presence of NAD$^+$, as this structure likely represents the

SirReal2-inhibited form of the enzyme. Structural comparison of the available Sirt2 structures with the Sirt2–SirReal2–H3 complex can be found in Supplementary Fig. 3.

Binding of SirReal2 to the EC-site is mainly driven by hydrophobic interactions (Fig. 3c,d). The naphthyl moiety of SirReal2 that protrudes into the acetyl-lysine-binding site is in van-der-Waals contacts with the NCA moiety of NAD$^+$, Phe131, Leu134, Ile169, Ile232, Val233 and Phe234. In the selectivity pocket, the DMP moiety forms π–π-stacking interactions with Tyr139 and Phe190 in the selectivity pocket that is shaped by Ile93, Ala135, Leu138, Pro140, Phe143, Leu206 and Ile213. In addition, Pro94 hydrogen bonds via a structural water molecule (W40) to the carbonyl-O of SirReal2. Besides its interactions with the Sirt2 protein, the SirReal2 inhibitor also forms an internal hydrogen bond between the amide N–H and one of the pyrimidine nitrogens. This results in a rigid conformation with ideal complementarity to the active site of Sirt2.

Binding of SirReal2 to Sirt2 rearranges the active site. The presence of SirReal2 results in a rearrangement of Sirt2's active
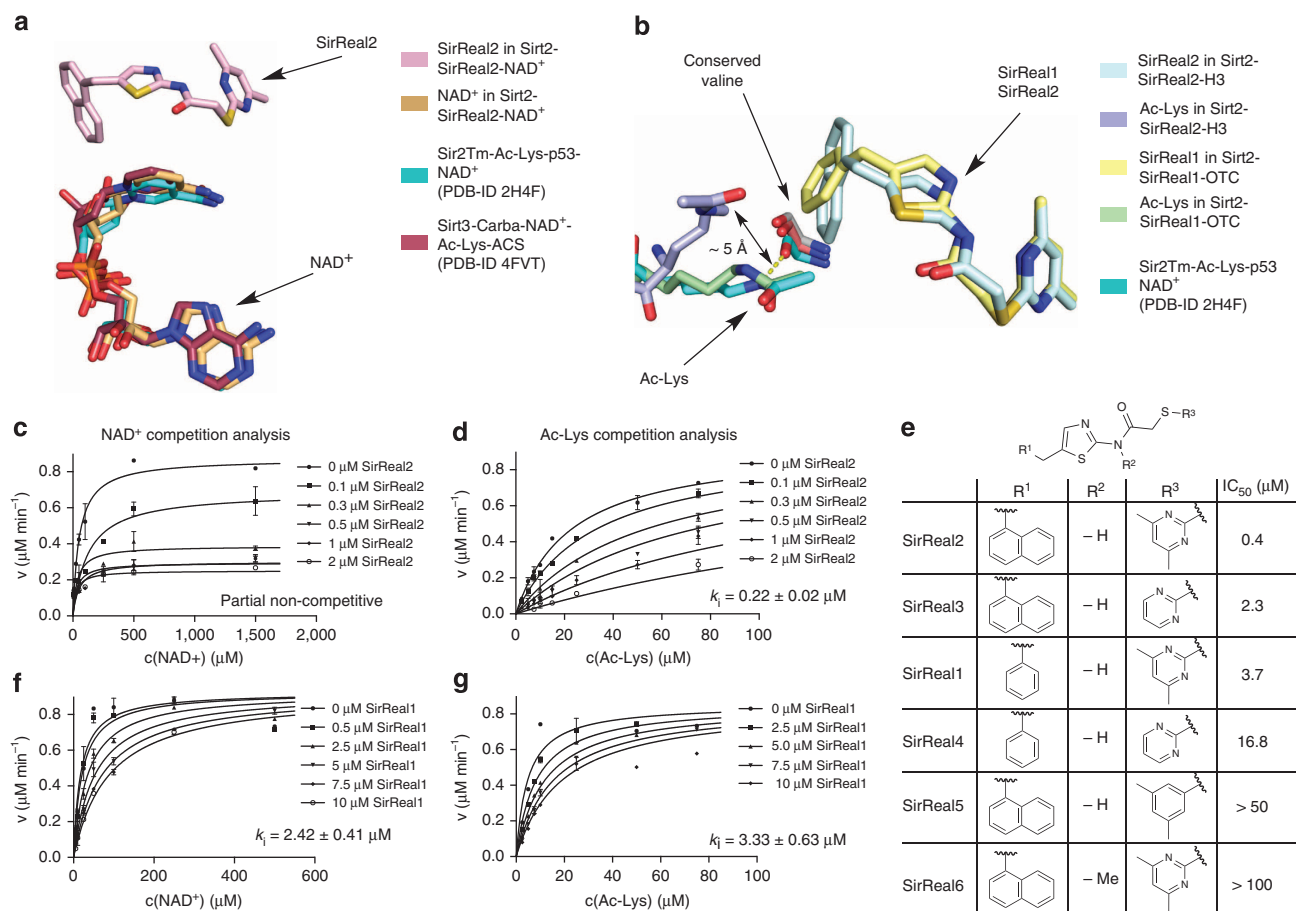
Figure 5 | SirReal inhibitors suppress Sirt2 activity via a unique mechanism. (a) Superposition of Sirt2–SirReal2–NAD$^+$ with ternary sirtuin complexes (Sir2Tm: PDB-ID 2H4F, aquamarine; Sirt3: PDB-ID 4FVT, raspberry) shows that NAD$^+$ in Sirt2–SirReal2–NAD$^+$ adopts a very similar kinked conformation to the one observed in ternary sirtuin complexes. The NCA ribose moiety of NAD$^+$ in Sirt2–SirReal2–NAD$^+$ shares more resemblance to the position of NCA ribose of NAD$^+$ in 2H4F than to the one in 4FVT. **(b)** Overlay of Sirt2–SirReal2–H3, Sirt2–SirReal1–OTC with 2H4F of Fig. 4a. The bulky naphthyl moiety of SirReal2 forces the acetyl-lysine out of its physiological position, which can be seen in the ternary sirtuin complex of Sir2Tm, by ~5 Å. In this new position, the N$_\epsilon$-group of the acetyl-lysine of Sirt2–SirReal2–H3 cannot hydrogen bond to the backbone carbonyl-O of the conserved Val232. The less bulky benzyl moiety of SirReal1 allows a similar acetyl-lysine binding to Sirt2 as observed in the ternary complex of Sir2Tm. However, the presence of SirReal1 slightly enlarges the distance between the backbone carbonyl-O of Val233 to the N$_\epsilon$ of the acetyl-lysine, thus disabling hydrogen bond formation. **(c,d,f,g)** Competition analyses of SirReal1/2-mediated inhibition. SirReal2 is a partial non-competitive inhibitor towards NAD$^+$, while SirReal1 functions as a NAD$^+$-competitive inhibitor. SirReal1 and SirReal2 are both competitive to the acetyl-lysine peptide. Data are presented as mean ± s.d. ($n = 2$). **(e)** Structure–activity relationships (SAR) for SirReal inhibitors. Only the combination of the bulky naphthyl moiety with the DMP and the non-methylated amide results in submicromolar Sirt2 inhibition. Inhibition data were determined using the substrate ZMAL ($n = 3$).

site. It is more pronounced in comparison with the Sirt2 structure in complex with ADPR (PDB-ID 3ZGV, Fig. 3e) than with the structure of Sirt2–apo (PDB-ID 3ZGO, Fig. 3e).

A site of major rearrangement is the selectivity pocket of the hinge region, where the DMP ring of SirReal2 is bound (Fig. 3e). Here the loop region from Lys136–Phe143 is substantially shifted upwards with respect to the Sirt2–apo structure and forms a lid above the DMP moiety. These residues seem to be more flexible, indicated by high *B*-factors, in structures of the closed conformation such as the Sirt2–ADPR or Sirt2–ADPR–NCA complexes (Supplementary Fig. 2) than in structures of the open conformation.

Another site of SirReal2-induced rearrangement is observed in the acetyl-lysine-binding site. Here the side chains of the residues forming the highly hydrophobic acetyl-lysine tunnel, Tyr104, Phe119, Phe131, Phe234 and Phe235 are shifted (Fig. 3e). In particular, the side chains of Phe235 and Tyr104 that usually cap the acetyl-lysine are rotated towards the surface of Sirt2. Surprisingly, this rearrangement does not prevent Sirt2 from

binding its acetyl-lysine peptide substrate, but deacetylation and the domain closure is blocked effectively.

Kinetic analyses of SirReal-mediated inhibition. In the course of the investigation SirReal-mediated inhibition, we also determined the crystal structure of another aminothiazole, termed SirReal1 (**2**, Fig. 4a), in complex with Sirt2 and a different acetyl-lysine peptide substrate. The latter is derived from ornithine transcarbamoylase (OTC, structure termed Sirt2–SirReal1–OTC). SirReal1 has a benzyl instead of a naphthyl-methyl substituent on the aminothiazole and is 26-fold less potent than SirReal2 in the same *in vitro* assay, but it retains high Sirt2 selectivity and shows similar behaviour in thermal stability assays (Supplementary Fig. 1b,c, Fig. 4b). Despite the presence of a different acetyl-lysine peptide, the structure of Sirt2–SirReal1–OTC bears a high resemblance to the Sirt2–SirReal2 complexes (r.m.s.d. (C$_\alpha$ atoms) = 0.44 Å to Sirt2–SirReal2–H3, 0.59 Å to Sirt2–SirReal2–NAD$^+$, Fig. 4c). SirReal1 also locks Sirt2 in the

a

```
Consensus                          .    .  .   ::   ***:*   .  .*:* :*.
Sirt1 244 ---------- ------EDAV KLLQE--CKK IIVLTGAGVS VSCGIPDFRS
Sirt2  65 ---------- ------EGVA RYMQSERCRR VICLVGAGIS TSAGIPDFRS
Sirt3 126 ---------- ------QDVA ELIRARACQR VVVMVGAGIS TPSGIPDFRS
Sirt4  29 IGLFVPASPP LDPEKVKELQ RFITL--SKR LLVMTGAGIS TESGIPDXRS
Sirt5  41 ---------- ------ADFR KFFAK--AKH IVIISGAGVS AESGVPTFRG
Sirt6  35 ---------- ------WELA RLVWQ--SSS VVFHTGAGIS TASGIPDFRG

Consensus                                                     .   .
Sirt1 277 RD-GIYARLA VDFPDLDPQ AMFDIEYFRK DPRPFFKF-- AKEIYPGQFQ
Sirt2  99 PSTGLYDN-L EKYH-LPYPE AIFEISYFKK HPEPFFAL-- AKELYPGQFK
Sirt3 160 PGSGLYSN-L QQYD-LPYPE AIFELPFFFH NPKPFFTL-- AKELYPGNYK
Sirt4  78 EKVGLYAR-T DRRP-IQHGD FVRSAPIR-- --QRWARNF VGWPQFSSSQ
Sirt5  73 AG-GYWRK-W -------QAQ DLATPLAFAH NPSRVWEFYH YRREVMGSAE
Sirt6  67 PH-GVWTM-E ---------- ---------- ERGLA-  KFDTTESAR

Consensus *.  . :          *        :**:*  *.  .:*      .  :  ** .*
Sirt1 324 PSLCHKFIAL SD----KEGK LLRNYTQNID TLEQVAGIQ- -RIIQCHGSF
Sirt2 145 PTICHYFMRL LK----DKGL LLRCYTQNID TLERIAGLEQ EDLVEAHGTF
Sirt3 206 PNVTHYFLRL LH----DKGL LLRLYTQNID GLERVSGIPA SKLVEAHGTF
Sirt4 122 PNPAHWALST WE----KLGK LYWLVTQNVD ALHTKAGSR- -RLTELHGCM
Sirt5 114 PNAGHRAIAE CETRLGKQGR RVVVITQNID ELHRKAGTK- -NLLEIHGSL
Sirt6  91 PTQTHMALVQ LE----RVGL LRFLVSQNVD G

Consensus      *        *
Sirt1 368 ATASCLI--C KYKVDIE--- ---------- ---------- ----AVRGDI
Sirt2 191 YTSHCVSASC RHEYPLS--- ---------- ---------- ----WMKEKI
Sirt3 252 ASATCTDV-- QRPFPSE--- ---------- ---------- ----DIRADV
Sirt4 166 DRVLCLD--C GEQTPPGVLQ ERFQVLNPTW SAEAHGLAPD GDVFLSEEQV
Sirt5 162 FKTRCTS--C GVVAENY--- ---KS--PIC PALSGKGAPE PGTQDASIPV
Sirt6 137 FVEECAK--C KTQYVRDTVV GT-------- ---------- ----MGLKAI

Consensus          .   ::   ::    :   :
Sirt1 388 FNQVVPRC-- --PRCPADEP LAIMKPEIVF FGENLPEQFH RAMKYDKDEV
Sirt2 214 FSEVTPKC-- --ED-----C QSLVKPDIVF FGESLPARFF SCMQSDFLKV
Sirt3 273 MADRVPRC-- --PV-----C TGVVKPDIVF FGEPLPQR-F LLHVVDFPMA
Sirt4 214 RSFQVPTC-- --VQ-----C GGHLKPDVVF FGDTVNPDKV DFVHKRVKEA
Sirt5 202 EKLPRCEE-- --AG-----C GGLLRPHVVA FGENLDPAIL EEVDRELAHC
Sirt6 163 GRLCTVAKAR GLRA-----C RGELRDTILD WEDSLPDRDL ALADEASRNA

Consensus *   :  :*:*   :     .                         .*
Sirt1 434 DLLIVIGSSL KVRPVALIPS SIP-HEVPQI LINREPLP-- ----------
Sirt2 255 DLLLVMGTSL QVQPFASLIS KAP-LSTPRL LINKEKAGQS DPFLGMIMGL
Sirt3 313 DLLLILGTSL EVEPFASLTE AVR-SSVPRL LINRDLVG-- ----------
Sirt4 255 DSLLVVGSSL QVYSGYRFIL TAWEKKLPIA ILNIGPTR-- ----------
Sirt5 243 DLCLVVGTSS VVYPAAMFAP QVAARGVPVA EFNTETTP-- ----------
Sirt6 208 DLSITLGTSL QIRPSGNLPL ATKRRGGRLV IVNLQPTK-- ----------

Consensus               .  .
Sirt1 471 ----HL---- -HFDVLLGD CDVIINELCH RL-GGEYA
Sirt2 305 GGGMDFDSKK AYRDVAWLGE CDQGCLALAE LL-GWKKE
Sirt3 350 ----PLAWHP RSRDVAQLGD VVHGVESLVE LL-GWTEE
Sirt4 293 ----SD---- DLACLKLNSR CGELLP---- ---LIDPC
Sirt5 281 ----AT---- NRFRFHFQGP CGTTLPEALA -CHENETV
Sirt6 246 ----HD---- RHADLRIHGY VDEVMTRLMK HL-GLEIP
```

b

Ile213 · Leu134 · Ile118 · Leu138 · Leu206 · Phe143 · Leu103 · Thr171

Sirt2-SirReal2-NAD$^+$
SirReal2

c

Met296 · Phe312 · Cys380 · Ile316 · Ile279

Sirt1-HM
SirReal2

d

Val272 · Gly265 · Gly232 · Tyr204

Sirt3-HM
SirReal2

Figure 6 | SirReal2 selectively inhibits Sirt2 via a Sirt2-specific amino acid network. (**a**) Structural sequence alignment of the Sirt1–6 deacylase domain. The residues that presumably interact with SirReal2 are highlighted in yellow if they are equivalent to the residues of Sirt2. If they differ from the residues of Sirt2, they are highlighted in red. The structural sequence alignment was generated using T-Coffee[35] and slightly modified. (**b–d**) Surface representation of the binding pockets of SirReal2 in Sirt2–SirReal2–NAD$^+$ and in the homology models of Sirt1 (Sirt1-HM) and Sirt3 (Sirt3-HM). The residues that differ in the three isotypes are represented as sticks (Sirt2, slate blue; Sirt1, brown; Sirt3, turquoise). SirReal2 is shown as light pink sticks (Sirt2–SirReal2–NAD$^+$), lime sticks (Sirt1-HM) and olive sticks (Sirt3-HM). Despite the highly conserved active site, the binding pockets appear in very different shapes due to differences in the amino acid sequence. In case of Sirt1 the amino acids that contribute to an unfavourable binding of SirReal2 are Ile279, Met296, Phe312, Ile316 and Cys380. In the case of Sirt3, the amino acids are Tyr204, Gly232, Gly265 and Val272.

open conformation and shows an almost identical interaction pattern as observed for SirReal2 (Fig. 4d,e).

To get insights into the inhibition mechanism, we first compared the structures of Sirt2–SirReal complexes with the available sirtuin structures lacking inhibitors. For the cosubstrate NAD$^+$, the binding mode does not differ substantially. NAD$^+$ of Sirt2–SirReal2–NAD$^+$ also adopts a kinked conformation with a similar network of hydrophilic and hydrophobic interactions as observed for NAD$^+$ or Carba-NAD$^+$ in ternary sirtuin complexes (PDB-ID 2H4F[34], Sir2Tm-Ac-Lys-p53-peptide-NAD$^+$, PDB-ID 4FVT[23], Sirt3-Carba-NAD$^+$-Ac-Lys-ACS-peptide, Fig. 5a). As the main difference, the NCA ribose moiety of Carba-NAD$^+$ is rotated ~30° around its glycosidic bond compared with NAD$^+$ in Sirt2–SirReal2–NAD$^+$ or Sir2Tm-Ac-Lys-p53-peptide-NAD$^+$. The binding mode of NAD$^+$ in Sirt2–SirReal2–NAD$^+$ therefore shares a higher resemblance to the conformation of NAD$^+$ in the ternary complex with Sir2Tm.

The acetyl-lysine-binding modes in ternary sirtuin complexes and Sirt2–SirReal2 structures on the other hand show substantial differences (Fig. 5b). In uninhibited sirtuin-acetyl-lysine-peptide structures, the acetyl-lysine-containing peptide binds in the cleft between the zinc-binding and NAD$^+$-binding domain, respectively, inserting its acetyl-lysine into a hydrophobic tunnel that is formed by several highly conserved phenylalanines. The binding of the acetyl-lysine is further stabilized by a hydrogen bond between the N$_\varepsilon$–H of the acetyl-lysine and the backbone carbonyl-O of a conserved valine. The hydrophobic acetyl-lysine–binding tunnel is not formed in all Sirt2–SirReal structures, since Phe235, which usually caps the acetyl-lysine, is rotated ~90° towards the surface. Moreover, the bulky naphthyl moiety of SirReal2 forces the acetyl-lysine ~5 Å out of its physiological position, which can be seen in ternary complexes of sirtuins (Sir2Tm-Ac-Lys-p53-peptide-NAD$^+$, PDB-ID 2H4F, Sirt3-Ac-Lys-ACS-peptide-Carba-NAD$^+$, PDB-ID 4FVT, Fig. 5b).

In the Sirt2 complex with SirReal1, the acetyl-lysine-binding mode is different. The acetyl-lysine adopts an almost physiological position, as it is observed in the above-mentioned ternary sirtuin complexes. However, even in case of SirReal1, the benzyl moiety of SirReal1 shifts the acetyl-lysine of the OTC peptide

7

Figure 7 | SirReal2 inhibits Sirt2 *in vivo*. (**a**) Acetylation level of the microtubule network (red) in the presence or absence of SirReal2 at a concentration of 20 μM. Treatment with SirReal2 leads to hyperacetylation of the microtubule network in a similar manner as observed for the Sirt2 inhibitor AGK2. Treatment with SirReal6 on the other hand results in no substantial change of acetylation level. The scale bar represents 5 μm ($n = 4$). (**b**) Abundance of BubR1 after incubation with SirReal2 ($n = 3$). (**c**) SirReal2 does not alter p53-Lys382-acetylation after ultraviolet damage ($n = 3$). Raw immunofluorescent images and uncropped blots are shown in the Supplementary Figs 8–10.

towards His187, weakening the formation of the hydrogen bond between the N_ε–H of the acetyl-lysine and the backbone carbonyl-O of the conserved valine (distance between carbonyl-O of valine and N_ε-KAc: 3.2 Å in Sirt2–SirReal1–OTC, 2.5–2.7 Å in ternary complexes).

To investigate the SirReal-mediated inhibition kinetics, we performed competition analyses for SirReal1 and SirReal2 (Fig. 5c,d,f and g). SirReal2 is partially non-competitive and SirReal1 is competitive towards NAD^+ (Fig. 5c,f). Both SirReal inhibitors also exhibit acetyl-lysine competition with inhibition constants of 0.22 μM for SirReal2 and 3.33 μM for SirReal1 (Fig. 5d,g). This is in line with the protrusion into the acetyl-lysine-binding site that was seen in the crystal structures. However, despite competition towards acetyl-lysine substrates or the cosubstrate NAD^+, the presence of SirReal1/2 inhibitors does not disable Sirt2 to bind its substrates.

For further exploration of the SirReal-mediated Sirt2 inhibition, we synthesized several SirReal derivatives (SirReal3–6, Supplementary Fig. 5, Supplementary Notes) and determined their inhibitory potencies (Fig. 5e). Only the combined presence of the naphthyl substituent with the DMP moiety and the non-methylated amide leads to a submicromolar Sirt2 inhibition. The substitution of the DMP moiety with a dimethylmercaptophenyl substituent or the methylation of the amide-nitrogen results in a significant loss of inhibition (>100-fold). This suggests that the formation of the intramolecular hydrogen bond and the resulting structural rigidity of Sirt2-bound SirReal2 are indispensable for potent Sirt2 inhibition.

Structural aspects of isotype-selective inhibition. One striking feature of the SirReal2-mediated inhibition is its isotype selectivity. SirReal2 inhibits Sirt2 >1,000-fold more potently than Sirt1, Sirt3, Sirt4, Sirt5 and Sirt6 and it is therefore one of the most selective sirtuin inhibitors known to date.

To analyse the basis of this high isotype selectivity, we created a structural sequence alignment of the deacylase domain of Sirt1–6

and compared the crystal structure of the Sirt2–SirReal2 complex with available crystal structures of sirtuins in their open conformation (Fig. 6a, Supplementary Fig. 7a,b)[35]. Assuming that SirReal2 binds to the other sirtuin isotypes in a similar fashion as observed for Sirt2, Sirt4–6 exhibit major differences in their amino acid sequence. The structural differences are also very pronounced (Supplementary Fig. 7a) rationalizing the observed lacking *in vitro* inhibition of Sirt4–6 by SirReal2. Sirt1 and Sirt3, on the other hand, are phylogenetically more closely related to Sirt2 and show only minor sequence variations[36]. Their conformation is more similar to the Sirt2–SirReal2–NAD^+ complex than to the conformation of the isotypes Sirt5/6 (Supplementary Fig. 7b). But they still show major structural differences (r.m.s.d. (C_α atoms) = 1.6 Å). As it was not possible to dock SirReal2 in any of the available Sirt1 and Sirt3 X-ray crystal structures (Supplementary Methods), we wanted to probe whether Sirt1 and Sirt3 were able to adopt a similar conformation as observed in the Sirt2–SirReal2 structures that would allow binding of SirReal2. This would enable us to see whether the minor sequence variations within the deacylase domain of Sirt1–3 would have an influence on SirReal2 binding. Therefore, we generated homology models of Sirt1 (Sirt1-HM) and Sirt3 (Sirt3-HM) based on our Sirt2–SirReal2 structures (Supplementary Methods). Stereochemical analyses as well as molecular dynamics simulations indicated high-quality model structures, and it was indeed possible to dock SirReal2 into these homology models (Supplementary Fig. 7c–h). However, the docking poses of SirReal2 in Sirt1-HM and Sirt3-HM gave less favourable docking scores compared with the requisite scores for the docking poses of SirReal2 in Sirt2–SirReal2 structures. Here the position and the conformation of SirReal2 were correctly predicted (Fig. 6b). In case of Sirt1, residues Leu103, Ile118, Leu134, Leu138 and Leu206 of Sirt2 are substituted with Ile279, Met296, Phe312, Ile316 and Cys380 (Fig. 6c). Cys380 gives the hypothetical selectivity pocket of SirReal2 in Sirt1-HM a very different shape and changes its surface characteristics. The bulky

Table 1 | Data collection and refinement statistics.

	Sirt2–SirReal1–OTC*	Sirt2–SirReal2–H3*	Sirt2–SirReal2–NAD$^+$*
Data collection			
Space group	$P2_1$	$P2_1$	$I2$
Cell dimensions (Å)			
a, b, c (Å)	36.21, 73.75, 55.86	35.99, 73.30, 55.29	83.7, 54.51, 96.69
α, β, γ (°)	90, 94.71, 90	90, 95.23, 90	90, 114.8, 90
Resolution (Å)†	44.43–1.45 (1.48–1.45)	44.02–1.42 (1.44–1.42)	48.28–1.88 (1.92–1.88)
R_{merge}	0.126 (1.009)	0.060 (0.922)	0.068 (1.351)
R_{pim}	0.054 (0.471)	0.035 (0.546)	0.029 (0.583)
$I/\sigma I$	9.2 (1.7)	11.9 (1.5)	19.3 (1.5)
Completeness (%)	99.9 (99.9)	99.6 (99.6)	100 (100)
CC1/2	0.995 (0.549)	0.999 (0.534)	0.999 (0.585)
Redundancy	6.5 (6.2)	3.7 (3.8)	6.6 (6.4)
Refinement			
Resolution (Å)	44.43–1.45	44.02–1.42	48.28–1.88
No. of reflections	334,389 (16,809)	199,366 (10,043)	213,173 (12,962)
R_{work}/R_{free} (%)	26.0/28.2	18.1/18.8	20.2/24.7
No. of atoms			
Protein	2,251	2,406	2,350
SirReal inhibitor	25	29	29
Ac-Lys peptide/NAD$^+$	32	12	44
Zn^{2+}	1	1	1
Water	156	242	99
B-factors (Å^2)			
Protein	17.3	21.1	38.4
SirReal inhibitor	27.0	25.1	32.2
Ac-Lys peptide/NAD$^+$	29.8	48.3	41.8
Zn^{2+}	11.7	14.8	30.7
Water	20.5	27.0	36.0
r.m.s. deviations			
Bond lengths (Å)	0.012	0.008	0.014
Bond angles (°)	1.58	1.33	1.65

Ac-Lys, acetyl-lysine; r.m.s., root mean squared.
*Each data set was obtained from one single crystal. Sirt2–SirReal1–OTC and Sirt2–SirReal2–H3 were collected at 1.0 Å at the Swiss Light Source (Villigen, Switzerland), Sirt2–SirReal2–NAD$^+$ was collected with an in-house X-ray source at 1.5418 Å.
†Values in parentheses are for highest-resolution shell.

Phe312 and Ile316 as well as Met296 and Ile279 also tighten the EC-site, resulting in an unfavourable orientation of the aminothiazole and naphthyl moieties in possible docking poses. In the case of Sirt3, the differences are mainly located at the selectivity pocket. Here Phe143, Thr171, Leu206 and Ile213 of Sirt2 are substituted by Tyr204, Gly232, Gly265 and Val272 (Fig. 6d). The less bulky Gly232, Gly265, Val272 of Sirt3 form a much wider and also more solvent-accessible selectivity pocket as compared with the Sirt2–SirReal2 structures. In contrast to the SirReal2-binding pockets of the homology models of Sirt1 and Sirt3, SirReal2 bound to Sirt2 can adopt a conformation that is in almost perfect complementarity with the protein, which is stabilized by the intramolecular hydrogen bond between the DMP substituent and the amide. This is not possible in Sirt1 and Sirt3 and also rationalizes the observed isotype selectivity.

In vivo inhibition of Sirt2. To validate that SirReal2 could be used as a tool to investigate the effects of Sirt2 inhibition in a cellular setting, we incubated HeLa cells with SirReal2 at various concentrations and determined the level of α-tubulin acetylation (Supplementary Fig. 8a,b). Incubation with SirReal2, but not with SirReal6, resulted in a significant increase of α-tubulin acetylation consistent with an *in vivo* inhibition of Sirt2 as shown previously[37]. These changes are not as pronounced when compared with the changes induced by the inhibition of the other main tubulin deacetylase KDAC6 (refs 38,39). KDAC6 activity is not affected *in vitro* in the presence of SirReal2 (Supplementary

Fig. 8c). To verify the observations from the western blot data, we also visualized the acetylation level by means of immunofluorescence microscopy. Again, the incubation with SirReal2 resulted in a partial increase of the acetylation of the microtubule network similar to the effects observed after treatment with the Sirt2-inhibitor AGK2 (Fig. 7a, Supplementary Fig. 9)[39,40]. SirReal6, on the other hand, does not alter microtubule acetylation. In addition, we analysed another Sirt2 target. Recently, we reported that the stability of spindle assembly checkpoint protein BubR1 is under control of Sirt2 (ref. 41). A decline in BubR1 over time has been linked to mammalian aging[42]. Deacetylation of Lys668 of BubR1 by Sirt2 inhibits the ubiquitination of BubR1 and its designation to the proteasome. Therefore, the abundance of BubR1 can be used as a functional measure for *in vivo* Sirt2 inhibition. Incubation with SirReal2 indeed significantly resulted in a dose-dependent depletion of BubR1, whereas SirReal5/6 did not influence BubR1 concentrations (Fig. 7b, Supplementary Fig. 8d,e). We also found that SirReal2 treatment did not alter cell cycle distribution, ruling out that the effect on BubR1 was indirect through induction of cell cycle changes (Supplementary Fig. 8f). To determine if SirReal2 selectively inhibits Sirt2 *in vivo*, we assessed p53 acetylation following genotoxic stress (Fig. 7c, Supplementary Fig. 10a). Acetylation of p53 occurs in response to ultraviolet exposure to cells[43] and this acetylation is regulated, in part, by the isotype Sirt1 (refs 44,45). On exposure to ultraviolet light, we detected an increase in acetylation of p53, which was further increased on treatment with the pan-sirtuin inhibitor

NCA. However, we did not observe an increase in acetylation of p53 following treatment with SirReal2/5/6. Similarly, we also tested if SirReal2 could inhibit Sirt3 in cells by assessing mitochondrial protein acetylation. Sirt3 has previously been demonstrated to regulate global mitochondrial protein acetylation[46]. Following treatment with SirReal2 or NCA as a positive control, we purified mitochondria and assessed protein acetylation by western blotting. We found that treatment with NCA leads to an increase in the acetylation of mitochondrial proteins, whereas treatment with SirReal2 did not, suggesting that SirReal2 is unable to regulate Sirt3 activity in cells (Supplementary Fig. 10b). These results confirm the *in vitro* observations and indicate that SirReal2 has a strong specificity towards Sirt2 *in vivo* when compared with the other members of Class-I sirtuins Sirt1 and Sirt3.

Discussion

There are many indications that sirtuins play an important role in neurodegeneration, cancer, bacterial infections and inflammation and that a modulation of Sirt2 activity could be a new strategy for pharmaceutical intervention. However, the physiological functions of Sirt2 are far from being completely understood and conclusive evidence for the suitability of Sirt2 as a pharmaceutical target is, at least in some cases, missing. To further explore Sirt2 function in a cellular environment, there is a definite need for selective and potent Sirt2 modulators.

So far, most sirtuin modulators lack either potency, selectivity or drug-like physicochemical properties. Recent screening campaigns have identified several potent and/or selective inhibitors[15,24–26]; however, with the exception of the macrocyclic peptide S2iL5, it is not clear how these inhibitors bind to Sirt2. And although several X-ray structures of sirtuins in complex with inhibitors have been reported lately[28,33,47–51], these structures do little to reveal a rationale for a Sirt2-selective inhibition.

With the identification of the SirReal inhibitors, we establish the structural basis for Sirt2-selective inhibition and report a new potent Sirt2-selective inhibitor scaffold. As noted above, the intramolecular hydrogen bond between the amide of the aminothiazole and a nitrogen atom of the DMP moiety gives the inhibitor a rigid form that can act as a molecular wedge locking the enzyme conformation with subsequent Sirt2 inhibition. Not only essential for the potency, the intramolecular bond also seems to play an important role for the compound's Sirt2 selectivity, as it can only be formed when bound in perfect complementarity to the active site of Sirt2. This seems not to be possible if bound to Sirt1 or Sirt3.

Another important aspect alongside the internal hydrogen bond of SirReal-mediated Sirt2 inhibition is the exploitation of the selectivity pocket by SirReal inhibitors. The only other isotype-selective sirtuin inhibitors with known structures, CHIC-35 (Sirt1-selective)[48], EX-527 (Sirt1-selective)[33] and SRT1720 (Sirt3-selective)[49] either bind to the EC-site and/or to the acetyl-lysine-binding site but neither the indole inhibitors nor SRT1720 or any of the inhibitors whose binding modes have been elucidated by means of X-ray crystallography occupy the selectivity pocket (Fig. 6). This pocket is formed by two loops that connect the Rossmann fold domain with the smaller zinc-binding domain. The residues that form this pocket significantly differ within the sirtuin family and targeting this pocket may present a new strategy for selective sirtuin inhibitor design. These particular findings would not have been discovered with the use of computational methods and the available Sirt2 structures.

In conclusion, with the identification of SirReal2, we provide an isotype-selective drug-like inhibitor with optimized potency and physicochemical properties in comparison with previously published Sirt2 inhibitors (Supplementary Table 1). We established valuable structural insights into selective Sirt2 inhibition and show that SirReal2 inhibits Sirt2 *in vivo* without affecting the activity of the other Class-I sirtuins Sirt1 and Sirt3. The observed selectivity towards Sirt3 may, in part, stem from a lack of penetration into the mitochondria but the cellular net result is as desired. SirReal2 may therefore be used for further cellular studies to probe Sirt2 biology. Our findings may constitute the basis for further selective sirtuin inhibitor development and provide a new tool for sirtuin biology.

Methods

Cloning. The gene sequences coding for human Sirt2$_{56-356}$ (Uniprot: Q8IXJ6) or human Sirt3$_{118-395}$ (Uniprot: Q9NTG) were cloned in a modified pET15b vector that contained His$_{10}$-Tag instead of a His$_{6}$-Tag and a cleavage site for TEV protease instead of one for thrombin.

Protein expression and purification. Human Sirt1$_{133-747}$ (Uniprot: Q96EB6), human Sirt2$_{25-389}$, human Sirt3$_{101-399}$, human Sirt5$_{34-302}$ (Uniprot: Q9NXA8) and human Sirt6$_{13-308}$ (Uniprot: Q8N6T7) were purified as described before[47,52,53]. Human Sirt4$_{25-314}$ (Uniprot: Q9Y6E7) was expressed and purified as described before[54] with the exception that autoinduction with 0.2% (w/v) lactose in TB media was used for expression.

Sirt2$_{56-356}$ and Sirt3$_{118-395}$ were expressed in *E. coli* strain BL21(DE3)Codonplus RIPL cells overnight at 18 °C. Overexpression was induced with isopropyl-β-D-thiogalactoside (0.1 mM) at an OD$_{600}$ of 0.6. Cells were harvested, resuspended in lysis buffer (Sirt2$_{56-356}$: 50 mM Tris/HCl, 500 mM NaCl, 5% (v/v) glycerol, 5 mM β-mercaptoethanol, pH 8.0; Sirt3$_{118-395}$: 50 mM HEPES, 500 mM NaCl, 5% (v/v) glycerol, 5 mM β-mercaptoethanol, pH 7.5) and lysed using a microfluidizer (Microfluidics). After the removal of cell debris, the supernatant was applied to a HisTrapFF 5 ml column (GE Healthcare), washed intensively before TEV protease (excess) was applied directly on the column. After an overnight digestion at 4 °C, the digested protein was eluted with lysis buffer, concentrated and further purified using a Superdex S75 26/60 gel filtration column (Sirt2$_{56-356}$: 25 mM Tris/HCl, 150 mM NaCl, pH 8.0; Sirt3$_{118-395}$: 25 mM HEPES, 200 mM NaCl, 5% (v/v) glycerol, 5 mM β-mercaptoethanol, pH 7.5). Sirtuin-containing fractions were collected and concentrated to 20 mg ml^{-1}. All purification steps were monitored using SDS-polyacrylamide gel electrophoresis (SDS–PAGE). Protein concentration was determined by the Bradford assay (Roth).

***In vitro* sirtuin assay.** Initial screens were conducted with a high-throughput fluorescence-based assay using the substrate ZMAL (Z-Lys(Acetyl)-AMC) that was synthesized according to published procedures[29]. For this human Sirt1$_{133-747}$, human Sirt2$_{25-389}$, human Sirt3$_{101-399}$ or Sirt3$_{118-395}$ were mixed with assay buffer (50 mM Tris/HCl, 137 mM NaCl, 2.7 mM KCl, 1 mM MgCl$_2$, pH 8.0), β-NAD$^+$ (final assay concentration 500 µM), the substrate ZMAL (final assay concentration 10.5 µM from a 12.6 mM stock solution in DMSO) and the respective inhibitor in DMSO at various concentrations or DMSO as a control (final DMSO concentration 5–20% (v/v)). The mixture was incubated at 37 °C for 4 h, with agitation at 150 r.p.m. Deacetylation was then stopped by the addition of a solution containing NCA and trypsin (50 mM Tris/HCl, 100 mM NaCl, 6.7% (v/v) DMSO, trypsin 5.5 U µl^{-1}, 8 mM NCA, pH 8.0, 60 µl) and the mixture was then incubated for tryptic digestion of the deacetylated product to release the fluorophor (20 min, 37 °C, 150 r.p.m.). Then the fluorescence intensity was measured in a microplate reader (BMG Polarstar, λ_{ex} 390 nm, λ_{em} 460 nm). The amount of inhibition was determined with respect to the mixture with only DMSO. IC$_{50}$ values were determined with Graphpad Prism software using a non-linear regression to fit the dose–response curve. SirReal1 and SirReal2 were also tested for Sirt1–3 inhibition with a non-labelled acetyl-lysine peptide substrate (based on α-tubulin with two additional tryptophans (residues 36–44, H-PSDK(Acetyl)TIGGWW-NH$_2$, 10 µM, Supplementary Methods). SirReal2 was also tested for Sirt5–6 inhibition with non-labelled acyl-lysine peptide substrates (Sirt5: Benzoyl-GVLK(Succinyl)EYGV-NH$_2$, 10 µM; Sirt6: Ac-EALPKK(Myristoyl)TGG-NH$_2$, 10 µM) The substrate was incubated (10 min, ~0.5 µM Sirt1/2/3/5/6, 500 µM β-NAD$^+$, 5–20% (v/v) DMSO, 50 mM Tris/HCl, 137 mM NaCl, 2.7 mM KCl, 1 mM MgCl$_2$, pH 8.0), stopped by the addition of trifluoroacetic acid (TFA, 10% (v/v), final concentration 1% (v/v)). The components of the stopped reaction mixture were separated by HPLC (Agilent 1100, Phenomenex reversed phase column Kinetex RP18 2.7 µm, 50 × 3 mm) using a linear gradient of acetonitrile (20–60% (v/v) acetonitrile, 0.1% (v/v) TFA, 0.6 ml min^{-1}). Peaks of acetylated and deacetylated substrate were quantified by absorption at 280 nm. Sirt4-dependent deacetylation reactions were performed with an acetylated Nnt397-peptide (H-NITKLLK(Acetyl)AISPDK-NH$_2$, 250 µM, GL Biochem.), in 50 mM Tris/HCl, 150 mM NaCl, pH 7.5). Samples were taken between 0 and 45 min and reactions were stopped by mixing 1:1 with 0.5% (v/v) TFA. The samples were then diluted to a peptide concentration of 5 µM with 0.1% (v/v) formic acid and analysed on an EASY-nLCII connected to a LTQ mass

spectrometer (Thermo Fisher Scientific). Peptides were separated by a linear gradient of acetonitrile (0–100% (v/v), 0.1% (v/v) TFA, 300 nl min^{-1}) on a reprosil C18 reversed phase column. Peak areas of acetylated and deacetylated peptides were extracted using Skyline[55]. A solution with DMSO was used as a negative control while a solution with the physiological inhibitor NCA served as a positive control (Fig. 1c). Owing to the lack of a suitable screening assay for human Sirt7, we focused our studies on isotypes Sirt1–6. Fluor-de-Lys assays (Enzo Life Sciences) were conducted according to the manual using the HDAC8 Fluor-de-Lys deacetylase substrate (BML-KI178-0005).

Protein crystallization. All crystallization trials were performed in 96-well plates (Intelli-Plate 96-3 Low Profile, Art Robbins Instruments) using an Oryx nano pipetting robot (Douglas Instruments). Reservoir solutions were precooled to 4 °C and screens were then pipetted at 20 °C.

For co-crystallization experiments with SirReal1 and SirReal2, a solution of the truncated Sirt2$_{56-356}$ (20 mg ml^{-1} final concentration) was preincubated with a saturated aminothiazole solution (100 mM stock solution in DMSO, 1–2% (v/v) DMSO final concentration) in the presence of H3 peptide (100 mM stock solution in 25 mM HEPES, 200 mM NaCl, 5% (v/v) glycerol, pH 7.5, 2 mM final concentration, derived from acetylated Histone H3 (residues 11–17), Peptide Specialty Laboratories), acetylated OTC oligopeptide (100 mM stock solution in DMSO, 2 mM final concentration, derived from ornithine transcarbamoylase (residues 83–92), Peptide Specialty Laboratories) or β-NAD$^+$ (Sigma-Aldrich, 100 mM stock solution in 25 mM Tris/HCl, 150 mM NaCl, pH 8.0, 10 mM final concentration) for 60 min at 4 °C, centrifuged (4 °C, 10 min, 16,100 g) and crystallized. Sirt2–SirReal1–OTC–peptide complex crystallized in 25% (w/v) polyethylene glycol (PEG) 3,350 and 0.1 M Bis–Tris buffer at pH of 6.5 and 4 °C, Sirt2–SirReal2–H3–peptide complex crystallized in 2.8 M (NH$_4$)$_2$SO$_4$ and 0.1 M Tris/HCl buffer at pH 9.0 and 4 °C. For both conditions, a protein solution to reservoir solution ratio of 1:3 was used. The Sirt2–SirReal2–NAD$^+$ complex crystallized in 0.1 M KSCN, 30% (w/v) PEG MME 2,000 at 4 °C with a protein solution to reservoir solution ratio of 3:1. The crystals were mounted in nylon loops and if required, cryoprotected by the addition of 20% (v/v) of glycerol before flash cooling in liquid nitrogen.

Crystals of Sirt2 in complex with ADPR (13 mg ml^{-1} final concentration, 20 mM ADPR, 1 M stock solution in 1 M Tris/HCl buffer at pH 9.0) were obtained using 18% (w/v) PEG 10,000 and 0.1 M Bis–Tris buffer at pH 5.75 and 20 °C. The crystals formed after 1 day and were then soaked in a buffer containing 18% (w/v) PEG 10,000, 0.1 M Bis–Tris buffer at pH 5.75, 200 mM NCA for 30 min. They were then mounted in nylon loops after addition of glycerol to a final concentration of 20% (v/v) before flash cooling in liquid nitrogen.

Data collection and processing. Data were collected at beamline X06SA (Sirt2–SirReal2–H3 complex) or X06DA (Sirt2–SirReal1–OTC complex, Sirt2–ADPR–NCA complex) with Pilatus detectors (Dectris) at the Swiss Light Source (Villigen, Switzerland). All experiments were carried out at 100 K with oscillations of 0.25 or 0.5° at an X-ray wavelength of 1.0 Å. The Sirt2–SirReal2–NAD$^+$ complex was determined from data collected on a MicroMax 007HF rotating anode X-ray generator (Rigaku) at an X-ray wavelength of 1.5418 Å, equipped with a mar345 image plate detector (Mar Research). All data sets were processed with Imosflm[56] or XDS[57] and scaled based on the CC* criterion[58] using Aimless[56].

Structure solution and refinement. All structures were solved by molecular replacement using either MOLREP[59] or PHASER[60] with a monomer of Sirt2–ADPR (PDB-ID 3ZGV)[19] or the initial Sirt2-aminothiazole-structure (Sirt2–SirReal2–H3) as a search model. Model building was carried out using Coot[61] and the structure was refined with REFMAC5 (ref. 62). Ligands were generated using the Grade Web Server (Global Phasing Ltd., Cambridge). All structures were validated using the Molprobity server[63].

Sirt2–SirReal1–OTC was refined to a final R_{work} of 26.0% and R_{free} of 28.2% with 98% of all amino acids of the refined model found in the most favored regions of the Ramachandran plot. Sirt2–SirReal2–H3 was refined to a final R_{work} of 18.1% and R_{free} of 18.8% with 98% of all residues falling into the most-favoured region of the Ramachandran plot. The Sirt2–SirReal2–NAD$^+$ complex was refined to a final R_{work} of 20.2% and R_{free} of 24.7% with 97% of all residues in the most-favoured Ramachandran plot regions. Finally, the Sirt2–ADPR–NCA complex was refined to a final R_{work} of 21.1% and R_{free} of 23.9% with 98% of all residues in the most favored Ramachandran plot regions. All structures do not have Ramachandran outliers. Further data collection and refinement statistics are found in Table 1 (Sirt2–SirReal1–OTC, Sirt2–SirReal2–H3, Sirt2–SirReal2–NAD$^+$) and in Supplementary Table 2 (Sirt2–ADPR–NCA).

Most of the residues of all new structures are well defined in the electron density maps except for some parts of the flexible cofactor-binding loop (residues 96–120, Sirt2–SirReal2–NAD$^+$, Sirt2–SirReal2–H3, Sirt2–SirReal1–OTC) and parts of the Sirt2-specific insertion loop (residues 295–305, Sirt2–SirReal2–NAD$^+$, Sirt2–SirReal2–H3, Sirt2–SirReal1–OTC). The weak density for NAD$^+$ in the Sirt2–SirReal2–NAD$^+$ complex may also be due to partial hydrolysis of NAD$^+$ and the formation of different conformers. The visible amino-terminal histidine and methionine visible in the Sirt2–ADPR–NCA complex and Sirt2–SirReal2–

NAD$^+$ complex structures originate from the NdeI restriction site of the modified pET15b vector. σ-weighted $F_o - F_c$ electron density OMIT maps were generated with the Phenix suite[64]. Images were prepared with Pymol (The Pymol Molecular Graphics System, Version 1.6, Schrödinger, LLC), r.m.s.d. values were calculated with SUPERPOSE[65] and the surface of the binding pockets was generated using HOLLOW[66]. The two-dimensional representation of the interactions of NCA with Sirt2 were generated with LigPlot+[67].

Determination of kinetic parameters for SirReal1/2. For SirReal-inhibition kinetics, a mixture of α-tubulin peptide substrate (residues 36–44, H-PSDK (Acetyl)TIGGWW-NH$_2$, 2.5–75 µM, for details about the α-tubulin peptide synthesis see Supplementary Methods), β-NAD$^+$ (5–1,500 µM), SirReal1/2 (various concentrations in 50 mM Tris/HCl, 137 mM NaCl, 2.7 mM KCl, 1 mM MgCl$_2$, 5% (v/v) DMSO, pH 8.0) was incubated (37 °C). The reaction was started by the addition of human Sirt2$_{56-356}$ (2 µM), stopped after 1–50 min with TFA (10% (v/v), final concentration 1% (v/v)) and analysed by HPLC as described above. The peak areas were integrated and converted to initial velocities calculated from the peak areas as the fraction of deacetylated peptide from total peptide. From this, reaction rates in µM min^{-1} were obtained by linear regression, while K_m and k_{cat} were obtained directly from Michaelis–Menten plots using Graphpad Prism software. β-NAD$^+$ (500 µM) was used for the determination of the kinetic parameters for the peptide substrate, 100 µM of peptide substrate was used for the determination of the kinetic parameters for β-NAD$^+$.

Thermal shift assays. Human Sirt2$_{56-356}$ (0.2 mg ml^{-1} final concentration) was mixed with or without ligand containing buffer (25 mM Tris/HCl, 150 mM NaCl, 5% (v/v) DMSO, 1:4,000 Sypro Orange, pH 8.0) in absence or presence of β-NAD$^+$ (100 mM stock solution in 25 mM Tris/HCl, 150 mM NaCl, pH 8.0, final assay concentration 5 mM) or acetylated H3-peptide (100 mM stock solution in 25 mM HEPES, 200 mM NaCl, 5% (v/v) glycerol, pH 7.5, final assay concentration 5 mM). Fluorescence was monitored during a temperature ramp from 25–95 °C (1 °C min^{-1}) using a Bio-Rad iCycler iQ5 (4titude, FrameStar 96-well plates, 4ti-0771, 4titude qPCR Seal, 4ti-0560). Melting temperatures were determined according to published procedures[68] using Graphpad Prism software.

Cell cultivation. HeLa cells (DSMZ accession no. 057) and U2OS cells (ATCC accession no. HTB-96) were grown in Dulbecco's modified Eagle's medium (PAA) containing 10% (v/v) fetal calf serum (FCS, PAA), 1% (v/v) penicillin (PAA), 1% (v/v) streptomycin (PAA), 1% (v/v), L-glutamine (PAA) at 37 °C in a 5% (v/v) CO$_2$ atmosphere.

Tubulin acetylation. HeLa cells were plated in petri dishes (5 cm, PAA), incubated overnight to a confluency of 30–40% and then treated with SirReal2 dissolved in RPMI1640 medium supplemented with fresh 20% (v/v) FCS (PAA), 1% (v/v) penicillin (PAA), 1% (v/v) streptomycin (PAA), 1% (v/v), L-glutamine (PAA), 1% (v/v) DMSO for 5 h at various concentrations. Cells were then washed with prewarmed PBS (2 ml), lysed in SDS–PAGE sample buffer (70 µl, 50 mM Tris/HCl, 0.5 mM EDTA, 1× Complete Protease Inhibitors (Sigma-Aldrich), 2% (v/v) IGEPAL (Sigma-Aldrich), 2% (w/v) SDS, 10% (v/v) glycerol, 50 mM NCA (Sigma-Aldrich), 3.3 µM trichostatin A (Sigma-Aldrich), 50 mM DTT, 0.01% (w/v) bromophenol blue, pH 6.8) and sonicated (5 min). Cell samples were then separated using SDS–PAGE (12.5% (w/v) polyacrylamide, transferred to an activated nitrocellulose membrane (Bio-Rad), blocked with non-fat dry milk (Roth, 5% (w/v), TBS, 0.1% (v/v) Tween 20) and probed with an anti-acetyl-α-tubulin antibody (1:1,000, Sigma-Aldrich, T6793) and an anti-GAPDH antibody (1:2,000–1:5,000, Sigma-Aldrich, G9545) as a loading control (Fusion SL, peqlab). An uncropped blot is shown in Supplementary Fig. 8.

Abundance of BubR1. HeLa cells plated in six-well plates were treated with SirReal2 dissolved in FCS (1% (v/v) DMSO, 16 h) at various concentrations. Cells were washed with PBS, lysed in IPLS (50 mM Tris/HCl, 150 mM NaCl, 0.5 mM EDTA, 0.5% (v/v) NP-40, pH 7.5, supplemented with Complete protease inhibitors (Roche)). Samples were pelleted and resuspended in 1× SDS–PAGE sample buffer and heated (95 °C, 5 min). Cell samples were separated using SDS–PAGE (10% (w/v) polyacrylamide), transferred to a nitrocellulose membrane (Bio-Rad), blocked with non-fat dry milk (Roth, 5% (w/v), TBS, 0.1% (v/v) Tween 20) and probed with the anti-BubR1 (1:5,000, BD Biosciences, 612502) and anti-tubulin (1:5,000, Sigma-Aldrich, T5168) as a loading control. Uncropped blots are shown in the Supplementary Fig. 8.

Immunocytochemistry. HeLa cells that were incubated with SirReal2 (20 and 50 µM), SirReal6 (50 µM), AGK2 (Sigma-Aldrich, 20 µM) or DMSO as a control in Dulbecco's modified Eagle's medium supplemented with 10% FCS, antibiotics and DMSO (1% (v/v)) for 4 h, were fixed with ice-cold methanol (10 min), washed with PBS and blocked with PBS supplemented with 0.1% (v/v) Triton-X-100 and 5% (v/v) FCS (30 min). Cells were then stained with an anti-acetyl-α-tubulin antibody (Sigma-Aldrich, T6793) and then probed with a secondary Alexa 546 conjugated anti-mouse-antibody (Invitrogen). Nuclei were counterstained with

DAPI (4′,6-diamidino-2-phenylindole). Coverslips were mounted with Fluor-oMount (Sigma-Aldrich) and sealed with DPX Mountant (Sigma-Aldrich). Images of the mounted samples were acquired on a Leica DM500 microscope equipped with a Leica DFC 395 FX camera and HBO 100 W lamp[40]. The microscope was run with the Leica Application Suite 4.4.0 software. Chroma UV filter set (No. C40888) and Leica N2.1 filter set (No. 513832) were used for DAPI and Alexa 546 signal acquisition, respectively, with a HCX FL Fluotar 40x/0.75 (dry) objective. Further details about the equipment and the settings that were used to acquire the images are found in the Supplementary Methods section. Unprocessed images are found in Supplementary Fig. 9.

p53 Acetylation. U2OS cells (ATCC accession no. HTB-96) were seeded and cultured until they reached 90% confluency. Cells were then pretreated for 1 h with NCA (Sigma-Aldrich), SirReal2, SirReal5 or SirReal6 at the indicated concentrations, and then subsequently exposed to 20 J cm^{-2} ultraviolet light. Cells were incubated for an additional 6 h in the presence of the inhibitor and then lysed in IPLS (50 mM Tris/HCl, 150 mM NaCl; 0.5 mM EDTA; 0.5% (v/v) NP-40; 1 × Complete Protease Inhibitors (Roche), pH 8.0) and resuspended in 1 × Laemmli Buffer. Samples were then separated on SDS–PAGE, transferred to a nitrocellulose membrane (Bio-Rad), blocked with non-fat dry milk (Roth, 5% (w/v), TBS, 0.1% (v/v) Tween 20) and probed with anti-acetyl-p53 K382 (Cell Signaling, #2522), anti-p53 DO.1 (Santa Cruz Biotechnology, sc-126) and anti-vinculin (Cell Signaling, #4650) as a loading control. Uncropped blots are shown in the Supplementary Fig. 10.

References

1. Feldman, J. L., Baeza, J. & Denu, J. M. Activation of the protein deacetylase SIRT6 by long-chain fatty acids and widespread deacylation by mammalian sirtuins. *J. Biol. Chem.* **288,** 31350–31356 (2013).
2. Jiang, H. *et al.* SIRT6 regulates TNF-α secretion through hydrolysis of long-chain fatty acyl lysine. *Nature* **496,** 110–113 (2013).
3. Du, J. *et al.* Sirt5 Is a NAD-dependent protein lysine demalonylase and desuccinylase. *Science* **334,** 806–809 (2011).
4. Du, J., Jiang, H. & Lin, H. Investigating the ADP-ribosyltransferase activity of sirtuins with NAD analogues and 32P-NAD. *Biochemistry* **48,** 2878–2890 (2009).
5. Vaquero, A., Sternglanz, R. & Reinberg, D. NAD$^+$-dependent deacetylation of H4 lysine 16 by class III HDACs. *Oncogene* **26,** 5505–5520 (2007).
6. North, B. J., Marshall, B. L., Borra, M. T., Denu, J. M. & Verdin, E. The human Sir2 ortholog, SIRT2, is an NAD$^+$-dependent tubulin deacetylase. *Mol. Cell* **11,** 437–444 (2003).
7. Beirowski, B. *et al.* Sir-two-homolog 2 (Sirt2) modulates peripheral myelination through polarity protein Par-3/atypical protein kinase C (aPKC) signaling. *Proc. Natl Acad. Sci. USA* **108,** E952–E961 (2011).
8. de Oliveira, R. M., Sarkander, J., Kazantsev, A. G. & Outeiro, T. F. SIRT2 as a therapeutic target for age-related disorders. *Front. Pharmacol.* **3,** 82 (2012).
9. Pais, T. F. *et al.* The NAD-dependent deacetylase sirtuin 2 is a suppressor of microglial activation and brain inflammation. *EMBO J.* **32,** 2603–2616 (2013).
10. Kim, H.-S. *et al.* SIRT2 maintains genome integrity and suppresses tumorigenesis through regulating APC/C activity. *Cancer Cell* **20,** 487–499 (2011).
11. Serrano, L. *et al.* The tumor suppressor SirT2 regulates cell cycle progression and genome stability by modulating the mitotic deposition of H4K20 methylation. *Genes Dev.* **27,** 639–653 (2013).
12. Yang, M. H. *et al.* HDAC6 and SIRT2 regulate the acetylation state and oncogenic activity of mutant K-RAS. *Mol. Cancer Res.* **11,** 1072–1077 (2013).
13. Liu, P. Y. *et al.* The histone deacetylase SIRT2 stabilizes Myc oncoproteins. *Cell Death Differ.* **20,** 503–514 (2013).
14. Eskandarian, H. A. *et al.* A role for SIRT2-dependent histone H3K18 deacetylation in bacterial infection. *Science* **341,** 1238858–1238858 (2013).
15. Outeiro, T. F. *et al.* Sirtuin 2 inhibitors rescue α-synuclein-mediated toxicity in models of Parkinson's disease. *Science* **317,** 516–519 (2007).
16. Chopra, V. *et al.* The sirtuin 2 inhibitor AK-7 is neuroprotective in Huntington's disease mouse models. *Cell Rep.* **2,** 1492–1497 (2012).
17. Bobrowska, A., Donmez, G., Weiss, A., Guarente, L. & Bates, G. SIRT2 ablation has no effect on tubulin acetylation in brain, cholesterol biosynthesis or the progression of Huntington's disease phenotypes *in vivo*. *PLoS ONE* **7,** e34805 (2012).
18. Finnin, M. S., Donigian, J. R. & Pavletich, N. P. Structure of the histone deacetylase SIRT2. *Nat. Struct. Biol.* **8,** 621–625 (2001).
19. Moniot, S., Schutkowski, M. & Steegborn, C. Crystal structure analysis of human Sirt2 and its ADP-ribose complex. *J. Struct. Biol.* **182,** 136–143 (2013).
20. Jin, L. *et al.* Crystal structures of human SIRT3 displaying substrate-induced conformational changes. *J. Biol. Chem.* **284,** 24394–24405 (2009).
21. Davenport, A. M., Huber, F. M. & Hoelz, A. Structural and Functional Analysis of Human SIRT1. *J. Mol. Biol.* **426,** 526–541 (2014).
22. Pan, P. W. *et al.* Structure and biochemical functions of SIRT6. *J. Biol. Chem.* **286,** 14575–14587 (2011).
23. Szczepankiewicz, B. G. *et al.* Synthesis of carba-NAD and the structures of its ternary complexes with SIRT3 and SIRT5. *J. Org. Chem.* **77,** 7319–7329 (2012).
24. Suzuki, T. *et al.* Design, synthesis, and biological activity of a novel series of human sirtuin-2-selective inhibitors. *J. Med. Chem.* **55,** 5760–5773 (2012).
25. Napper, A. D. *et al.* Discovery of indoles as potent and selective inhibitors of the deacetylase SIRT1. *J. Med. Chem.* **48,** 8045–8054 (2005).
26. Hoffmann, G., Breitenbücher, F., Schuler, M. & Ehrenhofer-Murray, A. E. A novel sirtuin 2 (SIRT2) Inhibitor with p53-dependent pro-apoptotic activity in non-small cell lung cancer. *J. Biol. Chem.* **289,** 5208–5216 (2014).
27. Cui, H. *et al.* Discovery of potent and selective sirtuin 2 (SIRT2) inhibitors using a fragment-based approach. *J. Med. Chem.* **57,** 8340–8357 (2014).
28. Yamagata, K. *et al.* Structural basis for potent inhibition of SIRT2 deacetylase by a macrocyclic peptide inducing dynamic structural change. *Structure* **22,** 345–352 (2014).
29. Heltweg, B., Trapp, J. & Jung, M. *In vitro* assays for the determination of histone deacetylase activity. *Methods* **36,** 332–337 (2005).
30. Avalos, J. L., Bever, K. M. & Wolberger, C. Mechanism of sirtuin inhibition by nicotinamide: altering the NAD$^+$ cosubstrate specificity of a Sir2 enzyme. *Mol. Cell* **17,** 855–868 (2005).
31. Avalos, J. L. *et al.* Structure of a Sir2 enzyme bound to an acetylated p53 peptide. *Mol. Cell* **10,** 523–535 (2002).
32. Cosgrove, M. S. *et al.* The structural basis of sirtuin substrate affinity. *Biochemistry* **45,** 7511–7521 (2006).
33. Gertz, M. *et al.* Ex-527 inhibits Sirtuins by exploiting their unique NAD$^+$-dependent deacetylation mechanism. *Proc. Natl Acad. Sci. USA* **110,** E2772–E2781 (2013).
34. Hoff, K. G., Avalos, J. L., Sens, K. & Wolberger, C. Insights into the sirtuin mechanism from ternary complexes containing NAD$^+$ and acetylated peptide. *Structure* **14,** 1231–1240 (2006).
35. Di Tommaso, P. *et al.* T-Coffee: a web server for the multiple sequence alignment of protein and RNA sequences using structural information and homology extension. *Nucleic Acids Res.* **39,** W13–W17 (2011).
36. Frye, R. A. Phylogenetic classification of prokaryotic and eukaryotic Sir2-like proteins. *Biochem. Biophys. Res. Commun.* **273,** 793–798 (2000).
37. Trapp, J. *et al.* Adenosine mimetics as inhibitors of NAD$^+$-dependent histone deacetylases, from kinase to sirtuin inhibition. *J. Med. Chem.* **49,** 7307–7316 (2006).
38. Hubbert, C. *et al.* HDAC6 is a microtubule-associated deacetylase. *Nature* **417,** 455–458 (2002).
39. Mangas-Sanjuan, V. *et al.* Tubulin acetylation promoting potency and absorption efficacy of deacetylase inhibitors. *Br. J. Pharmacol.* **172,** 829–840 (2014).
40. Tokési, N. *et al.* TPPP/p25 promotes tubulin acetylation by inhibiting histone deacetylase 6. *J. Biol. Chem.* **285,** 17896–17906 (2010).
41. North, B. J. *et al.* SIRT2 induces the checkpoint kinase BubR1 to increase lifespan. *EMBO J.* **33,** 1438–1453 (2014).
42. Baker, D. J. *et al.* Increased expression of BubR1 protects against aneuploidy and cancer and extends healthy lifespan. *Nat. Cell Biol.* **15,** 96–102 (2013).
43. Sakaguchi, K. *et al.* DNA damage activates p53 through a phosphorylation-acetylation cascade. *Genes Dev.* **12,** 2831–2841 (1998).
44. Vaziri, H. *et al.* hSIR2(SIRT1) functions as an NAD-dependent p53 deacetylase. *Cell* **107,** 149–159 (2001).
45. Luo, J. *et al.* Negative control of p53 by Sir2α promotes cell survival under stress. *Cell* **107,** 137–148 (2001).
46. Lombard, D. B. *et al.* Mammalian Sir2 homolog SIRT3 regulates global mitochondrial lysine acetylation. *Mol. Cell. Biol.* **27,** 8807–8814 (2007).
47. Schuetz, A. *et al.* Structural basis of inhibition of the human NAD$^+$-dependent deacetylase SIRT5 by suramin. *Structure* **15,** 377–389 (2007).
48. Zhao, X. *et al.* The 2.5Å crystal structure of the SIRT1 catalytic domain bound to nicotinamide adenine dinucleotide (NAD$^+$) and an indole (EX527 analogue) reveals a novel mechanism of histone deacetylase inhibition. *J. Med. Chem.* **56,** 963–969 (2013).
49. Nguyen, G. T. T., Schaefer, S., Gertz, M., Weyand, M. & Steegborn, C. Structures of human sirtuin 3 complexes with ADP-ribose and with carba-NAD$^+$ and SRT1720: binding details and inhibition mechanism. *Acta Crystallogr. D Biol. Crystallogr.* **69,** 1423–1432 (2013).
50. Nguyen, G. T. T., Gertz, M. & Steegborn, C. Crystal structures of Sirt3 complexes with 4′-bromo-resveratrol reveal binding sites and inhibition mechanism. *Chem. Biol.* **20,** 1375–1385 (2013).
51. Disch, J. S. *et al.* Discovery of thieno[3,2-d]pyrimidine-6-carboxamides as potent inhibitors of SIRT1, SIRT2, and SIRT3. *J. Med. Chem.* **56,** 3666–3679 (2013).
52. Maurer, B., Rumpf, T., Scharfe, M. & Stolfa, D. A. Inhibitors of the NAD$^+$-dependent protein desuccinylase and demalonylase Sirt5. *ACS Med. Chem. Lett.* **12,** 1050–1053 (2012).
53. Schlicker, C., Boanca, G., Lakshminarasimhan, M. & Steegborn, C. Structure-based development of novel sirtuin inhibitors. *Aging* **3,** 852–872 (2011).

54. Laurent, G. *et al.* SIRT4 coordinates the balance between lipid synthesis and catabolism by repressing malonyl CoA decarboxylase. *Mol. Cell* **50**, 686–698 (2013).

55. MacLean, B. *et al.* Skyline: an open source document editor for creating and analyzing targeted proteomics experiments. *Bioinformatics* **26**, 966–968 (2010).

56. Winn, M. D. *et al.* Overview of the CCP4 suite and current developments. *Acta Crystallogr. D Biol. Crystallogr.* **67**, 235–242 (2011).

57. Kabsch, W. XDS. *Acta Crystallogr. D Biol. Crystallogr.* **66**, 125–132 (2010).

58. Karplus, P. A. & Diederichs, K. Linking crystallographic model and data quality. *Science* **336**, 1030–1033 (2012).

59. Vagin, A. & Teplyakov, A. Molecular replacement with MOLREP. *Acta Crystallogr. D Biol. Crystallogr.* **66**, 22–25 (2010).

60. McCoy, A. J. *et al.* Phaser crystallographic software. *J. Appl. Crystallogr.* **40**, 658–674 (2007).

61. Emsley, P., Lohkamp, B., Scott, W. G. & Cowtan, K. Features and development of Coot. *Acta Crystallogr. D Biol. Crystallogr.* **66**, 486–501 (2010).

62. Murshudov, G. N. *et al.* REFMAC5 for the refinement of macromolecular crystal structures. *Acta Crystallogr. D Biol. Crystallogr.* **67**, 355–367 (2011).

63. Chen, V. B. *et al.* MolProbity: all-atom structure validation for macromolecular crystallography. *Acta Crystallogr. D Biol. Crystallogr.* **66**, 12–21 (2010).

64. Adams, P. D. *et al.* PHENIX: a comprehensive Python-based system for macromolecular structure solution. *Acta Crystallogr. D Biol. Crystallogr.* **66**, 213–221 (2010).

65. Krissinel, E. Enhanced fold recognition using efficient short fragment clustering. *J. Mol. Biochem.* **1**, 76–85 (2012).

66. Ho, B. K. & Gruswitz, F. HOLLOW: generating accurate representations of channel and interior surfaces in molecular structures. *BMC Struct. Biol.* **8**, 49 (2008).

67. Laskowski, R. A. & Swindells, M. B. LigPlot+: multiple ligand-protein interaction diagrams for drug discovery. *J. Chem. Inf. Model.* **51**, 2778–2786 (2011).

68. Niesen, F. H., Berglund, H. & Vedadi, M. The use of differential scanning fluorimetry to detect ligand interactions that promote protein stability. *Nat. Protoc.* **2**, 2212–2221 (2007).

Acknowledgements

Author contributions

Additional information

a

Nicotinamide
IC$_{50}$(Sirt1): 50-100 µM
IC$_{50}$(Sirt2): 1.2-100 µM
IC$_{50}$(Sirt3): 30 µM

EX-527 (racemic)
IC$_{50}$(Sirt1): 0.098 µM
IC$_{50}$(Sirt2): 20 µM
IC$_{50}$(Sirt3): 49 µM

CHIC-35
IC$_{50}$(Sirt1): 0.124 µM
IC$_{50}$(Sirt2): 2.8 µM
IC$_{50}$(Sirt3): > 100 µM

ELT inhibitor 11c
IC$_{50}$(Sirt1): 0.004 µM
IC$_{50}$(Sirt2): 0.003 µM
IC$_{50}$(Sirt3): 0.004 µM

ELT inhibitor 28
IC$_{50}$(Sirt1): 0.015 µM
IC$_{50}$(Sirt2): 0.010 µM
IC$_{50}$(Sirt3): 0.033 µM

ELT inhibitor 31
IC$_{50}$(Sirt1): 0.004 µM
IC$_{50}$(Sirt2): 0.001 µM
IC$_{50}$(Sirt3): 0.007 µM

SRT1720
IC$_{50}$(Sirt1): activation
IC$_{50}$(Sirt2): no inhibition
IC$_{50}$(Sirt3): 0.56 µM

4'-bromoresveratrol
IC$_{50}$(Sirt1): > 50 µM
IC$_{50}$(Sirt2): not determined
IC$_{50}$(Sirt3): 143 µM

S2iL5 peptide
YHTYHV-Lys(Tfac)-RRTNYY
k$_d$(Sirt1): not determined
k$_d$(Sirt2): 0.001 µM
k$_d$(Sirt3): 0.002 µM

b

SirReal1
IC$_{50}$ of 3.7 ± 1.8 µM

SirReal2
IC$_{50}$ of 0.14 ± 0.04 µM

c

DMSO control
SirReal1 100 µM

d

DMSO Control
Ac-Lys-H3 5 mM (ΔT = ~1 °C)
NAD$^+$ 5 mM (ΔT = ~1 °C)

Supplementary Figure 1 Structures and inhibition data for sirtuin inhibitors with published structural information, *in vitro* inhibition data for SirReal1/2 and thermal stability plots for Sirt2. **(a)** Chemical structures and IC$_{50}$ or k$_d$ values of sirtuin inhibitors with known binding modes: nicotinamide[1], indoles (EX-527, CHIC-35)[2-4], ELT inhibitors[5], SRT1720[6,7], 4'-bromoresveratrol[8] and the macrocyclic peptide S2iL5[9]. **(b)** Dose-response curves for Sirt2 inhibition in an HPLC-based absorption assay in the presence of SirReal1/2 using a non-labeled acetyl-lysine oligopeptide based on α-tubulin. Data are presented as mean ± s.d. (n=2). **(c)** *In vitro* inhibition data for Sirt1-3 in the presence of SirReal1 (100 µM) using an HPLC-based absorption assay with a non-labeled acetyl-lysine oligopeptide based on α-tubulin as a substrate. A solution containing DMSO was used as a negative control. SirReal1 shows a preference to inhibit Sirt2 but also affects the activity of Sirt1/3 at higher concentrations. Data are presented as mean ± s.d.

(n=2). **(d)** Representative thermal stability plots of Sirt2 in the presence of either the cosubstrate NAD$^+$ or an acetyl-lysine oligopeptide. The presence of either NAD$^+$ or an acetyl-lysine oligopeptide only leads to a slight stabilization of Sirt2 as compared to a combination of SirReal2 and cosubstrate or the substrate, respectively (n=3, Fig. 1d).
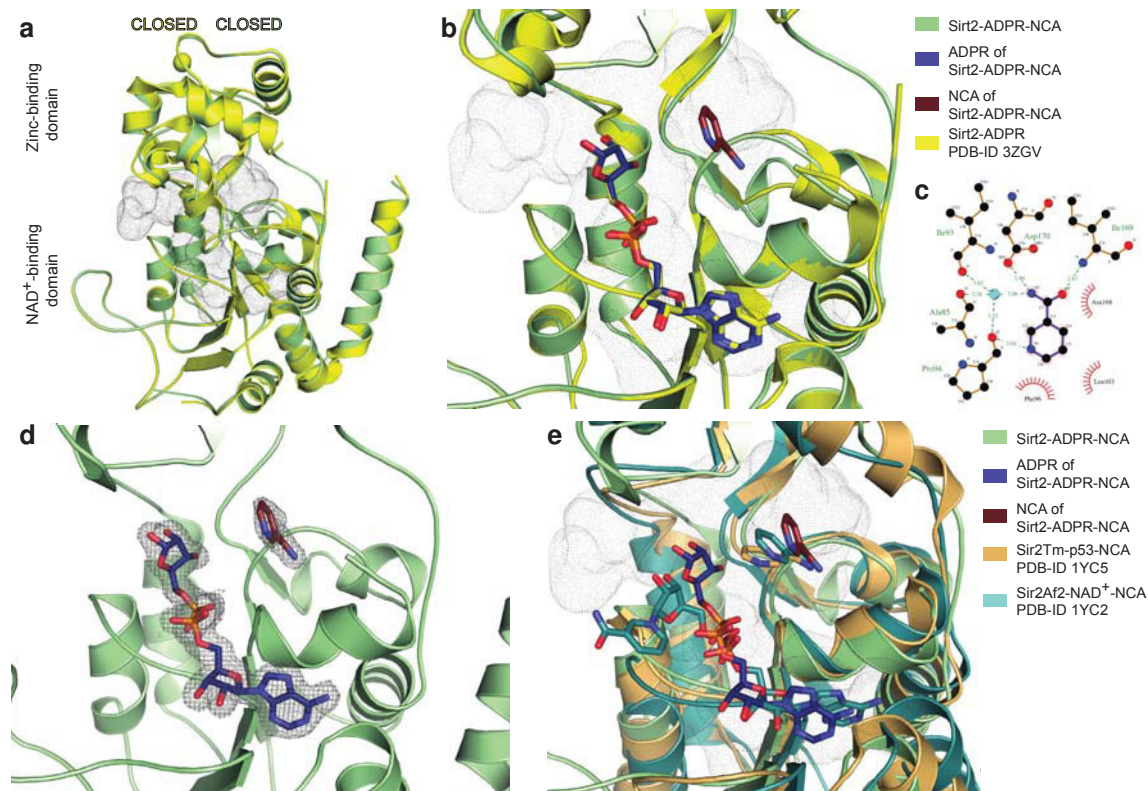
Supplementary Figure 2 Nicotinamide (NCA) of Sirt2-ADPR-NCA occupies the C-pocket and interacts over a network of highly conserved residues with Sirt2. **(a)** Superposition of the overall structure of Sirt2-ADPR-NCA (pale green) with the Sirt2-ADPR complex (PDB-ID 3ZGV[10], yellow). Both structures are very similar (r.m.s.d. (C_α atoms) = 0.44 Å) and resemble a 'closed' conformation, due to the binding of the Sirt2-specific insertion that acts as a pseudo-substrate for the neighboring Sirt2-molecule. The active site of Sirt2 is shown as small grey dots. Residues Tyr139-Gly141 of Sirt2-ADPR (PDB-ID 3ZGV) were not defined in the electron density map. **(b,d)** NCA (brown sticks) occupies the C-pocket in vicinity of ADPR (deep blue sticks). **(c)** The amide of the nicotinamide is tightly bound via hydrogen bonds to Ile169 and Asp170 while the pyridine ring undergoes $\pi-\pi$–stacking with Phe96. **(d)** Electron density maps of ADPR (overall B-factor 21.9 Å^2) and NCA (overall B-factor 46.3 Å^2) of Sirt2-ADPR-NCA. The position of the pyridine ring is more flexible relative to the amide as its B-factors are significantly higher than the B-factors of the amide (B-factor(Phenyl ring): 49.1 Å^2; B-factor(amide): 41.1 Å^2). The σ-weighted $2F_o$-F_c electron density map is contoured at 1.0 σ. A stereo image of **d** as well as a σ-

weighted F_o-F_c electron density OMIT map for ADPR and NCA are shown in Supplementary Fig. 4a,b. **(e)** The interactions of NCA with Sirt2 and its position within the C-pocket is similar to the ones observed in other sirtuin structures in complex with nicotinamide (Sir2Tm-Ac-Lys-p53-NCA, PDB-ID 1YC5[11], light orange, Sir2Af2-NAD$^+$-NCA, PDB-ID 1YC2[11], teal). However, in contrast to nicotinamide of Sir2Tm-Ac-Lys-p53-NCA and Sir2Af2-NAD$^+$-NCA the amide moiety and the phenyl ring of nicotinamide of Sirt2-ADPR-NCA do not lie in the same plane. The cofactor-binding loop in **b,d,e** is not shown for better clarity.
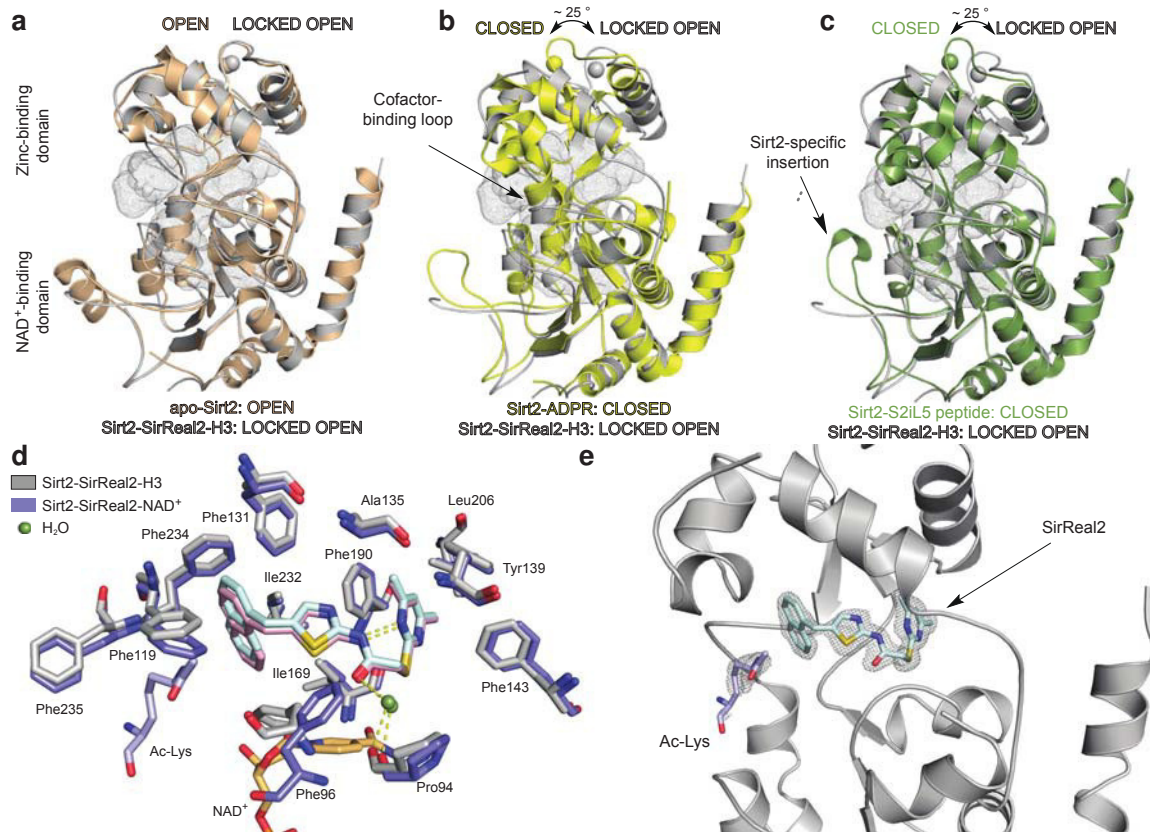
Supplementary Figure 3 SirReal2 functions as a molecular wedge and locks Sirt2 in an open conformation. **(a-c)** Superposition of Sirt2-SirReal2-H3 with Sirt2-apo (PDB-ID 3ZGO[10,12], salmon, residues 34-45 are omitted for better clarity), Sirt2 in complex with ADP ribose (PDB-ID 3ZGV, yellow, residues Tyr139-Gly141 were not defined in the electron density map) and the Sirt2-S2iL5-peptide complex (PDB-ID 4L3O[9], green). The active site is shown as small grey dots. As seen in Fig. 2 of the main article, the Sirt2-SirReal2 complex adopts an open state comparable to Sirt2-apo and in contrast to the Sirt2-ADPR and Sirt2-S2iL5 complex. Sirt2-SirReal2-H3 bears more resemblance to Sirt2-apo (r.m.s.d. (C_α atoms) = 1.3 Å) than to the Sirt2-ADPR complex (r.m.s.d. (C_α atoms) = 1.8 Å) or the Sirt2-S2iL5 peptide complex (r.m.s.d. (C_α atoms) = 1.6 Å). **(d)** Comparison of the interactions of SirReal2 in Sirt2-SirReal2-H3 (light cyan) with SirReal2 in Sirt2-SirReal2-NAD^{+} (light pink). Interacting residues are represented as sticks (Sirt2-SirReal2-H3: light grey; Sirt2-SirReal2-NAD^{+}: slate blue). Binding of SirReal2 is almost identical (r.m.s.d. of 0.47 Å) in both structures. This is also true for the positions of the

SirReal2-interacting residues of the Sirt2-SirReal2 structures except for Phe96 which is forced to adopt a different position upon NAD^+-binding. Hydrogen bonds are shown as dashed yellow lines. **(e)** Electron density maps for SirReal2 (pale cyan sticks, overall B-factor of 25.1 $Å^2$) and the acetyl-lysine peptide substrate (light blue sticks, overall B-factor of 48.3 $Å^2$). The σ-weighted $2F_o$-F_c electron density map is contoured at 1.0 σ. A stereo image of **e** as well as a σ-weighted F_o-F_c electron density OMIT map for SirReal2 and the Ac-Lys-H3 oligopeptide is shown in Supplementary Fig. 5a,b.
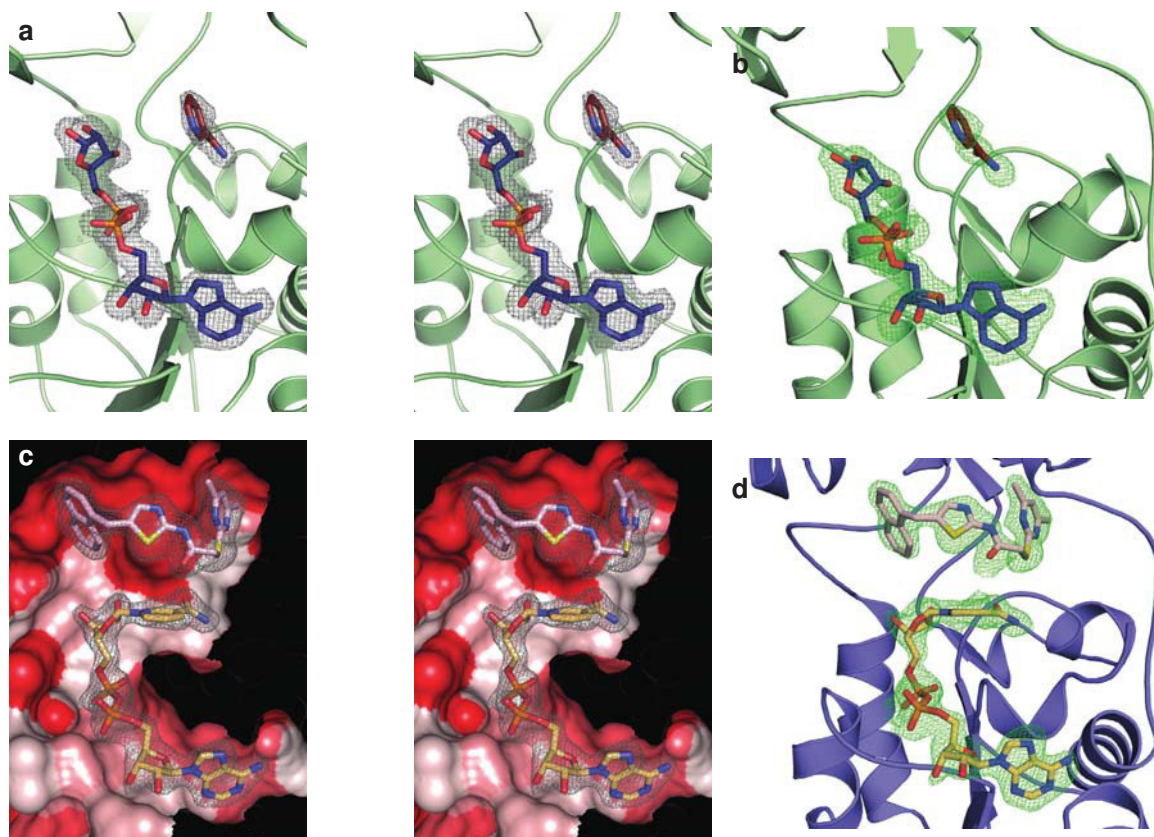
Supplementary Figure 4 Stereo images of the σ-weighted $2F_o$-F_c electron density and the σ-weighted F_o-F_c OMIT maps of presented inhibitors, cosubstrates and substrates. Wall-eyed stereo representation of the electron density of the ligands of **(a)** the Sirt2-ADPR-NCA structure and the Sirt2-SirReal2-NAD$^+$ complex **(c)**. Sirt2-ADPR-NCA is presented as a pale green cartoon and ADPR and NCA is shown as dark blue and dark brown sticks. Sirt2-SirReal2-NAD$^+$ is presented as a slate blue cartoon and SirReal2 and NAD$^+$ are shown as light pink and light orange sticks. The surface of Sirt2-SirReal2-NAD$^+$ of **c** is colored according to its hydrophobicity (red color indicating increasing hydrophobicity). The σ-weighted $2F_o$-F_c maps are contoured at 1.0 σ and shown as grey mesh . **(b,d)** The σ-weighted F_o-F_c electron density OMIT maps are contoured at 3.0 σ (ADPR, SirReal2) or 2.0 σ (NCA, NAD$^+$) and shown as green mesh. The cofactor-binding loop of **a-d** is omitted for clarity.
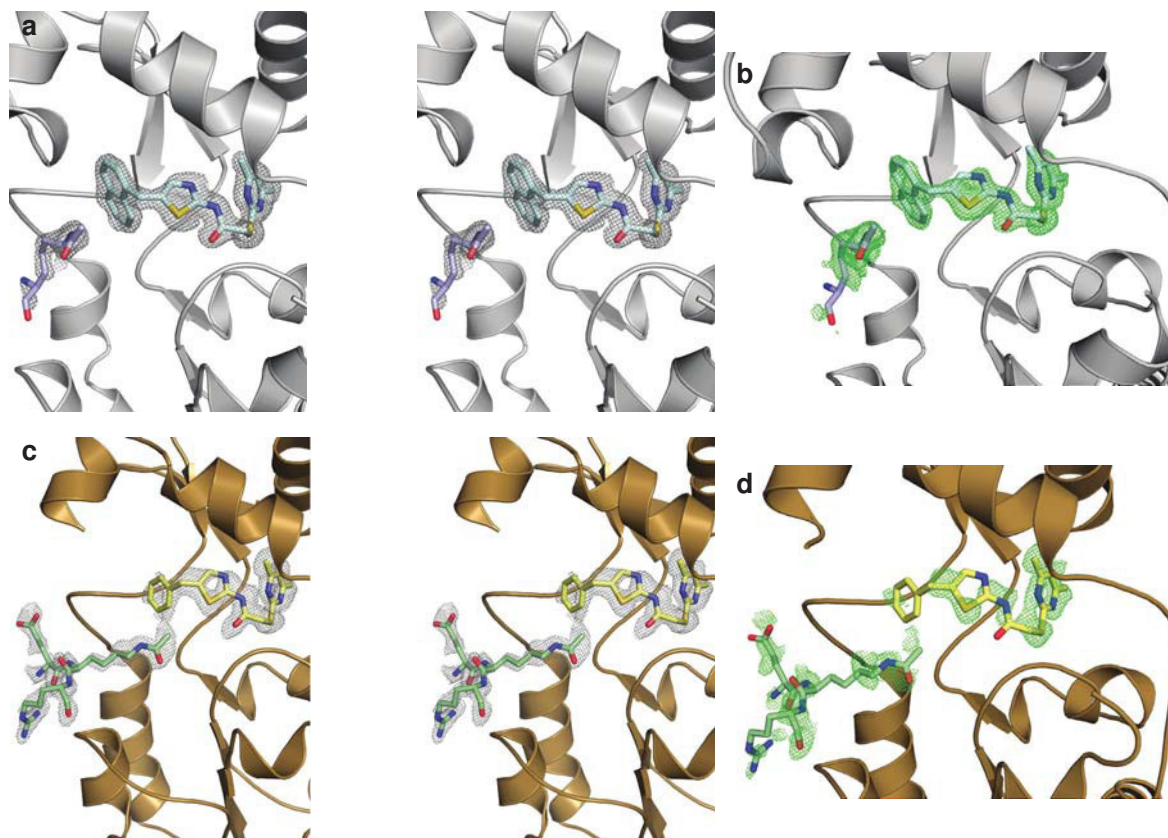
Supplementary Figure 5 Stereo images of the σ-weighted $2F_o$-F_c electron density and images of the σ-weighted F_o-F_c OMIT map of the Sirt2-SirReal2-H3 and Sirt2-SirReal1-OTC complexes. **(a,c)** Wall-eyed stereo representation of the electron density maps of the ligands of the Sirt2-SirReal2-H3 structure **(a)** and the Sirt2-SirReal1-OTC **(c)** complex. Sirt2-SirReal2-H3 is presented as a light grey cartoon and SirReal2 and the Ac-Lys-H3 oligopeptide are shown as light cyan and light blue sticks. Sirt2-SirReal1-OTC complex is presented as a brown cartoon and SirReal1 and the Ac-Lys-OTC oligopeptide are shown as pale yellow and light green sticks. The σ-weighted $2F_o$-F_c maps are contoured at 1.0 σ and shown as grey mesh. **(b,d)** The σ-weighted F_o-F_c electron density OMIT maps are contoured at 3.0 σ (SirReal2), 2.0 σ (Ac-Lys-H3, SirReal1) or 1.5 σ (Ac-Lys-OTC) and shown as green mesh. The poor electron density for the acetyl-lysine oligopeptides as well as the one of SirReal1 is probably due to a low occupancy. The cofactor-binding loop of **a-d** is omitted for clarity.
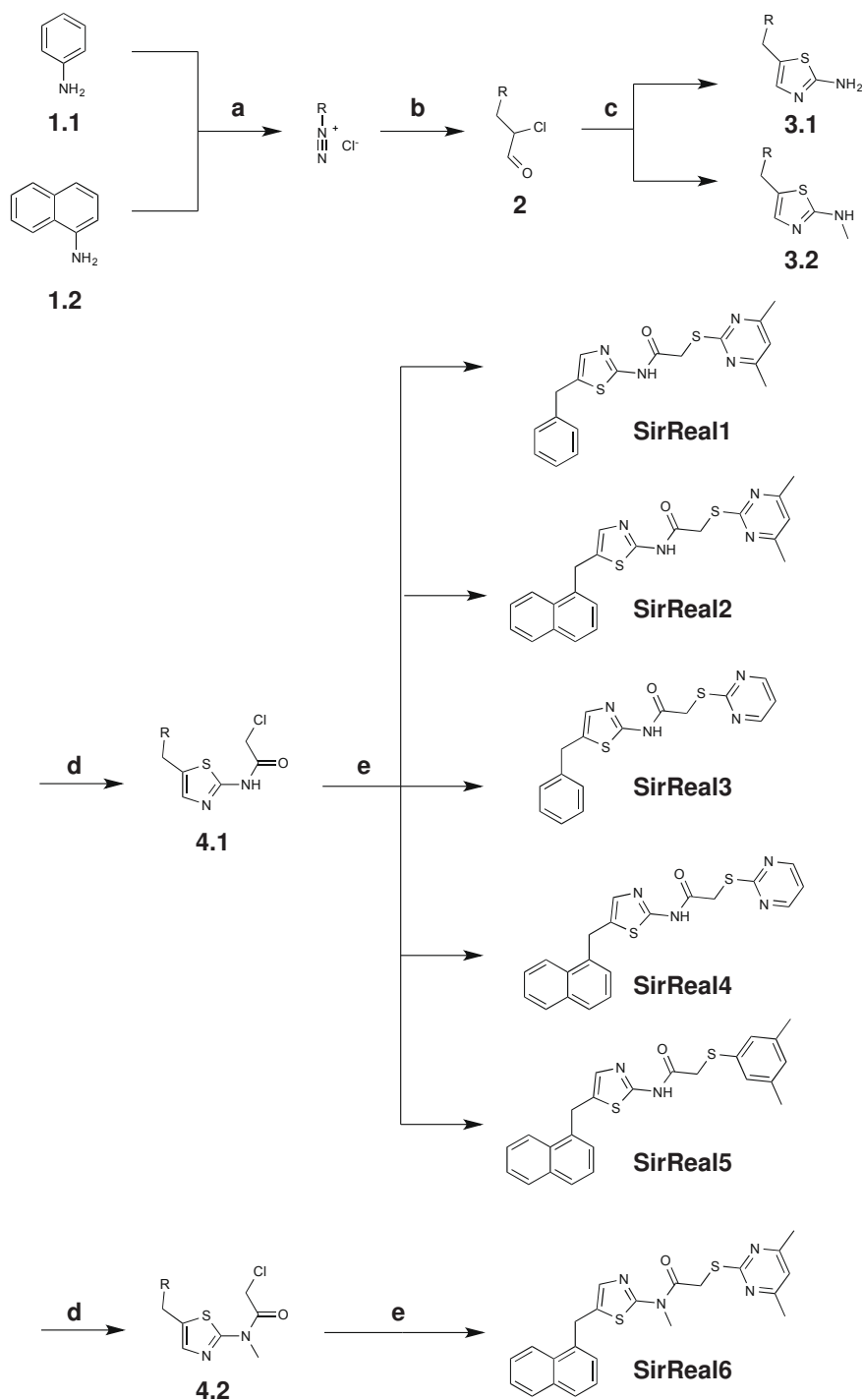
Supplementary Figure 6 Synthesis scheme for SirReal inhibitors. Preliminary tests with SirReal2 were performed with the commercially available compound (Chembridge, compound ID 7881488). For further characterization it was synthesized in our laboratory as the other SirReal inhibitors. Starting with the diazotization of aniline (**1.1**) for SirReal1/3 or

α-naphthylamine for SirReal2/4/5/6 (**1.2**), the α-chloropropanals (**2**) were generated via a Meerwein reaction[13,14]. Condensation of thiourea (SirReal1-5) or 1-methylthiourea (SirReal6) and the α-chloropropanals (**2**) led to formation of the aminothiazoles (**3.1 / 3.2**) which were then chloroacetylated to (**4.1 / 4.2**), followed by a nucleophilic substitution[15] with 2-mercapto-4,6-dimethylpyrimidine, 2-mercaptopyrimidine or 3,5-dimethylthiophenol to yield SirReal1-6. Identity and purity of all SirReal inhibitors were confirmed by ^{1}H-, ^{13}C-NMR, mass spectrometry respectively, and high performance liquid chromatography (HPLC) analysis. All synthesized SirReal inhibitors were of a purity of at least 95%. Spectroscopic data for all synthesized SirReal inhibitors can be found in the Supplementary Notes section. Reagents and conditions: (a) NaNO$_2$, HCl, water, 0 °C, 20 min; (b) acrolein, CuCl$_2$ × 2 H$_2$O, NaHCO$_3$, acetone, 20 °C, 3 h, 9% yield; (c) thiourea or 1-methylthiourea, ethanol, reflux, 2 h, 56% yield or 38%, respectively; (d) chloroacetyl chloride, DIPEA, acetonitrile, 20 °C, 2 h, 98% yield; (e) 2-mercaptopyrimidine, 2-mercapto-4,6-dimethylpyrimidine or 3,5-dimethylthiophenol, Na$_2$CO$_3$, KI, DMSO, 20 °C, 2 h, 80%, 89% or 13% yield.
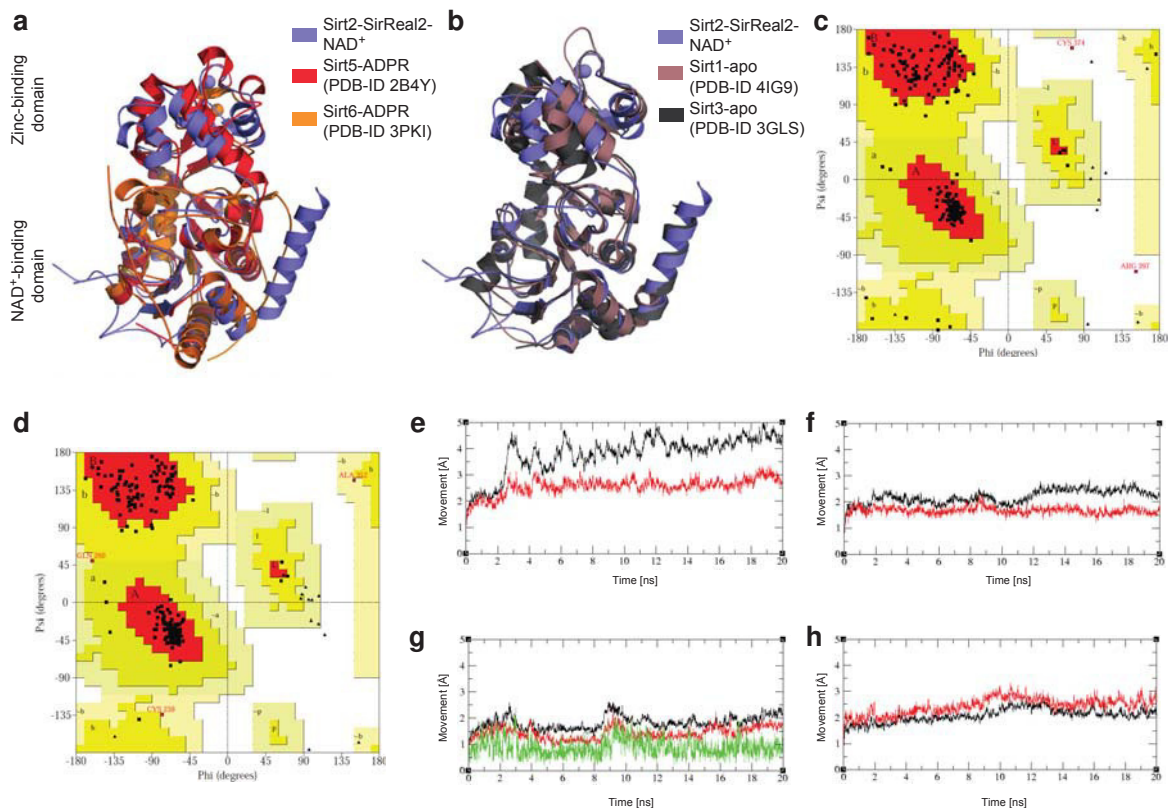
Supplementary Figure 7 Structural comparison of the Sirt2-SirReal2-NAD$^+$ complex with structures of available crystal structures of other sirtuins, stereochemical analysis, r.m.s.d. plots for molecular dynamics (MD) simulations of the Sirt1/3 homology models and the Sirt2-SirReal2-H3 structure. **(a,b)** Superposition of the Sirt2-SirReal2-NAD$^+$ complex with crystal structures of Sirt5 (red, PDB-ID 2B4Y[16]) and Sirt6 (orange, PDB-ID 3PKI[17]) in their open conformation **(a)** and with crystal structures of Sirt1 and Sirt3 **(b**, Sirt1-apo, brown, PDB-ID 4IG9[18]; Sirt3-apo, raspberry, PDB-ID 3GLS[19]). All structures adopt the 'open' conformation and show main differences in the conformation of the zinc-binding domain while the NAD$^+$-binding domain adopts a very similar conformation. The structural differences of the Sirt2-SirReal2-NAD$^+$ complex are more pronounced when compared to the crystal structures of Sirt5/6 than to the ones of Sirt1/3. This is also reflected by r.m.s.d. values: compared to Sirt5/6 (r.m.s.d. (C$_\alpha$ atoms) = 1.8–1.9 Å); to Sirt1/3 (r.m.s.d. (C$_\alpha$ atoms) = 1.6 Å). The C-terminal regulatory segment of Sirt1 is omitted for clarity. **(c)** PROCHECK stereochemical analysis of the Sirt1 homology model. 91.1% of the Φ and Ψ angles of the protein backbone are located in the most favored

regions, 8.1% are in the additional allowed regions and two residues are in the disallowed regions of the Ramachandran plot. Outlier residues are located outside of the binding pockets. **(d)** PROCHECK stereochemical analysis of the Sirt3 homology model. 92.2% of the Φ and Ψ angles of the protein backbone are located in the most favored regions, 6.5% are in the additional allowed regions and three residues are in the generously allowed regions of the Ramachandran plot. **(e-h)** r.m.s.d. plots for MD simulations of the Sirt1 homology model **(e)**, of the Sirt3 homology model **(f)**, of the Sirt2-SirReal2-H3 crystal structure with SirReal2 **(g)** and without SirReal2 **(h)**. The black line represents the r.m.s.d. value calculated for backbone heavy atoms (C_α, C and N) of the whole protein. The red line represents the r.m.s.d. value calculated for backbone heavy atoms of pocket residues only. The green line represents the r.m.s.d. value calculated for the heavy atoms of the inhibitor SirReal2.
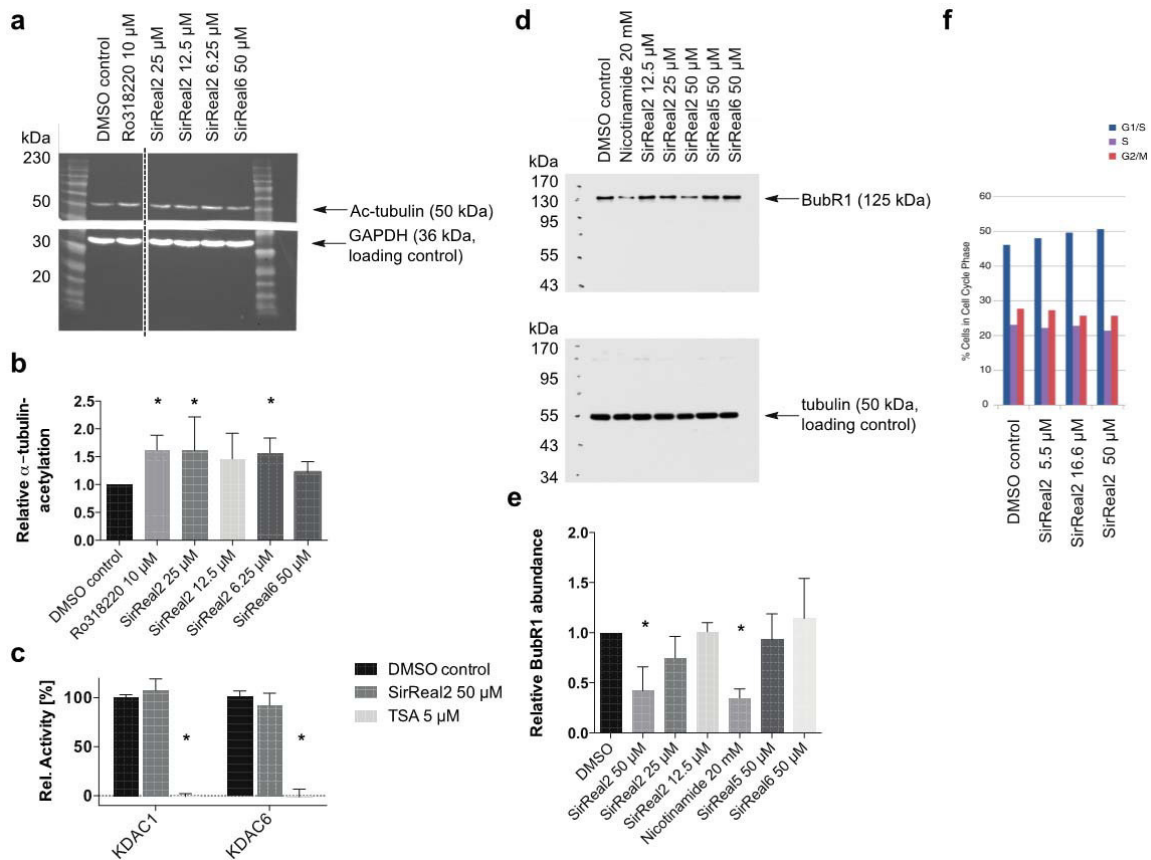
Supplementary Figure 8   SirReal2 induces a tubulin hyperacetylation and a significant depletion of BubR1. **(a)** Representative western blot of HeLa cell lysates after incubation with SirReal2 at the indicated concentrations. Ro318220 was used as a positive control[20]. The western blot was cut in half at around 40 kDa to detect acetyl-tubulin and GAPDH separately. **(b)** Quantification of the relative hyperacetylation after incubation with SirReal2. **(c)** *In vitro* inhibition data for the 'classical' KDAC1 and KDAC6. SirReal2 does not affect the activity of both KDACs. Only the positive control Trichostatin A (TSA) significantly inhibits both KDACs. **(d)** Representative western blot of HeLa lysates after incubation with SirReal2 at the indicated concentrations. SirReal2 induces a reduction of the spindle assembly checkpoint protein BubR1. **(e)** Statistical analysis of the abundance of BubR1 after incubation with SirReal2. At a SirReal2 concentration of 50 µM, BubR1 is significantly reduced in relation to the DMSO control. This is in line with a Sirt2-inhibition *in vivo*. **(f)** Cell cycle analysis after incubation of SirReal2 at the indicated concentrations. Treatment with SirReal2 did not alter the cell cycle. A description of

the cell cycle analysis can be found in the Supplementary Methods section. Colorplus™ Prestained Protein Ladder (New England Biolabs, tubulin hyperacetylation) and EZ-Run™ Prestained *Rec* Protein Ladder (Fisher Scientific, BubR1) were used as molecular weight markers. All data are presented as mean ± s.d. (n=3). *P* < 0.05 as compared to the control.
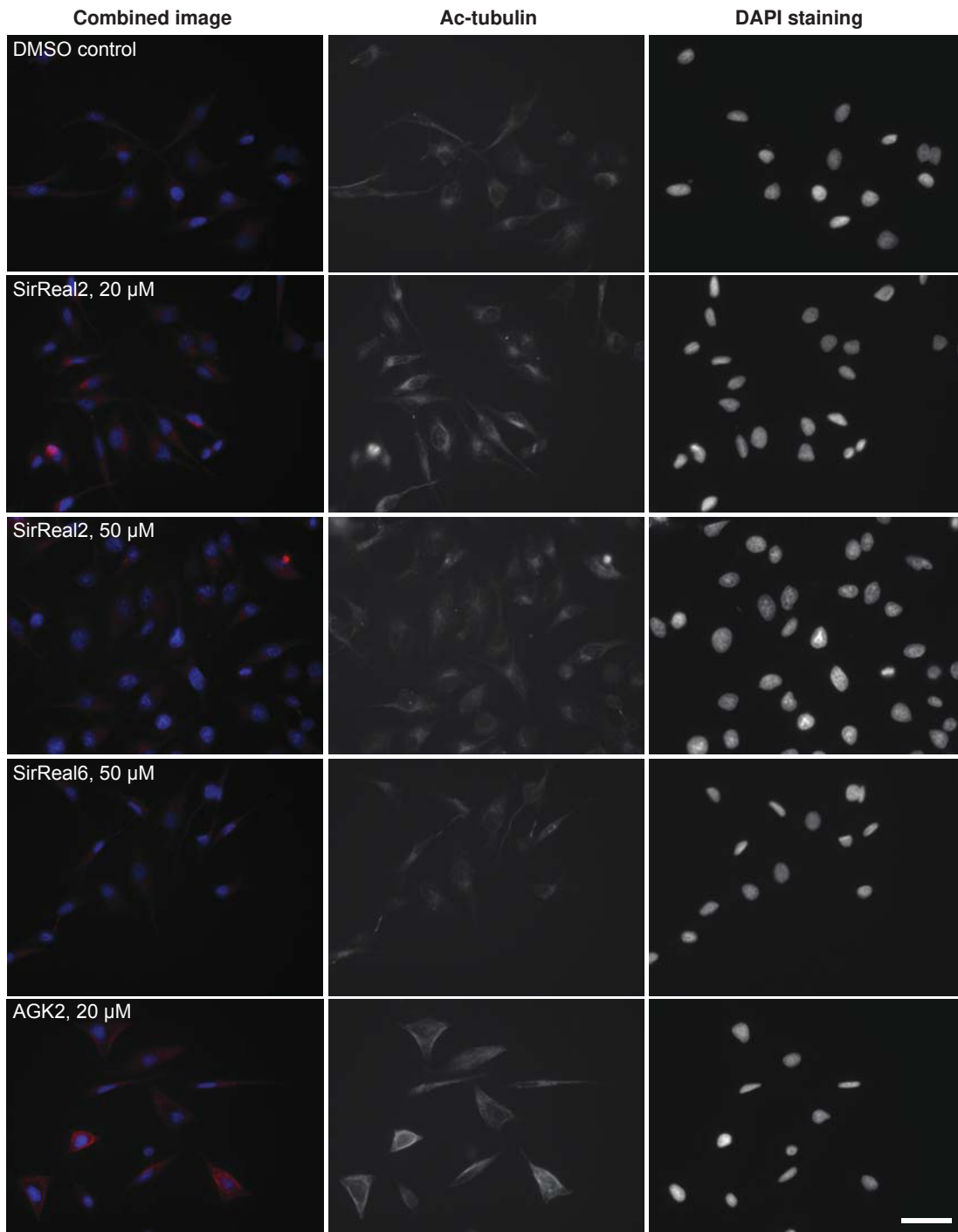
Supplementary Figure 9 SirReal2 induces tubulin-hyperacetylation in HeLa cells. Representative combined and raw images show that treatment with SirReal2 at a concentration of 20 µM and 50 µM induces hyperacetylation of the microtubule network as compared to the DMSO control. The effects are similar to the ones observed for the treatment with the Sirt2 inhibitor AGK2[21]. Treatment with SirReal6 on the other hand results in no substantial change of

acetylation level (n=4). The scale bar represents 10 µm .
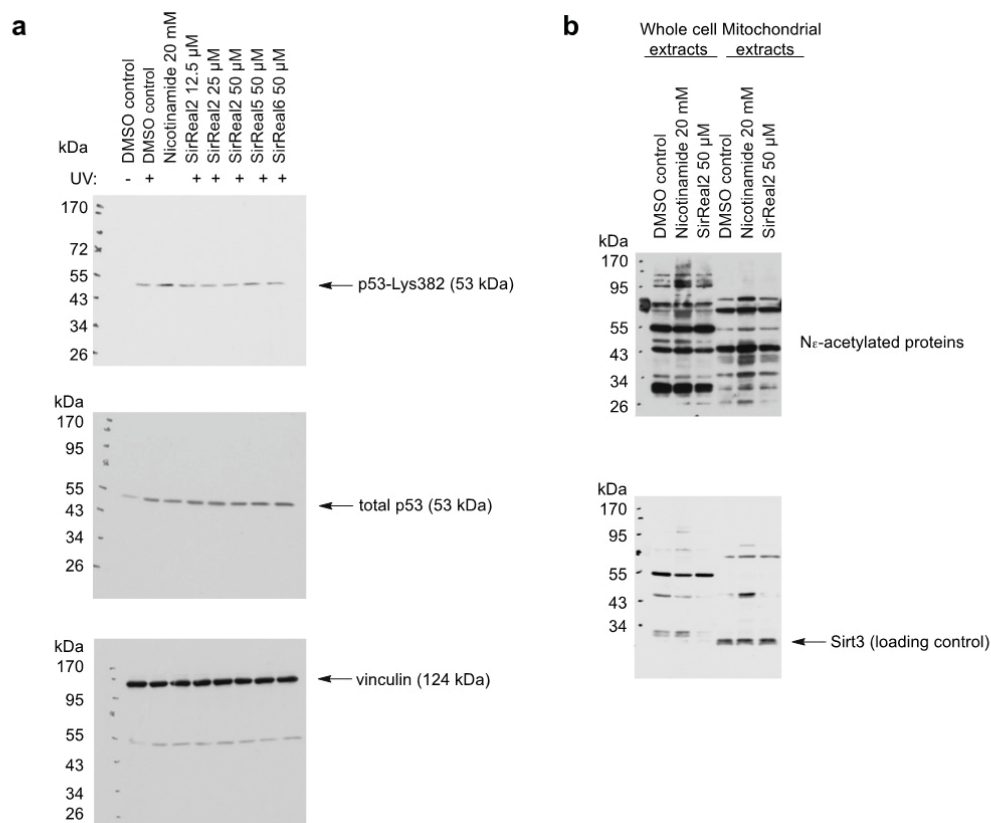
Supplementary Figure 10   SirReal2 does not alter the acetylation of p53-Lys382 or mitochondrial proteins. **(a)** Representative western blot of U2OS cell lysates after incubation with SirReal2. SirReal2 does not affect p53-Lys382-acetylation whereas treatment with nicotinamide, a pan-sirtuin inhibitor, results in an increase of p53-Lys382-acetylation (n=3). **(b)** Representative western blot of whole cell extracts and mitochondrial extracts of HEK293 cells. Treatment with SirReal2 does not alter the mitochondrial lysine-acetylation while incubation with the pan-sirtuin inhibitor nicotinamide leads to an increase of mitochondrial lysine acetylation. Sirt3 was used as a loading control. Sirt3 is enriched in the mitochondrial extracts as expected (n=3). EZ-Run™ Prestained *Rec* Protein Ladder (Fisher Scientific) was used as a molecular weight marker.

SUPPLEMENTARY TABLES

Supplementary Table 1 Physicochemical properties and selectivity profiles of sirtuin inhibitors (Supplementary Fig. 1).

	SirReal2	EX-527[2,3]	CHIC-35[2,4]	ELT inhibitor 11c[5]	ELT inhibitor 28[5]	ELT inhibitor 31[5]	SRT1720[6,7]	4'-bromo-resveratrol[8]	S2iL5[9]	Target values
IC_{50}/k_d for Sirt2 [μM]	0.14	20	2.4	0.003	0.01	0.001	n.d.*	n.d.*	0.001	
Selectivity Sirt1/	> 1,000	**1**	**1**	1.3	1.5	4	activation	**1**	n.d.*	
Sirt2/	**1**	200	23	**1**	**1**	**1**	n.d.*	n.d.*	**1**	
Sirt3 (fold)	> 1,000	500	> 833	1.3	3.3	7	**1**	3†	**1**	
Molar mass [g/mol]	420	249	263	487	389	383	470	291	2,039	< 500
log P^{22}	4.63	2.76	3.1	2.18	0.78	2.76	2.62	4.13	0.4	< 5
H-donors	1	2	2	3	2	2	2	2	31	< 5
H-acceptors	4	1	1	6	5	6	5	0	23	< 10
Number of atoms	49	30	33	59	54	46	57	28	266	20-70

n.d. – not determined; † - inhibition substrate-dependent

Among sirtuin ligands with structural data available, SirReal2 presents the most potent and Sirt2-selective inhibitor. Its physicochemical properties as well as its selectivity make SirReal2 a suitable compound for studies on Sirt2 *in vivo*.

Supplementary Table 2: Refinement statistics for the Sirt2-ADPR-NCA complex structure.

	Sirt2-ADPR-NCA[b]
Data collection	
Space group	$P2_1\,2_1\,2_1$
Cell dimensions (Å)	
a, b, c (Å)	77.60, 77.96, 114.30
α, β, γ (°)	90, 90, 90
Resolution (Å)[a]	34.74–1.87 (1.91–1.87)
R_{merge}	0.123 (1.247)
R_{pim}	0.051 (0.530)
CC1/2	0.995 (0.639)
$I/\sigma I$	8.2 (1.3)
Completeness (%)	100 (100)
Redundancy	6.8 (6.5)
Refinement	
Resolution (Å)	34.74–1.87
No. reflections	393,009 (23,929)
R_{work} / R_{free} (%)	21.1 / 23.9
No. atoms	
Protein	4,754
ADP ribose	72
Nicotinamide	9
Zn^{2+}	2
Other entities	30
Water	138
B-factors (Å^2)	
Protein	42.6
ADP ribose	23.1
Nicotinamide	46.4
Zn^{2+}	54.6
Other entities	36.4
Water	34.5
R.m.s. deviations	
Bond lengths (Å)	0.012
Bond angles (°)	1.58

[a] Values in parentheses are for highest-resolution shell. [b] Data were obtained from one single crystal and were collected at 1.0 Å at the Swiss Light Source (Villigen, Switzerland).

COMPOUND CHARACTERIZATION DATA

SirReal1 - *N*-(5-Benzylthiazol-2-yl)-2-((4,6-dimethylpyrimidin-2-yl)thio)acetamide

^{1}H NMR (400 MHz, DMSO-D$_6$): δ 11.53 (bs, 1H), 7.34–7.28 (m, 2H), 7.26-7.20 (m, 3H), 7.12–7.10 (m, 1H), 6.85 (s, 1H), 4.08 (s, 2H), 3.93 (s, 2H), 2.53 (s, 6H); **^{13}C NMR** (100 MHz, DMSO-D$_6$): δ 169.72, 167.96, 167.20, 157.17, 139.34, 134.16, 132.43, 128.63, 128.39, 126.68, 116.85, 34.37, 32.98, 23.82; HRMS (m/z): [M + Na]$^+$ calcd. for C$_{18}$H$_{18}$N$_4$NaOS$_2$, 393.0814; found, 393.0815; overall yield 9%; isolated mass 24 mg.

SirReal2 - 2-((4,6 -Dimethylpyrimidin-2-yl)thio)-*N*-(5-(naphthalen-1-ylmethyl)thiazol-2-yl)acetamide

^{1}H NMR (400 MHz, CDCl$_3$): δ 11.45 (bs, 1H), 8.05–8.00 (m, 1H), 7.89–7.84 (m, 1H), 7.80–7.76 (m, 1H), 7.51–7.46 (m, 2H), 7.45–7.38 (m, 2H), 7.07 (s, 1H), 6.83 (s, 1H), 4.53 (s, 2H), 3.90 (s, 2H), 2.52 (s, 6H); **^{13}C NMR** (100 MHz, CDCl$_3$): δ 169.79, 167.95, 167.11, 156.63, 135.15, 134.92, 133.91, 132.14, 131.50, 128.73, 127.71, 126.73, 126.15, 125.66, 125.51, 123.61, 116.82, 34.31, 30.43, 23.78; HRMS (m/z): [M + Na]$^+$ calcd. for C$_{22}$H$_{20}$N$_4$NaOS$_2$, 443.0971; found, 443.0973; overall yield 5%; isolated mass 45 mg.

SirReal3 - *N*-(5-Benzylthiazol-2-yl)-2-(pyrimidin-2-ylthio)acetamide

^{1}H NMR (400 MHz, DMSO-D$_6$): δ 12.23 (bs, 1H), 8.58 (d, *J* = 4.8 Hz, 2H), 8.17–8.12 (m, 1H), 7.96–7.90 (m, 1H), 7.86–7.80 (m, 1H), 7.58–7.43 (m, 4H), 7.31 (s, 1H); 7.17 (t, *J* = 4.8 Hz, 1H), 4.55 (s, 2H), 4.12 (s, 2H); **^{13}C NMR** (100 MHz, DMSO-D$_6$): δ 170.38, 166.67, 158.21, 156.94, 136.56, 135.13, 133.93, 131.84, 131.42, 129.01, 127.77, 127.02, 126.63, 126.23, 126.11, 124.28, 117.89, 34.46, 29.82; HRMS (m/z): [M + Na]$^+$ calcd. for C$_{20}$H$_{16}$N$_4$NaOS$_2$, 415.0659; found, 415.0659; overall yield 18%; isolated mass 102 mg.

SirReal4 - *N*-(5-(Naphthalen-1-ylmethyl)thiazol-2-yl)-2-(pyrimidin-2-ylthio)acetamide

^{1}H NMR (400 MHz, CDCl$_3$): δ 11.00 (bs, 1H), 8.66 (d, *J* = 4.9 Hz, 2H), 7.34–7.29 (m, 2H), 7.26–7.21 (m, 3H), 7.16–7.14 (m, 1H), 7.12 (t, *J* = 4.9 Hz, 1H), 4.08 (s, 2H), 3.99 (s, 2H); **^{13}C NMR** (100 MHz, CDCl$_3$): δ 170.64, 166.73, 157.81, 157.25, 139.09, 133.38, 132.78, 128.70, 128.40, 126.80, 117.58, 34.35, 32.96; HRMS (m/z): [M + Na]$^+$ calcd. for C$_{16}$H$_{14}$N$_4$NaOS$_2$, 365.0501; found, 365.0503; overall yield 11%; isolated mass 24 mg.

SirReal5 - 2-((3,5 -Dimethylphenyl)thio)-*N*-(5-(naphthalen-1-ylmethyl)thiazol-2-yl)acet-amide

^{1}H-NMR (400 MHz, DMSO-D$_6$): δ 12.13 (bs, 1H), 8.18–8.08 (m, 1H), 7.97–7.89 (m, 1H), 7.87–7.80 (m, 1H), 7.57–7.42 (m, 4H), 7.29 (s, 1H), 6.95 (s, 2H), 6.80 (s, 1H), 4.55 (s, 2H), 3.83 (s, 2H), 2.17 (s, 6H); **^{13}C-NMR** (100 MHz, DMSO-D$_6$): δ 167.38, 156.69, 138.56, 136.50, 135.20, 135.00, 133.95, 132.00, 131.44, 129.02, 128.37, 127.79, 127.02, 126.64, 126.44, 126.23, 126.11, 124.26, 36.31, 29.82, 21.16; HRMS (m/z): [M + Na]$^+$ calcd. for C$_{24}$H$_{22}$N$_2$NaOS$_2$, 441.1066; found, 441.1068; overall yield 2%; isolated mass 9 mg.

SirReal6 - 2-((4,6-Dimethylpyrimidin-2-yl)thio)-*N*-methyl-*N*-(5-(naphthalen-1-ylmethyl)-thiazol-2-yl)acetamide

^{1}H-NMR (400 MHz, DMSO-D$_6$,): δ 8.16–8.09 (m, 1H), 7.96–7.89 (m, 1H), 7.86–7.79 (m, 1H), 7.56–7.42 (m, 4H), 7.38 (s, 1H), 6.92 (s, 1H), 4.55 (s, 2H), 4.36 (s, 2H), 3.74 (s, 3H), 2.25 (s, 6H); **^{13}C-NMR** (100 MHz, DMSO-D$_6$): δ 169.23, 168.57, 167.38, 158.54, 136.50, 134.48, 133.94, 133.23, 131.45, 129.00, 127.77, 127.00, 126.59, 126.20, 126.07, 124.28, 116.48, 34.94, 34.36, 29.79, 23.65; HRMS (m/z): [M + Na]$^+$ calcd. for C$_{23}$H$_{22}$N$_4$NaOS$_2$, 457.1127; found, 457.1128; overall yield 21%; isolated mass 92 mg.

SUPPLEMENTARY METHODS

Homology Modeling . Homology models of human $Sirt1_{241-512}$ (UniProt: Q96EB6) and human $Sirt3_{122-395}$ (Uniprot: Q9NTG7) were generated using the Sirt2-SirReal2-H3 and Sirt2-SirReal2-NAD$^+$ crystal structures as templates. 10 protein conformations were generated and evaluated with the Modeller program version 9.11[23]. The model showing the most favorable DOPE (Discrete Optimized Protein Energy) assessment score[24] was selected. The stereochemical quality of the models was validated with PROCHECK[25] (Supplementary Fig. 6). All parameters indicate high-quality model structures. Assignment of correct protonation state and energy minimization of the homology models were carried out in MOE 2012.102[26].

Molecular dynamics s imulations. Molecular dynamics (MD) simulations were carried out for the Sirt2-SirReal2-H3 X-ray structure in uncomplexed form (inhibitor and substrate deleted) and in complex with SirReal2 (substrate deleted) as well as for the Sirt1 and Sirt3 homology models (uncomplexed) using the program AMBER 12 and the AMBER 2003 force field[27]. Missing residues in the Sirt2 structures were modelled using the loop search module of Modeller. Atom types and AM1-BCC atomic charges[28] were generated for the ligand using the Antechamber module. Ligand parameters were obtained from the general AMBER force field GAFF[29]. Preparation of the ligand-protein complex, addition of counter ions, solvation, preparation of parameter/topology and coordinate files was carried out using the LEaP module in AMBER. Parameters and libraries for zinc binding residues were defined as previously described[30].

The system was solvated using the water model TIP3BOX[31] and a margin of 10 Å. Two consecutive steps of minimization were carried out. In the first step 3,000 iterations (first 1,000 steepest descent and then 2,000 conjugate gradient) and in the second step 4,000 iterations (first 2,000 steepest descent and then 2,000 conjugate gradient) were applied to the

system. In the first step, atom coordinates for the amino acid residues and ligand atoms were restrained to their initial coordinates with a force constant of 500 kcal mol^{-1}Å^{-2} to relieve the unfavorable van-der-Waals contacts in the surrounding solvent and thus to minimize the positions of the water molecules and ions. In the second step, restraints to atoms were removed and the whole system was minimized freely to relieve bad contacts in the entire system.

The temperature of the system was then equilibrated at 300 K through 100 ps of MD with a time step of 2 fs per step. A constant volume periodic boundary was set to equilibrate the temperature of the system by the Langevin dynamics[32] using a collision frequency of 1 ps^{-1} during the temperature equilibration routine. The protein and ligand atoms were restrained to the initial coordinates with a weak force constant of 10 kcal mol^{-1}Å^{-2}. The final coordinates obtained after temperature equilibration step were then used for a 20 ns MD routine during which the temperature was kept at 300 K by the Langevin dynamics using a collision frequency of 1 ps^{-1}. Constant pressure periodic boundary was used to maintain the pressure of the system at 1 bar using isotropic pressure scaling with a relaxation time of 2 ps. During the temperature equilibration and MD routines a non-bonded cut-off distance of 10 Å was used applying the Particle Mesh Ewald (PME) method[33] for calculating the full electrostatic energy of the periodic system and the SHAKE algorithm[34] to adjust the constraints of all bonds involving hydrogen.

Docking studies . All protein structures were prepared by using the Structure Preparation module in MOE 2012.102[26]. Hydrogen atoms were added, for titratable amino acids the protonation state was calculated using the Protonate 3D module in MOE. All protein structures were energy minimized using the AMBER99 force field using a tethering force constant of 1.5 kT σ^{-2} with (σ = 0.5 Å) for all atoms during the minimization. Water molecules and ligand atoms except the zinc ion were removed from the structures. Docking

studies were performed using the Glide program (Schrödinger Suite 2012-5.8)[35]. All sirtuin structures were superimposed on their backbone atoms using the Superpose module in MOE 2012.102[26]. The position of the inhibitor SirReal2 in the crystal structure was used to define the binding site (10 Å radius). 20 docking poses were calculated for each ligand. All other options were left at their default values. The best-ranked pose from each docking run was included in the analysis and visually inspected together with the protein structure using the program MOE 2012.102[26]. The applied docking protocol used in Glide was able to correctly reproduce the location and conformation of the inhibitor SirReal2 in the corresponding X-ray structures (SirReal2: 0.32 Å and 0.31 Å, respectively). In case of the generated homology models of human Sirt1 and Sirt3 the docking protocol gave docking poses with less favorable Glide SP scores and larger deviations from the conformation and location observed in the Sirt2-SirReal2-H3 structure. To compare the three sirtuins we selected for both homology models docking poses that showed a comparable interaction with the residues of the extended C-site and the selectivity pocket. Docking of SirReal2 to the available crystal structures of Sirt1 and Sirt3 (apo-form and different inhibitor-complexes) was not possible due to the limited size of the extended C-site and the selectivity pocket (data not shown).

Synthesis of α-tubulin derivative H-PSDK(Ac)TIGGWW-NH$_2$. The peptide (residues 36–44 of α-tubulin with two additional C-terminal tryptophans) was synthesized with standard solid-phase-peptide synthesis using 9-fluorenylmethoxy-carbonyl (Fmoc) amino acids. The Rink amide MBHA resin was incubated with *N*,*N*-dimethylformamide (DMF) at RT for 20 min while stirring. The Fmoc group was removed by incubation with 20% (vol/vol) piperidine in DMF at RT for 15 min under stirring. After washing with DMF (5 min, 5 times) the resin was incubated with 4 equivalents (eq) of amino acid, 4 eq *N*,*N*,*N'*,*N'*-tetramethyl-*O*-(1*H*-benzotriazol-1-yl)uronium hexafluorophosphate (HBTU) and 8 eq *N*,*N*-diisopropylethylamine (DIPEA) in DMF at RT for 45 min under stirring. After washing the resin with DMF (5 min,

5 times), Fmoc deprotection and amino acid coupling were repeated until the last amino acid was coupled and the Fmoc group was removed. The resin was washed with dichloromethane (DCM, 3 min, 5 times), methanol (5 min, 3 times) and DCM (3 min, 5 times). The peptide was cleaved from the resin and deprotected by incubation with 97% (vol/vol) trifluoroacetic acid (TFA) at RT (1 h, 2 times). Cleaved peptide was precipitated with cold diethylether, filtrated and dried. The peptide was purified by semi-preparative HPLC (Merck-Hitachi High Speed LC system) using a Merck Hibar LiChrosorb RP-8 column (250–25 mm, 7 µm). For separation a linear gradient from 20–50% (vol/vol) acetonitrile (ACN) with 0.1% (vol/vol) TFA in 60 min was applied (flow-rate: 8 ml min^{-1}). The purification yielded > 97% of pure peptide. Identity was confirmed by MALDI-MS (calculated mass: 1186.5 Da, found: 1187.5 Da).

In vitro **KDAC1/6 assay**. Inhibition tests with SirReal2 and KDAC1/6 were conducted with a high-throughput fluorescence-based assay using the substrate ZMAL (Z-Lys(Acetyl)-AMC)[36]. ZMAL (12.6 µM final concentration) was mixed with assay buffer (50 mM Tris/HCl, 137 mM NaCl, 2.7 mM KCl, 1 mM MgCl$_2$, 0.1 mg mL^{-1} BSA, 5–10% (vol/vol) DMSO, 50 µL, pH 8.0) and SirReal2. A solution that contained DMSO was used a negative control. A solution with trichostatin A (TSA, Enzo Life Sciences) was used a positive control. The reaction was started through the addition of KDAC1 (Enzo Life Sciences, 10 µL) or KDAC6 (Enzo Life Sciences, 10 µL) and incubated (37 °C, 90 min, 150 rpm). To assure initial state conditions the substrate conversion was adjusted to 10–30% prior to inhibition tests. The reaction was stopped by the addition of a solution containing trypsin and TSA (50 mM Tris/HCl, 100 mM NaCl, 0.2% (vol/vol) DMSO, trypsin 5.5 U µL^{-1}, 16.5 µM TSA, pH 8.0, 60 µL) and further incubated (37 °C, 20 min, 150 rpm). Then fluorescence intensity of the released fluorophore of the deacetylated lysine derivative was measured in a microplate

reader (BMG Polarstar, λ_{ex} 390 nm, λ_{em} 460 nm). The amount of inhibition was determined with respect to the mixture with only DMSO.

Immunocytochemistry equipment and settings. The signal of Alexa 546 and DAPI of the same region were acquired with constant illumination parameters as grayscale 8-bit 600 dpi tiff files (1600×1200 pixels). Alexa 546 was acquired after 639.1 ms with a gamma factor of 0.65 without multiplying. The gain was set to 1. DAPI-stained images were acquired after about 20 ms with the same parameters as the one for Alexa 546 image acquisition. The temperature in the microscope room was kept at RT. Representative regions of each samples were processed with Adobe Photoshop CS2 to generate images in RGB mode by copying the appropriate original greyscale images to the blue (nuclei, DAPI) and the red (acetylated α-tubulin signal, Alexa 546) channel, respectively. As adjustment, a minimal background subtraction was applied on all images during processing in the same manner. The resolution was changed from 600 dpi (source images) to 450 dpi without resampling (Fig. 7 of the main article). LUT (CLUT) of grayscale images of the acetylated α-tubulin signal and of the DAPI signal are shown in Supplementary Fig. 8.

Cell Cycle Analysis . HeLa cells were treated as described in the Abundance of BubR1 section of the main article. Cells were harvested by trypsinization, washed in PBS, and fixed in ice-cold 70% (vol/vol) ethanol, and stored at –20 ºC for 2 h. Fixed cells were pelleted, washed in PBS, and stained in propidium iodide buffer (0.1% (wt/vol) sodium citrate, 0.3% (vol/vol) Triton X-100, 0.01% (wt/vol) propidium iodide, 0.02 mg mL^{-1} RNase A) as described previously[37] for 30 min. Stained cells were subjected to flow cytometric analysis using a FACSCaliber (BD Biosciences) and analyzed by FlowJo software (Tree Star, Inc.).

Cell cultivation. HEK-293 cells (ATCC accession no. CRL-1573) were grown in Dulbecco's modified Eagle's medium (DMEM, PAA) containing 10% (vol/vol) fetal calf serum (FCS, PAA), 1% (vol/vol) penicillin (PAA), 1% (vol/vol) streptomycin (PAA), 1% (vol/vol), L-glutamine (PAA) at 37 °C in a 5% (vol/vol) CO_2 atmosphere.

Mitochondrial extra ction. HEK-293 cells (ATCC accession no. CRL-1573) were treated with nicotinamide or SirReal2 at the indicated concentrations for 16 h. Cells were washed in PBS and lysed in 5 packed cell volumes of lysis buffer (20 mM HEPES/KOH, 250 mM sucrose; 10 mM KCl, 1.5 mM $MgCl_2$, 1 mM EDTA, 1 mM EGTA, 1 mM DTT; 0.1 mM PMSF, 1×Complete Protease Inhibitor Cocktail (Roche), pH 7.5). Cells were then homogenized in a Dounce homogenizer and 10% (vol/vol) of sample was removed for use as whole cell extract (WCE). To the remaining lysate, unbroken cells and nuclei were removed by centrifugation (10 min, 800g). The supernatant was transferred and centrifuged (10 min, 7,000g) to pellet mitochondria. Mitochondria were washed twice in lysis buffer, repeating centrifugation after each wash, followed by resuspending washed mitochondria in lysis buffer. NP-40 was added to both whole cell extracts and mitochondria fractions to a final concentration of 0.5% (vol/vol) and lysates were incubated at 4°C for 30 minutes. Lysates were cleared by centrifugation, protein concentrations were quantitated and normalized with 1×Laemmli Buffer. Whole cell and mitochondrial extracts were separated on SDS-PAGE and transferred to a nitrocellulose membrane (Bio-Rad), blocked with non-fat dry milk (Roth, 5% (wt/vol), TBS, 0.1% (vol/vol) Tween 20), and probed with anti-acetyl-lysine (Cell Signaling, #9814) and anti-Sirt3 (Cell Signaling, #2627) as a control for mitochondria enrichment and loading.

Statistical analysis . Statistical analysis for the BubR1 abundance and hyperacetylation of α-tubulin were performed with t-test option of Microsoft Excel using a one-tailed distribution.

For that the intensity of the bands were quantified (Fusion SL, peqlab) and normalized to the respective loading control.

SUPPLEMENTARY REFERENCES

1. Lawson, M. *et al.* Inhibitors to understand molecular mechanisms of NAD(+)-dependent deacetylases (sirtuins). *Biochim. Biophys. Acta* **1799,** 726–739 (2010).

2. Napper, A. D. *et al.* Discovery of indoles as potent and selective inhibitors of the deacetylase SIRT1. *J. Med. Chem.* **48,** 8045–8054 (2005).

3. Gertz, M. *et al.* Ex-527 inhibits Sirtuins by exploiting their unique NAD+-dependent deacetylation mechanism. *Proc. Natl. Acad. Sci.* **110,** E2772–E2781 (2013).

4. Zhao, X. *et al.* The 2.5 Å crystal structure of the SIRT1 catalytic domain bound to nicotinamide adenine dinucleotide (NAD+) and an indole (EX527 analogue) reveals a novel mechanism of histone deacetylase inhibition. *J. Med. Chem.* **56,** 963–969 (2013).

5. Disch, J. S. *et al.* Discovery of thieno[3,2-d]pyrimidine-6-carboxamides as potent inhibitors of SIRT1, SIRT2, and SIRT3. *J. Med. Chem.* **56,** 3666–3679 (2013).

6. Nguyen, G. T. T., Schaefer, S., Gertz, M., Weyand, M. & Steegborn, C. Structures of human sirtuin 3 complexes with ADP-ribose and with carba-NAD(+) and SRT1720: binding details and inhibition mechanism. *Acta Crystallogr. D Biol. Crystallogr.* **69,** 1423–1432 (2013).

7. Jin, L. *et al.* Biochemical characterization, localization, and tissue distribution of the longer form of mouse SIRT3. *Protein Sci.* **18,** 514–525 (2009).

8. Nguyen, G. T. T., Gertz, M. & Steegborn, C. Crystal structures of sirt3 complexes with 4'-bromo-resveratrol reveal binding sites and inhibition mechanism. *Chem. Biol.* **20,** 1375–1385 (2013).

9. Yamagata, K. *et al.* Structural Basis for Potent Inhibition of SIRT2 Deacetylase by a Macrocyclic Peptide Inducing Dynamic Structural Change. *Structure* **22,** 345–352 (2014).

10. Moniot, S., Schutkowski, M. & Steegborn, C. Crystal structure analysis of human Sirt2 and its ADP-ribose complex. *J. Struct. Biol.* **182,** 136–143 (2013).

11. Avalos, J. L., Bever, K. M. & Wolberger, C. Mechanism of sirtuin inhibition by nicotinamide: altering the NAD(+) cosubstrate specificity of a Sir2 enzyme. *Mol. Cell* **17,** 855–868 (2005).

12. Finnin, M. S., Donigian, J. R. & Pavletich, N. P. Structure of the histone deacetylase SIRT2. *Nat. Struct. Biol.* **8,** 621–625 (2001).

13. Krasavin, M. *et al.* Discovery and potency optimization of 2-amino-5-arylmethyl-1,3-thiazole derivatives as potential therapeutic agents for prostate cancer. *Arch. Pharm.*

342, 420–427 (2009).

14. Obushak, N. D., Matiichuk, V. S., Vasylyshin, R. Y. & Ostapyuk, Y. V. Heterocyclic Syntheses on the Basis of Arylation Products of Unsaturated Compounds: X. 3-Aryl-2-chloropropanals as Reagents for the Synthesis of 2-Amino-1,3-thiazole Derivatives. *Russ. J. Org. Chem.* **40,** 383–389 (2004).

15. Zav'yalov, S. I. *et al.* Synthesis of 2-aminothiazole derivatives. *Pharm. Chem. J.* **41,** 105–108 (2007).

16. Schuetz, A. *et al.* Structural basis of inhibition of the human NAD+-dependent deacetylase SIRT5 by suramin. *Structure* **15,** 377–389 (2007).

17. Pan, P. W. *et al.* Structure and biochemical functions of SIRT6. *J. Biol. Chem.* **286,** 14575–14587 (2011).

18. Davenport, A. M., Huber, F. M. & Hoelz, A. Structural and Functional Analysis of Human SIRT1. *J. Mol. Biol.* **426,** 526–541 (2014).

19. Jin, L. *et al.* Crystal structures of human SIRT3 displaying substrate-induced conformational changes. *J. Biol. Chem.* **284,** 24394–24405 (2009).

20. Trapp, J. *et al.* Adenosine mimetics as inhibitors of NAD+-dependent histone deacetylases, from kinase to sirtuin inhibition. *J. Med. Chem.* **49,** 7307–7316 (2006).

21. Outeiro, T. F. *et al.* Sirtuin 2 inhibitors rescue alpha-synuclein-mediated toxicity in models of Parkinson's disease. *Science* **317,** 516–519 (2007).

22. Tetko, I. V. *et al.* Virtual computational chemistry laboratory-design and description. *J. Comput.-Aided Mol. Des.* **19,** 453–463 (2005).

23. Sali, A. & Blundell, T. L. Comparative protein modelling by satisfaction of spatial restraints. *J. Mol. Biol.* **234,** 779–815 (1993).

24. Shen, M.-Y. & Sali, A. Statistical potential for assessment and prediction of protein structures. *Protein Sci.* **15,** 2507–2524 (2006).

25. Laskowski, R. A., MacArthur, M. W., Moss, D. S. & Thornton, J. M. PROCHECK: a program to check the stereochemical quality of protein structures. *J. Appl. Crystallogr.* **26,** 283–291 (1993).

26. Molecular Operating Environment (MOE), Version 2012.10, Chemical Computing Group Inc.: Montreal, QC, Canada, 2012.

27. Duan, Y. *et al.* A point charge force field for molecular mechanics simulations of proteins based on condensed phase quantum mechanical calculations. *J. Comput. Chem.* **24,** 1999–2012 (2003).

28. Jakalian, A. *et al.* Fast, efficient generation of high quality atomic charges. AM1

BCC model: II. Parameterization and validation. *J. Comput. Chem.* **23,** 1623–1641 (2002).

29.   Wang, J., Wolf, R. M., Caldwell, J. W., Kollman, P. A. & Case, D. A. Development and testing of a general amber force field. *J. Comput. Chem.* **25,** 1157–1174 (2004).

30.   Pang, Y.-P., Zinc Protein Simulations Using The Cationic Dummy Atom (CADA) Approach, http://www.mayo.edu/research/labs/computer-aided-molecular-design/projects/zinc-protein-simulationsusing-cationic-dummy-atom-cada-approach (2014).

31.   Jorgensen, W. L., Chandrasekhar, J., Madura, J. D., Impey, R. W. & Klein, M. L. Comparison of simple potential functions for simulating liquid water. *J. Chem. Phys.* **79,** 926–935 (1983).

32.   Pastor, R. W., Brooks, B. R. & Szabo, A. An analysis of the accuracy of Langevin and molecular dynamics algorithms. *Mol. Phys.* **65,** 1409–1419 (2006).

33.   Darden, T., York, D. & Pedersen, L. Particle mesh Ewald: An N log(N) method for Ewald sums in large systems. *J. Chem. Phys.* **98,** 10089–10092 (1993).

34.   Ryckaert, J.-P., Ciccotti, G. & Berendsen, H. J. C. Numerical integration of the cartesian equations of motion of a system with constraints: molecular dynamics of n-alkanes. *J. Comput. Phys.* **23,** 327–341 (1977).

35.   Glide, Schrödinger Suite v2012-5.8. Schrödinger Inc., New York, US, 2012.

36.   Heltweg, B., Trapp, J. & Jung, M. In vitro assays for the determination of histone deacetylase activity. *Methods* **36,** 332–337 (2005).

37.   Krishan, A. Rapid flow cytofluorometric analysis of mammalian cell cycle by propidium iodide staining. *J. Cell Biol.* **66,** 188–193 (1975).

5.5. Publication 5

Crystal structures of the mitochondrial deacylase Sirtuin 4 reveal isoform-specific acyl recognition and regulation features

Pannek, M., Simic, Z., Fuszard, M., Meleshin, M., Rotili, D., Mai, A., Schutkowski, M., Steegborn, C. (2017). Crystal structure of the mitochondrial deacylase Sirtuin 4 – unique structural features, acyl selectivity and regulation. *Nat. Commun.* 8:1513.

This publication resulted from a collaboration of the labs of Clemens Steegborn, Mike Schutkowski and Antonello Mai. Martin Pannek and Clemens Steegborn designed the project, analyzed data and drafted the manuscript. I did the activity studies, crystallization experiments, solved, refined and deposited the crystal structures. Mike Schutkowski, Zeljko Simic and Marat Meleshin synthesized acylated peptides and Cyclophilin A. Matthew Fuszard and me did the MS-experiments. Dante Rotili and Antonello Mai created the fluorogenic Z-Lys (HMG)-AMC substrate. All authors commented on the manuscript.

This work is publicly available and licensed under a Creative Commons Attribution 4.0 International License. This license can be found at the following adress:

https://creativecommons.org/licenses/by/4.0/legalcode

The whole publication including all supplementary information is shown on the following pages.

Crystal structures of the mitochondrial deacylase Sirtuin 4 reveal isoform-specific acyl recognition and regulation features

Martin Pannek[1], Zeljko Simic[2], Matthew Fuszard[1], Marat Meleshin[2], Dante Rotili[3], Antonello Mai[3], Mike Schutkowski[2] & Clemens Steegborn[1]

Sirtuins are evolutionary conserved NAD$^+$-dependent protein lysine deacylases. The seven human isoforms, Sirt1-7, regulate metabolism and stress responses and are considered therapeutic targets for aging-related diseases. Sirt4 locates to mitochondria and regulates fatty acid metabolism and apoptosis. In contrast to the mitochondrial deacetylase Sirt3 and desuccinylase Sirt5, no prominent deacylase activity and structural information are available for Sirt4. Here we describe acyl substrates and crystal structures for Sirt4. The enzyme shows isoform-specific acyl selectivity, with significant activity against hydroxymethylglutarylation. Crystal structures of Sirt4 from *Xenopus tropicalis* reveal a particular acyl binding site with an additional access channel, rationalizing its activities. The structures further identify a conserved, isoform-specific Sirt4 loop that folds into the active site to potentially regulate catalysis. Using these results, we further establish efficient Sirt4 activity assays, an unusual Sirt4 regulation by NADH, and Sirt4 effects of pharmacological modulators.

[1] Department of Biochemistry, University of Bayreuth, 95440 Bayreuth, Germany. [2] Department of Enzymology, Institute of Biochemistry and Biotechnology, Martin-Luther-University Halle-Wittenberg, 06108 Halle, Germany. [3] Department of Chemistry and Technologies of Drugs, Pasteur Institute Italy, Cenci-Bolognetti Foundation, Sapienza University of Rome, 00185 Rome, Italy. Correspondence and requests for materials should be addressed to C.S. (email: Clemens.Steegborn@uni-bayreuth.de)

Reversible acetylation of protein Lys side-chains is a post-translational modification in all domains of life. More than 7000 mammalian acetylation sites are known, and many of them regulate various target functions[1,2]. Among the protein Lys deacetylases, sirtuins form the evolutionary defined class III. They catalyze an unusual, NAD$^+$-dependent deacetylation reaction, coupling their activity to the metabolic state[3]. The seven mammalian sirtuin isoforms are primarily located in nucleus (Sirt1, 6, 7), cytosol (Sirt2), or mitochondria (Sirt3, 4, 5), and they regulate

processes from metabolism to stress responses[2,4]. Sirtuins have further been implicated in aging-related diseases, such as metabolic disorders and neurodegeneration, and are considered potential therapeutic targets[5,6].

Sirt4 acts as a metabolic regulator. It inhibits malonyl-CoA-decarboxylase (MCD), which represses fatty acid oxidation and promotes lipid anabolism[6,7], and it inhibits pancreatic glutamate dehydrogenase (GDH) to regulate insulin secretion[8,9]. Sirt4 further inhibits pyruvate dehydrogenase (PDH)[10] and stimulates
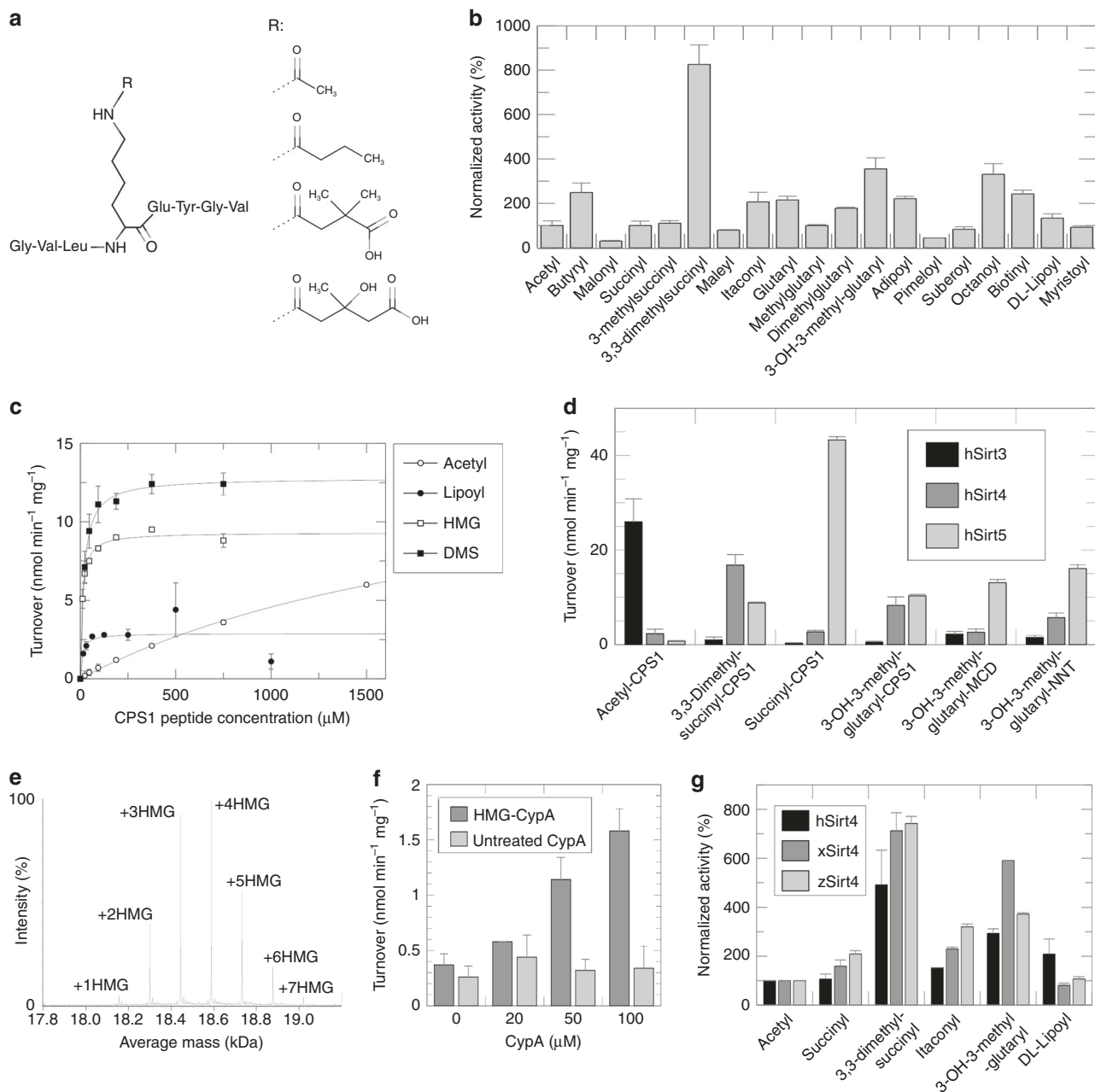
Fig. 1 Sirt4 deacylation activities. **a** Chemical structures of CPS1 peptide and Lys acylations; from top: acetylation, butyrylation, DMS-ylation, HMG-ylation. For the complete set of acyl modifications see Supplementary Fig. 1a. **b** Sirt4-dependent deacylation of differently acylated CPS1 peptides. ($n = 2$; error bars: s.d.). **c** Sirt4 titrations with CPS1 substrate peptide carrying an acetyl, lipoyl, HMG, or DMS modification, respectively. ($n = 2$; error bars: s.d.). **d** Comparison of Sirt3, 4, and 5 deacylation activities against substrate peptide with acetyl, succinyl, DMS, or HMG modification, respectively. ($n = 2$; error bars: s.d.). **e** Intact protein mass spectrometry of HMG-ylated CypA (unmodified molecular weight 18,012 Da). **f** Sirt4-dependent deacylation reactions with increasing amounts of untreated and HMG-ylated CypA protein, respectively, as a substrate. ($n = 2$; error bars: s.d.). **g** Comparison of the acyl selectivities of Sirt4 from human (hSirt4), clawed frog (xSirt4), and zebrafish (zSirt4) using CPS1 peptide substrates featuring an acetyl, succinyl, DMS, itaconyl, HMG, or lipoyl modification, respectively. ($n = 2$; error bars: s.d.)

mitochondrial ATP production[11]. Due to these effects on energy metabolism, Sirt4 is considered a therapeutic target for metabolic dysfunctions[6,7]. Furthermore, Sirt4 displays tumor suppressor activity through downregulation of glutamine metabolism and has been implicated in several cancer types[6,12].

Sirtuins are increasingly recognized as deacylases with isoform-specific acyl selectivities, catalyzing removal of acylations emerging as posttranslational protein modifications, such as succinylation or crotonylation[13–15]. While Sirt1–3 are strong deacetylases, Sirt5 shows low-deacetylation activity and acts primarily as a desuccinylase and deglutarylase[13,15,16], and Sirt6 deacetylates histones but displays more prominent demyristoylation activity[17]. Similarly, Sirt4 features weak deacetylation activity, which appears to regulate MCD[7], but for most of its functional effects the catalyzed target modification appears to differ or is unknown[6]. It can inhibit PDH through delipoylation[10], but the catalytic efficiency for this reaction appears much lower than for other primary sirtuin activities[13]. ADP-ribosyltransferase activity was also described for Sirt4 and Sirt6, but it is also inefficient and appears to constitute a side-activity[8,18], so that a prominent Sirt4 enzyme activity remains to be identified.

Sirtuins share a conserved catalytic core of ~275 amino acids[19]. Isoform-specific N-terminal and C-terminal domains contribute to regulation and cellular localization[6,20]. In Sirt4, the core has no C-terminal appendage and only a short, ~28 residue N-terminal extension that serves as mitochondrial localization sequence[6,9]. The sirtuin core comprises a Rossmann-fold subdomain and a smaller Zn^{2+}-binding module[21,22]. NAD^+ and the acylated substrate polypeptide are bound, with moderate sequence selectivity, to a cleft between the subdomains, accompanied by closure movements of the subdomains and a flexible "cofactor-binding loop"[1,21–24]. The ribose then releases nicotinamide (NAM), and via an 1′-O-alkylimidate and a bicyclic intermediate the products, deacetylated polypeptide and 2′-O-acyl-ADP-ribose, are formed[3,19]. This mechanism was deduced from biochemical studies and crystal structures including human Sirt1, 2, 3, 5, and 6[3,19,21,22,25,26], and it applies to all sirtuin-dependent deacylations. The isoform differences in preferred substrate acyls are caused by binding of the acyl moiety to an active site channel with isoform-specific features. For Sirt4, however, a lack of structural and enzymatic data hampers insights in Sirt4 acyl specificity and regulation.

Here we report crystal structure and enzymatic characterization of Sirt4. We identify an evolutionary conserved, Sirt4-specific acyl selectivity and dehydroxymethylglutarylation (de-HMG-ylation) as a potential physiological activity. A structure of Sirt4 from *X. tropicalis* reveals an unusual acyl binding site and a Sirt4-specific, potentially regulatory loop. Using these insights, we analyze and rationalize Sirt4 modulator effects and identify a Sirt4 regulation by NADH.

Results

Sirt4 shows an isoform-specific acyl preference. The seven mammalian sirtuins vary in their sequence and acyl preferences[16,19]. The Sirt4 deacylation activities reported so far, deacetylation and delipoylation, were weak, with orders of magnitude lower k_{cat}/K_M values as for other sirtuin/substrate acyl pairs[7,10,15]. Testing ~6800 mammalian acetylation site sequences yielded no dramatic activity improvements[1]. We therefore asked whether other acyl modifications would yield deacylation efficiencies expected for a physiologically dominant Sirt4 activity. Testing Sirt4 against an acyl library of CPS1 (carbamoyl phosphate synthetase 1)-Lys527 peptides in a coupled enzymatic assay monitoring NAM release from NAD^+ [27] indeed revealed a

Table 1 Kinetic parameters for Sirt4 and acyl substrates

	k_{cat} (10^{-3} s^{-1})	K_M (μM)	k_{cat}/K_M (M^{-1} s^{-1})
Acetyl-CPS1	8.7 ± 0.7	2341 ± 270	3.7 ± 0.7
Acetyl-DLAT[a]	ND[a]	ND (>2500)[a]	0.2 ± 0.0 (estimated)[a]
Lipoyl-CPS1	1.7 ± 0.3	10.1 ± 13.6	170 ± 230
Lipoyl-DLAT[a]	1.8 ± 0.1[a]	239 ± 51[a]	7.7 ± 1.3[a]
DMS-CPS1	7.3 ± 0.1	17.7 ± 1.5	412 ± 41
HMG-CPS1[b]	5.3 ± 0.1	9.7 ± 1.0	546 ± 67

[a]Values from[10]
[b]Not corrected for HMG-stimulated NAD^+ hydrolysis

particular specificity profile (Fig. 1a, b, Supplementary Fig. 1a). Consistent with previous reports[1,7,10], Sirt4 showed low-deacetylation activity but higher activity against lipoylated and biotinylated substrate (Fig. 1b). Further increased activity was obtained with butyryl and octanoyl substrate, but the highest activity—eightfold stronger than deacetylation—was observed with a 3,3-dimethylsuccinyl (DMS) substrate.

Comparing DMS to acyl moieties physiologically occurring as activated CoA-thioesters, and thus potentially modifying protein Lys side chains[28,29], revealed the 3-hydroxy-3-methylglutaryl (HMG) group as most closely related. Testing HMG-modified CPS1-Lys527 peptide indeed yielded Sirt4 activity similarly to DMS-CPS1 substrate (Fig. 1b), approximately threefold higher than for acetyl peptide and with the expected NAD^+ dependency (Supplementary Fig. 1b). To analyze the mechanistic basis of these differences, we compared through Michaelis-Menten kinetics the improved substrates, HMG- and DMS-CPS1, with lipoyl- and acetyl-CPS1 (Fig. 1c, Table 1). Consistent with previous data[10,16], catalytic efficiency k_{cat}/K_M for acetyl-CPS1 was low (3.7 ± 0.7 M^{-1} s^{-1}; Table 1). Sirt4 activity was strongly increased for DMS-CPS1 (412 ± 41 M^{-1} s^{-1}) and HMG-CPS1 (546 ± 67 M^{-1} s^{-1}). Strikingly, the preferred acyls showed comparable turnover rates to acetyl substrate but increased apparent affinities (two orders of magnitude lower K_M; Fig. 1c, Table 1). Interestingly, lipoyl-CPS1 yielded an only slightly lower k_{cat}/K_M (170 ± 230 M^{-1} s^{-1}), two orders of magnitude higher than a previously published value[10], due to a better K_M in our study, comparable to those for the DMS/HMG modifications (Table 1). These results indicate that lipoylated substrates bind much better to Sirt4 than so far known, but DMS/HMG still yield 3–5-fold higher efficiencies due to faster turnover. Importantly, the catalytic efficiencies with the DMS/HMG substrates are close to those of robust sirtuin activities, such as Sirt2-dependent deacetylation (e.g., 1400 M^{-1} s^{-1} for histone H3-K27[30]). Sirt4 thus features significant deacylation activity and appears to discriminate acyl substrates mainly via their apparent binding affinity.

Sirtuin-dependent NAM release from NAD^+ is normally coupled to deacylation. However, when we analyzed Sirt4-dependent turnover of HMG-CPS1 through MS detection of substrate and product peptide parallel to monitoring NAD^+ hydrolysis, HMG-CPS1 deacylation corresponded only to ~40 % of the NAD^+ turnover (Supplementary Fig. 1c). For Sirt4-dependent conversion of acetyl-CPS1, in contrast, no discrepancy to NAD^+ hydrolysis was observed (Supplementary Fig. 1c). Sirt4 thus shows significant NAD^+-dependent de-HMG-ylation activity, but it catalyzed even slightly better HMG-stimulated NAD^+ glycohydrolysis as an unusual, deacylation independent sirtuin activity.

We next compared the selectivities of the mitochondrial sirtuins Sirt3, 4, and 5 against CPS1 peptides carrying HMG-modifications and DMS-modifications or the generic Sirt3 and

Table 2 Data collection and refinement statistics

	xSirt4/ADPr	xSirt4/thioacetyl-ADPr	zSirt5/HMG-CPS1
Space group	C222$_1$	C222$_1$	P6$_5$22
Unit cell constants	$a = 69.4$ Å, $b = 74.7$ Å, $c = 109.7$ Å	$a = 69.0$ Å, $b = 74.9$ Å, $c = 109.6$ Å	$a = b = 87.5$ Å, $c = 316.9$ Å
Resolution[a]	20.00–1.58 Å (1.62–1.58 Å)	20.00–1.80 Å (1.85–1.80 Å)	50.00–3.10 Å (3.20–3.10 Å)
Unique reflections	39,280 (2868)	26,585 (1932)	13,919 (1214)
Multiplicity	5.1 (5.2)	6.8 (7.1)	10.3 (10.8)
Completeness	99.8% (99.9%)	99.7% (99.9%)	99.9% (99.9%)
R_{meas}	3.6% (85.3%)	5.5% (104.4%)	24.8% (151.2%)
CC1/2 (%)	100.0 (70.4)	99.9 (70.4)	99.4 (59.8)
I/σI	23.7 (2.1)	18.3 (2.1)	10.2 (1.6)
Protein atoms	2285	2177	4138
Ligand atoms	37	40	173
Solvent atoms	285	179	68
Resolution	19.73–1.58 Å (1.62 Å – 1.58 Å)	19.74–1.80 Å (1.85–1.80 Å)	48.67–3.10 Å (3.18–3.10 Å)
R_{cryst}/R_{free}[bc]	15.2%/18.6%	15.5%/20.8%	19.6%/26.6%
Average B-factors			
Protein	30.9	39.4	73.4
Ligands	21.8	30.4	74.3
Solvent	41.6	46.3	48.5
RMSD bond-lengths	0.03	0.03	0.01
RMSD bond-angles	2.6	2.4	1.5

[a] Values in parentheses refer to outermost shell

[b] $R_{cryst} = \frac{\sum ||F_{obs}| - k|F_{calc}||}{\sum |F_{obs}|}$. $|F_{obs}|$ is the observed and $|F_{calc}|$ the calculated structure factor amplitude

[c] R_{free} was calculated from 5% of reflections omitted from refinement

5 substrate modifications acetylation (Sirt3) and succinylation (Sirt5). Sirt4 showed the previous preference for DMS and HMG modifications, and very low-activity against acetylated or succinylated peptide (Fig. 1d). Sirt3, in contrast, featured pronounced selectivity for the acetyl modification, minor activity against DMS substrate, and no turnover with HMG and succinyl substrate (Fig. 1d). The other way round, Sirt5 showed no activity against acetyl substrate but high activity against succinyl peptide, and lower but still significant activity against DMS- and HMG-CPS1 consistent with reported parameters for HMG substrate ($K_M = 8$ μM, $k_{cat}/K_M = 500$ M^{-1} s^{-1})[15]. Sirt5 activity against HMG-CPS1 thus exceeds that of Sirt4 mainly due to faster turnover, and this Sirt5 activity appears even higher with other peptide sequences, but it is still 60–80% lower than the enzyme's desuccinylase activity (Fig. 1d). In summary, Sirt4 shows a particular acyl preference profile: it shares de-HMG-ylation but no desuccinylation activity with Sirt5 and shows no activity overlap with Sirt3, and it features unusual activity against DMS substrate and for HMG-stimulated NAD$^+$ hydrolysis. This distinct profile suggests that there might be additional protein Lys acylations that are specifically removed by Sirt4.

HMG-CoA acylates and Sirt4 de-HMG-ylates proteins. Acetyl transferases employ acetyl-CoA for modifying proteins. However, acetyl-CoA can also non-enzymatically modify proteins, and some other acyl-CoA, such as succinyl-CoA, do so even more efficiently, likely causing the emerging variety of protein acylations[14,28,29,31]. We thus analyzed whether HMG-CoA efficiently acylates peptides and proteins. HMG-CoA titrations revealed CPS1 peptide acylation with a bimolecular rate constant of $(4.0 \pm 0.8) \times 10^{-10}$ μM^{-1} s^{-1}, more than twice as fast as with acetyl-CoA ($k = (1.5 \pm 0.4) \times 10^{-10}$ μM^{-1} s^{-1})[29], in agreement with a recent study reporting more efficient protein acylation by glutaryl- and HMG-CoA as compared to acetyl-CoA[28]. Incubating recombinant Cyclophilin A (CypA) as a model protein with HMG-CoA resulted in 1–7 HMG-modifications as detected by intact protein mass spectrometry (MS; Fig. 1e) and confirmed by MS/MS

analysis of tryptic peptides, consistent with the protein's seven known Lys acetylation sites (Uniprot entry P62937).

To analyze whether Sirt4 is able to remove HMG modifications not only from peptides but also from HMG-ylated protein, we tried to de-HMG-ylate CypA. Modified and unmodified CypA was incubated with Sirt4, in the presence and absence of NAD$^+$, and the deacylation was monitored in the coupled enzymatic assay[27]. Unmodified CypA as substrate did not yield a significant deacylation signal, whereas HMG-CypA substrate resulted in a strong, substrate concentration dependent signal (Fig. 1f) that showed the expected dependency on the co-substrate NAD$^+$ (Supplementary Fig. 1d). To confirm that NAD$^+$-dependent CypA de-HMG-ylation causes or significantly contributes to the NAM release monitored in this assay, we also analyzed the reaction by intact protein mass spectrometry. Incubation with Sirt4 indeed caused a shift toward CypA species carrying fewer HMG-ylations (Supplementary Fig. 1e), confirming the deacylation. We thus conclude that HMG-CoA is reactive toward proteins and that Sirt4 can de-HMG-ylate the modified proteins, consistent with recently published work that furthermore confirmed the physiological occurrence of protein HMG-ylation and Sirt4-dependent de-HMG-ylation[28,32].

Crystal structure of Sirt4. For insights in the molecular basis of Sirt4's substrate preference and other isoform-specific features, we solved a Sirt4 crystal structure. Trials to crystallize our human Sirt4 protein construct (residues 25–314), which comprises the catalytic core with native C-terminus but lacks 24 residues of the N-terminal mitochondrial localization sequence (MLS; residues 1–28[9]), were not successful. Therefore, we used the Sirt4 orthologues from *Xenopus tropicalis* (clawed frog; xSirt4) and *Danio rerio* (zebrafish; zSirt4) as model systems. They show significant sequence deviations only in the ~30 N-terminal residues (Supplementary Fig. 2a), consistent with their function as MLS, which tend to show low-sequence conservation[33]. Within the catalytic core (hSirt4: 32–312; xSirt4: 31–314; zSirt4: 28–310), however, the sequence identity with hSirt4 is 67% (xSirt4; similarity 81%) and
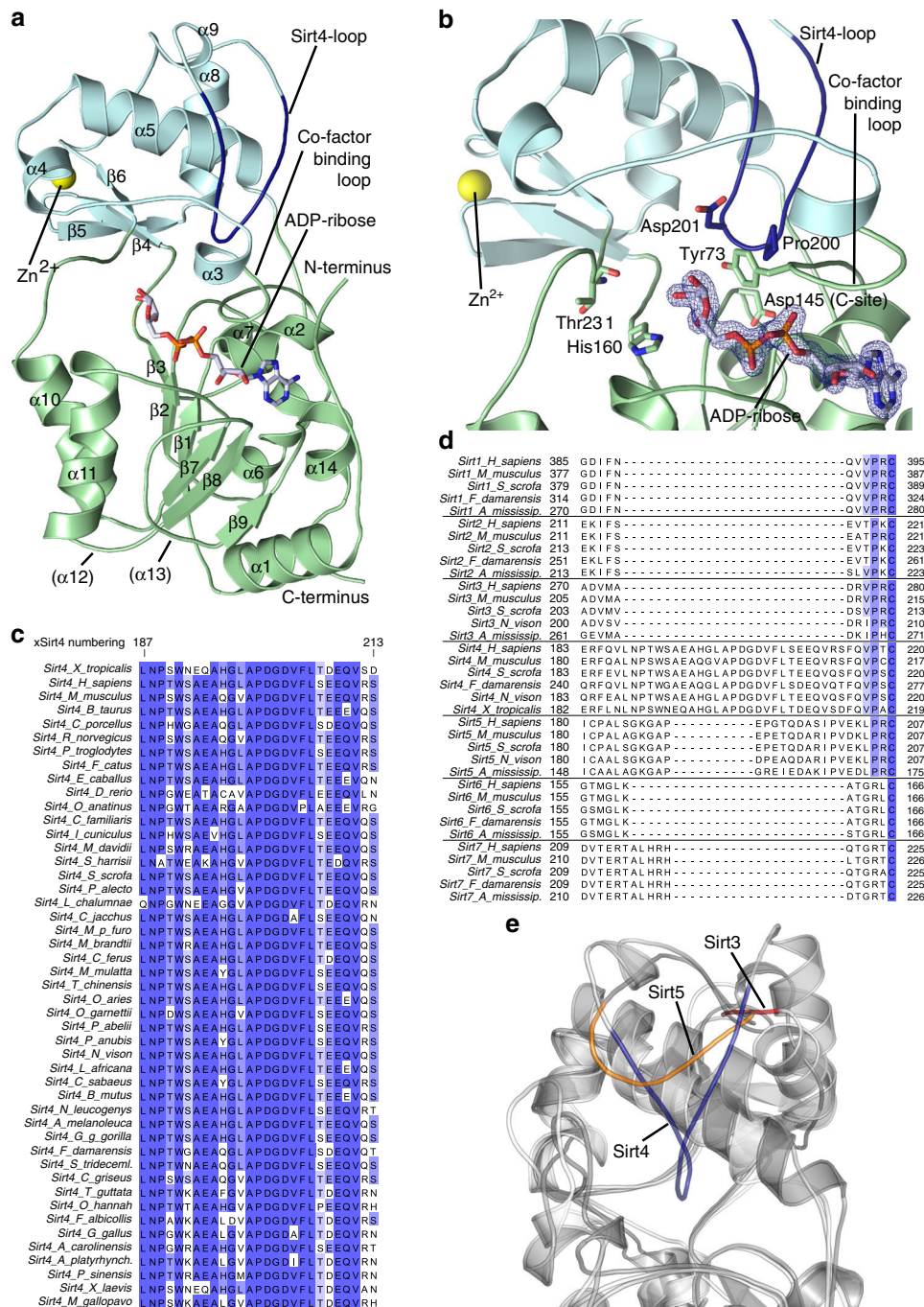
Fig. 2 Crystal structure of xSirt4. **a** Overall structure of the xSirt4/ADPr complex, with Rossmann-fold domain (green), Zn^{2+}-binding domain (cyan), and a Sirt4-specific loop (blue) indicated. ADPr is shown as sticks, colored according to atom type. Secondary structure elements are numbered equivalent to other sirtuins, elements missing in xSirt4 are indicated by brackets. **b** xSirt4 active site, with conserved sirtuin catalytic residues and key residues of the Sirt4-loop shown as sticks. ADPr sticks are colored according to atom type and overlaid with 2F$_o$–F$_c$ electron density (1σ). **c** Alignment of the Sirt4-loop region in Sirt4 sequences from various chordates (Full alignment: Supplementary Fig. 2c). **d** Section of a structure-based alignment of Sirt1–6, extended by chordate Sirt1–7 sequences, showing the isoform differences in the Sirt4-loop region (Full alignment: Supplementary Fig. 2d). **e** Overlay of xSirt4 (gray, blue) with Sirt3 (light gray, red; PDB ID 4BVH) and 5 (dark gray, orange; 4G1C) showing the extended Sirt4-loop, the shorter Sirt5 surface loop, and the short turn in Sirt1–3 (represented by Sirt3)

65% (zSirt4; similarity 78%), respectively (Supplementary Fig. 2a). Consistent with the high sequence conservation, xSirt4 and zSirt4 showed the same acyl preferences as hSirt4 (Fig. 1g), confirming that this acyl selectivity is an evolutionary conserved Sirt4 feature and that xSirt4 and zSirt4 are suitable models for the mammalian enzyme.

xSirt4 yielded well diffracting crystals in presence of ADP-ribose (ADPr). The xSirt4/ADPr structure was solved through Patterson searches with Sir2Af1 (PDB entry 4TWI) and refined at 1.58 Å resolution to R_{cryst}/R_{free} values of 15.2%/18.6% (Table 2). The xSirt4 overall structure shows the typical sirtuin architecture with Rossmann-fold domain and smaller Zn^{2+}-binding module,

Table 3 Kinetic parameters for xSirt4 wild-type and variants[a]

xSirt4 variant	Acetyl-CPS1 K_M (µM)	Acetyl-CPS1 v_{max} (10^{-3} s^{-1})	HMG-CPS1 K_M (µM)	HMG-CPS1 v_{max} (10^{-3} s^{-1})
Wild-type	663 ± 69	12.9 ± 0.6	6.8 ± 0.9	15.9 ± 0.4
Delta 196–205 + GSS	541 ± 51	10.7 ± 0.4	9.7 ± 0.7	18.4 ± 0.3
Delta 196–205	1599 ± 563	15.7 ± 3.4	8.5 ± 0.6	17.2 ± 0.2
Delta 198–203	1104 ± 110	17.1 ± 0.9	10.1 ± 0.7	19.9 ± 0.3
D201A	707 ± 127	9.1 ± 0.8	11.3 ± 1.4	13.0 ± 0.3
D203A	925 ± 136	10.5 ± 0.8	9.0 ± 1.1	14.1 ± 0.3
Y73F	640 ± 71	8.8 ± 0.4	9.0 ± 1.0	24.1 ± 0.5
R101A	ND	ND	23.2 ± 1.3	13.3 ± 0.2
Y104F	643 ± 40	13.3 ± 0.4	15.3 ± 1.3	15.2 ± 0.3
R107A	1097 ± 159	11.0 ± 0.9	17.2 ± 1.8	14.2 ± 0.3
Y104F R107A	918 ± 72	18.5 ± 0.8	22.6 ± 2.6	15.7 ± 0.4
N108A	1104 ± 254	14.8 ± 1.9	19.3 ± 2.8	12.2 ± 0.4

[a]Not corrected for HMG-stimulated NAD$^+$ hydrolysis

with the active-site located in between them and harboring the nucleotide that is well defined by electron density (Fig. 2a, b). The six-stranded β-sheet of the Rossmann-fold domain provides a docking patch for the nucleotide, orienting the reacting ribose close to the conserved catalytic sirtuin residue His160 (Fig. 2b; numbering refers to xSirt4 if not stated otherwise). Due to the occupied nucleotide binding site, the cofactor-binding loop between α2 and α3 is in the "closed" conformation[23], positioning the conserved Phe/Tyr (Tyr73) on top of the ADPr ribose. Thermal denaturation shift experiments showed significant Sirt4 stabilization by NAD$^+$ or ADPr, while substrate peptide and NAM had no pronounced effects (Supplementary Fig. 2b), indicating that the nucleotide-induced closed conformation stabilizes the protein and facilitates crystallization.

A Sirt4-specific loop and additional active site entry. Comparing the Sirt4 structure to other sirtuin isoforms reveals as most striking difference an extended, ~12 residues Sirt4 loop in the Zn^{2+}-binding module, between α8 and α9 (residues 195–206; Fig. 2a). The loop is oriented deep into the catalytic core and contributes to the active site lining (Fig. 2b). A sequence comparison of all higher eukaryotic Sirt4 orthologs in the UNIPROT database shows a high overall sequence homology (89%), and in particular a strict conservation of the presence and even sequence of this loop (G(L/V)APDGDVFL(T/S)(D/E)EQ motif; Fig. 2c, Supplementary Fig. 2c). Structure-based comparison of human Sirt1–6, with human Sirt7 and Sirt1–7 sequences from other chordates added based on homology, shows that the loop is absent in all other sirtuin isoforms (Fig. 2d, Supplementary Fig. 2d), and we therefore refer to it as "Sirt4-loop". The structure-based comparison shows that the Sirt4-loop is extended compared to a much smaller Sirt5 surface loop, and to a short turn in other isoforms, and only the Sirt4-loop is thus able to reach the active site (Fig. 2b, e). Removing the loop (Δ189–214 and Δ192–212) yielded insoluble protein, but deleting the loop's core (Δ196–205, Δ198–203) or replacing it with a GSS linker (Δ196–205 + GSS) resulted in soluble and active protein, which shows that the extended loop is not essential for Sirt4's structural integrity. The variants tended to show higher K_M values for the peptide substrate and at the same time slightly increased turnover (Table 3), which indicates that the loop contributes to substrate binding and restricts catalytically relevant active site dynamics (see also below). In a second xSirt4 structure, solved in complex with the product analog 2′-thioacetyl-ADPr, the Sirt4-loop was not defined by electron density (Table 2, Supplementary Fig. 2e), indicating that it is either flexible or can assume several conformations. Both xSirt4 complexes were solved from the same

crystal form, with residues 191–207 not participating in crystal contacts, excluding that crystal packing causes the loop differences. The Sirt4/2′-thioacetyl-ADPr structure might thus suggest that the loop is released from the active site during product formation, but functions and triggers of Sirt4-loop conformations remain to be studied in more detail.

Another unusual feature of the Sirt4 catalytic core is a channel that branches off from the acyl-Lys binding tunnel and leads to the protein surface (Fig. 3a, b). It is lined by residues from α4 and the preceding loop (86-ArgArgProIle, Glu93), α5 (Ala100, 103-ArgTyr, Arg107), and Ala199/Asp203 from the Sirt4-loop (Fig. 3a). They are mostly conserved in Sirt4, but differ in other isoforms (Fig. 3b). In Sirt6, the Sirt4 channel area is blocked by its isoform-specific N-terminus, but lack of α4, part of α5, and both loops results in a differently oriented, wide cleft that accommodates myristoyl substrates and activators[34]. Sirt1–3 and Sirt5 contain structure elements sized comparable to Sirt4, except for the missing Sirt4-loop, with sequences similar to each other but differing from Sirt4 (Fig. 3b, Supplementary Fig. 2d). The resulting fold in Sirt1–3 and Sirt5 comprises a more wiggled α3/α4 loop folded against α5 and blocking the Sirt4 channel area (Supplementary Fig. 3a). The Sirt4 channel has a small positively charged patch at the outer entrance but is generally rather hydrophobic, and we speculate that it contributes to accommodation of longer substrate acyls. Modeling a Sirt4/lipoyl-Lys complex indeed places the distal lipoyl end into the bottom of the channel (Fig. 3a), supporting an acyl binding function and rationalizing Sirt4's delipoylation activity. Interestingly, the channel could also accommodate a lipoyl group entering from outside as a substrate anchor, in a scenario related to SirTM, which catalyzes ADP-ribosylation of targets only after their lipoylation[35]. Furthermore, the channel might serve as a binding site for regulatory metabolites, similar to Sirt6 activation by free fatty acids[16]. Testing the effects of fatty acids, lipoic acid, and the ketone bodies beta-hydroxybutyrate and acetoacetate indeed revealed that free lipoic acid inhibits Sirt4's deacetylation and de-HMG-ylation activity (Supplementary Fig. 3b). However, the role of the Sirt4 channel in this and/or other regulation mechanisms remains to be studied in detail.

Using our structure-based alignment of Sirt4 and other structurally characterized sirtuins, extended by chordate Sirt1–7 sequences (Fig. 2d, Supplementary Fig. 2d), we analyzed phylogenetic relationships. The phylogenetic tree (based on 208 sequences; Fig. 3c) confirms some classifications based purely on sequence information[36] but also reveals modifications. Sirt4 forms a separate class (class II in ref. [36]) that is almost equally distant to classes I (Sirt1–3), III (Sirt5), and IV (Sirt6/7), despite its partial deacylation activity overlap with Sirt5. Prokaryotic
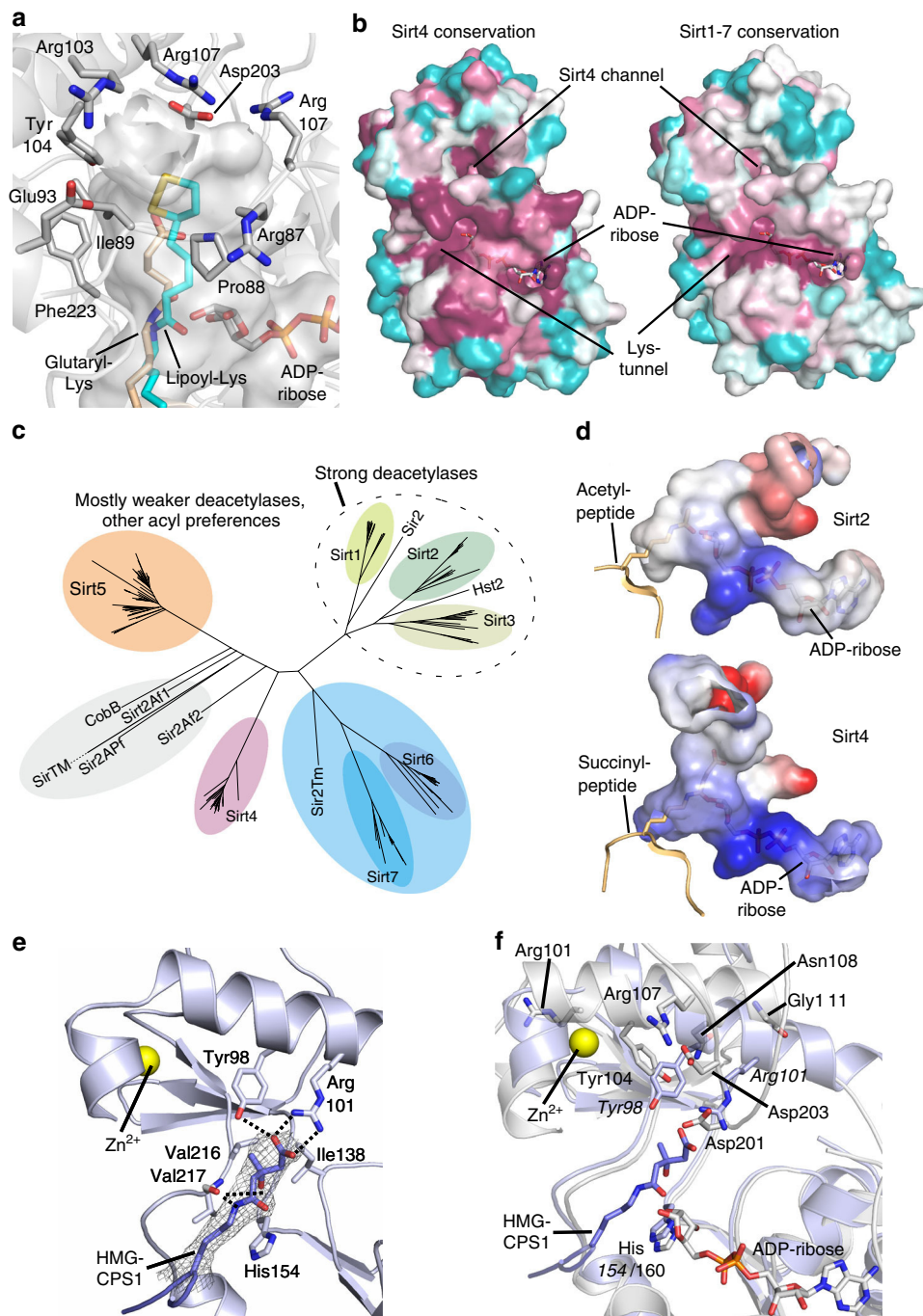
Fig. 3 Sirt4 structural features and phylogeny. **a** xSirt4 active site with the additional Sirt4 channel to the acyl pocket shown as transparent surface. ADPr and residues forming the channel are shown as sticks colored according to atom type. Glutaryl-Lys (beige) from an overlaid Sirt5 complex (PDB ID 4UTR) indicates the conventional acyl pocket, and the modeled lipoyl-Lys (cyan) the bottom of the Sirt4 channel. **b** xSirt4 surface colored according to sequence conservation within Sirt4 isoforms (left; from higher eukaryotic Sirt4 in UniProt) and within the complete Sirtuin family Sirt1–7 (right; from chordate Sirt1–7 in UniProt). Purple indicates high conservation, cyan high variability. **c** Phylogenetic tree generated from a structure-based sirtuin alignment, extended by aligning 195 chordate sirtuin sequences (see Supplementary Fig. 2c for a core alignment). **d** Active site inner surface of Sirt4 and Sirt2 (PDB ID 5D7O; see Supplementary Fig. 3d for all isoforms) colored according to electrostatic potential (red: −15 to blue:+15 $k_B T/e$). The succinyl- and acetyl-peptide are from overlays (PDB IDs 3RIY and 3GLR, respectively). **e** Crystal structure of zSirt5 in complex with HMG-CPS1 substrate peptide. Ligand and interacting residues are shown as sticks, and 2F$_o$–F$_c$ electron density for the peptide is contoured at 1.0σ. Dotted lines indicate hydrogen bonds. **f** Active site overlay of xSirt4/ADPr (gray) and zSirt5/HMG-CPS1 (blue). Catalytic His and residues analyzed for acyl recognition contributions are shown as sticks and labeled (italics: zSirt5)

sirtuins form a cluster in the Sirt5 branch, separate from chordate Sirt5 and almost equidistant to Sirt4. The Sirt6/7 branch also comprises a prokaryotic member, Sir2Tm. The three subclusters for the strong deacetylases Sirt1, 2, and 3 are clearly separated from the other branches but contain yeast enzymes, indicating

that a deacetylase developed still early during evolution and diversified further, possibly reflecting the prominent role of acetylation among the protein acylations. All other branches appear to constitute subfamilies with mostly weak deacetylases, which developed different acyl preference profiles for each cluster
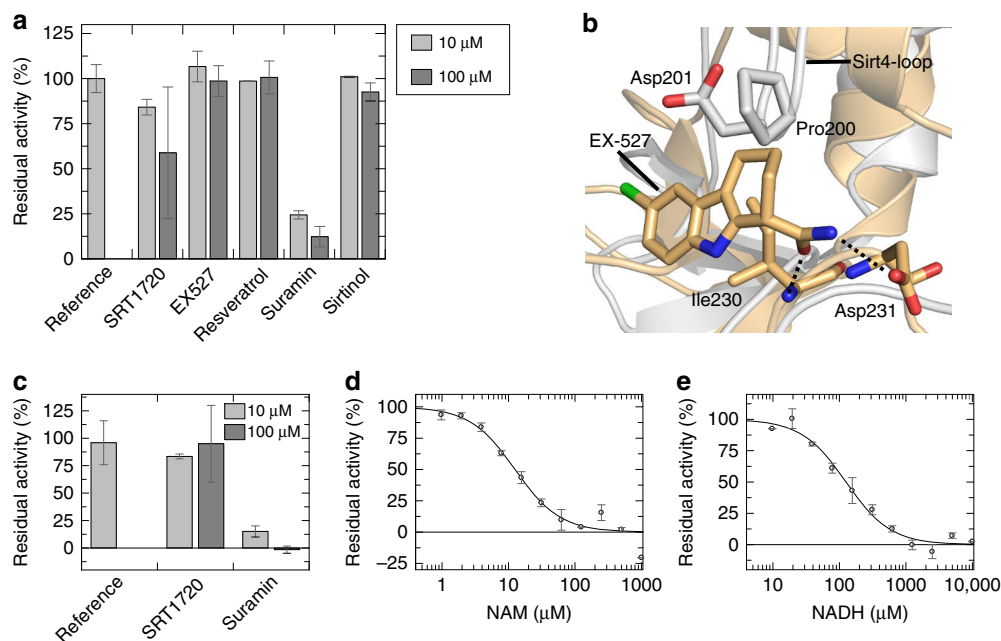
Fig. 4 Sirt4 modulation by physiological metabolites and pharmacological compounds. **a** Effects of known sirtuin modulators on Sirt4 de-HMG-ylation activity. SRT1720 caused effects in controls, indicating incompatibility with the coupled enzymatic assay. ($n = 2$; error bars: s.d.). **b** C-site regions of xSirt4 (gray) and Sirt3/Ex527 (gold; PDB ID 4BVB), showing that Ex-527 would clash with the Sirt4-loop residue Pro200. Dotted lines: conserved hydrogen bonds for carbamide recognition. **c** Effects of SRT1720 and suramin on Sirt4 activity in a HMG-FdL assay. ($n = 2$; error bars: s.d.). **d** NAM titration of Sirt4 activity in a HMG-FdL assay. ($n = 2$; error bars: s.d.). **e** NADH titration of Sirt4 activity in a HMG-FdL assay (see Supplementary Fig. 4b for a titration in a MS assay). ($n = 2$; error bars: s.d.)

that remained conserved in later stages of evolution as indicated by our Sirt4 ortholog comparison. These major branches apparently separated early during evolution, consistent with a variety of acylations occurring non-enzymatically[28,29,31] and thus likely being evolutionary early posttranslational modifications that existed before the protein modifying enzymes emerged.

Sirt4 nucleotide and acyl binding sites. All sirtuins share NAD+ as an essential cosubstrate, but the Sirt4 nucleotide binding site differs from those of other isoforms. The Sirt4-loop tightens the entry of the C-site, where the conserved Asp145 recognizes the NAM moiety of NAD+[25], and its tip around Pro200 will have to rearrange slightly to allow productive NAD+ binding (Supplementary Fig. 3c), consistent with a switch function. However, NAD+ titrations revealed similar apparent NAD+ affinities for wild-type Sirt4 ($K_M = 70 \pm 14\,\mu M$ for xSirt4; $62 \pm 14\,\mu M$ for hSirt4) and a Sirt4 loop deletion variant ($K_M = 66 \pm 9\,\mu M$; Supplementary Fig. 3d), suggesting that a regulatory factor stabilizing the inactive conformation might be missing, consistent with the loop variability observed in our structures (see above). Positive electrostatic potential in the nucleotide site supports binding of the negatively charged ligand in all isoforms, but in Sirt4 the positive potential is more pronounced than in most isoforms (Fig. 3d, Supplementary Fig. 3e), rationalizing its low K_M(NAD+) within the 14–600 μM range reported for sirtuins[15,37,38]. Sirt4's cosubstrate site might also facilitate binding of NADH, compared to NAD+, due to its lacking positive charge at the nicotinamide, and we indeed find a distinctive sensitivity of this sirtuin isoform to NADH (see below). In the peptide binding cleft, Sirt4 also features positive potential in regions accommodating the substrate sequence immediately N-terminal and C-terminal from the substrate acyl-Lys (Supplementary Fig. 3f). Consistently, peptide array studies with its weaker deacetylase activity had shown a

Sirt4 substrate sequence preference for polar residues around the acetyl-Lys, in particular with negative charges in positions +1/2 and −3/4[1].

In the active site, Sirt4 comprises the conserved sirtuin catalytic residues His160 and the Leu/Thr/Val (Thr231) whose backbone oxygen orients the substrate through a hydrogen bond to the acyl-Lys ε-amide (Fig. 2b)[15]. The cofactor-binding loop in "closed" conformation[23] positions the conserved Phe/Tyr (Tyr73) on top of the ribose, shielding this reacting group. Mutating Tyr73 to the Phe found in most sirtuins increased k_{cat} (Table 3), confirming its catalytic relevance and indicating that its hydroxyl group might contribute to an auto-inhibitory mechanism. In the region accommodating a distal carboxyl group in short and medium long dicarboxylates, such as HMG, mildly positive electrostatic potential rationalizes the affinity of such substrates (Fig. 3d). Attempts to solve a Sirt4 structure in complex with substrate peptide to study acyl recognition details failed, possibly due to the lacking stabilization by this ligand (Supplementary Fig. 2b), but we were able to solve a complex of zebrafish Sirt5 (zSirt5) with HMG-CPS1 peptide. The structure, refined at 3.1 Å resolution to R_{cryst}/R_{free} values of 19.5%/26.6% (Table 2, Fig. 3e), reveals a similar substrate conformation as in zSirt5/glutaryl-CPS1. The HMG length is reduced through a helical conformation, albeit with opposite handedness compared to glutaryl-CPS1, to position the 3-hydroxy and 3-methyl moieties toward Ile138/His154 and Tyr98/Val216, respectively (Fig. 3e, Supplementary Fig. 3g). The distal carboxylate interacts with Tyr98 and Arg101, which also recognize the carboxylates of succinyl and glutaryl substrates[15]. Interestingly, Sirt4 also features such a Tyr-X-X-Arg motif in α5. The Sirt4 motif is shifted one helix turn, however, with Sirt4-Tyr104 oriented back to the region occupied by Sirt5-Tyr98, but Sirt4-Arg107 pointing away from the acyl channel (Fig. 3f). Sirt4 residues in the positions of Sirt5-Tyr98/Arg101 would be Asn108 and Gly111. Due to a slightly different conformation, however,

Gly111 is shifted and the area of Sirt5-Arg101 is occupied by the Sirt4-loop residue Asp201 (Fig. 3f), which would result in close contacts between the carboxylates of Asp201 and an HMG substrate. To test the roles of these residues, we analyzed deacetylation and de-HMG-ylation kinetics of xSirt4 Ala variants (Table 3). Exchanging Asp201 or Asp203 caused only a moderate decrease in apparent HMG-peptide affinity, consistent with Sirt4-loop deletion effects. They thus appear not directly involved in substrate binding but to rearrange dynamically, as expected from the repellent effect Asp201 would have on substrate carboxylates and in line with our crystallographic results. Consistently, testing β-Ala-, γ-aminobutyryl-, and 6-aminocaproyl-CPS1 substrates (Supplementary Fig. 1a), which have positively charged end groups that could favorably interact with Asp201 in this position, yielded no Sirt4-dependent deacylation (Supplementary Fig. 3h). Replacing Tyr104 (to Phe) or Arg107 of the Sirt4 Tyr-X-X-Arg motif had a stronger, approximately twofold effect on HMG-peptide K_M values, and a Tyr104Phe/Arg107Ala double mutant even showed an additive effect (Table 3). They thus seem to contribute—directly or indirectly—to substrate binding despite Arg107's orientation away from the active site. In fact, replacing the neighboring Asn108, which points toward the acyl channel, caused a significant, approximately threefold decrease in apparent HMG-substrate affinity, suggesting a contribution to acyl binding and possibly an indirect role for Arg107, via its salt bridge to the Sirt4-loop residue Asp203 (Fig. 3f). Interestingly, mutating Arg101 from a 101-ArgArgArg-103 motif on the opposite side of Tyr104 caused a strong, approximately fourfold decrease in apparent HMG-peptide affinity (Table 3), indicating an important role in substrate recognition despite its distance to the acyl site. These results indicate that as in Sirt5, α5 plays a key role in Sirt4 acyl recognition. Residue differences seem to contribute directly to their different acyl selectivity profiles, but also to a more dynamic Sirt4 acyl site, which we speculate to adapt to acyl substrates (α5 N-terminus) and to contribute to a regulatory Sirt4-loop function (α5 center).

Sirt4 substrates and structure enable modulator studies. Our insights in Sirt4 catalytic activity and structure now enable activity studies for Sirt4 modulator development and a structure-based analysis of compound effects. Using the HMG-CPS1 peptide, we analyzed the effects of the Sirt1 activators resveratrol and SRT1720[39,40], the moderately Sirt1 selective inhibitors Ex527 and sirtinol[25,41], and the pan sirtuin inhibitor suramin[42,43]. At 10 and 100 μM compound concentration, respectively, there was no significant effect for resveratrol, Ex527, and sirtinol (Fig. 4a). Suramin caused potent Sirt4 inhibition, similar to its effects on other sirtuin isoforms[42,43], and 100 μM SRT1720 led to a weak signal decrease but with a high error and significant effect already in a control reaction, indicating a compound incompatibility with the coupled enzymatic assay used here. Suramin is a huge polyanionic compound occupying the complete active site of sirtuins and other targets[44]. Ex-527, in contrast, is accommodated by a small region around the C-site[25], and an overlay of Sirt3/Ex-527 with our Sirt4 structure rationalizes Sirt4's insensitivity (Fig. 4b): The compound would clash with its A ring with Pro200 from the Sirt4-loop, and omitting the A ring and instead attaching the carbamide via a methylene group to ring B might yield a Sirt4-specific compound.

As a convenient and complementary, fluorescence-based alternative to the coupled enzymatic assay with HMG-peptides, we established substrate and assay corresponding to the popular "Fluor-de-Lys" (FdL) deacylation assays[19]. Attaching the HMG group to a Lys with Z-protected amino group and 7-aminomethylcoumarin (AMC) coupled to the carboxyl group,

analog to the Sirt1–3 acetyl substrate Z-MAL[45], yielded an HMG-FdL substrate readily accepted by Sirt4 and sensitively monitored via fluorescence using the FdL procedure[19]. Testing suramin with the HMG-FdL substrate confirmed the potent Sirt4 inhibition observed in the coupled enzymatic assay (Fig. 4c), and a dose-response experiment yielded an IC_{50} of $1.8 \pm 0.2\,\mu M$ (Supplementary Fig. 4a). Assays with SRT1720 showed no incompatibilities in control reactions and revealed that the compound has no effect on Sirt4 activity (Fig. 4c). We then employed the FdL-like Sirt4 assay for studying the effects of NAM and NADH, which are not compatible with the coupled assay. NAM appears to act as a physiological regulator for most sirtuin isoforms[37], and a NAM dose-response experiment with Sirt4 revealed potent inhibition with $IC_{50} = 13 \pm 2\,\mu M$ (Fig. 4d). The effect on Sirt4 is even more potent than on other isoforms[37,46] and possibly supported by the Sirt4-loop at the NAM accommodating C-site entrance. An NADH dose-response experiment (Fig. 4e), corrected through NADH spiking controls for its fluorescence overlap with AMC[47], also indicated pronounced Sirt4 inhibition ($IC_{50} = 126 \pm 12\,\mu M$ at 500 μM NAD$^+$). Analyzing the NADH titration with the robust MS assay confirmed this Sirt4 inhibition potency ($IC_{50} = 142 \pm 54\,\mu M$; Supplementary Fig. 4b) that exceeds NADH effects on other sirtuins (IC_{50} 1.3–27.9 mM)[47,48], consistent with Sirt4 nucleotide site features (see above and discussion). The response of Sirt4 activity to NADH levels around ~30 μM, which is estimated to be the mitochondrial concentration of free NADH[47], suggests NADH or the NAD$^+$/NADH ratio to act as a physiological Sirt4 regulator.

Discussion

Posttranslational modifications are a ubiquitous mechanism of protein regulation and rely on activated metabolites, which are now realized also to cause non-enzymatic modifications[14,28,29,49]. For emerging acyl modifications, such as succinylation and crotonylation, acyl-CoAs act as major activated metabolites[14] whose concentrations thus influence modification levels, together with deacylating enzymes. Elevated HMG-CoA levels in a HMG-CoA-Lyase deficiency model indeed increased protein HMG-ylation[28], and similar changes are expected under fasting conditions and during ketogenic protein catabolism, suggesting that de-HMG-ylating enzymes will regulate target functions during starvation. Sirtuins convert several acyl substrates but with isoform-specific selectivity profiles[15,38], and we find that Sirt4 also has a particular acyl preference profile. It shares de-HMG-ylation activity with Sirt5 but they differ, e.g., in their desuccinylase activity, and Sirt3–5 might have developed complementary selectivities to cover a range of acyls reflecting the variety of activated metabolites in mitochondria. Sirt5's higher de-HMG-ylation activity might suggest that other, even better Sirt4 substrate acyls might exist, but also shared deacylation activities can be complementary due to sirtuin differences in substrate sequence preference and tissue distribution[1,50]. The substrate acylations might be accidental "damage", which would render sirtuins repair enzymes, but many of them regulate dedicated target functions, consistent with specific regulatory effects of sirtuins[4,6]. The additional HMG-dependent NAD$^+$ hydrolase activity of Sirt4 could serve a signaling function, similar to NAD$^+$ depletion caused by poly-(ADP-ribose) polymerases, but a functional role of this unusual sirtuin activity remains to be studied further.

Sirtuin isoforms differ in acyl channel architecture and dynamics. Sirt5 provides a rather rigid binding site for succinylations, but related dicarboxylate modifications can adapt to this site, rationalizing Sirt5's activity against glutarylations[15,51] and HMG-ylations (present study). Sirt6, in contrast, has a long, hydrophobic channel to accommodate myristoyl substrates, and

also the smaller channels in Sirt2 and, in particular, Sirt3 can rearrange to efficiently accommodate and hydrolyze longer acylations such as myristoylations[23,38,52,53]. Sirt4 seems even more adaptable. Sirt4 structure and mutagenesis data suggest that, similar to Sirt5[13], the α5 center contributes to acyl recognition, but in Sirt4 even the remote α5 N-terminus influences acyl binding. Furthermore, the α5 center is connected via an Arg107/Asp203 salt bridge to the Sirt4-loop, an isoform-specific element of the Sirt4 acyl site, and the Sirt4-loop further to the nucleotide binding loop through the packing of Pro200 on the auto-inhibitory Tyr73. The Sirt4-loop assumes at least two states in our structures and for productive NAD+ binding it indeed has to rearrange (Supplementary Figs. 2e, 3c)—possibly triggered by a yet to be identified activator in a physiological setting—which will induce conformational changes in the acyl site. Shifting Asp201 away from the conventional acyl binding pocket should support binding of dicarboxyl substrates such as HMG-ylations. A complete loop release, possibly, would open an area accommodating longer acyls in other isoforms[53] and could extend the observed Sirt4 deoctanoylation activity to longer modifications. Interestingly, Sirt4 accommodates extended lipoyl modifications as substrates despite its length restriction for fatty acids, likely by exploiting a Sirt4-specific channel branching off from the conventional acyl pocket. The bulkier lipoyl group might exploit this channel better than slim alkyl chains, and the two acyl sites might serve, alternatively or even in combination, to expand the acyl substrate spectrum of Sirt4. Interestingly, a lipoyl moiety would also fit into the Sirt4-specific channel coming from outside, as a target label in analogy to the bacterial sirtuin SirTM, which ADP-ribosylates targets only after their lipoylation[35], or as a potential regulatory metabolite (this study). Sirt4 substrate selection indeed appears dominated by K_M, and its de-HMG-ylation activity is still slightly lower than major activities of other sirtuin isoforms. Our comparison of HMG-peptides indicates a relevance for the substrate sequence, consistent with Sirt4 deacetylation studies[1], indicating that better de-HMG-ylation substrates might exist. Sequence differences might in fact account for our higher Sirt4-dependent delipoylation and Sirt5-dependent de-HMG-ylation activity compared to other studies[10,32]. It will be interesting to see whether better Sirt4 substrate sequences or acylations can be identified, and further mechanistic studies, supported by our structural data, should enable a full understanding of Sirt4-loop and acyl channel, their substrate adaptations, and possible external triggers that would regulate Sirt4.

Our Sirt4 substrates and assays enabled analyzes on drug effects and physiological Sirt4 regulators. The continuous coupled assay allows excellent quantification[27], and the FdL assay provides a sensitive set-up that is easily parallelized for screening campaigns[19]. Using these assays, we find a very potent NAM inhibition for Sirt4, which renders it the isoform most sensitive to NAM regulation so far[46,54]. Physiological NAM concentrations are assumed to reach up to 100 μM[54], which would inhibit Sirt4 almost completely, and in vivo Sirt4 activity will thus strongly depend on NAM levels. It will be interesting to see how Sirt4 contributes to the physiological effects of NAM. We further find that Sirt4 activity seems sensitive to physiological NADH levels or the NAD+/NADH ratio. Sirtuin regulation by NADH or NAD+/NADH had been suggested based on inhibitory NADH effects on other isoforms but was discarded due to its weak potency ($IC_{50} \geq 1.3$ mM; $K_i \geq 0.7$ mM), which rules out significant in vivo effects at assumed NADH concentrations (~30 μM in mitochondria) and NAD+/NADH ratios (10:1 and higher)[47,48]. We now find an at least one order of magnitude higher NADH sensitivity for Sirt4, which causes significant effects under such conditions, and it will be exciting to see how this Sirt4-specific regulation contributes to its function. Mechanistically, NADH

likely inhibits through nucleotide site binding in an extended, non-productive conformation also observed for NAD+ under certain conditions[25] (Supplementary Fig. 3c). It places the NAM moiety outside the C-pocket—which prefers oxidized nucleotide due to its conserved negative charge—into regions that show positive electrostatic potential, in particular in Sirt4, which favors NADH over NAD+. Assays and structural insights also provide a basis for Sirt4 modulator development. The identified nucleotide binding site differences should enable Sirt4-specific inhibition, for example through Ex-527 derivatives that can enter Sirt4's tightened C-site. The particular Sirt4 acyl site could be exploited with thio-DMS-Lys, analog to the alkylimidate forming thio-acetyl peptides for deacetylases[25], and the additional Sirt4 channel provides another docking site for specific small molecule inhibitors and possibly also activators. Such Sirt4 modulators would be excellent tools for physiological studies and lead compounds for drug development, for example for diabetes treatment[7].

Methods

Chemicals. If not stated otherwise, chemicals were from Sigma (St. Louis, MO, USA).

Expression and purification of Sirt4 and Sirt5 proteins. hSirt4(25–314) in pQE30 coding for an N-terminal His6-tag, and xSirt4(32–315) and zSirt4(29–310) in a modified pET-19b coding for an N-terminal His6-SUMO-tag (see Supplementary Table 1 for primer sequences), were expressed in *Escherichia coli* CodonPlus(DE3) (Agilent, Santa Clara, CA, USA) in LB medium supplemented with 100 μM zinc acetate. Cells were resuspended in 50 mM Tris/HCl pH 7.5, 200 mM NaCl (and 20% glycerol for xSirt4) and lysed by adding lysozyme and sodium desoxycholate and subsequent pressure homogenization in an Emulsiflex-C5 (Avestin, Ottawa, Canada). After centrifugation (75,000×g, 4 °C, 1 h), supernatants were incubated for 1 h with NiNTA beads in presence of 10 mM imidazole. After transfer in a column, the resin was washed with 20 column volumes (CV) 50 mM Tris/HCl pH 7.5, 500 mM NaCl and 20 CV 50 mM Tris/HCl pH 7.5, 200 mM NaCl, 10 mM imidazole, and the protein eluted with 50 mM Tris/HCl pH 7.5, 200 mM NaCl, 250 mM imidazole.

For hSirt4(25–314), the buffer of the eluted protein was changed to 50 mM Tris/HCl pH 7.5, 30 mM NaCl in a HiPrep Desalting Column (GE Healthcare, Chicago, IL, USA) and the sample applied to a SOURCE15S cation exchange column (GE Healthcare). The proteins were eluted in a linear gradient 30–1000 mM NaCl and Sirt4 fractions were pooled and diluted fivefold with 50 mM Tris/HCl pH 7.5. Sirt4 was then loaded on a HiTrap Heparin column (GE Healthcare) and eluted with a linear gradient 30–1000 mM NaCl. The protein was concentrated to ~1 mg ml⁻¹ in a Microsep concentrator (Pall Corporation, Port Washington, NY, USA), flash-frozen in liquid nitrogen, and stored at −80 °C.

For xSirt4(32–315) and zSirt4(29–310) eluted from the NiNTA material, the buffer was changed to 50 mM Tris/HCl pH 7.5, 200 mM NaCl, (supplemented with 20% glycerol for xSirt4) in a HiPrep Desalting column and subjected to Senp2-proteolysis for 30 min on ice. The protein was loaded on a HisTrap HP 1 mL column (GE Healthcare) and eluted with 50 mM Tris/HCl pH 7.5, 200 mM NaCl, 30–50 mM imidazole. It was subsequently subjected to gel filtration on a Superdex 75 10/300 GL (xSirt4) or Superdex 200 10/300 GL (zSirt4) column (both GE Healthcare) in 25 mM Tris/HCl pH 7.5, 150 mM NaCl (+20 % glycerol for xSirt4), concentrated in a Microsep concentrator, flash-frozen in liquid nitrogen, and stored at −80 °C. xSirt4 single-site variants were generated using the QuickChange protocol (see Supplementary Table 1 for primer sequences) and verified by DNA sequencing, and the proteins were produced as described for wild-type xSirt4.

zSirt5(30–298) was expressed in *E.coli* and purified through Talon affinity chromatography, TEV-proteolysis, reverse affinity chromatography, and gel filtration on a Sephacryl S-200 column[15].

Synthesis of Lys- and peptide-based substrates. HMG-ylated peptides CPS1 (Bz-GVL(acyl-K)EYGV-NH2), MCD (Ac-TSYLGS(HMG-K)IIKASE-NH2), and NNT (Ac-NITKLL(HMG-K)AISPDK-NH2) were synthesized using Fmoc-based solid-phase peptide synthesis protocols. Fmoc-Lys(Nosyl)-OH was used as building block enabling selective on resin deprotections and acylations using HMG-anhydride. As acyl peptide library, the panel of acyl CPS1-Lys527 peptides described in ref. [15] was used and extended through analog synthesis of β-Ala-CPS1, γ-aminobutyryl-CPS1, 6-aminocaproyl-CPS1, butyryl-CPS1, octanoyl-CPS1, lipoyl-CPS1, and biotinyl-CPS1.

The Sirt4 substrate Z-Lys(HMG)-AMC (MC3659; 5-(((S)−5-(((benzyloxy)carbonyl)amino)-6-((4-methyl-2-oxo-2H-chromen-7-yl)amino)-6-oxohexyl)amino)-3-hydroxy-3-methyl-5-oxopentanoic acid) was synthesized by reaction between the (S)-benzyl (6-amino-1-((4-methyl-2-oxo-2H-chromen-7-yl)amino)-1-oxohexan-2-yl)carbamate (Z-Lys-AMC), prepared as reported in literature[55], and

the commercially available 3-hydroxy-3-methylglutaric (HMG) anhydride in dry THF in the presence of DIPEA at room temperature (Supplementary Fig. 5). All chemicals were purchased from Aldrich Chimica, Milan (Italy), and were of the highest purity. Z-Lys-AMC (170 mg, 0.388 mmol) was dissolved at 0 °C in 4 mL dry THF together with diisopropylethylamine (DIPEA) (140 μL, 0.777 mmol) under nitrogen atmosphere. A solution of 3-hydroxy-3-methylglutaric anhydride (67 mg, 0.777 mmol) in dry THF (4 mL) was added dropwise at 0 °C, and the resulting mixture was left under stirring at room temperature overnight. At the end of the reaction, water (10 mL) was added, the resulting mixture was made acidic (pH ~2) with potassium bisulphate 1 M and then extracted with ethyl acetate (6 × 10 mL). The collected organic phases were washed with brine (2 mL), dried, and concentrated under reduced pressure to provide a crude residue that was purified by a silica gel flash chromatography (SNAP 25, Biotage Isolera One) using a linear gradient of methanol (3–25%) in chloroform, giving the expected compound Z-Lys (HMG)-AMC as a white solid, with a yield of 72%. Melting point was determined on a Buchi 530 melting point apparatus and is uncorrected. ^{1}H- and 13C-NMR spectra were recorded at 400 MHz (^{1}H) respective 100 MHz (^{13}C) on a Bruker AC 400 spectrometer; reporting chemical shifts in δ (p.p.m.) units relative to the internal reference tetramethylsilane (Me$_4$Si). All compounds were routinely checked by TLC and ^{1}H-NMR. TLC was performed on aluminum-backed silica gel plates (Merck DC, Alufolien Kieselgel 60 F254) with spots visualized by UV light. Yield of reaction refers to the purified product. Mass spectrum was recorded on an API-TOF Mariner by Perspective Biosystem (Stratford, TX, USA), and samples were injected by a Harvard pump, using a flow rate of 5–10 μL min^{-1}, in the Electrospray system. Elemental analysis was performed by a PE 2400 (Perkin-Elmer) analyzer and has been used to determine purity of the described compound, which is >95%. Analytical result is within ±0.40% of the theoretical value.

mp 128–129 °C; yield 72%. ^{1}H-NMR (DMSO) δ 1.18 (s, 3H, C(OH)CH$_3$), 1.32–1.41 (m, 4H, CHCH$_2$CH$_2$CH$_2$NH), 1.61–1.67 (m, 2H, CHCH$_2$CH$_2$CH$_2$NH), 2.33 (s, 2H, C(OH)(CH$_3$)CH$_2$CONHCH$_2$), 2.38–2.41 (m, 5H, CH$_2$COOH and coumarin-CH$_3$), 3.04 (m, 2H, CH$_2$CONHCH$_2$), 4.15 (m, 1H, α-CH), 5.04 (s, 2H, OCH$_2$Ph), 6.28 (s, 1H, C–H coumarin), 7.18–7.37 (m, 5H, C–H phenyl ring), 7.51–7.54 (m, 1H, C–H coumarin), 7.67 (m, 1H, C–H coumarin), 7.73 (d, 1H, Z–NHCHCO), 7.80 (bs, 1H, C–H coumarin), 8.01 (t, 1H, CH$_2$CONHCH$_2$), 10.61 (bs, 1H, CONH-coumarin). ^{13}C-NMR (DMSO) δ: 174.2, 172.6, 170.9, 161.4, 156.5, 154.2, 153.5, 142.5, 136.8, 128.6 (2C), 128.2 (2C), 127.8, 124.5, 116.7, 112.5, 110.7, 105.2, 71.5, 66.8, 54.1, 47.6, 46.9, 39.1, 30.5, 29.7, 27.4, 22.5, 18.9. Anal. (C$_{30}$H$_{35}$N$_3$O$_9$) Calcd. (%): C, 61.95; H, 6.07; N, 7.22. Found (%): C, 62.03; H, 6.05; N, 7.19. MS (ESI), m/z: 580 (M–H)$^-$.

CypA modification and de-HMG-ylation and intact protein MS. The recombinant CypA was prepared through expression of a full-length CypA construct in pQE70 (Qiagen) in *E. coli* M15 cells and purification by ion exchange chromatography on Fractogel EMD DEAE-650(M), Fractogel TSK AF-Blue, and Fractogel SO3–650(M) (Merck Millipore)[29]. CypA protein (0.4 mg ml^{-1}) was modified using 8 mM HMG-CoA in 100 mM Tris-HCl buffer pH 8.3 at 37 °C for 4 h. Formation of HMG-ylated protein was confirmed by peptide-MS analyzes after tryptic digest[29], and by intact HMG-CypA mass analyzes through HPLC-coupled ESI-MS[56]. For intact mass determination, 25 μM HMG-CypA in 10 mM Tris/HCl pH 7.5, 50 mM NaCl was HPLC-separated with the setting described below for peptide MS, using a 30 min gradient from 1 to 55% buffer B (90% ACN, 9.9% H$_2$O, 0.1% FA; buffer A: 5% ACN, 94.9% H$_2$O, 0.1% FA) followed by 1 min of 55–90% buffer B with 70 μL min^{-1} flow-rate. MS-analyzes were done with the settings described for peptide assays (below), except that the IntactProtein script was activated, which reduces CEM to 100. Acquired data were extracted with PeakView and deconvoluted in MassLynx in the range of 950–1500 m/z using the MaxEnt I algorithm to a resolution of 1 Da. Peak intensity values were recorded and overlaid with MassLynx.

For MS-based CypA deacylation analyzes, 50 μM HMG-modified CypA was incubated for 2 h at 37 °C with 20 μM hSirt4 and 2 mM NAD$^+$, as well as 0.5 mg mL^{-1} nicotinamidase to prevent Sirt4-inhibition by released nicotinamide. Control reactions without Sirt4 were incubated for 22 h. All reactions were stopped through mixing 1:1 with 0.5% TFA and analyzed by ESI-MS as described above[56]. CypA de-HMG-ylations in the coupled continuous assay were performed as described for peptide-based assays.

Peptide- and FdL-based activity assays. The coupled continuous assay was performed as reported[27]. Briefly, assays in 20 mM sodium phosphate buffer pH 7.8 contained 5 μM hSirt4 or 3–5 μM xSirt4, 0.05 mg ml^{-1} nicotinamidase, 2 U ml^{-1} GDH, 3.3 mM a-ketoglutarate, 0.2 mM NADPH, 10% DMSO, and NAD$^+$ at 2 mM or as indicated, and substrate peptide at 500 μM or as indicated. Reactions were monitored in microplates at room temperature for 1 h through absorption measurements at 340 nm in a LAMBDAScan plate reader (MWG Biotech, Ebersberg, Germany).

The Fluor-de-Lys (FdL) assay was performed at 37 °C in 25 mM Tris/HCl, 150 mM NaCl with 1 μM hSirt4, 500 μM HMG-FdL substrate and 500 μM NAD$^+$. After 20 min, developer solution (2 mM NAM and 10 mg mL^{-1} trypsin) in assay buffer was added 1:1 and samples were incubated for 45 min at room temperature. Fluorescence was measures using a FluoDia T70 with excitation wavelength 365 nm and emission wavelength 465 nm.

For MS and UV analyzes of deacylation reactions, samples were prepared as described for the coupled continuous assay, stopped by mixing 1:1 with 0.5% TFA after 0 and 60 min, diluted to 20 μM peptide using 0.1% FA, and analyzed by HPLC-separation using a Shimadzu Prominence UFLC (Shimadzu, Duisburg, Germany) coupled to ESI-MS and UV detection. Samples were washed on a Piccolo Proto 200 C4 5 μm 2.5 × 0.5 mm trap column (Higgins Analytical, Mountain View, California) and subsequently subjected to a Jupiter C4 5 μm 300 Å 150 × 1 mm analytical column (Phenomenex, Torrance, California) for reversed phase separation, with 99.9% H$_2$O, 0.1% TFA as buffer A and 99.9% ACN, 0.1% TFA as buffer B. Peptides were eluted over a 20 min gradient from 1 to 55% buffer B, followed by 1 min from 55 to 90% buffer B with 70 μL min^{-1} flow-rate. UV-detection was done using a Shimadzu SPD-20A detector at 280 nm. MS analysis was performed by ESI-TOF-MS on an AB Sciex TripleTOF 5600+ mass spectrometer (Sciex, Darmstadt, Germany) with a DuoSpray Ion Source using the following settings: floating voltage of 5500 V and declustering potential of 100 with one TOF experiment summing over four time bins. We detected in a mass range from 300 to 2500 m/z. XIC of substrate and product peptides were extracted using their respective mass in singly, doubly, or triply charged state within a window of 0.2 m/z in PeakView version 1.2.0.3.

Thermal denaturation shift assays. Thermal shift assays were performed in 96-well PCR plates using 3 μM xSirt4 (32–315) or 3 μM zSirt4 (29–310) and SYPRO orange (Thermo Fisher, Waltham, MA, USA) covered with 15 μL mineral oil. Heating and fluorescence measurements were performed in a FluoDia T70 with 1 K steps from 20 to 73 °C (excitation: 465 nm, emission: 580 nm). The data were analyzed in GraFit (Erithacus Software Ltd, Horley, UK) by nonlinear fitting using a two state model.

Statistical information. Data points for activity assays were determined in duplicates, and all experiments were done in at least two repetitions.

Sirt4 crystallization and structure determination. xSirt4(32–315) protein (5 mg ml^{-1}) in 25 mM Tris/HCl 7.5, 150 mM NaCl, 20% glycerol) was incubated with 10 mM ADPr (xSirt4/ADPr complex) or 1 mM thioacetyl H3K9 peptide and 5 mM NAD$^+$ (xSirt4/thioacetyl-ADPr complex) on ice for 30 min. The xSirt4 complexes crystallized at 4 °C in sitting drops (1:1 ratio protein to reservoir solution) with 100 mM BICINE pH 8.5, 20% PEG6000 (xSirt4/ADPr) or 500 mM Na/K-tartrate, 0.5% PEG5000MME, 100 mM TRIS/HCl pH 8.5 (xSirt4/thioacetyl-ADPr) as reservoir. zSirt5 (10 mg mL^{-1} in 20 mM TRIS/HCl pH 8.5, 150 mM NaCl) was incubated with 1 mM HMG-CPS1-peptide (10% v/v DMSO final concentration) on ice for 30 min and crystallized in sitting drops at 20 °C using 20% PEG3350, 100 mM HEPES pH 7.6 as reservoir solution. Crystals appeared within 3 days (xSirt4) or 2 weeks (zSirt5), were transferred to a drop of reservoir solution supplemented with the co-crystallization ligand and 25% glycerol for 1 min, and flash-frozen in liquid nitrogen.

Data collection was done at BESSY II beamline MX14.1 (operated by the Helmholtz Zentrum Berlin, Germany) using a wavelength of 0.912 Å and a Pilatus 6 M detector (Dectris, Baden, Switzerland). Indexing, scaling and merging of diffraction data was performed with XDS[57]. Structures were solved by molecular replacement with PHASER[58] using as a search model a Sir2Af1/peptide complex (PDB-Code 4TWI[59]) for xSirt4/ADPr, this initial xSirt4 structure for xSirt4/thioacetyl-ADPr, and a zSirt5/peptide complex (PDB ID 4UTV[15]) for zSirt5/HMG-CPS1. Refinement was performed with Refmac5[60], using partially anisotropic B-factors and TLS for the protein chain and the Zn ion for the xSirt4/ADPr complex. Models were built and validated using Coot[61] and structure figures were generated with PyMol (Schrödinger, LLC). Docking of Lipoyl-Lys in the xSirt4/ADPr active-site was done with LeadIT (BiosolveIT GmbH, Sankt Augustin, Germany).

Sequence alignments and phylogenetic trees. Structure-based sequence alignments were created using STRAP with the integrated Aligner3D algorithm[62], and manual editing and phylogenetic tree generation were done with BioEdit[63]. Conservation levels were mapped on the xSirt4 structure surface using ConSurf[64].

References

1. Rauh, D. et al. An acetylome peptide microarray reveals specificities and deacetylation substrates for all human sirtuin isoforms. *Nat. Commun.* **4**, 2327 (2013).

2. Choudhary, C., Weinert, B. T., Nishida, Y., Verdin, E. & Mann, M. The growing landscape of lysine acetylation links metabolism and cell signalling. *Nat. Rev. Mol. Cell Biol.* **15**, 536–550 (2014).

3. Sauve, A. A., Wolberger, C., Schramm, V. L. & Boeke, J. D. The biochemistry of sirtuins. *Annu. Rev. Biochem.* **75**, 435–465 (2006).

4. Michan, S. & Sinclair, D. Sirtuins in mammals: insights into their biological function. *Biochem. J.* **404**, 1–13 (2007).

5. Baur, J. A., Ungvari, Z., Minor, R. K., Le Couteur, D. G. & de Cabo, R. Are sirtuins viable targets for improving healthspan and lifespan? *Nat. Rev. Drug Discov.* **11**, 443–461 (2012).

6. Gertz, M. & Steegborn, C. Using mitochondrial sirtuins as drug targets - disease implications and available compounds. *Cell Mol. Life Sci.* **73**, 2871–2896 (2016).

7. Laurent, G. et al. SIRT4 coordinates the balance between lipid synthesis and catabolism by repressing malonyl CoA decarboxylase. *Mol. Cell* **50**, 686–698 (2013).

8. Haigis, M. C. et al. SIRT4 inhibits glutamate dehydrogenase and opposes the effects of calorie restriction in pancreatic beta cells. *Cell* **126**, 941–954 (2006).

9. Ahuja, N. et al. Regulation of insulin secretion by SIRT4, a mitochondrial ADP-ribosyltransferase. *J. Biol. Chem.* **282**, 33583–33592 (2007).

10. Mathias, R. A. et al. Sirtuin 4 is a lipoamidase regulating pyruvate dehydrogenase complex activity. *Cell* **159**, 1615–1625 (2014).

11. Ho, L. et al. SIRT4 regulates ATP homeostasis and mediates a retrograde signaling via AMPK. *Aging* **5**, 835–849 (2013).

12. Jeong, S. M. et al. SIRT4 has tumor-suppressive activity and regulates the cellular metabolic response to DNA damage by inhibiting mitochondrial glutamine metabolism. *Cancer Cell* **23**, 450–463 (2013).

13. Du, J. et al. Sirt5 is a NAD-dependent protein lysine demalonylase and desuccinylase. *Science* **334**, 806–809 (2011).

14. Lin, H., Su, X. & He, B. Protein lysine acylation and cysteine succination by intermediates of energy metabolism. *ACS Chem. Biol.* **7**, 947–960 (2012).

15. Roessler, C. et al. Chemical probing of the human sirtuin 5 active site reveals its substrate acyl specificity and peptide-based inhibitors. *Angew. Chem. Int. Ed. Engl.* **53**, 10728–10732 (2014).

16. Feldman, J. L., Baeza, J. & Denu, J. M. Activation of the protein deacetylase SIRT6 by long-chain fatty acids and widespread deacylation by mammalian sirtuins. *J. Biol. Chem.* **288**, 31350–31356 (2013).

17. Jiang, H. et al. SIRT6 regulates TNF-alpha secretion through hydrolysis of long-chain fatty acyl lysine. *Nature* **496**, 110–113 (2013).

18. Du, J., Jiang, H. & Lin, H. Investigating the ADP-ribosyltransferase activity of sirtuins with NAD analogues and 32P-NAD. *Biochemistry* **48**, 2878–2890 (2009).

19. Schutkowski, M., Fischer, F., Roessler, C. & Steegborn, C. New assays and approaches for discovery and design of Sirtuin modulators. *Exp. Opin. Drug Discov.* **9**, 183–199 (2014).

20. Tennen, R. I., Berber, E. & Chua, K. F. Functional dissection of SIRT6: identification of domains that regulate histone deacetylase activity and chromatin localization. *Mech. Ageing Dev.* **131**, 185–192 (2010).

21. Sanders, B. D., Jackson, B. & Marmorstein, R. Structural basis for sirtuin function: what we know and what we don't. *Biochim. Biophys. Acta* **1804**, 1604–1616 (2010).

22. Moniot, S., Weyand, M. & Steegborn, C. Structures, substrates, and regulators of Mammalian sirtuins - opportunities and challenges for drug development. *Front. Pharmacol.* **3**, 16 (2012).

23. Moniot, S., Schutkowski, M. & Steegborn, C. Crystal structure analysis of human Sirt2 and its ADP-ribose complex. *J. Struct. Biol.* **182**, 136–143 (2013).

24. Jin, L. et al. Crystal structures of human SIRT3 displaying substrate-induced conformational changes. *J. Biol. Chem.* **284**, 24394–24405 (2009).

25. Gertz, M. et al. Ex-527 inhibits Sirtuins by exploiting their unique NAD+-dependent deacetylation mechanism. *Proc. Natl Acad. Sci. USA* **110**, E2772–E2781 (2013).

26. Zhou, Y. et al. The bicyclic intermediate structure provides insights into the desuccinylation mechanism of human sirtuin 5 (SIRT5). *J. Biol. Chem.* **287**, 28307–28314 (2012).

27. Smith, B. C., Hallows, W. C. & Denu, J. M. A continuous microplate assay for sirtuins and nicotinamide-producing enzymes. *Anal. Biochem.* **394**, 101–109 (2009).

28. Wagner, G. R. et al. A class of reactive Acyl-CoA species reveals the non-enzymatic origins of protein acylation. *Cell Metab.* **25**, 823–837 (2017). e828.

29. Simic, Z., Weiwad, M., Schierhorn, A., Steegborn, C. & Schutkowski, M. The epsilon-amino group of protein lysine residues is highly susceptible to nonenzymatic acylation by several physiological Acyl-CoA thioesters. *Chembiochem* **16**, 2337–2347 (2015).

30. Jin, J., He, B., Zhang, X., Lin, H. & Wang, Y. SIRT2 reverses 4-oxononanoyl lysine modification on histones. *J. Am. Chem. Soc.* **138**, 12304–12307 (2016).

31. Wagner, G. R. & Payne, R. M. Widespread and enzyme-independent Nepsilon-acetylation and Nepsilon-succinylation of proteins in the chemical conditions of the mitochondrial matrix. *J. Biol. Chem.* **288**, 29036–29045 (2013).

32. Anderson, K. A. et al. SIRT4 Is a lysine deacylase that controls leucine metabolism and insulin secretion. *Cell Metab.* **25**, 838–855 (2017). e815.

33. Emanuelsson, O., Brunak, S., von Heijne, G. & Nielsen, H. Locating proteins in the cell using TargetP, SignalP and related tools. *Nat. Protoc.* **2**, 953–971 (2007).

34. You, W. et al. Structural basis of sirtuin 6 activation by synthetic small molecules. *Angew. Chem. Int. Ed. Engl.* **56**, 1007–1011 (2017).

35. Rack, J. G. et al. Identification of a class of protein ADP-ribosylating sirtuins in microbial pathogens. *Mol. Cell* **59**, 309–320 (2015).

36. Frye, R. A. Phylogenetic classification of prokaryotic and eukaryotic Sir2-like proteins. *Biochem. Biophys. Res. Commun.* **273**, 793–798 (2000).

37. Sauve, A. A. Sirtuin chemical mechanisms. *Biochim. Biophys. Acta* **1804**, 1591–1603 (2016).

38. Feldman, J. L. et al. Kinetic and structural basis for acyl-group selectivity and NAD(+) dependence in sirtuin-catalyzed deacylation. *Biochemistry* **54**, 3037–3050 (2015).

39. Lakshminarasimhan, M., Rauth, D., Schutkowski, M. & Steegborn, C. Sirt1 activation by resveratrol is substrate sequence-selective. *Aging* **5**, 151–154 (2013).

40. Milne, J. C. et al. Small molecule activators of SIRT1 as therapeutics for the treatment of type 2 diabetes. *Nature* **450**, 712–716 (2007).

41. Peck, B. et al. SIRT inhibitors induce cell death and p53 acetylation through targeting both SIRT1 and SIRT2. *Mol. Cancer Ther.* **9**, 844–855 (2010).

42. Suenkel, B., Fischer, F. & Steegborn, C. Inhibition of the human deacylase Sirtuin 5 by the indole GW5074. *Bioorg. Med. Chem. Lett.* **23**, 143–146 (2013).

43. Gertz, M. & Steegborn, C. Function and regulation of the mitochondrial Sirtuin isoform Sirt5 in Mammalia. *Biochim. Biophys. Acta* **1804**, 1658–1665 (2010).

44. Schuetz, A. et al. Structural basis of inhibition of the human NAD+-dependent deacetylase SIRT5 by suramin. *Structure* **15**, 377–389 (2007).

45. Heltweg, B., Dequiedt, F., Verdin, E. & Jung, M. Nonisotopic substrate for assaying both human zinc and NAD+-dependent histone deacetylases. *Anal. Biochem.* **319**, 42–48 (2003).

46. Fischer, F. et al. Sirt5 deacylation activities show differential sensitivities to nicotinamide inhibition. *PLoS ONE* **7**, e45098 (2012).

47. Madsen, A. S. et al. Investigating the sensitivity of NAD+-dependent sirtuin deacylation activities to NADH. *J. Biol. Chem.* **291**, 7128–7141 (2016).

48. Schmidt, M. T., Smith, B. C., Jackson, M. D. & Denu, J. M. Coenzyme specificity of Sir2 protein deacetylases: implications for physiological regulation. *J. Biol. Chem.* **279**, 40122–40129 (2004).

49. Wagner, G. R. & Hirschey, M. D. Nonenzymatic protein acylation as a carbon stress regulated by sirtuin deacylases. *Mol. Cell* **54**, 5–16 (2014).

50. Michishita, E., Park, J. Y., Burneskis, J. M., Barrett, J. C. & Horikawa, I. Evolutionarily conserved and nonconserved cellular localizations and functions of human SIRT proteins. *Mol. Biol. Cell* **16**, 4623–4635 (2005).

51. Tan, M. et al. Lysine glutarylation is a protein posttranslational modification regulated by SIRT5. *Cell Metab.* **19**, 605–617 (2014).

52. Teng, Y. B. et al. Efficient demyristoylase activity of SIRT2 revealed by kinetic and structural studies. *Sci. Rep.* **5**, 8529 (2015).

53. Gai, W., Li, H., Jiang, H., Long, Y. & Liu, D. Crystal structures of SIRT3 reveal that the alpha2-alpha3 loop and alpha3-helix affect the interaction with long-chain acyl lysine. *FEBS Lett.* **590**, 3019–3028 (2016).

54. Yang, T. & Sauve, A. A. NAD metabolism and sirtuins: metabolic regulation of protein deacetylation in stress and toxicity. *AAPS J.* **8**, E632–E643 (2006).

55. Maurer, B. et al. Inhibitors of the NAD dependent protein desuccinylase and demalonylase Sirt5. *ACS Med. Chem. Lett.* **3**, 1050–1053 (2012).

56. de Oliveira, R. M. et al. The mechanism of sirtuin 2-mediated exacerbation of alpha-synuclein toxicity in models of Parkinson disease. *PLoS Biol.* **15**, e2000374 (2017).

57. Kabsch, W. Xds. *Acta Crystallogr. D Biol. Crystallogr.* **66**, 125–132 (2010).

58. McCoy, A. J. et al. Phaser crystallographic software. *J. Appl. Crystallogr.* **40**, 658–674 (2007).

59. Ringel, A. E., Roman, C. & Wolberger, C. Alternate deacylating specificities of the archaeal sirtuins Sir2Af1 and Sir2Af2. *Protein Sci.* **23**, 1686–1697 (2014).

60. Murshudov, G. N., Vagin, A. A. & Dodson, E. J. Refinement of macromolecular structures by the maximum-likelihood method. *Acta Crystallogr. D Biol. Crystallogr.* **53**, 240–255 (1997).

61. Emsley, P. & Cowtan, K. Coot: model-building tools for molecular graphics. *Acta Crystallogr. D Biol. Crystallogr.* **60**, 2126–2132 (2004).

62. Gille, C. & Frommel, C. STRAP: editor for structural alignments of proteins. *Bioinformatics* **17**, 377–378 (2001).

63. Hall, T. A. BioEdit: a user-friendly biological sequence alignment editor and analysis program for Windows 95/98/NT. *Nucleic Acids Symp. Ser.* **41**, 95–98 (1999).

64. Ashkenazy, H. et al. ConSurf 2016: an improved methodology to estimate and visualize evolutionary conservation in macromolecules. *Nucleic Acids Res.* **44**, W344–W350 (2016).

Acknowledgments

Author contributions

M.P. and C.S. designed the project, analyzed data, and drafted the manuscript, and all authors contributed to the refinement of the manuscript. M.P. solved the crystal structures and did the activity studies. M.S., Z.S., M.P. and M.F. did acylation studies, and M.S. and M.M. synthesized acyl peptides. D.R. and A.M. created the fluorogenic Z-Lys (HMG)-AMC substrate.

Additional information

Supplementary Information accompanies this paper at doi:10.1038/s41467-017-01701-2.

Competing interests: The authors declare no competing financial interests.

Reprints and permission information is available online at http://npg.nature.com/reprintsandpermissions/

Publisher's note: Springer Nature remains neutral with regard to jurisdictional claims in published maps and institutional affiliations.

Supplementary Figures

a

R:

Acetyl

3,3-dimethyl-succinyl

3,3-dimethyl-glutaryl

Malonyl

Itaconyl

3-hydroxy-3-methyl-glutaryl

Octanoyl

Butyryl

Maleyl

Adipoyl

Biotinyl

Succinyl

Glutaryl

Pimeloyl

3-methyl-succinyl

3-methyl-glutaryl

Suberoyl

DL-Lipoyl

Beta-alanin

Gamma-aminobutyryl

6-Aminocaproyl

b

c

d **e**

Supplementary Figure 1. Enzymatic activity of Sirt4. **a,** Peptide acyl library for Sirt4 activity screening. A peptide derived from human CPS1 (residues 524-531) was modified with the given acyls (R) on its lysine ε-amino group (covalent linkage indicated by dotted lines). **b,** hSirt4-dependent deacylation reactions with acetyl-, DMS- and HMG-CPS1 peptide substrate performed in presence and absence of 2 mM NAD$^+$ to confirm their NAD$^+$ dependency. (n=2; error bars: s.d.) **c,** Analysis of Sirt4-dependent de-HMG-ylation and deacetylation by MS detection of substrate and product peptide (left). The identical de-HMG-ylation analyzed in the coupled enzymatic assay is shown on the right. (n=2; error bars: s.d.) **d,** NAD$^+$ titration of the hSirt4-dependent de-HMG-ylation of HMG-CypA as a substrate protein. Error bars indicate the correlation coefficient of the linear fit of assay progression. (n=2; error bars: s.d.) **e,** Intact protein MS analysis of Sirt4-dependent de-HMG-ylation of HMG-CypA. The ratios (left) of lower to higher HMG-modification levels (numbered in spectra on the right) increased in presence of Sirt4 but not in control reactions without enzyme.

a

```
Sirt4_homo_sapiens        1 MKMSFALTFRSAKGRWIANPSQPCSKASIGL - -  31
Sirt4_xenopus_tropicalis  1 - - - MWKNVREGSKVFWGINNITRSHKSHLALSE  30
Sirt4_danio_rerio         1 - - - - MLLSCRYLPPPVAVGRCASTIQAGVQQ - -  27

Sirt4_homo_sapiens       32 FVPASPPLDPEKVKELQRFITLSKRLLVMTGAG  64
Sirt4_xenopus_tropicalis 31 FVPACPPPNPHQVEQLQDFVSQSQRLFVMTGAG  63
Sirt4_danio_rerio        28 FVPASGSFDSSALEQLQAFISQASRLFVISGAG  60

Sirt4_homo_sapiens       65 ISTESGIPDYRSEKVGLYARTDRRPIQHGDFVR  97
Sirt4_xenopus_tropicalis 64 ISTESGIPDYRSEGVGLYSRTERRPIQHSEFVQ  96
Sirt4_danio_rerio        61 LSTESGIPDYRSEGVGLYARTNRRPMQHSEFVR  93

Sirt4_homo_sapiens       98 SAPIRQRYWARNFVGWPQFSSHQPNPAHWALST 130
Sirt4_xenopus_tropicalis 97 SQAARRRYWARNFVGWPSFSSHEPNSAHVNLCK 129
Sirt4_danio_rerio        94 SEKSRQRYWARNYVGWPQFSSHQPNSAHLALRD 126

Sirt4_homo_sapiens      131 WEKLGKLYWLVTQNVDALHTKAGSRRLTELHGC 163
Sirt4_xenopus_tropicalis 130 WERAGRLHWLVTQNVDALHTKAGQCRLSELHGC 162
Sirt4_danio_rerio       127 WEEKGKLHWLVTQNVDALHLKAGQQRLTELHGS 159

Sirt4_homo_sapiens      164 MDRVLCLDCGEQTPRGVLQERFQVLNPTWSAEA 196
Sirt4_xenopus_tropicalis 163 THRVICLGCQTVTKRSELQERFLNLNPSWNEQA 195
Sirt4_danio_rerio       160 THRVVCLDCGELTLRAELQKRFTALNPGWEATA 192

Sirt4_homo_sapiens      197 HGLAPDGDVFLSEEQVRSFQVPTCVQCGGHLKP 229
Sirt4_xenopus_tropicalis 196 HGLAPDGDVFLTDEQVSDFQVPACTKCGGILKP 228
Sirt4_danio_rerio       193 CAVAPDGDVFLEEEQVLNFRVPACNACGGVLKP 225

Sirt4_homo_sapiens      230 DVVFFGDTVNPDKVDFVHKRVKEADSLLVVGSS 262
Sirt4_xenopus_tropicalis 229 QVTFFGDTVNRGFVFSIYEQMKQADAMLIVGSS 261
Sirt4_danio_rerio       226 EVTFFGDVVKRNTVHFVHNKLAESDAVLVAGSS 258

Sirt4_homo_sapiens      263 LQVYSGYRFILTAWEKKLPIAILNIGPTRSDDL 295
Sirt4_xenopus_tropicalis 262 LQVYSGYRFALNAKELHLPIAILNIGPTRADHL 294
Sirt4_danio_rerio       259 LQVFSGYRFLLAASERKLPIAIVNIGATRADHL 291

Sirt4_homo_sapiens      296 ACLKLNSRCGELLP - - - LIDPC - - - - - -     314
Sirt4_xenopus_tropicalis 295 AKVKVSARCGDVLPHILLQDQWHKEIQS      322
Sirt4_danio_rerio       292 TDIRVSARCGEVLPAIKLS - - - - - - - - -     310
```

b

3

d

e
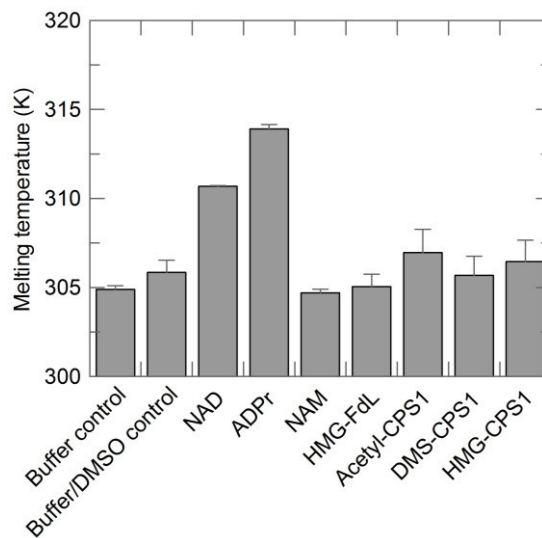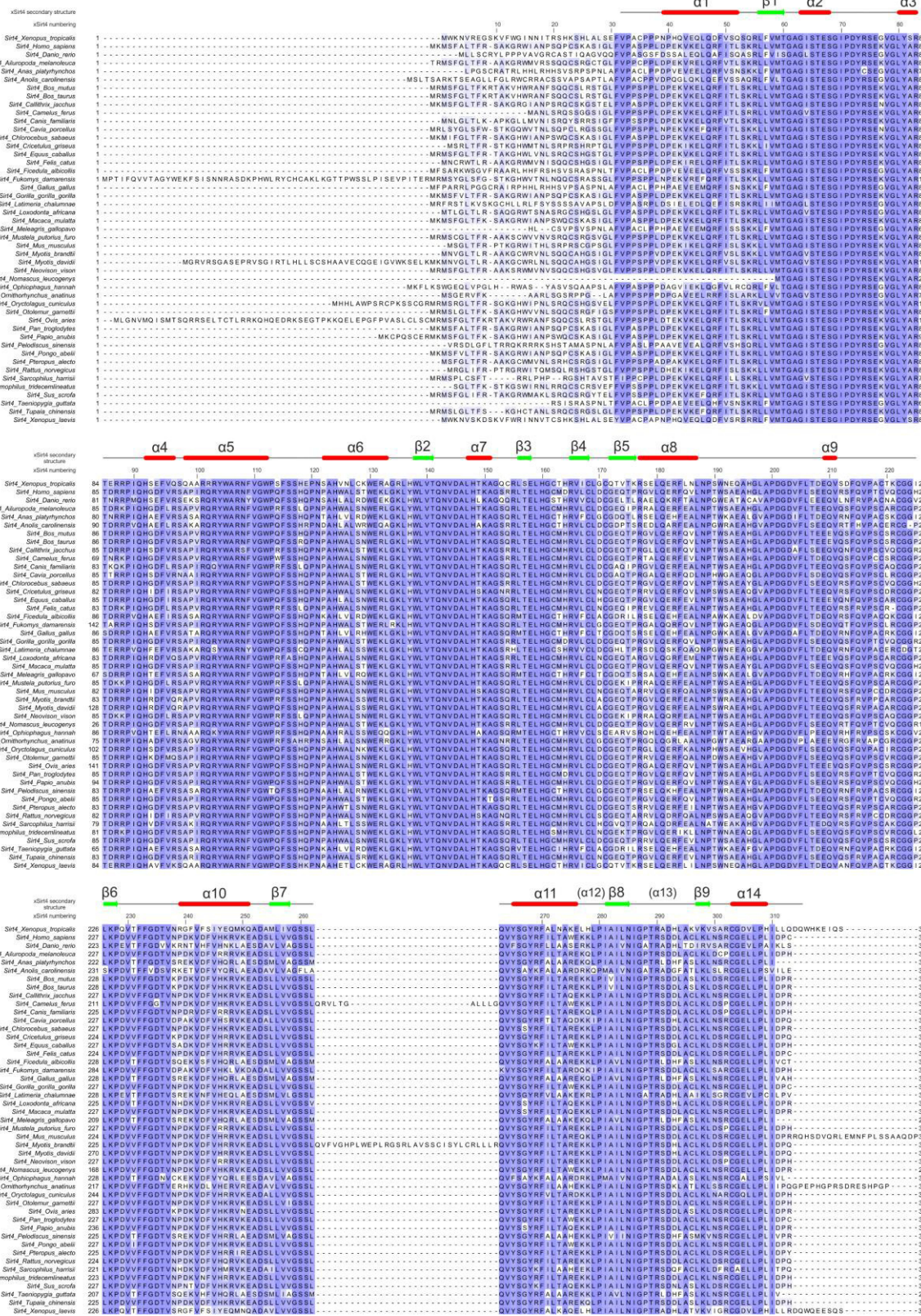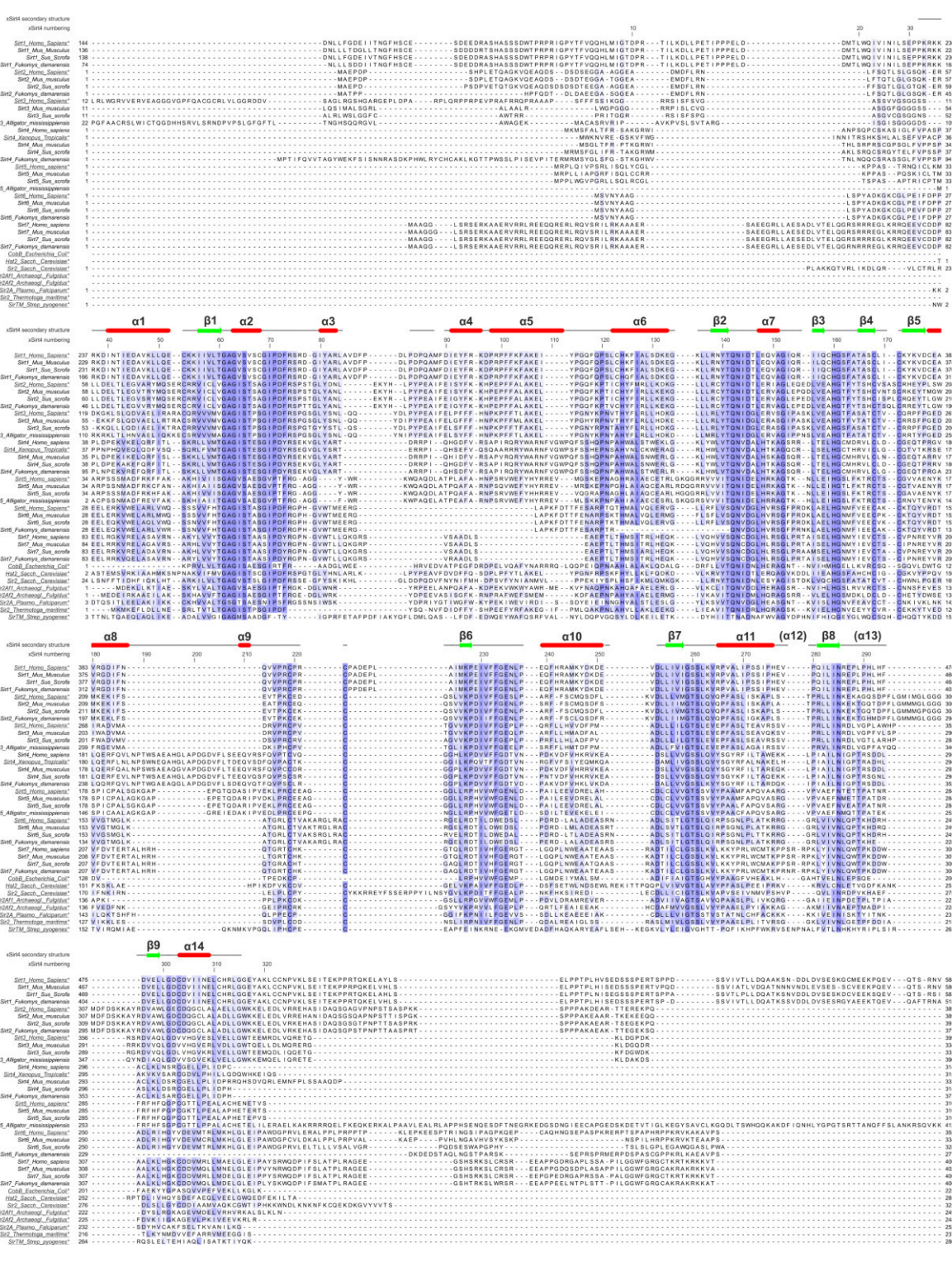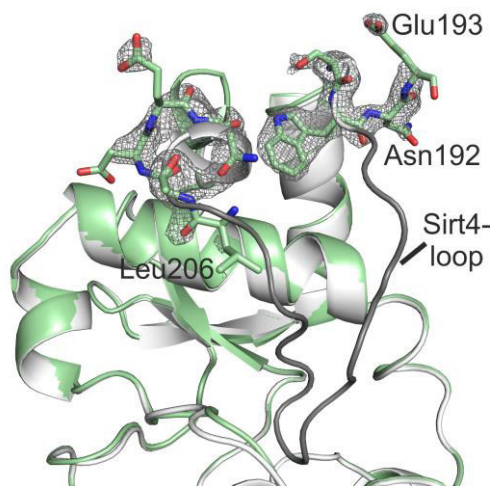
Supplementary Figure 2. Sirt4 conservation and structure. **a,** Sequence alignment of hSirt4, xSirt4 and zSirt4 showing high conservation except for the N-terminal MLS. The coloring encodes conservation (BLOSUM62 score). **b,** Melting temperatures of xSirt4 with various ligands in thermal denaturation shift assays. HMG-FdL, CPS1 peptide, and DMSO control contained 10% DMSO. (n=2; error bars: s.d.) **c,** Multiple sequence alignment of all chordate Sirt4 sequences available from UniProt. The coloring encodes conservation (BLOSUM62 score). Numbering and secondary structure elements are from xSirt4. **d,** Structure-based sequence alignment of the catalytic cores of Sirt1-7 and bacterial sirtuins. Our xSirt4/ADPr complex, the most similar structures of human Sirt1,2,3,5,6 and of the bacterial sirtuins (determined using PDBeFOLD) were aligned, the alignment refined manually according to conserved secondary structure elements, and subsequently all chordate sequences of Sirt1-7 available from UniProt were added. Sequences of the structurally characterized sirtuins (highlighted by underlining and *) and four representative sequences of Sirt1-7 are shown. Coloring indicates conservation (BLOSUM62 score). Numbering and secondary structure elements are from xSirt4. **e,** Crystal structure of an xSirt4/thioacetyl-ADP-ribose complex (green). The Sirt4-loop features a different conformation than in the Sirt4/ADPr complex (grey) and is largely undefined as indicated by the 2Fo-Fc electron density contoured at 1σ (gray mesh).

e

Sirt1   Sirt2

Sirt3   Sirt4

Sirt5   Sirt6
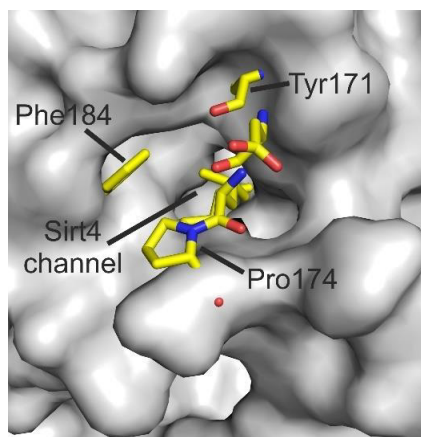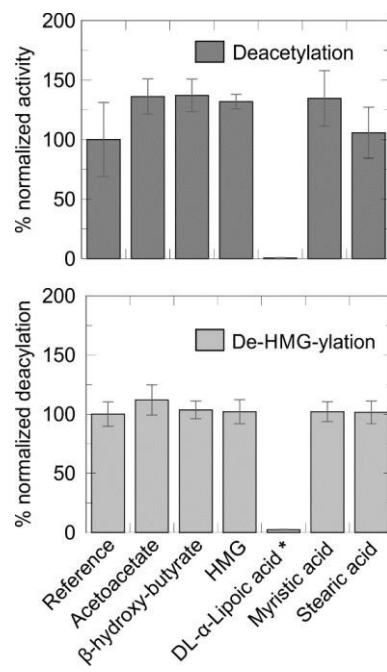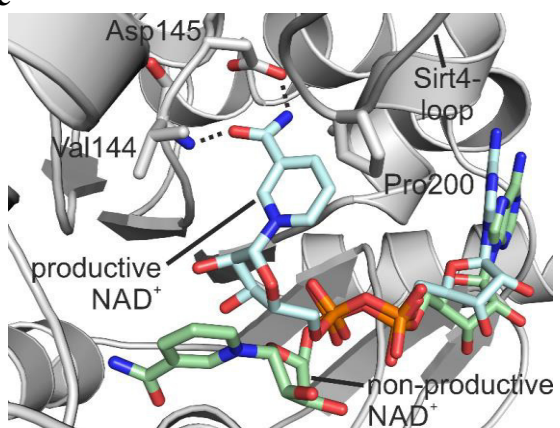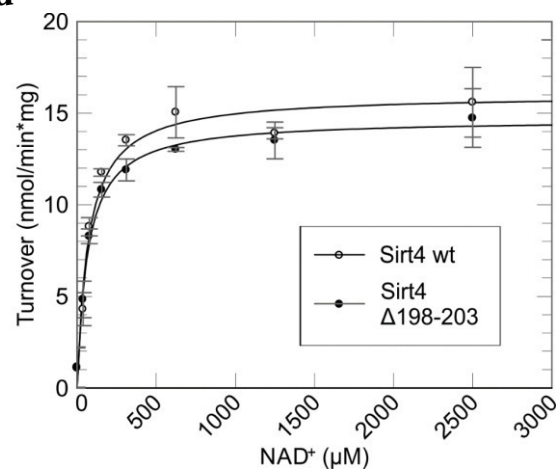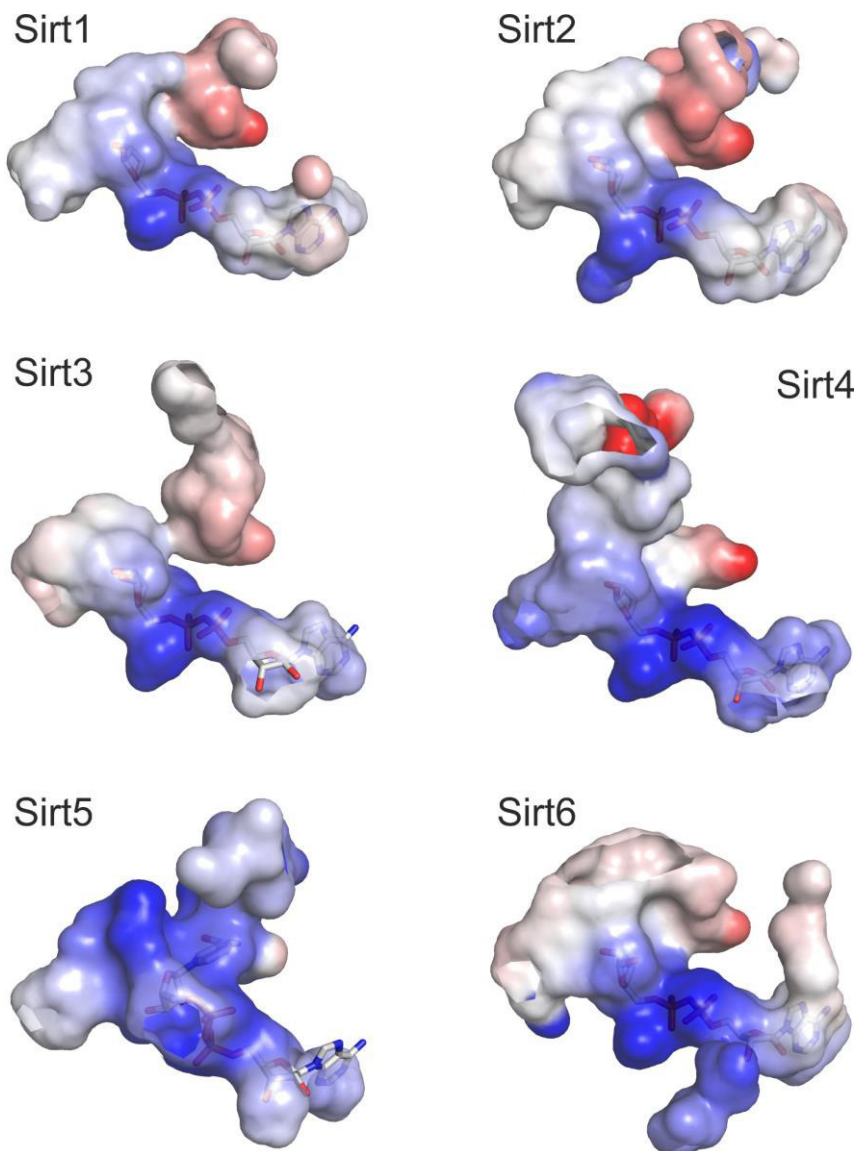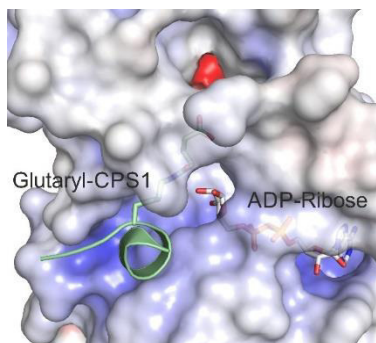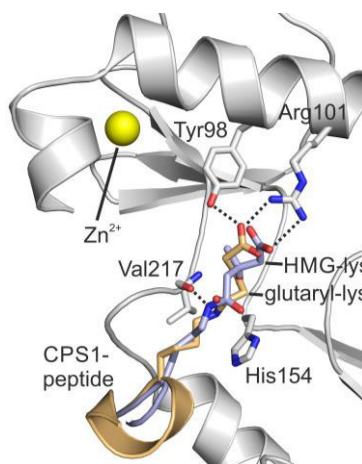
f   g   h
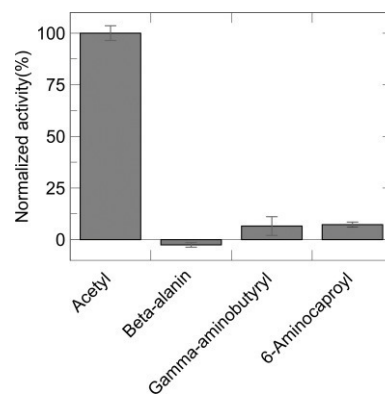
Supplementary Figure 3.   Active site features. **a,** Overlay of xSirt4 (grey surface) and as a representative of other isoforms Sirt3 (PDB ID 3GLR; yellow sticks), showing that the Sirt4 channel is blocked in other isoforms. **b,** Effect of metabolites on xSirt4-dependent deacetylation (top) and de-HMGylation activity (bottom). Metabolites were tested in the coupled enzymatic assay, except for lipoic acid (*****), which was incompatible and therefore examined in MS-based assays. (n=2; error bars: s.d.) **c,** Overlay of xSirt4 (grey cartoon and sticks) with NAD^+ in productive conformation (cyan sticks) from an overlaid Sir2Tm complex (PDB ID 4BUZ) and non-productive NAD^+ (green) from an overlaid Sirt3 complex (PDB ID 4BV3). **d,** NAD^+ titrations for xSirt4 wildtype (wt) and Sirt4-loop deletion mutant (Δ198-203) with HMG-CPS1 peptide substrate. (n=2; error bars: s.d.) **e,** Inner surfaces of the nucleotide binding sites of Sirt1-6, colored by electrostatic potential calculated with APBS2.1 in PyMOL using PDB IDs 4KXQ (Sirt1), 5D7O (Sirt2), 4BN4 (Sirt3), our xSirt4 structure, PDB IDs 3RIY (Sirt5) and 3K35 (Sirt6). ADPr complexes were used for comparability, except for Sirt5 (Sirt5/ADPr complex in open conformation) where we used a Sirt5/succinyl-H3K9/NAD^+ complex. ADPr/NAD^+ are shown as sticks. The surfaces are colored according to electrostatic potential (red/-15 to blue/+15 k_BT/*e*). **f,** xSirt4 surface colored by electrostatic potential calculated using APBS2.1 in PyMOL (red/-15 to blue/+15 k_BT/*e*). ADP-ribose is shown as white sticks, and a glutaryl-CPS1 peptide from an overlaid zSirt5 complex (PDB ID 4UTR) is shown in pale green. **g,** Overlay of the active sites of the zSirt5/HMG-CPS1 complex (white, light-blue ligand) with zSirt5/glutaryl-CPS1 (orange; PDB ID 4UTR). Polar contacts are indicated by dashed lines. **h,** xSirt4-dependent deacylation of CPS1-K527 peptides carrying modifications with a positive charge at the distal end (acyl structures shown in **Supplementary Fig. 1a**). Activities are normalized to acetyl-CPS1 substrate. (n=2; error bars: s.d.)
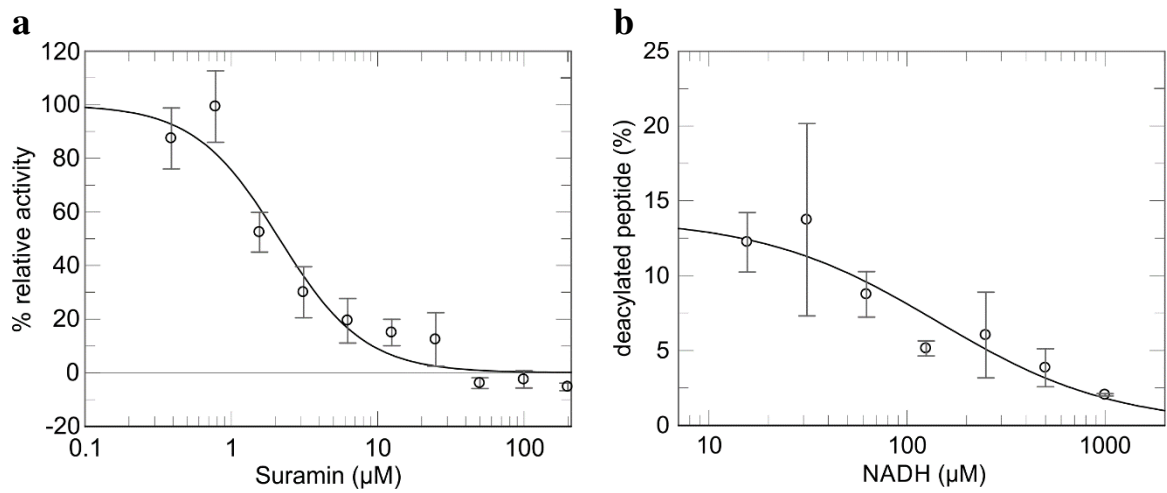
Supplementary Figure 4. Sirt4 inhibition. **a,** Suramin titration to determine the IC$_{50}$ for hSirt4 in the FdL-like de-HMG-ylation assay. (n=2; error bars: s.d.) **b,** NADH-dependent Sirt4 inhibition analyzed with HMG-CPS1 substrate in the MS-based assay. (n=2; error bars: s.d.)
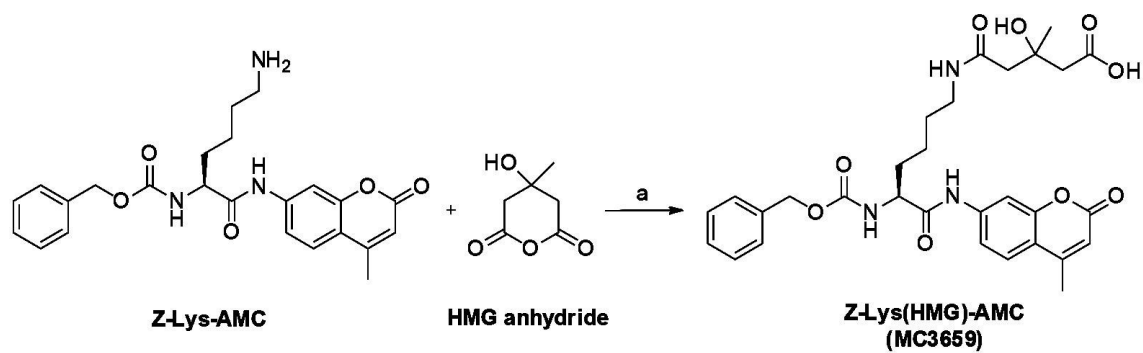
Reagents and conditions: a) DIPEA, dry THF, N₂, rt.

Supplementary Figure 5. Reaction scheme for synthesis of the fluorogenic Sirt4 substrate Z-Lys(HMG)-AMC (HMG-FdL).

Supplementary Table 1 – Primer sequences

Primer	Sequence
hSirt4_25_BamHI_forward	TATAGGATCCTCGAAAGCCTCCATTGGGTTATT
hSirt4_314_HindIII_reverse	TATAAAGCTTTCAGCATGGGTCTATCAAAG
xSirt4_21_NdeI_forward	ATACATATGAGCCACAAATCCCACCTTGCATTGTCAG
xSirt4_32_NdeI_forward	ATACATATGGTCCCTGCATGTCCCCCACCAAATC
xSirt4_315_XhoI_reverse	TATACTCGAGCTATTGGTCCTGTAGCAATATGTGTGGCAATAC
xSirt4_D201A_forward	GTTGGCTCCCGCGGGTGATGTCTTTCTGAC
xSirt4_D201A_reverse	TGTACCCAACCGAGGGCGCCCACTACAGAA
xSirt4_D203A_forward	AGGGCTACCACGCCAGAAAGACTGTCTAC
xSirt4_D203A_reverse	AGGGCTACCACGCCAGAAAGACTGTCTAC
xSirt4_Y73F_forward	GGAATCCCAGACTTTCGCTCAGAAGGG
xSirt4_Y73F_reverse	CCCTTCTGAGCGAAAGTCTGGGATTCC
xSirt4_R101A_forward	GAGTCAGGCTGCAGCACGGAGATATTGGG
xSirt4_R101A_reverse	CCCAATATCTCCGTGCTGCAGCCTGACTC
xSirt4_Y104F_forward	GCTGCAAGACGGAGATTTTGGGCTCGTAACTTTG
xSirt4_Y104F_reverse	CAAAGTTACGAGCCCAAAATCTCCGTCTTGCAGC
xSirt4_R107A_forward	CGGAGATATTGGGCTGCGAACTTTGTAGGATG
xSirt4_R107A_reverse	CATCCTACAAAGTTCGCAGCCCAATATCTCCG
xSirt4_Y104F-R107A_forward	CAGGCTGCAAGACGGAGATTTTGGGCGGCGAACTTTGTAGGATGGCCTAG
xSirt4_Y104F-R107A_reverse	CTAGGCCATCCTACAAAGTTCGCCGCCCAAAATCTCCGTCTTGCAGCCTG
xSirt4_N108A_forward	GAGATATTGGGCTCGTGCGTTTGTAGGATGGCCTAG
xSirt4_N108A_reverse	CTAGGCCATCCTACAAACGCACGAGCCCAATATCTC
xSirt4_Δ189-214_forward	GGTTTCTGAATCTCAATGGATCTAGTCAGGTCCCAGCCTGTACCAAGTG
xSirt4_Δ189-214_reverse	GGCTGGGACCTGACTAGATCCATTGAGATTCAGAAACCTTTCCTGCAGC
xSirt4_Δ192-212_forward	CTCAATCCATCCTGGGGTAGTTCTGACTTTCAGGTCCCAGCCTGTACC
xSirt4_Δ192-212_reverse	GGGACCTGAAAGTCAGAACTACCCCAGGATGGATTGAGATTCAGAAAC
xSirt4_Δ196-205_forward	CCTGGAATGAGCAGGCACTGACAGATGAGCAGG
xSirt4_Δ196-205_reverse	CCTGCTCATCTGTCAGTGCCTGCTCATTCCAGG
xSirt4_Δ196-205+GSS_forward	CAATCCATCCTGGAATGAGCAGGCAGGCTCTTCTCTGACAGATGAGC
xSirt4_Δ196-205+GSS_reverse	GTCTGACACCTGCTCATCTGTCAGAGAAGAGCCTGCCTGCTCATTCC
xSirt4_Δ198-203_forward	GAGCAGGCACATGGGGTCTTTCTGACAGATG
xSirt4_Δ198-203_reverse	CATCTGTCAGAAAGACCCCATGTGCCTGCTC
zSirt4_29_NdeI_forward	ATACATATGGTTCCTGCAAGTGGCTCCTTTGACTCCAG
zSirt4_310_XhoI_reverse	TATACTCGAGTCAGGACAGTTTAATGGCTGGCAGCACTTCTCC

12

6. **Danksagung**

An dieser Stelle möchte ich mich bei den Menschen bedanken, die mich während meiner Promotion besonders unterstützt haben.

Zunächst gilt mein Dank meinem Doktorvater Prof. Dr. Clemens Steegborn, der mir die Doktorarbeit in seiner Arbeitsgruppe ermöglicht und die spannenden Themen angeboten hat. Ich danke Dir weiterhin, dass Du mir immer mit Diskussionen und Ratschlägen zur Seite standest, aber mir auch den notwendigen wissenschaftlichen Freiraum gelassen hast.

Bei unseren Kollaborateuren der Arbeitsgruppen von Prof. Dr. Mike Schutkowski, Prof. Dr. Wolfgang Sippl (beide Martin-Luther-Universität Halle-Wittenberg), Prof. Dr. Antonello Mai (Sapienza Universitá di Roma), Prof. Dr. Manfred Jung (Albert-Ludwigs-Universität Freiburg) und Prof. Dr. Christian Olsen (University of Copenhagen) möchte ich mich für die spannenden, intensiven und erfolgreichen Kooperationen bedanken.

Dr. Sebastien Moniot und Dr. Michael Weyand, euch danke ich für die vielen theoretischen und praktischen Hilfestellungen zur Röntgenkristallographie. Bei Dr. Matt Fuszard und Dr. Frank Fischer möchte ich mich für die detaillierte Einführung in die Massenspektrometrie sowie Hilfestellungen beim Experimentdesign und der Auswertung bedanken.

Dr. Benjamin Sünkel, Dr. Sebastien Moniot, Dr. Melanie Fischer, Julian Pfahler und Soorubaan Shanmugaratnam möchte ich für die intensiven Diskussionen zu Kinetiken, Konstrukt- und Experimentdesign sowie für die vielen lustigen Stunden während und nach der Arbeit danken.

Den (langjährigen) Mit-Doktoranden Jonathan Quast, Holly Towell, Ramona Adolph und You Weijie sowie den Angehörigen der Arbeitsgruppen von Prof. Dr. Andreas Möglich und Prof. Dr. Birte Höcker danke ich für die angenehme Zeit und gegenseitige Unterstützung.

Für ihre Unterstützung danke ich unseren technischen Assistenten Martina Lenk und Susanne Schäfer. Sabrina Wischt, vielen Dank, dass Du mich so unterstützt hast in meiner krankheitsbedingten Ausfallzeit. Lisa Meisel und Norbert Grillenbeck - ich finde, wir waren ein klasse Team und ich danke Euch für alles, was Ihr in den letzten vier Jahren für mich geleistet habt. Auch unseren Sekretärinnen Renate Crowe und Gabi Kassler möchte ich für Eure Unterstützung danken, die meist im Hintergrund abläuft und leider zu oft gar nicht richtig gewürdigt wird.

Dr. Benjamin Sünkel, Dr. Sebastien Moniot und Joschka Bauer danke ich für die Kommentierung und Diskussion meiner Dissertationsschrift.

Für die tolle Zeit im Studium und der Promotion (Mensa!) in Bayreuth danke ich meinen Freunden Joschka Bauer, Manuel Mönnich, Manuel Braun, Michael Magdeburg, Christopher Thiel und Moritz Joop. War eine mega Zeit, an die wir uns immer gerne erinnern werden!

Mein besonderer Dank gilt meiner Familie und den Eltern meiner Freundin, die immer für mich da und mir ein großer Rückhalt waren.

Maren, mein Schatz, Dir danke ich für alles, was Du mir gibst. Ich liebe Dich!

7. **(Eidesstattliche) Versicherungen und Erklärungen**

(§ 9 Satz 2 Nr. 3 PromO BayNAT)

Hiermit versichere ich eidesstattlich, dass ich die Arbeit selbständig verfasst und keine anderen als die von mir angegebenen Quellen und Hilfsmittel benutzt habe (vgl. Art. 64 Abs. 1 Satz 6 BayHSchG).

(§ 9 Satz 2 Nr. 3 PromO BayNAT)

Hiermit erkläre ich, dass ich die Dissertation nicht bereits zur Erlangung eines akademischen Grades eingereicht habe und dass ich nicht bereits diese oder eine gleichartige Doktorprüfung endgültig nicht bestanden habe.

(§ 9 Satz 2 Nr. 4 PromO BayNAT)

Hiermit erkläre ich, dass ich Hilfe von gewerblichen Promotionsberatern bzw. -vermittlern oder ähnlichen Dienstleistern weder bisher in Anspruch genommen habe noch künftig in Anspruch nehmen werde.

(§ 9 Satz 2 Nr. 7 PromO BayNAT)

Hiermit erkläre ich mein Einverständnis, dass die elektronische Fassung meiner Dissertation unter Wahrung meiner Urheberrechte und des Datenschutzes einer gesonderten Überprüfung unterzogen werden kann.

(§ 9 Satz 2 Nr. 8 PromO BayNAT)

Hiermit erkläre ich mein Einverständnis, dass bei Verdacht wissenschaftlichen Fehlverhaltens Ermittlungen durch universitätsinterne Organe der wissenschaftlichen Selbstkontrolle stattfinden können.

……………………………………………………………………………………………………….

Ort, Datum, Unterschrift